Measuring nanometer-scale distances by high-field pulsed electron-electron double resonance using MnII spin labels

Paul Demay-Drouhard

THESE DE DOCTORAT DE L'UNIVERSITE PIERRE ET MARIE CURIE

Spécialité : Chimie Moléculaire

Présentée par

Paul Demay-Drouhard

Pour obtenir le grade de

Docteur de l'Université Pierre et Marie Curie

Measuring Nanometer-Scale Distances by High-Field Pulsed Electron-Electron Double Resonance Using Mn^{II} Spin Labels

Soutenue le 22 octobre 2015

Devant un jury constitué de :

Pr. Clotilde POLICAR	Directrice de thèse
Dr. Hélène BERTRAND	Encadrante de thèse
Pr. Marcel MAYOR	Rapporteur
Dr. Eva TOTH	Rapporteur
Pr. Bernold HASENKNOPF	Examinateur
Pr. Thomas PRISNER	Examinateur

Remerciements

Ce travail de thèse a été effectué au Laboratoire des Biomolécules (à l'Ecole Normale Supérieure et à l'Université Pierre et Marie Curie), ainsi qu'au CEA-Saclay, sous la direction de Clotilde Policar et d'Hélène Bertrand. Il n'aurait jamais été possible sans l'aide de nombreuses personnes que je tiens vivement à remercier.

Tout d'abord, j'exprime ma gratitude à Clotilde pour son encadrement et pour la liberté qu'elle ma laissé au cours de ce projet, toujours supervisé d'une manière très dynamique. J'adresse ensuite mes plus profonds remerciements à mon encadrante, Hélène. Tu m'as accompagné dans la réalisation de ce projet d'une manière idéale et tu as toujours été présente pour moi, en particulier dans les moments difficiles où la chimie sait se montrer coriace... A la fois sur le plan scientifique et sur le plan humain, tes qualités sont remarquables et pour tout cela je t'admire beaucoup.

Je remercie vivement Solange et Sandrine pour leur accueil dans l'UMR. Je tiens à remercier chaleureusement Eva Tóth et Marcel Mayor pour avoir accepté d'évaluer ce travail et d'être rapporteurs, ainsi que Thomas Prisner et Berni Hasenknopf pour avoir accepté le rôle d'examinateurs.

Mes deux premières années de thèse se sont déroulées à l'ENS, et j'aimerais remercier Isabelle pour m'avoir accueilli au P12, ainsi que Sylvie pour ta gentillesse sans pareil. Je profite de l'occasion pour remercier Sandrine pour m'avoir permis d'utiliser la DLS, ainsi que les thésards et post-docs de l'UMR Pasteur, Fabrice en particulier.

Parmi ceux avec qui j'ai partagé le bureau, je tiens à remercier Géraldine pour les commandes toujours impeccables et François pour ta grande culture chimique ainsi que pour avoir assuré sans faille le transport de mes échantillons entre l'ENS et Orsay ! Merci également aux anciens, Anne-Sophie et Sylvain, pour avoir rendu mon quotidien très agréable. Une mention spéciale pour Sarah, avec qui j'ai souvent pesté contre la chimie qui refuse souvent de marcher comme on veut ! Merci à Emilie et Lucas pour leur sympathie, à Nico pour avoir pris le temps de nous aider avec l'ITC, ainsi qu'à Eliane et Karine pour leur aide précieuse avec les tâches administratives. Et bonne chance aux nouveaux, Julien et Meng Lan.

Un grand merci à l'équipe de Jean-Maurice, les sucriers du LBM : Laure et Anaïs pour les nombreux bars et restaurants (parfois sur le toit de l'ENS ou même au CEA), Laurent pour ta gentillesse et ton aide, sans oublier Mayeul (même si je sais que tu es jaloux de mon pantalon vert), Guillaume et mon collègue ESCOMien Pascal (bon courage avec tes mayonnaises !). Mes remerciements vont également à Laurence, Catherine et Alexandra pour leur aide et pour les nombreuses molécules empruntées. Un grand merci à Hakim, que j'ai eu plaisir à retrouver, pour ton aide avec la DFT des complexes de Mn, ainsi qu'à Geoff pour la dynamique moléculaire.

Passons maintenant aux peptidistes… Merci à Rodrigue pour ton expérience en matière de synthèse peptidique (et pour m'y avoir initié, même si le premier essai n'était pas très fructueux), ainsi que pour tes rappels hygiène et sécurité (ma blouse n'était pas si sale !). Merci à Cillian pour

m'avoir bien aidé avec l'HPLC, et pour tes super bières home-made. Un grand merci à Cécile pour ton énergie et pour les nombreux conseils en synthèse, ainsi qu'à Roba et Benjamin.

Mes remerciements vont également à tous les thésards et post-docs avec qui j'ai pu discuter, et qui ont grandement contribué à rendre ces trois années de thèse très agréables : Jean-Marie « Jeannot », Marghe, Maryline, May Lee, Héloïse, Jean-Philippe, Mathilde, Mehdi, les deux Anaïs, Aude, Lucile, Tom… et mes excuses à ceux que j'oublie certainement. Nombreux d'entre vous ont fait de la fête de la science un grand succès ! Je tiens aussi à remercier les stagiaires que j'ai eu l'occasion de côtoyer, dont certains ont contribué à ce travail : Marie, JB, Rahaman et Martha.

Une partie de ce travail repose sur la cristallographie aux rayons X, c'est pourquoi je tiens à remercier Régis de l'ICMMO et Lise-Marie de l'IPCM pour leur travail impeccable et leur disponibilité. Merci également à Christophe pour son aide avec le dichroïsme circulaire, ainsi qu'à Gilles et Gérard pour les discussions très utiles concernant la spectrométrie de masse. La grande majorité des spectres de masse des molécules synthétisées au cours de cette thèse a d'ailleurs été obtenue grâce au service de spectrométrie de masse de l'ICMMO par les soins de Delphine et Tanya, que je remercie vivement. Une partie des HRMS a également été effectuée par Claude et Hristo à l'IPCM. Merci enfin à Sandrine et Astrid pour m'avoir permis d'utiliser l'ITC.

Merci également à tous ceux avec qui j'ai pu interagir pour le monitorat : Sylvie, Marie et Khalil pour la chimie physique, Delphine et Anny pour la chimie organique, Catherine et Annie pour l'insertion professionnelle et Jacques pour la PAES. Merci aussi à Jean-Philippe lors des tests de TP d'orga… Je remercie aussi mon comité de suivi de thèse, Pierre et Rodrigue.

Now switching into English… This project would not have been possible without the group of Biological High-field Magnetic Resonance in CEA-Saclay. I would like to deeply thank Sun for allowing me to use his 285 GHz EPR spectrometer as well as the W-band Bruker. I will never forget itc set 23 and magnet goto 9.7 heater off, as well as my frozen fingers when removing the stick from the Bruker. Then a very special thank you to Vincent for these days at CEA. I really learnt a lot about EPR with you and our discussions about the black magic of Mn-DOTA have always been very fruitful! Thank you very much for your careful reading of this manuscript and for your constant help with the 285 GHz (that I finally managed to like) and with the Golden Shovel. And I also wish to thank Leandro (I could write this in French!) for your help with the W-band, with you we saw the first encouraging Mn-Mn PELDOR results with the rigid compounds!

The third group I would like to thank is the Center for Biomolecular Magnetic Resonance in Goethe University directed by Thomas Prisner. Thank you for your welcome in Frankfurt during these three weeks in January, they contributed a lot to improve my knowledge about PELDOR. And of course, a very big thank you to Dimi. Thank you so much for correcting the pulsed EPR part of this manuscript. Your kindness and your knowledge about physics are both very impressive, you really know how to explain it simply, and with you and Vincent I will always remember these nights in Frankfurt behind the G-band and the ice hockey matches (Löwen Frankfurt!). I also thank Vasyl for his nice help with the G-band, Jörn for his advices in synthesis as well as Andriy, Burkhard and all the PhD and post-docs in Frankfurt that made my stay very enjoyable.

Pour finir, et de manière plus personnelle, je tiens à remercier mes amis de longue date dont le soutien a été si important, plus particulièrement Quentin, Camille (venue de Lille !), Benoît (bientôt ton tour !), The Flew, Danny, Fred, Anto, Max, Jérôme, Niou, Zoé, Apo, Jojo, Karim, Carotte, Beulette et Léa (la coloc de l'amour), Malcolm et Popy (les anciens ESCOMiens)… Merci d'avoir fait le déplacement pour la plupart et d'avoir rendu ma journée de soutenance (et la soirée) inoubliable. Merci enfin à mes parents et à mes deux petits frères pour m'avoir toujours épaulé dans ces études plutôt longues… Et merci à Gri, pour ton soutien tellement précieux pendant la rédaction de ce manuscrit et pour tout ce que tu m'apportes.

Contents

Abbreviations

18C6	18-crown-6
3MDPA	3-mercaptodipicolinic acid
4MMDPA	4-methylmercaptodipicolinic acid
abs.	absolute
AIBN	azobisisobutyronitrile
AMBER	Assisted Model Building with Energy Refinement
ANR	Agence Nationale de la Recherche
APCI	Atmospheric Pressure Chemical Ionization
aq.	aqueous
BARF	sodium tetrakis[(3,5-trifluoromethyl)phenyl]borate
BImP	bis(imino)pyridine
BINAP	2,2'-bis(diphenylphosphino)-1,1'-binaphthyl
BMC	Ballester-Molinet-Castañer reagent
Bn	benzyl
Boc	*tert*-butyloxycarbonyl
BOP	(benzotriazol-1-yloxy)tris(dimethylamino)phosphonium hexafluorophosphate
Cbz	carboxybenzyl
CD	circular dichroism
CNRS	Centre National de la Recherche Scientifique
conc.	concentrated
CuAAC	copper-catalyzed azide-alkyne cycloaddition
cw	continuous wave
Cy	cyclohexane
DAP	2,6-diacetylpyridine
DB18C6	dibenzo-18-crown-6
dba	dibenzylideneacetone
DCC	*N*,*N*'-dicyclohexylcarbodiimide
DCE	1,2-dichloroethane
DCM	dichloromethane
DEER	Double Electron-Electron Resonance
DEPT	Distorsionless Enhanced Polarization Transfer
DFT	Density Functional Theory
DIPEA	*N*,*N*-diisopropylethylamine
DMAP	4-dimethylaminopyridine
DMF	*N*,*N*-dimethylformamide
DMSO	dimethyl sulfoxide
DNA	deoxyribonucleic acid
DNP	Dynamic Nuclear Polarization
DO2A	1,4,7,10-tetraazacyclododecane-1,7-diacetic acid
DO3A	1,4,7,10-tetraazacyclododecane-1,4,7-triacetic acid
DOTA	1,4,7,10-tetraazacyclododecane-1,4,7,10-tetraacetic acid
DOTAM	1,4,7,10-tetrakis(carbamoylmethyl)-1,4,7,10-tetraazacyclododecane
DPA	dipicolinic acid
DOPC	1,2-dioleoyl-*sn*-glycero-3-phosphocholine
dppf	1,1'-bis(diphenylphosphino)ferrocene
DQC	Double-Quantum Coherence
DTPA	diethylenetriaminepentaacetic acid
EDC	1-ethyl-3-(3-dimethylaminopropyl)carbodiimide
EDT	1,2-ethanedithiol

ED-EPR	echo-detected Electron Paramagnetic Resonance
EDTA	ethylenediaminetetraacetic acid
EPR	Electron Paramagnetic Resonance
ESI	Electrospray Ionization
Fmoc	9-fluorenylmethyloxycarbonyl
FRET	Förster Resonance Energy Transfer
FS	field-swept
FT	Finland trityl
HATU	1-[bis(dimethylamino)methylene]-1*H*-1,2,3-triazolo[4,5-*b*]pyridinium 3-oxid hexa-fluorophosphate
HBTU	2-(1*H*-benzotriazol-1-yl)-1,1,3,3-tetramethyluronium hexafluorophosphate
HCCA	α-cyano-4-hydroxycinnamic acid
HEPES	2-[4-(2-hydroxyethyl)piperazin-1-yl]ethanesulfonic acid
HFEPR	High-Field Electron Paramagnetic Resonance
HMPA	hexamethylphosphoramide
HOBt	*N*-hydroxybenzotriazole
HOMO	Highest Occupied Molecular Orbital
HPLC	High Performance Liquid Chromatography
HSQC	Heteronuclear Single Quantum Coherence
HWE	Horner-Wadsworth-Emmons
ITC	Isothermal Titration Calorimetry
ITO	Indium Tin Oxide
LDA	lithium diisopropylamide
MALDI-TOF	Matrix-Assisted Laser Desorption Ionization – Time of Flight
MBHA	4-(2',4'-dimethoxyphenyl-Fmoc-aminomethyl)-phenoxyacetamido-methylbenzhydryl amine
MD	Molecular Dynamics
MRI	Magnetic Resonance Imaging
Ms	mesyl
MTSL	S-(1-oxyl-2,2,5,5-tetramethyl-2,5-dihydro-1*H*-pyrrol-3-yl)methylmethanesulfono-thioate
mw	microwave
MW	molecular weight
NBS	*N*-bromosuccinimide
NMP	*N*-methyl-2-pyrrolidone
NMR	Nuclear Magnetic Resonance
Ns	nosyl
OMRI	Overhauser-enhanced magnetic resonance imaging
OPE	oligo(phenylene-ethynylene)
OPV	oligo(phenylene-vinylidene)
ORTEP	Oak Ridge Thermal Ellipsoid Plot
PCMA	pyridyltriazacyclododecane monoacetate
PCTA	pyridyltriazacyclododecane triacetate
PELDOR	Pulsed Electron-Electron Double Resonance
PET	polyethylene terephthalate
Pin	pinacolato
Pp	phenyl-isopropyl
PSII	photosystem II
PTM	perchlorotriphenylmethyl
PTMTC	perchlorotriphenylmethyl-tricarboxylic acid
PTMTE	perchlorotriphenylmethyl-triethylester

PTSA	*para*-toluenesulfonic acid
PyMDPDA	pyridinedimethylenenitrilo-dipyridyldiacetate
PyMTA	pyridinedimethylenenitrilo-tetraacetate
RIDME	Relaxation-Induced Dipolar Modulation Enhancement
RNA	ribonucleic acid
rt	room temprature
SAM	self-assembled monolayer
sat.	saturated
SDSL	site-directed spin labeling
SNR	signal-to-noise ratio
SOD	superoxide dismutase
SPP	shots per point
SPPS	solid-phase peptide synthesis
SRT	shot repetition time
TAM	tetrathiatriarylmethyl
TBAF	tetra-*n*-butylammonium fluoride
TBDMS	*tert*-butyldimethylsilyl
TCEP	*tris*(2-carboxyethyl)phosphine
TEA	triethylamine
TFA	trifluoroacetic acid
TEMPO	(2,2,6,6-tetramethylpiperidin-1-yl)oxyl
Tf	triflate
TFE	trifluoroethanol
THF	tetrahydrofuran
TIPS	triisopropylsilyl
TIPSA	triisopropylsilylacetylene
TIS	triisopropylsilane
TLC	thin layer chromatography
TMEDA	tetramethylethylenediamine
TMS	trimethylsilyl
TMSA	trimethylsilylacetylene
TNPTM	trinitroperchlorotriphenylmethyl
Tpy	2,2’:6’,2”-terpyridine
Trt	trityl
Ts	tosyl
TSPTM	perchlorotriphenylmethyl trisulfonic acid
TTF	tetrathiafulvalene
VMD	Visual Molecular Dynamics
XPhos	2-dicyclohexylphosphino-2’,4’,6’-triisopropylbiphenyl
XRD	X-ray diffraction
ZFS	zero-field splitting

List of figures

List of schemes

List of tables

General introduction

Biomacromolecules such as proteins or nucleic acids play an essential role in living organisms. They are involved in numerous tasks: catalysis of metabolic reactions (enzymes), cell signaling, or the encoding, transmission and expression of the genetic information. Understanding the function of biomacromolecules is crucial to investigate the processes that occur in a cell, in order to improve our knowledge on life. The function of a biological macromolecule closely depends on its structure. The two most popular techniques for structure elucidation are X-ray crystallography[1] and nuclear magnetic resonance (NMR) spectroscopy.[2] Both are complementary methods that display advantages and drawbacks.

X-ray diffraction (XRD) can provide a microscopic picture of various molecules at the atomic resolution. For instance, the Nobel Prize in Chemistry in 2009 was awarded to V. Ramakrishnan, T. A. Steitz and A. E. Yonath for studies of the structure and function of the ribosome,[3] in which XRD played a decisive role. This technique has led to major progress, but still suffers from limitations. It only applies to crystallized molecules, and growing crystals of proteins can be a tedious task. In particular, making membrane proteins crystallize often requires the use of detergents[4] that can lead to structure disruption. Moreover, XRD offers a static view of a molecule in the solid state, which does not necessarily reflect its structure in solution. The crystallized form of a protein may therefore not correspond to its biologically active conformation. On the contrary, NMR spectroscopy applies to proteins in solution. Using multidimensional experiments, one can assign the different chemical shifts to a specific nucleus, in order to generate a complete map of the protein of interest. Structures can be determined on a very short time scale, providing a description of a protein that better reflects its native environment. However, protein NMR is often limited to rather small objects (< 50 kDa) because the overlap of the different NMR peaks renders the interpretation very difficult for larger structures.[5]

In this context, alternative methods for structural studies are highly desirable. Among them, the determination of long-range (nanometer-scale) distances appears as a very valuable tool. Collecting a set of long-range constraints in a biomacromolecule gives insight into its global structure, information on the formation of oligomers or on conformational changes upon ligand binding.[6] Förster Resonance Energy Transfer (FRET) has been widely used for this purpose,[7] but it is sometimes quite difficult to extract the corresponding distance from a difference in fluorescence intensities. Nanometer-scale distances can also be measured using electron paramagnetic resonance (EPR), and especially pulsed EPR techniques such as pulsed electron double resonance (PELDOR).[6] Together with XRD and NMR, this method has emerged as a powerful complement in the biostructural toolbox. It is also very efficient as a stand-alone technique to study the conformational distribution of biomacromolecules in the nanometer scale.[8]

EPR spectroscopy only applies to paramagnetic compounds. As many proteins are diamagnetic, stable paramagnetic labels have to be grafted on them at specific positions. This method, known as site-directed spin labeling (SDSL), is commonly performed with nitroxide derivatives.[9] A popular spin label is S-(1-oxyl-2,2,5,5-tetramethyl-2,5-dihydro-1*H*-pyrrol-3-

yl)methylmethanesulfonothioate (MTSL), which can be grafted on cysteine residues of proteins, either native or introduced by site-directed mutagenesis (Scheme 1).

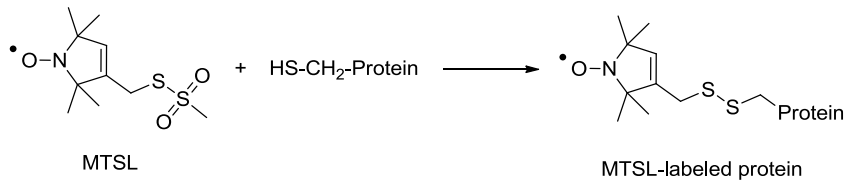

Scheme 1: Spin-labeling of a protein with MTSL

It is then possible to study every kind of protein, even large ones, by tagging them with two MTSL spin labels and measuring the interspin distance using pulse sequences like PELDOR. Briefly, the dipolar coupling between the two nitroxides, which is proportional to the inverse cube of the distance between them, can be separated from the other contributions to the spin Hamiltonian using a relevant pulse sequence.[10] Unlike protein NMR, the detected signal only comes from the two spin labels: the rest of the doubly labeled molecule is EPR-silent, so the obtained information is very specific. Other nitroxide-based spin labels and labeling methods have been developed so that virtually every kind of molecule can be studied by the PELDOR technique. Accordingly, this approach has been applied to proteins,[11,12] nucleic acids[13,14,15] or purely synthetic systems.[16,17,18,19]

Nevertheless, stable nitroxide have some limitations. The measurement time usually varies from 12 to 24 h to obtain a single distance, and the required concentration typically ranges from 0.1 to 1 mM. This rather low sensitivity can be greatly improved by increasing the frequency of the EPR spectrometer (Table 1, p. 9). PELDOR experiments with nitroxides are commonly performed at X-band (9.5 GHz), so the use of other wavebands (Q-band, 34 GHz; W-band, 95 GHz; G-band, 180 GHz) could be envisioned. However, the gain in sensitivity would be compensated by the broadening of the EPR spectrum of nitroxide moieties, which decreases the number of spins that are inverted by the pump pulse of the PELDOR pulse sequence.[20] Alternative spin labels would thus be highly desirable, and, among them, high-spin metal complexes are very promising candidates.[20] Unlike nitroxides, the central transition of their EPR spectrum narrows when the frequency increases, leading to a high signal-to-noise ratio (SNR). Additionally, high-spin metal complexes are stable in the cellular medium, offering the possibility of performing PELDOR measurements *in vivo*: this is much more difficult with nitroxides that are readily reduced into EPR-silent hydroxylamines. The use of Gd^{III} complexes as new spin labels for the PELDOR methodology has been initiated by the group of D. Goldfarb in 2007.[21] The same group reported the first successful high-spin Mn^{II}-Mn^{II} PELDOR measurement in 2011,[22] but Mn^{II} complexes as paramagnetic centers for PELDOR measurements have been much less investigated since. However, they appear attractive, notably in a biological perspective. Mn^{II} is endogenous, less toxic than Gd^{III}, and can replace Mg^{II} in many other biological systems due to similarities in charge and size.[23]

Unraveling the potential of high-spin Mn^{II} complexes as paramagnetic centers for high-field PELDOR measurements is the purpose of this thesis. The basics of EPR, with a particular emphasis on pulsed EPR and especially PELDOR, will be discussed and applied to high-spin Mn^{II} complexes and nitroxide spin labels. A focused literature review of distance measurements involving metal centers, especiall high-spin Gd^{III} and Mn^{II} complexes, using PELDOR and related pulse sequences will then be

presented. With this in mind, we will determine what should be the relevant features of an ideal Mn^{II} complex employed as a spin label: parameters such as the symmetry of the coordination sphere, the zero-field splitting (ZFS) parameters and the thermodynamic stability will be taken into account. The design of model systems incorporating two Mn^{II} complexes connected to a central rigid molecular rod will be described: such compounds will serve as "Mn^{II} standards" to calibrate the PELDOR method. In the first chapter of this manuscript, the screening of ligands for Mn^{II} that correspond to the parameters specified above will be presented. The synthetic methodologies to generate ligands for Mn^{II} with a graftable moiety, in order to connect them to a rigid rod, will be described in details. The corresponding Mn^{II} complexes have been characterized using continuous-wave high-field EPR (*cw*-HFEPR), and this screening procedure have led to the identification of 1,4,7,10-tetraazacyclododecane-1,4,7,10-tetraacetic acid (DOTA) as the most promising ligand for Mn^{II}. The synthesis of stiff linkers with various anchoring groups have also be performed, and methods will be presented to graft them on selected ligands. A variety of rigid model systems with Mn-Mn distances covering the 1.5 – 6 nm range have been obtained this way, and the expected Mn-Mn distances have been calculated using density functional theory (DFT) and molecular dynamics (MD) calculations. The corresponding bis-nitroxide modules have also been synthesized for comparison purposes.

In the second chapter, W-band PELDOR measurements on the previously synthesized Mn^{II}-Mn^{II} model systems will be presented. Preliminary measurements on platforms incorporating two Mn^{II}-bis-terpyridine complexes proved difficult, but the Mn-Mn distance was successfully measured on platforms with two Mn^{II}-DOTA centers connected to a polyproline spacer. The use of Mn^{II} complexes with small ZFS parameters led to an improved sensitivity. The Mn-Mn distances and distribution profiles obtained with PELDOR were in good agreement with MD calculations. We will show that under certain conditions, shorter components in the distance distributions can appear. They likely result from the contribution of the pseudo-secular term of the dipolar Hamiltonian. This interaction cannot be neglected for our systems because pumped and detected spins are similar. For the polyproline bis-Mn^{II} platforms, the pseudo-secular interaction is certainly hidden under the flexibility of the system, so the distance distribution profiles obtained with PELDOR were found to be reliable. In the case of a rigid linker, for short distances, the routinely performed Tikhonov analysis could not fully account for the experimental frequency-domain traces, meaning that the Mn-Mn distance was not reliable. However, the Mn-Mn distance was successfully measured when the rigid linker was longer, and we will show that in this case, the pseudo-secular interaction increases the width of the distance distribution. Insights in the coordination sphere of Mn^{II}-DOTA will be provided using measurements with Gd^{III}-DOTA complexes.

The last chapter of this manuscript deals with an emerging class of paramagnetic centers for pulsed EPR distance measurements: substituted persistent trityl radicals such as perchlorotriphenylmethyl (PTM) and tetrathiatriarylmethyl (TAM). These radicals display a very narrow EPR signal, which explains their attractiveness as PELDOR spin labels but also in numerous active fields. Methodologies toward new platforms incorporating a Mn^{II}-DOTA center and a PTM or TAM label will be presented. To understand the relationship between the structure of these radicals and their specific applications, the *g*-tensors of tricarboxylic derivatives will be accurately measured using *cw*-HFEPR with Mn^{II} as a field standard. We will show that despite the similar structure of PTMs

and TAMs, their electronic properties are very different. These findings will be rationalized using DFT calculations.

This work was performed in the frame of an ANR international project (MnHFPELDOR) that gathered three research groups, two from France and one from Germany:

- The group of Inorganic Cellular Chemistry, led by Prof. C. Policar, in the Laboratory of BioMolecules (Ecole Normale Supérieure - PSL Research University, Département de Chimie, Sorbonne Universités, UPMC Univ Paris 06, CNRS UMR 7203)

- The group of Biological High-field Magnetic Resonance (BHMR) directed by Dr. Sun Un in the Institute for Integrative Biology of the Cell (I2BC) (Department of Biochemistry, Biophysics and Structural Biology, Université Paris-Saclay, CEA, CNRS UMR 9198)

- The group directed by T. Prisner in the Institute of Physical and Theoretical Chemistry and Center for Biomolecular Magnetic Resonance (BMRZ), Department of Biochemistry, Chemistry and Pharmacy, Goethe University.

In the course of this PhD work, the bis-Mn^{II} platforms, the bis-nitroxides systems along with the mixed Mn-Mn and Mn-TEMPO modules were chemically designed and synthesized at LBM under the supervision of Hélène Bertrand and Clotilde Policar, as well as the PTM derivatives. The EPR experiments were performed at BHMR with Vincent Ching under the supervision of Sun Un and Leandro Tabares. I have also spent three weeks in Frankfurt to perform experiments at G-band with Dmitry Akhmetzyanov and Vincent Ching under the supervision of Thomas Prisner.

Introduction: theory, literature review and aim of the project

1. THEORETICAL BACKGROUND

1.1 EPR: introduction and scope of application

Electron Paramagnetic Resonance (EPR) was discovered by the Russian physicist Yevgeny Zavoisky in Kazan State University in 1944. Numerous similarities exist between EPR and the more commonly used nuclear magnetic resonance (NMR). Both rely on the interaction between the magnetic component of an electromagnetic radiation and a sample placed in a magnetic field. The magnetic field splits the degeneracy of the energy levels, and an absorption of energy may occur when the energy of an incident photon is equal to the energy difference between two levels. In NMR, the energy is absorbed by atomic nuclei, while in EPR, the energy is absorbed by paramagnetic centers.

A paramagnetic center is a molecule that contains unpaired electrons. Two main categories of paramagnetic centers can be distinguished:

- Radicals are molecules with one unpaired electron. They are often transient species, as they can quickly react with other molecules. They can be intermediates in reaction mechanisms, or generated by various kinds of radiations. Radicals such as nitric oxide $NO^{\bullet}$, hydroxyl radical $HO^{\bullet}$ or superoxide $O_2^{\bullet -}$ are involved in many physiological and pathological processes.

  In some cases, radicals can be long-lived: they are called stable radicals when the unpaired electron can be delocalized through π-bonds, thus reducing the reactivity of the system. When the steric hindrance around the unpaired electron is so high that the radical cannot readily react with another molecule, the term persistent radical is employed. Nitroxides like (2,2,6,6-tetramethylpiperidin-1-yl)oxyl (TEMPO) or substituted trityl radicals like perchlorotriphenylmethyl (PTM) are persistent radicals that are stable for decades at room temperature and are unaffected by numerous reagents (Figure 1).

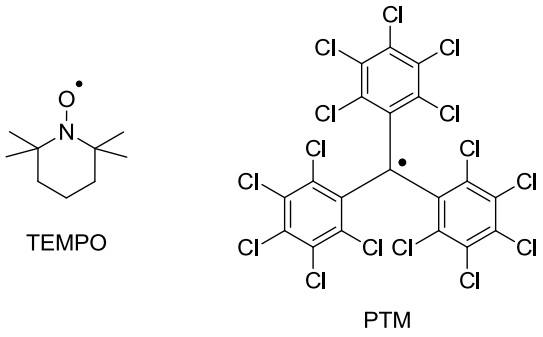

Figure 1: Structure of TEMPO and PTM

- Coordination complexes with transition metals, lanthanides or actinides can also be paramagnetic, containing one or more unpaired electrons. They can be found in metalloproteins like hemoglobin and notably in metalloenzymes such as superoxide dismutase and vitamin B_{12}.

Other paramagnetic centers can be described such as conduction electrons in metals or electrons trapped in crystallographic defects. EPR spectroscopy is thus a valuable method to study all these systems.

1.2 Theoretical background

In this part, vectors are written in bold and tensors are written with breves.

1.2.1 Magnetic moment of the electron

Let us consider an electron in motion, with a mass m_e and an elementary charge e. This electron creates a magnetic moment $\boldsymbol{\mu}$ defined by:[24]

$$\boldsymbol{\mu} = -(e/2m_e)(\boldsymbol{\sigma}_l + g_e\boldsymbol{\sigma}_s) \quad [1]$$

where g_e is the free electron spin g-factor, $\boldsymbol{\sigma}_l$ is the orbital angular momentum and $\boldsymbol{\sigma}_s$ is the spin angular momentum. These quantities can only take discrete values:

$$\boldsymbol{\sigma}_l^2 = \ell(\ell+1)\hbar \text{ and } \boldsymbol{\sigma}_s^2 = s(s+1)\hbar \quad [2]$$

where $\hbar = h/2\pi$ is the reduced Planck constant. ℓ can be any natural number but s can only be equal to ½. s is an intrinsic property of the electron which is called spin.

For a determined value of ℓ, one component of $\boldsymbol{\sigma}_l$ (σ_{lz} for instance) can only take values defined by:

$$\sigma_{lz} = m_\ell\hbar \text{ with } m_\ell = -\ell, -\ell+1 \ldots \ell \quad [3]$$

The same holds for s, but because s = ½, m_s can only take two values: -½ or +½.

$\sigma_{sz} = m_s\hbar$ with $m_s = -½, +½$ [4]

For the sake of simplification, equation [1] can be written:

$\boldsymbol{\mu} = -\beta(\mathbf{l}+g_e\mathbf{s})$

where $\mathbf{l} = \boldsymbol{\sigma}_l/\hbar$ and $\mathbf{s}=\boldsymbol{\sigma}_s/\hbar$ are reduced angular momentums. β is called Bohr magneton and is equal to:

$\beta = e\hbar/2m_e$ [5]

1.2.2 Interaction between a paramagnetic center and a magnetic field

All the equations discussed above are true for an isolated electron. We will now consider the more complex case of a paramagnetic center. In the absence of a magnetic field, the magnetic moment of its electrons can be written:

$\boldsymbol{\mu} = -g\beta\mathbf{S}$ [6]

where **S** is a reduced angular moment, implying that $\mathbf{S}^2 = S(S+1)$ and that S_z can take the 2S+1 electronic spin quantum numbers $M_S = -S, -S+1…S$. This angular moment is called electron spin of the paramagnetic center, and encompasses what was referred before as orbital and spin momentums. It takes into account the difference between an isolated electron and a paramagnetic center.

The *g*-value characterizes the paramagnetic center and is measured during an EPR experiment. It is comparable to the chemical shift δ in NMR spectroscopy. We can also say that $g = g_e + \Delta g$ where Δg is characteristic of the studied system. To measure *g*, the paramagnetic sample is placed in a magnetic field **B**. The interaction energy between **μ** and **B** can be written:

$H = -\boldsymbol{\mu}\mathbf{B}$ [7]

When **B** is aligned along the +*z* axis, this equation becomes:

$H = g\beta BSz$ [8]

H can thus take only discrete values:

$E(M_S) = g\beta BM_S$ [9]

This shows that the interaction between the magnetic moment of a paramagnetic center **μ** and a magnetic field **B** creates 2S+1 energy levels. The energy difference between the levels is equal to:

$\Delta E = g\beta B$ [10]

This splitting is centered on the energy level of the paramagnetic center without magnetic field, and is known as Zeeman effect.

When an electromagnetic radiation is applied on the paramagnetic center in a magnetic field, transitions between the energy levels will occur, provided that the energy of the incident photons (proportional to their frequency ν) is equal to the energy difference between two levels: this is the resonance condition.

$$h\nu = g\beta B_0 \quad [11]$$

This situation is depicted on Figure 2, for a paramagnetic center with S = 1/2. Importantly, magnetic dipolar transitions only occur with the selection rule $\Delta M_S = \pm 1$.

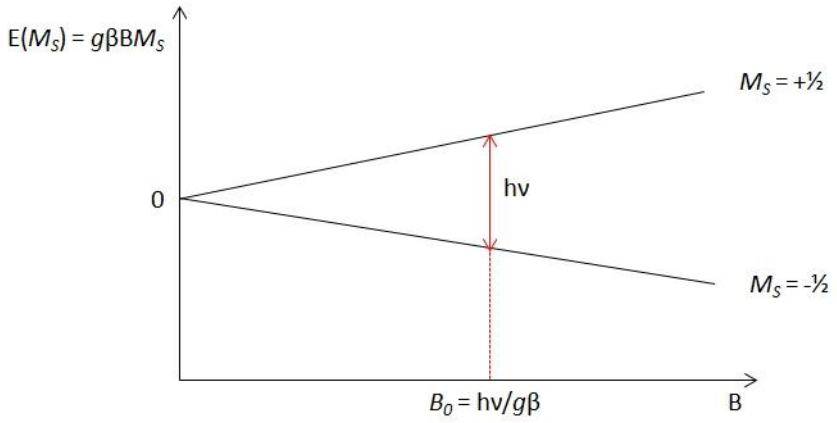

Figure 2: Zeeman effect and the resonance condition for S = 1/2

Finally, let us consider a sample with N paramagnetic centers at thermal equilibrium, and with S = 1/2. Some centers will occupy the M_S = ½ state (N_+ population), some other the M_S = -½ state (N_- population). These centers obey the Boltzmann equation:

$$N_+/N_- = \exp(-\Delta E/k_B T) \text{ with } N = N_+ + N_- \quad [12]$$

where k_B is the Boltzmann constant. At the resonance, the absorbed power P_{abs} can then be written:

$$P_{abs} = W(N_- - N_+)\Delta E \quad [13]$$

where W is the transition probability per second (Figure 3).

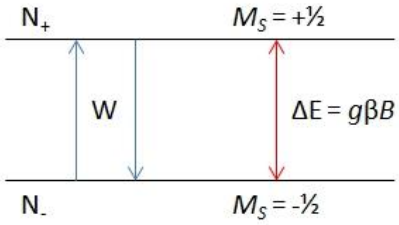

Figure 3: Transitions between energy levels when S = 1/2

1.2.3 Continuous-wave EPR

Continuous-wave EPR (*cw*-EPR) is the original method for acquiring an EPR spectrum and is still widely used (unlike *cw*-NMR). The idea is to work at a constant frequency and to sweep the magnetic field **B** to detect resonances, which occur when:

$$\nu/B = g\beta/h \qquad [14]$$

Usually *g*-values are around 2. This implies that ν/B is around 28 GHz.T^{-1}. Using electromagnets, fields up to around 13 T can be obtained: the corresponding frequency range corresponds to the microwave (*mw*) domain (from 1 to 350 GHz). This domain is divided in several bands using a terminology originally developed for radar technology (Table 1).

Table 1: Frequency range of the wavebands used in EPR spectroscopy. Commonly encountered wavebands along the text are highlighted in grey, and bold numbers in brackets refer to the frequency of the spectrometers used in this work

Waveband	Frequency range (GHz)
L	1 to 2
S	2 to 4
C	4 to 8
X	8 to 12
Ku	12 to 18
K	18 to 27
Ka	27 to 40
Q	30 to 50
U	40 to 60
V	50 to 75
E	60 to 90
W	75 to 110 **(94)**
F	90 to 140
D	110 to 170
G	130 to 230 **(180)**
J	230 to 350 **(285)**

A standard *cw*-EPR spectrometer is constituted of the following elements:

- An electromagnet creates a magnetic field **B** of fixed direction. By varying the intensity of the current in the coil, B can be swept.
- A generator gives the *mw* radiation. Usually a Gunn diode is employed, and the power of the radiation can be set between 1 µW and 200 mW. The microwaves travel in a waveguide.
- A resonant cavity contains the sample. This setup, which is not always used, is employed to improve the sensitivity.
- A diode is used to detect the absorption signal.

The detection of the signal is based on a technique called modulation of the magnetic field. A small sinusoidal magnetic field parallel to **B** is added, which make it possible to extract the first derivative of the absorption signal with a very good signal-to-noise ratio (SNR). Hence, *cw*-EPR spectra are very often represented with the first derivative of the absorption signal relative to the field on the *y* axis, and the field on the *x* axis.

1.2.4 The case of a real EPR spectrum

In fact, the shape of an EPR spectrum is usually more complicated, meaning that much more information can be extracted. The main features that influence the shape of an EPR spectrum are listed below:

- The way the molecules are organized in the sample deeply affects the spectral shape. This is because the magnetic moment of the molecules is not always isotropic: the interaction between **µ** and **B** depends on the direction of **B** compared to the molecules. This means that the *g*-value in equation [6] must be replaced with an anisotropic *g*-tensor $\check{g}$.

- The unpaired electrons of a paramagnetic center can interact with the magnetic moment of a nucleus. This is called a hyperfine interaction, which has a great effect on the EPR spectrum. It is analogous to *J*-coupling in NMR.

- For paramagnetic centers with S > 1/2 (certain metal complexes for example), some energy levels are already separated without any applied magnetic field. This phenomenon is called zero-field splitting (ZFS) and significantly modifies the spectral shape.

In the next part we will go into more details in the case of the transition metal that is of interest to us, namely Mn^{II}.

1.3 Spin Hamiltonian for Mn^{II}

To take into account every phenomenon that influences the shape of the EPR spectrum of Mn^{II}, we need to express its spin Hamiltonian. The electronic configuration of Mn^{II} is $3d^5$. Generally Mn^{II} complexes have the high-spin S = 5/2 configuration, with the five unpaired electrons in their ground state. Only the ^{55}Mn isotope is stable (100% natural abundance): its nuclear spin is I = 5/2. It is worth noting that I is an angular moment that obeys the same rules as S, except that the selection

rule is $\Delta M_I = 0$ instead of $\Delta M_S = \pm 1$.

The major terms in the spin Hamiltonian for Mn^{II} are:[25,26]

- The Zeeman interaction H_Z, which results from the interaction between the electron spin **S** and the applied magnetic field **B**:

$$H_Z = \beta \mathbf{B} \check{g} \mathbf{S} \quad [15]$$

For most Mn^{II} complexes at X-band (Table 1, p. 9), the Zeeman interaction is the dominant term in the spin Hamiltonian. Moreover, $\check{g}$ is usually isotropic and its values are close to g_e.

- The hyperfine coupling interaction H_{HF}, which results from the interaction between the electron spin **S** and the nuclear spin **I**:

$$H_{HF} = \mathbf{I} \check{A} \mathbf{S} \quad [16]$$

where $\check{A}$ is the hyperfine tensor, which is usually isotropic for octahedral Mn^{II} complexes because of the symmetrical electron distribution. The hyperfine constant |A| typically ranges between 160 and 300 MHz. The number of energy levels generated by the hyperfine splitting is thus equal to (2S+1)(2I+1), i.e. 36 for high-spin Mn^{II}, corresponding to 30 possible transitions following the selection rules $\Delta M_S = \pm 1$ and $\Delta M_I = 0$.

- The zero-field interaction (or ZFS), which results from the interaction between the electron spins in the absence of magnetic field:

$$H_{ZFS} = \mathbf{S} \check{D} \mathbf{S} \quad [17]$$

where $\check{D}$ is the zero-field splitting tensor. The ZFS reflects the symmetry of the ligand sphere around Mn^{II} and is related to the crystal field. Distortion of the coordination sphere which affects the axial ligands induces a change in the energy levels governed by the axial ZFS parameter *D*. Distortion which affects the equatorial ligands induces further shifting of these energy levels by a function of the rhombic ZFS parameter *E*. H_{ZFS} thus depends on these two parameters *D* and *E*:

$$H_{ZFS} = (D/3)[3S_z^2 - S(S+1)] + (E/2)(S_x^2 - S_y^2) \quad [18]$$

There are other terms in the spin Hamiltonian, but they are either negligible, or not contributing to the EPR spectrum such as the nuclear Zeeman interaction (which results from the interaction between the nuclear spin and the applied magnetic field). The simplified spin Hamiltonian that governs the EPR spectrum of a Mn^{II} complex is thus given by:

$$H = \beta \mathbf{B} \hat{g} \mathbf{S} + \mathbf{I} \hat{A} \mathbf{S} + \mathbf{S} \check{D} \mathbf{S} \quad [19]$$

The contributions from these three terms for a high-spin $^{55}Mn^{II}$ ion are depicted in Figure 4.[27]

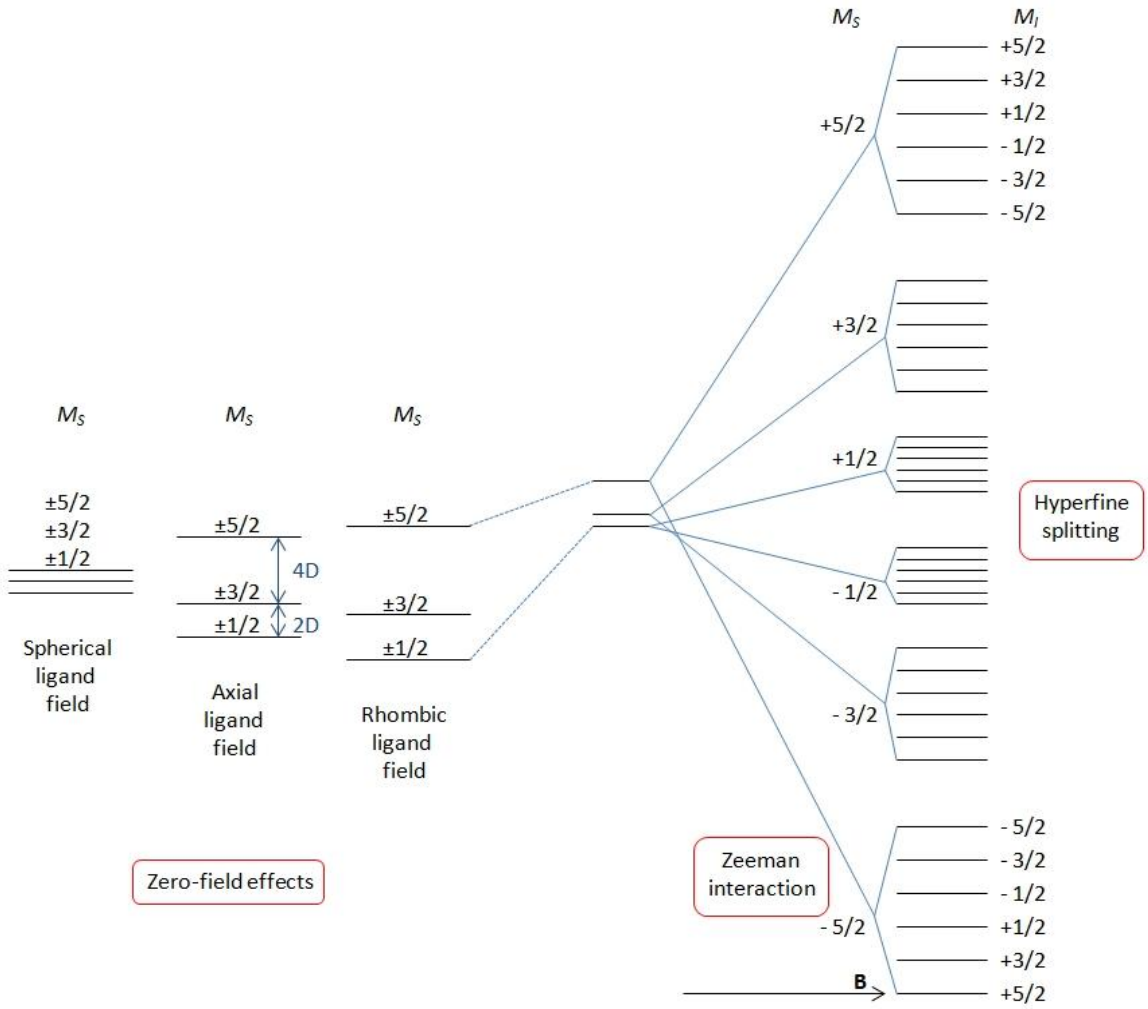

Figure 4: Energy levels diagram for a high-spin $^{55}Mn^{II}$ ion. Adapted from [27]

1.4 Continuous-wave high-field EPR

Continuous-wave high-field EPR (*cw*-HFEPR) corresponds to the situation where high fields (and thus high frequencies) are employed. This has a marked effect on the EPR spectrum. The concept of high field depends on the radical or metal complex that is studied: it corresponds to a situation where a good resolution can be achieved (W-band and above for Mn^{II} complexes). All *cw*-HFEPR spectra have been recorded at CEA on a locally built spectrometer operating in *cw*-mode at 285 GHz[28] (J-band, see Table 1, p. 9).

1.4.1 Design of the J-band cw-HFEPR spectrometer

This spectrometer was built fifteen years ago by Sun Un and does not use a cavity. The sensitivity is thus low, but this can be partially compensated by the use of large volumes (up to 1 mL compared to a few µL for cavity-based spectrometers). Moreover, the use of a field-calibration standard that can be coaxially mounted with the sample is possible.

The *mw* source is a 95 GHz generator, followed by a frequency tripler. The microwaves travel in a waveguide until they reach the sample that lies on the superconducting magnet. The absorbed microwave energy is then measured by a bolometer. The sample is contained in a polyethylene terephthalate (PET) tube, frozen in liquid nitrogen and loaded into the spectrometer by dropping into the waveguide. A high vacuum is then generated by a pump. A flow of helium coupled with a heater is used to thermostat the system, and the magnetic field is then swept to record the *cw*-HFEPR spectrum. The phase of the signal can be adjusted using a polarizer. The modulation and the sensitivity can be adjusted as well.

1.4.2 Influence of the high-field on the EPR spectrum

1.4.2.1 The case of Mn^{II}

At high field, according to equation [19] (total spin Hamiltonian), the Zeeman interaction becomes overwhelmingly dominant. In the case of Mn^{II}, this effect is very beneficial because it greatly simplifies the EPR spectrum by obscuring effects from the ZFS interaction (see below).

According to Figure 5, at 23 K the M_S = -½ ↔ +½ (ΔM_S = 1) transition (referred to as the central transition) is the most prominent feature of the spectrum. The maximum probability of this transition is near 23 K, as the spin populations can be modified with the temperature according to equation [12]: other transitions are less prominent at this temperature. The *cw*-HFEPR spectrum of Mn^{II} is then composed of six sharp lines (peak-to-trough linewidth: 7 G) arising from the hyperfine interaction, which are the six transitions that follow the selection rule ΔM_I = 0. These lines are centered at hν/*g*β and separated by the hyperfine constant |A|, because both the *g*-tensor and the *A*-tensor are isotropic. For the free Mn^{II} ion (*i.e.* the $[Mn(H_2O)_6]^{2+}$ complex), |A| = 267 MHz and *g* = 2.00107 (Figure 5).

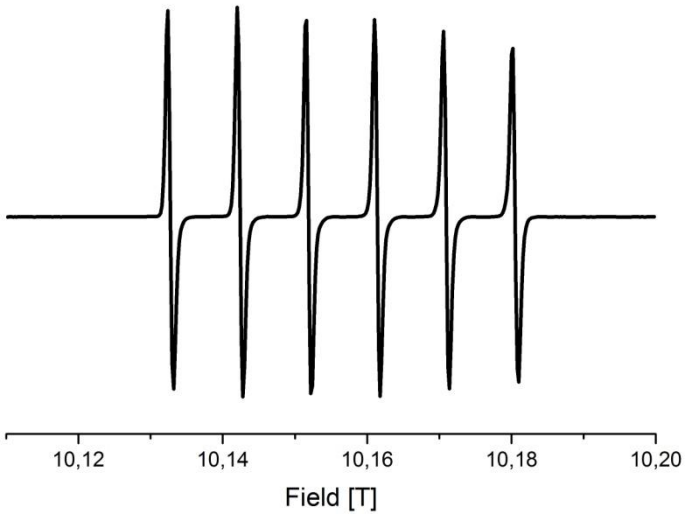

Figure 5: 285 GHz *cw*-HFEPR of $[Mn(H_2O)_6]^{2+}$ (from $Mn(ClO_4)_2$) at 23 K (in 8:2 H_2O/glycerol)

One could wonder why the central transition is the most intense. This is because the ZFS does not interact similarly with every Zeeman transition. The central transition is only perturbed by

the ZFS in the second order in the magnetic field, and thus stays sharp, but the intensity of the other transitions is dominated by the ZFS in the first order which renders them broad. The zero-field contribution to the central transition linewidth is proportional to D^2/ν_0, where ν_0 is the spectrometer frequency. Hence, the EPR spectrum of the central transition of Mn^{II} becomes narrower at higher fields.

When the temperature is decreased, it is possible to observe other features. At 4.2 K, the six hyperfine lines are then superposing a broad component arising from other Zeeman transitions (mainly the M_S = -5/2 to -3/2, referred to as the outer transitions) (Figure 6). The reason why the central transition is still intense at this temperature is complex.

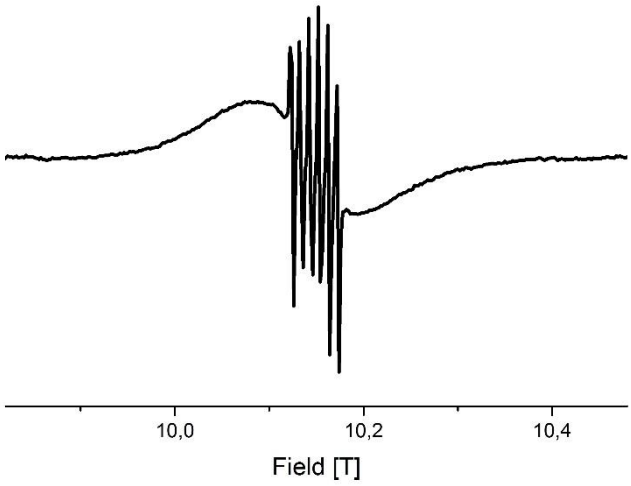

Figure 6: 285 GHz *cw*-HFEPR of $[Mn(H_2O)_6]^{2+}$ (from $Mn(ClO_4)_2$) at 4.2 K (in 8:2 H_2O/glycerol)

1.4.2.2 The case of TEMPO

We can now consider the case of the most commonly used paramagnetic center for PELDOR measurements: the nitroxide radical. When incorporated into a molecule where the spin density is only located in the N-O bond, which is made possible by shielding the adjacent carbons with methyl groups for instance, the corresponding structure is known as TEMPO (Figure 1, p. 6) and is a radical with a shelf life of decades. The nuclear spin of ^{14}N (99.6% natural abundance) is I = 1, while the nuclear spin of ^{16}O (99.8% natural abundance) is I = 0. The electron spin of a nitroxide is S = 1/2, and because there is no ZFS for systems with S = ½, six energy levels corresponding to three transitions ($\Delta M_I = 0$) should be observed. The energy levels are depicted in Figure 7.

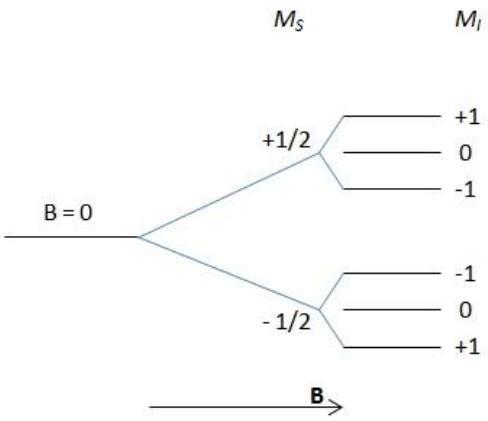

Figure 7: Energy levels diagram for a nitroxide

At X-band, the *cw*-EPR of the TEMPO radical is thus constituted of three sharp lines separated by a hyperfine constant |A|. But if we move to higher field/frequency, the situation becomes more complicated. Unlike Mn^{II}, the *g*- and *A*-tensors of TEMPO are anisotropic. The *g*-anisotropy becomes resolved at high field, while the resolution of the *A*-anisotropy does not depend on the field (see equation [16]) but becomes more visible at high field because of the higher reolution in *g*. Different cases can occur:

- When $g_x = g_y = g_z$, the symmetry is cubic. The *g*-tensor is thus isotropic.
- When $g_x = g_y \neq g_z$, the symmetry is axial. In this case, $g_x = g_y$ is usually written $g_\perp$, and g_z is usually written $g_\parallel$.
- When $g_x \neq g_y \neq g_z$, the symmetry is rhombic.

The *g*-anisotropy for the TEMPO radical comes from its molecular structure. Assuming that the *g*- and *A*-axes systems are collinear, let us consider a TEMPO radical where the piperidine ring lies in the *x*-*y* plane and the *z* axis is perpendicular to the N-O bond. Unlike Mn^{II}, for which the spin density is nearly symmetric, for TEMPO the spin density is localized on the N-O bond (and almost equally distributed between both atoms), so that all directions are not equivalent with respect to **B**. This situation is depicted in Figure 8. At X-band, the EPR spectrum of a typical nitroxide is dominated by the hyperfine splitting of A_z (red lines) while A_x (blue lines) and A_y (green lines) are hidden under the central peak. The *g*-anisotropy, which is not resolved at this field, becomes resolved at G-band (Table 1, p. 9): g_x, g_y and g_z are clearly separated. A_z is still resolved and can be seen on g_z, but the hyperfine splitting A_x on g_x and A_y on g_y are not resolved. The spectra displayed on this figure represent the absorption signal and not its first derivative: this kind of spectra will be discussed in the next section (p. 18).

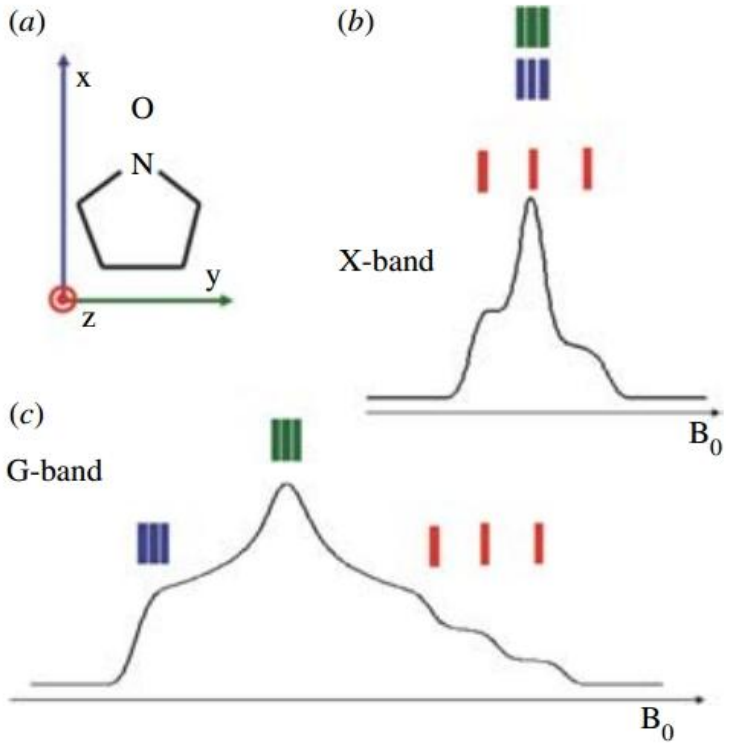

Figure 8: Typical EPR spectra of a nitroxide. (a) - Axis system of a nitroxide; (b) - X-band EPR spectrum of nitroxide; (c)- G-band EPR spectrum of a nitroxide. Adapted from [6]

1.5 Pulsed EPR

1.5.1 Introduction and main pulse sequences

In 1958, R. J. Blume reported the first pulsed EPR experiment: an electron spin echo could be observed from a solution of sodium in ammonia.[29] During the 1960s, in parallel with pulsed NMR, important advances were performed in pulsed EPR, notably by W. B. Mims. Progress in *mw* electronics have led to the development of commercial pulsed EPR spectrometers at X-, W-, and J-bands (Table 1, p. 9).

In a pulsed EPR experiment, instead of sweeping the magnetic field to detect resonances in the sample, a short and intense *mw* pulse is applied with a specific bandwidth. This generates a free induction decay (FID) signal created by the sample magnetization, corresponding to the time-domain spectrum, which is finally Fourier transformed to obtain the frequency-domain EPR spectrum. A more complete explanation will be given in the next pages, but it is worth noting that this methodology is quite similar to pulsed NMR experiments. However, this type of pulsed EPR measurements are not as routinely performed as pulsed NMR experiments: short *mw* pulses should be applied in the case of EPR.

Let us consider a single electron placed in a constant magnetic field $\mathbf{B_0}$, aligned along the +*z* axis (longitudinal direction). The magnetic moment $\boldsymbol{\mu}$ of the electron spin will precess around $\mathbf{B_0}$ at an angular frequency called Larmor frequency ω (in Hz). The relationship between ω and $\mathbf{B_0}$ is:

$$\omega = -\gamma \mathbf{B_0} \quad [20]$$

where γ is called gyromagnetic ratio (in $Hz.T^{-1}$). In a paramagnetic sample with many electron spins, each spin can be aligned either parallel (m_s = -1/2) or antiparallel (m_s = +1/2) to $\mathbf{B_0}$. Because the parallel state has a lower energy, at thermal equilibrium the Boltzmann equation implies that more electrons will be aligned parallel to $\mathbf{B_0}$. Thus, a vector called magnetization $\mathbf{M_0}$, aligned along the +*z* axis, is created.

To apply *mw* pulses, a resonator creates a polarized *m*w field $\mathbf{B_1}$. The polarization of these *mw* pulses is usually chosen perpendicular to the much stronger applied magnetic field $\mathbf{B_0}$ (*i.e.* in the *x*-*y* plane, also called transverse plane). The essential idea behind pulsed EPR is to perturb $\mathbf{M_0}$ using $\mathbf{B_1}$ *mw* pulses to detect the response of the spin system by probing the FID. Using pulse sequences with various shapes and durations, numerous properties of paramagnetic compounds can be studied, thus making pulsed EPR a powerful analytical tool.

At this stage, it is very convenient to use the rotating frame convention to describe the magnetization. In the laboratory frame, the magnetic moments of the electron spins precess around $\mathbf{B_0}$, but they are stationary in the rotating frame, thus allowing a much easier representation of their behavior when microwave pulses are applied. Pulses are often named by the rotation angle (or flip angle) of $\mathbf{M_0}$ that they induce. The π/2 pulse will flip $\mathbf{M_0}$ by 90°, thus making it lie in the *x*-*y* plane. The π pulse will flip $\mathbf{M_0}$ by 180°, making it pointing along the –*z* axis. This pulse inverts the populations of the spin states and is thus called inversion pulse.

The relaxation phenomenon is in fact characterized by two processes: the spin-lattice relaxation (or longitudinal relaxation, with a time constant T_1) and the spin-spin relaxation (or transverse relaxation, with a time constant T_2).

- The spin-lattice relaxation is characterized by the recovering rate of $\mathbf{M_0}$ to the thermodynamic (Boltzmann) equilibrium. This reflects how fast the spins give back the energy they obtained from the microwave pulses to the lattice, *i.e.* the neighboring molecules.

- The spin-spin relaxation is characterized by the vanishing time of the M_{xy} component of $\mathbf{M_0}$. It defines how long $\mathbf{M_0}$ "lives" in the transverse plane. Spins affected by the $\mathbf{B_1}$ *mw* pulses can be gathered into groups called spin packets: in a spin packet, all spins have the same Larmor frequency and experience the same magnetic field. The spin-spin relaxation is caused by the interaction between the spin packets: as there are local magnetic field inhomogeneities, each spin packet experience a different magnetic field, which leads to different Larmor frequencies. Spin packets will thus rotate at different speeds according to their respective Larmor frequencies: the precession of the spins is then progressively randomized and the M_{xy} component of $\mathbf{M_0}$ progressively disappears. We can also say that the spins dephase or lose their coherence due to spin-spin interaction. T_2 is at least one order of magnitude less than T_1 for high-spin metal complexes, and two orders of magnitude less for nitroxides, in frozen solution.

EPR spectra can be obtained by several methods. Accordingly, the easiest way to detect a signal would be to record the FID after a π/2 pulse. Hence, $\mathbf{M_0}$ would be stationary in the rotating frame and would start decaying. But now switching to the laboratory frame, $\mathbf{M_0}$ would rotate in the transverse plane while decaying, thus generating a FID. Fourier transform of this FID would give the frequency-domain EPR spectrum. Unfortunately, the EPR signal cannot be recorded this way because it would be masked by the much more superior power of the pulses: there is a time delay between the end of the π/2 pulse and the beginning of the signal recording, called dead time. Moreover, the linewidth of the sample is usually not narrow enough to excite the whole spectrum with the π/2 pulse. To circumvent this problem, we can use a pulse sequence called spin echo (or Hahn echo, Figure 9).

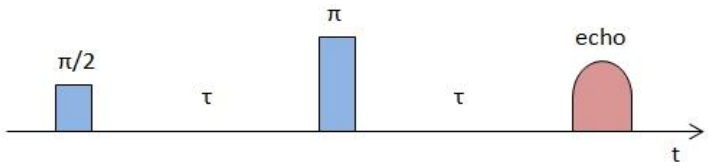

Figure 9: Spin echo pulse sequence

This sequence can be decomposed this way, in the rotating frame:

- A π/2 pulse is applied. $\mathbf{M_0}$ is then flipped in the transverse plane.

- The transverse magnetization starts to decay due to dephasing of the spin packets. We can also say that the transverse magnetization "fan out".

- A π pulse is applied a time τ after the π/2 pulse. $\mathbf{M_0}$ is then inverted in the transverse plane. At a time 2τ, $\mathbf{M_0}$ will refocus, creating a so-called spin echo. A usual illustration is to compare spin packets to runners. The race begins when the π/2 pulse is applied: some runners will run fast, some will run slow. At time τ, when the π pulse is applied, the runners must all stop, immediately turn back and run in the opposite direction. Whatever their individual speed, they will all cross the finish line at the same time 2τ, corresponding to the refocusing of $\mathbf{M_0}$. The interpulse delay τ should be shorter than T_2 to avoid loss of spin coherence.

Measuring the time constant of the echo decay would give the T_2 value. This can be done by recording the intensity of the echo for different values of τ. In reality, the dephasing of the spin packets also depends on other processes, like spin diffusion or dipolar coupling, so that the spin-spin relaxation is not purely exponential. The time constant for the echo decay is in fact called phase memory time T_m.

Using the spin echo sequence is an efficient way to record an EPR spectrum. By sweeping $\mathbf{B_0}$ while monitoring the echo intensity, one can obtain an EPR spectrum with a very high spectral resolution.[6] Such spectra are called 2-pulse (2P) echo-detected (ED) field-swept (FS) EPR spectra, or more simply ED-EPR spectra. Contrary to *cw*-EPR spectra, the signal is directly recorded, not its first derivative.

T_1 can be measured using the inversion-recovery sequence depicted in Figure 10.

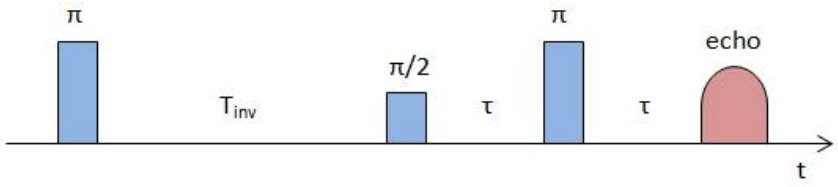

Figure 10: Inversion-recovery pulse sequence

This sequence is identical to the spin echo sequence, but a first π pulse rotates $\mathbf{M_0}$ down to the *–z* axis. The signal will start decaying as $\mathbf{M_0}$ will return towards its equilibrium position along the *+z* axis, *i.e.* undergo spin-lattice relaxation. After a certain inversion time T_{inv}, a π/2 pulse will flip $\mathbf{M_0}$ in the transverse plane, and the signal will be refocused by the last π pulse to create an echo that will recover with a T_1 time constant.

1.5.2 The PELDOR pulse sequence

1.5.2.1 Theory

Pulsed electron-electron double resonance (PELDOR), also called double electron-electron resonance (DEER), has emerged as a powerful method to accurately determine the distance between two paramagnetic centers. The original three-pulse version of this technique was invented by A. D. Milov and Y. D. Tsvetkov in Novosibirsk in the beginning of the 1980s,[30,31] and was refined about twenty years later in a more efficient dead-time-free four-pulse version.[32] The PELDOR method relies on the magnetic dipole-dipole interaction between the magnetic moments of two electron spins μ_A and μ_B,[6] which depends on the distance R between these two spins. The energy of the magnetic dipole-dipole interaction can be described by the dipolar Hamiltonian H_{dip}:

$$H_{dip} = (g_1 g_2 \beta^2/R^3)(A+B+C+D+E+F) \quad [21]$$

where g_1 and g_2 are the *g*-values of the paramagnetic centers 1 and 2, respectively. A is called the secular term, B is known as the pseudo-secular term, and C-F are the non-secular terms. They are products of the electron spin **S** of the paramagnetic centers 1 and 2 and angular expressions describing the orientation of the molecule with respect to $\mathbf{B_0}$. The aim of a PELDOR experiment is to determine the dipolar coupling ω_{dip} (in Hz), which reflects the magnetic dipolar interaction between the two paramagnetic centers 1 and 2, using a relevant pulse sequence, as it will be discussed later. Indeed, ω_{dip} is directly linked to R.

Fortunately, when ω_{dip} is small compared to the Zeeman interaction, when g_1 and g_2 are weakly anisotropic, and when the weak coupling condition is obeyed (see below), only the secular term A is significant. The dipolar coupling can then be written

$$\omega_{dip} = (D_{dip}/R^3)(1-3\cos^2\theta) \quad [22]$$

where D_{dip} is called the splitting constant (in Hz.m^3) and θ is the angle between $\mathbf{B_0}$ and the interspin (or dipolar) vector. When $g_1 = g_2 = 2$, D_{dip} is equal to 2π×52 MHz.nm^3. According to equation

[22], when $\mathbf{B_0}$ is parallel to the dipolar vector ($\theta = 0°$), ω_{dip} is equal to $-2D_{dip}/R^3$, and when $\mathbf{B_0}$ is perpendicular to the dipolar vector ($\theta = 90°$), ω_{dip} is equal to D_{dip}/R^3.

Let us consider a sample constituted of biradicals in liquid solution: they will all have random dynamic orientations relative to $\mathbf{B_0}$, thus ω_{dip} will be averaged out. But if this sample is frozen, the resulting spectrum will be a static superposition of spectra corresponding to each possible orientation. Such a spectrum is called a Pake doublet (or Pake pattern, figure 11).

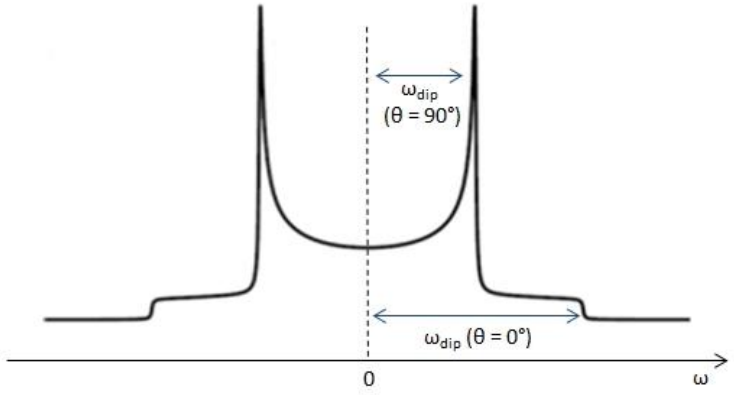

Figure 11: Pake doublet. Adapted from [6]

The two "horns" of the Pake doublet correspond to interspin vectors which are aligned perpendicularly to $\mathbf{B_0}$, and the two "feet" correspond to interspin vectors which are aligned parallel to $\mathbf{B_0}$. The "horns" are more intense than the "feet", which means that the former case reflects a more probable situation. Indeed, if we consider a sphere whose center is the paramagnet 1 and whose radius is the interspin vector, there are more possible locations of paramagnet 2 perpendicularly to $\mathbf{B_0}$ than parallel to $\mathbf{B_0}$. Thus, the distance from the center to a "horn" is equal to ω_{dip} when $\theta = 90°$, and the distance from the center to a « foot » is equal to ω_{dip} when $\theta = 0°$.

The Pake doublet corresponds to what was previously referred to as the frequency-domain spectrum, and is thus obtained by Fourier transform of the PELDOR signal. As it can be seen from equation [22], if we know ω_{dip} (from the Pake doublet), we can calculate the interspin distance R. Unfortunately, this procedure is not reliable since the interspin distance is distributed, and the parallel and perpendicular singularities of the Pake doublet can be poorly resolved in this case. The presence of noise and uncertainties in the data treatment greatly influence the shape of the Pake doublet. This is called an ill-posed problem, and this is why we use mathematical treatments adapted to this kind of situation. Among them, the Tikhonov regularization is the most widely employed.[33] It finds a compromise between the smoothness and the narrowness of the distance distribution.

1.5.2.2 Pulse sequence

As seen before, if we want to know the interspin distance R, we need to measure the dipolar coupling ω_{dip}. Unfortunately, this interaction is very weak compared to other contributions to the spin Hamiltonian (hyperfine couplings and *g*-tensor anisotropy),[10] meaning that in general, ω_{dip} does not significantly influence the shape of the EPR spectrum. Accordingly, the aim of the PELDOR pulse

sequence is to separate ω_{dip} from all the other contributions. The four-pulse version of PELDOR is the most commonly used (Figure 12, top).[32]

Let us consider a biradical that consist in two stable nitroxides connected to a rigid central linker (Figure 12, middle), and its ED-EPR spectrum (Figure 12, bottom). The four-pulse PELDOR consists of two sequences called detection (or observe) and inversion (or pump) sequences, operating at two different frequencies ν_{det} and ν_{inv}, respectively. The difference between these two frequencies is called offset.

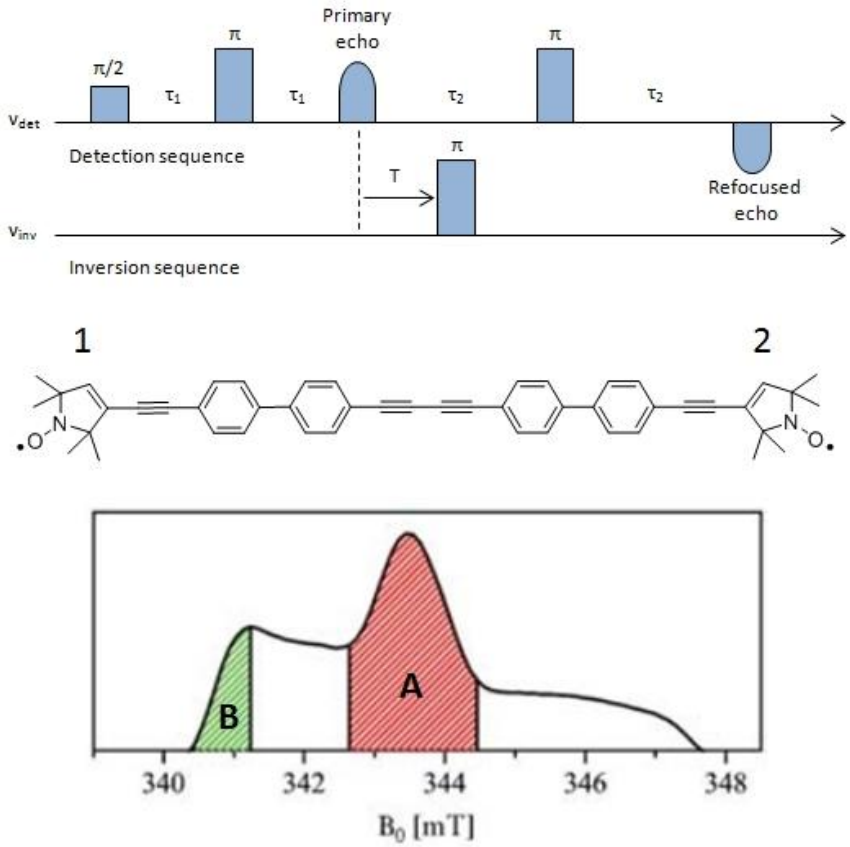

Figure 12: Top: Four-pulse version of the PELDOR pulse sequence. Middle: Structure of the studied rigid biradical model. The two paramagnetic centers are denoted 1 and 2. Bottom: Its X-band ED-EPR spectrum. The portion of the spectrum denoted A is excited by the inversion sequence while the portion denoted B is excited by the detection sequence. Adapted from [6]

The first two pulses of the detection sequence consist in a Hahn echo, which results in a selective spin echo of the spins of the region B (also called observer spins), resonant with ν_{det}. The subsequent decay in the echo intensity contains, among other contributions, the dipolar coupling ω_{dip}. A π pulse is then applied to selectively invert the spins of the region A (also called pumped spins) at a frequency ν_{inv}. Accordingly, a $\pm\omega_{dip}$ term will be added in the Larmor frequency of the spin B, depending on the quantum state of spin A. As a result, the spins B will then precess with an altered frequency, inducing a dephasing effect, and thus will not be refocused properly when the last π pulse (on the detection sequence) is applied. The π pump pulse can be applied at different times T to induce a periodic modulation of the intensity of the spins B echo according to:

$$V(T) = V_0(1-\lambda+\lambda\cos(\omega_{dip}T)) \quad [23]$$

where V_0 is the echo intensity at T = 0, and λ is called the modulation depth (in %). This parameter characterizes the fraction of spins that are excited by the inversion pulse. The echo intensity as a function of time V(T) is also called dipolar evolution function or PELDOR time trace, and this is what is recorded during a PELDOR experiment (Figure 13).

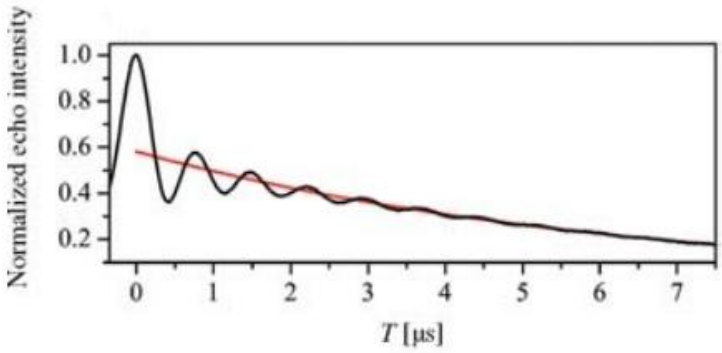

Figure 13: Dipolar evolution function V(T) (black) for the biradical depicted in Figure 12. The red line is the background contribution and is discussed below. Adapted from [6]

As mentioned above, we need to be in the weak coupling regime to consider the secular term of the dipolar Hamiltonian only. The weak coupling means that ω_{dip} has to be smaller than the absolute value of the resonance frequency difference between pumped and detected spins. This situation is commonly encountered for nitroxides at X-band by using an appropriate offset, but for high-spin metal complexes of Gd^{III} and Mn^{II} it is more complex.[34]

The measurable distance range varies from 1.8 nm to 8.3 nm.[34] Below 1.8 nm, the contribution from a process called exchange coupling cannot be negligible. This situation can also occur when the spin is fully delocalized between the two paramagnetic centers, in the case of a fully conjugated system for instance. Above 8.3 nm, it is difficult to distinguish the dipolar coupling from the noise because a very long dipolar evolution window is needed (see below).

1.5.2.3 Optimization of parameters

A compromise between all PELDOR parameters must be found in order to obtain the highest sensitivity. This sensitivity is directly related to the echo intensity and to the modulation depth, which can be tuned by choosing the appropriate pump-detect strategy. The T_1 value determines the repetition rate (or shot repetition time, SRT) of the experiment, *i.e.* the time between two pulse sequences. To achieve the highest possible SNR, the experiment needs to be repeated as many times as possible, but we need to wait for $\mathbf{M_0}$ to recover along the +*z* axis before applying another pulse sequence. The T_2 (or more exactly the T_m) is crucial because it determines the dipolar evolution window, *i.e.* the time during which the pump pulse is applied. If the T_m is too short, a first complete oscillation may not be observed. As the dipolar coupling becomes smaller when the interspin distance increases, the period of the PELDOR oscillations becomes bigger: hence, a long T_m is required to measure long distances.

To sum up, the sensitivity of a PELDOR measurement η is proportional to product of the intensity of the detected echo V and the modulation depth λ, but it also depends on other factors such as T_m and T_1. Ideally, large V, large λ, long T_m and short enough T_1 values are desired.[35] Other parameters that affect the SNR are the measurement time and the number of shots per point (SPP), *i.e.* the number of acquisitions of the echo intensity per increment of the time delay of the pump pulse before averaging.

1.5.2.3.1 Concentration

As described earlier, the Fourier transform of V(T) will give the frequency-domain spectrum, theoretically shaped like a Pake doublet. Tikhonov regularization of the signal will give the distance distribution (Figure 14).

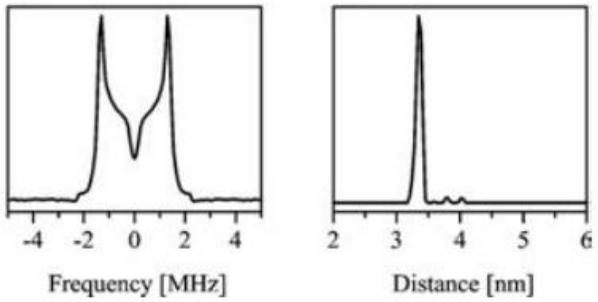

Figure 14: Left: Fourier transform of the dipolar evolution time V(T) shown in Figure 13 (after background correction), shaped like a Pake doublet. Right: its Tikhonov regularization. Adapted from [6]

Nevertheless, an additional step is required. The echo intensity is the product of two contributions: the form factor F(T) and the background factor B(T).[36]

$$V(T) = F(T)B(T) \quad [24]$$

The studied system (biradical for instance) cannot be considered as isolated: indeed, intermolecular contribution from other biradicals impacts the signal and must be taken into account. Accordingly, the form factor represents the contribution from the spins within the studied biradical (intramolecular interaction), and the background factor represents the contribution from neighboring spins on other biradicals (intermolecular interaction). To extract F(T), the background factor can be modeled as an exponential decay while taking into account the distribution of the biradical, assuming a homogeneous distribution:

$$B(T) = B_0\exp(-kTD/3) \quad [25]$$

where B_0 is a pre-exponential factor, k is a time constant (in s^{-1}) and D is the number of dimensions of the system (T is the time shown in Figure 12). For a biradical, D = 3, because the molecule is homogeneously distributed, but for more particular systems such as lipid bilayers, D can be set to 2. The background factor can be adjusted by choosing an appropriate concentration: the sample must be sufficiently concentrated to keep the SNR reasonably high, but not too concentrated. Otherwise, a phenomenon known as instantaneous diffusion occurs: when a pulse is applied to invert a spin, a neighboring spin (on another molecule) will also experience a slight change in

frequency. This will interfere with the refocusing of the spin echo, reducing its intensity and thus reducing the phase memory time T_m.

F(T) can then be separated from B(T) by fitting the time constant k: this is the background subtraction. To be as accurate as possible, at least two modulations should be observed. Noteworthy, F(T) does not depend on the concentration while B(T) is affected.

1.5.2.3.2 Pulses

The duration of the pulses, as well as the time between them, has a crucial influence on the echo intensity and the modulation depth. The length of a pulse controls its bandwidth: the shorter the pulse duration, the larger the bandwidth, *i.e.* the frequency range that a pulse can cover in the ED-EPR spectrum. As an example, a π pulse length of aboutd 20 corresponds to 40 MHz. It is preferable to use short π pulses to excite as much spins as possible, but if the bandwidths of the inversion and detection pulses overlap, the echo intensity of the detected spins is reduced. This spectral overlap can be controlled by changing the offset.

Additionally, to obtain a high λ, the inversion frequency must be set where the intensity of the EPR spectrum is the highest, so that the pump pulse will invert as much spins as possible. However, to obtain a high V, the detection frequency must correspond to the maximum of the spectrum. Usually the first option is preferred, but the choice also depends on the distance range. The time between the pulses must be set by taking into account T_1 and T_2.

1.5.2.3.3 Temperature

The choice of the temperature is more crucial for high-spin metal complexes than for nitroxides, because for the former, the shape of the spectrum strongly depend on spin populations. Furthermore, relaxation becomes slower at low temperature, meaning that both T_1 and T_2 increase when decreasing the temperature. The SNR increases with the square root of the repetition rate, so a relatively short T_1 is desirable.

1.5.2.3.4 Solvent

The molecule of interest must be dissolved in an adequate glass-forming solvent, while avoiding the formation of aggregates. Usually mixtures of water and a glass-forming agent (also called cryoprotectant) such as glycerol or ethylene glycol are used (see Annex 1, p. 205). For hydrophobic samples, 2-Me-THF, toluene or mixtures thereof are adequate. Perdeuterating the solvent is advantageous because it increases T_m by diminishing proton spin diffusion, *i.e.* the continuous exchange of energy between proton spins and electron spins.

1.5.2.4 High-spin metals *vs* nitroxide spin labels

As we will see later, high-spin metals such as Gd^{III} or Mn^{II} are emerging as a new promising class of paramagnetic centers for PELDOR. They display numerous advantages compared to the

widely employed nitroxide derivatives, but also new difficulties because of the more complex spin physics associated with the larger number of unpaired electrons.

A first notable improvement is the absence of orientation selection at high field. Usually, PELDOR measurements involving nitroxides are performed at X-band and Q-band where the *g*-anisotropy is very weakly resolved (Table 1, p. 9). This *g*-anisotropy becomes resolved at high field: as a consequence, the PELDOR detection sequence excites only a relatively small fraction of the EPR spectrum, because the pulse bandwidth cannot cover it totally. As a result, only a fraction of molecules with a particular orientation with respect to $\mathbf{B_0}$ will contribute to the PELDOR signal. The interspin distance can still be obtained, but a set of measurements at different positions of the EPR spectrum is required, leading to a complex data analysis.[20] Orientation selection can also occur at X-band on a semi-rigid system if the orientations of the two nitroxides are correlated, where different orientations of the anisotropic A-tensor can be probed.[37,38] In contrast, effects of orientation selection at X-band are removed (averaged) when the motion of a nitroxide label is not restricted.

For Gd^{III} and Mn^{II}, the orientation selection disappears for three reasons: the *g*-tensor is isotropic for most cases, the ZFS only contributes to the central transition in the second order to $\mathbf{B_0}$ and the ZFS parameters *D* and *E* are relatively largely distributed. This leads to the second advantage of high-spin metals: because the central transition of their EPR spectrum narrows at higher field, they will better perform at high field compared to nitroxides for which issues associated with orientation selection and pumping efficiency will reduce their interest. Hence, the sensitivity of PELDOR measurements can be greatly improved with the high-spin metal/high-field magnet combination by pumping or detecting on the central transition, implying that less sample can be used, which is of great interest for proteins that are not easily obtained. This also leads to reduced measurement times.

The third advantage regards biological applications. It is of great interest to perform PELDOR experiments in a cell, but this turns into a challenging task with nitroxides, because they are readily converted into EPR-silent hydroxylamines in the reducing environment of a cell. In contrast, Gd^{III} and Mn^{II} complexes are redox-stable in a cell,[39] provided ligand exchange does not occur.

On the other hand, high-spin metals are intrinsically more complex than nitroxides, which are only S = ½ and which have been extensively used. This means that additional difficulties are likely to arise. Notably, a very important point is that the pseudo-secular term of the dipolar Hamiltonian H_{dip} can only be neglected when the dipolar coupling ω_{dip} is small compared to the energy difference between the pumped and detected spins. This weak coupling approximation is usually fulfilled for nitroxides, but it has been shown[35] that in some cases, the pseudo-secular effect needs to be taken into account for high-spin metal complexes. However, the potential of high-spin metals is progressively unraveled over the years. Under certain conditions, Gd^{III} can be treated as an effective S = ½ system and data analysis can be performed using DeerAnalysis like for nitroxides.

1.5.2.5 Mn^{II} *vs* Gd^{III}

Today, Gd^{III} is much more used than Mn^{II} as a PELDOR spin label. Several reasons can explain this fact: for labels with comparable *D*-values, the echo intensity for Gd^{III} is larger than for Mn^{II} by a

factor 6 because the hyperfine interaction splits the Mn^{II} central transition into a sextet. This also reduces the modulation depth by the same factor, but this loss of sensitivity is partially compensated by the lower spin multiplicity of Mn^{II} compared to Gd^{III} which can result in as much as a 2-fold increase in the population of the central transition at optimal temperature.

However, in a biological perspective, Mn^{II} has some advantages. Contrary to Gd^{III}, it is endogenous in biological environment and found in numerous proteins (concanavalin A or enzymes such as superoxide dismutase and oxalate decarboxylase). Moreover, due to similarities in charge and size, it can replace Mg^{II} in many other enzymes or nucleic acids.[23] This means that a single tagging with an exogenous Mn^{II} complex will lead to a bis-Mn^{II} system that can be studied by PELDOR.

2. PULSED EPR MEASUREMENTS INVOLVING METALS

As mentioned above, PELDOR measurements using nitroxide spin labels at X-band have been successfully used in many systems. For instance, they proved useful to probe the flexibility of oligo(phenylene-ethynylene) (OPE) rods[16,17] or porphyrin-based wires.[40] Systems using the same OPE rods have also been employed to measure the distance between three or four nitroxide groups.[41,42] The conformation of other original constructs could be probed using PELDOR with nitroxides, for instance catenanes[18] or rotaxanes.[19] Besides these synthetic systems, the structure and dynamics of nitroxide-labeled biological objects have been intensely investigated, for instance oligonucleotides[14,15] or proteins.[12,43] PELDOR measurements involving nitroxides have been thoroughly reviewed.[10,30,44] Experiments using tyrosyl radicals have also been reported.[45,46]

Similarly to the widely employed distance measurements between nitroxide spin labels, low-spin (S = 1/2) metals (essentially Cu^{II} complexes, Fe-S clusters or Mn in photosystem II in the dark-stable S_2 state) have also been employed to a lesser extent for metal-metal or metal-radical distance measurements. High-spin complexes of Gd^{III} (S = 7/2) and Mn^{II} (S = 5/2) have also started to emerge as a new promising class of paramagnetic centers for pulsed EPR-based distance measurements. Like nitroxides, but unlike high-spin metals, the width of the EPR spectrum of low-spin metals widens at high fields. This width is even larger than for nitroxides, such that the *g*-anisotropy of low-spin metal complexes is often already resolved even at X-band, where most of the measurements are performed. Hence, sensitivity and orientation selection are crucial issues, but despite these drawbacks, pulsed EPR distance measurements on biological systems that contain native Cu, Fe or Mn centers have led to important advances.[6,47] In this part, we will shortly mention selected examples dealing with low-spin metals, and we will concentrate on high-spin Gd^{III} (S = 7/2) and Mn^{II} (S = 5/2) complexes.

2.1 Low-spin metals

2.1.1 Cu^{II} complexes

2.1.1.1 Cu^{II}-Cu^{II} distance measurements

Like Mn^{II}, Cu^{II} is involved in numerous biological processes. Hence it is very attractive as a paramagnetic label for EPR-based distance measurements, which could reveal structural details that complement NMR or X-ray investigations. Unlike Mn^{II}, Cu^{II} complexes are S = 1/2 and display a large *g*- and A-anisotropy, so orientation selection is a crucial point of concern. Their EPR spectrum widens with increasing field, so measurements are usually performed at X-band. Like Mn^{II} and Gd^{III}, PELDOR is the most popular pulse sequence.

The parameters that govern the efficiency of Cu^{II}-Cu^{II} PELDOR were analyzed in details on a polyproline system[48] with two Cu^{II}-binding PHGGGW sequences in the ends. As this object is flexible, the X-band PELDOR oscillations were identical at different magnetic field positions. Using a similar peptide,[49] parameters that lead to high SNR PELDOR traces were addressed. By systematically varying the pulses, a pump π-pulse of 16 ns and an observe π-pulse of 20-48 ns were found to be ideal. A frequency offset of 100 MHz was sufficient for a good SNR, affording a modulation depth of 9%. These results could be achieved at 20 K with concentrations around 1.5 mM and a measurement time of 2-12 h, using SRT of 2-3 ms.

Measurements between Cu^{II} centers in biological systems were first peformed on a covalently linked dimer of azurin[50]. Because of the high *g*- and *A*-anisotropy of Cu^{II} compounds, leading to strong orientation selection, the task was challenging, but quite noisy but clear PELDOR modulations could be observed at X-band. The maximum intensity of the corresponding frequency-domain spectrum was observed at 2.7 MHz, translating into a distance of 2.6 nm, in accordance with the X-ray structure. In another study, the two Fe^{III} ions of human serum transferring (Tf) and lactoferrin (Lf) could be replaced by two Cu^{II} ions without altering the overall protein structure.[51] Orientation selection was found to be low for these systems at X-band, thus easing measurements. Distances of 4.2 nm were obtained for both proteins that were only 2-3% lower than the X-ray distances, possibly accounting for small conformational differences in solution and in the solid state. The frequency-domain spectra were found to be well shaped Pake doublets, confirming minimal orientation selection (Figure 15).

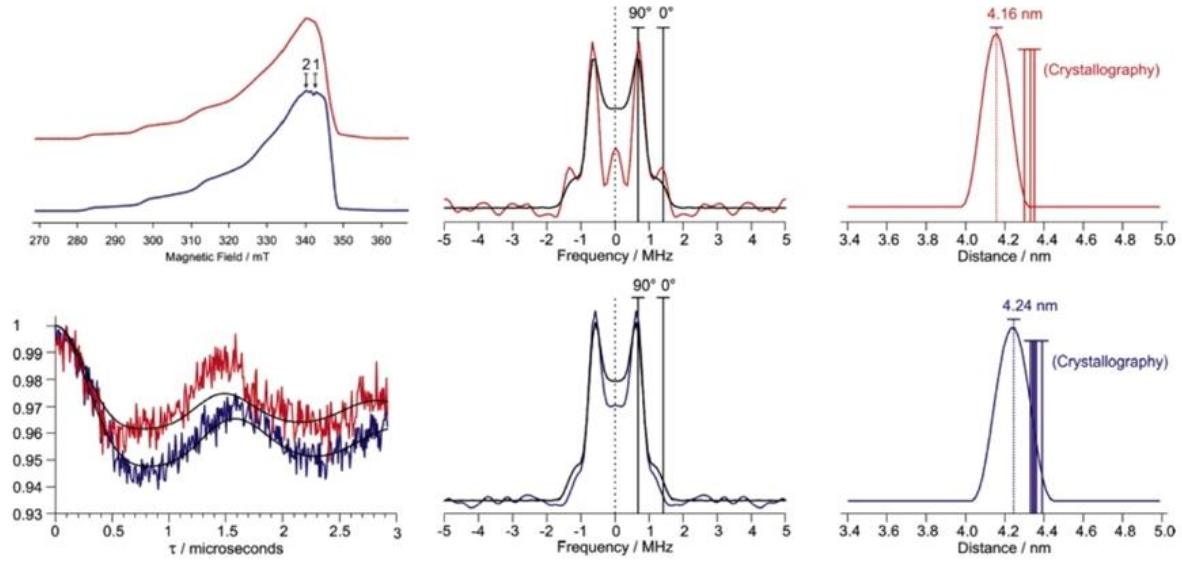

Figure 15: PELDOR results on Cu_2Tf (red) and Cu_2Lf (blue). Left side: X-band ED- EPR spectra (top) with pump (1) and detect (2) positions marked with arrows, and background-corrected PELDOR time traces (bottom) with their respective Tikhonov fits in black. Middle: Corresponding frequency-domain spectra showing the perpendicular and parallel components of the Pake doublets as well as their respective Tikhonov fits in black. Right side: Distance distributions obtained with Tikhonov regularizations, as well as distances from X-ray crystallography. Adapted from [51]

Recent developments in PELDOR methodology have encouraged researchers to tackle to more complex biological systems, like the multi-copper nitrite reductase from *Achromobacter xylosoxidans* (AxNiR), a homo-trimer with two Cu^{II} ions per subunit in two different geometries (T1 and T2).[52] Using improved PELDOR sequences, it was possible to eliminate either the intersubunit T1 Cu – T1 Cu or the T2 Cu – T2 Cu distances, showing that the PELDOR technique can be successfully applied to biomacromolecules containing multiple paramagnetic centers by deconvoluting the complex distance distributions that are obtained.

2.1.1.2 Cu^{II}-nitroxide distance measurements

The specific parameters that ensure a successful Cu^{II}-NO PELDOR measurement were addressed using polyproline and polyalanine peptides with a Cu^{II}-PHGGGW site and a MTSL label.[49,53,54] A modulation depth of 19% could be achieved by pumping on top of the nitroxide peak and using a 260 MHz offset, with π pump and detection pulses of 16 and 20 ns, respectively, within a few hours of acquisition. Weak orientation selection was observed due to the flexibility of the system.

More rigid objects were also studied such as model compound consisting in a Cu^{II}-bis(Tpy) (terpyridine) complex linked to two nitroxide moieties.[55] Because of the moderate overlap of the EPR spectra of the nitroxide and the Cu^{II} moieties at X-band, these two paramagnetic species could be selectively excited by the pulses, leading to the selective measurement of the Cu-Cu or the Cu-nitroxide distance. A platform with a Cu^{II}-porphyrin at one end and a nitroxide at the other was crystallized and X-band PELDOR measurements led to a distance of 2.06 nm, in excellent agreement

with the 2.07 nm from the crystal structure, and with a modulation depth of 40%, analogous to nitroxide-nitroxide pairs.[56]

PELDOR distance measurements on Cu^{II}-containing proteins tagged with MTSL were applied to Cu-Zn superoxide dismutase (SOD), and revealed noticeable differences between wild-type SOD and three single-residue mutants implied in familial amyotrophic lateral sclerosis.[57] Identifying Cu^{II} binding sites by PELDOR triangulation with nitroxides could be performed in the EcoRI endonuclease homodimer.[58] This EPR-based approach for the localization of Cu^{II} ions in biomolecules was also experimented on azurin: the idea was to determine the position of the Cu^{II} ion by tagging mutants of the protein with MTSL and measuring the Cu^{II}-nitroxide distance for each mutant, in a way similar to a GPS.[59] This trilateration method gave a position for the Cu^{II} consistent with the X-ray results (Figure 16).

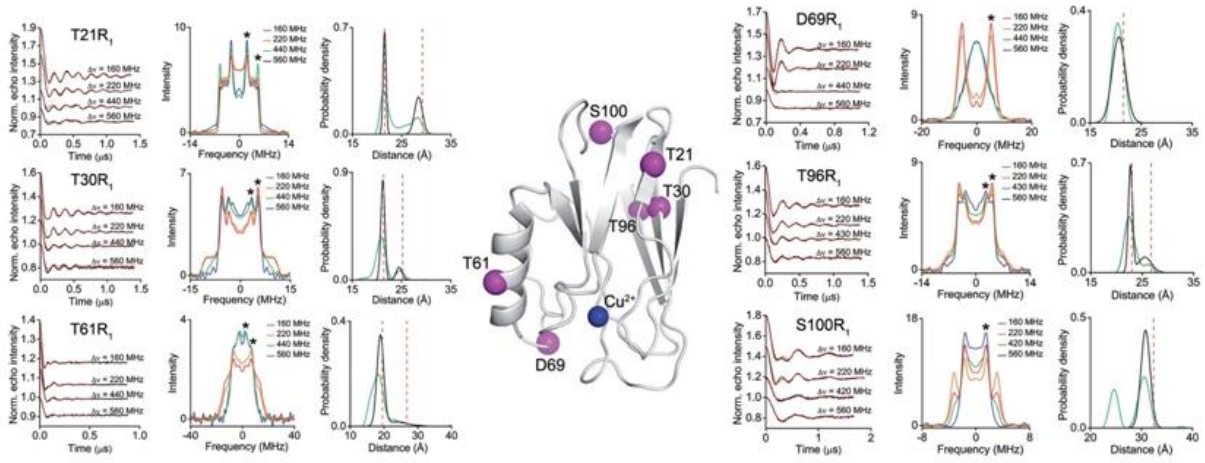

Figure 16: Middle: Structure of azurin showing the Cu^{II} as a blue sphere and the six MTSL labeling positions as pink spheres. Left and right sides: Left panel: X-band background-corrected PELDOR time traces (black) and their fits obtained with PeldorFit (red) for each mutant. The pump position was set on the maximum of the ED-EPR spectrum (nitroxide region) and four offsets were used for each mutant (detection in the Cu^{II} region). Middle panel: Frequency-domain spectra. The perpendicular component of the Pake doublet is indicated with an asterisk. Right panel: Distances obtained from the perpendicular component (dashed red lines), from Tikhonov regularization (green) and from PeldorFit (black). Adapted from [59]

Noteworthy, Double-Quantum Coherence (DQC), a single-frequency pulse sequence,[6] have also been used to measure Cu^{II}-Cu^{II} distances. DQC was more demanding than PELDOR in the case of Cu^{II}, but in a polyproline platform, a Pake pattern from which a peak at ±7.4 MHz could be safely attributed to an intramolecular dipolar interaction between the two Cu^{II} electron spins was obtained.[60] A Cu-Cu distance of 3.5 nm could also be measured in the Cu^{II}-EcoRI-DNA by division of two DQC traces recorded with two different pump pulses.[61]

2.1.2 Fe-S clusters

Fe-S constitute a very interesting target for pulsed EPR distance measurement as they are present in numerous enzymes where they are involved in electron transfer processes. For instance, PELDOR experiments have led to a better understanding of the interactions between multinuclear

metal clusters in the hydrogenase from *D. Vulgaris* Miyazaki F,[62] which contains two paramagnetic species in the oxidized state, a $[3Fe\text{-}4S]^+$ cluster and a [NiFe] center (both S = 1/2). Clear PELDOR oscillations were observed and the correct distance could be determined by taking into account the contribution of each individual spin to the total spin of the multimetallic centers. PELDOR was also used to identify which Fe-S was reduced during the catalytic cycle of pyruvate ferredoxin oxidoreductase (PFOR) by measuring the distance between the hydroxyethylidene-thiamine pyrophosphate radical (HE-TPP) and the Fe-S clusters.[63] The distance between Mo^V and the Fe^{III} heme center in human sulfite oxidase (SO) was also determined.[64,65]

2.1.3 Mn-tyrosyl measurements in the S_2 state of PSII

PELDOR measurements on high-spin Mn^{II}, studies involving the Mn-cluster in oxygen-evolving Photosystem II (PS II) in the dark-stable S_2 state (S = 1/2) and tyrosyl radicals have also been reported. A Y_D^+-Mn cluster distance of 2.71 nm could be measured using PELDOR[66] and an estimation of the distance between the Mn cluster and Y_Z^+ (1.5-2 nm) was also obtained.[67] These studies contributed to a deeper structural understanding of the PSII.

2.2 High-spin Gd^{III} complexes

The most widely used high-spin metal for PELDOR distance measurements is Gd^{III}. It has to be coordinated to a ligand and then grafted onto the studied system. The structures of these tags are depicted in Figure 17.

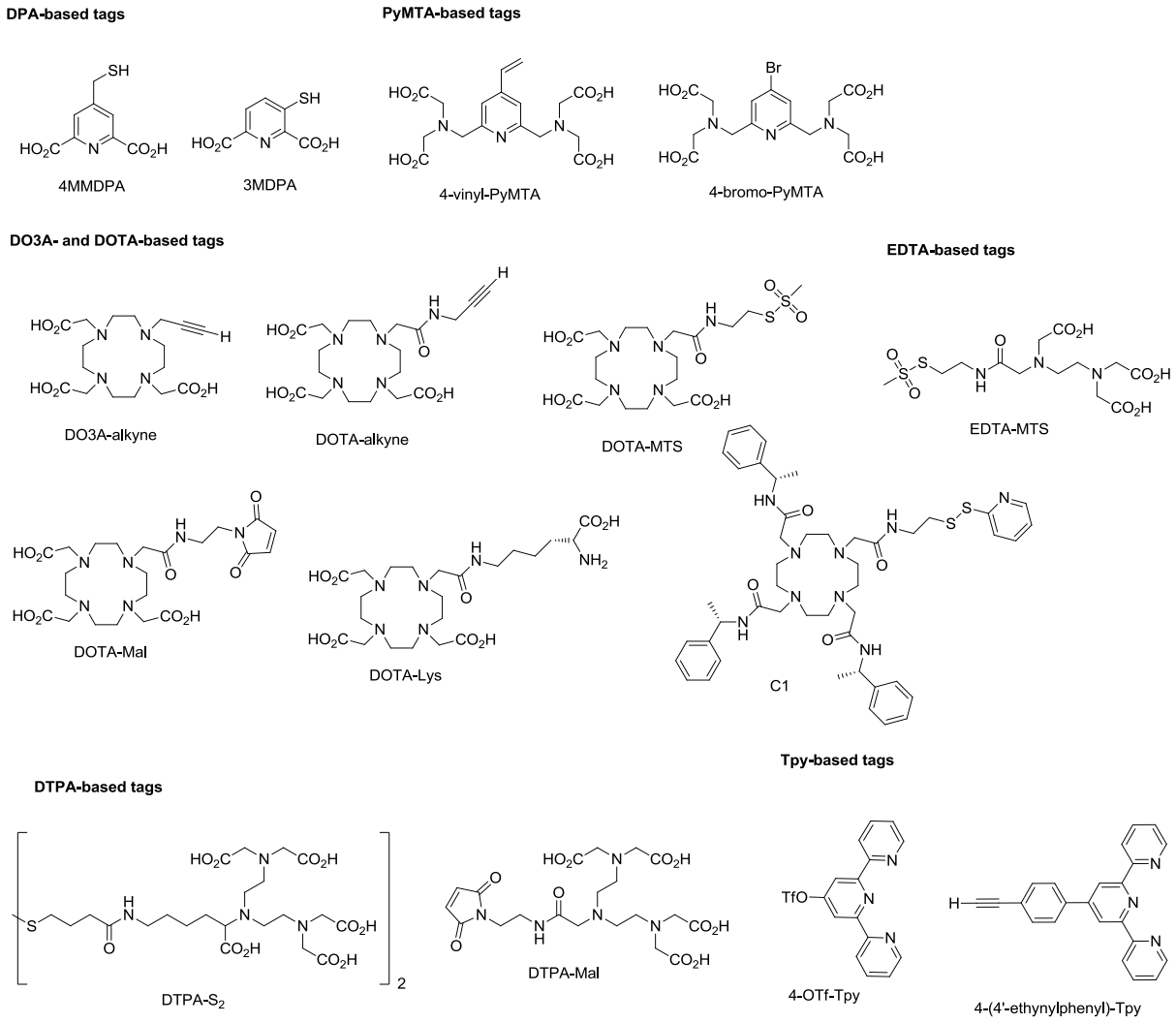

Figure 17: Commonly used ligands for Gd^{III} and Mn^{II} for spin-labeling cited in this chapter

Most of these tags, which contain a thiol, disulfide, maleimide or dithiopyridyl group, are designed to react with thiol groups to form a disulfide bond. In the case of DO3A- and DOTA-based labels, coordination with Gd^{III} is often performed before grafting, whereas the contrary occurs for other ligands. Coordination before grafting is advantageous to avoid the presence of free Mn^{II} or Gd^{III} in solution.

If the object of interest is a biomacromolecule, this spin-labeling method is mandatory for Gd^{III} complexes because Gd^{III} is not endogenous in biological environments. To the best of our knowledge, even if numerous proteins contain a native high-spin Mn^{II} center, there is no reported pulsed EPR distance measurement on such a protein: two identical Mn^{II} artificial tags have always been introduced.

2.2.1 PELDOR distance measurements between two GdIII complexes

2.2.1.1 Gd-Gd measurements on rigid models compounds

The very first PELDOR distance measurement between two Gd^{III} centers has been performed by the group of D. Goldfarb in 2007, at Ka- and W-bands.[21] The model system consisted of two Gd-PyMTA complexes linked with a rigid spacer: the key step of the synthesis was a double Sonogashira reaction between the tetra-*tert*-butyl ester of 4-bromo-PyMTA (Figure 17, p. 31) and *p*-diethynylbenzene (Figure 18). The central idea was that the sensitivity of the PELDOR method could be improved by using high-field spectrometers, but that this gain would be negligible in the case of nitroxides because the width of their EPR spectrum widens at high field, thus reducing the number of spins that are inverted by the pump pulse, which may also introduce orientation selection effects. By contrast, the central transition of Gd^{III} spin labels narrows at higher fields. Another advantage of Gd^{III}-based spin labels compared to nitroxides is their very short spin-lattice relaxation time (T_1 < 300 µs) that allow fast repetition rate, greatly increasing the SNR for a given experiment time. The negligible orientation selectivity of Gd^{III} complexes is also an appreciable feature that eases data analysis.

Shallow but clear PELDOR oscillations were observed that led to an estimation of the Gd-Gd distance of 2-2.05 nm, in quite good agreement with the 2.21 nm distance obtained from DFT calculations and the 2.11 nm distance obtained later from the X-ray structure.[68] However, the very steep decay of the PELDOR signal associated with the shallowness of the oscillations (λ = 1.9 to 3.6%) made the shape of the frequency-domain spectrum very sensitive to background removal, inducing artifacts in the distance distribution, which was also broader than expected for such a rigid system (Figure 16). The quick damping of the PELDOR modulations compared to a bis-nitroxide system with the same distance was also unexpected. An alternative explanation for these additional features could be the inherent higher complexity of high-spin systems. Nevertheless, the proof of concept that Gd^{III} spin labels could be suitable for high-field PELDOR was established. Compared to nitroxides at X-band, the sensitivity was actually better: the measurement time could be shorter (5-9 h *vs* 12 h) for a sample volume that was much lower (2 µL *vs* 50 µL).

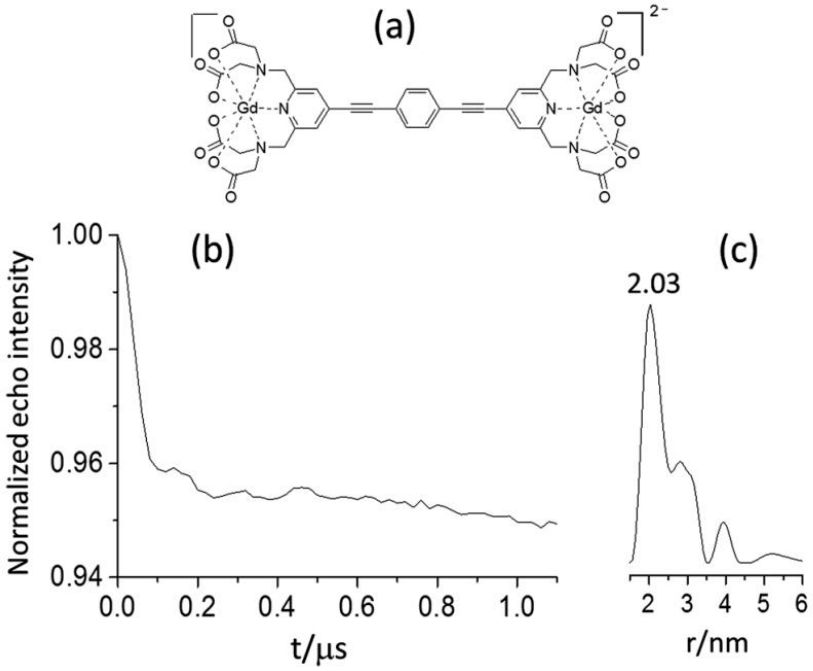

Figure 18: (a) Structure of the bis-Gd-PyMTA rigid model system. (b) W-band PELDOR time trace (25 K, pump pulse 16 ns, detection pulses 16 and 32 ns, offset 83 MHz). (c) Distance distribution obtained with DeerAnalysis. Adapted from [20]

The potential and specificity of Gd^{III}-based spin-labels was progressively unraveled over the years, and a complete study on a series of rigid compounds appeared only very recently.[34] A family of rigid systems with two Gd-PyMTA labels attached to a central oligo(phenylene-ethynylene) (OPE) linker of varying length, including a derivative of the bis-PyMTA compound shown above, was synthesized. The use of ethylene glycol chains on the OPE backbone was chosen to ensure good solubility in water-glycerol mixtures. Distances from 2.1 to 8.3 nm could be accurately measured at Q- and W-bands. However, for distances in the 2.1 – 2.9 nm range, the frequency-domain spectra showed severe distortions from the expected Pake patterns, which translated into broadened distance distribution profiles with satellite peaks, as observed before for the bis-PyMTA compound. For distances above 3.4 nm, clean distance distributions without spurious peaks could be obtained, but a broadening up to 0.4 nm was still observed (Figure 19).

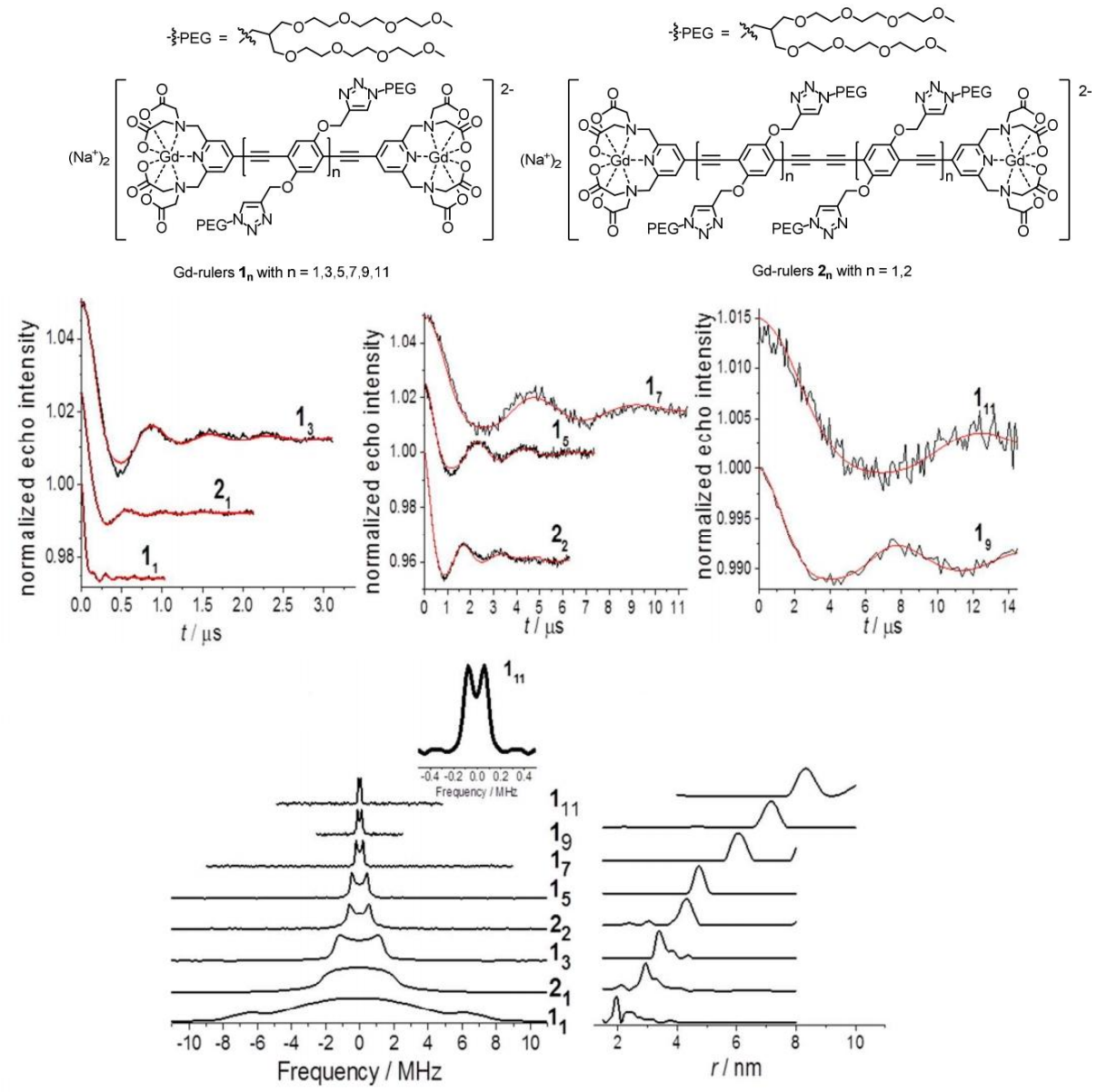

Figure 19: Structure of the rigid bis-Gd-PyMTA platforms (top), Background-corrected W-band PELDOR time traces (middle), Corresponding frequency-domain spectra (bottom, left) and distance distributions obtained with Tikhonov regularization (bottom, right). Conditions: D_2O/glycerol-d_8 7/3, 10 K. Adapted from [34]

The additional features of the distance distribution profiles could be attributed to the violation of the weak coupling approximation, which neglects the influence of the pseudo-secular term of the dipolar Hamiltonian. Data analysis is usually performed using DeerAnalysis,[33] a tool originally developed for nitroxide pairs. Gd^{III} complexes display two major differences with nitroxides: their spin is S = 7/2 compared to S = 1/2, which induces a zero-field splitting (ZFS) term in the spin Hamiltonian. For distances around 2 nm, the weak coupling approximation is fulfilled for nitroxide pairs, but not for Gd^{III}-based spin labels because of the overlapping of their central transition. This can be controlled by chemical design of the Gd^{III} complex by tuning the ZFS *D*-value as well as its distribution. Three cases can appear:

- For short distances, the distance distribution is broadened due to the pseudo-secular interaction, and does not reflect the real rigidity of the system. Ghost peaks are present, which does not have any real meaning.
- When the Gd-Gd distance increases, the pseudo-secular broadening decreases and ghost peaks disappear, but the distance distribution becomes larger because of the higher bending amplitude of OPE linkers. The observed distance distribution is the sum of these two contributions.
- As the distance becomes longer, the influence of the pseudo-secular term disappears. The distance distribution only reflects the intrinsic rigidity of the system.

Hence, the extra broadening from the pseudo-secular term hampers the assessment of the structure and conformation of the system in a large range of distances. Disentangling this contribution on the distance distribution profile from the one induced by the real flexibility of the system is a difficult task. Choosing a ligand with a specific *D*-value can tune this contribution, as it becomes stronger when the *D*-value is lower. Gd-PyMTA (D = 1150 MHZ) should be more appropriate for short distances than Gd-DOTA (D = 280 MHz).[34] In both cases, a large distribution of the *D*-values is essential for a successful measurement.

Another major conclusion of this study is that any effect of the pseudo-secular term should be negligible for investigations on biological systems, because Gd^{III}-based spin-labels are often attached with a flexible tether. The broadening of the distance distribution caused by the pseudo-secular interaction will be masked under the already large distance distribution.

As a transition between model systems and biological objects such as proteins, a platform consisting of two Gd-DOTA complexes (Figure 17, p. 31) linked by a flexible bridge was synthesized using a click chemistry reaction between the Gd complex of DOTA-alkyne and 1,4-bis(azidomethyl)benzene,[69] to obtain a primitive model for a protein tagged with two flexible Gd^{III} spin labels in which the distance is distributed over the 0.5-2.8 nm range. The complexity of high-spin systems was deeply analyzed in order to pave the way for further biological studies. As mentioned before, it was found that Gd^{III} complexes could be treated as an effective S = 1/2 system for such flexible geometries, thus easing data analysis. Even if the spin populations are distributed over numerous spin states compared to nitroxides, the resulting loss in sensitivity (lower modulation depth) is compensated by higher signal intensity and repetition rate. Additionally, shorter distances could be measured because of the possibility of generating shorter pulses and a large pump-probe offset.

In the context of Gd^{III}-spin-labeled biomolecules, the influence of the ZFS was considered, and it was surmised that systems with low *D*-values could be beneficial by reducing the width of the central transition, thus increasing the number of pumped spins for a given pump pulse length. This implies that the symmetry of the Gd^{III} complex, and hence of the chelator, has to be taken into account. It was also anticipated that Gd^{III} spin labels would be more suitable to measure distances on flexible systems like proteins, because the low number of PELDOR oscillations leads in itself to a broad distance distribution. This effect was rationalized later by introducing the pseudo-secular

contribution, as shown by Goldfarb *et al*.[34] Hence it was concluded that Gd^{III} and nitroxide centers, which do not exhibit a fast oscillation damping behavior, could be complementary spin labels.

These three studies are important milestones, as they encompass the scope and limitations of Gd^{III}-based PELDOR measurements. They have paved the way for further studies on Gd^{III}- or Gd^{III}/nitroxide-spin-labeled peptides and proteins, which will be presented in the next two parts, respectively. In addition, the optimal parameters for long-distance (above 6 nm) Gd^{III}-Gd^{III} measurements at Ka- and W-bands have been scrutinized.[70] In this context, the factors that affect the absolute PELDOR effect $\eta = \lambda V$ (where V is the echo intensity) must be carefully optimized. Contrary to short distance measurements, the observation frequency instead of the pump frequency should be applied at the maximum of the EPR spectrum. The optimal temperature at W-band was determined to be between 6 and 9 K, and this waveband was shown to be superior to the Ka-band: the higher the spectrometer frequency, the better the sensitivity. As expected, the use of short π-pulses also improves the absolute PELDOR effect.

To conclude, a recent promising report dealt with an original way to improve the sensitivity of Gd^{III} spin labels: the population transfer of the energy levels with frequency-swept passage pulses.[71] This resulted in a signal enhancement of the central line of the Q-band EPR spectrum of Gd-DOTA, Gd-PyMTA and Gd-DTPA by more than 80%. Gd-DOTA displayed the best results because of its low *D*-value. Combining this method with PELDOR distance measurement on two bis-Gd-PyMTA rigid model systems led to a more than 3 times higher modulation depth compared to standard monochromatic rectangular pulses. It must be emphasized that this pre-polarization technique using chirp pulses can be employed for every kind of pulse sequence and for distance measurements involving a Gd^{III} complex and a nitroxide center.

2.2.1.2 Gd-Gd measurements on biological objects

2.2.1.2.1 In vitro PELDOR

2.2.1.2.1.1 Gd-DPA-based tags

The first work on a Gd^{III}-labeled biological system was described by Goldfarb *et al*.[72] Two nitroxide MTSL labels as well as two derivatives of dipicolinic acid incorporating thiol groups (3-mercaptodipicolinic acid (3MDPA) and 4-mercaptopethyldipicolinic acid (4MMDPA), Figure 17, p. 31) were reacted with two cysteine residues (native or introduced by site-directed mutagenesis) of two proteins, p75ICD and τ_C14. PELDOR experiments on these six doubly-labeled proteins were performed at W-band to compare the relevance of nitroxide and Gd^{III} systems (Figure 20).

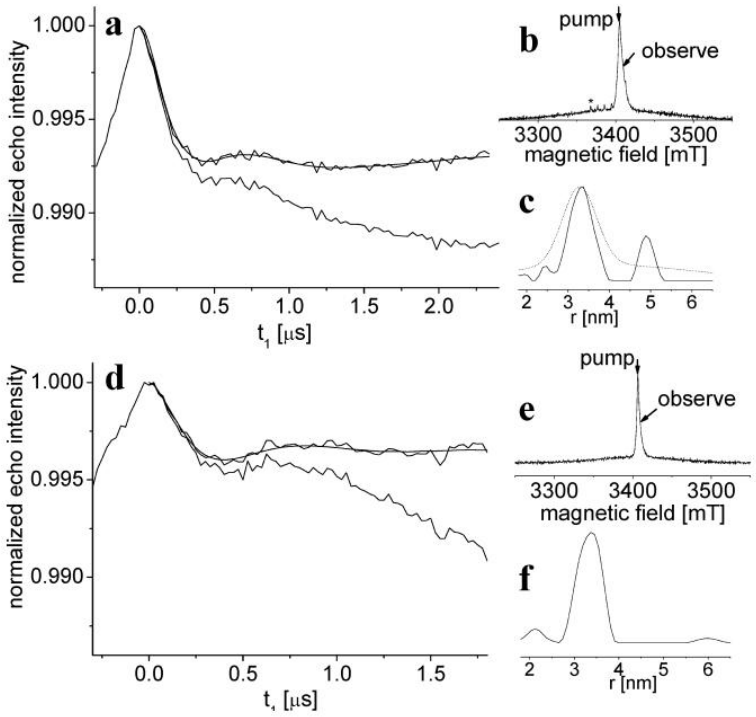

Figure 20: W-band PELDOR results from τ_C14 doubly labeled with Gd-4MMDPA (top) or Gd-3MDPA (bottom). (a) Time trace after (top) and before (bottom) background subtraction. Gaussian fit of the time-domain is also displayed on the top trace. (b) ED-EPR spectrum of τ_C14 doubly labeled with Gd-4MMDPA. The pump-detect strategy is indicated with arrows. (c) Distance distribution obtained with Tikhonov regularization (plain line) or Gaussian fit (dashed line). (d-f) Same as (a-c) but using Gd-3MDPA instead of Gd-4MMDPA. Conditions: ≈ 100 μM, 25 K. Adapted from [72]

For both proteins, the distance between the two Gd-DPA labels was found to be higher than the distance between the two nitroxide labels (2.9 nm *vs* 2.5 nm for p75ICD and 3.4 nm vs 2.5 nm for τ_C14) (Figure 21), which was attributed to a different orientation of the Gd/nitroxide tags relative to the protein backbone. Moreover, while no orientation selection was found for the MTSL-labeled p75ICD, a strong correlation was observed between the nitroxide labels of τ_C14, hampering straightforward distance extraction. Rotamer analyses gave distances in good agreement with experimental ones for the DPA-labeled proteins, taking into account the Gd-coordination of a neighboring Asp for p75ICD. The agreement was not as good for MTSL-labeled proteins, certainly due to hydrophobic bias.

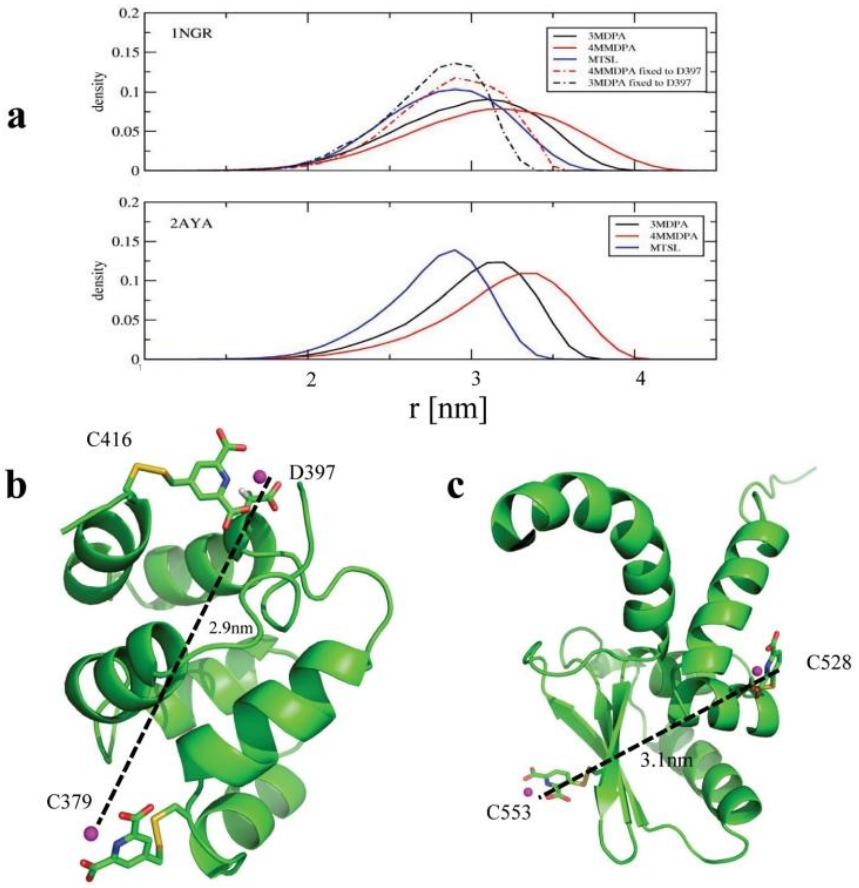

Figure 21: Distributions of Gd-Gd and nitrogen-nitrogen distances in p75ICD (INGR) and τ_C14 (2AYA) from rotamer analysis. (a) Distance distributions for p75ICD (top) and τ_C14 (bottom). Dashed-dotted lines take coordination of a neighboring Asp into account. (b) Cartoon of the NMR structure of p75ICD doubly labeled with Gd-4MMDPA. (c) Cartoon of the NMR structure of τ_C14 doubly labeled with Gd-3MDPA. Adapted from [72]

For the first time it was hypothesized that the lower experimental modulation depth than predicted for Gd^{III}-Gd^{III} PELDOR could arise from contribution of other terms than the secular term, as definitely assessed later.[34] This study clearly showed the relevance of Gd^{III} spin labels for distance measurements on biological systems.

This comparative work between nitroxide and Gd^{III}-based spin labels was later extended to mellitin, a common model for antimicrobial peptides.[73] A variant of this compound incorporating two Cys residues was labeled with two MTSL or two 4MMDPA tags. A Gd-Gd distance of 3.3-3.4 nm was measured from PELDOR experiments. The R = Gd^{III}:peptide ratio was found to be crucial (ideally 0.6-0.8) because excess Gd^{III} masked the PELDOR effect and too little Gd^{III} led to the formation of peptide dimers linked by a Gd^{III}. It was also shown that a temperature of 10 K was preferable to 25 K, which was unexpected because the central transition of the EPR spectrum is more intense at 25 K, leading to a higher experimental modulation depth λ_{exp}. The random flips of the pumped spins due to spectral diffusion was proposed as an explanation, so that the effective modulation depth is better at 10 K (Figure 22).

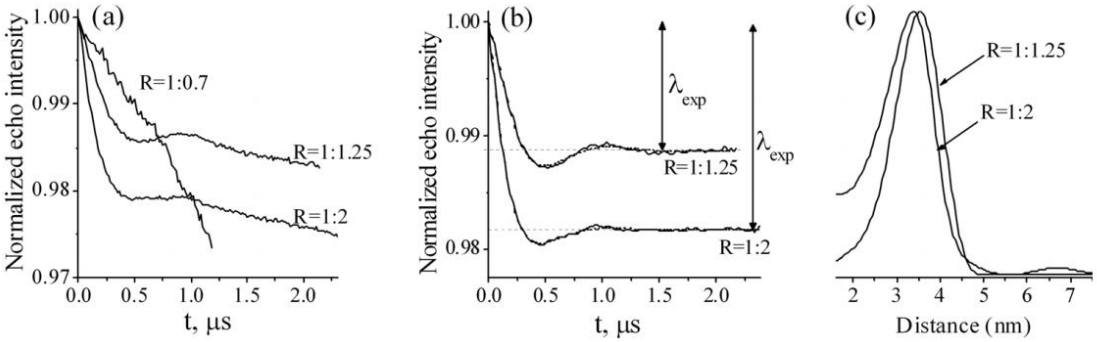

Figure 22: W-band PELDOR results on mellitin doubly labeled with Gd-4MMDPA. (a) Raw time traces (T = 10 K for R = 1:1.25 and 1:2, T = 25 K for R = 1:0.7). (b) Background-corrected traces, λ_{exp} = 1.2% for R = 1:1.25 and 1.7% for R = 1:2. (c) Corresponding distance distributions obtained with Tikhonov regularization. Adapted from [73]

Concerning the MTSL-labeled mellitin, distances of 2.2 nm (at X-band) and 2.5 nm (at W-band) were found, with some orientation selection at this waveband, as shown by the different distance distributions obtained for several positions of the detection and inversion sequences on the ED-EPR spectrum. The distance discrepancy between Gd^{III} and nitroxide tags was explained by the difference in conformation and orientation of these two labels, again showing that complementary information could be obtained.

The efficiency of Gd^{III}-Gd^{III} distance determination was further exploited to analyze the structural organization of a complex biological system, the green-absorbing proteorhodopsin (G-PR) hexamer in membrane-mimetic surfactant micelles.[74] Two mutants of this hexamer were tagged (on each subunit) with 4MMDPA or MTSL to assess how the interunit distances could contribute to the measured distance distribution. PELDOR results on the mutant that incorporate a Cys residue instead of the native Trp at position 58 are displayed in Figure 23.

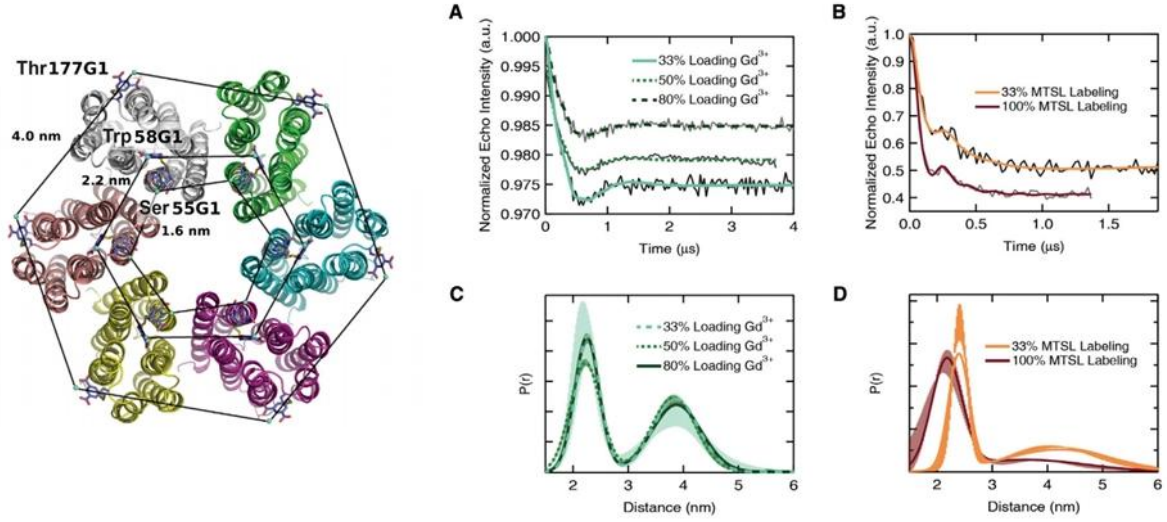

Figure 23: PELDOR results for the G-PR mutants at position 58. Left: structure of the G-PR hexamer showing the positions of the Gd-4MMDPA tags. Right: (A) W-band background-corrected time-domains of 4MMDPA-labeled G-PR for various Gd^{III} loadings. (C) Corresponding distance distributions using a two-Gaussian model. (B) and (D)

Same as (A) and (C) but for MTSL-tagged mutants at X-band. All fits are from a two-Gaussian model, and the shaded regions are the errors on the distance distribution obtained from different background subtractions. Adapted from [74]

The influence of the Gd^{III} loading was assessed, and as previously shown,[73] 80% per monomer gave the better results. Two dominant profiles in the distance distribution for the Gd-4MMDPA-labeled sample were observed, showing that the reliable extraction of the nearest neighbor and the next-nearest neighbor distances is feasible as the results agreed well with the crystal structure. For the MTSL-labeled sample, the next-neighbor distance was obscured due to the short phase memory time that hampered recording the time trace for a long dipolar evolution time. Moreover, the distance distribution varies significantly with the labeling amount. This proves that Gd^{III}-based spin labels are more adapted to multispin systems than nitroxides, again confirming their interest for high-field PELDOR measurements.

2.2.1.2.1.2 Gd-DO3A and Gd-DOTA-based tags

Measurements of longer distances are more demanding in terms of sensitivity. To improve the absolute PELDOR effect, the echo intensity as well as the modulation depth needs to be higher, and this can be achieved using Gd^{III} complexes with a lower *D*-value than the Gd-DPA compounds used in the work discussed above. To this aim, the previously described Gd-DOTA-alkyne as well as a Gd-DO3A-alkyne complex (Figure 17, p. 31) were clicked on the 5' end of an oligonucleotide, which was then annealed to form the corresponding Gd^{III}-labeled DNA duplexes (Figure 24).[75]

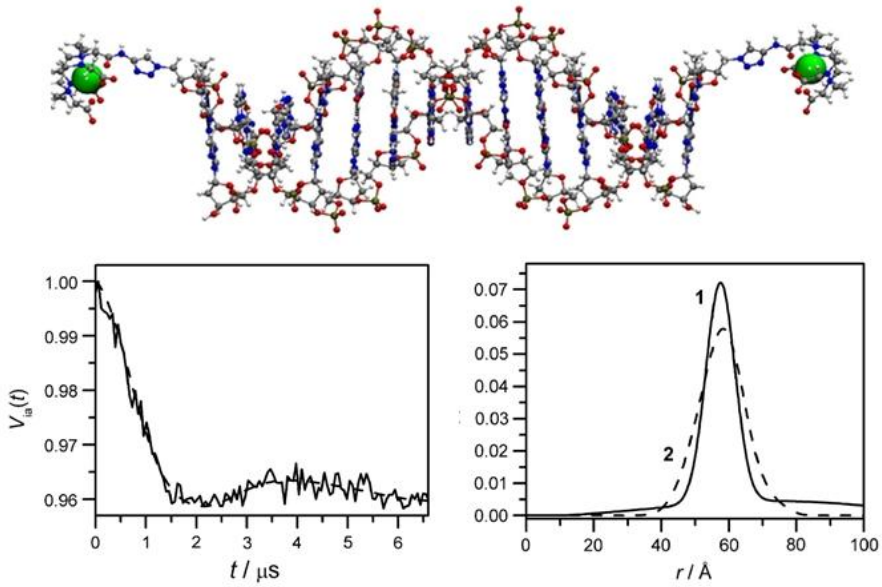

Figure 24: Top: Example of structure of DNA duplex doubly labeled with Gd-DOTA-alkyne. Bottom, left: Corresponding background-correected Ka-band time trace. The dashed line is the two-Gaussian fit. Right: Distance distribution using a two-Gaussian fit. The dashed line is obtained using MD simulations. Adapted from [75]

A Gd-Gd distance of 5.8 nm was determined at Ka-band for both spin labels, although the use of DO3A-alkyne was less convenient than DOTA-alkyne because of its larger *D* value, which needed a

much longer measurement time (16 h vs 1 to 4 h). An accurate background subtraction was performed because two samples at two different concentrations were employed. Detailed calculations indicated that for a given frequency, Gd^{III} tags could give a 4- to 16-fold improvement in sensitivity compared to nitroxide tags, as well as a decrease in measurement time by an order of magnitude for the same SNR.

This extension of the measurable distance range was further confirmed the same year[76] on two mutants of the homodimeric rat protein ERp29, grafted with the new Gd-DOTA complex C1 on two Cys residues (Figure 15). PELDOR measurements at W-band on these two doubly Gd-C1-tagged proteins revealed distances of 5.68 and 6.05 nm, in excellent agreement with the data extracted from the crystal structure and NMR experiments (Figure 25).

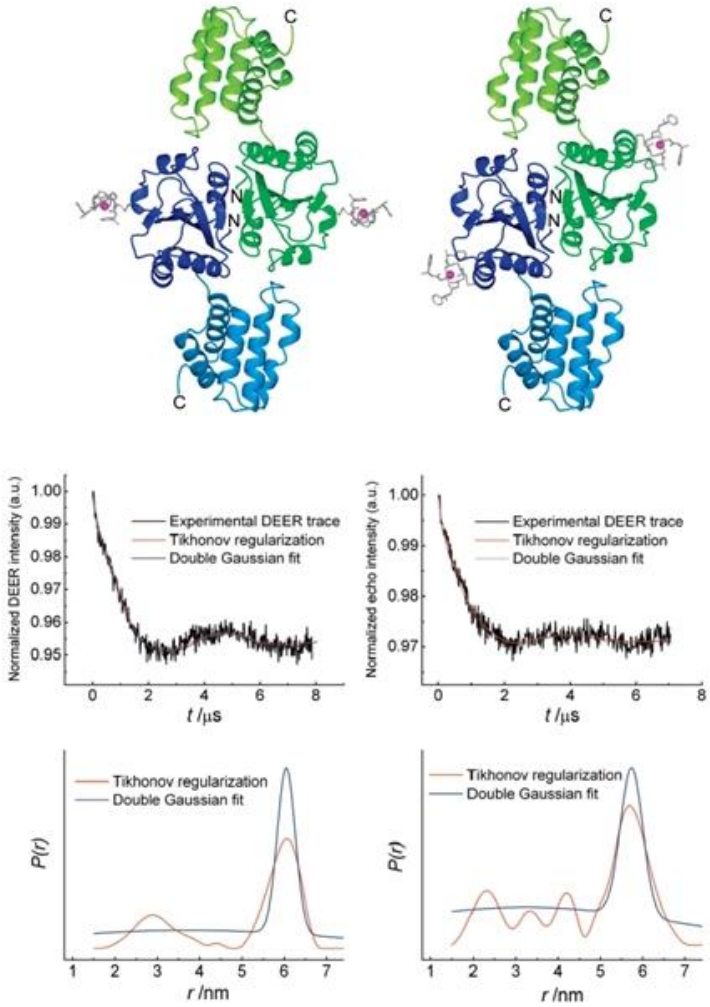

Figure 25: Top: Structure of the two ERp29 mutant dimers with the Gd-C1 tag at position 114 (left) or 147 (right). Middle: Corresponding W-band PELDOR background-corrected time traces with their fits. Bottom: Corresponding distance distributions (maxima at 6.05 nm, left; 5.68 nm, right) with their fits. Conditions: 10 K, 100 µM in 8:2 D_2O/glycerol-d_8. Adapted from [76].

The use of the bulky chiral Gd-C1 tag is responsible for this high precision, narrowing the distance distribution by a factor of two compared to MTSL-labeled proteins. Its bulkiness limits the

conformational freedom and its enantiomeric purity leads to only one position for the Gd^{III} ion, compared to standard DOTA tags that generate diastereomers with different average Gd positions when attached on a protein. These results confirmed the presence of the dimeric proteic structure in solution, and proved that Gd-DOTA-based PELDOR measurements are a powerful tool to assess the oligomeric states of large biological objects.

PELDOR measurements on model membrane systems were also reported.[77] Ala-Leu-rich WALP helical peptides with variable lengths were tagged at both ends at the Cys residue with Gd-DOTA-MTS (Figure 17, p. 31), Gd-C1 or MTSL and inserted into 1,2-dioleoyl-*sn*-glycero-3-phosphocholine (DOPC) vesicles. The end-to-end PELDOR distances were found to be quite different (3.1 nm for MTSL, 3.7 nm for Gd-C1 and 4.3 nm for Gd-DOTA-MTS, for the same peptide length) relative to the nature of the spin label, accounting for the different interaction with the membrane according to the differences in hydrophobicity of the tags. Additionally, the position of the labels with respect to the helix axis could be probed, because of the nonlinear distance variation expected for helical peptides (Figure 26). This kind of experiment is particularly interesting as it can provide structural information on transmembrane proteins, which are difficult to crystallize.

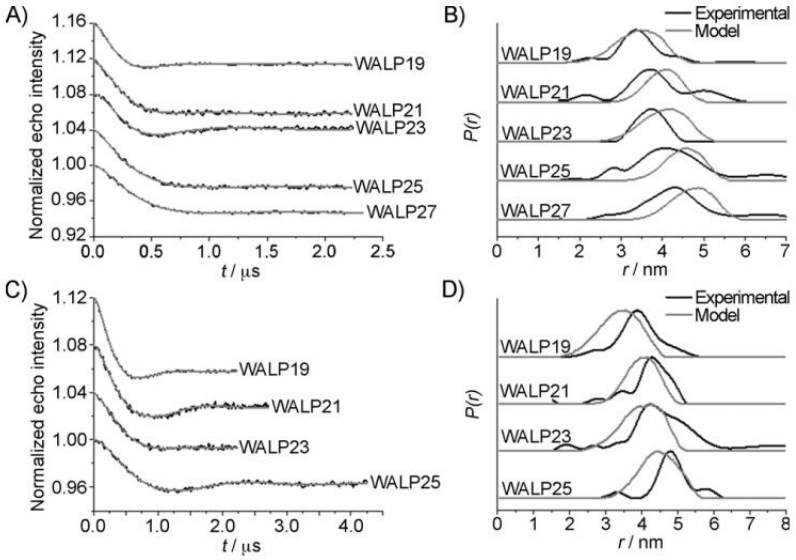

Figure 26: W-band PELDOR results obtained with doubly-labeled WALP peptides. A) Background-corrected time traces with their Tikhonov fits for the doubly-Gd-C1 labeled peptides. B) Corresponding distance distributions obtained with Tikhonov regularization (black) and rotamer analysis (gray). C) and D) Same as A) and B) but with Gd-DOTA-MTS instead of Gd-DOTA-C1. Adapted from [77]

2.2.1.2.2 In-cell PELDOR

2.2.1.2.2.1 Gd-PyMTA tags

The success of these experiments prompted researchers to tackle the more difficult task of performing a PELDOR experiment in a living cell. A 4-vinyl-PyMTA spin label (Figure 15) was attached at two Cys residues of a polyproline peptide,[39] which is known to adopt a relatively rigid PPII helix structure in aqueous solution. A rigid model system consisting in two PyMTA labels separated by a

rodlike stiff spacer, similar to the one used by Goldfarb *et al*,[34] was also designed. These constructs were coordinated with Gd^{III}, microinjected into *Xenopus laevis* oocytes and the Gd-Gd distance was measured at Q-band (Figure 27), after having established that the Gd-PyMTA label is intact (by monitoring its EPR signal) and does not affect the morphology of oocytes during a few hours. A distance of 3 nm, in agreement with what was expected, was determined for the rigid model compound both in cell and *in vitro*. The situation was different for the spin-labeled polyproline: a major peak at 3.5 nm was observed *in vitro*, while a bimodal distribution (two maxima at 2.6 and 3.8 nm) was determined in cell (Figure 27). This could suggest a partial change of conformation from a PPII to a PPI helix, indicating incorporation in the less polar environment of membranes.

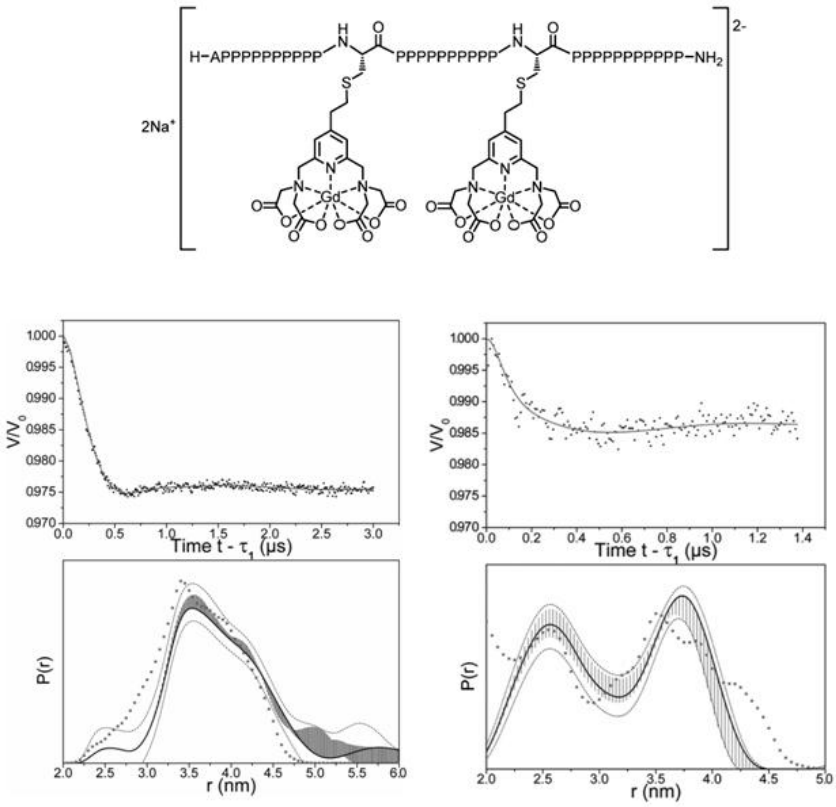

Figure 27: Top: Structure of the doubly-Gd-PyMTA-tagged polyproline peptide. Middle: Corresponding Q-band background-corrected PELDOR time trace in 7:3 D_2O/glycerol-d_8 (left) and inside *Xenopus laevis* oocytes after 1 h of incubation (right). Solid lines are Tikhonov fits. Bottom: Corresponding distance distributions in the deuterated buffer (left) and in cell (right). Errors bars are the full variation of the probability of given distances, dotted lines are errors on the distance distribution obtained from different Tikhonov fits, and squares are obtained from rotamer analysis assuming a PPII conformation (left) or a 10:9 PPI:PPII conformation (right). Adapted from [39]

2.2.1.2.2.2 Gd-DOTA-based tags

Another in-cell PELDOR distance measurement using Gd^{III} spin labels appeared the same year.[78] A mutant of human ubiquitin was tagged with a Gd-DOTA-Mal spin-label (Figure 17, p. 31) on two Cys residues and introduced into human HeLa cells through hypo-osmotic shock. The in-cell and *in vitro* Gd^{III}-Gd^{III} distance was identical (3.2 nm) as revealed by PELDOR measurements at W-band,

even if in-cell experiments displayed lower λ and SNR and required longer acquisition time (Figure 28).

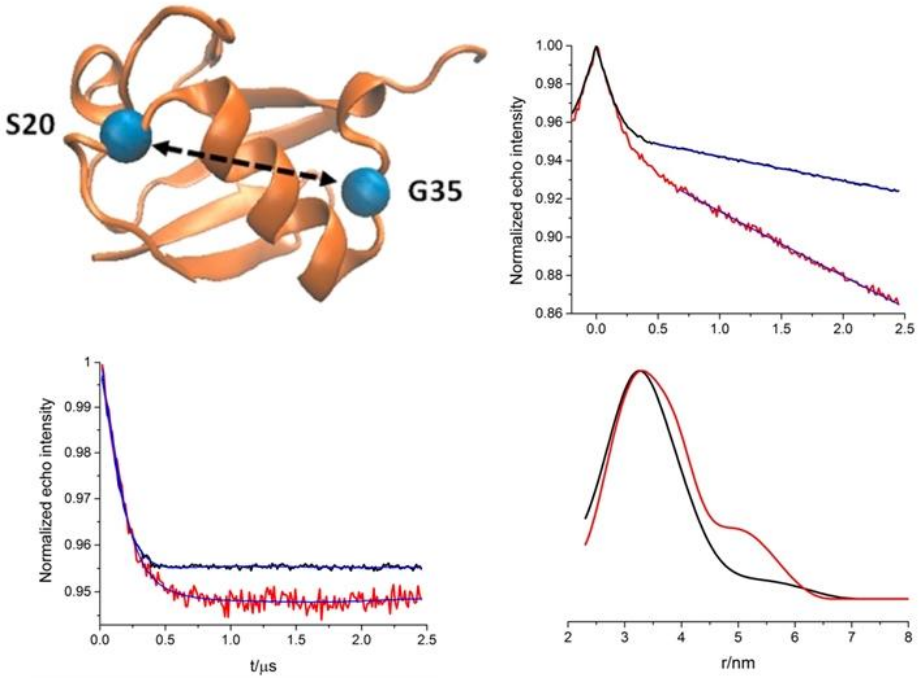

Figure 28: Top, left: Ribbon structure of ubiquitin showing the two mutation sites. Top, right: W-band PELDOR raw time trace of ubiquitin doubly labeled with Gd-DOTA-Mal (black: *in vitro*, SNR of 43 in 3 h; red: in cell, SNR of 11 after 18 h). Bottom, left: Background-corrected time traces. Blue lines are Tikhonov fits. Bottom, right: Corresponding distance distribution obtained with Tikhonov regularization. Adapted from [78]

Using Gd^{III} spin labels at high field has advantages compared to nitroxides, as they tolerate the reducing environment of the cell that converts nitroxides into EPR-silent hydroxylamines within hours. The sensitivity is much higher, and proteins could be studied at a concentration closer to the physiological one. Moreover, analysis of the background decay of the echo analysis gave insights into the localization and distribution of the protein in the cell. Hence, snapshots of a biomolecule during an aggregation process for instance could be obtained.

Another impetus to the development of in-cell PELDOR was reported very recently.[79] A novel strategy for attaching a Gd-DOTA label to the C5 position of uracil in a DNA duplex was designed, with spin-labeling in an internal position to extend the range of nucleic acid structures that can be studied using PELDOR. A iodohexyl tether was coupled to uracil and this building block was incorporated in the automated synthesis of two oligodeoxynucleotides. Conversion into azide and click chemistry using Gd-DOTA-alkyne (Figure 17, p. 31) was directly performed on the two resin-bound nucleotides. Q-band PELDOR was performed on the doubly-labeled DNA duplex, first in deuterated Tris-HCl buffer, where a mean distance of 4.8 nm was determined with a 2% modulation depth. The DNA duplex was then injected into *Xenopus laevis* oocytes. As reported by Drescher *et al*,[39] a reduction of the SNR was observed, as the T_2 is shorter than *in vitro*, where D_2O was employed instead of H_2O. The presence of endogenous Mn^{II} species, easily visible in the ED-EPR spectra, also contributes to the reduction of the SNR. The in-cell and *in vitro* distances were comparable (Figure 29), but a cytotoxic effect of the Gd-labeled DNA for the oocytes was observed, as shown by the

disruption of the vitelline membrane after one hour of incubation after injection. This might prevent investigations on a longer time scale.

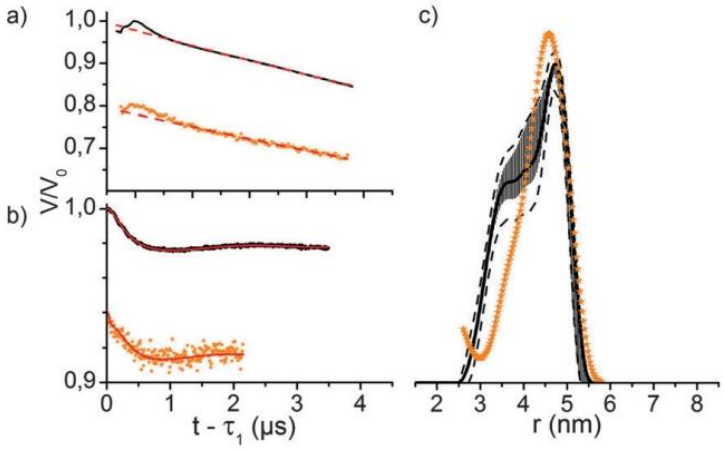

Figure 29: Q-band PELDOR results on the doubly-labeled DNA duplex (black lines, in buffer; orange lines: in oocytes after 15 min incubation). a) Raw time traces with background fits in dashed red lines. b) Background-corrected time traces with Tikhonov fits in red. c) Corresponding distance distributions obtained with Tikhonov regularization. Errors bars are the full variation of the probability of given distances and dotted lines are errors estimations corresponding to the mean value ± two times the standard deviation of the different Tikhonov fits. Adapted from [79]

2.2.1.3 Gd-nitroxide measurements

2.2.1.3.1 With Gd-Tpy or Gd-DTPA labels

The idea that the advantages of Gd^{III} and nitroxide spin labels could be combined was put into practice by the first Gd^{III}-nitroxide distance measurement in a model system at X- and Q-bands.[80] The rigid compound was synthesized through a Sonogashira coupling between 4-OTf-Tpy (Figure 17, p. 31) and a nitroxide attached to an OPE linker, followed by coordination with $GdCl_3$. Gd^{III} complexes display much larger transition probabilities and a much shorter T_1 than nitroxides: this almost independent detection of these two species was possible after optimizing the pulses and shot repetition times (SRT) (Figure 30).

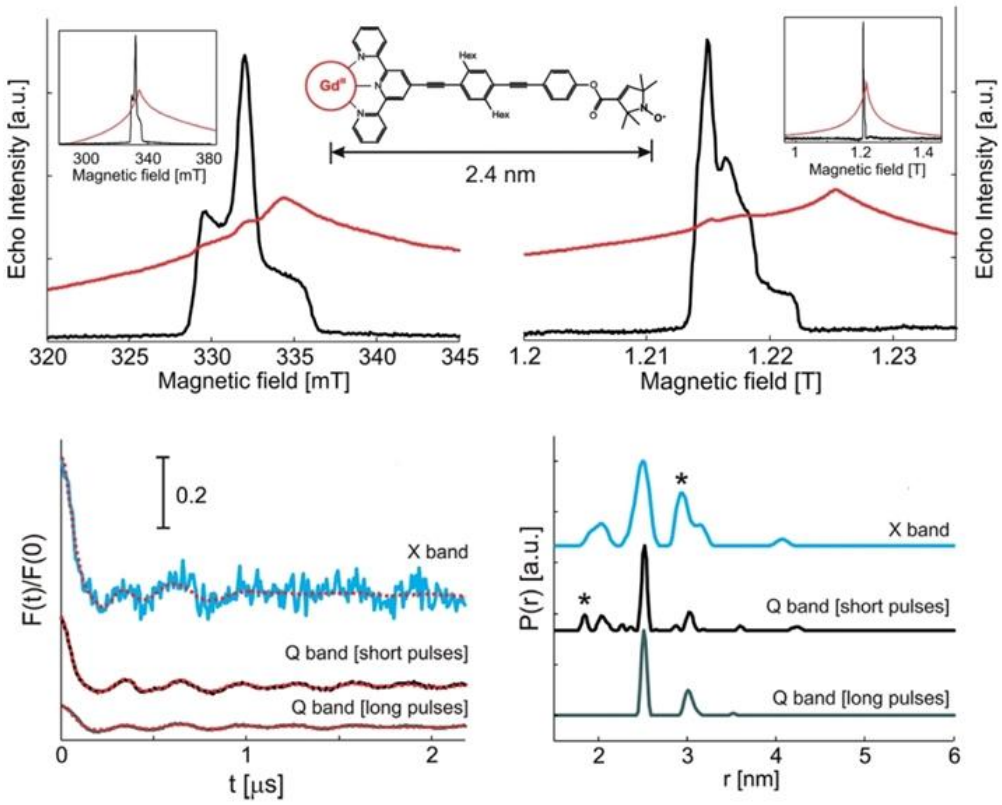

Figure 30: Top: ED-EPR spectra (left: X-band; right: Q-band) of the $TpyGdCl_3$-nitroxide compound (structure shown in center) optimized for the detection of the nitroxide (black, SRT = 16000 µs) or the Gd^{III} center (red, SRT = 337 µs). Bottom: X-band (cyan) and Q-band (black and green) PELDOR results. Left: Background-corrected time traces with Tikhonov fits in red. Right: Corresponding distance distributions obtained with Tikhonov regularization. Asterisks indicate artifacts due to ^2H modulation. Conditions: 10 K, 600 µM in Gd^{III}, SRT = 357 µs. Adapted from [80]

The pump pulse was set on top of the nitroxide spectrum to provide high modulation depth, and the detection position was set on the maximum absorption of Gd^{III} to minimize anisotropy and thus orientation selection effects. With this setup, narrow distance distribution profiles with a main peak at 2.54 nm were obtained at both X- and Q-bands. This value was in good agreement with the 2.43 nm obtained from the crystal structure of the analogous Cu^{II}-complex. The results also reflect the importance of the performance of the spectrometer. With a home-build spectrometer, short pump pulses could be generated, leading to a higher modulation depth (20%) than with the commercial spectrometer (6%) that could not accommodate such short pulses. Apparently, the origin of the satellite peaks in the distance distribution was not related to the negligence of the pseudo-secular term but rather to effects arising from excitation of other transition than the central one. This work highlights the interest of combining the advantages of nitroxides (high modulation depth) and Gd^{III} complexes (high signal intensity, short SRT and absence of orientation selection).

The selective measurement of Gd-Gd, nitroxide-nitroxide and Gd-nitroxide distances in the same object, taking advantage of the different spin physics of these spin labels, was put into practice in an original system.[81] Gold nanoparticles were synthesized and coated with the penta-*tert*-butyl ester of DTPA-S_2 (Figure 17, p. 31). Ligand exchange with a nitroxide tag containing a disulfide moiety

followed by deprotection of the ^{t}Bu groups and coordination with Gd^{III} generated nanoparticles that contained at their surface a mixture of Gd-DTPA and nitroxide labels, in which the distances between the tags could be independently and reliably measured at X- and Q-bands (Figure 31).

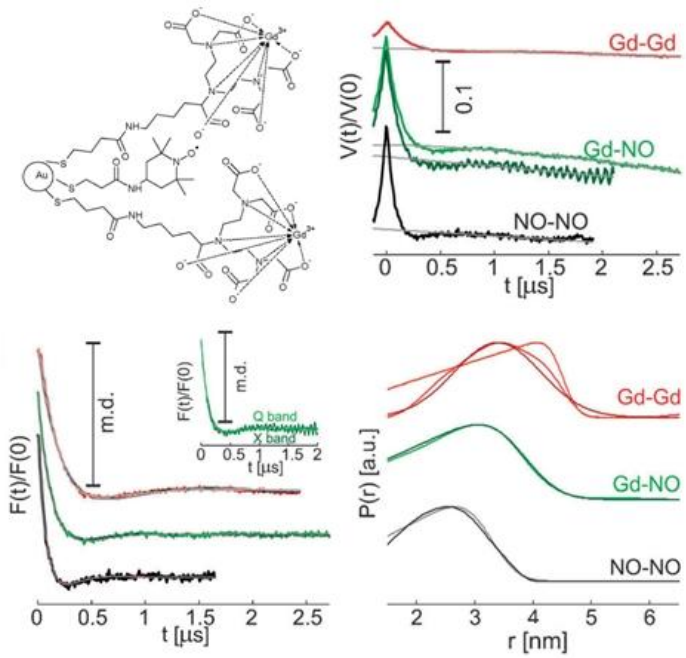

Figure 31: Top, left: Structure of the studied functionalized gold nanoparticles. Top, right: Raw PELDOR time traces with a 4% Gd^{III} loading for Gd-Gd pairs (red, Q-band), Gd-NO pairs (light green, Q-band; dark green, X-band) and NO-NO pairs (black, Q-band), with backgrounds in gray. Bottom, left: Background-corrected time traces normalized by the modulation depth (m.d.) with their Tikhonov fits in gray. Bottom, right: Corresponding distance distributions obtained with Tikhonov regularization (dark colors). Sphere surface fits are shown in intermediate color, and for Gd-Gd a Gaussian fit is shown in light red color. Adapted from [81]

A good correlation was obtained with models assuming a spherical distribution of the tags around the nanoparticle, except for the Gd-Gd distance. Moreover, it was shown that the pseudosecular term only caused minor distortions in the distance distribution. A useful correlation between the *D*-value and the Gd^{III}-nitroxide distance resolution of the PELDOR measurement was also established. This work can be seen as a proof of concept for selective measurements in nitroxide- and Gd^{III}-containing systems.

2.2.1.3.2 With Gd-DOTA labels

Combining the advantages of nitroxides and low *D*-value DOTA derivatives led to a handful of insightful studies. The concept of selective measurements between different paramagnetic species was also demonstrated on a double mutant of the ERp29 protein dimer.[82] A mixture of 25% doubly Gd-C1-labeled, 25% doubly MTSL-labeled and 50% MTSL/Gd-C1 labeled protein was employed, so that three different distances corresponding to Gd-Gd, Gd-NO and NO-NO pairs should be measurable. Optimizing the pulses and repetition rates led to selective measurements. W-band PELDOR measurements led to three different distances corresponding to those expected between the tags according to molecular modeling (Figure 32).

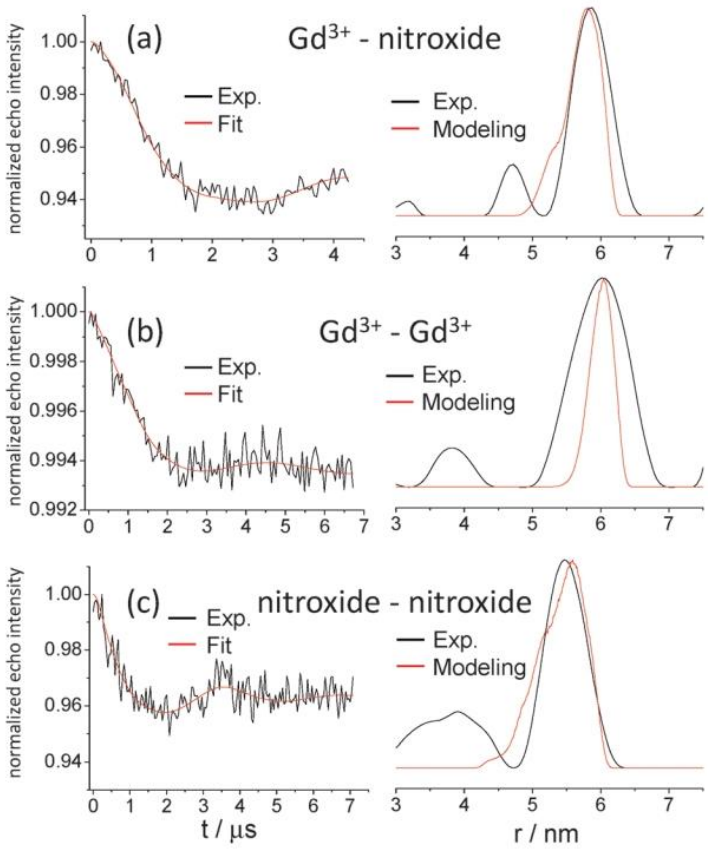

Figure 32: W-band PELDOR results on the mixed spin-labeled ERp29 dimers. Left: Background-corrected time traces (black) with their Tikhonov fits (red). Right: Corresponding distance distributions obtained with Tikhonov regularization (black) and molecular modeling (red). (a) Gd-NO pair, pump pulse 17.5 ns, repetition rate 5 kHz, 10 K. (b) Gd-Gd pair, pump pulse 15 ns, repetition rate 5 kHz, 10 K. (c) NO-NO pair, pump pulse 30 ns, repetition rate 0.2 kHz, 50 K. Sum of two traces with offsets of +65 and -65 MHz. Adapted from [82]

For the Gd-NO pair, the pump pulse was set on top of the nitroxide spectrum and little orientation selection was detected. To selectively measure the Gd-Gd distance, both the pump and detection frequencies were set outside of the nitroxide spectrum, and to extract the NO-NO distance, the measurement was performed at 50 K, were the Gd^{III} center contribution nearly disappears from the EPR spectrum. Orientation selection was taken into account by summing traces with two different offsets. This work extends the concept of spectroscopic selection of distance measurements in the 6 nm range.

More complex assemblies could also be studied. To simulate membrane proteins, a set of WALP peptides, incorporating a Gd-DOTA-Lys tag (Figure 17, p. 31) at the N-terminus and MTSL labels on Cys residues at variable positions, were embedded in DOPG vesicles.[83] Gd^{III}-nitroxide PELDOR measurements at X- and Q-bands revealed distances of 2 to 4 nm in accordance with the expected α-helical pitch of 0.54 nm (Figure 33). The nitroxide-nitroxide distance between the peptides could also be safely measured to give insights into the aggregation within the lipid bilayer, owing to the pulse settings that can spectroscopically select which paramagnetic center will be affected. This proves that useful information on the conformation of biological systems can be extracted knowing the distance thanks to the PELDOR method.

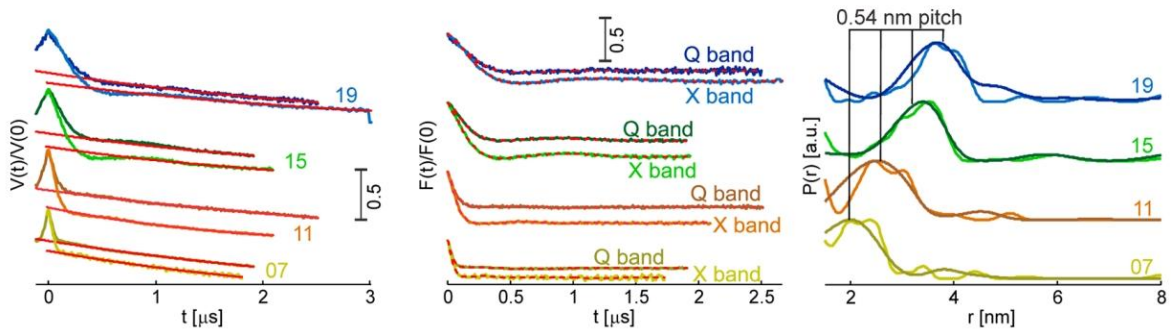

Figure 33: PELDOR results on the four doubly-tagged WALP peptides (light colors, X-band; dark colors, Q-band). Left: Raw time traces with backgrounds in red. Numbers correspond to the position of the nitroxide label. Middle: Background-corrected time traces with their Tikhonov fits indicated by dashed red lines. Right: Corresponding distance distributions obtained with Tikhonov regularization. Adapted from [83]

This concept of orthogonal spin labeling was further refined with the chemoselective site-specific spin-labeling of a T4 lysozyme (T4L) mutant.[84] A nitroxide radical with a hydroxylamine anchor was able to react specifically with a genetically encoded unnatural amino acid, *p*-AcPhe, while a Gd-DOTA-Mal or Gd-DTPA-Mal (Figure 17, p. 31) was grafted on a Cys residue. It was shown that a high buffer ionic strength greatly increased the modulation depth, which was attributed to nonspecific binding of the Gd complexes. An identical Gd^{III}-NO distance (3.8 nm) was obtained from PELDOR measurements with both Gd tags, albeit with a lower λ for Gd-DTPA, as expected from its lower *D*-value (Figure 34).

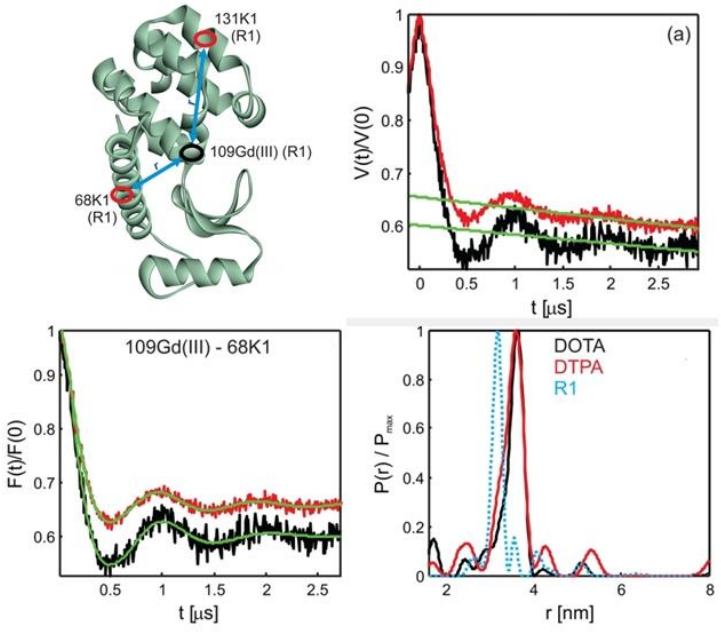

Figure 34: Top, left: Ribbon model of T4L showing the spin-labeled sites. Top, right: Raw Q-band PELDOR time traces for the 109C/68AcPhe T4L mutant incorporating a nitroxide moiety in position 68 and a Gd-DOTA (black) or a Gd-DTPA (red) in position 109. Backgrounds are shown as a green line. Bottom, left: Background-corrected time traces with their respective Tikhonov fit in green. Bottom, right: Corresponding distance distributions

obtained with Tikhonov regularization. The distance distribution obtained from a T4L mutant incorporating two MTSL-tagged Cys in the same positions in shown in dotted cyan. Adapted from [84]

A broad component can be observed in the distance distributions (see the shoulder in the distance distribution clearly seen for DTPA in Figure 32). It was tentatively assigned to some degree of protein misfolding, as it cannot be totally explained by the flexibility of the spin labels. The broad component was also present in the doubly-MTSL-labeled sample, and the mean distance was shorter, as observed by Goldfarb *et al*. Interestingly, the SNR could be optimized by tuning the flip angle of the pump pulse.

As no pseudo-secular interaction could be observed during Gd-NO PELDOR measurements, they appear to be an efficient tool to probe the real rigidity of a system. To confirm it, the shape persistence of a series of PPII octadecamers helices incorporating a Gd-DOTA tag at the N-termini (introduced as a tri-^{t}Bu-protected DOTA) and a MTSL every nanometer was probed. Because of the complete decay of the Q-band dipolar PELDOR modulations, the shape of the distance distribution could be safely interpreted in two solvents (trifluoroethanol (TFE) and 7:3 H_2O/glycerol).[85] An increased broadening of the distance distribution with the Gd-NO distance was observed, which could be traced either to backbone flexibility of the PPII helix or the occurrence of *cis* amide bonds (Figure 35). These two contributions were disentangled using Monte-Carlo simulations and led to an upper limit of 2% and 0% of *cis* amide bonds in TFE and 7:3 H_2O/glycerol, respectively. This confirms the attractiveness of PPII as molecular rulers as they display a high degree of rigidity, and the potential of Gd-NO PELDOR to evaluate the flexibility of shape-persistent macromolecules.

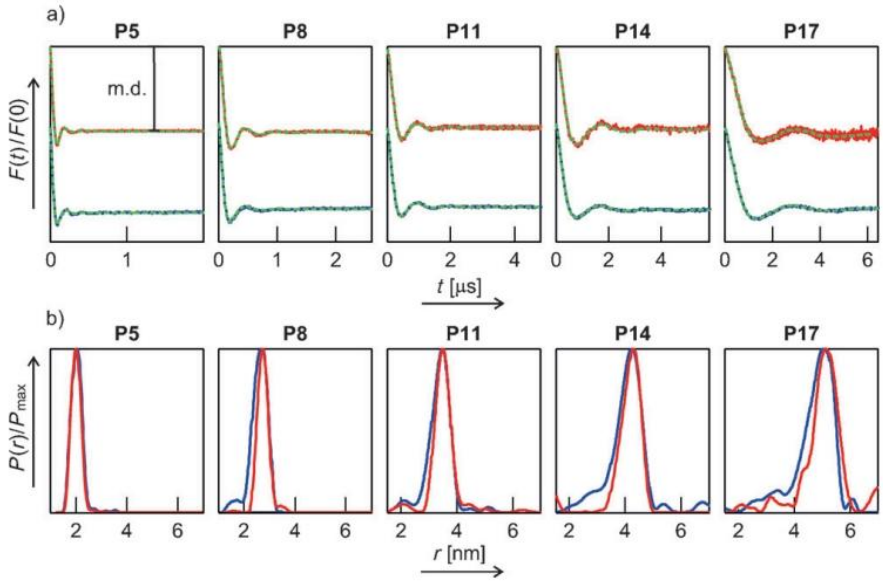

Figure 35: Q-band PELDOR results on the spin-labeled polyprolines. A) Background-corrected time traces (red, in TFE; blue, in 7:3 H_2O/glycerol) with their Tikhonov fits in dotted green. B) Corresponding distance distributions obtained with Tikhonov regularization. Adapted from [85]

Meanwhile, a new impetus was given to Gd^{III}-nitroxide measurements with the realization of a W-band dual mode cavity[86] that unraveled the full potential of Gd^{III} spin labels. Using the previously studied ERp29 mutant labeled with a Gd-C1 complex and a MTSL tag, this new setup allowed setting

the pump pulse to the local maxima (g_x, g_y and g_z) of the nitroxide and the observe pulse to the maximum of the Gd^{III} spectrum, which are about 700 MHz apart. This resulted in a dramatic improvement of the SNR, while a dipolar evolution time up to 12 µs could be observed, implying that distances up to 8 nm and above could be measured. Because of the resolved orientation selection, the orientation of the interspin vector relative to the axis system of the nitroxide *g*-tensor was obtained, providing useful structural information (Figure 36). This procedure is much easier on a Gd^{III}-nitroxide pair than on a bis-nitroxide system, where five angles instead of two have to be determined.

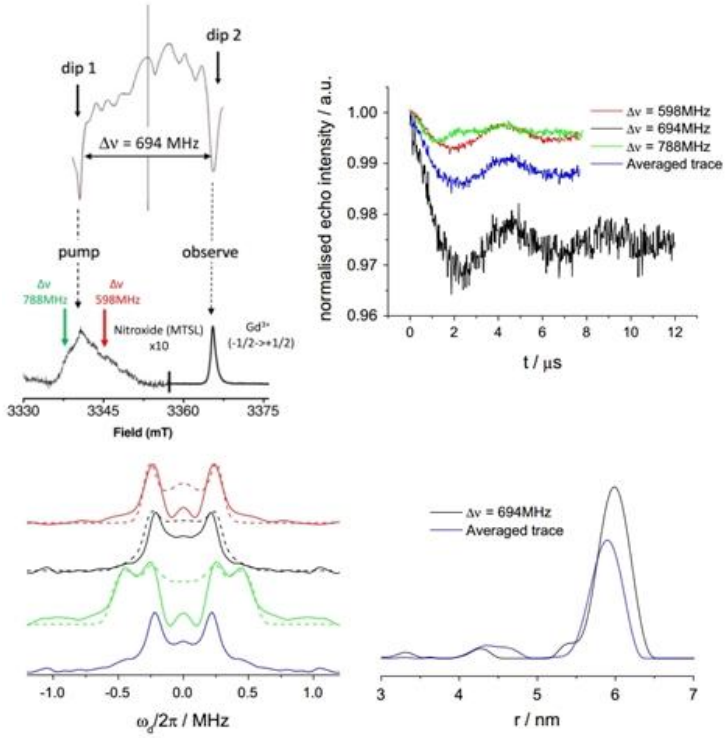

Figure 36: Top, left: Characteristic tuning curve of the dual-mode cavity along with the EPR spectrum of the doubly-labeled ERp29 mutant. Top, right: W-band background-corrected PELDOR time traces with different offsets. Bottom, left: Corresponding frequency-domain traces with their Tikhonov fits as dashed lines. Bottom, right: Distance distributions obtained with Tikhonov regularization. Adapted from [86]

To conclude, PELDOR distance measurements between a Gd^{III} center and a nitroxide are very promising for several reasons: the Gd^{III} center brings high echo intensity, abolishes orientation selection and allow fast repetition rates, while the nitroxide gives a deep modulation depth. No pseudo-secular contribution was observed because the two spin labels are different. The resulting high SNR is very profitable and turns PELDOR into a powerful tool to explore the structure of numerous biomacromolecules. The spectroscopic selection between these two spin labels associated with the development of spectrometers with a dual mode cavity foreshadows further insightful developments.

2.2.2 RIDME

Only report about Gd^{III}-Gd^{III} distance measurements that do not use PELDOR have been released. The relaxation-induced dipolar modulation enhancement (RIDME) pulse sequence[6] was successfully applied at W-band to extract the Gd-Gd distance (3.5 nm) on a rigid model system with two Gd-PyMTA labels connected to a central OPE linker, as described previously.[87] Modulation depths up to ten times higher compared to PELDOR were observed, even if the removal of the background decay was much less straightforward.

This considerable amount of results indicated that pulsed EPR-based distance measurements using Gd^{III} spin labels are an active and successful field of research. A recent perspective article[35] reviewed these findings.

2.3 Mn^{II} complexes

Compared to Gd^{III}-based tags, Mn^{II} spin labels have been much less studied. Nevertheless, they display some advantages, notably in a biological perspective (ref int). Like Gd^{III}, the sensitivity of Mn^{II}-based pulsed EPR methods could be improved by population transfer from the -5/2 and -3/2 levels to the -1/2 level using a rapid magnetic field sweep under *mw* irradiation.[88] This led to a 25-30% enhancement of the ED-EPR spectrum of Mn^{II}-doped MgO. So far, all reports involving Mn^{II} spin labels rely on the PELDOR method.

2.3.1 Mn-Mn distance measurements

The first report of a Mn^{II}-Mn^{II} distance measurement was released a few years ago.[22] The two Cys residues of the p75DD neurotrophin receptor were tagged with EDTA-MTS (Figure 17, p. 31) and loaded with Mn^{II}. The ED-EPR spectrum shows a broad central transition with a poorly resolved six-line hyperfine pattern, superimposed with sharp spikes that arise from a very low amount of free (hexaaqua) Mn^{II}. The broadness directly arises from the very large *D*-value (3000 MHz) of Mn-EDTA (Figure 37).

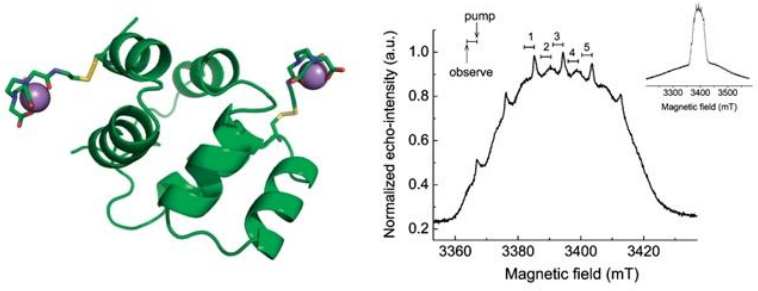

Figure 37: Left: Ribbon structure of the doubly-labeled p75DD. Right: Its ED-EPR spectrum showing the pump-detect strategy. Conditions: 10 K, 0.1 mM in 20 mM pD 7 HEPES buffer in 8:2 D_2O/glycerol-d_8. Adapted from [22]

PELDOR measurements at W-band were performed at five different pump-detect combinations with the same 75 MHz offset and revealed a Mn-Mn distance of 3.2 nm, in excellent

agreement with molecular models. However, there was room for optimization. The observed modulation depth was very low (0.4 %) because of the very shallow PELDOR modulations, giving rise to well-defined but noisy Pake doublets (Figure 38).

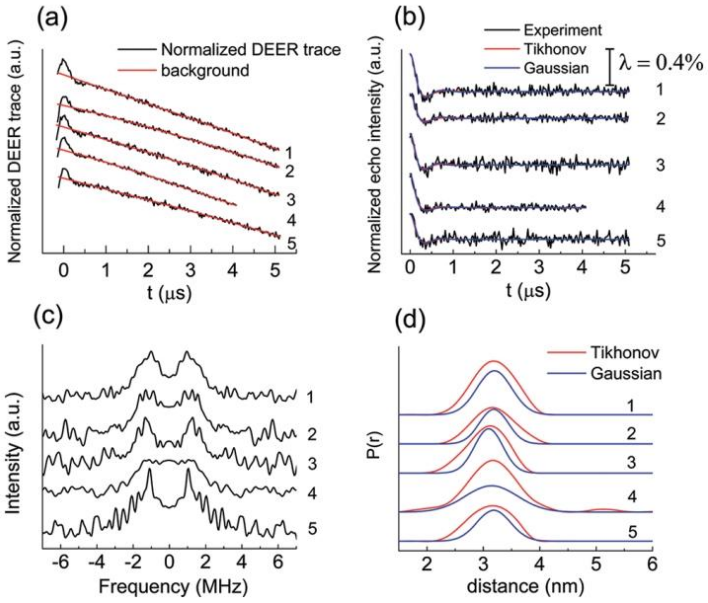

Figure 38: W-band PELDOR results on the doubly-labeled p75DD. (a) Raw time traces with backgrounds in red. (b) Background-corrected time domains with Tikhonov (red) and Gaussian (blue) fits. (c) Corresponding frequency domains. (d) Distance distributions obtained with Tikhonov regularization or Gaussian fit. The numbers of the traces correspond to the positions on the EPR spectrum on Figure X. Conditions: 10 K, pump pulse 15 ns, detection pulses 30 and 60 ns, repetition time 1 ms, acquisition time 7 to 12 h. Adapted from [22]

The lowered modulation depth was expected because of the Mn^{II} hyperfine interaction that splits the central transition into a sextet, thus dividing the modulation depth by a factor 6 compared to a Gd^{III} tag with the same *D*-value, even if the lower spin multiplicity of Mn^{II} can result in as much as a twofold increase of the population of the central transition. It has been postulated that systems with lower *D*-values could result in better sensitivity. This hypothesis is the central idea of this thesis: the design of Mn^{II} complexes with low *D*-values depend on the geometry of the coordination sphere and the screening of various ligands, based on the EPR spectrum and *D*-values of the corresponding Mn^{II} complexes, will be detailed in the first chapter of this manuscript.

2.3.2 Mn-nitroxide measurements

The first Mn^{II}-nitroxide PELDOR measurement was reported by our collaborators in Frankfurt.[89] A Mn^{II}-bisTpy model system was synthesized using a Sonogashira coupling between 4-(4'-ethynylphenyl)-Tpy (Figure 17, p. 31) and a nitroxide attached to a iodobiphenyl spacer, followed by coordination with $TpyMnCl_2$ (Figure 39). As shown for Gd^{III}-NO measurements, the spectroscopic selectivity between Mn^{II} and NO can be achieved, even if the I = 5/2 spin associated with the sensitivity loss induced by the splitting of the central transition are more demanding. The ED-EPR spectra of the Mn^{II}-NO compound are depicted in Figure 39.

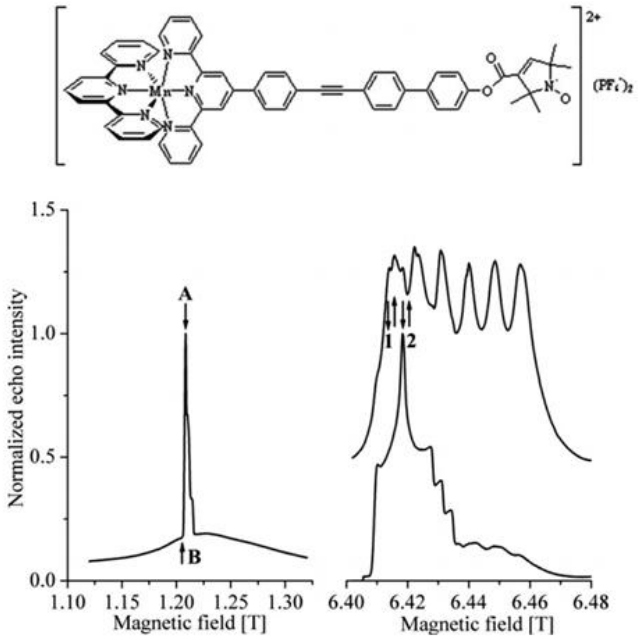

Figure 39: Top: Structure of the Mn^{II}bis(Tpy)-NO model compound. Bottom: its ED-EPR spectra at Q-band (left) with settings optimized for Mn^{II} at position B and at G-band (right) with settings optimized for Mn^{II} at one of the central hyperfine lines (top) and for the nitroxide at its maximum absorption (bottom). The pump-detect strategy is indicated with arrows and numbers. Adapted from [89]

At Q-band, despite the much shorter T_1 of Mn^{II}, the nitroxide signal is still present on the EPR spectrum. The large ZFS parameters of Mn^{II}-bis(Tpy) complexes are highlighted by the unresolved hyperfine Mn^{II} sextet at this waveband. This is not the case at G-band, and the Mn^{II} or nitroxide contributions can be distinguished by optimizing the pulse length and the repetition rate, as demonstrated for Gd-NO systems. Q-band PELDOR measurements led a modulation depth of 2% when pumping on the nitroxide and detecting on the Mn^{II} compared to 11% when the pump-detect combination was reversed, with 90 MHz offset in both cases. Pronounced oscillations were recorded in both cases, which corresponded to a distance of 2.7 nm with a very narrow distribution, in accordance to what was expected from the crystal structure of similar compounds. Negligible orientation selectivity was observed at this waveband because of the broad distribution of the ZFS parameters (Figure 40).

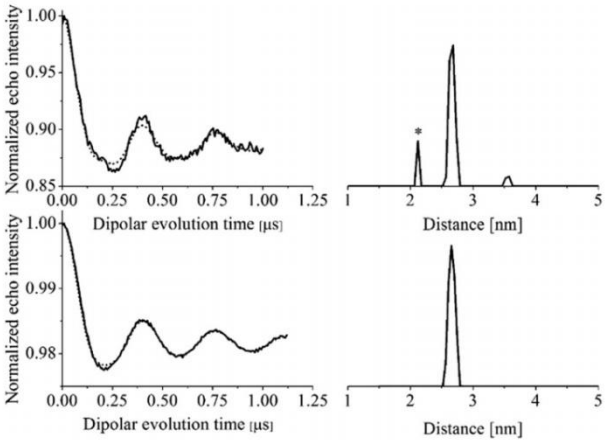

Figure 40: Q-band PELDOR results with the pump pulse set at position A (top) or B (bottom) in Figure 22. Left: Background-corrected time traces with their Tikhonov fits in dotted lines. Right: Corresponding distance distributions obtained with Tikhonov regularization. The ghost peak marked with as asterisk likely arise from nuclear modulation effects. Adapted from [89]

Noteworthy, orientation selection was noticeable at G-band when pumping on the nitroxide and detecting on the Mn^{II}: this prevented direct distance extraction using DeerAnalysis. The dipolar oscillations strongly depend on the position of the pump pulse and could be adequately fitted by simulations. This work showed that measurements on Mn^{II}-NO systems are as attractive as Gd^{III}-NO systems and even more if one envision biological applications.

Accordingly, Mn^{II}-NO PELDOR was recently employed to identify a Mn^{II} binding site in a RNA derived from hairpin 92 of the 23S ribosomal RNA (HP92).[90] Two RNAs were singly-labeled with a nitroxide moiety at positions 3 and 31 (RNA3 and RNA31, respectively) and a doubly-labeled RNA (RNA3,31) was also synthesized (Figure 41). W-band measurements on this construct, without adding Mn^{II}, gave a broad distance distribution with a maximum at 4.5 – 4.9 nm. The orientation selection was assumed to be negligible owing to the similarity between three traces recorded at different detection positions because of their large width (Figure 41).

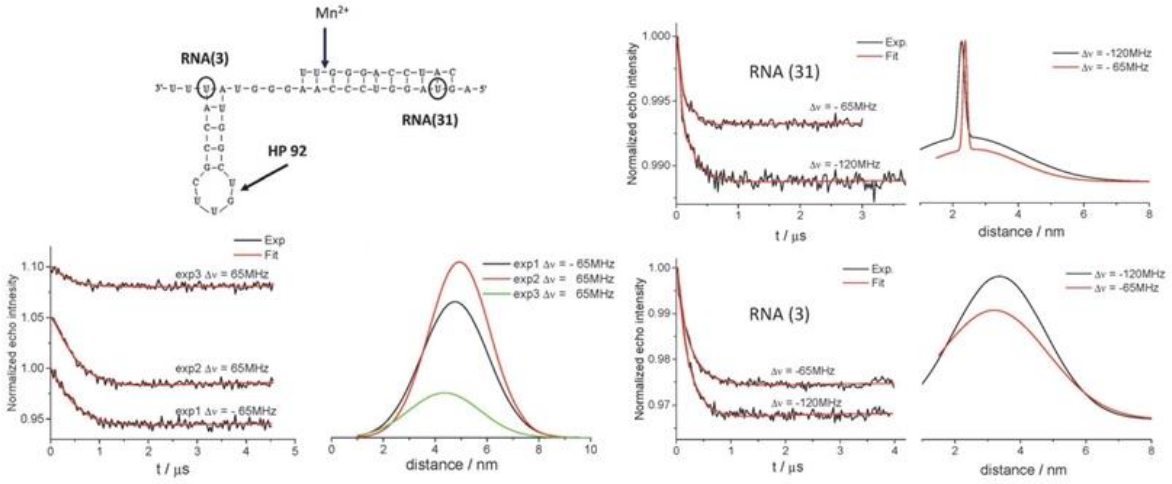

Figure 41: Left: Structure of the studied RNA construct with labeling positions (top) and W-band background-corrected PELDOR time traces for RNA3,31 and corresponding distance distributions. Right: W-band PELDOR results for the RNA31 (top) and RNA3 (bottom) with equimolar amounts of Mn^{II}. Time traces are obtained and distance distributions are fitted using single (for RNA3,31 and RNA3-Mn^{II}) or double (for RNA31-Mn^{II}) Gaussian fits. Adapted from [90]

The singly-labeled RNAs were then mixed with equimolar amounts of Mn^{II}. Using appropriate pulse settings, the modulation depth could be optimized. For RNA31-Mn^{II}, a narrow distribution superimposed on a broad one was observed, while for RNA3-Mn^{II} only a broad distribution could be seen. This shows that either non-specific Mn^{II} binding takes place or the constructs are very flexible. However, the narrow peak observed for RNA31-Mn^{II} suggests that a specific binding site in the 5' extension could exist, along with a non-negligible amount of free Mn^{II} in solution that would explain the low modulation depth. This work proves that Mn-NO PELDOR is a useful tool for localizing paramagnetic species in biological systems.

All these results proved that the potential of Mn^{II} as a high-field PELDOR spin-label for distance measurements has been underestimated and that it stands out as a useful tool for the structural elucidation of biological systems. Noteworthy, Mn^{II}-nitroxide measurements at high field do not require a dual-mode cavity, unlike Gd^{III}-nitroxide systems. This prompted us to investigate the use of Mn^{II}-based spin labels with low *D*-values to perform PELDOR measurements with an improved sensitivity.

3. AIM OF THE PROJECT

The purpose of this PhD thesis is to use Mn^{II} complexes as paramagnetic centers for high-field PELDOR distance measurements. This will be realized in several steps: first, an ideal Mn^{II} complex has to be found. Crucial parameters are to be considered:

- The Mn^{II} complex must display narrow HFEPR lines, such as what is observed for $Mn(H_2O)_6^{2+}$. Hence, a high modulation depth would be obtained when pumping on top of a hyperfine line or the echo intensity would be maximized by detecting on top of a hyperfine line. This means

that we need a Mn^{II} complex with a low *D*-value. The relationship between the ZFS and the coordination sphere is complex, but it is well-known that a symmetrical environment is to be preferred, like the octahedral coordination of $Mn(H_2O)_6^{2+}$.

- The corresponding ligand must have a high affinity for Mn^{II}, to ensure that no unspecific binding will take place.

- This ligand must be easily graftable, either on a protein or on a synthetic model system.

Once a relevant candidate is found, a model system will be designed for an in-depth study of the parameters that govern the success of a Mn^{II}-Mn^{II} PELDOR distance measurement. The model platform will thus be constituted of two Mn^{II} complexes linked to a central spacer. The critical parameters for this spacer are:

- An intrinsic rigidity, in order to have a constrained distance between the two Mn^{II} centers. This is more convenient to predict the distance using DFT or X-ray crystallography. A unidirectional linker would be more appropriate as it is more easily synthesized.

- An incrementation possibility, in order to have access to a set of different sizes to probe the accessible distance range (1.8 to 8 nm).

- A possibility of desymmetrization, *i.e.* the introduction of two different end groups to assess the influence of two different paramagnetic centers.

- Various end groups to determine which grafting strategy on the ligand is the most relevant. It must be pointed out that this tether must be as short as possible to keep the global rigidity of the platform as high as possible.

A schematic picture of the targeted model platforms is depicted in Figure 42.

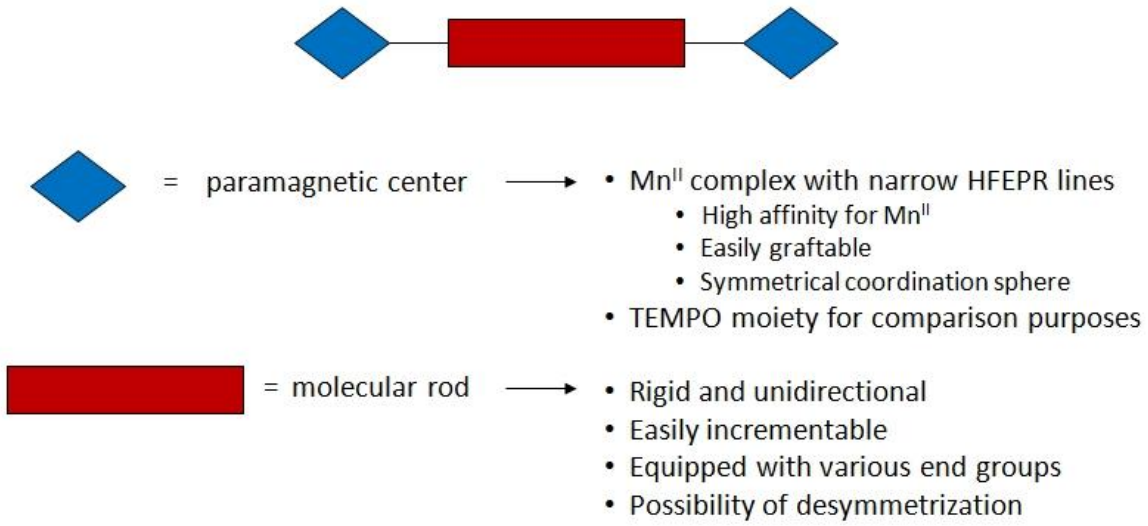

Figure 42: Targeted model platforms

These steps will be described in the first chapter of this manuscript. The synthesis of various Mn^{II}-Mn^{II} model platforms have been performed, and X-ray crystallography in combination with DFT calculations or MD simulations have been used to predict the end-to-end distance of these model systems. In the second chapter, high-field PELDOR measurements on selected platforms have been performed. The last chapter of this manuscript deals with persistent substituted trityl spin labels, which were studied by *cw*-HFEPR at *J*-band.

Chapter I – Synthesis of platforms with a constrained distance between two Mn^{II} complexes

In this chapter, the synthesis of platforms incorporating two Mn^{II} complexes connected to a central rigid molecular rod will be discussed. We will show that it tis possible to obtain systems that comply with the specifications shown in Figure 42. To this aim, the screening of several ligands will be performed to find the ideal candidate. In the meantime, various rigid linkers have been synthesized and efficient methodologies to attach the selected ligands on these spacers have been employed.

1. LIGAND SCREENING

1.1 Bis(imino)pyridines

Bis(imino)pyridines (BImP) are a well-known class of compounds[91] consisting of a central pyridine core linked with a methylene-imino bridge to two aromatic rings bearing various substituents. The general structure of BImPs is depicted in Figure 43.

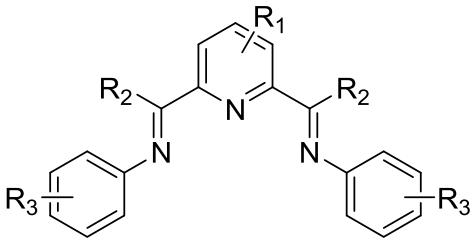

Figure 43: General structure of BImPs

Since the late 1990s, these ligands have attracted interest owing because it was shown that their Fe^{II} and Co^{II} complexes were able to catalyze the polymerization of ethylene with very high efficiency.[92] Indeed, these catalysts promote the production of highly linear high-density poly(ethylene), with an activity comparable to the most active Ziegler-Natta systems. Many useful reactions can be catalyzed by Fe- or Co-BImPs, as shown by the group of P. J. Chirik: alkene hydrosilylation,[93] enyne cyclization,[94] asymmetric alkene hydrogenation[95] and many others. The choice of the substituents on the BImP core is crucial to the catalytic activity, as well as the metal: chromium[96] and vanadium[97] still perform well for ethylene polymerization, but manganese[98] is essentially inactive. Hence, numerous metals have been screened to expand the scope of BImPs: cadmium,[99] mercury[100] and copper[101] display interesting luminescence properties, while silver[102] and ruthenium[103] have been used for structural and theoretical studies.

Due to their absence of catalytic activity, Mn-BImPs have been studied much. The crystal structure of a five-coordinate dibromo Mn^{II}-BImP complex has been determined,[104] and various

stable Mn-BImPs bearing alkyl ligands have been prepared[105] for an attempted ethylene polymerization. Modulation of the nature of the R_3 group (in the *ortho* position) led to Mn^{II}-BImP complexes displaying antifungal and antibacterial activity[106] when R_3 = SH or CO_2H. This prompted us to use Mn^{II}-BImPs as paramagnetic centers for PELDOR distance measurements, because they can be easily modulated. Derivatives incorporating an anchoring group in the *para* position of the pyridine ring would be directly grafted on a rigid linker using Pd-catalyzed couplings, inducing minimal loss of flexibility.

The majority of BImPs incorporate a R_2 = Me group. The synthesis of these BImPs relies on an imine bond formation between aniline or its derivatives (mainly di-*ortho*-substituted) and 2,6-diacetylpyridine (DAP **3**), which can be obtained by various methods starting from dipicolinic acid (DPA **1**) (Scheme 2).

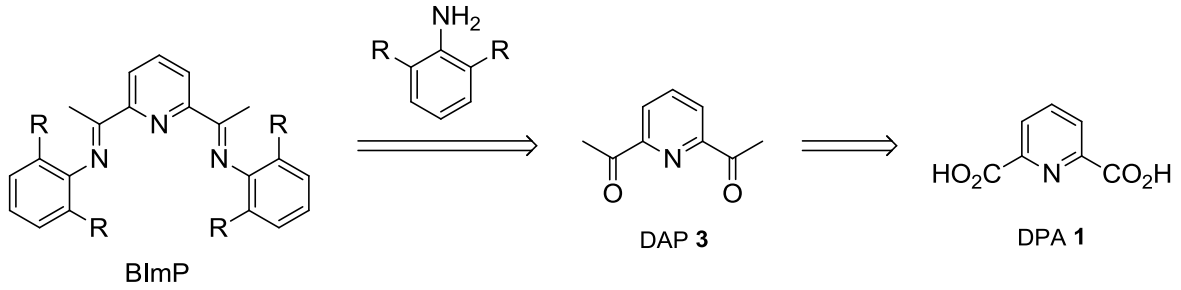

Scheme 2: Retrosynthetic analysis of BImPs. R = alkyl group

Three methods have been explored to synthesize DAP **3** starting from DPA **1** (Scheme 3). According to the *method A*, DPA **1** was engaged in a Fischer esterification with ethanol in the presence of a catalytic amount of *p*-toluenesulfonic acid (PTSA) to give dipicolinic acid diethyl ester **2** in good yield. This compound was reacted first with sodium ethoxide in AcOEt, and then refluxed with concentrated aqueous HCl to give DAP **3** with a slightly lower yield than the literature (46% vs. 59%).[107] This difference could be explained by the fact that AcOEt must be rigorously dried and NaOEt must be free from impurities. The use of fresh NaOEt (prepared from anhydrous EtOH and sodium) did not improve the yield. In contrast, another report[108] stated that traces of EtOH and H_2O in AcOEt improved the yield of DAP **3** to 86%. In our hands, this method only resulted in a drop of yield to 10%.

Aiming to improve the yield of DAP **3**, we decided to use a Gilman reagent as described in *method B* (Scheme 3). DPA **1** was chlorinated with thionyl chloride to give dipicolinic acid dichloride **4** in nearly quantitative yield. In the presence of CuI and MeLi, compound **4** was readily converted to DAP **3**, but the yield was only 40%.

Recently, a convenient approach for the synthesis of DAP **3** based on the reaction between a 2,6-pyridinedicarboxamide and a Grignard reagent was described.[109] As shown in *method C* (Scheme 3), addition of pyrrolidine to dipicolinic acid dichloride **4** afforded diamide **5** in excellent yield. Addition of methylmagnesium chloride to compound **5** gave DAP **3**, but with a yield nearly three times lower than described (32% *vs.* 88%).

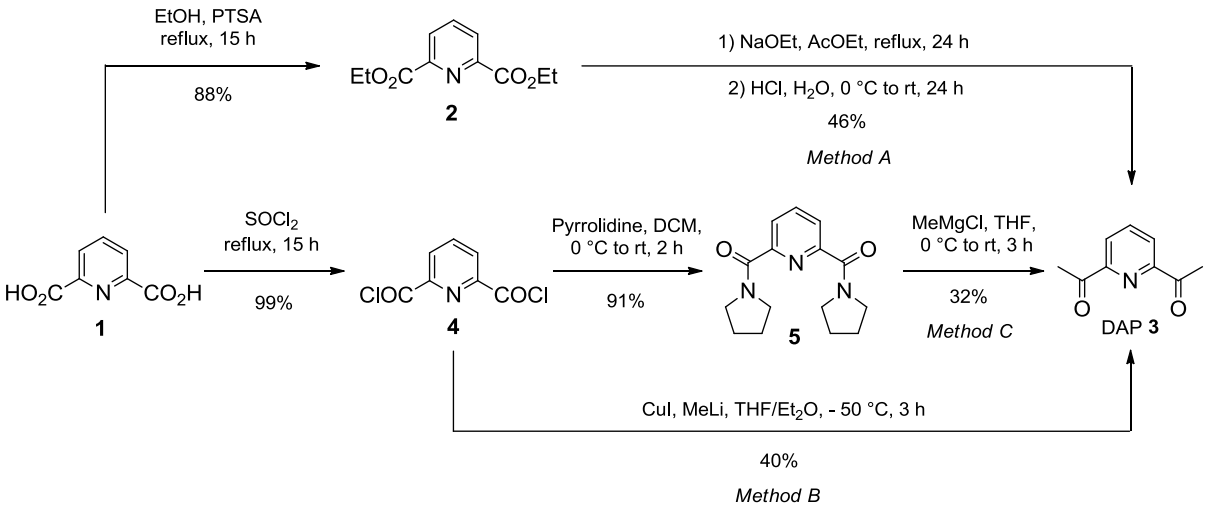

Scheme 3: Synthetic methods for the synthesis of DAP **3**

After trialing these synthetic procedures, we decided to choose the *method A* because of the higher yield. The starting material is cheap and the reaction can easily be scaled up to obtain gram-scale quantities of DAP **3**.

In order to obtain functionalizable BImPs that can be attached to a rigid linker, we synthesized analogs incorporating a halogen atom in the *para* position of DAP **3**. To do so, a convenient starting material is chelidamic acid **6**, a dipicolinic acid bearing a hydroxy moiety in the *para* position. Starting from this compound, a Fischer esterification in EtOH with a catalytic amount of H_2SO_4 afforded chelidamic acid diethyl ester **7** in 75% yield. This lower yield compared to dipicolinic acid diethyl ester can be explained by the formation of a byproduct, 4-ethoxydipicolinic acid diester. Chlorination of the hydroxyl group using $SOCl_2$ with traces of DMF afforded diester **8** in good yield, whereas bromination with PBr_5 gave diester **9** in high yield. Finally, these two compounds were converted to the corresponding *para*-substituted diacetylpyridines, as described in *method A*, affording *p*Cl-DAP **10** and *p*Br-DAP **11** in modest to moderate yield (Scheme 4).

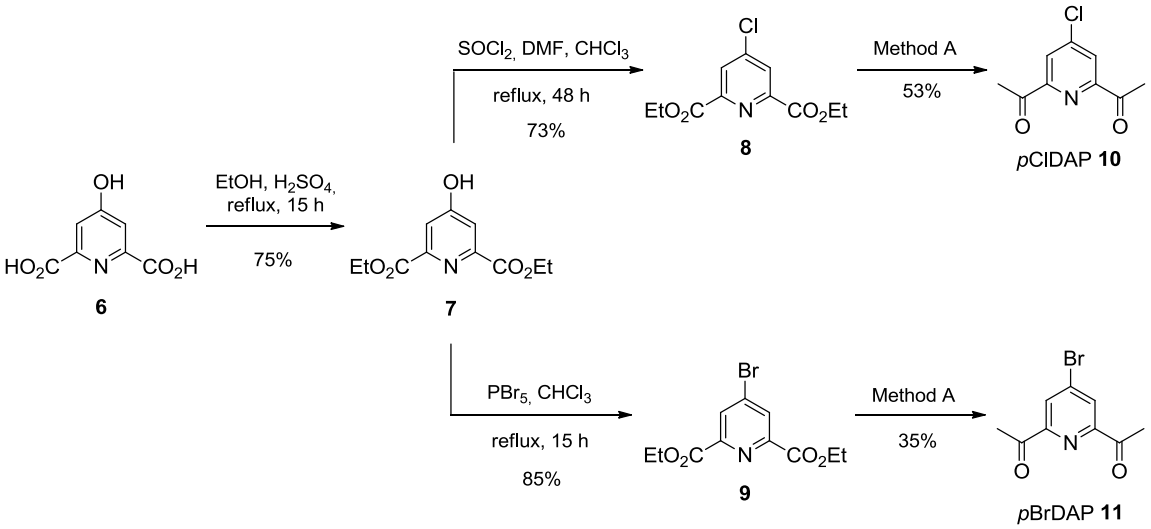

Scheme 4: Synthesis of *para*-substituted diacetylpyridines **10** and **11**

Next, DAP **3** and its *para*-substituted analogues **10** and **11** were mixed with two equivalents of aniline **12** or a di-*ortho*-substituted aniline (with a Me group, **13**, and with a ^{i}Pr group, **14**) in an acidic alcoholic solvent to give the corresponding BImPs **15**-**21** in moderate to high yield. The yield is directly linked with the size of the *ortho*-substituent: bulky ^{i}Pr group induces fast precipitation of the product during the course of the reaction, with an equilibrium shift and a nearly quantitative yield. In contrast, when unsubstituted aniline is used, the product crystallized after one month at 4 °C, EtOH/AcOH was used instead of MeOH/HCO_2H. Coordination with $MnBr_2$ afforded the corresponding Mn-BImPs **22**-**26** in moderate to high yield. Again, the pure products precipitated out immediately after addition of $MnBr_2$ (Scheme 5).

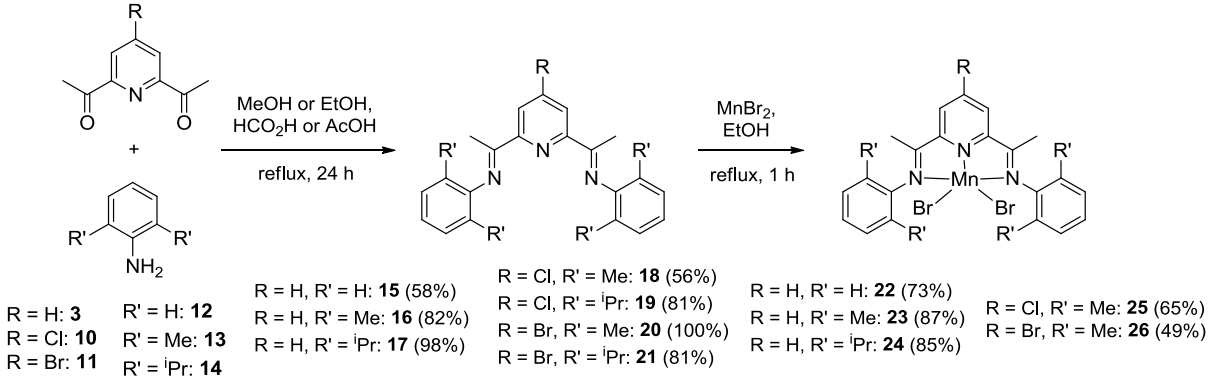

Scheme 5: Synthesis of substituted Mn-BImPs **22**-**26**

Yellow crystals of *p*Cl-Me-BImP-$MnBr_2$ **25** suitable for X-ray diffraction were grown by slow evaporation of an acetonitrile solution of the complex. This compound crystallizes in the P-1 space group (triclinic system), where two molecules of the complex constitute the asymmetric unit, along with three cocrystallized MeCN. The geometry around the Mn center can be described as a distorted trigonal bipyramid, where the trigonal plane consists of the pyridyl nitrogen and the two bromine atoms, the two imino nitrogen atoms being the apical donor atoms. The mean distance of the Mn-Br bond is 2.488 Å, very close from the the literature value (2.477 Å) for compound **22**.[104] The distances

between Mn and the nitrogen atoms are 2.195 Å for the pyridyl nitrogen and 2.335 Å for the imino nitrogen, with small deviations from the literature values (2.177 Å and 2.255 Å, respectively). Noteworthy, the two xylyl rings are nearly perpendicular (mean angle of 82°) to the pyridyl ring, due to steric constraints between the methyl groups and the bromine atoms. Hence, no interaction between aromatic rings is observed in the packing (Figure 44).

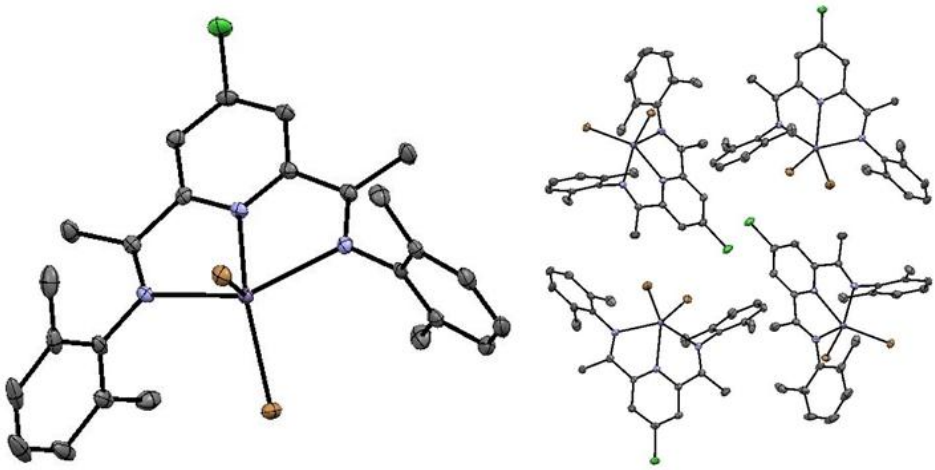

Figure 44: ORTEP drawings of *p*Cl-Me-BImP-$MnBr_2$ **25**. Hydrogen atoms and cocrystallized solvent molecules have been omitted for clarity. Left: one molecule of the asymmetric unit; Right: view of the packing

The J-band *cw*-HFEPR spectrum of a MeCN sample containing ^{i}Pr-BImP-$MnBr_2$ **24** was recorded (Figure 45).

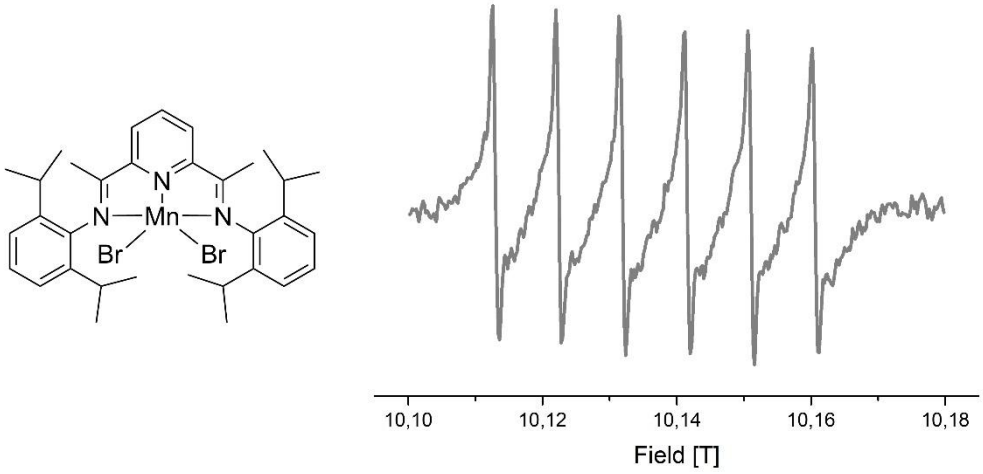

Figure 45: Structure of ^{i}Pr-BImP-$MnBr_2$ **24** (left) and J-band *cw*-HFEPR spectrum of a MeCN sample (1 mM, 23 K, right)

This spectrum displays the expected six hyperfine lines, but the narrow component corresponds to the release of free Mn^{II} in solution, indicative for notable decoordination. Each narrow line is superimposed on a broad line that could correspond to the signal of the complex, but also to artifacts such as precipitation of the complex during the freezing process or poor glass formation. This spectrum is poorly reproducible and its aspect seems to depend on factors such as the freezing time or the delay between the dissolution in MeCN and the freezing of the solution.

These issues led us to the conclusion that BImP-$MnBr_2$ complexes are not suitable as paramagnetic centers for the PELDOR method because MeCN samples gave poorly defined *cw*-HFEPR spectra with too broad lines. We hypothesized that problems linked to the release of Mn^{II} from the ligand could stem from the coordination sphere incorporating two bromine atoms, easing the decoordination to generate $MnBr_2$. A Mn^{II} complex with only nitrogen-based coordinated Lewis bases thus seemed appropriate. Keeping the pyridine moiety, we also decided to move toward hexacoordinated complexes to increase the symmetry around Mn^{II}. Among them, Mn^{II}-bis(terpyridine) complexes could constitute a relevant choice.

1.2 Terpyridines

2,2':6',2"-terpyridine (Tpy **47**, Figure 46) is a commonly employed building block in supramolecular assemblies,[110] colorimetric titrations (for instance mercury[111]), light-emitting complexes[112] and biological applications such as DNA ligands (recognition of quadruplex-DNA when complexed with Cu or Pt for instance[113,114]). Tpy has also been used as a ligand for Cu^{II}, Gd^{III} and Mn^{II} for metal-nitroxide PELDOR measurements.[55,80,89]

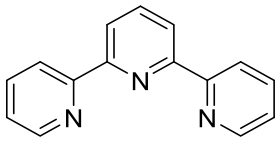

Figure 46: The Tpy ligand **47**

Several syntheses of the Tpy ligand have been described.[115] They mainly rely on couplings between pyridine units or construction of the central pyridine ring using variations of the Hantzsch pyridine synthesis, generally with low yields and difficult purification. In contrast, *para*-phenylterpyridines can be synthesized in only one step starting from 2-acetylpyridine and a benzaldehyde derivative,[116] and they are more convenient for the present work because they already incorporate a phenyl ring to increase the length of the molecular rod. This cascade reaction involves the formation of an α-enone from the aldehyde and the 2-acetylpyridine, followed by the Michael addition of a second equivalent of 2-acetylpyridine to form a 1,5-diketone which is finally cyclized in the presence of ammonia and atmospheric oxygen to generate the central pyridine ring. An alternative stepwise method[117] consists in the isolation of the alpha-enone, which can then react with a pyridinium compound to form the *p*-phenylterpyridine (Scheme 6).

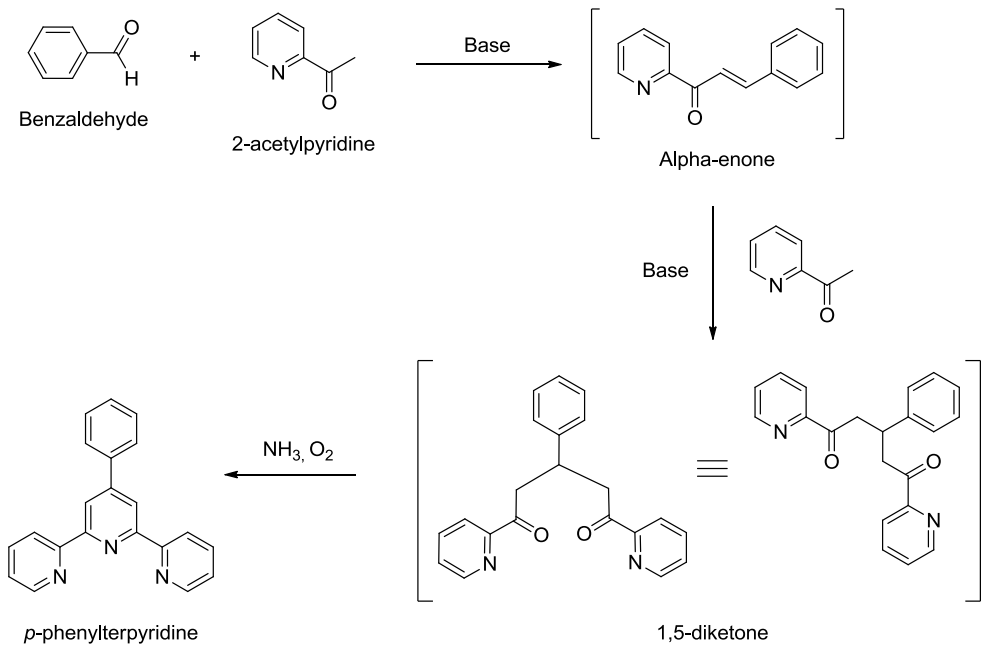

Scheme 6: Main intermediates in the synthesis of *p*-phenylterpyridine

To obtain a family of *para*-functionalized phenylterpyridines, a number of *para*-substituted benzaldehydes were needed. Some are commercially available, while the others needed to be synthesized. A benzaldehyde bearing a *para*-ethynyl moiety would be a useful precursor for further functionalization, either by Sonogashira couplings or click chemistry reactions. Sonogashira coupling of 4-bromobenzaldehyde **27** with trimethylsilylacetylene (TMSA) in the presence of catalytic amounts of $Pd(PPh_3)_2Cl_2$ and CuI afforded aldehyde **28** in high yield. Removal of the trimethylsilyl (TMS) group with K_2CO_3 in MeOH gave aldehyde **29** in nearly quantitative yield (Scheme 7).[118]

Alternatively, a phenylterpyridine incorporating an azido moiety would also be a valuable building block. Treatment of 4-nitrobenzaldehyde **30** with sodium azide in hexamethyl-phosphoramide (HMPA) afforded aldehyde **31** in high yield (Scheme 7).[119]

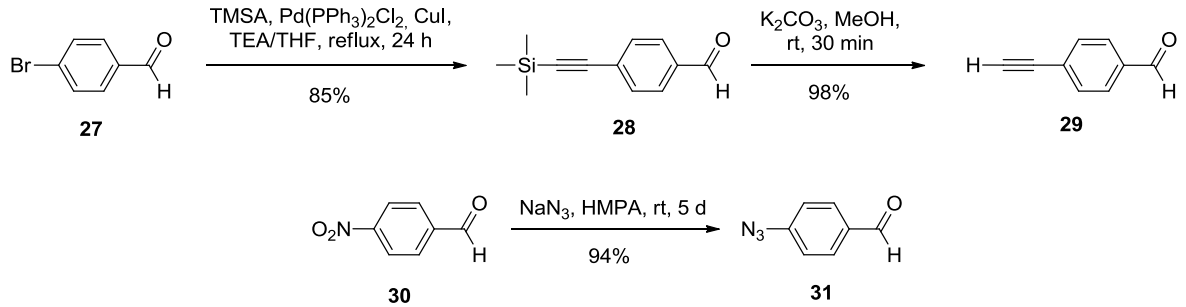

Scheme 7: Synthesis of *para*-substituted benzaldehydes **29** and **31**

Compounds **29** and **31** as well as commercially available aldehydes (with a Br group, **27,** and with Cl, F and Me groups, **32**-**34**) were reacted with two equivalents of 2-acetylpyridine **35** in EtOH, in

the presence of KOH and aqueous concentrated ammonia, under atmospheric oxygen, to afford the corresponding *para*-substituted phenylterpyridines *p*RPhTpy **36**-**41** in low yields (Scheme 8, *method A*). Harsher conditions were necessary (reflux for 72 h instead of rt for 4 h) in the case of the fluorinated terpyridine **33**, maybe because the electron-withdrawing effect of the fluorine atom would decrease the kinetics of the steps depicted in Scheme 8.

To improve the yields of the general procedure, alternative conditions were tried (NaOH instead of KOH, NH_4OAc instead of ammonia,[120] MeOH instead of EtOH, or refluxing). No improvement was observed, even with other methods such as the use of microwaves[121] or solventless chemistry.[122] The stepwise method was thus tried. Reaction of *p*-chlorobenzaldehyde **32** with 2-acetylpyridine **35** in the presence of NaOH gave the corresponding azachalcone **42**, and iodine was also condensed with 2-acetylpyridine to give pyridinium iodide **43**, but in low yield. These two compounds were then refluxed in the presence of NH_4OAc under atmospheric oxygen to give the corresponding *p*-chlorophenylterpyridine **39** in a better yield (Scheme 8, *method B*). Nevertheless, this method was not further exploited because of the lower overall yield and higher number of synthetic steps.

The crude products were easily isolated as they precipitate from the reaction medium, and were sometimes pure enough for further reactions. When an additional purification step was needed, column chromatography on Al_2O_3 was used because these compounds proved unstable on silica gel. More conveniently, simple recrystallization from EtOH gave very pure products and the possibility to perform the reaction on a large scale. This compensates the low yields, which can be explained by the large number of side products[123] that are formed during this cascade reaction.

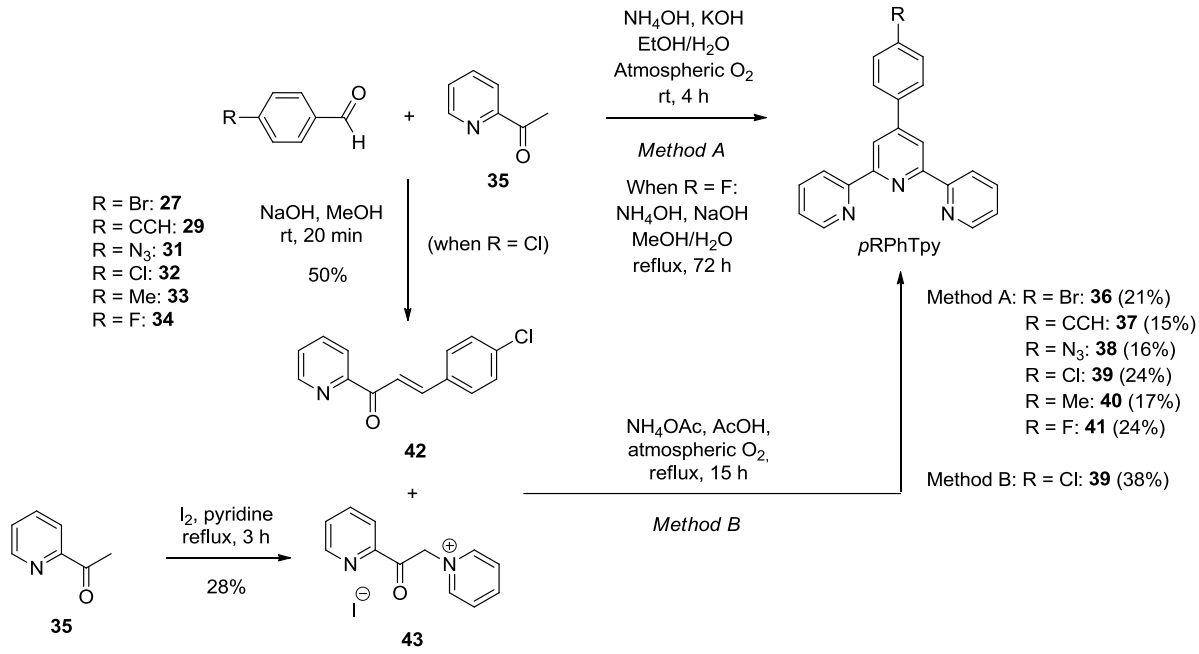

Scheme 8: Synthesis of *para*-substituted phenylterpyridines **36**-**41**

Other graftable phenylterpyridines can be obtained by functional group modification. Notably, radical bromination of *p*-tolylterpyridine **40** with *N*-bromosuccinimide (NBS) in the presence

of azobisisobutyronitrile (AIBN) afforded brominated terpyridine **44** in moderate yield after recrystallization. An Arbuzov reaction with neat triethylphosphite cleanly gave phosphonate **45** in excellent yield.[124] Moreover, the Miyaura borylation of *p*BrPhTpy **36** (with bis(pinacolato)diboron $(Bpin)_2$ in the presence of $PdCl_2$, 1,1'-bis(diphenylphosphino)ferrocene (dppf) and KOAc) cleanly gave boronate **46** in good yield (Scheme 9).[125] The synthesis of *p*N_3PhTpy **38** was first envisoned starting from *p*BrPhTpy **36**, but no conversion took place (NaN_3/DMF with or without H_2O).

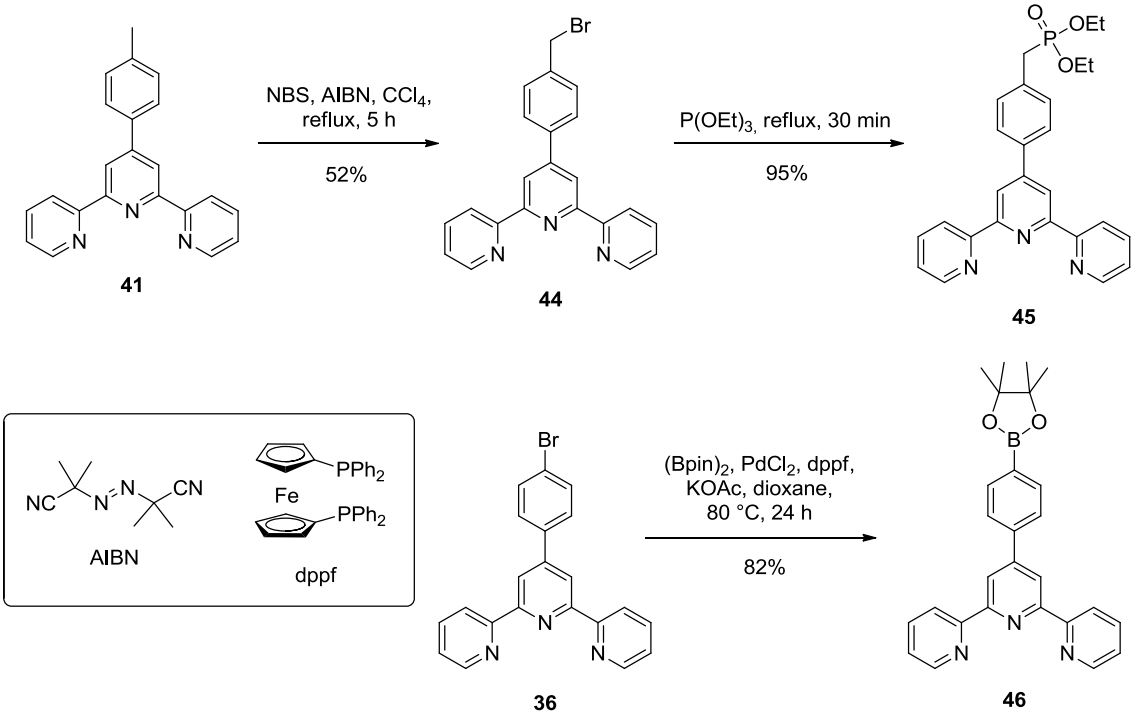

Scheme 9: Functionalization of *p*-phenylterpyridines

To assess the suitability of Mn-Tpys for PELDOR distance measurements, we prepared different Mn-complexes of synthesized as well as commercially available Tpy ligands. Reaction between $MnCl_2$ and two simple terpyridines (Tpy **47** and *p*ClTpy **48**) afforded the corresponding complexes $TpyMnCl_2$ **49** and *p*ClTpy$MnCl_2$ **50** in very high yield (Scheme 10).[120]

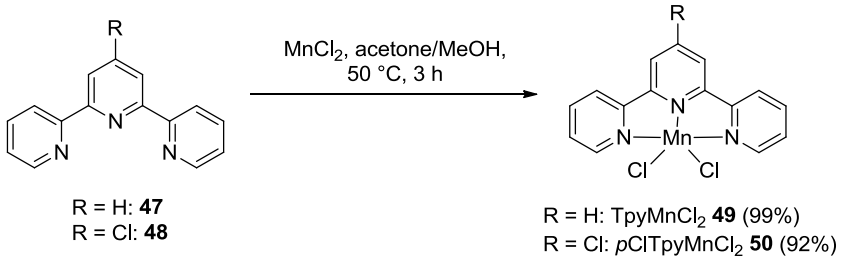

Scheme 10: Synthesis of dichloro Mn-Tpy complexes **49** and **50**

Similarly, coordination of the previously synthesized *p*-phenylterpyridines **36**, **37**, **39** or **41** with $MnBr_2$[126] gave the corresponding Mn-complexes **51**-**54** in good to high yield (Scheme 11).

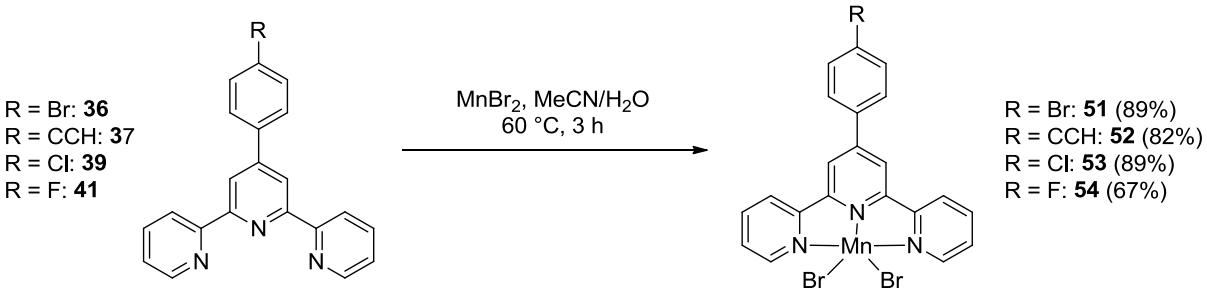

Scheme 11: Synthesis of dibromo Mn-Tpy complexes **51**-**54**

Symmetric Mn-bis(Tpys) complexes can also be made by mixing two equivalents of a *p*-Tpy derivative (**40**, **41**, **47**, **48**, and **55** bearing a pyrrolidinyl moiety) with one equivalent of $MnCl_2$. Precipitation with excess NH_4PF_6 and purification by precipitation in Et_2O[127] gave a family of $Mn(Tpy)_2^{2+}$, $2PF_6^-$ compounds **56**-**60** (Scheme 12)

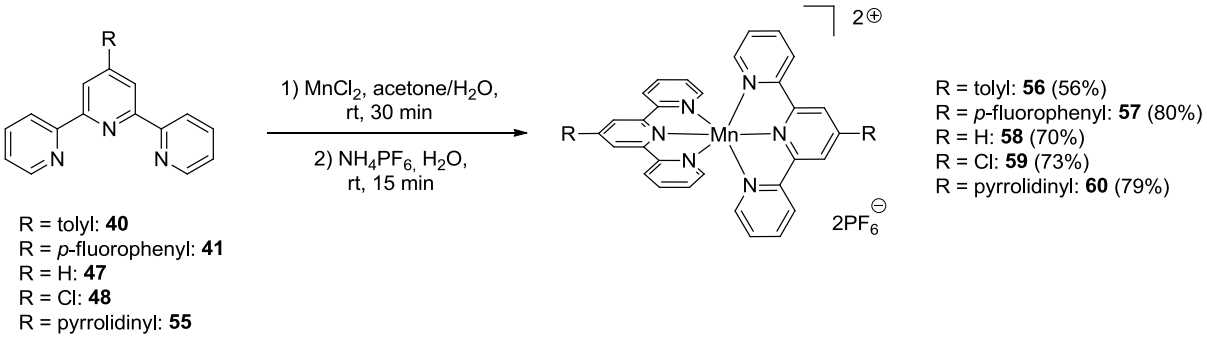

Scheme 12: Synthesis of symmetric Mn-bis(Tpy) complexes **56**-**60**

The J-band *cw*-HFEPR spectrum of Mn^{II}-bis(Tpy) **58** was recorded (Figure 47).

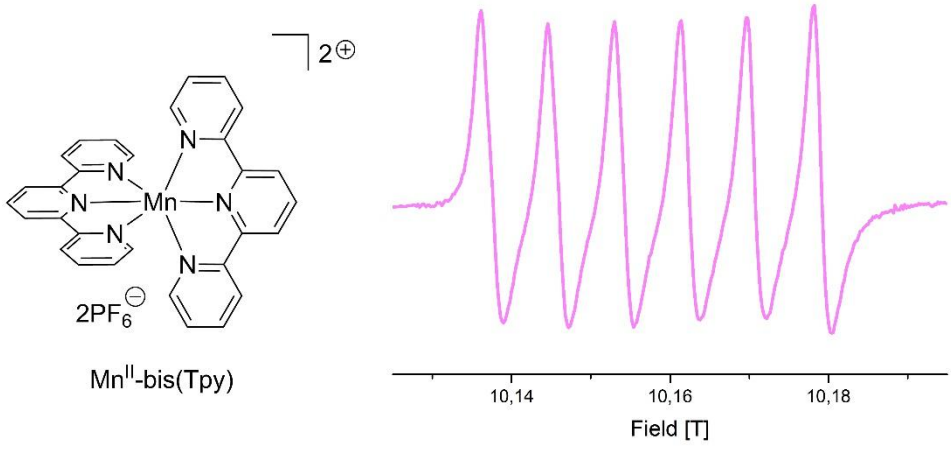

Figure 47: Structure of Mn^{II}-bis(Tpy) **58** (left) and its J-band *cw*-HFEPR spectrum (2 mM in MeCN with 100 mM *n*-BuN_4PF_6 at 23 K, right)

The improvement on Mn^{II}-BImP complexes is notable: no release of free Mn^{II} was detected, and six well-defined hyperfine lines were observed. These lines are quite broad (peak-to-trough linewidth: 27 G) but it seemed reasonable to select Mn^{II}-bis(Tpy) complexes for PELDOR

measurements. The dissymmetric Mn-bis(Tpy) **61** and **62** were also synthesized by ligand exchange between the dibromo Mn-Tpy complexes **51** and **54**, and Tpy **47**, in an analogous manner as found in the literature for Ru^{III}-Tpy complexes (Scheme 13).[128]

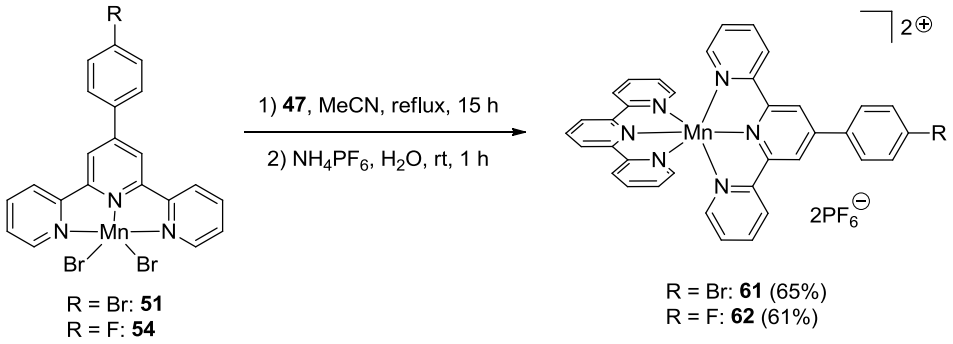

Scheme 13: Synthesis of dissymmetric Mn-bis(Tpy) complexes **61** and **62**

The J-band *cw*-HFEPR spectra of Mn^{II}-bis(*p*FTpy) **57** and of Mn^{II}(Tpy)(*p*FPhTpy) **62** were recorded (Figure 48).

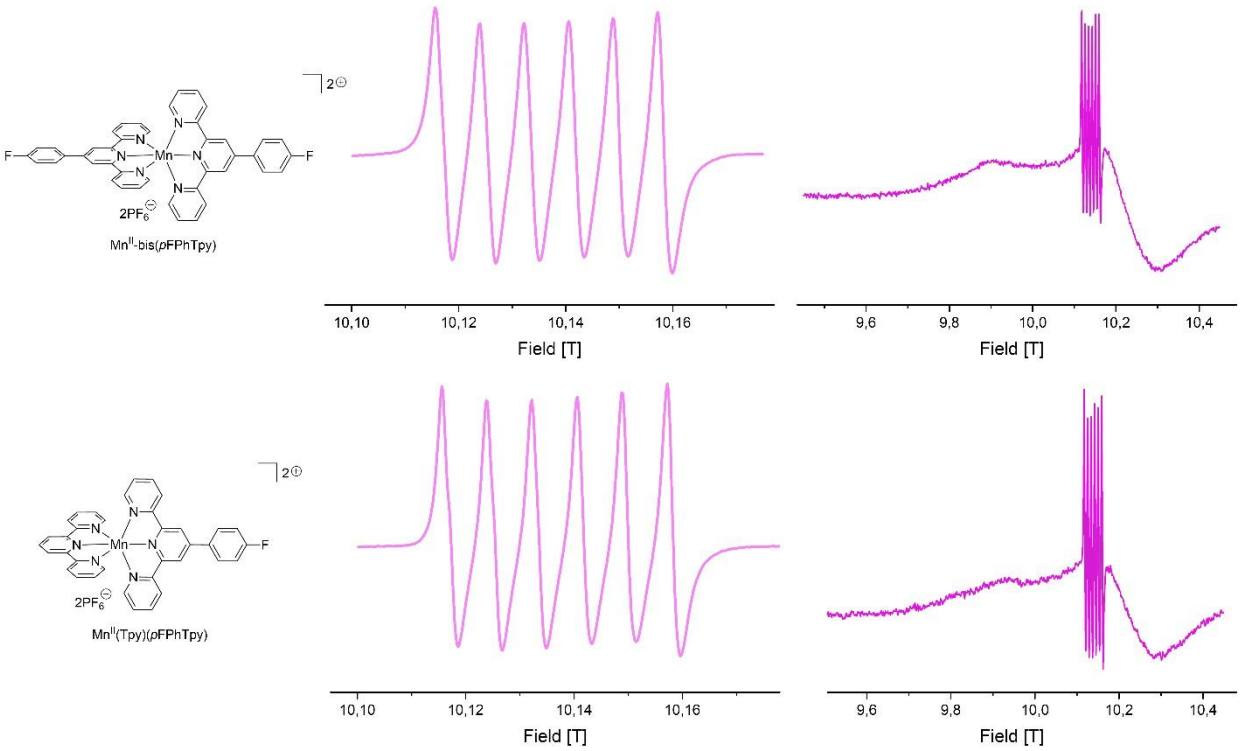

Figure 48: *cw*-HFEPR spectra of fluorinated Mn^{II}-bis(Tpy) complexes **57** and **62**. From left to right: top: structure of Mn^{II}-bis(*p*FTpy) **57** and its *cw*-HFEPR spectra at 23 K and 4.2 K, bottom: structure of Mn^{II}(Tpy)(*p*FPhTpy) **62** and its *cw*-HFEPR spectra at 23 K and 4.2 K. All spectra have been recorded at 2 mM in MeCN with 100 mM *n*-Bu_4NPF_6

The 23 K spectra were very similar to each other and to the spectrum of Mn^{II}-bis(Tpy) **58**. The 4.2 K spectra could allow the extraction of the ZFS parameters *D* and *E*.[129]

In conclusion, Mn^{II}-bis(Tpy) complexes appear to be a better choice than Mn^{II}-BImPs as they display a *cw*-HFEPR spectrum with a well-defined hyperfine sextet and no Mn decoordination. The broadness of the lines is higher than free Mn^{II}, but it seemed reasonable to try these complexes for PELDOR distance measurements. In the meantime, moving toward a more biological context, we looked for water-soluble Mn^{II} complexes. Adding carboxylate groups seemed appropriate, as they provide good water-solubility. We decided to explore this possibility, because numerous ligands incorporating carboxylate arms display a high affinity for Mn^{II},[130] with $\log K_{MnL}$ values in the 7 – 20 range. Moreover, the binding environment of Mn^{II} in proteins often includes a carboxylate group from an aspartic or a glutamic acid, and the *cw*-HFEPR spectra of such proteins can display very narrow lines, as it is the case for Concanavalin A or oxalate decarboxylase at pH 8.[26,131]

1.3 Dipicolinic acid and derivatives (PyMTA and PyMDPDA)

Accordingly, we decided to combine a pyridine ring with carboxylate moieties. The already mentioned dipicolinic acid (DPA **1**, see pp. 37 – 40) is an example, and increasing the denticity leads to derivatives known as pyridinedimethylenenitrilo-tetraacetate (PyMTA **66**). The structure of these ligands is depicted in Figure 49. Functionalized DPA[72,73,74] and PyMTA[21,34,39] have already been used with gadolinium as spin labels for PELDOR distance measurements. This strengthened our intent to investigate their use with Mn^{II}.

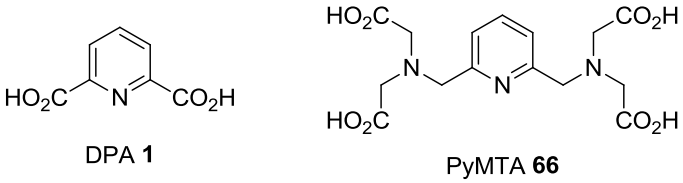

Figure 49: Structures of DPA **1** and PyMTA **66**

The synthesis of PyMTA has been achieved starting from pyridine 2,6-dimethanol **63**. Bromination with hydrobromic acid afforded 2,6-dibromomethylpyridine **64** in modest yield. Double nucleophilic substitution with ethyl iminodiacetate gave Et-PyMTA **65** in good yield, and a final saponification with lithine followed by anion exchange with an Amberlite resin led to the formation of PyMTA **66** in quantitative yield.[132] The corresponding Mn^{II} complex **67** was prepared using $MnCl_2$ at controlled pH for elucidation of the coordination sphere using X-ray crystallography (Scheme 14). However, no crystals could be obtained, so the coordination sphere depicted in Scheme 14 is hypothetical and based on the corresponding Gd^{III}-PyMTA complex without the coordinated water molecule, even if numerous related Mn^{II} complexes include a water molecule in their coordination sphere.[133]

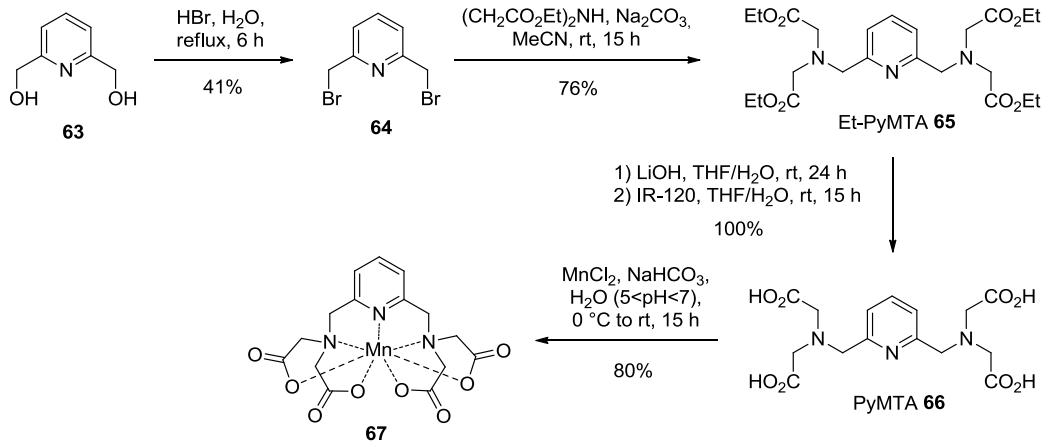

Scheme 14: Synthesis of PyMTA **66** and its corresponding Mn^{II} complex **67**

A bromo or an azido group in the *para* position of the pyridine ring of PyMTA were introduced for further functionalization. A relevant starting point is the previously synthesized diester **9** (p. 62). Reduction of the ester moieties with $NaBH_4$ in refluxing EtOH gave diol **68** in high yield.[134] The subsequent steps were analogous the synthesis of the non-functionalized PyMTA **66**. Bromination using PBr_3 afforded dibromide **69** in moderate yield,[134] then addition of ethyl or *tert*-butyl iminodiacetate gave the corresponding Et- and ^{t}Bu-*p*BrPyMTA (**70** and **71**, respectively) in high yield. Aromatic nucleophilic substitution on these compounds with sodium azide in hot DMF resulted in the formation of Et- and ^{t}Bu-*p*N_3PyMTA (**74** and **75**, respectively) in good yields.[135] Moreover, TFA removal of the ^{t}Bu groups of compound **71** afforded *p*BrPyMTA **72** after HPLC purification, and the corresponding Mn^{II} complex **73** was also generated employing the procedure used for complex **67** (Scheme 15).

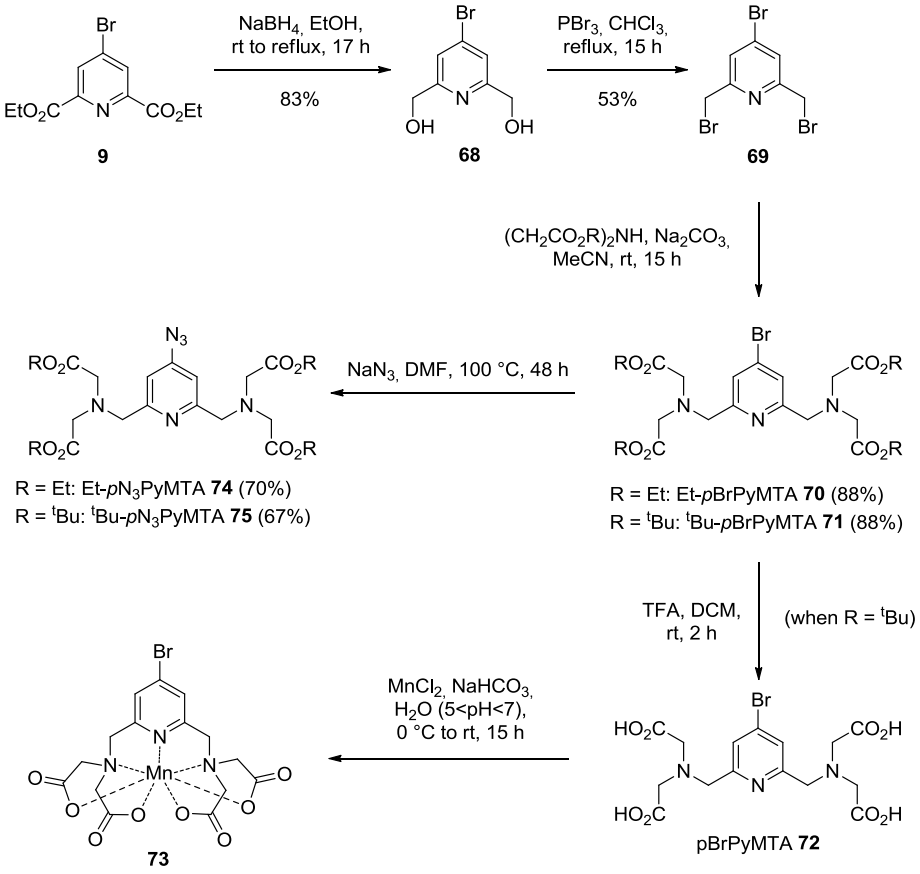

Scheme 15: Synthesis of para-functionalized PyMTA derivatives

The affinity of PyMTA for Mn^{II} has not been reported. We undertook an evaluation using isothermal titration calorimetry (ITC). This technique is very useful as it provides the affinity constant as well as the stoichiometry and the changes in enthalpy (ΔH) and entropy (ΔS) during the reaction. Briefly, during the reaction of the ligand with a Mn^{II} salt, a heat exchange will occur. The amount of power needed to maintain a constant temperature is measured. To perform the titration, aliquots of a Mn^{II} salt are regularly injected, generating a spike of heat flow. These spikes will become less and less intense as we approach stoichiometry and negligible when we exceed the stoichiometry, because no more reaction takes place.

In our case, the ITC cell (983 µL) was filled with a solution of *p*BrPyMTA **72** (780 µM in 100 mM pH 8 HEPES buffer) and titrated with a solution of $MnCl_2$ (6 mM in 100 mM pH 8 HEPES buffer) in a 250 µL syringe. Each 5 min (time necessary to go back to baseline in the thermogram), 10 µL of Mn^{II} solution was injected, which corresponds to 25 injections. This was performed in triplicate, and a typical thermogram is displayed in Figure 50, as well as the fit of the experimental data.

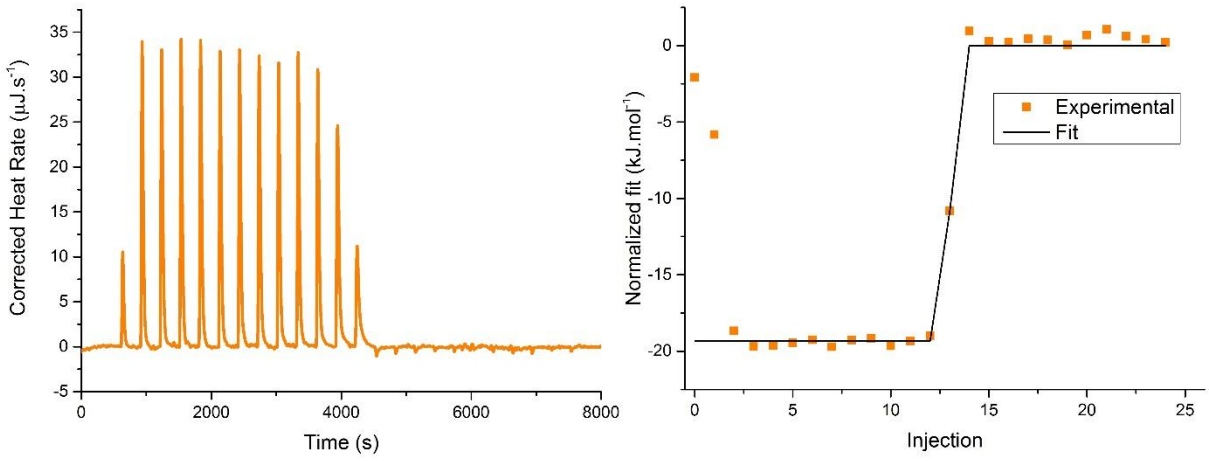

Figure 50: Typical thermogram of the titration of pBrPyMTA **72** with Mn^{II} (left), and fit of the experimental data (right)

For a 1:1 ligand:metal stoichiometry, according to the concentration and volumes of *p*BrPyMTA **72** and Mn^{II}, the equivalence should be reached at the 13th injection: this is compatible with the existence of a mononuclear complex, providing a first information on the coordination sphere. Fitting of the data using a one-site model gave a $\log K_{MnL}$ of 7.9, a ΔH of -19.2 kJ.mol^{-1} and a ΔS of 83.5 J.mol^{-1}.K^{-1}. This proves that the affinity of *p*BrPyMTA **72** for Mn^{II} is quite high.

The J-band *cw*-HFEPR of the *in situ*-generated Mn^{II} complex of *p*BrPyMTA **72** was recorded (Figure 51).

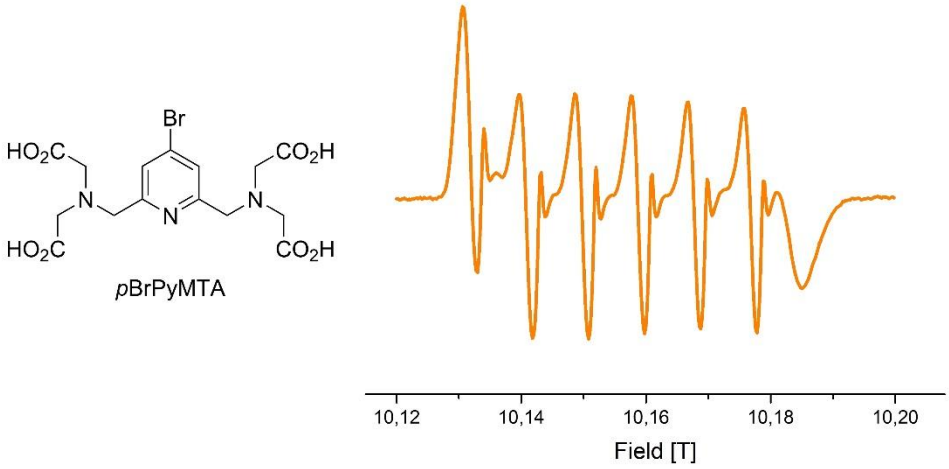

Figure 51: Structure of *p*BrPyMTA **72** (left) and J-band cw-HFEPR spectrum of the corresponding Mn^{II}-complex (1 mM in ligand, 500 µM in Mn^{II}, in 100 mM pH 8 HEPES buffer with 20% glycerol at 23 K, right)

The Mn^{II}-*p*BrPyMTA complex is water-soluble (at pH 8) and displays six narrow lines, with each line being flanked by a much smaller feature, reflecting the complexity of the coordination sphere, most probably due to a large ZFS interaction. No free Mn^{II} could be observed, justifying our assumption that ligands with numerous carboxylate groups would be interesting candidates for

PELDOR distance measurements. As we could not obtain crystals of Mn^{II}-PyMTA **67**, we surmised that a complex with extended aromaticity could crystallize more easily.

The azido moiety of Et-*p*N_3PyMTA **74** appeared as an ideal anchor to graft aromatic groups. Phenylacetylene was reacted with Et-*p*N_3PyMTA **74** in the presence of CuI to form the click chemistry adduct Et-PhTPyMTA **76** in good yield. The rather unusual conditions employed (CuI/MeCN) can be explained by the fact that Cu^{II} is complexed by the PyMTA moiety.[135] The usual saponification procedure with LiOH afforded PhTPyMTA **77** in high yield, and the corresponding Mn^{II} complex **78** was generated with the procedure used above (Scheme 16).

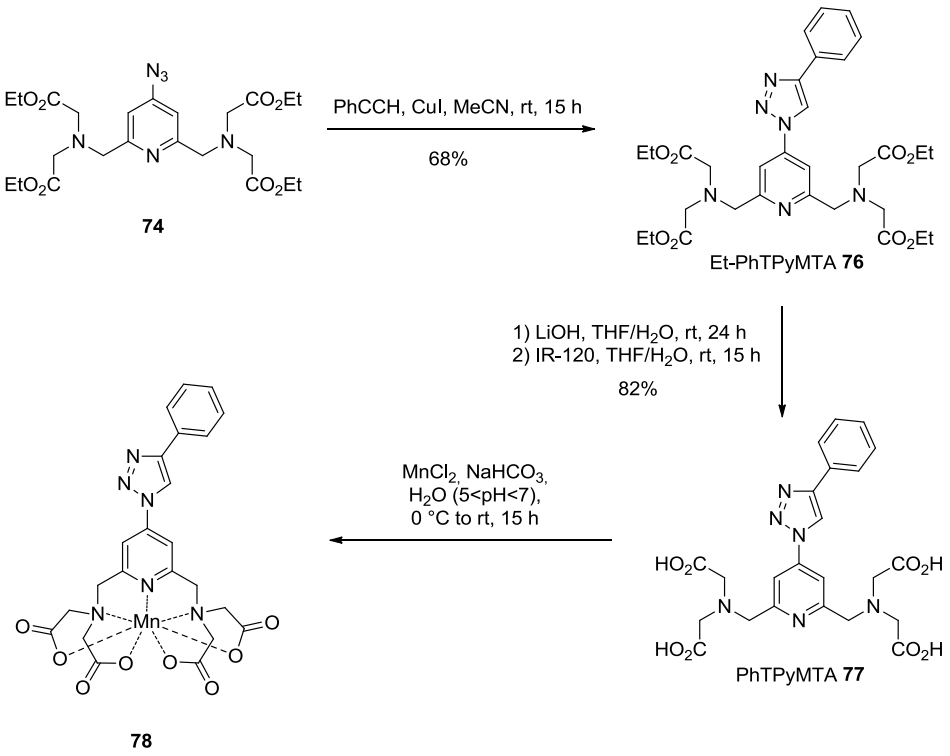

Scheme 16: Synthesis of PhTPyMTA **77** and its corresponding MnII complex **78**

The J-band *cw*-HFEPR of the Mn^{II} complex of PhTPyMTA **77** (generated *in situ*) was recorded (Figure 52).

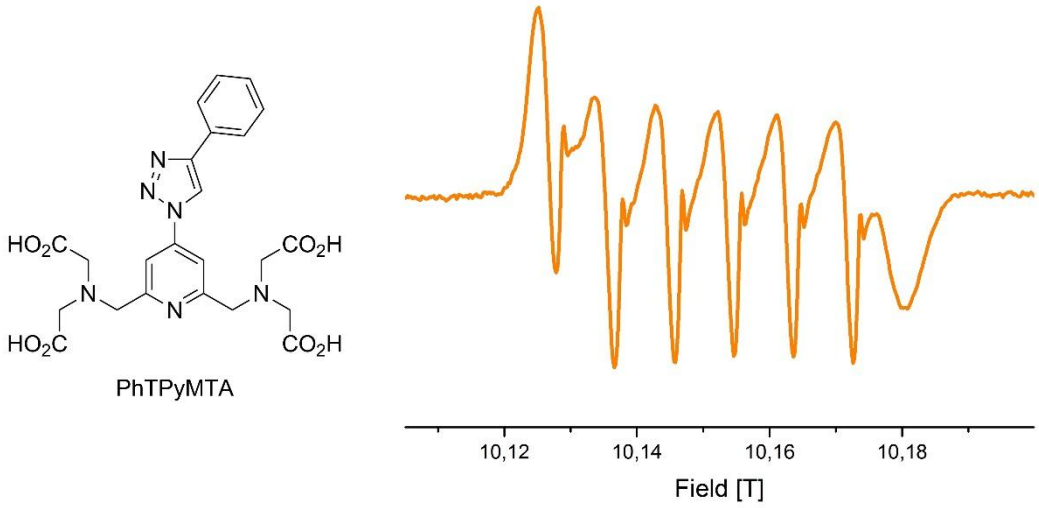

Figure 52: Structure of PhTPyMTA **77** (left) and J-band cw-HFEPR spectrum of the corresponding Mn^{II}-complex (1 mM in ligand, 450 µM in Mn^{II}, in 100 mM pH 8 HEPES buffer with 20% glycerol at 23 K, right)

This spectrum is comparable to the spectrum of the Mn^{II} complex of *p*BrPyMTA **72**. However, the lines appear to be broader with the minor feature being obscured, suggesting that the phenyl-triazole moiety could have a small influence on the coordination sphere. Crystallization procedures are in progress to elucidate its solid state structure.

We also decided to introduce aromatic boronic acids starting from Et-*p*BrPyMTA **70**. However, a Suzuki coupling with 2-naphthylboronic acid ($Pd(PPh_3)_4$/DIPEA) did not prove efficient. Thus, we decided to introduce the naphthyl moiety earlier in the synthesis (Scheme 17).[136] Triflation of chelidamic acid diethyl ester **7** with Tf_2O in the presence of 2,6-lutidine gave triflate **79** in good yield. In this case, the Suzuki coupling with 2-naphthylboronic was efficient, affording diester **80** also in good yield. The ester groups were then reduced with $NaBH_4$ to generate the corresponding diol **81**, which was in turn chlorinated with $SOCl_2$ to give dichloride **82**. This compound reacted with *tert*-butyl iminodiacetate to give ^{t}Bu-NpPyMTA **83** in moderate yield. This result could have been improved by using a dibrominated equivalent of **82**. Finally, treatment with TFA afforded ligand NpPyMTA **84** (Scheme 17).

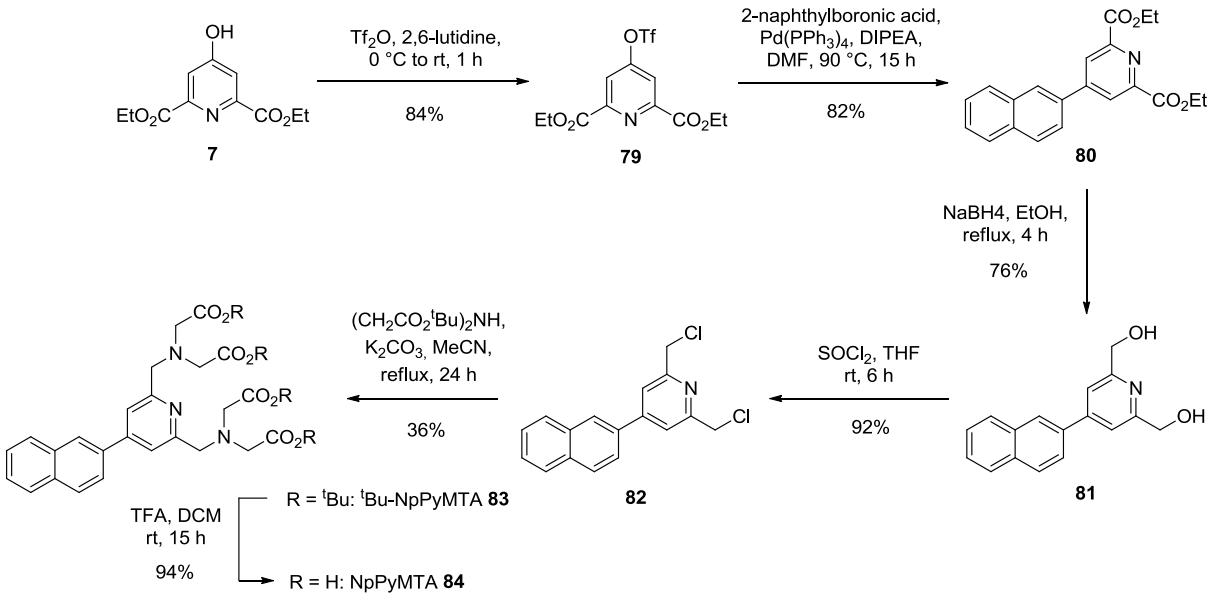

Scheme 17: Introduction of a naphthyl substituent on PyMTA: synthesis of NpPyMTA **84**

Crystals (colorless needles) suitable for X-ray diffraction were obtained by layering a chloroform solution of diester **80** with Et_2O. This structure, which crystallizes in the $P2_1/c$ space group (monoclinic system), reveals a dihedral angle between the pyridyl and the naphthyl rings of 35°. A similar structure with a 9-anthracenyl moiety[136] showed a dihedral angle of 70°, indicating that the steric interactions between the *meta* proton of the pyridyl ring and the naphthyl proton in the α position are much less pronounced. The molecules form antiparallel sheets in the packing, indicative for π-stacking interactions. However, the mean intersheet distance of 3.6 Å suggests a weak effect (Figure 53).

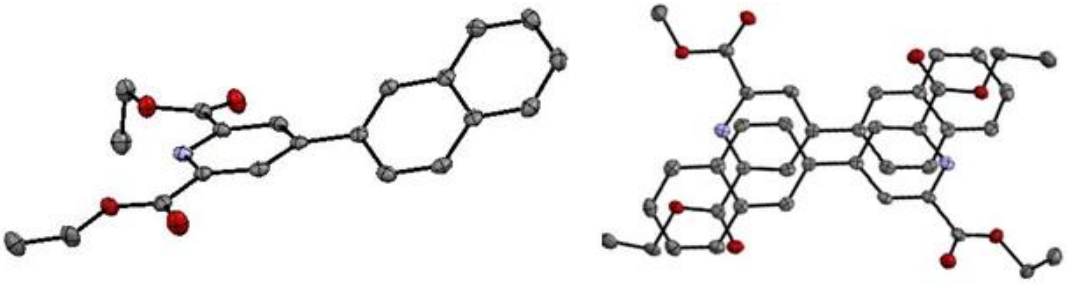

Figure 53: ORTEP drawings of diester **80**. Hydrogen atoms have been omitted for clarity. Left: structure of the molecule, right: view of the packing interactions

PhTPyMTA **77** and NpPyMTA **84** are two ligands incorporating a fluorescent group. As a perspective, we could envision to study their potential use for the detection of cations by fluorescence, as the fluorescence could change when coordinated to cations.[137]

Variations in the coordination sphere of the PyMTA ligand were explored as they can induce a drastic change in the EPR spectrum. To do so, we decided to substitute two carboxylic acid moieties with two pyridines to obtain pyridinedimethylenenitrilo-dipyridyldiacetate (PyMDPDA). Addition of ethyl bromoacetate on 2-picolylamine **85** afforded ester **86** in good yield after distillation under

reduced pressure.[138] This product could not be purified by column chromatography because of its degradation on silica gel. Ester **86** readily coupled with dibromide **69** to give Et-*p*BrPyMDPDA **87** in excellent yield. Without any further purification, compound **87** was saponified with NaOH to afford the desired *p*BrPyMDPDA **88** which was purified by HPLC purification (Scheme 18).

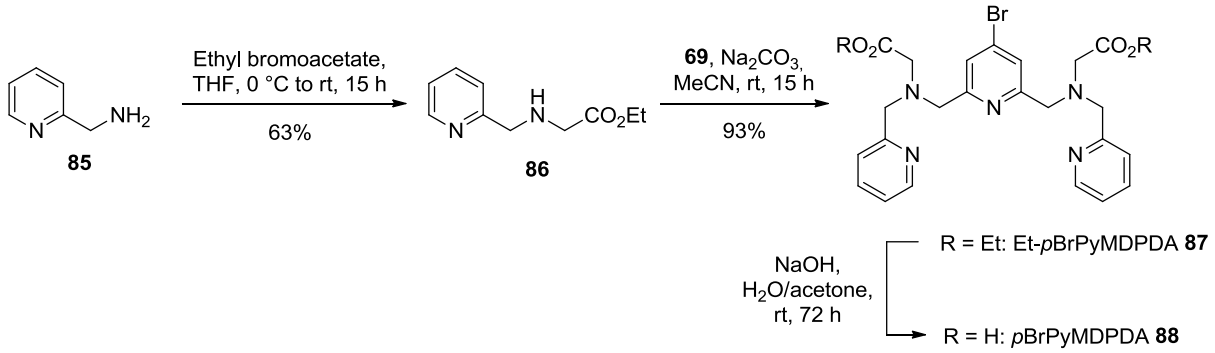

Scheme 18: Synthesis of *p*BrPyMDPDA **88**

The J-band *cw*-HFEPR of the *in situ*-generated Mn^{II} complex of *p*BrPyMDPDA **88** was recorded (Figure 54).

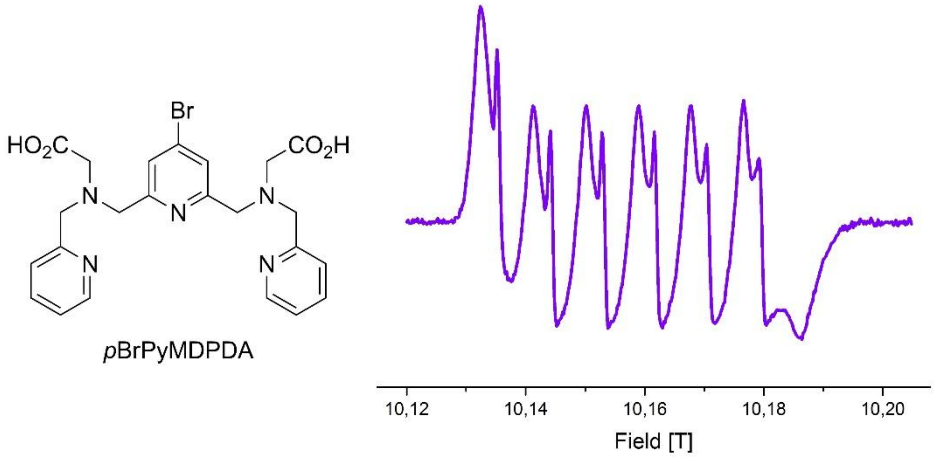

Figure 54: Structure of *p*BrPyMDPDA **88** (left) and J-band *cw*-HFEPR spectrum of the corresponding Mn^{II}-complex (500 µM in ligand, 440 µM in Mn^{II}, in 100 mM pH 8 HEPES buffer with 20% glycerol at 23 K, right)

The expected six-line pattern is clearly visible, but compared to PyMTA, the minor feature became prominent. It seems that the replacement of two carboxylates with two pyridines leads to much broader lines. However, it could be interesting to compare Mn^{II}-PyMTA and Mn^{II}-PyMDPDA in PELDOR to see directly the influence of the broadening on the performance of the distance measurement.

Looking for narrower lines, we surmised that using a macrocyclic version of PyMTA could change the coordination sphere in a favorable way, because the affinity for Mn^{II} is in general higher than for acyclic ligands. A macrocycle could also induce conformational constraints, reducing the number of conformations to obtain a higher symmetry. These ligands are known as pyridyltriazacyclododecane triacetate (PCTA) and pyridyltriazacyclododecane monoacetate (PCMA).

1.4 PCTA and PCMA

PCTA and PCMA (Figure 55) are macrocyclic ligands incorporating a pyridine in a triaza ring. They display high $\log K_{MnL}$ values of 18.59 and 11.54, respectively,[130] and could thus constitute good candidates, even if their synthesis is less straightforward than PyMTA derivatives.

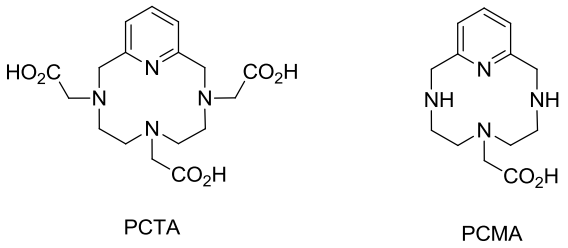

Figure 55: Structures of PCTA and PCMA

Our first synthetic efforts were directed toward PCTA. Using a classical procedure,[139] diethylenetriamine **89** was protected with three nosyl (Ns) groups with NsCl, affording the tri-Ns compound **90** in low yield. This compound was then engaged in a macrocyclisation with 2,6-dibromomethylpyridine **64** in the presence of Na_2CO_3, giving the expected Ns-protected macrocycle **91** in excellent yield. Surprisingly, the reaction does not require dilute conditions, as it is usually the case (around 0.1 M was found to be very effective). However, the next step was problematic. In our hands, the usual conditions employed for the removal of the Ns group ($PhSH/Na_2CO_3$/DMF) systematically afforded a mono-nosylated product. The use of high temperatures for a long time, a large excess of PhSH, or other conditions (PhSH/KOH/MeCN) did not solve the problem (Scheme 19).

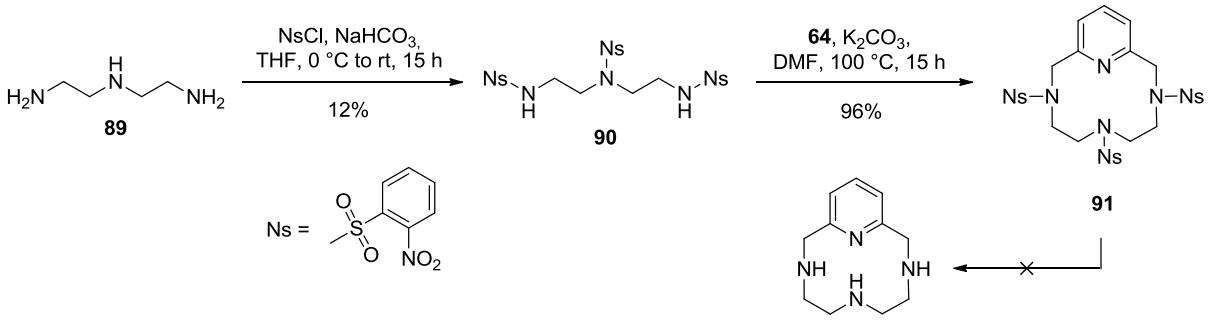

Scheme 19: Attempted denosylation of **91** toward PCTA

Thus, we decided to directly introduce masked acetic acid groups (protected as ^{t}Bu esters) on diethylenetriamine **89**. Accordingly, the two primary amine groups of this reactant were protected with Bn moieties using a reductive amination with benzaldehyde and $NaBH_4$ to give compound **92**. The three remaining secondary amine groups were reacted with *tert*-butyl bromoacetate in the presence of K_2CO_3 to afford triester **93** in moderate yield. Catalytic hydrogenation with Pd/C removed the Bn groups in nearly quantitative yield to give intermediate **94**,[140] which was then engaged in a macrocyclization in the same conditions as before. However, the expected macrocycle could not be isolated pure (Scheme 20). As a commercial source provided us at this point with a small

amount of PCTA to allow us recording the EPR spectrum, we did not pursue our synthetic efforts any further.

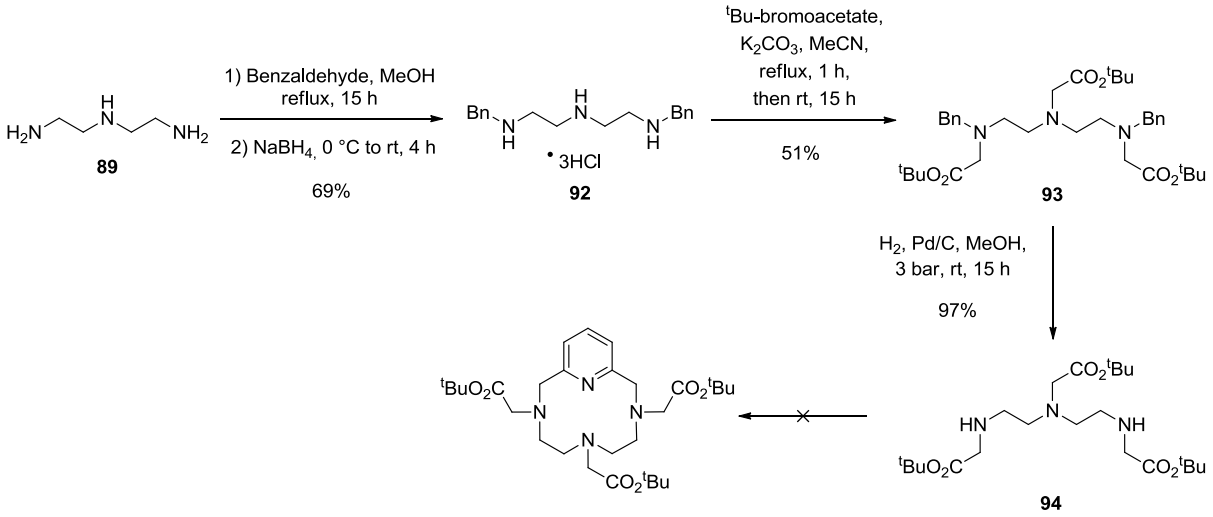

Scheme 20: Attempted macrocyclization of **94** toward PCTA

We explored in the meantime the synthesis of PCMA. The two primary amine groups of diethylenetriamine **89** were protected with two equivalents of NsCl to give the di-Ns product **95**, which was reacted with tert-butyl chloroacetate in the presence of TEA to afford ester **96** in moderate yield. Macrocyclization with 2,6-dibromomethylpyridine **64** as described before proceeded smoothly, giving ^{t}Bu-2Ns-PCMA **97** in 55% yield. In this case, the removal of the two Ns groups with thiophenol and Na_2CO_3 proceeded without difficulties to generate ^{t}Bu-PCMA **98**.[141] Finally, the carboxylic acid was regenerated with TFA, again without problems, to afford pure PCMA **99**. Futhermore, another way toward PCTA was tried: ester **98** was reacted with *tert*-butyl bromoacetate but here again, the purification proved difficult and the expected product could not be obtained in a satisfactory purity (Scheme 21).

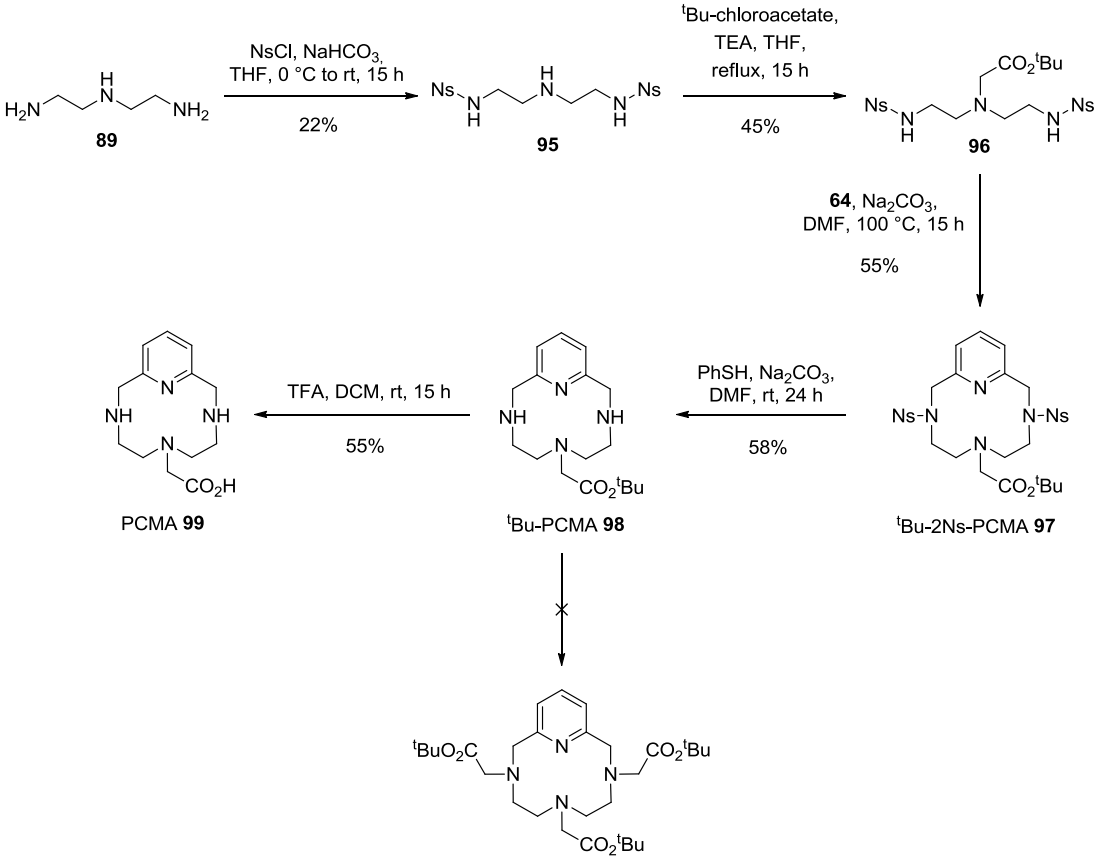

Scheme 21: Synthesis of PCMA **99**

The J-band *cw*-HFEPR of the Mn^{II} complex of PCMA (generated *in situ*) was recorded (Figure 56).

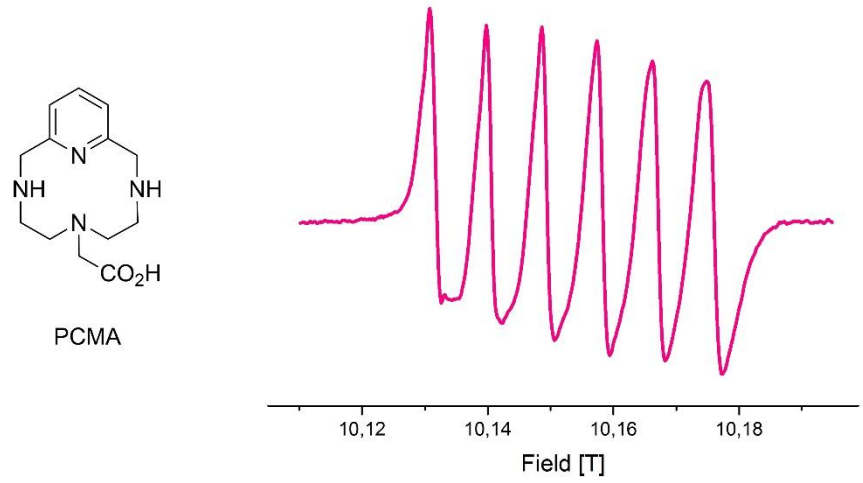

Figure 56: Structure of PCMA **99** (left) and J-band *cw*-HFEPR spectrum of the corresponding Mn^{II}-complex (500 µM in ligand, 450 µM in Mn^{II}, in 100 mM pH 8 HEPES buffer with 20% glycerol at 23 K, right)

Here the broadness of the lines is identical to PyMTA **66** but much narrower than *p*BrPyMDPDA **88** (peak-to-trough linewidth: 21 G). The usual minor feature is certainly hidden under

the lines. We also recorded the J-band *cw*-HFPER spectrum of the *in situ*-generated Mn^{II} complex of PCTA (Figure 57).

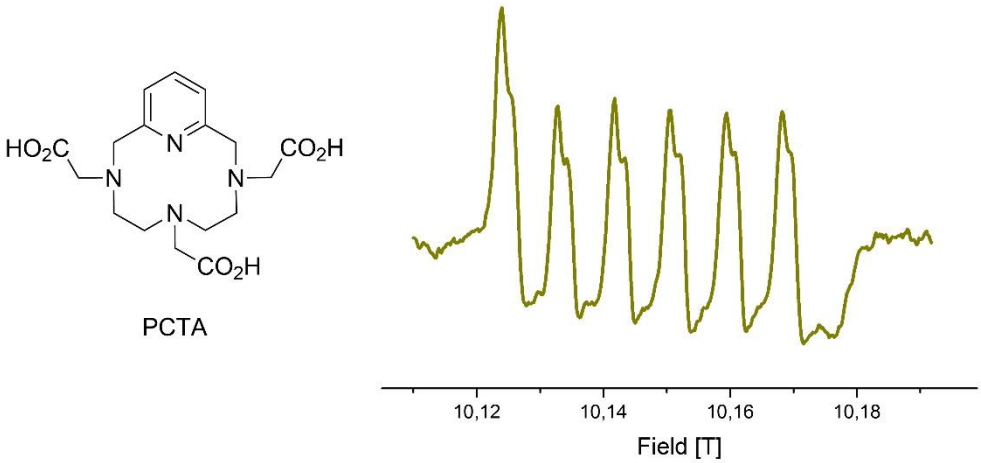

Figure 57: Structure of PCTA (left) and J-band *cw*-HFEPR spectrum of the corresponding Mn^{II}-complex (500 µM in ligand, 250 µM in Mn^{II}, in 100 mM pH 8 HEPES buffer with 20% glycerol at 23 K, right)

Here the broadness appears to be comparable to *p*BrPyMDPDA **88** (peak-to-trough linewidth: 32 G). The minor feature is this time visible but the whole spectrum resembles Mn^{II}-PCMA, suggesting that the two additional carboxylate arms have a marked influence. This shows that a higher affinity constant does not necessarily leads to narrower hyperfine lines, highlighting the complexity of the ligand screening process.

All these experiments led us to envision that the pyridine ring could be linked to the relative broadness of the hyperfine lines, so we started to study the analogue of PCTA where an azaacetate arm replaces the pyridine ring, known as tetraazacyclododecane-tetraacetic acid (DOTA).

1.5 DOTA and DO3A

The DOTA ligand was first described in 1976.[142] This well-know chelator exhibits very high formation constants for the coordination of various transition metals and lanthanides. The coordination number is usually 6 or 7 for transition metals, and 8 or 9 (with a coordinated water molecule) for lanthanides.[143] Gadolinium complexes of DOTA are widely used as contrast agents in magnetic resonance imaging (MRI), whereas yttrium-90 complexes have proved efficient for cancer treatment.[144] Some Mn^{II} complexes have also started to emerge as potential MRI agents.[133] Gd-DOTA and its derivatives have been widely used for Gd-Gd[69,70,75,76,78,82] or Gd-NO[83,84,85,86] PELDOR distance measurements. Using DOTA as a spin label for Mn^{II}-based distance measurements on rigid systems did not seem attractive in the beginning, because it is usually grafted using one of the acetate arms, which inherently induces flexibility.

Manganese complexes of DOTA have been less studied. The $\log K_{MnL}$ is equal to 19.89, which is the highest known stability constant amongst mononuclear Mn^{II} complexes.[145] Dissociation kinetics have also been studied,[146] and revealed the high kinetic inertness of Mn^{II}-DOTA (k_0 = $1.8.10^{-7}$ s^{-1}). Crystals of the Mn^{II} complex of DOTA have been obtained by mixing equimolar amounts of DOTA and

$MnSO_4 \bullet H_2O$ in water: after stirring at rt for 30 min, diffusion of acetone gave crystals suitable for X-ray crystallography.[147] The crystal structure reveals a coordination number of 6: the Mn atom is bound to the four nitrogen atoms of the cyclen ring and to two carboxylate groups, the two other being protonated and uncoordinated (Figure 58.

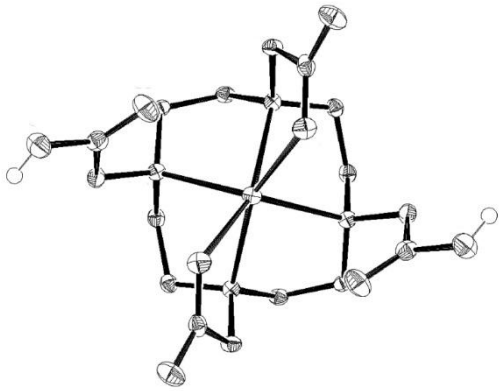

Figure 58: Crystal structure of Mn^{II}-DOTA. Adapted from [147]

The synthesis of a large number of functionalized DOTA has also been described, while DOTA and numerous functionalized derivatives are commercially available. The J-band *cw*-HFEPR spectrum of the Mn^{II}-DOTA complex, generated *in situ*, is displayed in Figure 59 as well as the J-band *cw*-HFEPR spectrum of $Mn(H_2O)_6^{2+}$ for comparison purposes.

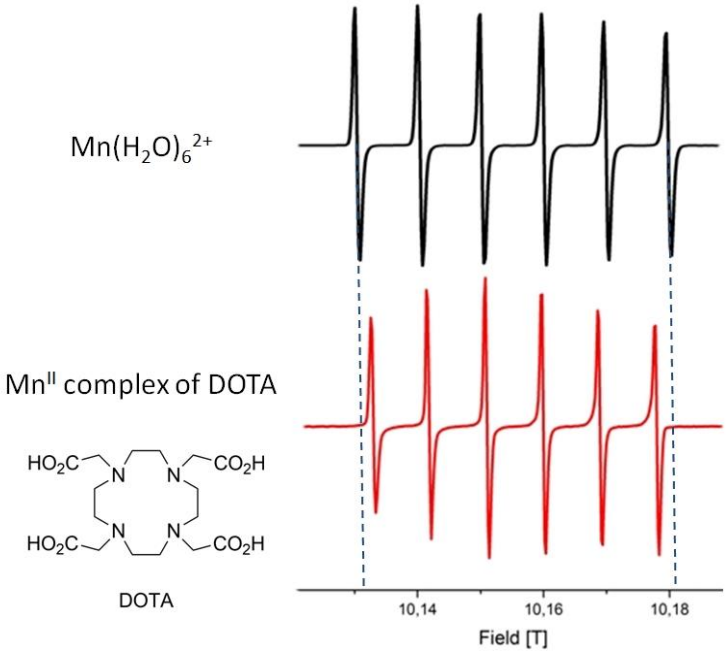

Figure 59: Left: Structure of DOTA. Right: J-band *cw*-HFEPR spectrum of $Mn(H_2O)_6^{2+}$ (top) and of the Mn^{II} complex of DOTA (bottom, 1 mM in ligand, 500 µM in Mn^{II}, in 100 mM pH 8 HEPES buffer with 20% glycerol). Blue dashed lines show the difference in the hyperfine constants

The J-band *cw*-HFEPR spectrum of Mn^{II}-DOTA displays six narrow lines, slightly narrower than those of $Mn(H_2O)_6^{2+}$ (peak-to-trough linewidths of 6 and 7 G, respectively). This sextet is centered at

g = 2.00122, and the hyperfine coupling is |A| = 252 MHz. These values are quite comparable to the $Mn(H_2O)_6^{2+}$ parameters, *g* = 2.00107 and |A| = 267 MHz, which is in agreement with the apparent similarity between these spectra, even if we will show in the next chapter that the ZFS *D*-value is different (610 MHz[27] for $Mn(H_2O)_6^{2+}$ compared to 280 MHz[148] for Mn^{II}-DOTA). The difference in the hyperfine constants can easily be seen with the blue dashed lines of Figure 77. The very high symmetry of the Mn^{II} coordination sphere suggested by the crystal structure as well as the very high K_{MnL}[145] could explain the comparable narrowness of the hyperfine lines of $[Mn(H_2O)_6]^{2+}$ and Mn^{II}-DOTA, which appears as the ideal candidate for PELDOR distance measurements.

However, attaching DOTA on a linker could generate issues, because contrary to the other ligands that we studied, the coordination sphere is likely to be modified upon grafting. For instance, a common DOTA derivative, where one of the acetate arms is removed, is known as tetraazacyclododecane-triacetic acid (DO3A, see Figure 58). When the three carboxylate groups are protected, the free amine group can be used for tagging purposes, but this could disrupt the geometry of the coordination sphere and thus the narrowness of the lines. To confirm this hypothesis, we recorded the J-band *cw*-HFPER spectrum of the *in situ*-generated Mn^{II}-DO3A complex (Figure 60).

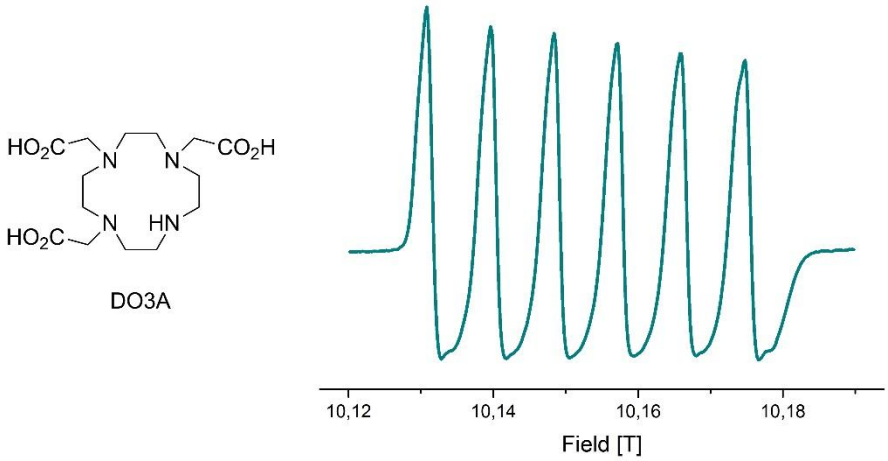

Figure 60: Structure of DO3A (left) and J-band *cw*-HFEPR spectrum of the corresponding Mn^{II}-complex (500 µM in ligand, 450 µM in Mn^{II}, in 100 mM pH 8 HEPES buffer with 20% glycerol at 23 K, right)

It is clear that the symmetry breaking of the coordination sphere leads to the broadening of the lines (peak-to-trough linewidth: 27 G). Indeed, the crystal structure of Mn^{II}-DO3A derivatives are heptacoordinated.[149] According to this spectrum, the use of DO3A most probably would not improve the sensitivity of PELDOR distance measurements, but it could still be useful as higher ZFS parameters can lower the contribution of the pseudo-secular term of the dipolar Hamiltonian, leading to ligands that are more adequate for short distance measurements.[34]

DOTA derivatives are also commonly attached by one of the carboxylic acid arms to form an amide bond.[150,151,152,153] This grafting mode is to be preferred as the whole DOTA core is conserved. Indeed, the carbonyl group of the amide bond is known to complex Gd^{III} for instance, inducing negligible changes in the coordination sphere compared to Gd-DOTA.

However, in the crystal structure depicted in Figure 58, Mn^{II} is hexacoordinated, meaning that when one the carboxylate arms of DOTA is functionalized, Mn^{II} can coordinate through two opposite carboxylate arms or through one carboxylate and the oxygen atom of the amide tether. The latter case may lead to a different EPR spectrum, but as we will show later (Figure 119, p. 172), this is not the case. This also raises the question: is Mn^{II}-DOTA hexacoordinated in solution? If this is the case, the spectrum of Mn^{II}-DO2A should not be different from that of Mn^{II}-DOTA. To further investigate this question, we recorded the J-band *cw*-HFPER spectrum of the *in situ*-generated Mn^{II}-DO2A complex displayed in Figure 61.

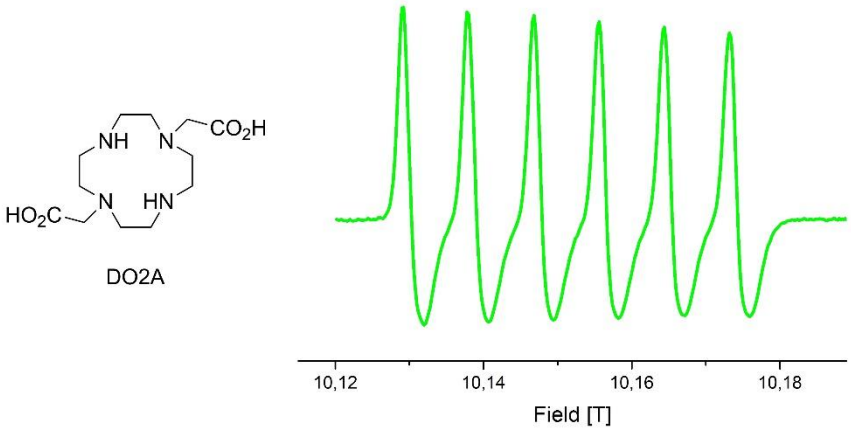

Figure 61: Structure of DO2A (left) and J-band *cw*-HFEPR spectrum of the corresponding Mn^{II}-complex (500 µM in ligand, 450 µM in Mn^{II}, in 100 mM pH 8 HEPES buffer with 20% glycerol at 23 K, right)

We can clearly see that the lines are again much broader than Mn^{II}-DOTA (peak-to-trough linewidth: 20 G) but narrower than Mn^{II}-DO3A. These experiments suggest that Mn^{II}-DOTA could be octacoordinated in solution, whereas it is hexacoordinated in the solid state (see Figure 76).[147] This is not surprising as it is known that the solid state structure does not always reflect the actual solution structure. Indeed, solution studies have shown that the carboxylic arms of Mn^{II}-DOTA are fully deprotonated at pH 6 to 8.[146] As shown above, high coordination numbers, up to seven and eight, are not uncommon for Mn^{II} with macrocyclic or tripodal ligands.[149,154,155,156,157] This hypothesis is supported by the fact that the Mn^{II} complex of tetraazacyclododecane-tetracarboxamide (DOTAM) is octacoordinated in the solid state (as shown by the crystal structure depicted in Figure 63, obtained by recrystallization of the complex from water[147]) and displays a nearly identical J-band *cw*-HFEPR spectrum as Mn^{II}-DOTA (peak-to-trough linewidth: 8 G, Figure 62). A more detailed investigation have been performed in the second chapter of this manuscript.

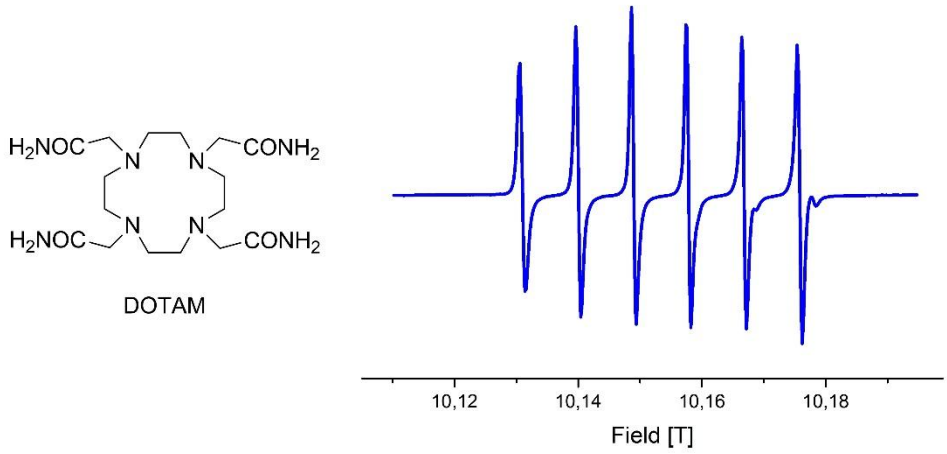

Figure 62: Structure of DOTAM (left) and J-band *cw*-HFEPR spectrum of the corresponding Mn^{II}-complex (500 µM in ligand, 495 µM in Mn^{II}, in 100 mM pH 8 HEPES buffer with 20% glycerol at 23 K, right). The small peaks around 10.17-10.18 T are due to a slight excess of free Mn^{II}

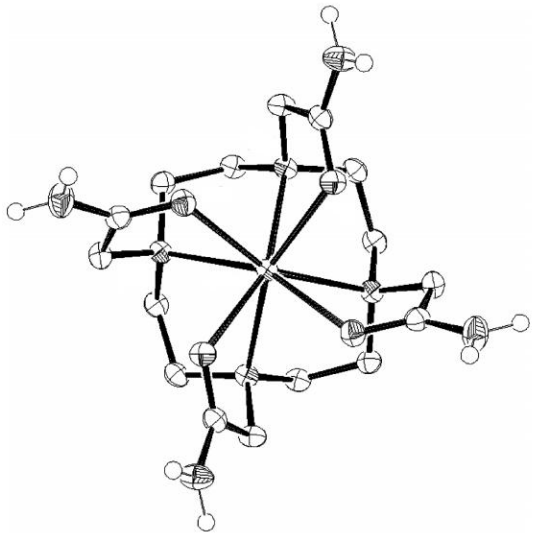

Figure 63: Crystal structure of Mn^{II}-DOTAM. Adapted from [147].

To conclude, the screening of numerous ligands based on the J-band *cw*-HFEPR of the corresponding Mn^{II} complexes has led to the identification of DOTA as a very attractive candidate for the PELDOR method. Starting from Mn^{II}-BImP, we saw that the use of two bromide anions in the coordination sphere was detrimental because of the corresponding poorly defined *cw*-HFEPR spectrum. Mn^{II}-bis(Tpy) derivatives constituted a first improvement as six well-defined lines were observed. They constitute acceptable candidates and platforms with two Mn^{II}-bis(Tpy) connected to a central linker will be developed and studied (see below). Moving toward water-soluble Mn^{II} complexes of PyMTA and PyMDPDA that include carboxylate groups narrowed the EPR lines, but the use of the pyridine-containing macrocyclic ligands PCMA and PCTA did not improve their narrowness. Keeping the macrocycle but removing the pyridine led to the identification of DOTA as the ideal ligand for Mn^{II} to graft on rigid spacers. A comparison between the crystal structure of Mn^{II}-DOTA and *cw*-HFEPR spectra of derivatives suggested that Mn^{II}-DOTA could be octacoordinated in solution.

We will now discuss the synthesis of different linkers and present the methodology to graft them on some of these ligands.

2. LINKERS AND GRAFTING OF LIGANDS

We have a set of ligands for Mn^{II} to be used as paramagnetic centers for the PELDOR method. We now need to graft two of them on a central linker to obtain bis-Mn^{II} systems and to test them in PELDOR. This central spacer has to comply with the specifications of a "molecular rod". It must be rigid (in order to obtain a constrained distance between the two paramagnetic centers), easily incrementable (to have access to a broad range of distances) and must possess functional groups allowing straightforward coupling to the magnetic centers. Moreover, these two groups should be either identical (to incorporate the same paramagnetic center) or different (to obtain dissymmetrical platforms containing, for instance, a Mn^{II} complex and a stable radical, or two different Mn^{II} complexes). Readily crystallizable rods are desirable to determine the distance from X-ray crystallography for comparison with the distances obtained with the PELDOR methodology. To this aim, DFT calculations will also be employed. Finally, the ideal linker should also be water-soluble, so that the PELDOR experiment could be performed in water in order to be as close as possible to the conditions that will be used in future biological applications.

2.1 Oligo(piperidine) linker

2.1.1 Synthesis of the oligo(piperidine) linker

To fulfill these requirements, we turned our attention to a quite recently described oligo(piperidine) linker.[158] This spacer consists of an oligomeric backbone of piperidines, which adopt a chair conformation, both in solution (as shown by NMR experiments) and in the solid state (as revealed by the crystal structure depicted in Figure 64). Furthermore, this rod is water-soluble and suitable for asymmetric platforms, bearing a keto group at one side and an amino group at the other side.

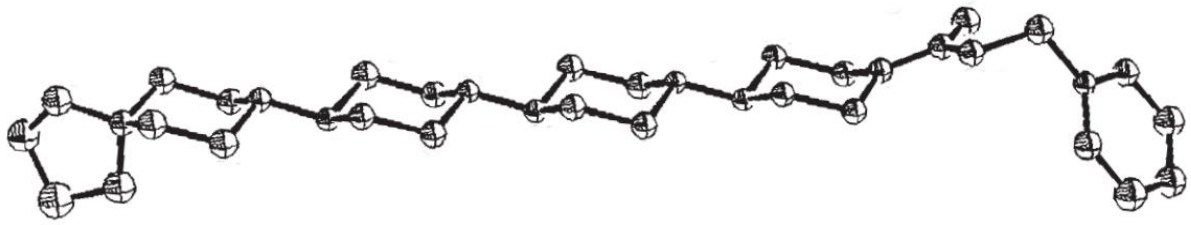

Figure 64: ORTEP drawing of a tetrapiperidine linker. Adapted from [158]

The elongation methodology is based on iterative reductive aminations (Scheme 22).[158] First, 4-piperidone **100** was protected with a benzyl (Bn) or a carboxybenzyl (Cbz) group to give the corresponding *N*-protected piperidones (**101** and **102**, respectively) in good to high yield. The Cbz and the Bn groups have been chosen because they can be removed by hydrogenation: in the first case, we followed the literature conditions, but in the second case, the Bn group was used because it

can also be removed using 1-chloroethyl chloroformate,[159] which could be useful if hydrogenation-sensitive moieties are also present.

Next, reductive amination with 4-piperidone ethylene ketal **103** in the presence of $NaBH(OAc)_3$ and AcOH afforded the orthogonally protected bis(piperidines) **104** and **105** (with a Bn or a Cbz group, respectively) in good yields. Optimization was needed for this step, as the literature conditions[158] (no AcOH) afforded the product in non reproducible yields (30 to 60%) with a slow conversion, even when a large excess of $NaBH(OAc)_3$ was employed. In our hands, the use of AcOH[160] gave consistent good yields and conversions.

The orthogonally protected compound **105** was then either hydrogenated under pressure to give the free amine **106** in nearly quantitative yield, or treated with HCl to regenerate the ketone **107** by removal of the ketal group (Scheme 22). This step was problematic, as the conditions described[158] (37% aq. HCl for 25 min) led to poor yields (around 15%), presumably due to degradation. The use of more diluted HCl (6 M) improved the yield to 36%. With higher dilutions of cold HCl (4M), smooth deprotection of the ketone was obtained with excellent yields (> 90%), albeit in one week. This procedure was also successful in the synthesis of ketone **108**, but the Bn group could not be removed using 1-chloroethyl chloroformate in DCM and then refluxing the mixture with MeOH,[159] maybe because of the cleavage of the other C-N bond.

Lastly, a second reductive amination between **106** and **107** with $NaBH_3CN$ in the presence of $Ti(O^iPr)_4$[160] afforded the orthogonally protected tetra(piperidine) **109** in low yield. Again, the original conditions[158] ($NaBH(OAc)_3$) did not allow for the formation of the desired product, even when AcOH was added, or when freshly distilled DCE was used. Replacing $NaBH_3CN$ for $NaBH_4$ led to poorer yields. The difficulty to perform reductive aminations on bis(piperidines) **106** and **107** was confirmed by the fact that no reaction took place between **107** and piperazine, while the coupling between amine **106** and cyclohexanone led to the isolation of the adduct with only 15% yield using $NaBH(OAc)_3$ with AcOH (Scheme 22).

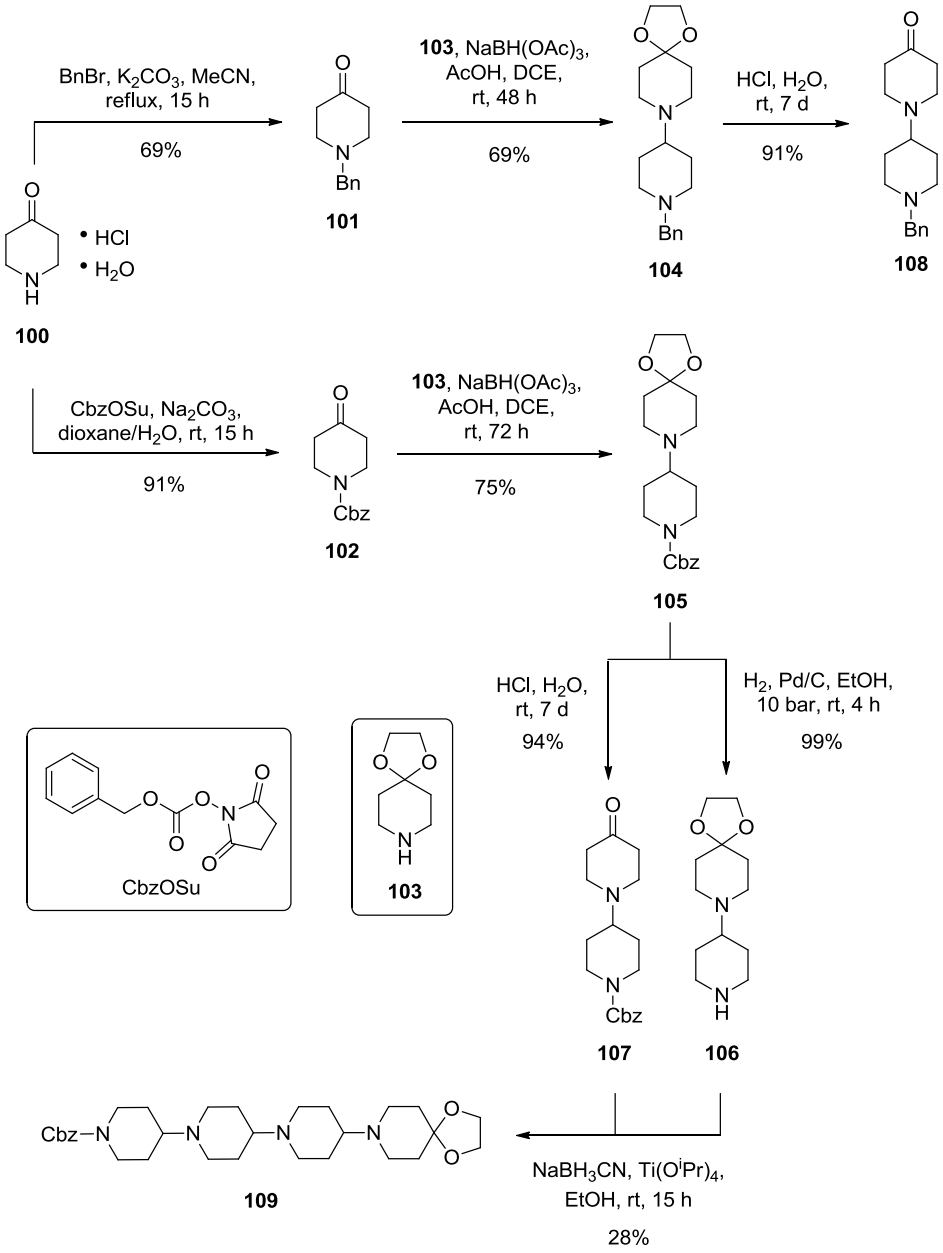

Scheme 22: Synthesis of the orthogonally protected tetrapiperidine linker **109**

The same synthetic steps were performed starting from a Fmoc-protected linker, but numerous stability and degradation issues were encountered during the synthesis.

To improve the efficiency of the last step, ketone **107** was reduced to alcohol **110** with $NaBH_4$ in high yield. Mesylation of this compound with MsCl in the presence of pyridine generated mesylate **111** quantitatively. Unfortunately, no nucleophilic substitution between this compound and amine **106** took place (K_2CO_3 in refluxing MeCN, Scheme 23).

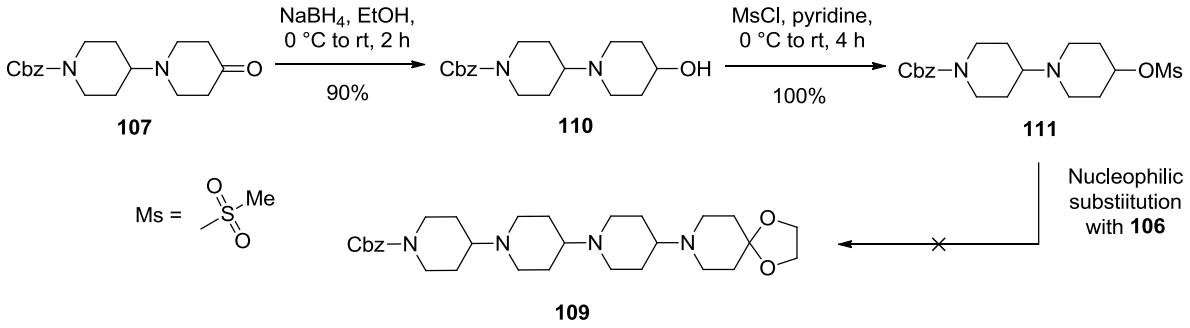

Scheme 23: Synthesis of a bis(piperidine) linker with a mesylate group

To overcome these difficulties, we decided to use only the bis(piperidines) **106** and **107** as rigid rods, and to extend their length with aromatic groups. An idea was the addition of a building block with an ethynyl moiety suitable for further grafting. To this end, *p*-bromoethynylbenzene **112** was protected with a trimethylsilyl (TMS) group with TMSOTf in the presence of a catalytic amount of $Zn(OTf)_2$ to give bromoarene **113** in high yield.[161] Hartwig-Buchwald coupling with amine **106** in the original Buchwald conditions[162,163] (tris(dibenzylideneacetone)dipalladium ($Pd_2(dba)_3$), (2,2'-bis (diphenylphosphino)-1,1'-binaphthyl (BINAP) and NaO^tBu in refluxing toluene) generated ketal **114** in moderate yield. Noteworthy, this coupling failed whatever the conditions ($Pd_2(dba)_3$/BINAP/NaO^tBu or $Pd(OAc)_2$/$P(^tBu)_3$/Cs_2CO_3) when the alkyne partner was not TMS-protected. Finally, the TMS group was removed with K_2CO_3 in MeOH to give the corresponding alkyne **115** in high yield (Scheme 24).

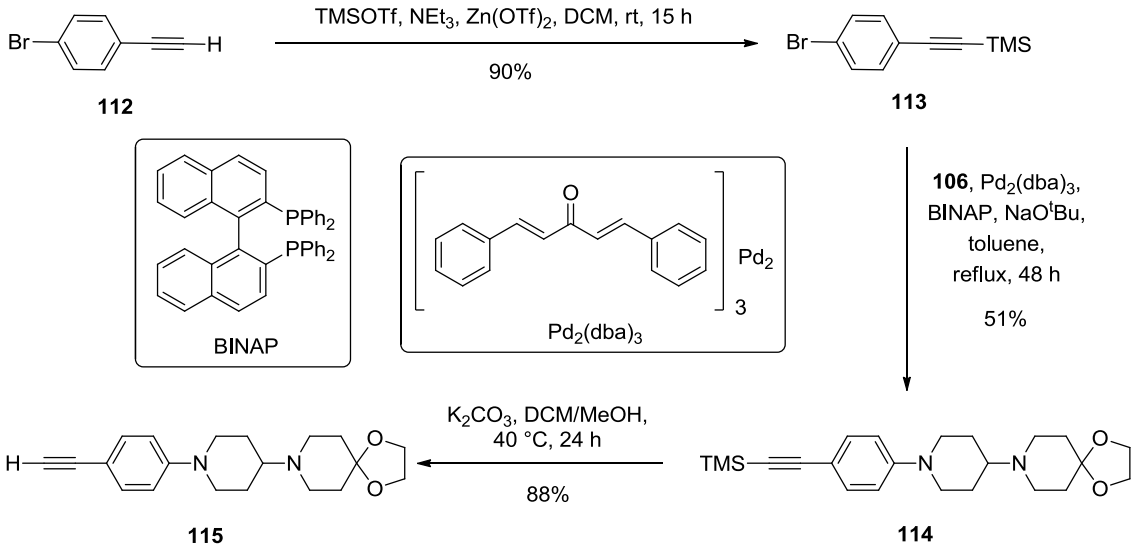

Scheme 24: Incorporation of an ethynyl group in the oligo(piperidine) linker

We will now describe how the ligands synthesized in the first part of this chapter will be coupled to these oligo(piperidine) linkers.

2.1.2 Coupling with ligands

2.1.2.1 Grafting of BImPs

The first approach we chose was to directly build a bis-BimP platform with a bis(piperidine) linker from the BImPs synthesized above (p. 62). The direct Hartwig-Buchwald coupling between *p*Br-^{i}Pr-BImP **21** and bis(piperidine) **106** in the original Buchwald conditions[162] afforded only traces of the expected product as shown by mass spectroscopy (Scheme 25).

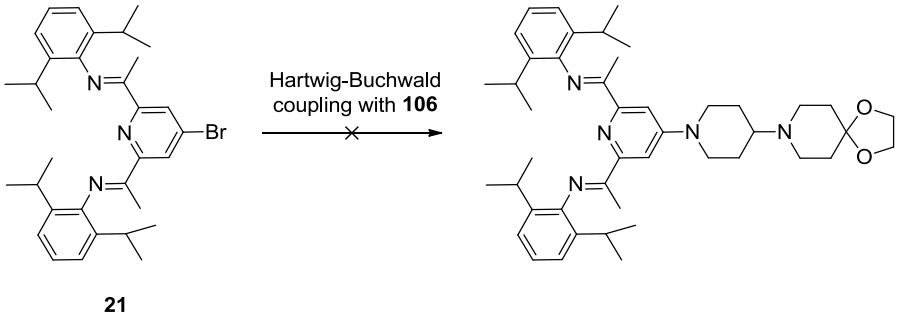

Scheme 25: Attempted direct coupling between a BImP and a bis(piperidine)

We surmised that the imino moiety could be detrimental, so we decided to use *p*BrDAP **11** instead of *p*Br-^{i}Pr-BImP **21**. The coupling between *p*BrDAP **11** and bis(piperidine) **106** ($Pd_2(dba)_3$/BINAP/NaO^{t}Bu, $Pd_2(dba)_3$/BINAP/Cs_2CO_3 or $Pd(OAc)_2$/BINAP/Cs_2CO_3) gave only 4%, 10% or none of the desired product, respectively, with tedious purification. Moreover, a Sonogashira coupling ($Pd(PPh_3)_4$/CuI/DMF/TEA) between *p*BrDAP **11** and alkyne **115** was not conclusive (Scheme 26).

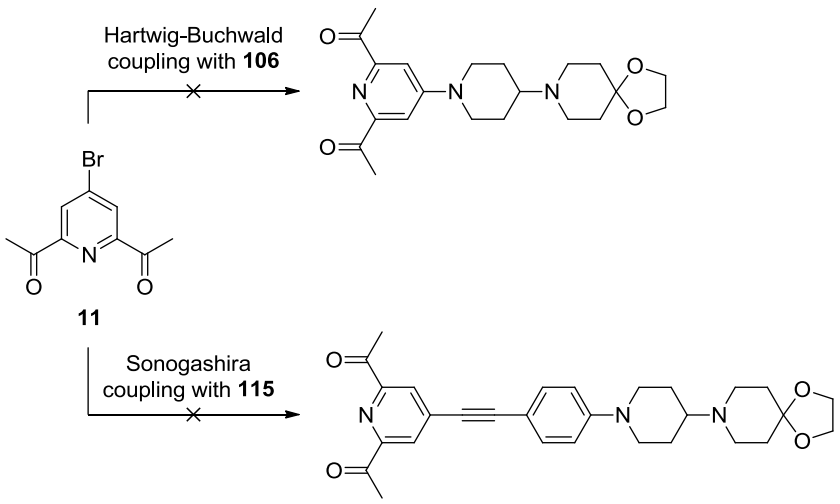

Scheme 26: Attempted couplings of *p*BrDAP **11** on bis(piperidine) linkers **106** and **115**

Instead of ketone **11**, a "protected" BimP was chosen in the form of a functionalized bis(pyrrolidino)pyridine that could be easily converted to the corresponding ketone later using the *method C* described earlier (p. 61). A one-pot sequence in which chelidamic acid **6** was successively

brominated and added on pyrrolidine generated diamide **116**, albeit in low yield. A Hartwig-Buchwald coupling with amine **106** gave ketal **117** in good yield, and the ketal group was removed with HCl to obtain ketone **118** (Scheme 27).

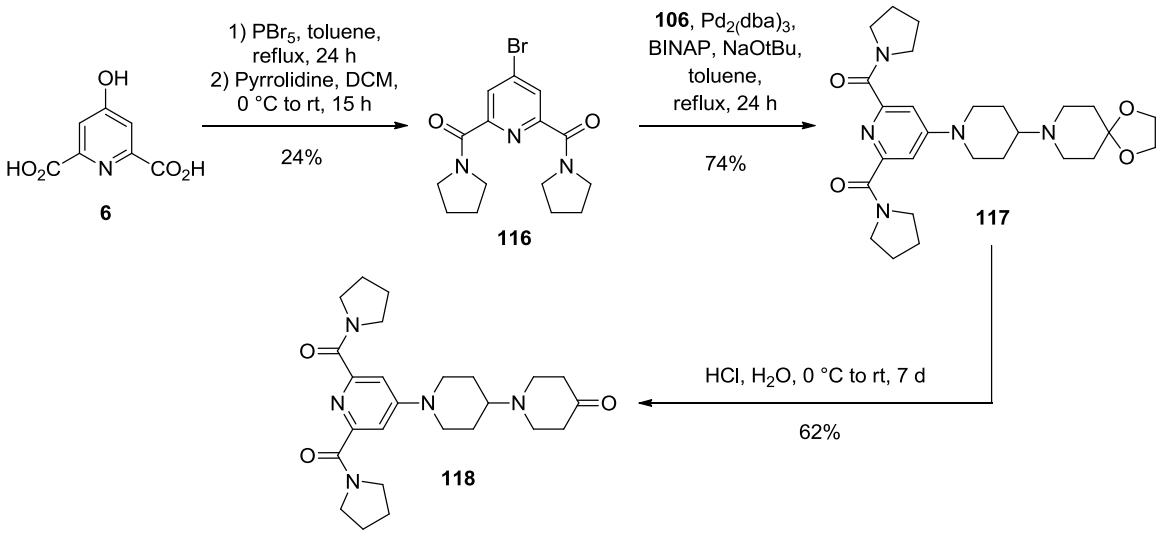

Scheme 27: Possible starting point for a bis(BimP) platform

As we became aware that Mn^{II}-BimPs were not suitable for the PELDOR method, we developed strategies to graft phenylterpyridines instead on the bis-piperidine linkers.

2.1.2.2 Grafting of Tpys

We first started with the amino side. A Hartwig-Buchwald coupling between amine **106** and *p*BrPhTpy **36** led to the formation of ketal **119** in nearly quantitative yield. No coupling product could be detected when *p*ClPhTpy **39** was used in the same conditions. Ketal group removal in acidic conditions regenerated the ketone **120** (Scheme 28).

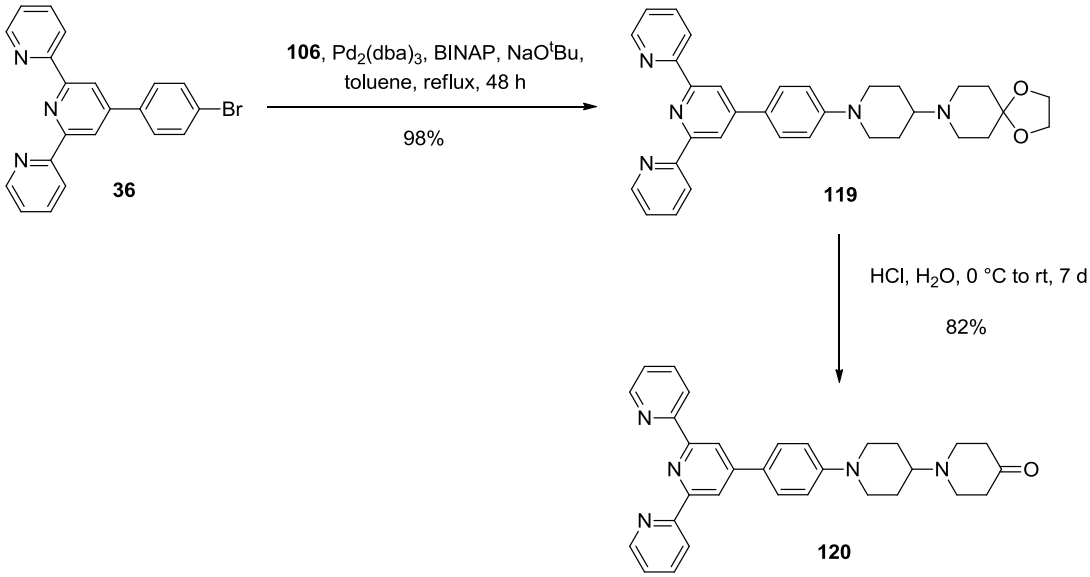

Scheme 28: Coupling on the amino side of the bis(piperidine) linker

The structure of ketone **120** was confirmed by X-ray crystallography. Orange needles suitable for X-ray diffraction were grown by slow evaporation from a deuterated chloroform solution. This molecule crystallizes in the Cc space group (monoclinic system), forming nearly perpendicular sheets. The four aromatic rings are roughly coplanar: two consecutive pyridine are coplanar and the third one is tilted by 16°, while the phenyl ring is twisted by 10°. The two piperidine rings adopt a chair conformation, but are not linearly arranged as the tetrapiperidine linker[158] because of the keto group (Figure 65).

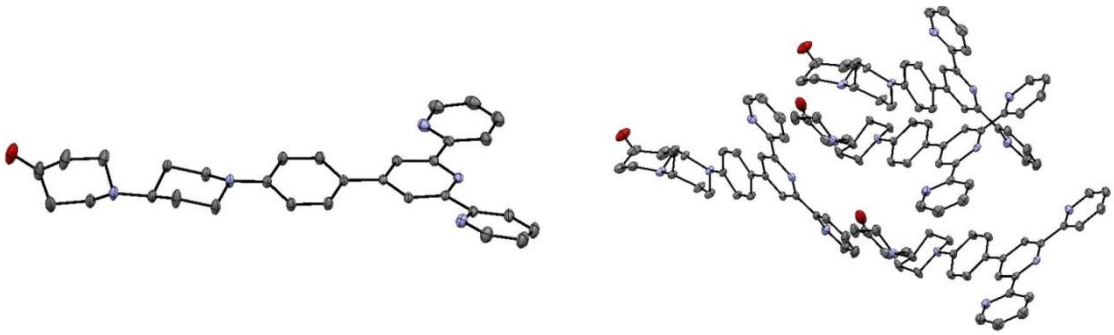

Figure 65: ORTEP drawings of ketone **120**. Hydrogen atoms have been omitted for clarity. Left: view of the asymmetric unit, right: view of the packing

Despite several attempts, ketone **120** could not be carried forward in further syntheses. A McMurry reaction[164,165] was attempted ($TiCl_4$/Zn/pyridine) without success, maybe because of the coordination of titanium by the terpyridine, the double reductive amination with piperazine ($NaBH(OAc)_3$/AcOH or $Ti(O^iPr)_4$/$NaBH_3CN$) failed, and the Horner-Wadsworth-Emmons reaction with phosphonate **45** (NaH, DMF or THF) did not proceed (Scheme 29).

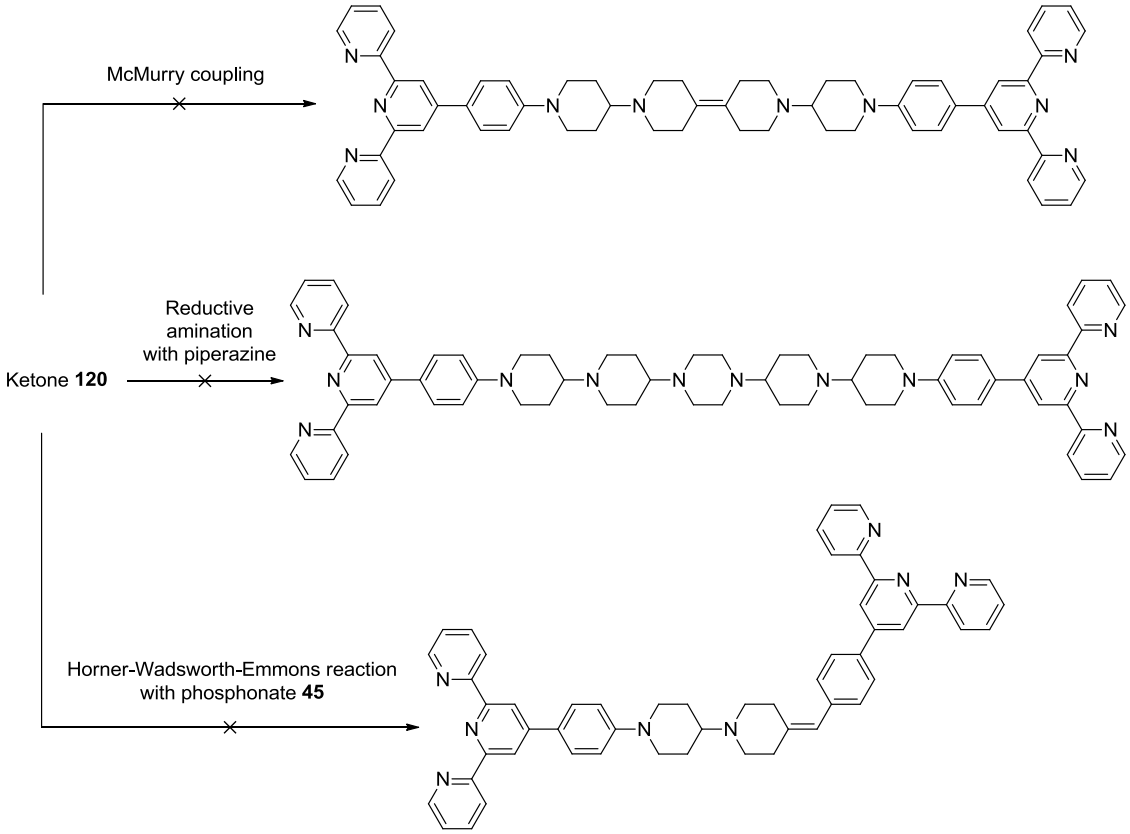

Scheme 29: Attempted syntheses of bis-Tpy platforms incorporating a bis(piperidine) linker

We also tried to convert ketone **120** into a more reactive group. The addition of ethynylmagnesium bromide to this compound to obtain an ethynyl group suitable for a subsequent Sonogashira coupling was not effective. Triflation of ketone **120** using LDA with *N*-phenyl-bis(trifluoromethanesulfonimide[166] ($PhNTf_2$) led to an impure product which could not be purified using column chromatography (Scheme 30).

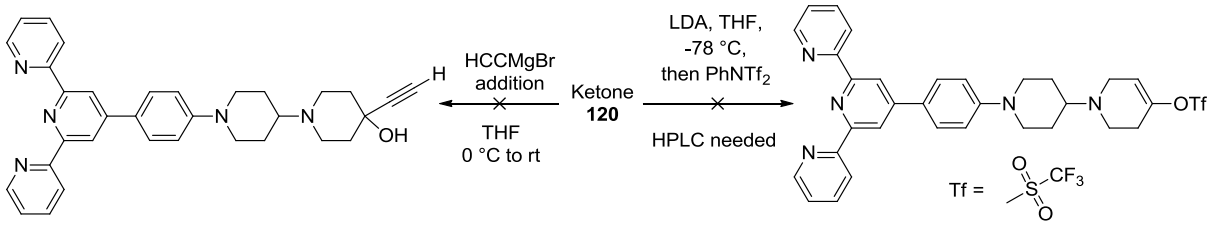

Scheme 30: Attempted conversion of ketone **120**

The same difficulties were encountered starting directly from ketones **107** and **108**. The addition of ethynylmagnesium bromide suffered from poor reproducibility and the couplings of the ethynyl compounds obtained this way failed systematically. We surmised that the hydroxy moiety could be an issue, but any attempt of dehydration failed under several different conditions (TFA, MsCl/TEA or $POCl_3$/pyridine, Scheme 31).

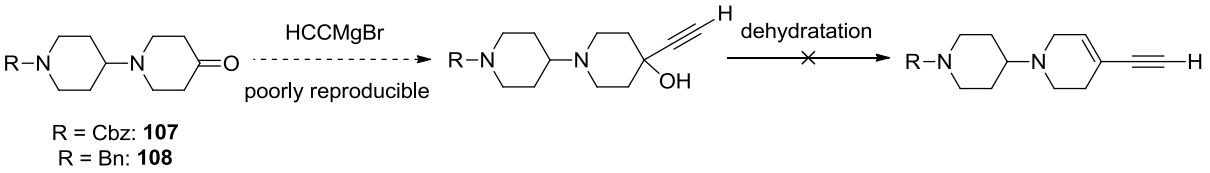

Scheme 31: Attempted conversion of the keto group of bis(piperidine)

However, the conversion of ketones **107** and **108** into the corresponding triflates **121** and **122** was successful. Unfortunately, these compounds proved unreactive for further Sonogashira couplings. The conversion into the corresponding boronate (bis(pinacolato)diboron $(Bpin)_2$/Pd(dppf)Cl_2/dppf/KOAc) was not effective.[167] So we decided to couple triflates **121** and **122** directly to boronate **46**. Under different conditions (Pd(dppf)Cl_2/K_2CO_3, Pd(dppf)Cl_2/Cs_2CO_3, Pd$(PPh_3)_2Cl_2$/Na_2CO_3 or Pd$(PPh_3)_4$/LiCl/Na_2CO_3), the maximum yield was around 40% for a purity of 50% as determined by HPLC (Scheme 32).

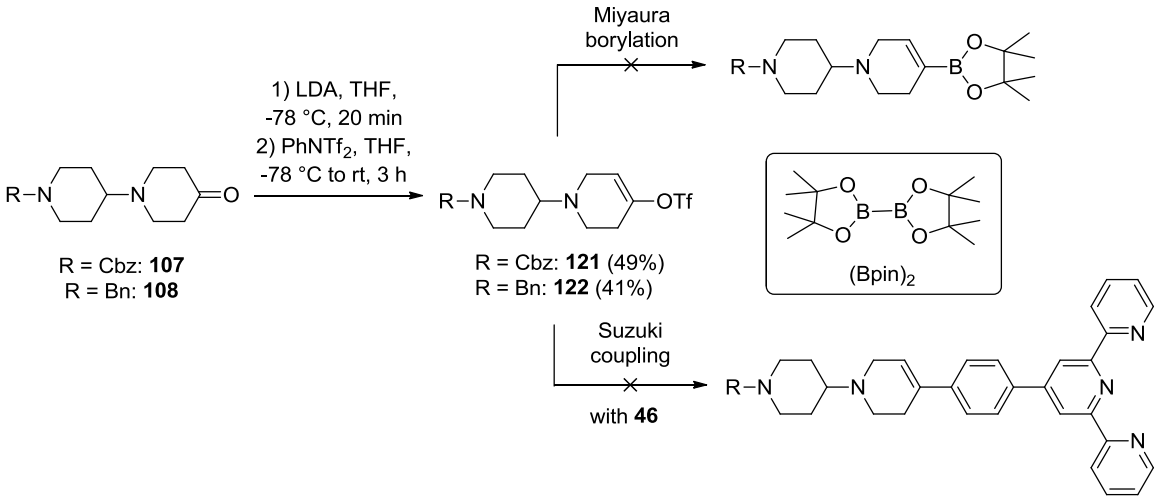

Scheme 32: Attempted couplings on triflates **121** and **122**

Alternatively, ketone **107** was allowed to react with hydrazine to give hydrazone **123** quantitatively, but the subsequent conversion into the bromoalkene ($CuBr_2$/TEA) failed.[168,169] Furthermore, the formation of a stannane derivative (*n*-BuLi/Bu_3SnH/MsCl) that could be used in a further Stille coupling did not proceed[170] (Scheme 33).

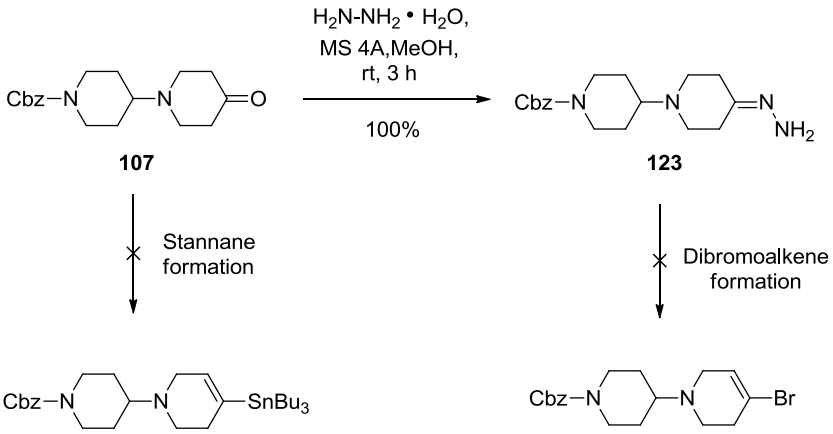

Scheme 33: Attempted synthesis of oligo(piperidine) coupling partners

Another strategy was to directly add the terpyridyl moiety as a Grignard reagent on the keto side. Using bromobenzene as a model compound for *p*BrPhTpy **36**, addition on ketone **107** allowed the formation of alcohol **124** in moderate yield. Elimination of water with TFA gave alkene **125** in good yield. Concomitant reduction of the double bond and deprotection of the amine using catalytic hydrogenation yielded amine **126** (Scheme 34).

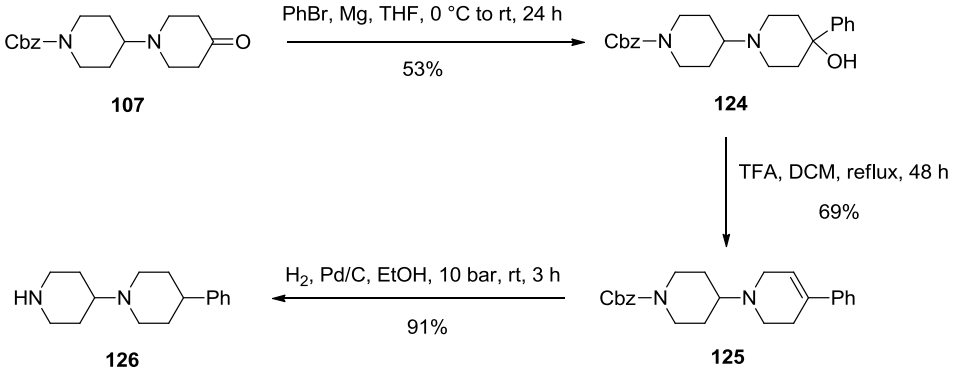

Scheme 34: Grafting of a phenyl ring on an oligo(piperidine) linker

Unfortunately, this sequence could not be reproduced when *p*BrPhTpy **36** was used, as no Grignard reagent could be formed from this compound, as well as other bromoarenes such as alkyne **113**, despite numerous attempts (use of sonication or chemical initiators, trials with *p*ClPhTpy **39** instead of *p*BrPhTpy **36**) (Scheme 35).

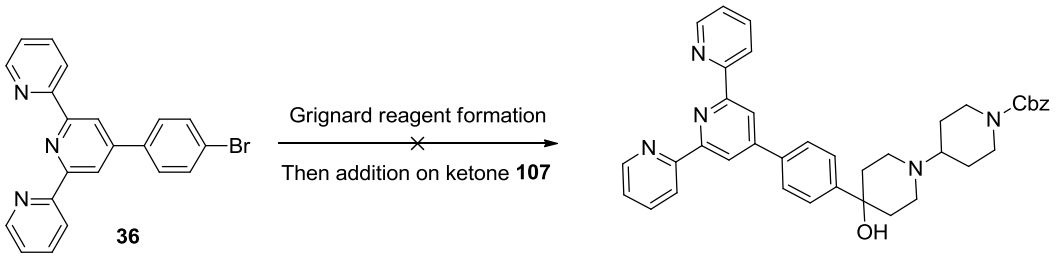

Scheme 35: Attempted formation of a Grignard reagent from *p*BrPhTpy **36** and subsequent coupling on ketone **107**

All these efforts led us to the conclusion that the oligo(piperidine) linker was not the ideal choice. Numerous modifications from the literature had to be realized to obtain a bis-piperidine rod and the final generation of a tetra-piperidine linker was difficult. Furthermore, even if couplings on the amino side proceeded well, this was not the case at all for the keto side, where numerous trials were performed without any conclusive result. We decided not to pursue with this linker any further and to explore other chemical scaffolds.

2.2 Phenyl-piperazine linker

2.2.1 Symmetric version

We hypothesized that a spacer with alternating benzene and piperazine rings could be well-suited for the requirements of this project. Indeed, the only efficient couplings with the oligo(piperidine) linker were Hartwig-Buchwald couplings, so we surmised that spacer with two amino end groups would be readily graftable on ligands for Mn^{II}. The idea was to attach one of the amino groups of the piperazine to a benzene ring to build the linker and the other amino group to a ligand or to another benzene ring to extend the linker. Accordingly, the retrosynthetic analysis for the smallest linker relies on a coupling between a central *p*-dibromobenzene and a monoprotected piperazine (Scheme 36).

Scheme 36: Retrosynthetic analysis of the phenyl-piperazine linker. R = protecting group

To prepare this spacer, the first step was to synthesize monoprotected piperazines. Treatment of di-*tert*-butyl dicarbonate (Boc_2O) with an excess of piperazine readily afforded Boc-Pip **127** in good yield.[171] Similarly, Bn-Pip **128** was obtained by reacting benzyl chloride with a large excess of piperazine[172] (Scheme 37).

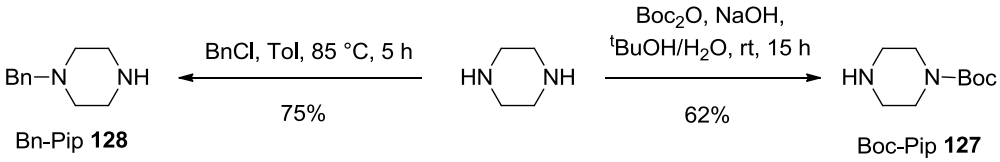

Scheme 37: Synthesis of the monoprotected piperazines **127** and **128**

A double Hartwig-Buchwald coupling between Boc-Pip **127** and *p*-dibromobenzene **129** using $Pd_2(dba)_3$ and BINAP in the presence of NaO^tBu gave the protected linker **130** in good yield, even if a long reaction time was needed. Removal of the Boc group with TFA afforded the phenyl-piperazine linker PipPhPip **131** (Scheme 38).

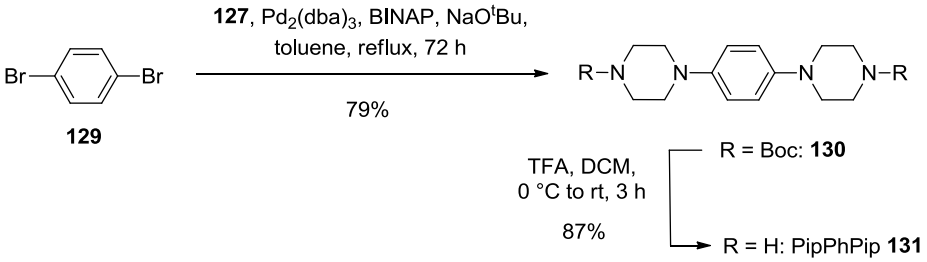

Scheme 38: Synthesis of the phenyl-piperazine linker **131**

Crystals of compound **130** were grown from a chloroform/toluene mixture. This molecule crystallizes in the $P2_1/m$ space group (monoclinic system), forming roughly perpendicular sheets in the packing. The two piperazine rings adopt a chair conformation but are not perfectly symmetrically arranged relative to the benzene ring. The distance between the two carbons of the carbamate group is 13.7 Å (Figure 66).

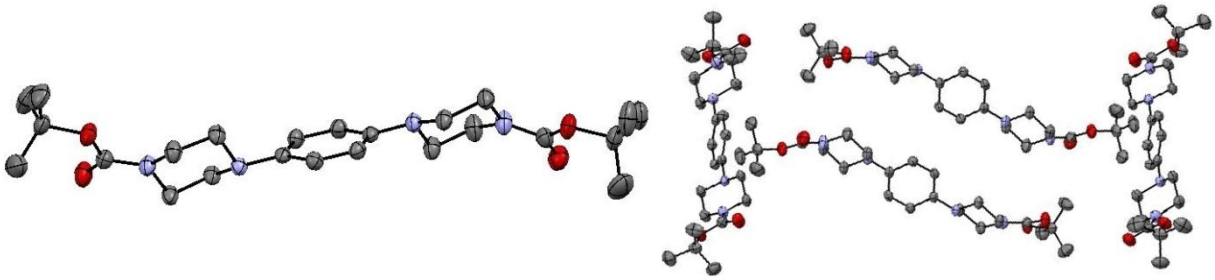

Figure 66: ORTEP drawings of compound **130**. Hydrogen atoms have been omitted for clarity. Left: view of the asymmetric unit, right: view of the packing

This distance is in excellent agreement with the 13.9 Å in the corresponding structure minimized with DFT (UB3LYP/6-311G**, using the *Gaussian 09* program)[173] where the -O^{t}Bu was replaced for a -Me group to reduce calculation time. The small difference can be explained by the fact that, in the structure obtained by DFT calculations, the two piperazine rings are perfectly symmetric with respect to the benzene ring (Figure 67).

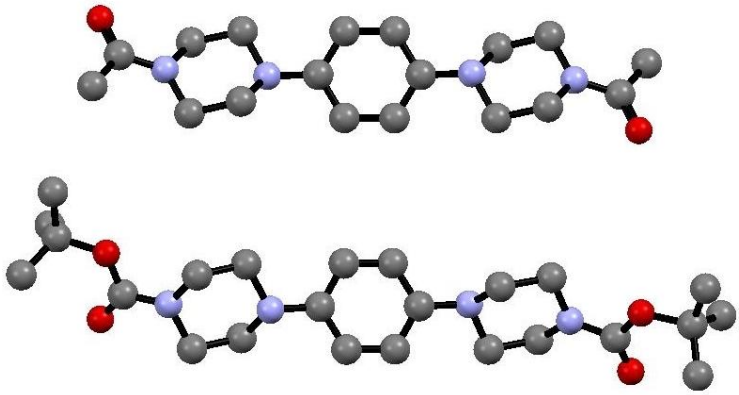

Figure 67: Ball and stick drawings of compound **130**. Top: DFT structure of the corresponding simplified model, bottom: X-ray structure

2.2.2 Dissymmetric version

Targeting a dissymmetric version of this linker, we exploited the different reactivity of the bromo and the iodo group on 1-bromo-4-iodobenzene **132** to sequentially introduce Boc-Pip **127** and Bn-Pip **128**.[174] The Boc and the Bn protecting groups being orthogonal, it would permit the sequential introduction of two different paramagnetic moieties. The replacement of bromo for iodo moities should not be detrimental to the efficiency of the Hartwing-Buchwald coupling, as special conditions have been developed in this case: the addition of 18-crown-6 (18C6) activates NaO^tBu by increasing the solvation of Na^+,[175] allowing efficient couplings on aryl iodides.

Indeed, a coupling with Boc-Pip **127** in the same conditions as above afforded bromoarene **133**, but with a low yield (24%). As described by Buchwald,[175] adding 18C6 enhanced considerably the yield to 57%. We found that dibenzo-18C6 gave better results (91%), which could be traced to its superior affinity for Na^+. It is worth noting that Ullmann-like versions of this coupling[176] (CuI/ethylene glycol/K_3PO_4 or CuI/proline/K_3PO_4) did not afford the desired product. Good yields were also obtained when Bn-Pip **128** was used to give the expected bromoarene **134** (Scheme 39).

Optimization of the next coupling step was also necessary. The coupling between bromoarene **133** and Bn-Pip **128** in the original Buchwald conditions afforded equimolar amounts of the desired product **135** and recovered **133**. The conversion was not complete even after extended reflux time and could not be improved using other classical ($Pd(OAc)_2$/BINAP/Cs_2CO_3) conditions. Low yields were also observed when bromoarene **134** was coupled with Boc-Pip **127** to give compound **135**. We solved this issue using 2-dicyclohexylphosphino-2',4',6'-triisopropylbiphenyl (XPhos[177]) in combination with $Pd_2(dba)_3$ and Cs_2CO_3, which afforded the orthogonally protected linker BocPhPipPhBn **135** in 66% yield. The global yield of this Pd/Pd method is higher than the Cu/Pd literature method (Scheme 39).[174]

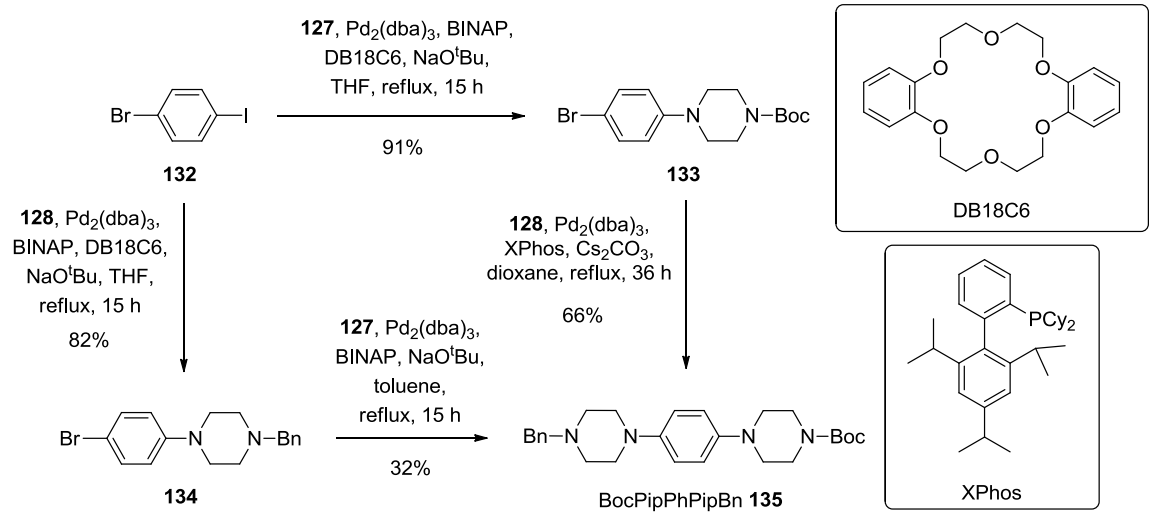

Scheme 39: Synthesis of the orthogonally protected phenyl-piperazine linker **135**

Removal of the Boc group of **135** was easily performed with TFA, giving BnPipPhPip **136** in nearly quantitative yield. However, the Bn moiety was more difficult to remove. Pd/C hydrogenation under pressure with traces of acetic acid led to a nearly total recovery of the reactant as shown by NMR. The addition of DMF to improve the solubility was not effective, nor the use of $Pd(OH)_2/C$ (Pearlman's catalyst). This lack of reactivity could be due to poisoning of the catalyst by the reactant. The problem was solved by the use of ammonium formate with Pd/C[178], which cleanly afforded the desired linker BocPipPhPip **137** in nearly quantitative yield (Scheme 40).

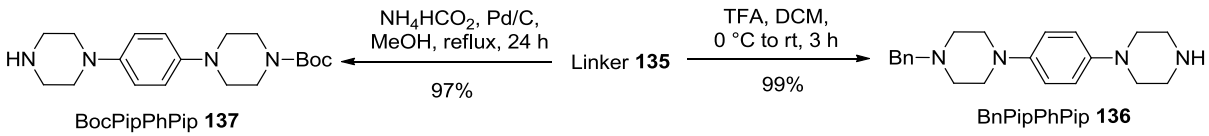

Scheme 40: Synthesis of dissymmetrical phenyl-piperazine linkers **136** and **137**

2.2.3 Elongation

With the optimized conditions in hand, we decided to build longer linkers with alternating phenyl and piperazine units. However, and despite all our efforts, no condition led to efficient procedures. The coupling between BnPhPipPh **136** and bromoarene **133** under various conditions (CuI/proline/K_3PO_4, $Pd_2(dba)_3$/BINAP/NaO^tBu or $Pd_2(dba)_3$/XPhos/Cs_2CO_3) only gave traces of the expected product with the XPhos procedure. Moreover, the coupling between PhPipPh **131** (or piperazine) and bromoarene **133** or between *p*-dibromobenzene **129** and BnPhPipPh **136** to give long symmetrical oligo(phenyl-piperazine) linkers failed with the original Buchwald conditions (Scheme 41).[162]

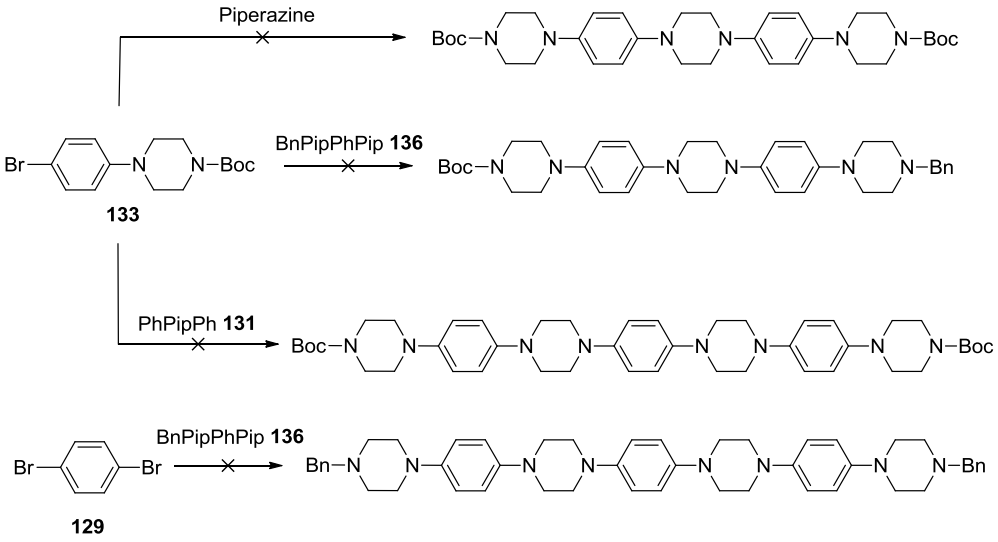

Scheme 41: Attempted elongation of the phenyl-piperazine linker

To overcome these difficulties, we employed a longer central aromatic core. The same coupling strategy was repeated using *p*-dibromobiphenyl **138** instead of *p*-dibromobenzene **129**. However, the reactivity was lower: when Boc-Pip **127** was reacted with biphenyl **138** in the standard Buchwald conditions, no di-coupled product could be detected even after one week, but the mono-coupled product **139** was isolated in acceptable yield. Starting from this compound, Boc-Pip **127** could not be coupled in the same conditions as the previous step. Again, the XPhos procedure proved more efficient, affording the protected linker **140** in 55% yield. The usual TFA-removal of the Boc group gave the biphenyl-piperazine linker PipPh$_2$Pip **141** (Scheme 42).

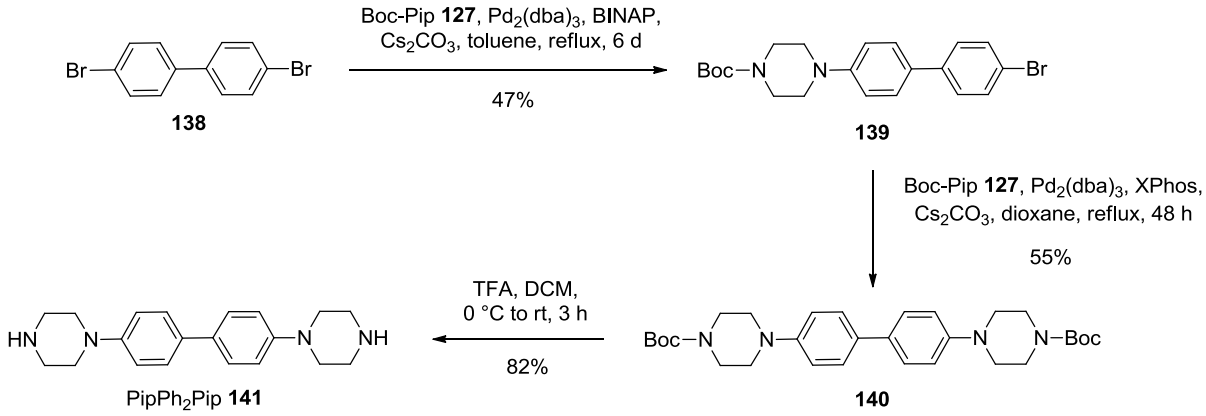

Scheme 42: Synthesis of the biphenyl-piperazine linker **141**

To further extend the aromatic core, the same strategy was employed starting from *p*-dibromoterphenyl. However, due to the poor reactivity of this compound linked to its low solubility, efforts were not pursued in this direction.

DFT calculations (UB3LYP/6-311G**) were performed on compound **140**, with -O^{t}Bu replaced for -Me to reduce calculation time. The distance between the two carbons of the carbamate group is 18.3 Å. The addition of one benzene ring compared to compound **130** corresponds to an additional

length of 4.4 Å. The two benzene rings are not coplanar (dihedral angle of 37°) because of the steric hindrance imposed by the hydrogen atoms in *ortho* from the C-C benzene-benzene bond (Figure 86).

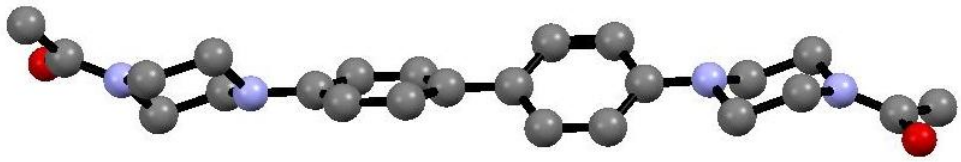

Figure 68: DFT structure of a simplified model of **140**. Hydrogen atoms have been omitted for clarity

2.2.4 Couplings with ligands

2.2.4.1 with terpyridines

As a first approach, we envisioned to directly graft two terpyridines on a symmetrical spacer. To develop the PELDOR method with Mn^{II}, the shortest Mn-Mn distance should be around 20 Å. We decided to introduce a piperazine spacer between two *p*-phenylterpyridines, as the resulting platform can be seen as two Tpy attached to a phenyl-piperazine linker. A double Hartwig-Buchwald coupling in the standard Buchwald conditions between piperazine and *p*BrPhTpy **36** generated the first Tpy-Tpy ligand bis-PhTpy-Pip **142** in modest yield (41%). This compound was then allowed to react with $TpyMnCl_2$ **49** or *p*$ClTpyMnCl_2$ **50** to afford, after precipitation with NH_4PF_6, the shortest bis[Mn^{II}-bis(Tpy)] platforms bis-(Tpy)Mn^{II}(PhTpy)-Pip **143** and bis-(*p*ClTpy)Mn^{II}(PhTpy)-Pip **144** (Scheme 43).

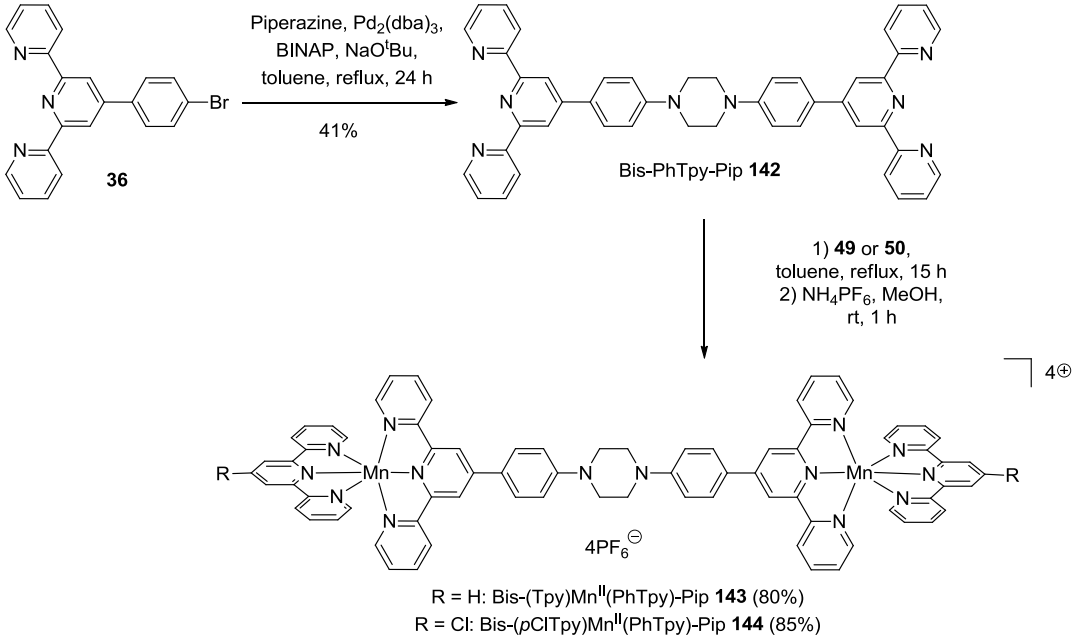

Scheme 43: Synthesis of the bis[Mn^{II}-bis(Tpy)] platforms **143** and **144**

The distance between the two nitrogen atoms of the central pyridine rings of the two terpyridines of Tpy-Tpy **142** was estimated using DFT calculations (UB3LYP/6-31G**), and was found

to be exactly 20 Å. The dihedral angle between the benzene and the central pyridine rings is 32°, while the two terpyridine groups are coplanar (Figure 69).

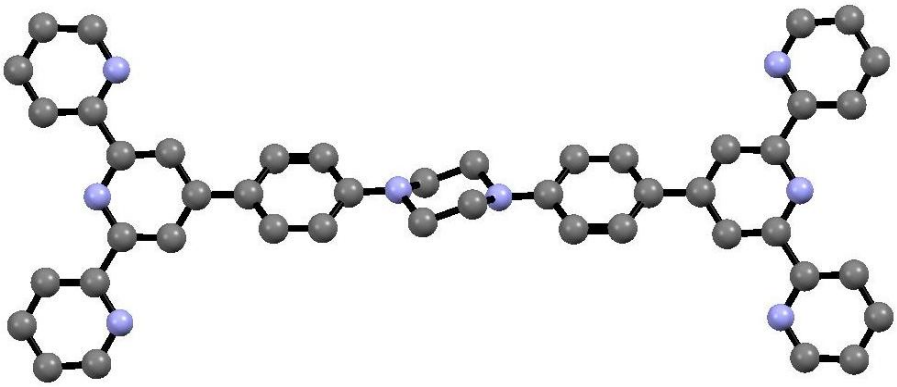

Figure 69: DFT structure of **142**. Hydrogen atoms have been omitted for clarity

The J-band *cw*-HFEPR spectrum of the Mn^{II}-bisTpy **143** was recorded (Figure 70).

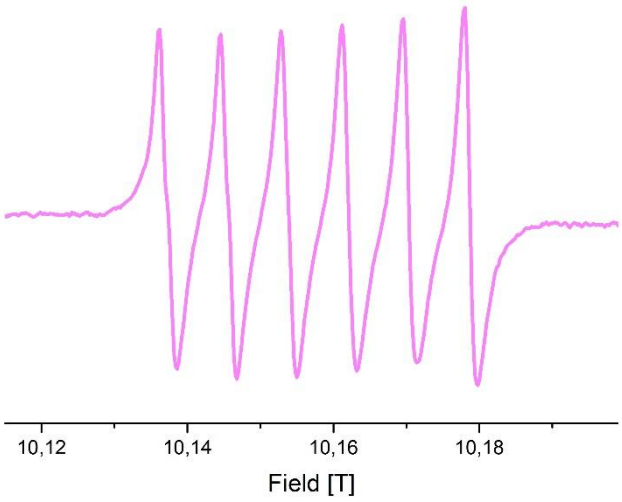

Figure 70: J-band *cw*-HFEPR spectrum of the Mn^{II}-bisTpy **143** (0.5 mM in MeCN with 100 mM *n*-Bu_4PF_6 at 23 K)

This spectrum appears very similar to Mn^{II}-bis(Tpy) complexes such as **57**, **58** and **62** (ref interne). This suggests that there is no extra broadening induced by the dipolar coupling between the two Mn-bis(Tpy) at such a distance (around 20 Å).

Moving towards higher distances, the same strategy was used with spacer **131** instead of piperidine. This time, no Hartwig-Buchwald coupling took place between *p*BrPhTpy **36** and compound **131** in the same conditions as above (Scheme 44). However, a Hartwig-Buchwald coupling between *p*BrPhTpy **36** and Boc-Pip **127** afforded terpyridine **144** in high yield. The corresponding amine **145** was then regenerated with TFA, but the coupling between *p*-dibromobenzene **129** and amine **145** failed again (Scheme 44).

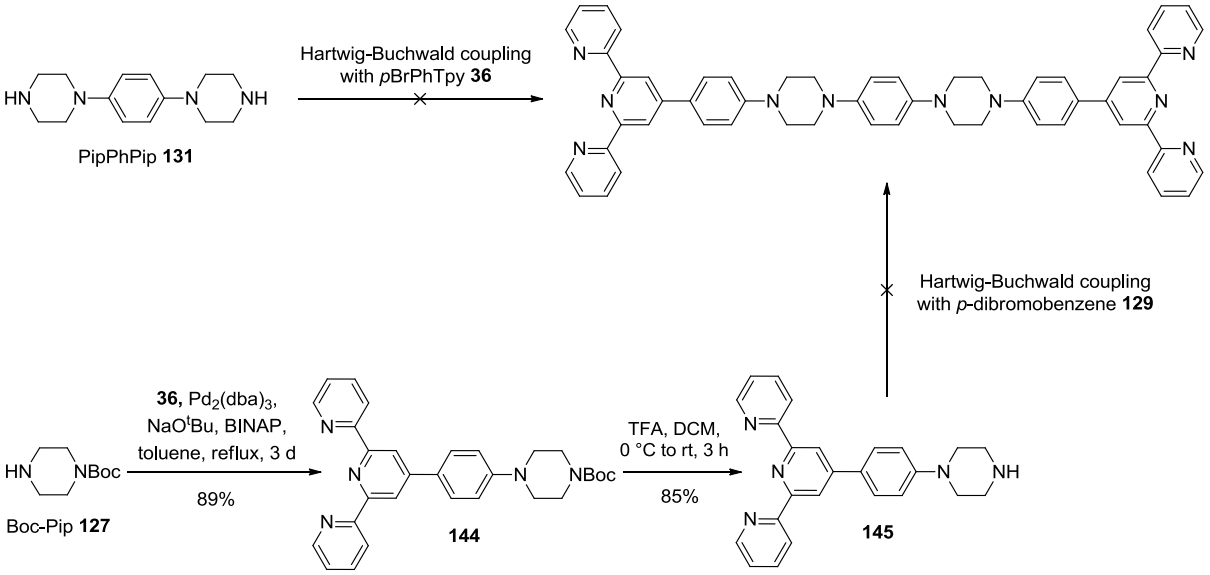

Scheme 44: Attempted Hartwig-Buchwald couplings between linker **131** and *p*BrPhTpy **36**, and between *p*-dibromobenzene **129** and amine **145**

Together with the difficulties we encountered on the elongation methodology, these results suggest that the grafting of ligands on phenyl-piperazine linkers using Pd-catalyzed C-N bond formation is more difficult than anticipated. The next part will confirm this behavior.

2.2.4.2 with DPA, PyMTA and PyMDPDA derivatives

Despite this lack of reactivity, we still tried to couple pyridine-based ligands to the phenyl-piperazine linkers. No reaction was observed between Et-*p*BrPyMTA **70** and Bn-Pip **128** ($Pd_2(dba)_3$/BINAP/NaO^tBu or $Pd(OAc)_2$/XPhos/NaO^tBu). The coupling between Et-*p*BrPyMTA **70** and asymmetric BocPipPhPip **137** was attempted several times ($Pd_2(dba)_3$/BINAP/NaO^tBu, $Pd_2(dba)_3$/X-Phos/NaO^tBu, $Pd(OAc)_2$/BINAP/NaO^tBu, $Pd(OAc)_2$/BINAP/Cs_2CO_3 or $Pd(OAc)_2$/$P(^tBu)_3$/Cs_2CO_3) but when the reactants seemed to be consumed, only intractable mixtures were obtained. The use of Et-*p*BrPyMDPDA **87** instead of Et-*p*BrPyMTA **70** did not improve the results. Finally, when phenyl-piperazine linker **132** was reacted with Et-*p*BrPyMTA **70**, diester **9** or triflate **79**, no desired product could be isolated (Scheme 45).

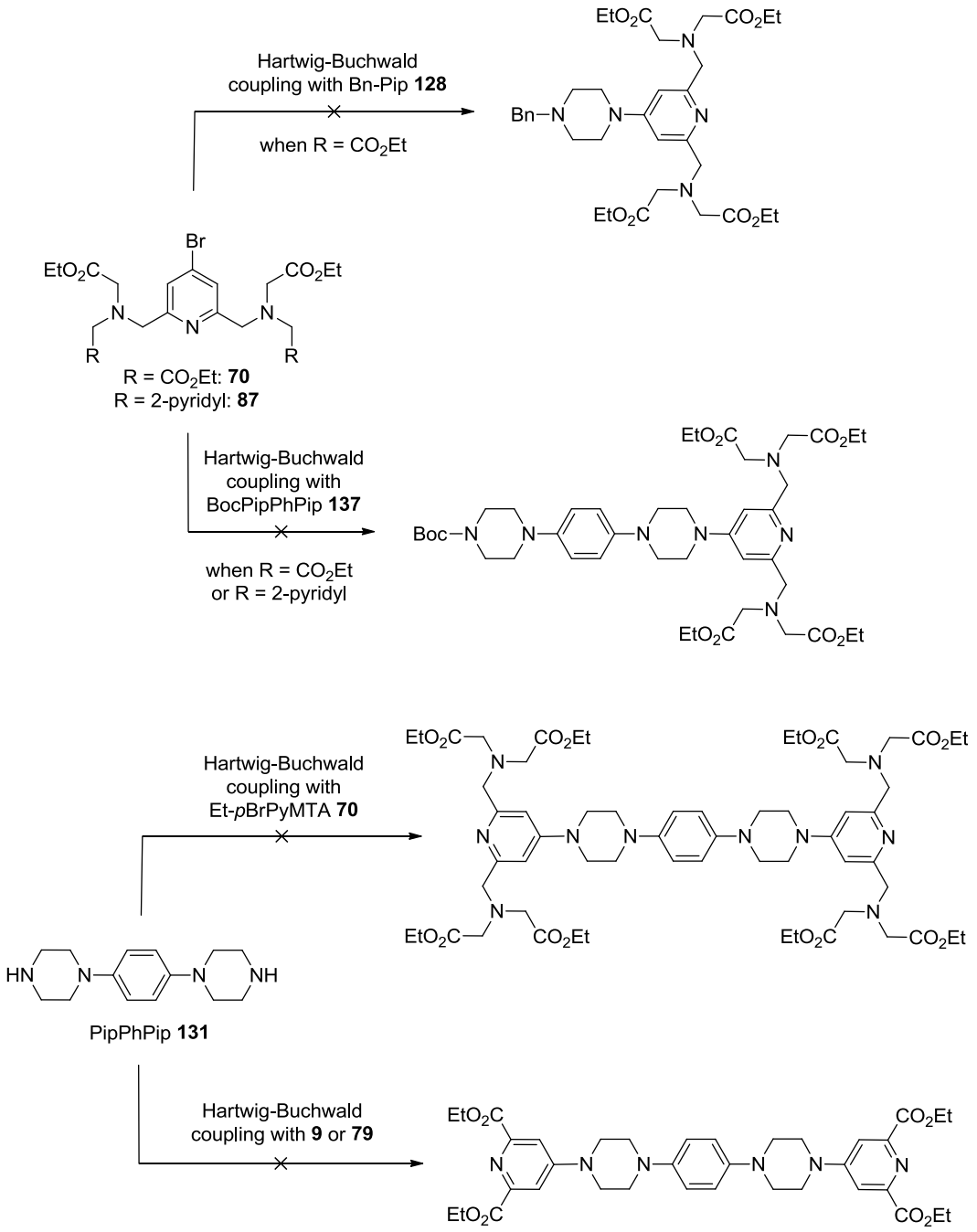

Scheme 45: Attempted couplings of PyMTA, PyMDPDA and DPA derivatives on phenyl-piperazine linkers

These results led to the conclusion that phenyl-piperazine linkers are not adequate for further elongation and that their lack of reactivity hampers any direct C-N bond formation using Pd-catalyzed couplings. However, as we will see in the next part, other efficient methodologies can be used to attach ligands for Mn^{II} on these linkers.

2.2.4.3 with DOTA derivatives

As we became aware that grafting methodologies using Hartwig-Buchwald couplings on phenyl-piperazine linkers are not optimal, we explored the formation of amide bonds. The DOTA ligand was perfectly suited for that purpose, as the carboxylic acid derivative tri-^{t}Bu-DOTA **146** is commercially available. The coupling between this compound and phenyl-piperazine linkers PipPhPip **131** and PipPh$_2$Pip **141** in the presence of 1-[bis(dimethylamino)methylene]-1*H*-1,2,3-triazolo[4,5-*b*]pyridinium 3-oxid hexafluorophosphate (HATU) afforded the protected bis-DOTA **147** and **148** in good to excellent yield. Removal of the ^{t}Bu groups with TFA was performed to lead to the formation of the bis-DOTA platforms **149** and **150** after reversed-phase HPLC purification (Scheme 46).

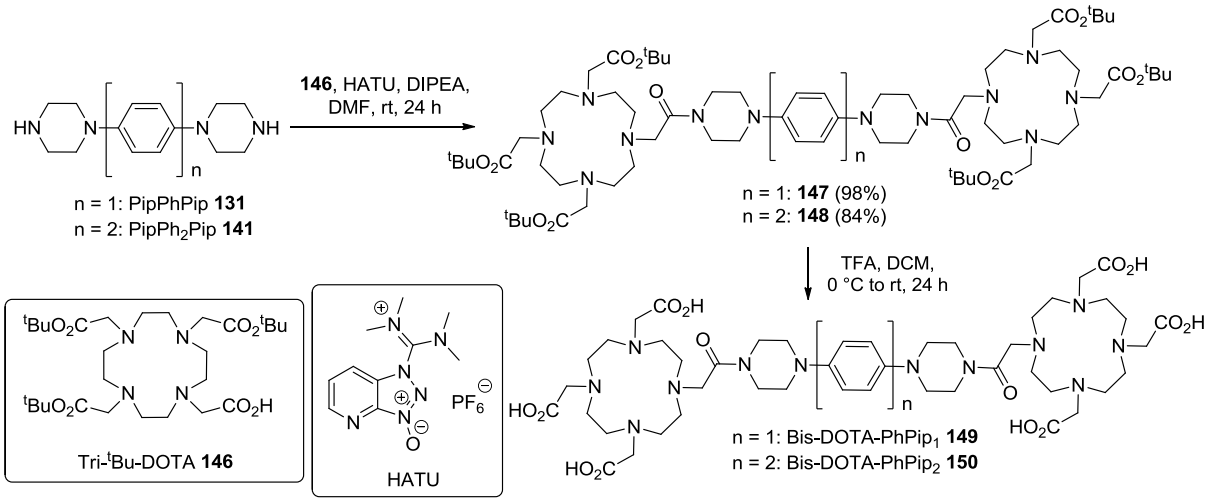

Scheme 46: Synthesis of the two bis-DOTA platforms **149** and **150** with a phenyl-piperazine linker

DFT calculations on bis-DOTA **149** and **150** are not adequate owing to the very large degree of conformational freedom of the DOTA ring. Molecular dynamics (MD) calculations, which can generate a set of conformers for bis-DOTAs **149** and **150**, are more suited as the distance distribution can also be obtained. MD calculations will be presented in detail in the second chapter. The estimated mean Mn-Mn distance was found to be 2.07 and 2.45 nm for the Mn^{II} complexes of **149** and **150**, respectively.

The J-band *cw*-HFEPR spectra of the Mn^{II} complex of bis-DOTA-PhPip$_1$ **149**, generated *in situ*, were recorded (Figure 71). To ensure that the two DOTA are coordinated, a titration with Mn^{II} was performed. As expected, the amount of Mn^{II} needed before the appearance of free Mn lines corresponds to twice the concentration of ligand, accounting for four trifluoroacetate counterions resulting from the HPLC purification.[179,180] For this bis-DOTA platform and the following ones, 1.8 eq of Mn^{II} are added to ensure that both DOTA sites are occupied and that no excess Mn^{II} is visible, which would perturb PELDOR measurements.

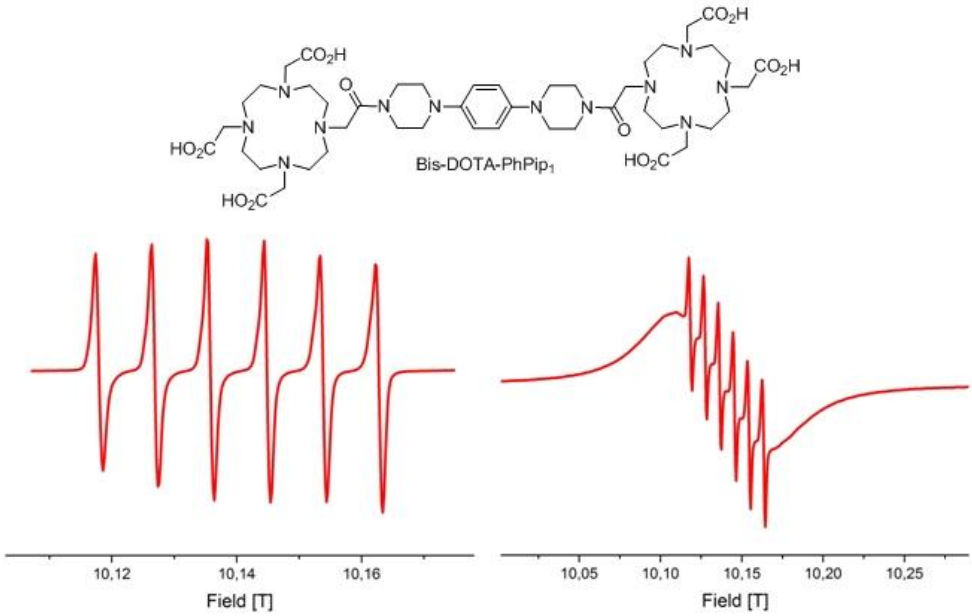

Figure 71: Structure of bis-DOTA-PhPip$_1$ **149** (top) and J-band *cw*-HFEPR spectra of the corresponding Mn^{II} complex (bottom, 250 µM in ligand, 200 µM in Mn^{II}, in 50 mM pH 8 HEPES buffer with 10% glycerol, left: 23 K, right: 4 K)

These spectra display the expected six narrow lines, superimposed on a broader component arising from outer transitions in the case of the spectrum recorded at 4 K. They are comparable to the spectra of Mn^{II}-DOTA but with broader lines (peak-to-trough linewidth: 12 G). This could come from the fact that a carboxylate group is replaced with an amide moiety, changing the Mn^{II} coordination to some extent. However, the ZFS parameters of the Mn^{II} complex of bis-DOTA **149** are identical to those of Mn^{II}-DOTA, meaning that the broadening is not likely to come from a change of the coordination sphere. The observed broadening could directly come from the dipolar coupling: this point will be detailed in the second chapter.

In conclusion, we developed in this part an efficient methodology to synthesize symmetric and dissymmetric phenyl-piperazine linkers. Good yields were obtained using improved Hartwig-Buchwald couplings. The bis[Mn^{II}-bis(Tpy)] platform **143** with relatively narrow lines was generated, as well as the two bis-DOTA platforms **149** and **150** with narrow lines. DFT calculations in combination with X-ray crystallography allowed us to estimate the Mn-Mn distance (20 to 25 Å), which is at the start of the measurable PELDOR range. PELDOR results on these three platforms will be discussed in the second chapter. Grafting of other ligands on phenyl-piperazine linkers using Pd-catalyzed couplings proved difficult, which was traced to the poor reactivity of piperazine moieties. These issues were circumvented by the use of efficient amide bond formation using HATU, as illustrated with the bis-DOTA platforms **149** and **150**, which appear to be very promising. All these results constitute a decisive improvement on the oligo(piperidine) linker described above in this chapter (pp. 86 – 96).

2.3 Oligo(phenylene-ethynylene) linker

We have also used oligo(phenylene-ethynylene)s[181] (OPE) as a third type of spacers. These shape-persistent, fully conjugated, stiff nanowires consist of alternating phenyl-acetylene repeat unit. PELDOR measurements at X-band on these linkers grafted with two nitroxides at both ends have led to narrow distance distributions[16,17,182] confirming their rigidity. Systems containing more than two nitroxides have also been constructed using OPE linkers.[41,42] These linkers are often derivatized with alkyl chains to enhance their solubility in organic solvents. We have chosen small poly(ethylene)glycol (PEG) chains, as systems incorporating two charged Mn^{II} complexes at both ends in combination with PEG chains should provide sufficient water solubility.

2.3.1 Symmetric version

Retrosynthetically, a symmetric OPE linker could be obtained by a coupling reaction between a central diiodinated building block equipped with PEG chains **154** and a *para*-substituted ethynylbenzene, also substituted with PEG chains, that could be obtained by desymmetrization of the central diiodinated building block **154**. This strategy is analogous as the construction of the phenyl-piperazine linker, but Sonogashira couplings would be employed instead of Hartwig-Buchwald couplings (Scheme 47).

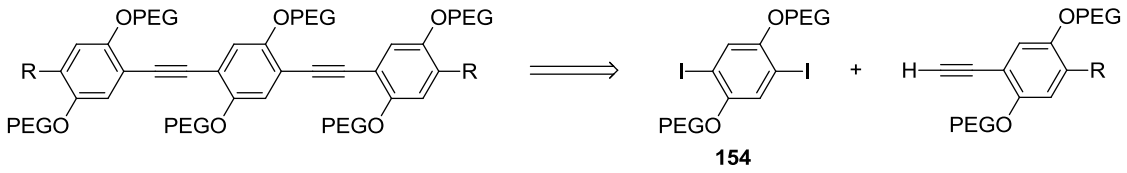

Scheme 47: Retrosynthetic analysis of an OPE linker with PEG chains on each benzene ring

The synthesis of key intermediate **154** was achieved in three steps. Tosylation of diethylene glycol monomethyl ether **151** gave tosylate **152** in good yield.[183] This compound was then allowed to react with hydroquinone (*p*-dihydroxybenzene) in a double Williamson reaction to afford $Ph(OPEG)_2$ **153** in a similar yield.[184] Diiodination of this compound using iodine in conjunction with KIO_3 in AcOH led to the formation of $Ph(OPEG)_2I_2$ **154** in good yield after recrystallization.[185] A scale-up of this protocol gave us an easy access to nearly 30 g of building block **154** (Scheme 48).

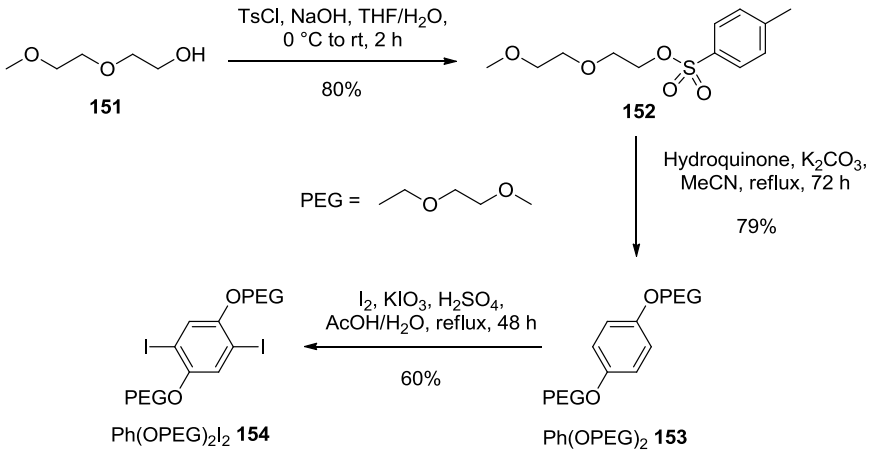

Scheme 48: Synthesis of the diiodinated building block **154**

We encountered numerous issues in the desymmetrization of $Ph(OPEG)_2I_2$ **154**. A first successful Sonogashira coupling with TMSA ($Pd(PPh_3)_2Cl_2$, CuI, TEA/THF) afforded the mono-coupled product with 47% yield, along with 15% of di-coupled adduct. This reaction could not be reproduced, even with other conditions (2-methyl-3-butyn-2-ol or triisopropylsilylacetylene (TIPSA) instead of TMSA, piperidine instead of TEA, addition of PPh_3 or refluxing the reaction medium). Another attempted reaction with building block **154** was the metal-halogen exchange/trapping with DMF to form the mono-aldehyde. This strategy is particularly interesting because the bis-aldehyde is much more difficult to generate than the mono-aldehyde.[186] However, all conditions failed (*n*-BuLi/Et_2O or ^{i}PrMgCl/THF with different temperatures), maybe because of the poor solubility of compound **154** in these solvents. Another idea was to directly desymmetrize intermediate $Ph(OPEG)_2$ **153** by the successive introduction of a bromo group and an iodo group, but the mono-bromination of this compound[185] (Br_2/NaOAc) led to an inseparable mixture (Scheme 49).

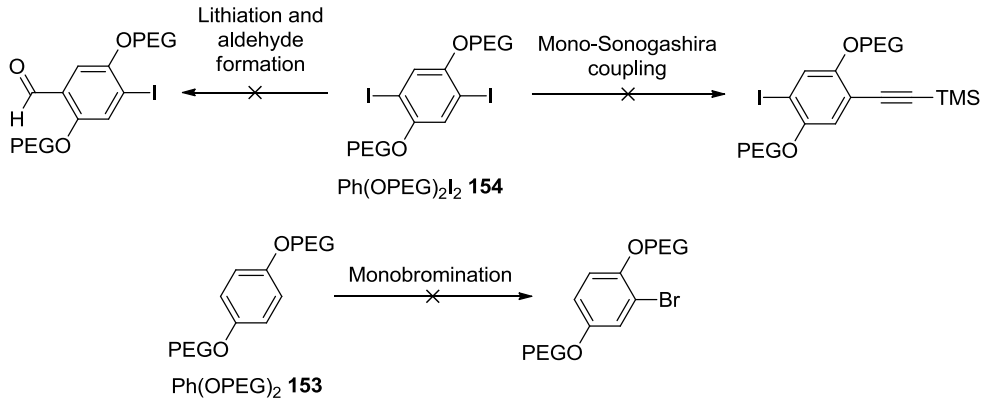

Scheme 49: Attempted desymmetrization of compounds **153** and **154**

We revised our strategy accordingly, and surmised that the solubility of these linkers should not be much lowered if only one phenyl ring out of two was derivatized with PEG chains (Scheme 50). This strategy is advantageous because it is more convergent: *para*-functionalized ethynylbenzenes are commercially available or easy to synthesize, and we already have in hands *p*-ethynylbenzaldehyde **29** (p. 65).

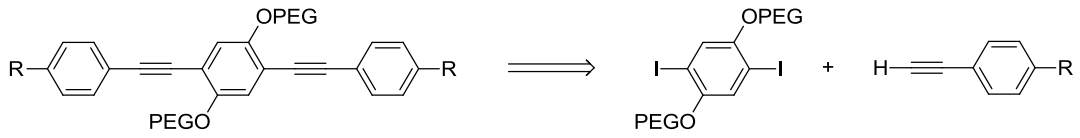

Scheme 50: Retrosynthetic analysis of an OPE linker

To diversify our ethynylbenzene coupling partners, the synthesis of a monoprotected diethynylbenzene[187] was undertaken in order to generate an ethynyl-terminated OPE linker. A first strategy was to start from 1-bromo-4-iodobenzene **155**, which would react successively with TIPSA and TMSA according to the different reactivity of the iodo group and the bromo group. The TMS group would then be removed under basic conditions that do not affect the triisopropylsilyl (TIPS) group. Accordingly, a first Sonogashira coupling with TIPSA ($Pd(PPh_3)_2Cl_2$/CuI/piperidine) afforded bromoarene **156** in nearly quantitative yield,[188] but the following coupling with TMSA ($Pd(PPh_3)_2Cl_2$/PPh_3/CuI in piperidine at rt) was not efficient (Scheme 51).

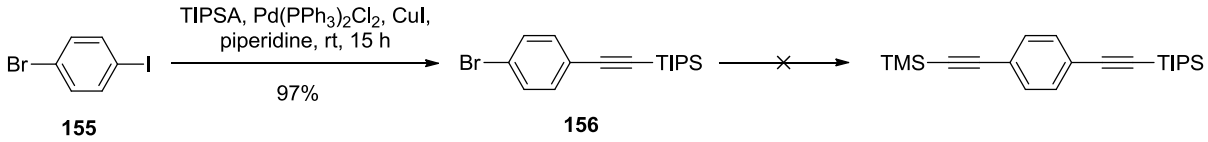

Scheme 51: Attempted synthesis of a monoprotected diethynylbenzene from **155** with two subsequent Sonogashira couplings

Another strategy was envisioned. Starting from 4-bromobenzaldehyde **27**, a Sonogashira coupling with TIPSA in the presence of $Pd(PPh_3)_2Cl_2$, PPh_3 and CuI gave aldehyde **157** in high yield. A Corey-Fuchs reaction was then used to convert the aldehyde moiety into the ethynyl moiety. First, treatment of aldehyde **157** with CBr_4 and PPh_3 gave the corresponding dibromoalkene **158** in nearly quantitative yield. This compound was then engaged in a Fritsch-Buttenberg-Wiechell rearrangement using LDA to afford a mixture of the desired alkyne **159** and the bromoalkyne intermediate.[187] Finally, this mixture was allowed to react with *tert*-BuLi to convert the remaining bromoalkyne into alkyne **159** in good yield (Scheme 52).

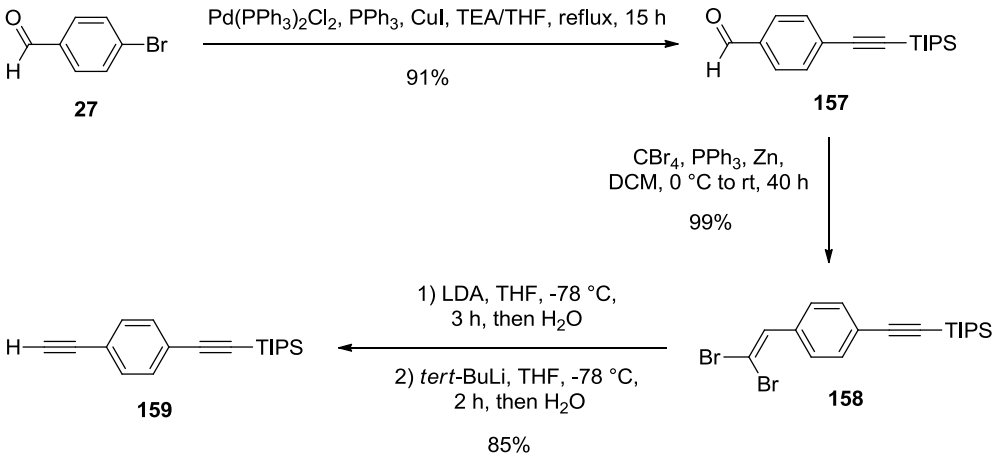

Scheme 52: Synthesis of the monoprotected TIPS-diethynylbenzene **159**

We then built a small library of functionalized OPE linkers with various end groups for further coupling using a double Sonogashira coupling between $Ph(OPEG)_2I_2$ **154** and three *para*-substituted ethynylbenzenes (the already synthesized *p*-ethynylbenzaldehyde **29** and monoprotected TIPS-ethynylbenzene **159** as well as the commercially available *p*-ethynylaniline **160**) using the $Pd(PPh_3)_2Cl_2$/CuI/TEA/THF conditions. We found that better yields and kinetics were obtained with a rather high catalytic loading (0.1 eq of $Pd(PPh_3)_2Cl_2$ and 0.2 eq of CuI). These conditions will be hereafter called *usual Sonogashira conditions*. The di-coupled products **161** (OPE-diCOH), **162** (OPE-diCCTIPS) and **163** (OPE-diNH_2) were generated in reproducible modest to good yields. For OPE-diCCTIPS **162**, removal of the TIPS group with tetra-*n*-butylammonium fluoride (TBAF) gave OPE-diCCH **164** in good yield (Scheme 53).

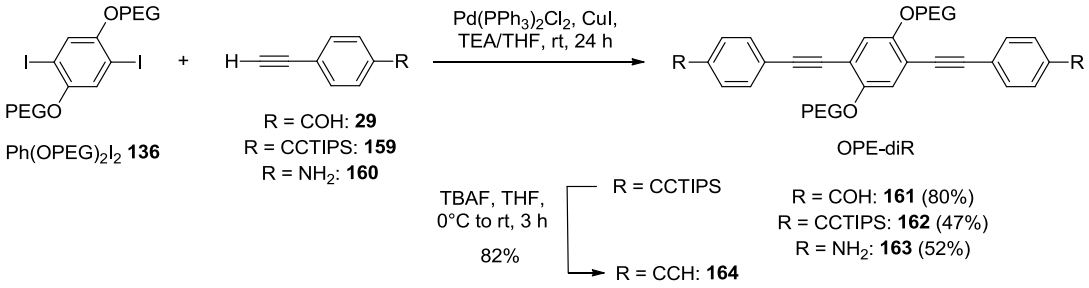

Scheme 53: Synthesis of a family of PEGylated OPEs

Orange crystals of OPE-diCOH **161** and yellow needles of OPE-diCCH **164** suitable for X-ray diffraction were grown by slow evaporation from chloroform/ethyl acetate and toluene/dichloromethane mixtures, respectively. Despite their structural similarity, these molecules crystallize in two different space groups: P-1 for OPE-diCOH **161** (triclinic system) and $P2_1$ for OPE-diCCH **164** (monoclinic system), with two molecules per asymmetric unit in this case. This reflects the difference in the arrangement of the aromatic rings, which is far from coplanarity: in the case of OPE-diCOH **161**, the two benzaldehyde rings are nearly perpendicular to the central one (84°), while for OPE-diCCH **164**, all rings are twisted from each other (with dihedral angles of 18° and 31° relative to the central ring for one molecule and 24° and 54° for the other). Both molecules are slightly bended, reflecting the non-ideal unidirectional arrangement of OPE linkers. However, the C-C end-to-end

distance (calculated between the aldehyde carbons or between the first ethynyl carbons) is very similar for these two molecules (19.3 Å for OPE-diCOH **161** and 19.2 Å for OPE-diCCH **164**). No π-stacking is observed for any of these molecules, presumably because of the non-linear arrangement of the benzene rings and because of the steric hindrance imposed by the PEG chains (Figure 72).

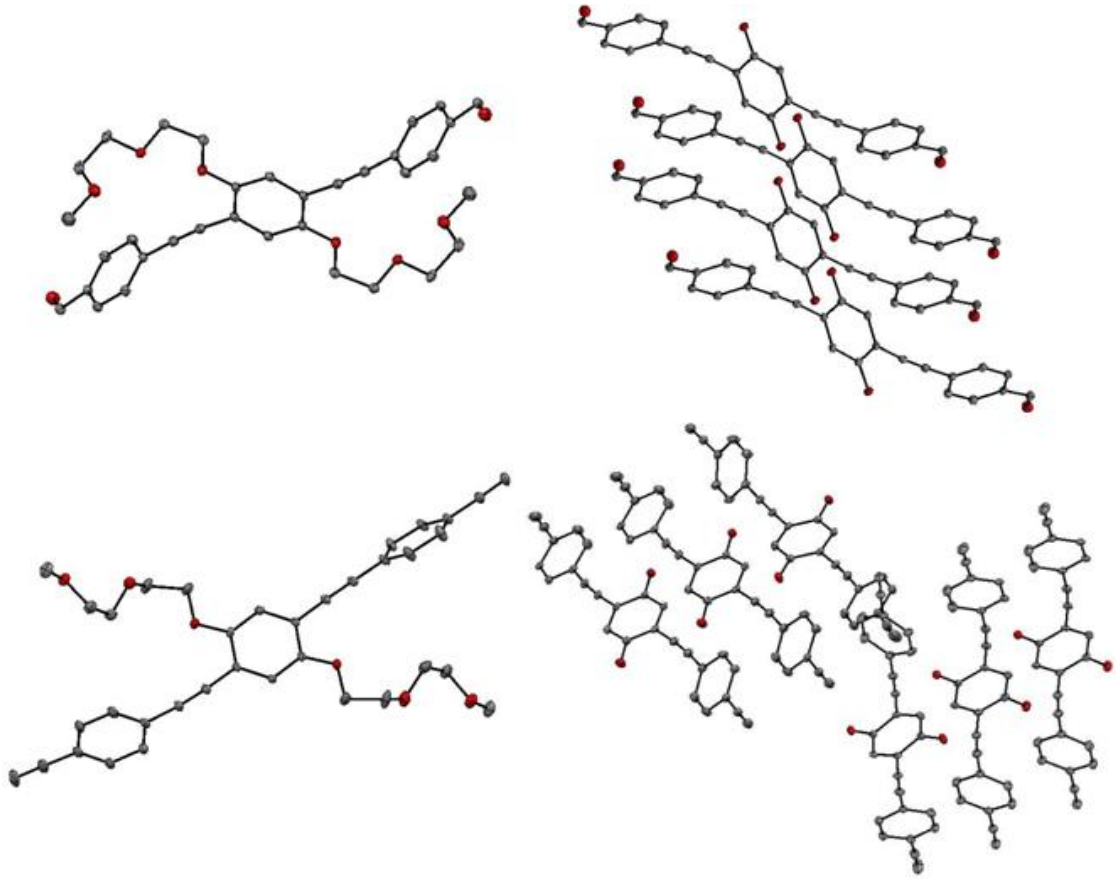

Figure 72: ORTEP drawings of OPE-diCOH **161** and OPE-diCCH **164**. Hydrogen atoms have been omitted for clarity. Left: structures of OPE-diCOH **161** (top) and OPE-diCCH **164** (bottom, only one molecule of the asymmetric unit is depicted). Right: corresponding packing interactions, with PEG chains omitted for clarity

To extend the library, further reactions were performed, which gave access to linkers with diversified end groups. For instance, treatment of OPE-diCOH **161** with $KHSO_5 \bullet KHSO_4 \bullet K_2SO_4$ (Oxone®) cleanly afforded the corresponding dicarboxylic acid OPE-diCO_2H **165** in good yield without any further purification.[189] Moreover, a diazotation followed by a Sandmeyer reaction with NaN_3 readily converted OPE-diNH_2 **163** into diazide OPE-diN_3 **166**, again in good yield and with no need for further purification (Scheme 54).[190]

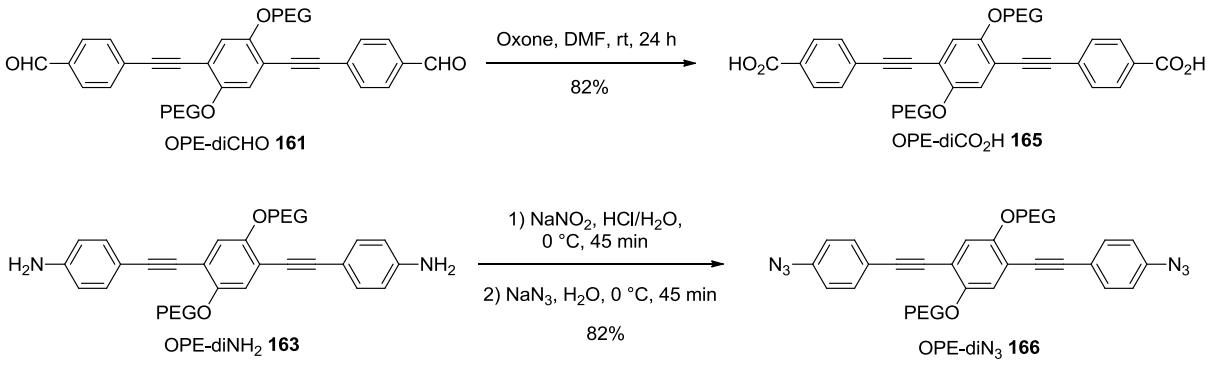

Scheme 54: Functional group modification on PEGylated OPEs

All these linkers, equipped with useful end groups, could be used for amide bond formation (OPE-diNH_2 **163** and OPE-diCO_2H **165**), click chemistry (OPE-diCCH **164** and OPE-diN_3 **166**), Sonogashira coupling (OPE-diCCH **164**) and Horner-Wadsworth-Emmons (HWE) reaction (OPE-diCOH **161**). This extends the range of grafting possibilities compared to phenyl-piperazine linkers, which only possess an amine end group.

2.3.2 Dissymmetric version

We also designed a strategy to have access to a dissymmetric OPE linker using only a few synthetic steps. Having in hands the optimized coupling conditions, the mono-coupling between $Ph(OPEG)_2I_2$ **154** and 0.75 eq of *p*-ethynylaniline **160** under the usual Sonogashira conditions allowed the formation of amine **167** in reproducible and acceptable yield with a very limited formation of the di-coupled product **163**. In the meantime, *p*-ethynylaniline **162** was also Boc-protected in good yield to give alkyne **168**,[191] which was coupled with amine **167** using the usual Sonogashira conditions to give the mono-Boc-protected OPE linker **169** in good yield (Scheme 55).

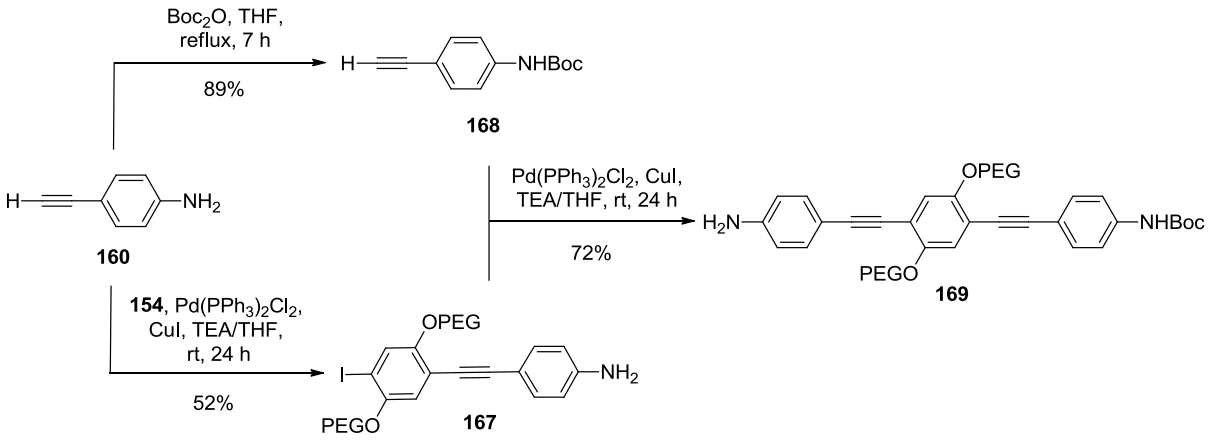

Scheme 55: Synthesis of the mono-Boc-protected OPE linker **169**

Alternatively, the mono-Boc-protection of OPE-diNH_2 **163** to give **169** has been attempted but it failed even with a 5:1 **163**:Boc_2O ratio, leading to a complex mixture. Moreover, the mono-silylation of OPE-diCCH **164** (*n*-BuLi or EtMgBr followed by *tert*-butyldimethylsilyl chloride (TBDMSCl)

[192,193]) led to the recovery of the reactant, and the mono-deprotection of OPE-diCCTIPS **162** with one equivalent of TBAF led to the fully deprotected product OPE-diCCH **164** in high yield (Scheme 56).

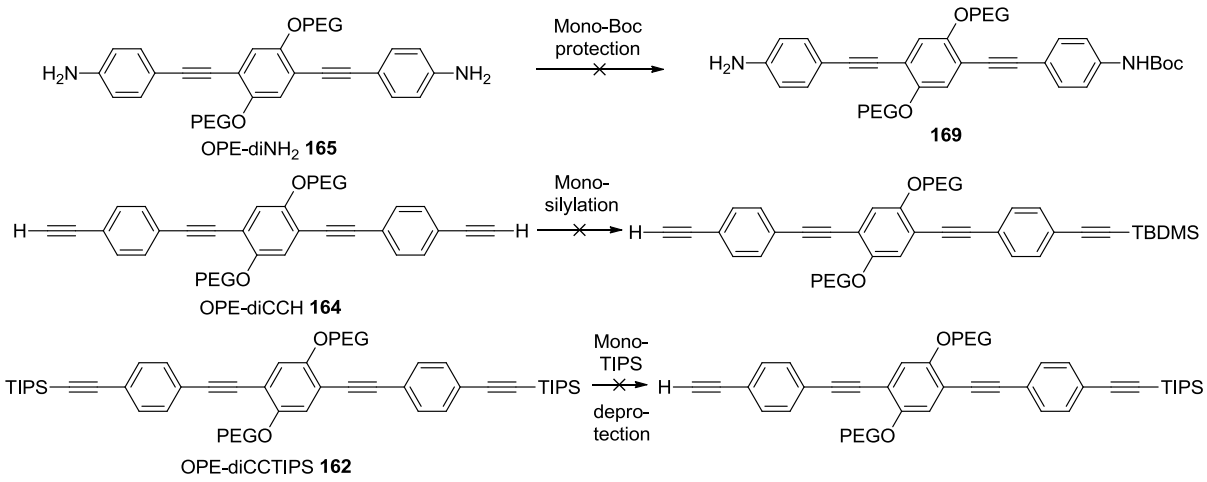

Scheme 56: Attempted desymmetrization of OPE linkers **162**, **164** and **165**

To conclude, we developed an efficient methodology based on Sonogashira couplings to synthesize a library of symmetric and dissymmetric OPE linkers in a few synthetic steps. The use of small PEG chains allows for crystallization: without them, the compounds would not be soluble enough, but too long chains would probably give oils. This means that growing crystals of Mn-Mn platforms with these linkers should be possible.

2.3.3 Elongation

All the linkers we have in hand correspond to short distances. Longer lengths are desirable to probe the efficiency of the PELDOR methodology, and building block **167** is precisely suitable for obtaining longer OPE linkers. This compound was thus engaged in two subsequent couplings with *p*-diethynylbenzene **170** or OPE-diCCH **164** in the usual Sonogashira conditions to give linkers OPE_2-$diNH_2$ **171** and OPE_3-$diNH_2$ **172** with 5 and 7 phenyl-acetylene repeat units, respectively (Scheme 57).

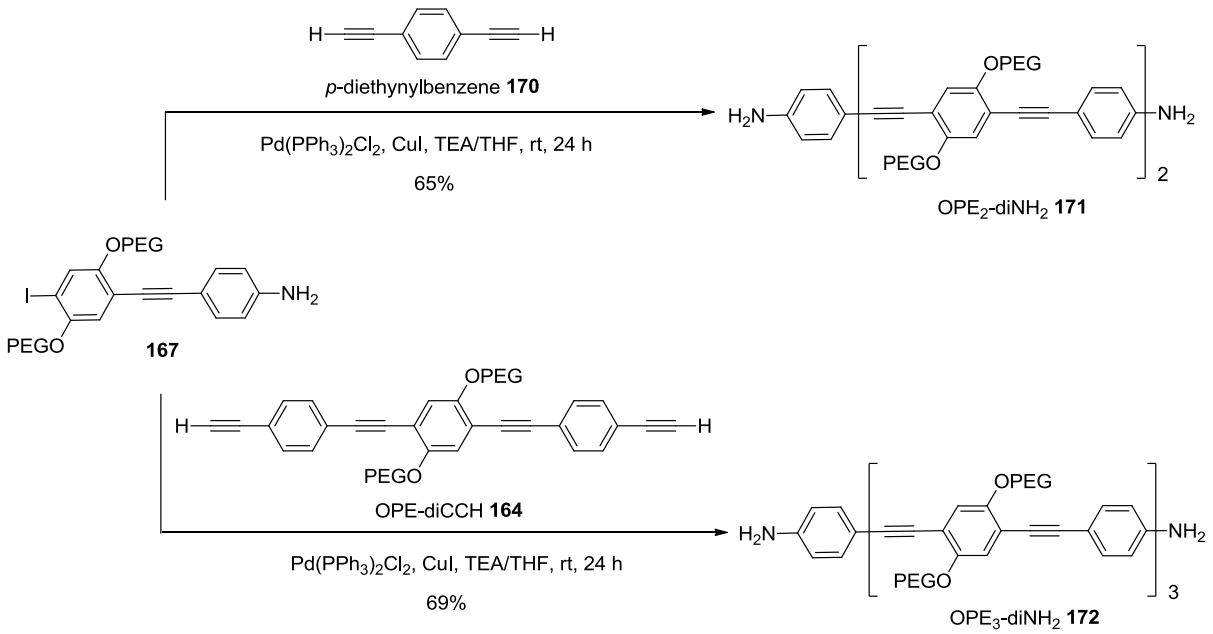

Scheme 57: Synthesis of OPE linkers **171** and **172** with 5 and 7 phenylene-ethynylene repeat units.

DFT calculations (UB3LYP/6-311G**) performed on OPE_n-diNH_2 linkers **165**, **171** and **172** (with -OMe or -OH groups instead of PEG chains to reduce calculation time) led to N-N distances of 19.4, 33.1 and 46.8 Å, respectively. This means that a phenyl-acetylene moiety increments by 6.9 Å the length of the linker (Figure 73).

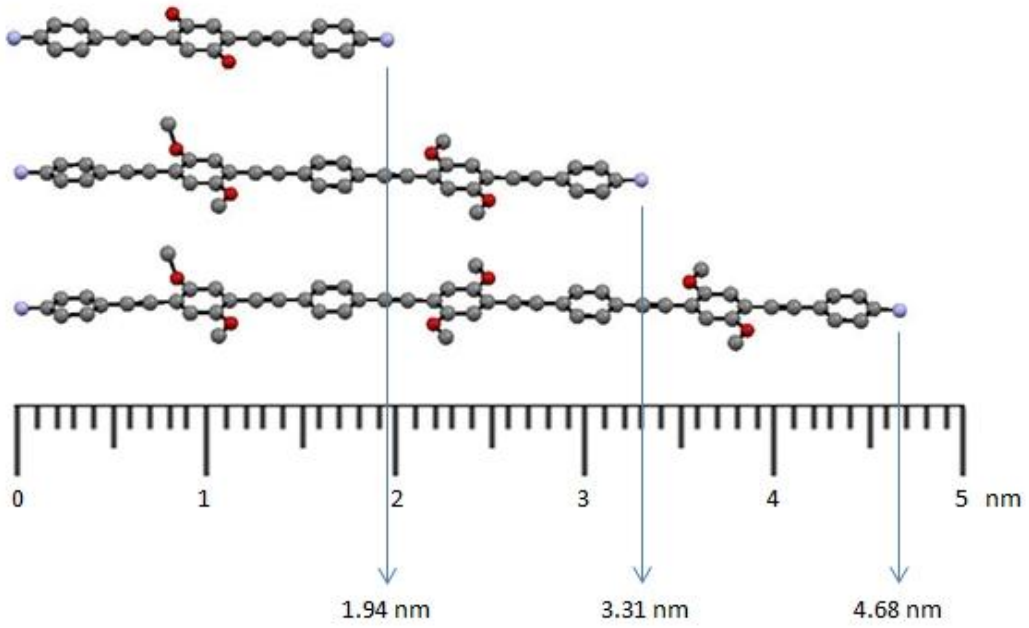

Figure 73: DFT structures of simplified models of linkers **165**, **171** and **172** and their respective N-N length

We now have a set of three OPE linkers of predictable length, equipped with the useful amine group for further coupling with ligands, for generating Mn^{II}-Mn^{II} structures that will cover a large range of distances (from around 2.5 to 6 Å) within the PELDOR measurable range.

2.3.4 Coupling with ligands

2.3.4.1 with terpyridines

The coupling between *p*CCHPhTpy **37** and $Ph(OPEG)_2I_2$ **154** led to the formation of the corresponding Tpy-Tpy ligand bis-CCPhTpy-$Ph(OPEG)_2$ **173** in the usual Sonogashira conditions, even if it was necessary to heat the mixture up to 50 °C.[194] Reaction with $TpyMnCl_2$ **49** and precipitation gave the corresponding bis[Mn^{II}-bis(Tpy)] module bis-(Tpy)Mn^{II}(PhTpy)-$CC_2Ph(OPEG)_2$ **174** (Scheme 58).

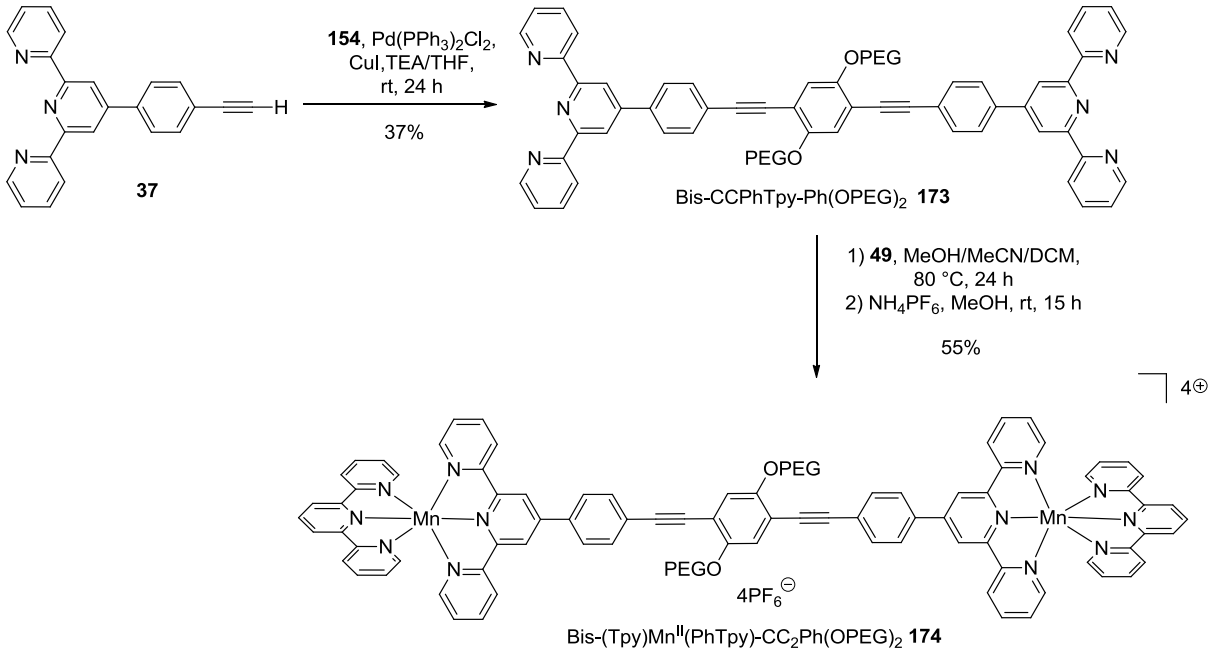

Scheme 58: Synthesis of the bis[Mn^{II}-bis(Tpy)] platform **174**

DFT calculations (UB3LYP/6-311G**) performed on Tpy-Tpy **173** (without PEG chains to reduce calculation time) revealed a N-N distance of 25.2 Å for this ligand, around 5 Å longer that the previous platform. Here the dihedral angle between the two terpyridine groups is 53°: the aromatic rings are all tilted along the linker (Figure 74).

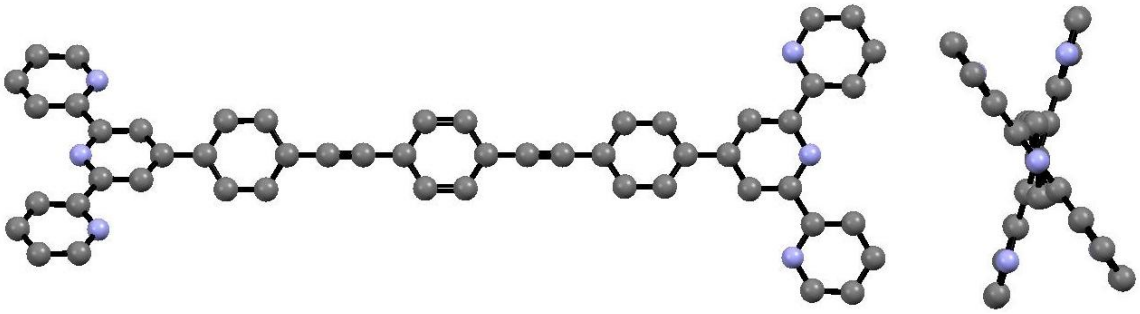

Figure 74: Two views of the DFT structure of a simplified model of **173**. Hydrogen atoms have been omitted for clarity

To have access to another short distance, we also performed a Suzuki coupling between boronate **46** and $Ph(OPEG)_2I_2$ **154** to afford the Tpy-Tpy module bis-PhTpy-$Ph(OPEG)_2$ **175** in good yield. The usual reaction with $TpyMnCl_2$ **49** followed by precipitation with excess NH_4PF_6 gave the corresponding bis[Mn^{II}-bis(Tpy)] module bis-(Tpy)Mn^{II}(PhTpy)-$Ph(OPEG)_2$ **176** (Scheme 59).

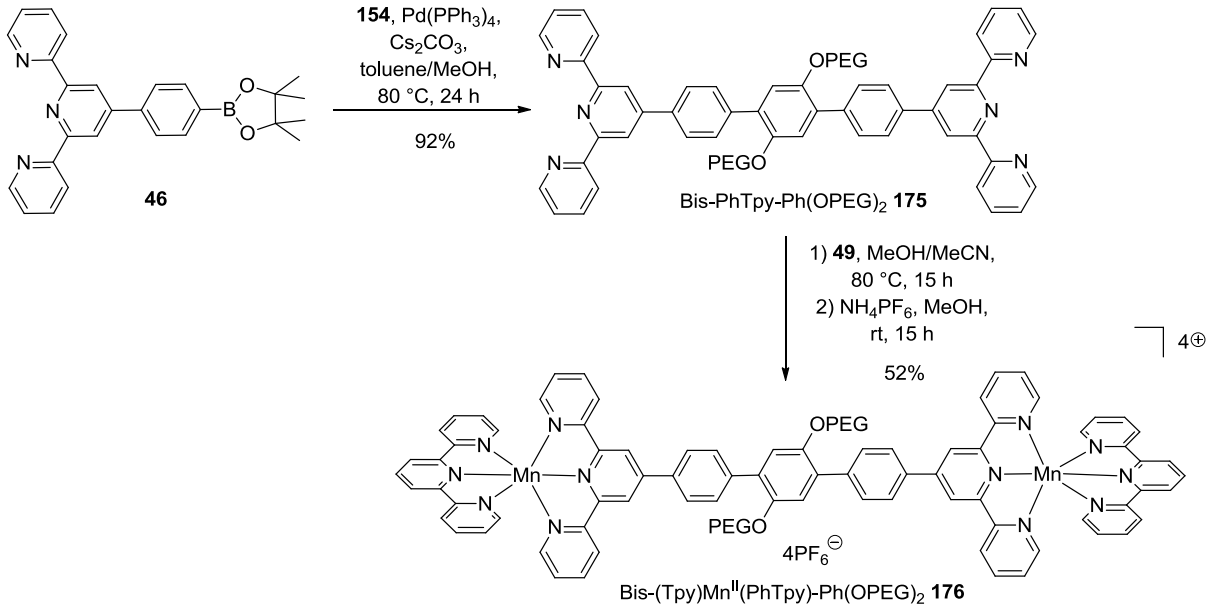

Scheme 59: Synthesis of the bis[Mn^{II}-bis(Tpy)] platform **176**

DFT calculations (UB3LYP/6-311G**) performed on Tpy-Tpy **175** (with -OMe groups instead of PEG chains to reduce calculation time) gaved a N-N distance of 20.1 Å, nearly identical to ligand **142**. The angle between the two Tpy planes was found to be 21°, and the aromatic rings are twisted all along the linker in a similar fashion for ligand **173** (Figure 75).

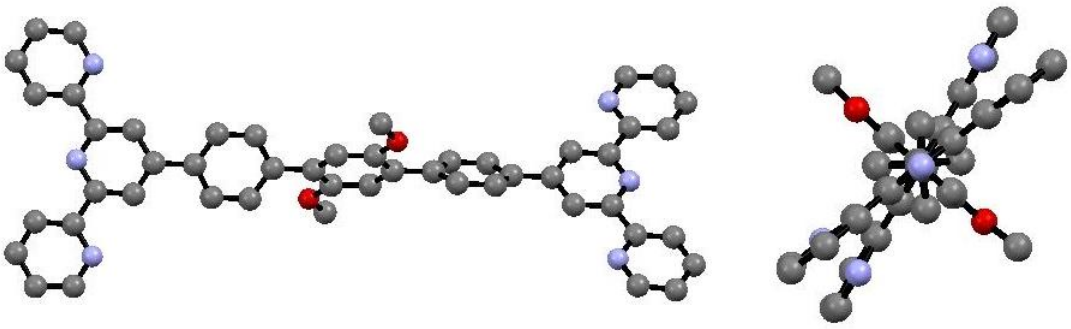

Figure 75: Two views of the DFT structure of a simplified model of **175**. Hydrogen atoms have been omitted for clarity.

We then decided to use an OPE spacer to connect two phenylterpyridines, as we had in hands OPE-diCCH **164** (for click chemistry) and OPE-diCOH **161** (for HWE reaction). A first inconclusive trial was the click reaction between *p*N_3PhTpy **38** and OPE-diCCH **164** (CuI with DMSO or EtOH/H_2O, Scheme 60).

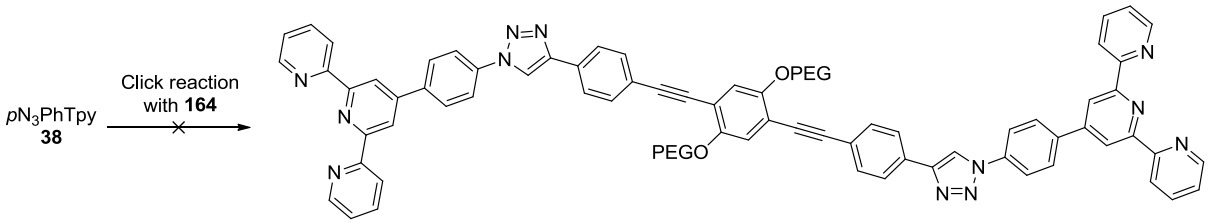

Scheme 60: Attempted click reaction between *p*N_3PhTpy **38** and OPE-diCCH **164**

A double Horner-Wadsworth-Emmons (HWE) reaction between phosphonate **45** and OPE-diCOH **161** in the presence of NaH as a strong base proved more efficient, affording the long Tpy-Tpy rod bis-PhTpy-OPE **177** in good yield. Curiously, the literature conditions[124] advised the use of KO^{t}Bu instead of NaH, but in our hands, no conversion was observed. A crucial feature of the HWE reaction is the exclusive generation of C=C bonds with the *E* configuration: the *Z* isomer would considerably reduce the N-N distance between the two central pyridine rings. A doublet at 7.67 ppm with a coupling constant of 8.6 Hz was assigned to the C=C double bond, but this value could correspond to an *E* or *Z* isomer. However, the structural similarity between the NMR spectrum of compound **177** and a similar molecule[124] strongly suggests that only the *E* isomer is obtained. The usual TpyMnCl_2/precipitation generated the corresponding bis[Mn^{II}-bis(Tpy)] module bis-(Tpy)Mn^{II}(PhTpy)-OPE **178**. Alternatively, ligand **177** could also be coordinated with $Mn(ClO_4)_2$, giving the corresponding bis-Mn^{II}-Tpy complex **179** (Scheme 61).

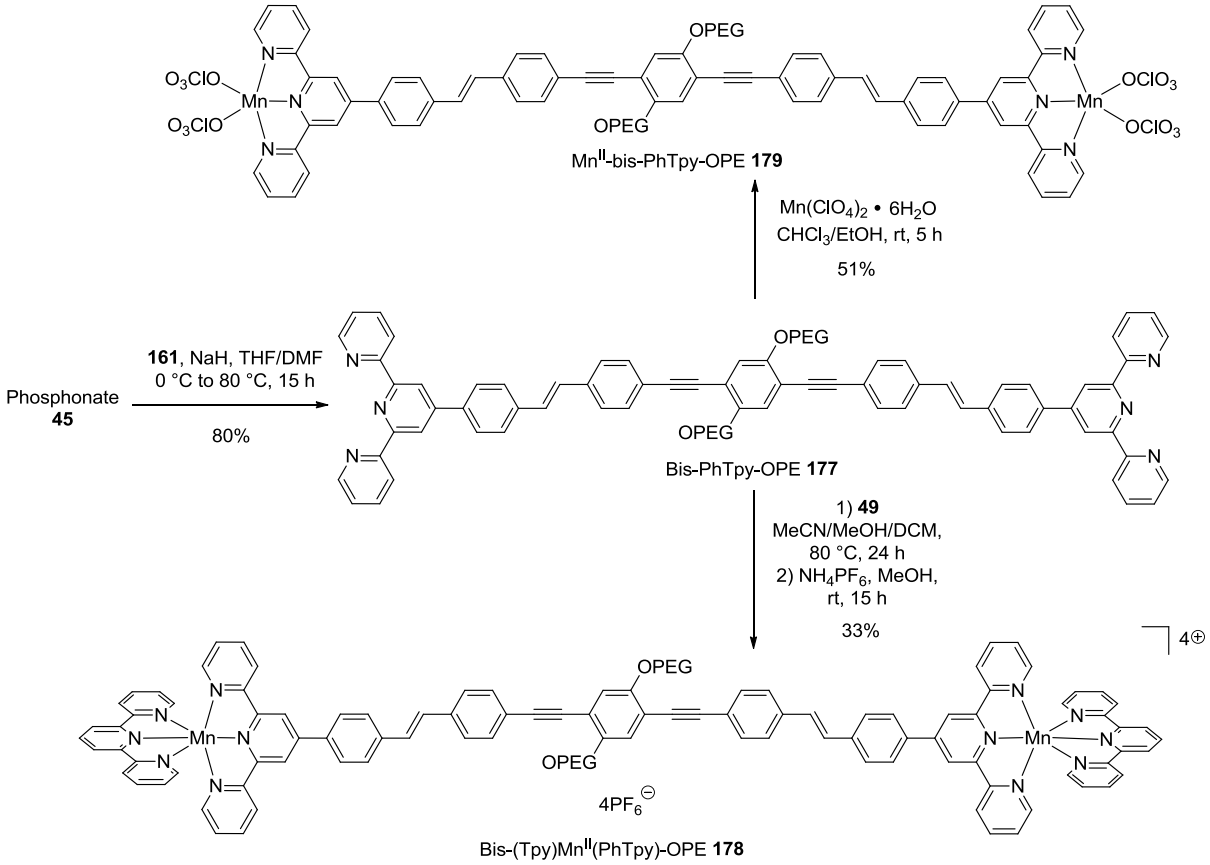

Scheme 61: Synthesis of the bis[Mn^{II}-bis(Tpy)] platform **178** and the bis-Mn^{II}-Tpy complex **179**

DFT calculations (UB3LYP/6-311G**) performed on Tpy-Tpy **177** (without PEG chains to reduce calculation time) have led to a 38.4 Å N-N distance. The two terpyridine groups are coplanar, and inclined by 33° relative to the linker (in which the five benzene rings are also nearly coplanar, Figure 76).

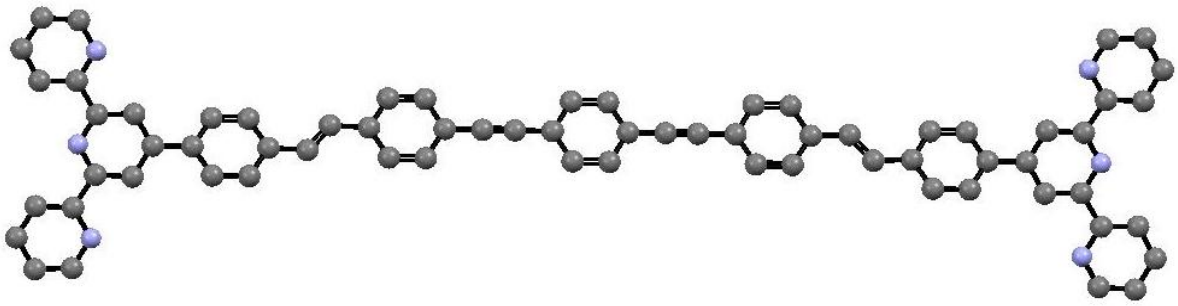

Figure 76: DFT structure of a simplified model of **179**. Hydrogen atoms have been omitted for clarity.

Attempts to record J-band *cw*-HFEPR spectra of bis[Mn^{II}-bis(Tpy)] platforms **174** and **178** (MeCN, DMF or DMSO/toluene with *n*-Bu_4PF_6) did not give any satisfactory results. Only free Mn^{II} resulting from decoordination was observed. This is most probably due to the very low solubility of these platforms in common glass-forming solvents, or to ligand exchange with coordinating solvents such as DMSO or DMF. However, an anion exchange between PF_6^- and tetrakis[3,5-bis(trifluoromethyl)phenyl]borate $[BAr^F{}_4]^-$ (or simply BARF) followed by dissolution in 2-Me-THF

allowed the dissolution of platform **176**.[89] The use of the non-coordinating anion BARF, with its negative charge being distributed all over the structure because of the electron-withdrawing CF_3 groups, greatly improves the solubility in organic solvents. PELDOR experiments on platform bis-(Tpy)Mn^{II}(PhTpy)-Ph$(OPEG)_2$ **176** will be discussed in the second chapter.

To conclude on the four bis[Mn^{II}-bis(Tpy)] platforms we synthesized (Figure 77), even if solubility issues prevented modules **174** and **178** to be used for PELDOR experiments, we managed to dissolve the short platforms **143** and **176** and to record their EPR spectrum showing that little or no decoordination takes place. Solubility appeared to be an important issue, and lowering the *D*-value would also be desired to improve the sensitivity. As we have in hand water-soluble ligands that form Mn^{II} complexes with low *D*-values (*i.e.* narrow EPR lines), namely DOTA and its derivatives, the synthesis of modules incorporating two DOTA ligands connected to a rigid linker is the next logical step. This will be discussed in details in pp. 125 – 132.

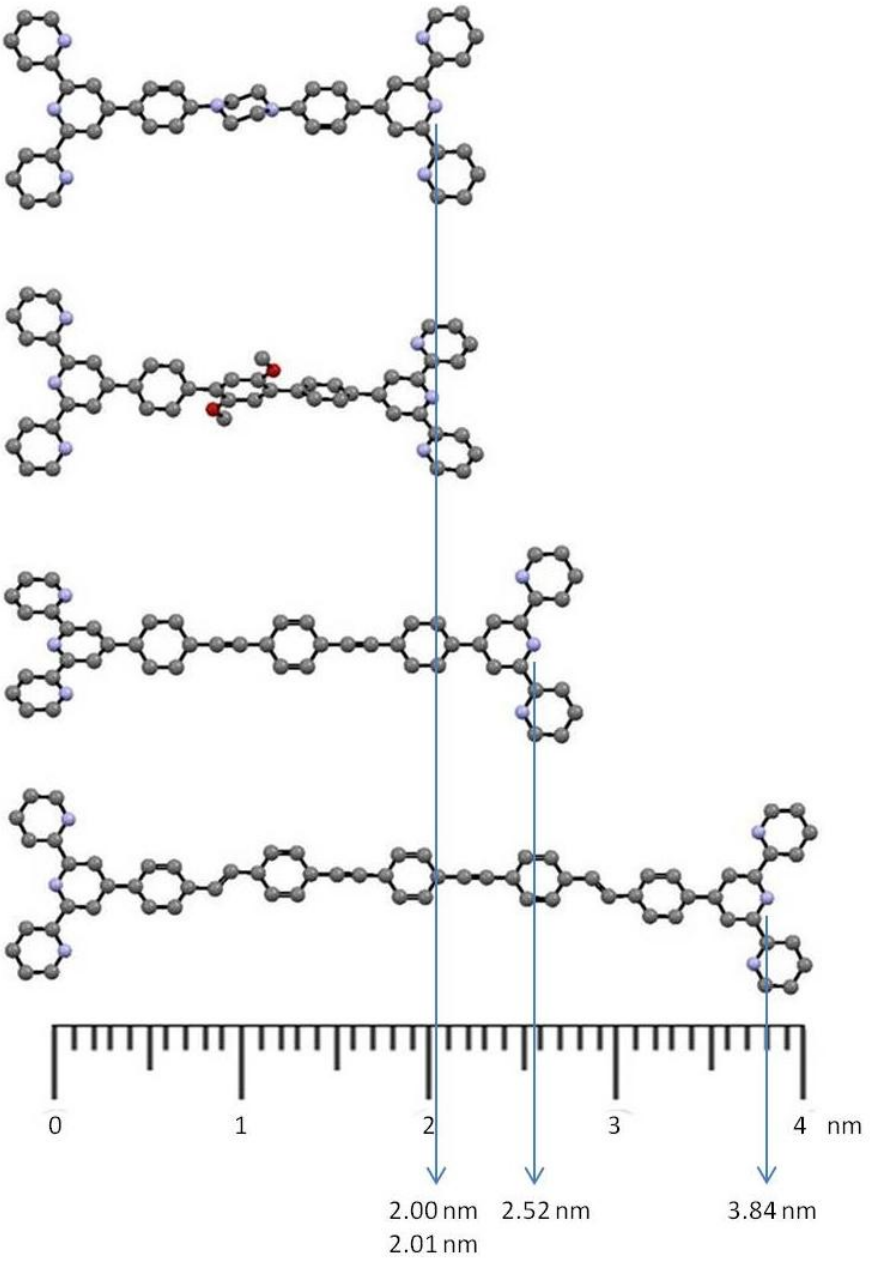

Figure 77: DFT structures of simplified models of the four bis-Tpy platforms **143**, **174**, **176** and **178**

2.3.4.2 DPA and PyMTA derivatives

Concerning the other ligands, even if their EPR spectra could be too broad for PELDOR purposes, we decided to perform the same methodological developments, as the resulting platforms could find other applications than PELDOR (in supramolecular chemistry notably). Hence, a double Sonogashira coupling between diester **9** and OPE-diCCH **164** afforded tetraester **180** in good yield. DMF was used instead of THF to improve the solubility of the reagents. A saponification led to the formation of the fully conjugated rod bis-DPA-OPE **181**, and coordination with $Mn(ClO_4)_2$ led to the corresponding Mn^{II} complex **182** in good yield (Scheme 62).

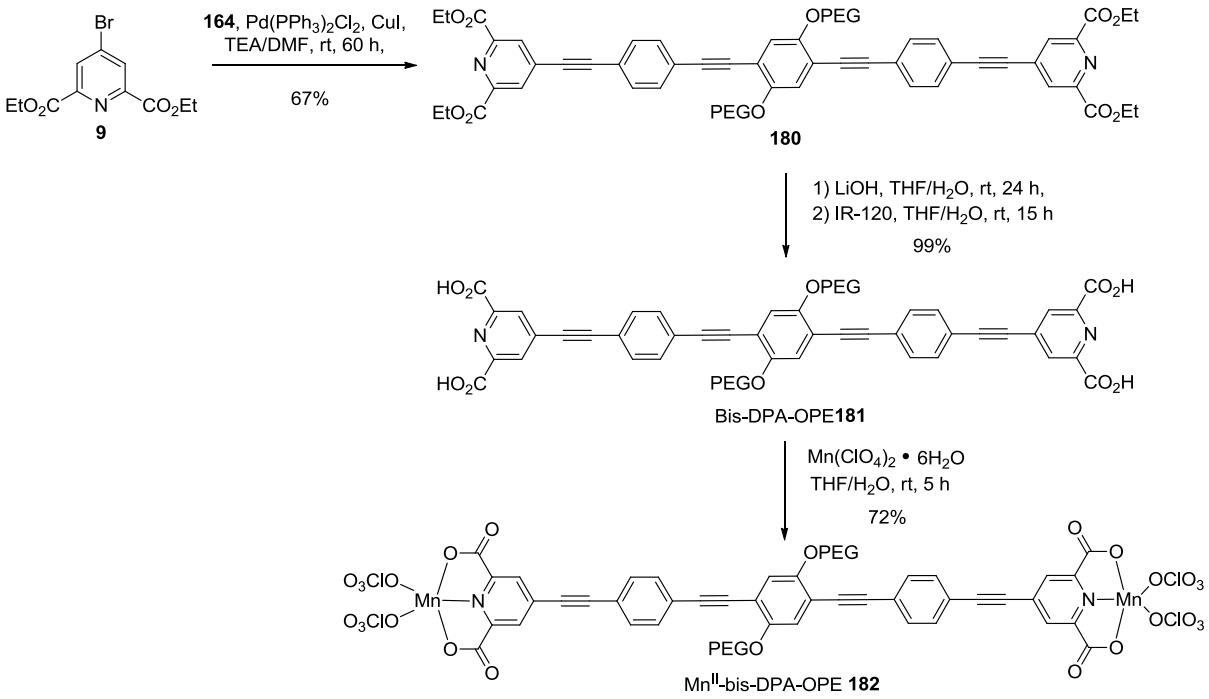

Scheme 62: Synthesis of the bis-DPA-OPE platform **181** and its corresponding Mn^{II} complex **182**

Crystals of tetraester **180** suitable for X-ray diffraction were grown by slow evaporation from a deuterated chloroform solution. This molecule crystallizes in the P-1 space group (triclinic system), one of the ethyl groups being slightly disordered, with a N-N distance of 30.1 Å. Parallel sheets are formed in the packing unit, with weak π-stacking (3.6-3.7 Å) between one benzene ring with PEG chains and another benzene ring without PEG chains. The five aromatic rings are nearly coplanar: the three benzene rings are strictly coplanar while the two pyridine rings are twisted by 10° (Figure 78).

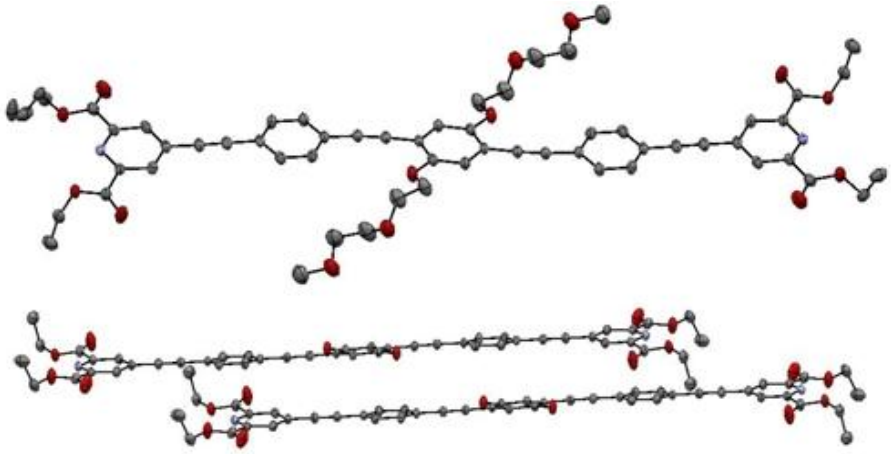

Figure 78: ORTEP drawings of tetraester **180**. Hydrogen atoms have been omitted for clarity. Top: view of the asymmetric unit, bottom: view of the packing interactions (PEG chains omitted for clarity)

DFT calculations (UB3LYP/6-311G**) performed on bis-DPA-OPE **181** (with PEG chains replaced with -OMe groups to reduce calculation time) have led to the structure depicted in Figure 79. The N-N distance is 30.3 Å, in excellent agreement with the crystal structure. This can be explained by the intrinsic rigidity of the system, limiting the number of conformations of minimal energy. The only difference is the perfect planarity of the structure obtained by DFT.

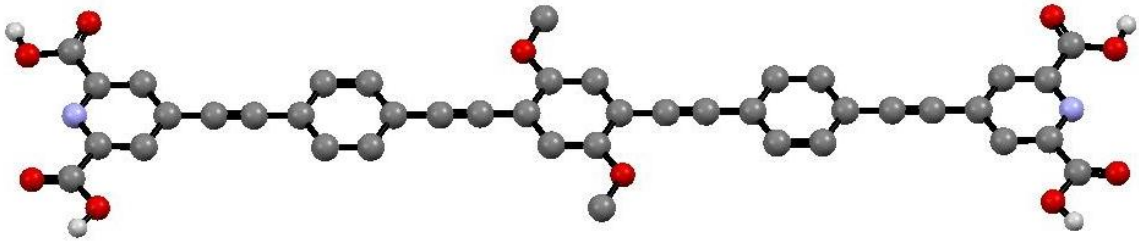

Figure 79: DFT structure of a simplified model of bis-DPA-OPE **181**. Hydrogen atoms (except on carboxylic acid groups) have been omitted for clarity.

The bis-DPA-OPE platform **181** is soluble in 100 mM HEPES buffer at pH 8, but despite our efforts, we could not manage to dissolve the corresponding Mn^{II} complex **182**, owing to its very low solubility in most common solvents. This prevented any PELDOR assay as the *in situ*-generated Mn^{II} complex of bis-DOTA-OPE **181** precipitates out as soon as Mn^{II} is added.

We used the same strategy to graft ^{t}Bu-*p*BrPyMTA **71** on an OPE linker. The coupling between ^{t}Bu-*p*BrPyMTA **71** and *p*-diethynylbenzene **170** is described in the literature.[21] However, in our hands this reaction could not be reproduced, either in the original conditions ($Pd(PPh_3)_2Cl_2$/CuI/$^{i}Pr_2NH$) or using modified procedures (replacing the base for piperidine or TEA/DMF, or replacing the catalyst for $Pd(PPh_3)_4$). The fact that this reaction was originally performed on multigram scale could be an explanation for this lack of reproducibility. The same issue was observed when *p*-diethynylbenzene **170** was replaced for OPE-diCCH **164**, despite many attempts ($Pd(PPh_3)_4$/CuI/TEA/THF or $Pd(PPh_3)_2Cl_2$/CuI with either TEA/THF, $^{i}Pr_2NH$/DMF or piperidine). In each case complex mixtures were obtained. It also failed when Et-*p*BrPyMDPDA **87** or

Et-*p*BrPyMTA **70** were used under classical conditions ($Pd(PPh_3)_2Cl_2$/CuI/THF with TEA or $HNEt_2$, Scheme 63).

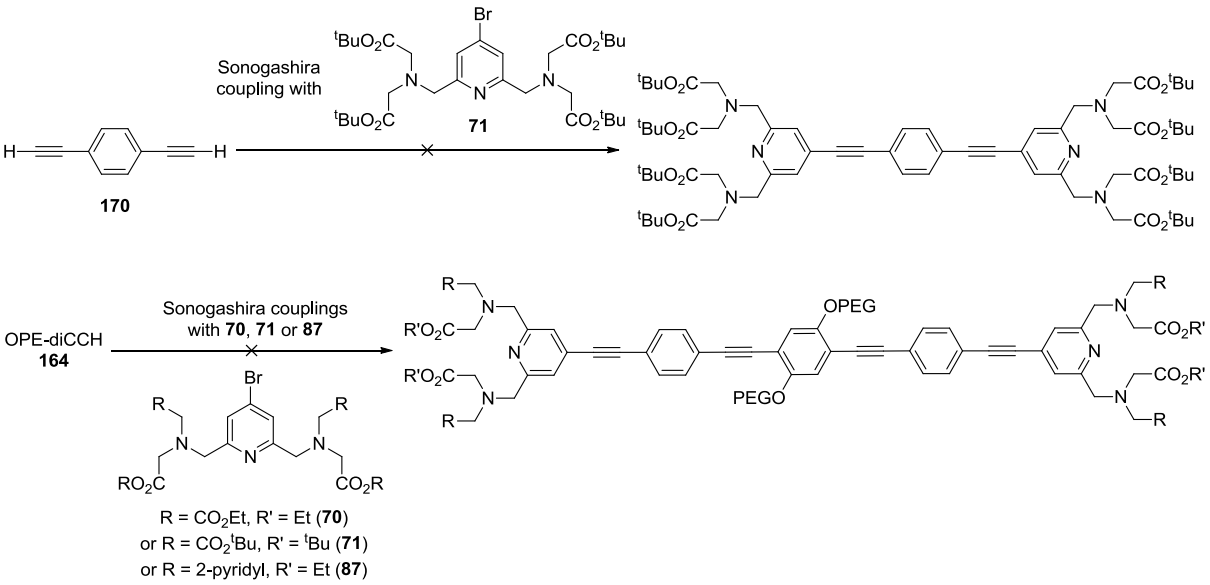

Scheme 63: Attempted Sonogashira couplings between PyMTA and PyMDPDA derivatives **70**, **71** and **87** and linkers **170** or **164**

This problem was solved by the use of click chemistry (CuAAC – Copper-catalyzed azide-alkyne cycloaddition).[135] Using the strategy we employed for the synthesis of compound **76** (ref interne), reaction between Et-*p*N_3PyMTA **74** and OPE-diCCH **164** afforded the expected protected octaester rod **183** in modest yield. Basic hydrolysis generated the bis-PyMTA-OPE platform **184**, and coordination with $MnCl_2$ afforded the corresponding Mn^{II} complex **185** (Scheme 64).

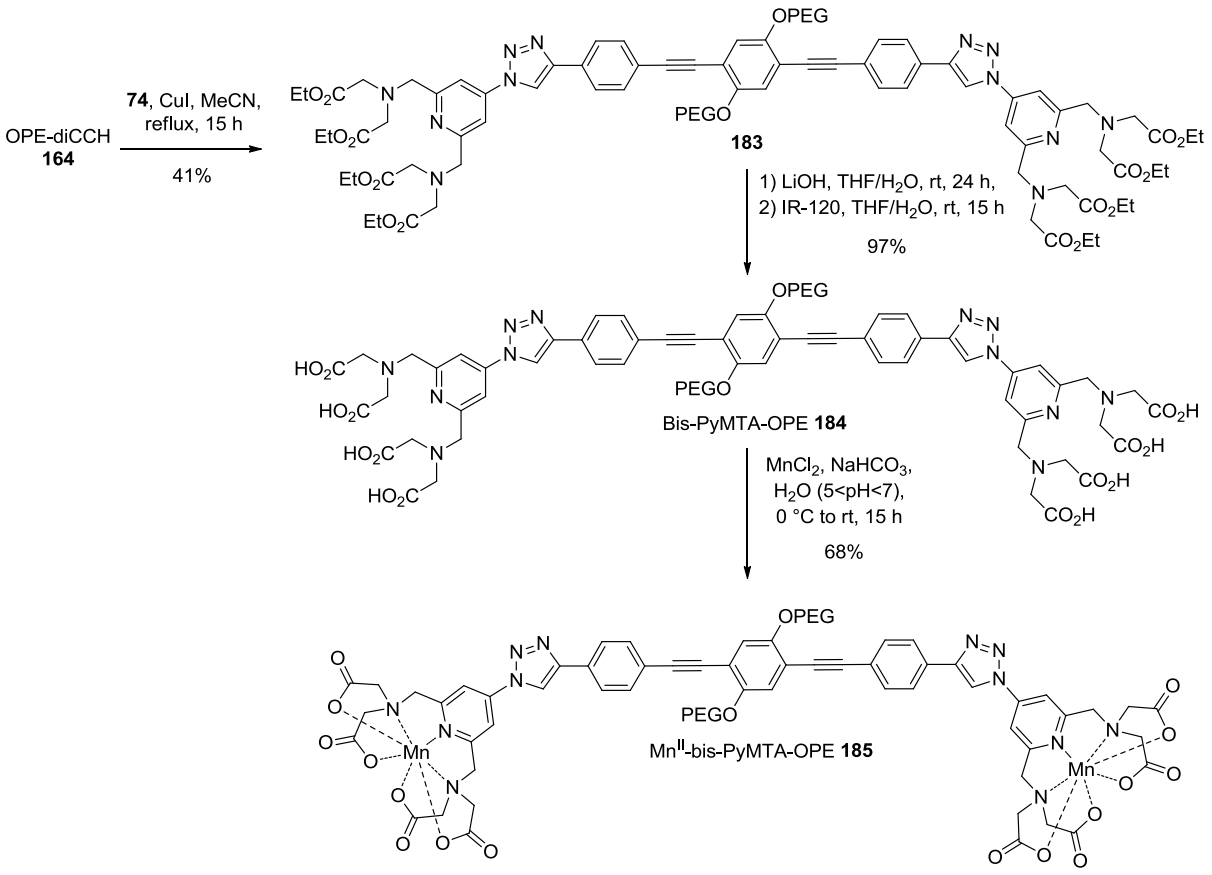

Scheme 64: Synthesis of the bis-PyMTA-OPE module **184** and its corresponding Mn^{II} complex **185**

DFT calculations (UB3LYP/6-311G**) were realized on an analogue of the bis-PyMTA platform **184**, where the acetate moieties have been removed and the PEG chains have been replaced with -OMe groups to reduce calculation time. The corresponding structure is depicted in Figure X and indicates a N-N distance of 31.3 Å. The OPE rod is roughly planar, while the two pyridine moieties are tilted by 13° (Figure 80).

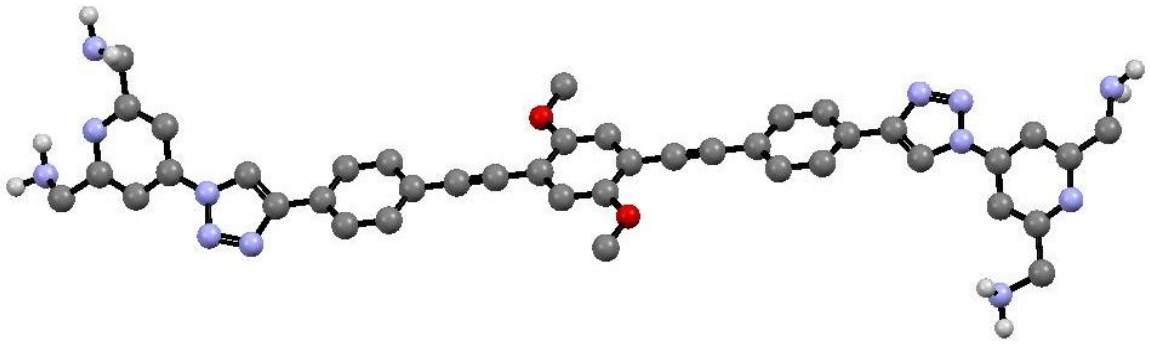

Figure 80: DFT structure of a simplified model of **184**. Hydrogen atoms (except on amino groups) have been omitted for clarity

The J-band *cw*-HFEPR spectrum of Mn^{II}-bis-PyMTA-OPE **185** was recorded (Figure 81).

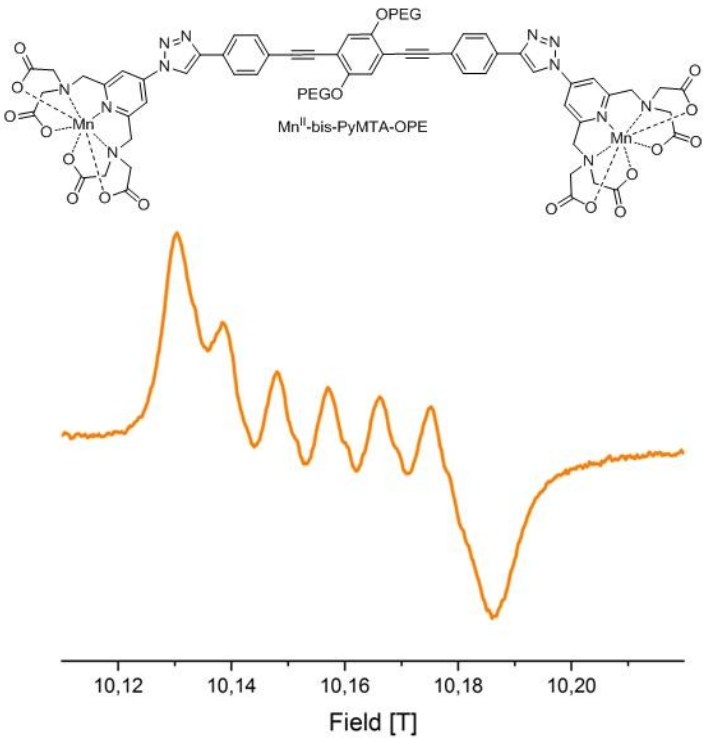

Figure 81: Structure of Mn^{II}-bis-PyMTA-OPE **185** (top) and its J-band *cw*-HFEPR spectrum (1 mM in ligand, 0.8 mM in Mn^{II}, in 100 mM pH 8 HEPES buffer with 20% glycerol, bottom)

Compared to the Mn^{II} complexes of the mono-PyMTA derivatives pBrPyMTA **72** and PhTPyMTA **77**, this spectrum looks very different: all lines are much broader and obscure the minor feature. The same result was observed when the Mn^{II} complex was generated *in situ* from the corresponding ligand. It was shown (p. 75) that the addition of a triazole moiety on PyMTA induced some broadening, but not to that extent. An explanation could be the electronic communication between the two Mn centers because the structure is fully conjugated. This broadening is detrimental for the PELDOR method, but this platform could be used to assess the effect of Mn^{II} complexes with broad lines on the SNR.

2.3.4.3 DO3A and DOTA derivatives

Among the library of OPE linker, OPE-diNH_2 **163** and OPE-diCO_2H **165** appeared particularly relevant for grafting on DO3A and DOTA derivatives, in a way similar to the strategy used for phenyl-piperazine linkers (p. 105). In a first approach, we used the commercially available tri-^{t}Bu-DO3A **186**, equipped with an amino group that would form an amide bond with OPE-diCO_2H **165**. As shown by the *cw*-HFEPR of the Mn^{II} complex of DO3A (Figure 60, p. 83), we can expect broad lines from a bis-DO3A platform. However, these compounds are different (a NH group on DO3A and an amide bond on bis-DO3A).

The reaction between tri-^{t}Bu-DO3A **186** and OPE-diCO_2H **165** in the presence of hydroxybenzotriazole (HOBt) and *N*,*N'*-dicyclohexylcarbodiimide (DCC) resulted in the formation of the corresponding protected bis-DO3A **187** in moderate yield. No improvement was observed when

HATU was used. The carboxylic acids were then regenerated with TFA to afford the bis-DO3A-OPE platform **188** after purification by reversed-phase HPLC (Scheme 65). The mean N-N distance between the DO3A rings was roughly estimated to be 2.3 nm using Spartan.[195]

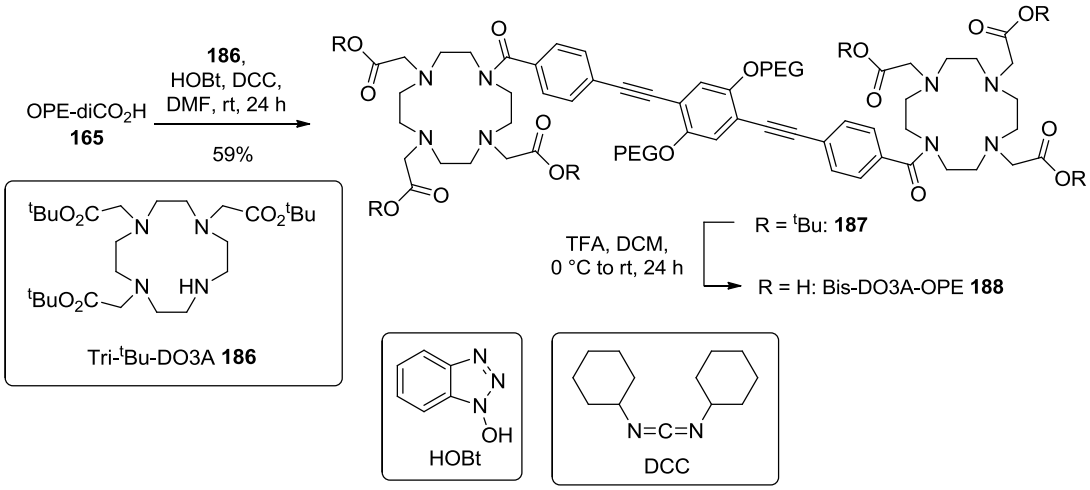

Scheme 65: Synthesis of the bis-DO3A-OPE platform **188**

The J-band *cw*-HFEPR spectrum of the Mn^{II} complex of bis-DO3A-OPE **188** is depicted in Figure 820. As anticipated, broad and complex lines are observed because the symmetry of the coordination sphere is broken, again illustrating the striking difference compared to the Mn^{II} complex of the bis-DOTA-$PhPip_1$ platform **149** (p. 106) for instance.

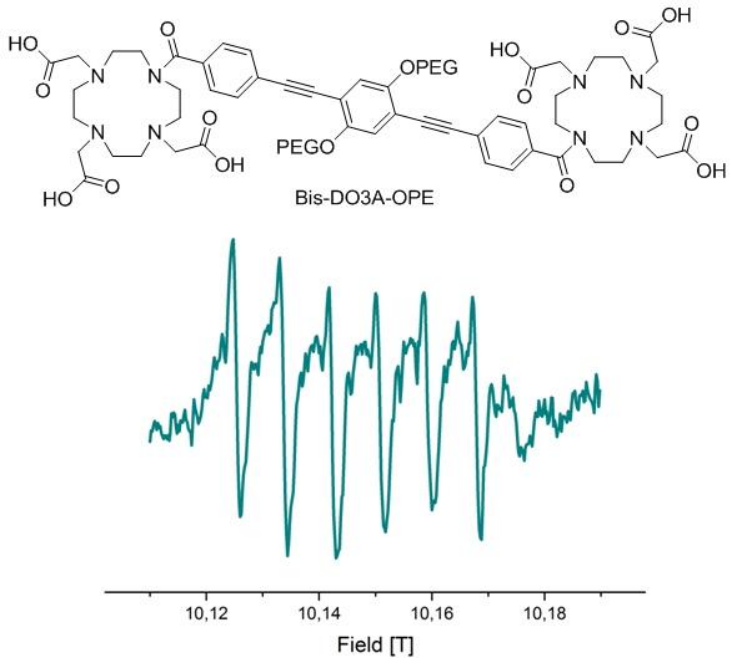

Figure 82: Structure of bis-DO3A-OPE **188** (top) and J-band *cw*-HFEPR spectrum of the corresponding Mn^{II}-complex (100 µM in ligand, 80 µM in Mn^{II}, in 100 mM pH 8 HEPES buffer with 20% glycerol at 23 K, bottom)

We obtained the first bisDOTA platforms **149** and **150** on a phenyl-piperazine linker using an amide bond formation with HATU. Under the same conditions, the coupling between OPE-diNH_2 **163**

and tri-^{t}Bu-DOTA **146** afforded the corresponding protected bis-DOTA **189**, in modest yield (33%) after laborious purification using column chromatography on silica gel (Scheme 66).

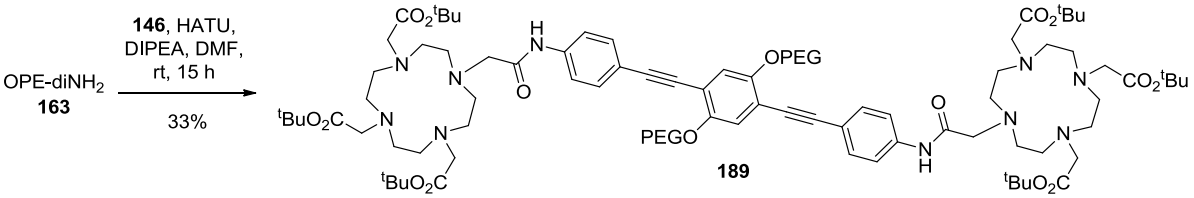

Scheme 66: Synthesis of the protected bis-DOTA platform **189** using an amide bond formation

We modified the strategy by introducing the last DOTA arm directly on the linker and allowing the product to react with tri-^{t}Bu-DO3A **186**, a commonly used procedure.[153,196,197,198,199,200] Starting from the three OPE$_n$-diNH$_2$ linkers **163**, **171** and **172**, addition of bromoacetyl bromide in the presence of K_2CO_3 afforded bromides **190**, **191** and **192** in modest to good yields. The use of TEA instead of K_2CO_3 led to inferior yields. A double nucleophilic substitution with tri-^{t}Bu-DO3A **186** gave the three protected bis-DOTA **193**, **194** and **195** platforms in good yields with straightforward column chromatography purification (Scheme 67).

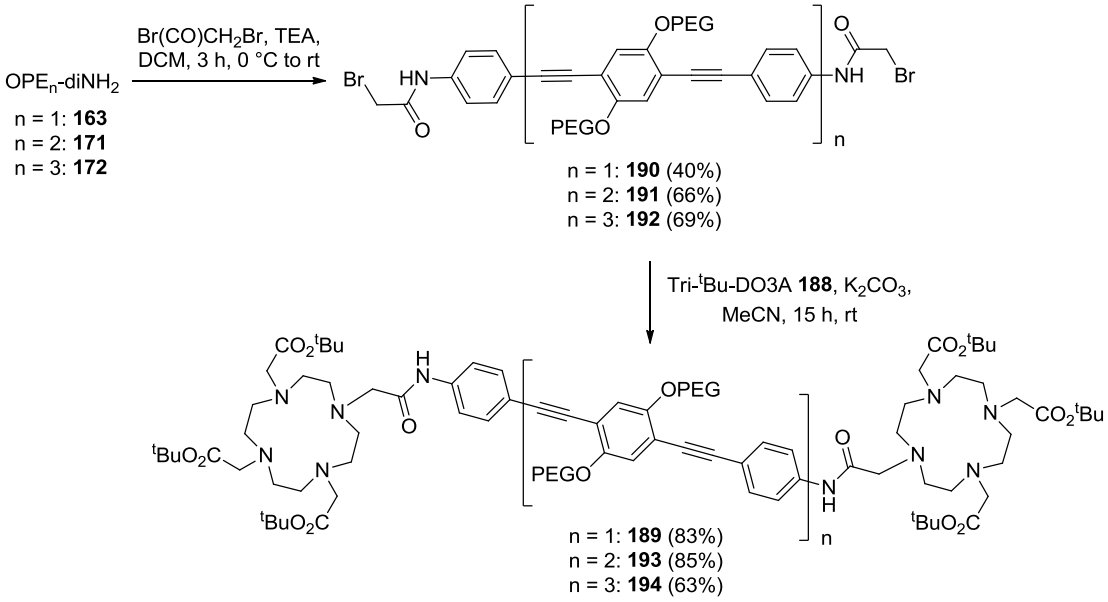

Scheme 67: Synthesis of the three protected bis-DOTA platforms **189**, **193** and **194**

The same TFA treatment used for protected bis-DOTAs **147** and **148** (p. 105) and protected bis-DO3A **187** (p. 126, 50:50 TFA/DCM, 0 °C to rt, 24 h) was then performed on the three protected bis-DOTA platforms **189**, **193** and **194**. However, a very surprising result was obtained. On these systems, under a vast range of conditions (TFA/DCM with or without scavengers,[196] HCO_2H,[201] and aq. HCl), the expected deprotected products have never been isolated. Other pure products were isolated instead after HPLC purification, but with lower molar masses (Figure 83).

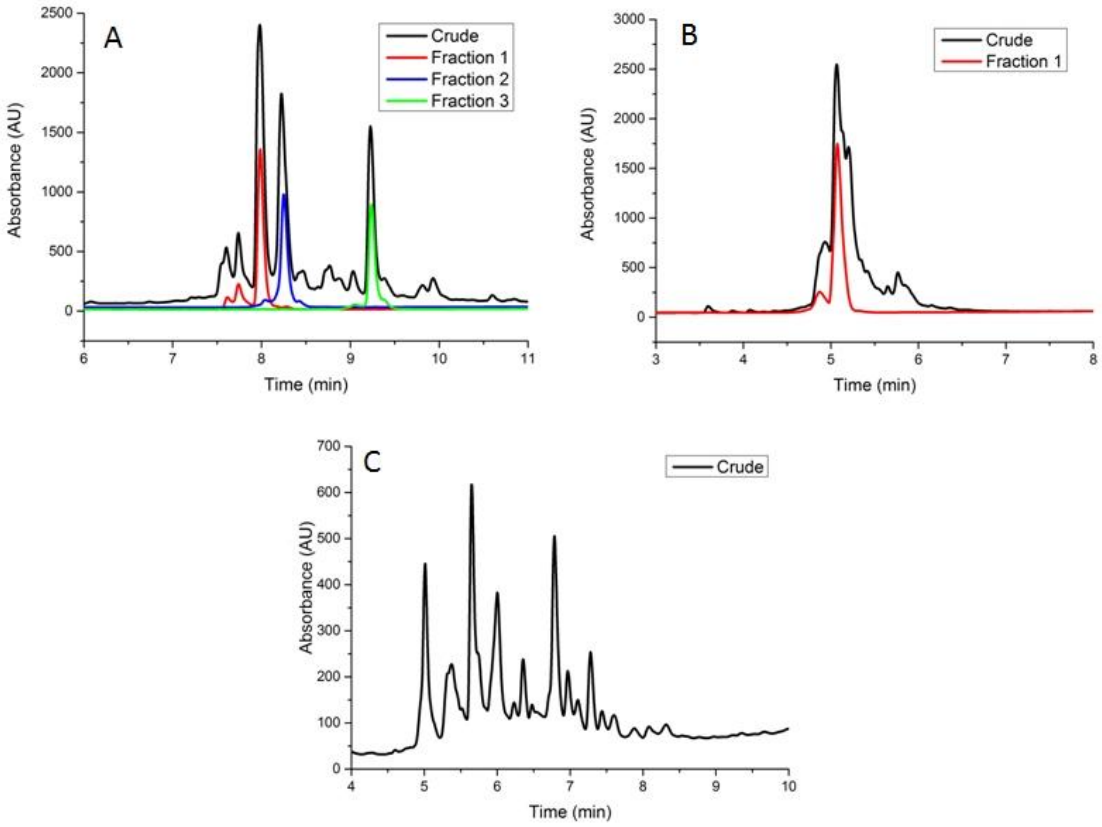

Figure 83: HPLC traces of the crude and purified compounds after deprotection of the protected bis-DOTA modules **189**, **193** and **194** in different conditions. A: 1:1 TFA/DCM, 24 h, 0 °C to rt. B: Aq. 6M HCl, 24 h, 0 °C to rt. C: HCO_2H, 12 h, 60 °C. Gradients: 0 to 50% MeCN (A), 5 to 100% MeCN (B), 0 to 70% MeCN (C) in 10 min

As shown in Figure 83, whatever the deprotection conditions, rather complex chromatograms were obtained. The isolated products have the expected molar mass minus 66 or 84 $g.mol^{-1}$, depending on the conditions. No obvious fragmentation could be identified. This behavior is surprising if we consider that the ^{t}Bu-deprotection of DOTA compounds usually proceeds cleanly in the literature, even on related compounds.[197] However, low yields were sometimes observed,[196] so this deprotection step is not so straightforward.

We concluded that the strong acidic conditions used for the ^{t}Bu group deprotection could be responsible for the degradation of compounds **189**, **193** and **194**. A strong acidic medium is necessary because the deprotection of ^{t}Bu-protected DOTA derivatives is known to be sluggish.[202] To circumvent this problem, we looked for a more acid-sensitive protecting group. The phenyl-isopropyl (Pp) group mentioned by Mier *et al.*[203] seemed particularly relevant as it is easily cleaved with only 2% TFA in DCM. This group has been successfully employed by the authors to generate peptides incorporating a DOTA core with a much cleaner HPLC profile after cleavage from the resin than with the standard ^{t}Bu-protected DOTA.[204]

The synthesis of the Pp counterpart of tri-^{t}Bu-DO3A **186** was achieved by reacting bromoacetic acid with 2-phenyl-2-propanol **195** in the presence of DCC and 4-dimethylaminopyridine (DMAP) to give ester **196**. Interestingly, the use of bromoacetyl bromide was inefficient, as well as the use of HATU, maybe due to the steric hindrance around the -OH group. The yield of this method

is slightly inferior to the one of Mier *et al.*[203] (isolation of the trichloroacetimidate and reaction with bromoacetic acid) but can be performed in only one step. Next, the reaction between 1,4,7,10-tetraazacyclododecane (cyclen) **197** and 3 equivalents of ester **196** afforded the expected tri-Pp-DO3A **198** in low yield, which was not surprising because of the presence of other alkylated cyclen derivatives as side-products. However, the purification was straightforward and gram amounts of tri-Pp-DO3A **198** could be readily obtained (Scheme 68).

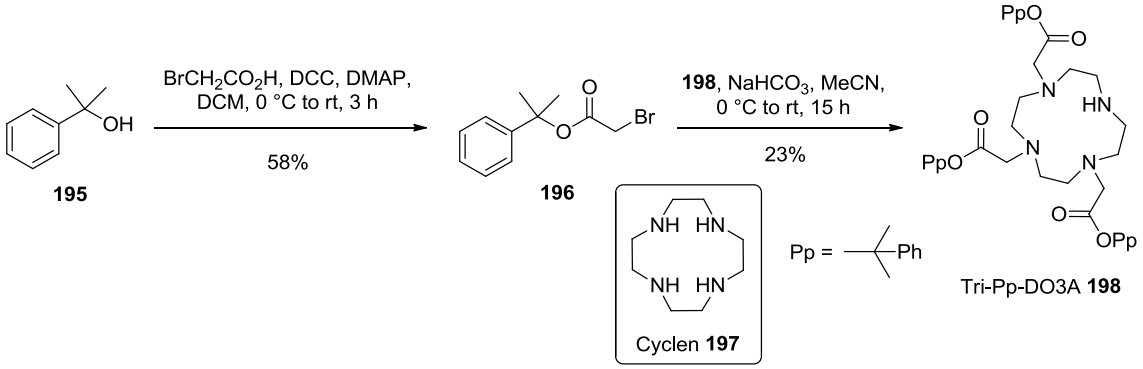

Scheme 68: Synthesis of tri-Pp-DO3A **198**

The reaction between tri-Pp-DO3A **198** and linkers **190**, **191** and **192** afforded the Pp-protected bis-DOTA modules **199**, **200** and **201**. As anticipated, the deprotection of Pp groups with a 2:2:96 TFA:TIS:DCM cleavage cocktail proceeded smoothly and cleanly afforded the expected bis-DOTA-OPE$_n$ platforms **202**, **203** and **204** (with n = 1, 2 and 3, respectively) after HPLC purification (Scheme 69).

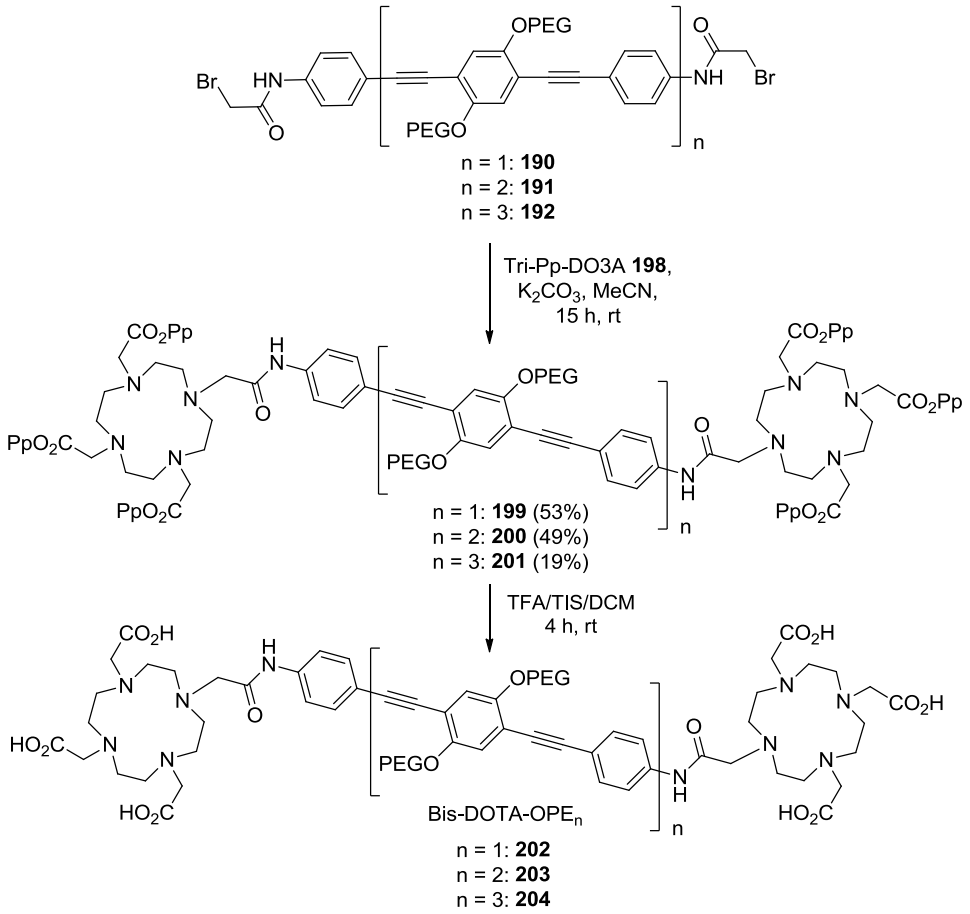

Scheme 69: Synthesis of the three bis-DOTA-OPE$_n$ modules **202**, **203** and **204**

The efficiency of this deprotection step was monitored by reversed-phase HPLC. Treatment of 30 mg of compound **199** with 1 mL of cleavage cocktail gave, after 1 h, a mixture of reactant, product and partially deprotected compounds. Two additional mL of the cleavage cocktail were added and the reaction went to completion after 3 h, giving only the expected fully deprotected product **202** that was already 95% pure, in striking contrast with the deprotection of the ^{t}Bu-protected platforms (Figure 84).

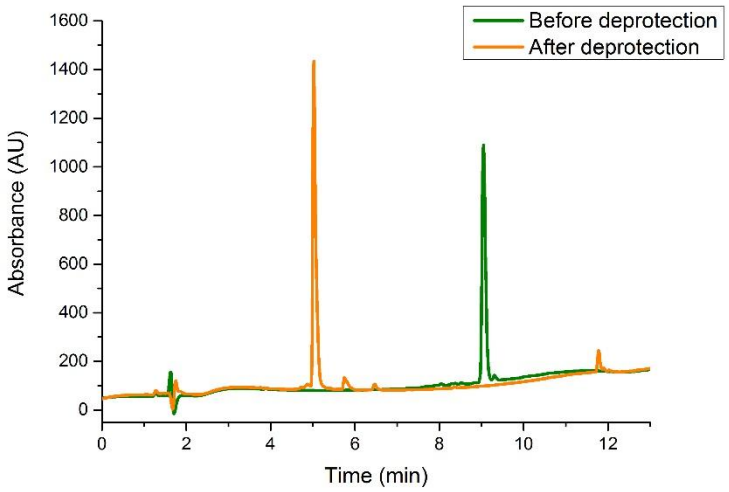

Figure 84: HPLC traces of pure Pp-protected bis-DOTA-OPE$_1$ **199** (green) and of the crude mixture after completion of the deprotection (orange) containing 95% of bis-DOTA-OPE$_1$ **202**. Gradient: 5 to 100% MeCN in 10 min.

The mean Mn-Mn distance of the Mn^{II} complexes of platforms **202**, **203** and **204** was obtained with MD simulations (values of 2.83, 4.12 and 5.46 nm, respectively). These results are in good agreement with the 0.69 nm distance increase per phenyl-acetylene moiety found using DFT calculations (Figure 73, p. 114). More details will be provided in the next chapter.

The J-band *cw*-HFEPR spectrum of the Mn^{II} complex of bis-DOTA-OPE$_1$ **202**, generated *in situ*, was recorded (Figure 85). The same titration procedure performed for bis-DOTA-PhPip$_1$ **149** was performed, and here again, it indicated the presence of four trifluoroacetate counterions resulting from HPLC.

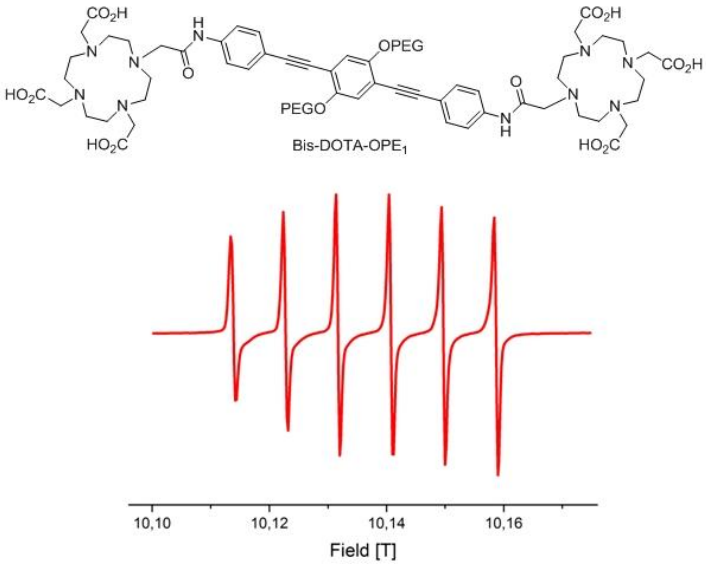

Figure 85: Structure of bis-DOTA-OPE_1 **202** (top) and J-band *cw*-HFEPR spectra of the corresponding Mn^{II} complex (25 µM in ligand, 20 µM in Mn^{II}, in 100 mM pH 8 HEPES buffer with 20% glycerol at 23 K, bottom)

This spectrum displays the expected six narrow lines. Unlike bis-DOTA-$PhPip_1$ **149**, the hyperfine sextet is as narrow as Mn^{II}-DOTA.

As a conclusion, numerous platforms incorporating two ligands for Mn^{II}, including the most promising DOTA, attached to a central rigid molecular rod have been successfully synthesized. X-ray crystallography in combination with DFT calculations and MD simulations were used to predict the Mn^{II}-Mn^{II} distance, which is in the 2-5 nm range for all modules.

2.4 Polyprolines

The last kind of linker we employed can be seen as a first step toward biological applications: it is a polypeptide spacer that consists of an oligomer of prolines, known as polyproline. Polyproline linkers have already been used for PELDOR measurements in various reports, where they were tagged with one or two MTSL,[48,49,53,60,205] two Gd-PyMTA labels,[39] or with one Gd-DOTA and a TEMPO moiety.[85] The interest of polyprolines lies in their quite rigid helical structure in aqueous solution[206,207] where the amide groups adopt an all-*trans* conformation known as polyproline II (PPII): this explains the popularity of polyprolines as a molecular ruler. The size of a PPII structure is highly predictable, as a recent crystallographic study[208] showed that the length increase per proline residue is 0.3 nm. However, FRET studies[209,210] have suggested that for long polyprolines (> 20 residues), chain bending considerably shortens the end-to-end distance. In less polar environments, like aliphatic alcohols such as isopropanol, the amide moieties can adopt a *cis* conformation. The all-*cis* conformation is known as polyproline I (PPI) and is more compact: the length increase per proline is only 0.18 nm.[207,211,212]

The literature strategies that have been employed to spin-label a polyproline are all different. The incorporation of one or two nitroxides on the Cys residues of a CP_6C peptide has been performed using the standard MTSL.[48,49,53,60,205] Similarly, Cys residues of a $AP_{10}CP_{10}CP_{10}$ peptide have been

tagged with a thiol-ene reaction using a PyMTA label incorporating a vinyl group.[39] Finally, a tri-^{t}Bu-DOTA label was attached using a peptide coupling directly to the NH group of a polyproline octadecamer.[85]

Our strategy also relied on the introduction of cysteine residues, but they were designed to react with maleimides, specifically DOTA-Mal **205** (Figure 17, p. 31), which has already be employed for the Cys labeling of proteins[78,84] (Figure 28, p. 44 and Figure 34, p. 49) (Scheme 70). Peptides incorporating 6, 9 and 12 prolines with a cysteine at the N- and C-terminus (CysPro$_n$Cys **206**, **207** or **208** with n = 6, 9 or 12, respectively) were thus synthesized using solid-phase peptide synthesis (SPPS) in Fmoc strategy. Briefly, the 4-(2′,4′-dimethoxyphenyl-Fmoc-aminomethyl)-phenoxyacetamido-methylbenzhydryl amine (Rink Amide MBHA) resin was first Fmoc-deprotected (NMP/piperidine) and coupled with a trityl-protected cysteine (Fmoc-Cys(Trt)-OH) (coupling conditions: HATU/DIPEA/NMP). After Fmoc deprotection, iterative coupling-deprotection steps with Fmoc-protected prolines (Fmoc-Pro-OH) (HBTU/DIPEA/NMP) were performed. When the adequate number of prolines was reached, at last coupling with Fmoc-Cys(Trt)-OH was performed. After a last deprotection step, the NH_2 group was capped (Ac_2O/DCM) and the peptide was cleaved from the resin with an adequate cleavage cocktail (degassed 1,2-ethanedithiol (EDT)/triisopropylsilane (TIS)/H_2O/TFA) to avoid the oxidation of thiol groups. HPLC analysis showed that the peptides were pure enough (more than 90%) to be engaged in further coupling with DOTA-Mal **205**.

Accordingly, a thiol-maleimide coupling was performed between the polyprolines CysPro$_n$Cys **206**, **207** or **208** and DOTA-Mal **205**, in 200 mM pH 7 HEPES buffer with tris-(2-carboxyethyl)phosphine (TCEP) as a reducing agent, to avoid thiol oxidation to disulfides. The reaction proceeded smoothly and the corresponding bis-DOTA-polyprolines DOTA$_2$P$_n$ **209**, **210** and **211** were isolated in moderate to good yields after HPLC purification (Scheme 70).

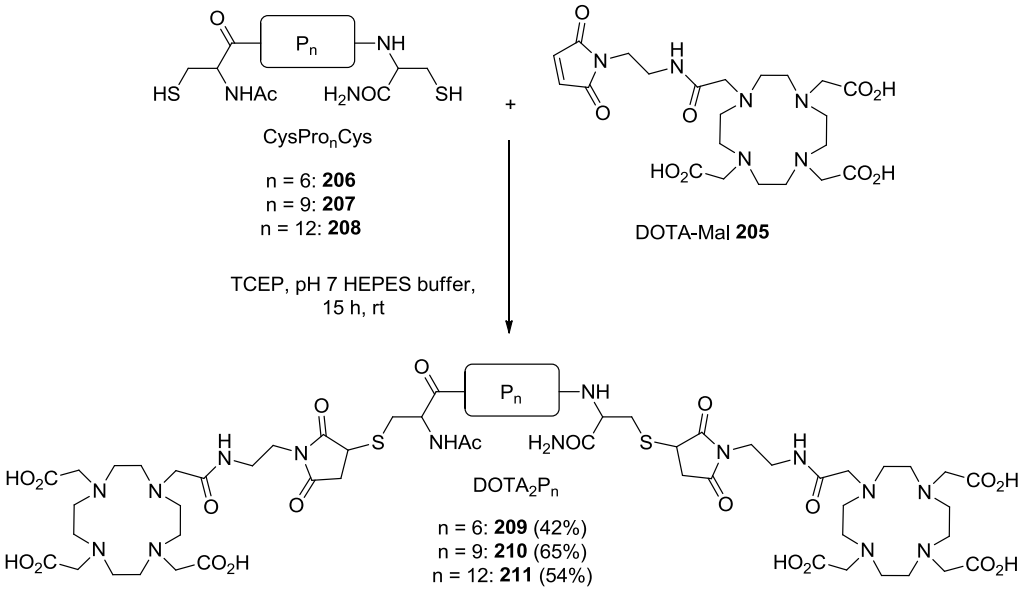

Scheme 70: Polyproline labeling with DOTA-Mal **205**

Alternatively, a dissymmetric version of a polyproline linker would be desirable to introduce two different paramagnetic centers. Thus, the same SPPS was repeated, but the peptide was cleaved

before the introduction of the second cysteine at the N-terminus: the free amino group of the last proline residue would be the attachment point. Again, the $(Pro)_nCys$ peptides **212**, **213** or **214** (with n = 6, 9 or 12, respectively) obtained were found to be at least 95% pure.

To determine whether the grafting of DOTA moieties could disrupt the PPII structure of the $DOTA_2P_n$ modules, we performed circular dichroism (CD) experiments. Platforms were dissolved in the closest possible conditions as those used for PELDOR experiments (200 µM in 100 mM pH 7.5 phosphate buffer with 5% glycerol and 200 mM NaCl). The CD spectra are displayed in Figure 86.

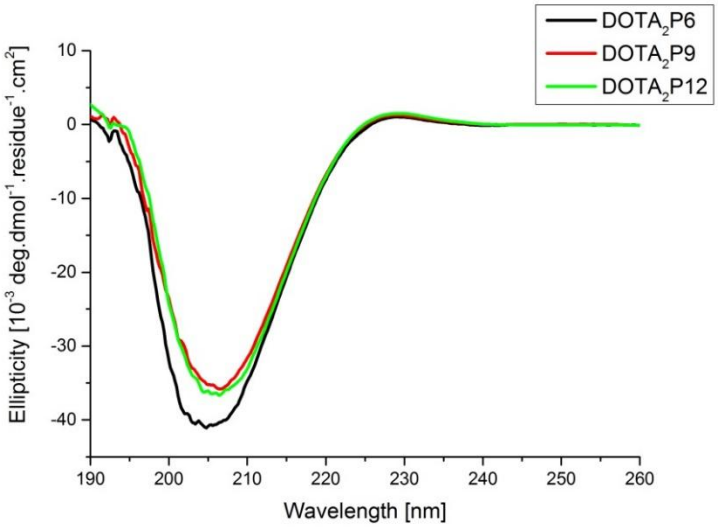

Figure 86: CD spectra of $DOTA_2P_n$ (n = 6, black, n = 9, red, n = 12, green) at 20 °C. See above for experimental conditions

These spectra show typical features of a PPII helix signature, with a small positive band around 228 nm and a large negative band around 206 nm.[207,211,213] Analogous spectra were obtained using the same platforms metallated with 1.8 equivalents of $Mn(ClO_4)_2 \bullet 6H_2O$. PPII helix contents were evaluated at 92%, 87% and 85% for $DOTA_2P_6$, $DOTA_2P_9$ and $DOTA_2P_{12}$, respectively, using a home-written program (CD Friend, S. Buchoux, PhD thesis, University of Bordeaux 1, 2008). This proves that the PPII helix conformation is still largely dominating in solution in these conditions and that the effect of the DOTA moieties is likely to be negligible. The J-band *cw*-HFEPR spectra of the Mn^{II} complexes of $DOTA_2P_n$ were recorded and found to be identical to Mn^{II}-DOTA (p. 151).

In this chapter, we explored four types of linkers to build modules with a constrained distance between two Mn^{II} complexes. Oligo(piperidine)s first seemed adequate, but issues in the synthesis of the linker and in the grafting of ligands incited us to explore other possibilities. Phenyl-piperazine linkers were designed, but elongation and grafting with various ligands using Hartwig-Buchwald couplings proved difficult. However, these linkers could be coupled to the promising DOTA ligand to obtain two bis-DOTA platforms in the estimated 2.1 – 2.4 nm range (bis-DOTA-$PhPip_n$ **149** and **150** with n = 1 and 2, respectively). OPE linkers, known to be very stiff, were then synthesized and their length was efficiently incremented using iterative Sonogashira couplings. These linkers could be coupled to various ligands including DOTA to obtain three bis-DOTA modules (bis-DOTA-

OPE_n **202**, **203** and **204** with n = 1, 2 or 3, respectively) in the approximate 2.4 – 5.3 nm range. Finally, polyproline spacers were then synthesized and coupled to DOTA to generate the three $DOTA_2P_n$ modules **209**, **210** and **211** (n = 6, 9 or 12, respectively) that should roughly cover the 3 – 4.5 nm range. PELDOR measurements on the Mn^{II} complexes of these eight bis-DOTA platforms (Figure 87), as well as on bis-Mn-Tpy platform **176**, will be discussed in Chapter II.

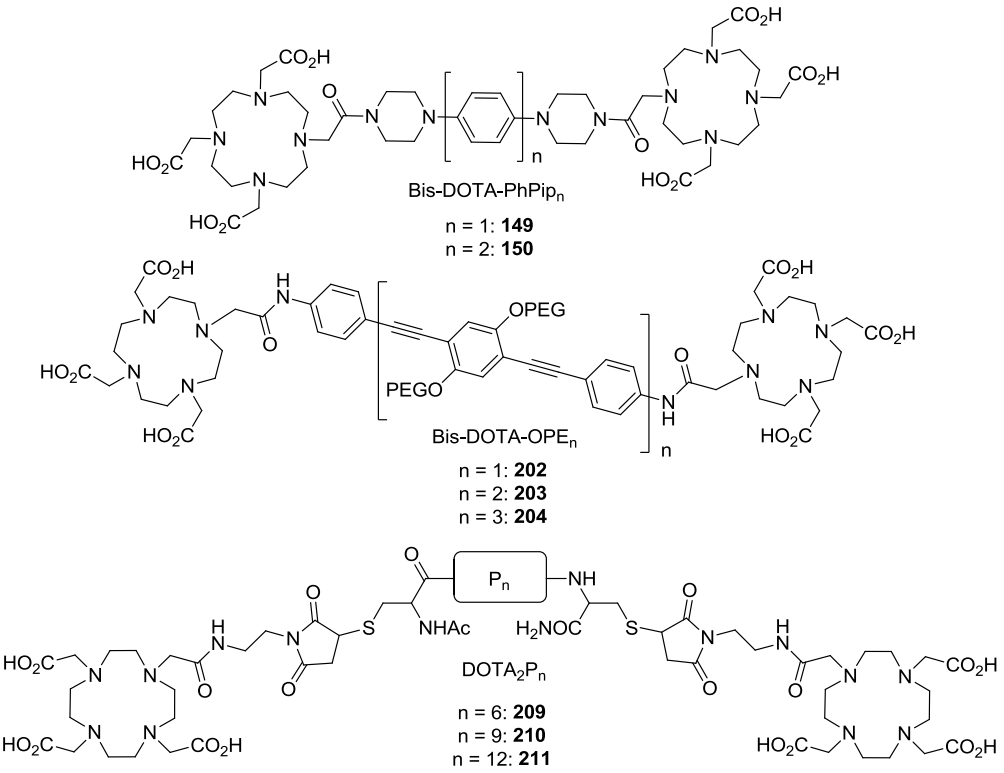

Figure 87: Structure of the eight bis-DOTA platforms that will be used for PELDOR distance measurements

3. BIS(NITROXIDES)

Stable nitroxide radicals such as TEMPO have found a wide range of applications, notably as mild oxidants in synthetic chemistry. They are also the most commonly used spin labels for PELDOR experiments,[10,36,44] and constitute a highly informative comparison point with high-spin metal-based distance measurements. This is why in the frame of this project, a set of platforms using the linkers previously developed attached to two TEMPO was then developed, to obtain the bis-nitroxide analogue of the most promising bis-Mn^{II} modules. For this purpose, numerous functionalized TEMPO derivatives are commercially available (Figure 88), which can also be modified to obtain the same grafting moieties present on the ligands for Mn^{II} that we have selected for PELDOR measurements.

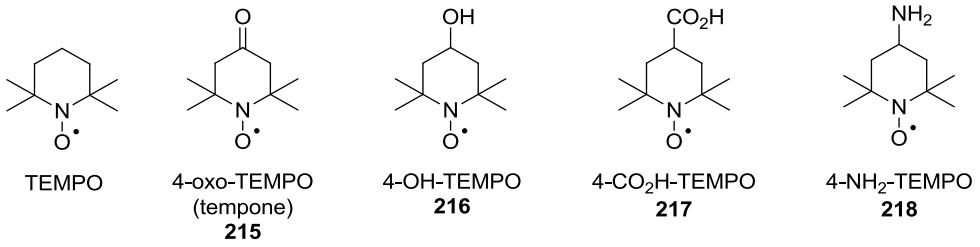

Figure 88: Common commercially available functionalized TEMPO derivatives

3.1 Platforms with a phenyl-piperazine linker

To obtain a bis-TEMPO analogue of bis-(Tpy)Mn^{II}(PhTpy)-Pip **143** (p. 101), a double reductive amination between 4-oxo-TEMPO **215** and PipPhPip **131** allowed the formation of bis-TEMPO **219**, but in low yield (Scheme 71).

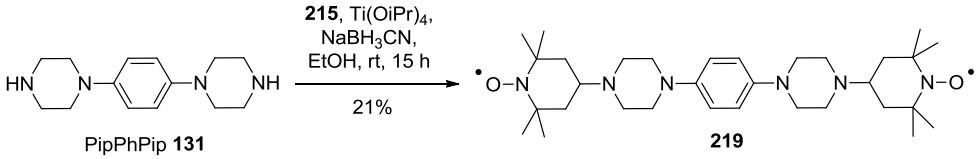

Scheme 71: Synthesis of the bis-TEMPO platform **219**

DFT calculations (UB3LYP/6-31G*) performed on the bis-TEMPO **219** (with NO groups replaced with N-OH to avoid complications linked to spin states) revealed a perfectly symmetric structure where the distance between the middle of the two N-O bonds (point-dipole approximation) was 21.4 Å. (Figure 89).

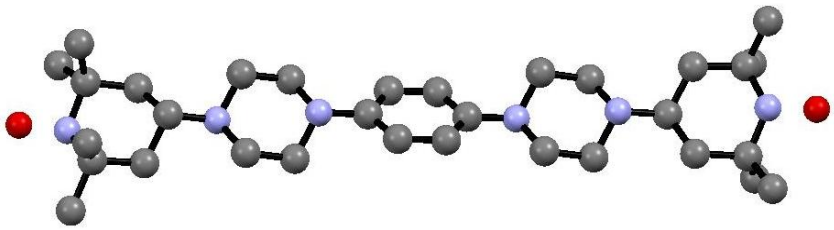

Figure 89: DFT structure of the bis-hydroxylamine corresponding to bis-TEMPO **219**. Hydrogen atoms have been omitted for clarity

The J-band *cw*-HFEPR spectrum of the bis-TEMPO **219** was recorded (Figure 90).

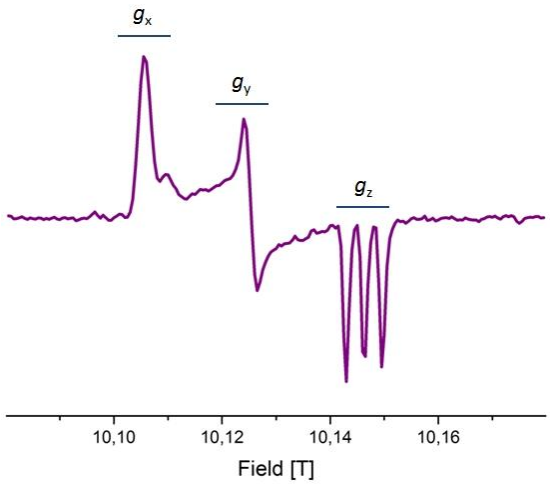

Figure 90: J-band *cw*-HFEPR spectrum of bis-TEMPO **219** (1 mM in toluene, 20 K)

As expected, the *g*-anisotropy is clearly resolved at this field. The A_z component is well-resolved, as it is usually the case for TEMPO derivatives, because the resonance position of g_z is far enough from g_x and g_y at this field. The A_x component is partially resolved, while the A_y is not: higher fields could be used to better separate g_x from g_y. A similar spectrum was obtained at 40 K.

An analogue of the Mn^{II} complex of bis-DOTA-PhPip$_1$ **149** (p. 105) was also synthesized using an amide bond formation between PipPhPip **131** and 4-CO_2H-TEMPO **217** in the presence of HOBt and 1-ethyl-3-(3-dimethylaminopropyl)carbodiimide (EDC) to give the bis-TEMPO **220** in acceptable yield (Scheme 72).

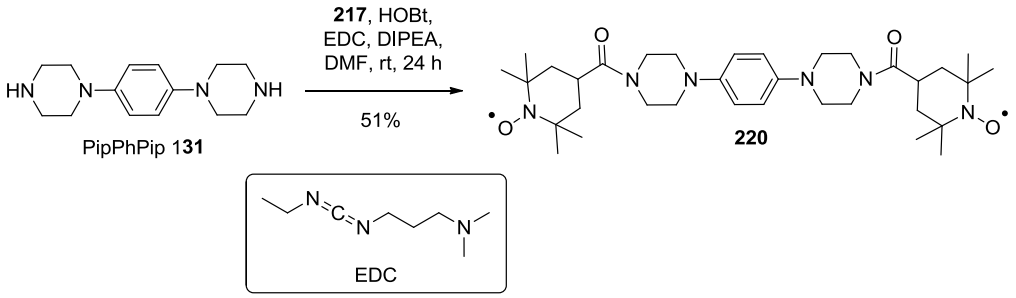

Scheme 72: Synthesis of the bis-TEMPO platform **220**

Orange crystals of bis-TEMPO **220** were obtained by slow evaporation of a chloroform/methanol mixture. This compound crystallizes in the P-1 space group (triclinic system), with a slightly disordered benzene ring, and forms parallel sheets. The piperazine and piperidine rings all adopt the expected chair conformation, but compared to compound **130** (p. 97), the piperazine moieties are symmetrical to the benzene ring in the solid state (Figure 91). The distance between the middle of the two N-O bonds is 19.8 Å.

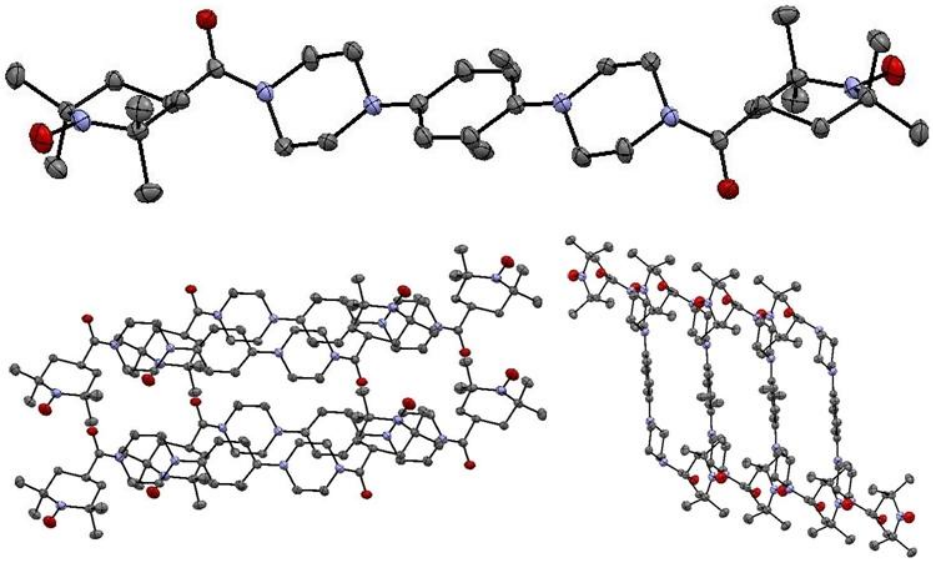

Figure 91: ORTEP drawings of bis-TEMPO **220**. Hydrogen atoms have been omitted for clarity. Top: view of the asymmetric unit, bottom: two different views of the packing

DFT calculations (HF/STO-3G) revealed a NO-NO midpoint distance of 21.7 Å for this platform. The distance obtained this way is quite different from the 19.8 Å from X-ray crystallography. This can be rationalized by a different arrangement of the piperazine and piperidine rings that leads to a more constrained structure in the solid state, as shown in Figure 92.

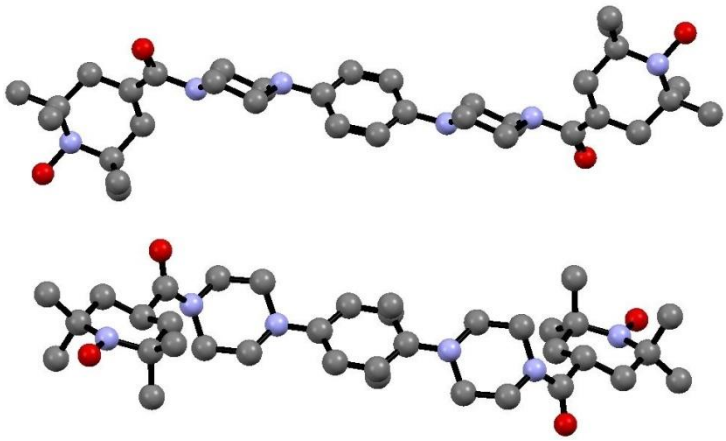

Figure 92: Ball and stick drawings of bis-TEMPO **220**. Top: DFT structure of the corresponding bis-hydroxylamine, bottom: X-ray structure

3.2 Platforms with an OPE linker

The synthesis of the bis-TEMPO analogues of bis-(Tpy)Mn^{II}(PhTpy)-CC_2Ph$(OPEG)_2$ **174** and bis-(Tpy)Mn^{II}(PhTpy)-Ph$(OPEG)_2$ **176** was also attempted. Starting from 4-oxo-TEMPO **215**, the corresponding triflate 4-OTf-TEMPO **221** was generated in moderate yield using LDA followed by $PhNTf_2$. The Sonogashira coupling between 4-OTf-TEMPO **221** and OPE-diCCH **164** was tried, but an inseparable mixture was obtained (Scheme 73).

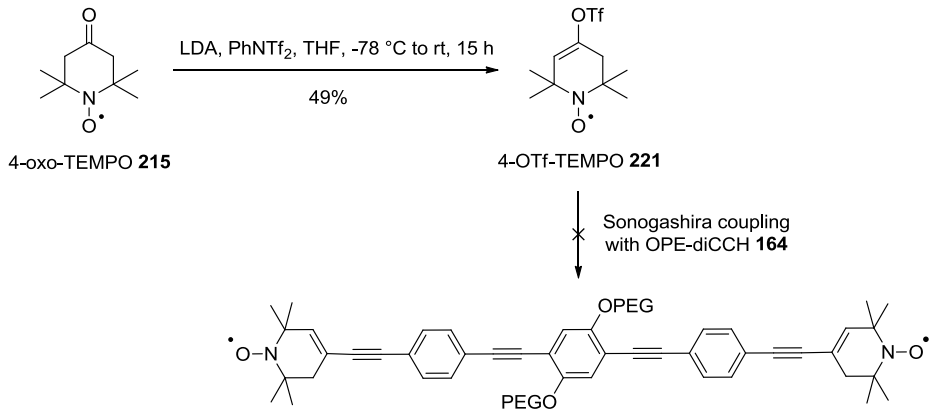

Scheme 73: Attempted Sonogashira coupling between OPE-diCCH **164** and 4-OTf-TEMPO **221**

To form the bis-nitroxide analogue of Mn^{II}-bis-PyMTA-OPE **185** (p. 124), 4-OH-TEMPO **216** was mesylated to afford 4-OMs-TEMPO **222** in excellent yield without further purification. Reaction with sodium azide cleanly gave orange needles of the corresponding azide 4-N_3-TEMPO **223** in good yield, again with no need for purification (Scheme 74).[214] 4-N_3-TEMPO **223** and OPE-diCCH **164** were clicked in the presence of CuI to give the corresponding bis-triazole **224** in low yield. The use of a Cu^{I} salt instead of the more common Cu^{II}/ascorbate conditions is compulsory, because the nitroxide moiety would be reduced into hydroxylamine during the course of the reaction by the ascorbate.

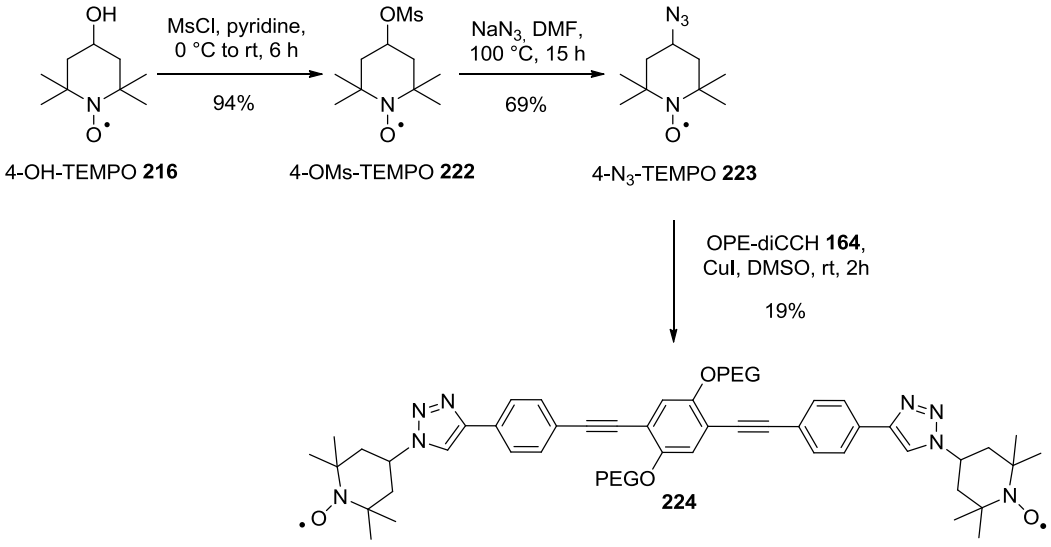

Scheme 74: Synthesis of the bis-TEMPO platform **224**

DFT calculations (UB3LYP/6-31G*) were been performed for the bis-TEMPO platform **224**, but with an -OMe group instead of the PEG chains to reduce calculation time. The distance between the middle of the two N-O bonds is 32.3 Å, in a structure where all aromatic rings are nearly coplanar and in the same plane as the N-O bonds (Figure 93).

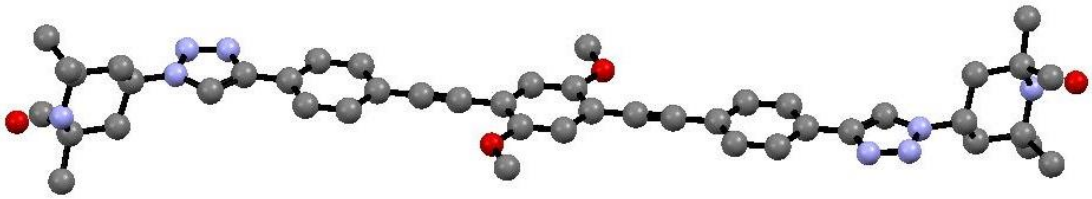

Figure 93: DFT structure of a simplified model of the bis-hydroxylamine corresponding to bis-TEMPO **224**. Hydrogen atoms have been omitted for clarity

The J-band *cw*-HFEPR spectrum of the bis-TEMPO **224** was recorded (Figure 94). It shows globally a pattern similar to the other bis-TEMPO platforms.

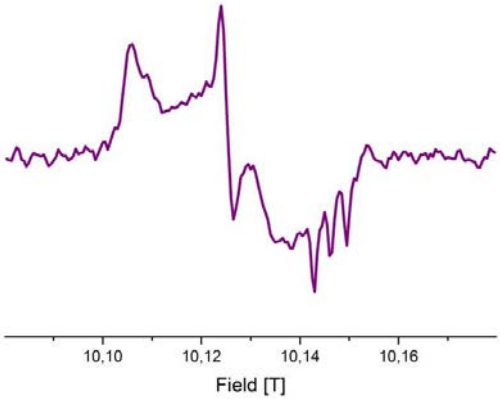

Figure 94: J-band *cw*-HFEPR spectrum of bis-TEMPO **224** (1 mM in 9:1 MeOH/toluene, 20 K)

Finally, the analogue of the Mn^{II} complex of bis-DOTA-OPE_1 **202** (p. 130) was generated using an amide bond formation between 4-NH_2-TEMPO **218** and OPE-diCO_2H **165** in the presence of DCC and HOBt to afford bis-TEMPO-OPE **225** in excellent yield. The use of different linkages between a TEMPO moiety and the OPE spacer can affect the conformational freedom of the TEMPO, which is useful to probe orientation selection phenomena. For that purpose, bis-TEMPO **226** was synthesized using a Steglich esterification with DCC and DMAP[215] between 4-OH-TEMPO **216** and OPE-diCO_2H **165**. The use of the water-soluble EDC, known to ease the purification step, lowered the yield to 10% (Scheme 75).

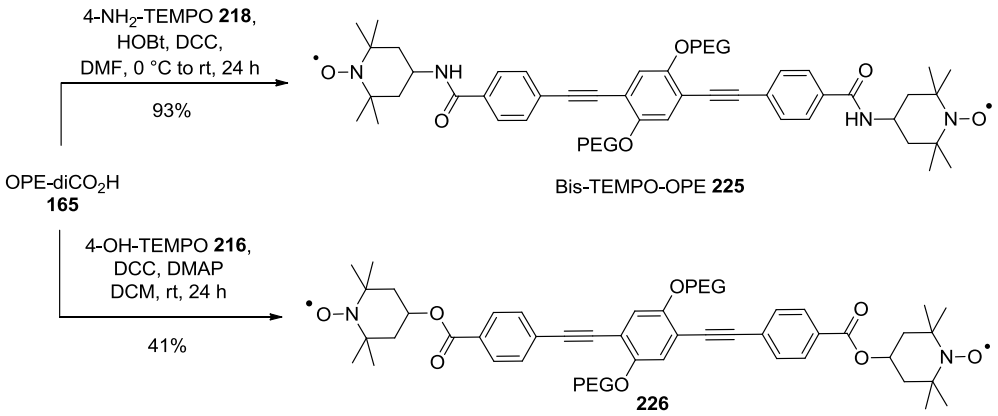

Scheme 75: Synthesis of bis-TEMPO platforms **225** and **226**

Orange prisms of bis-TEMPO **225** suitable for X-ray diffraction were grown by slow evaporation of a toluene solution of the biradical. This compound crystallizes in the $P2_1/m$ space group (monoclinic system), with one disordered cocrystallized toluene molecule. The three aromatic rings are twisted by 39° from each other, while the two piperidine rings adopt the expected chair conformation. The distance between the middle of the two N-O bonds (point-dipole approximation) is 30.2 Å. The packing shows that the molecules adopt a parallel arrangement, with four biradicals pointing in a direction intercalated with two other ones pointing 47° out (Figure 95).

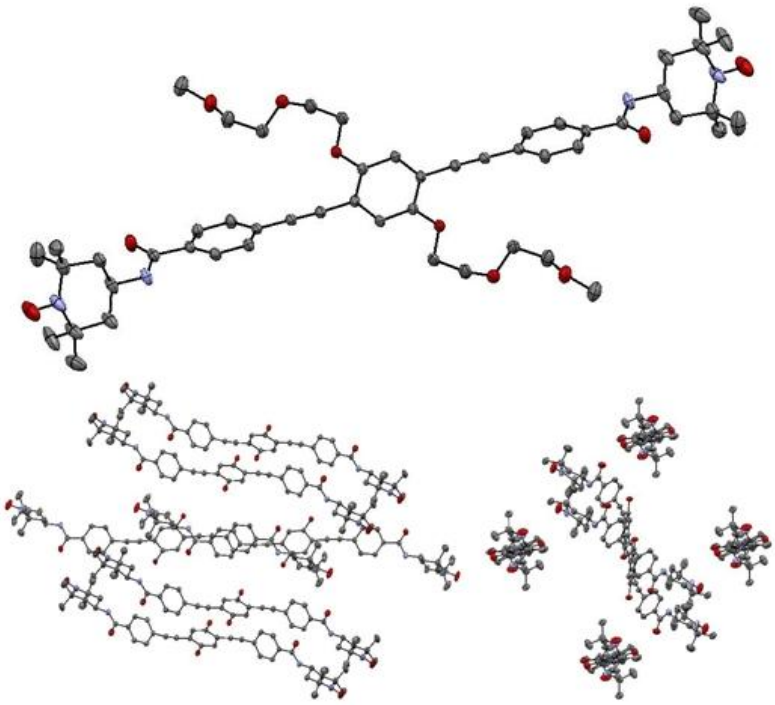

Figure 95: ORTEP drawings of bis-TEMPO **225**. Hydrogen atoms and cocrystallized solvent have been omitted for clarity. Top: view of the asymmetric unit, bottom: two different views of the packing with PEG chains omitted for clarity

DFT calculations (UB3LYP/6-31G*) were performed for bis-TEMPO **225**, without PEG chains to reduce calculation time. The difference between the X-ray structure is striking: the C=O and N-C

bonds of the amide group are in *cis* conformation in the solid state, while the DFT predicts a *trans* conformation, leading to a NO-NO midpoint distance of 25.1 Å, more than 0.5 nm less than the X-ray distance. The benzene rings are also found to be coplanar in the DFT structure, and no bending of the OPE linker is observed. This illustrates the difference of behavior between the solid state and a calculation performed in the gas phase (Figure 97).

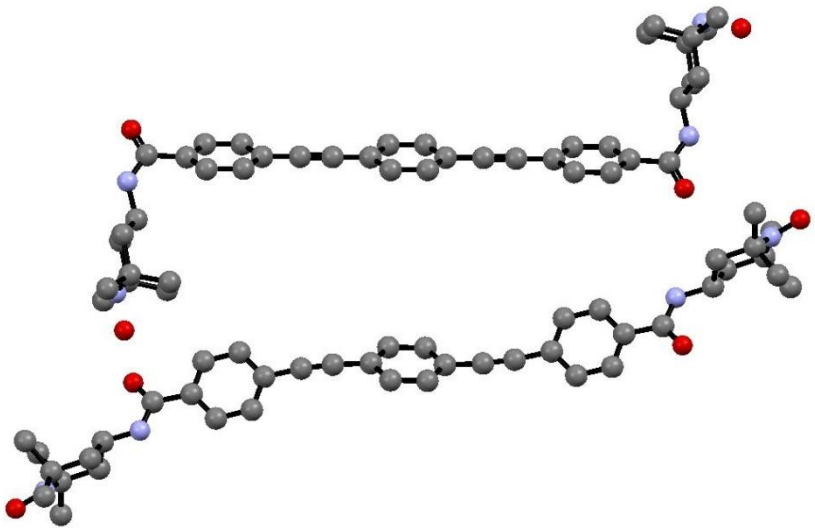

Figure 96: Ball and stick drawings of bis-TEMPO **225**. Top: DFT structure of a simplified model of the corresponding bis-hydroxylamine, bottom: X-ray structure. Hydrogen atoms and PEG chains have been omitted for clarity.

The J-band *cw*-HFEPR spectrum of the bis-TEMPO **225** was also recorded (Figure 97). A MeOH/toluene mixture, known to make a good glass, was chosen for solubility reasons. It is comparable to bis-TEMPO **219**, even if the resolution of the A_x component is quite different.

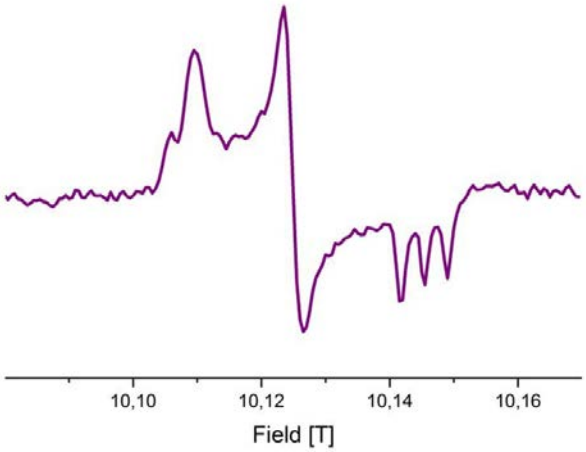

Figure 97: J-band *cw*-HFEPR spectrum of bis-TEMPO **225** (200 µM in 9:1 MeOH/toluene at 20 K)

DFT calculations (UB3LYP/6-31G*) were also performed for bis-TEMPO platform **226**, but with an -OMe group instead of the PEG chains to reduce calculation time. The *cis* arrangement of the TEMPO groups relative to the linker is here again surprising: the predicted NO-NO midpoint distance

of 22.9 Å is expected to be clearly underestimated by comparison to what it would be in solution (Figure 98). MD calculations would be more adequate for this kind of situation.

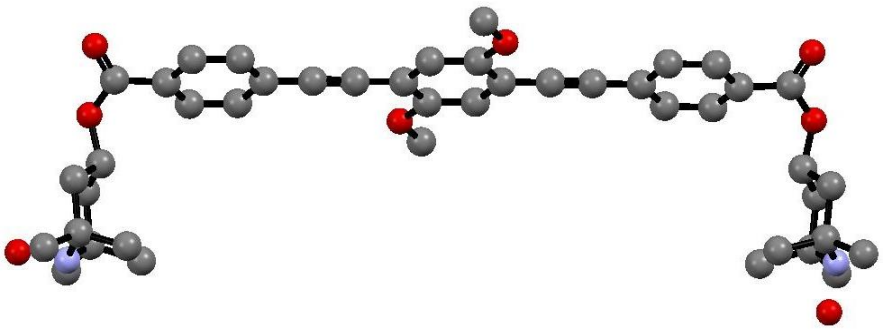

Figure 98: DFT structure of a simplified model of the bis-hydroxylamine corresponding to bis-TEMPO **226**. Hydrogen atoms have been omitted for clarity

The J-band *cw*-HFEPR spectrum of the bis-TEMPO **226** was recorded (Figure 99). This spectrum is very similar to the spectrum of bis-TEMPO **219**, suggesting that no exchange coupling takes place.

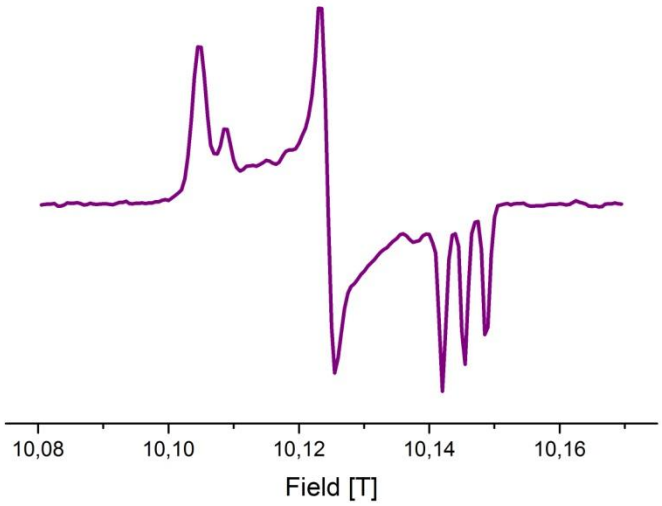

Figure 99: J-band *cw*-HFEPR spectrum of bis-TEMPO **226** (200 µM in 9:1 MeOH/toluene at 20 K)

To conclude, five bis-TEMPO platforms have been synthesized to serve as a useful comparison point with the corresponding bis-Mn^{II} complex systems. It will be also interesting to compare the results obtained from PELDOR distance measurements (which reflects a behavior in frozen solution) to the distance obtained from X-ray crystallography (*i.e.* in the solid state) and from DFT calculations (in the gas phase). The distance distributions could also be compared and discussed using MD simulations.

4. DISSYMMETRIC PLATFORMS

Having synthesized several platforms incorporating two identical Mn^{II} complexes, we decided to move towards modules containing two different paramagnetic centers. These centers can be two different Mn^{II} complexes, or one Mn^{II} center coupled to a TEMPO radical.

4.1 With the phenyl-piperazine linker

Being aware of the poor reactivity of phenyl-piperazine linkers, we extended the reflux time to 5 days to perform the Hartwig-Buchwald coupling with *p*BrPhTpy **36** and BocPipPhPip **137** to afford compound **227** in high yield. Deprotection of the amine group with TFA gave terpyridine **228**. Amide bond formation between BocPipPhPip **137** and 4-CO_2H-TEMPO **217** gave the expected nitroxide **229** (Scheme 76).

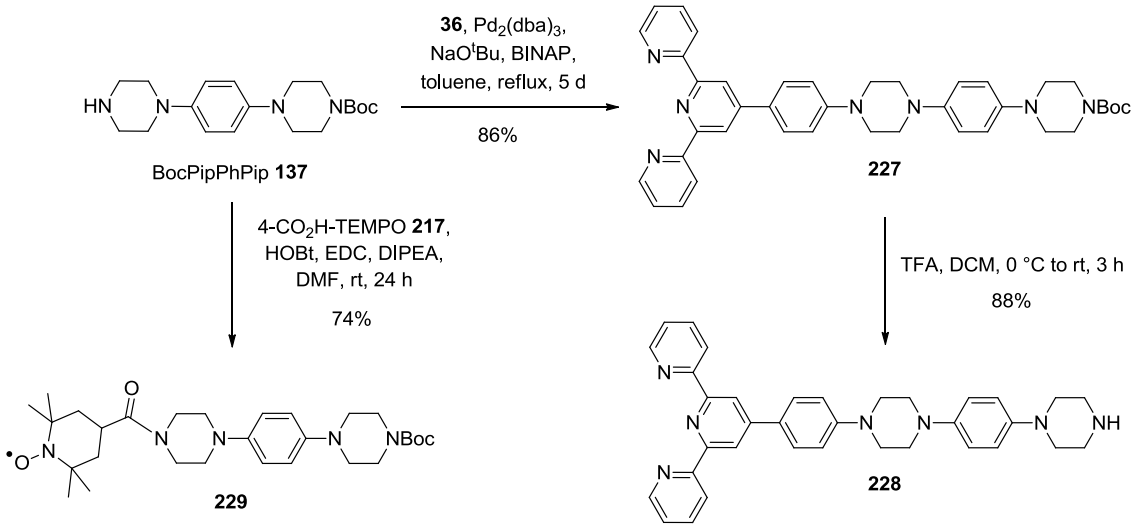

Scheme 76: Synthesis of terpyridine **228** and nitroxide **229**

Terpyridine **228** was reacted with tri-^{t}Bu-DOTA **146** using HATU to afford the protected DOTA-Tpy platform **230**. Preliminary calculations with Spartan on this module have led to a distance of 22.5 Å between Mn and the four nitrogens of the DOTA ring. An amide bond formation between terpyridine **228** and 4-CO_2H-TEMPO **217** was also readily performed with HOBt and EDC to give the Tpy-TEMPO ligand **231** (Scheme 77).

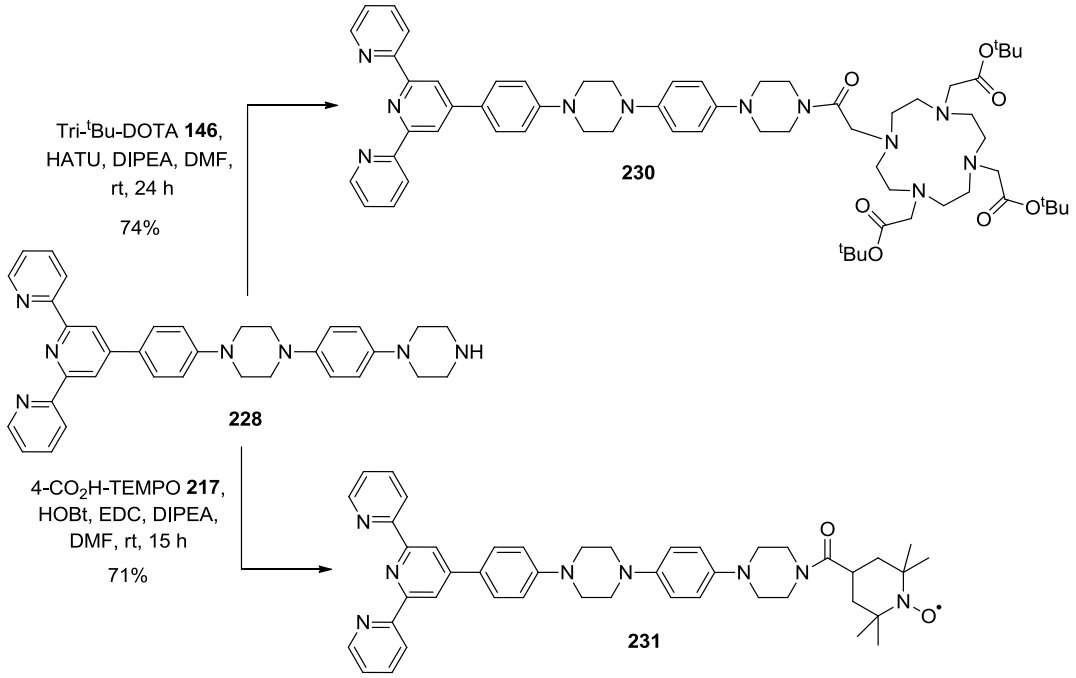

Scheme 77: Synthesis of dissymmetric platforms **230** and **231**

Using the same strategy, the reaction between BocPipPhPip **137** and tri-^{t}Bu-DOTA **146** led to the formation of intermediate **232** in good yield. The ^{t}Bu and the Boc groups were then simultaneously removed with TFA to give compound **233**, and the amide bond formation with 4-CO_2H-TEMPO **217** yielded the DOTA-PipPhPip-TEMPO module **234** after HPLC purification (Scheme 78). The mean distance between the middle of the N-O bond and the four nitrogens of the DOTA ring on module **234** was estimated to be 17.6 Å with Spartan.

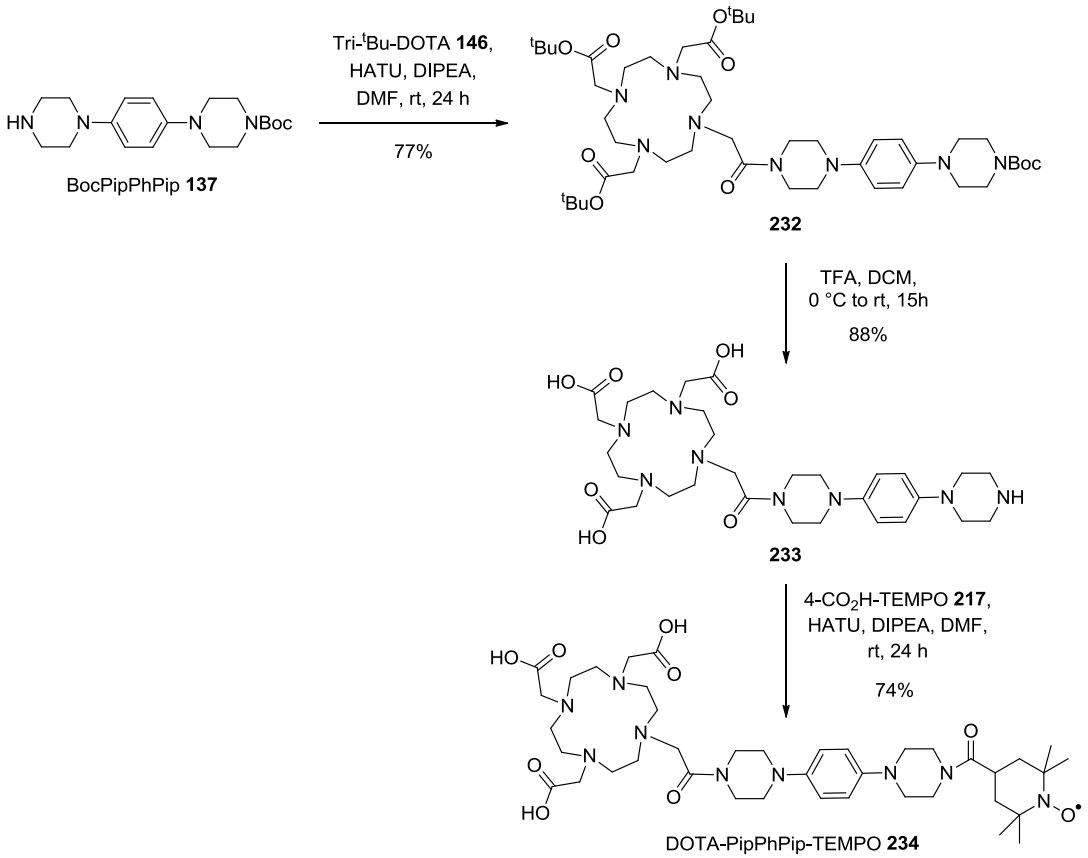

Scheme 78: Synthesis of the DOTA-PipPhPip-TEMPO module **234**

4.2 With the OPE linker

The synthesis of asymmetric OPE linkers with one DOTA at one end was also undertaken. The mono-Boc-protected OPE linker **169** reacted with bromoacetyl bromide to give intermediate **235** in good yield. Reaction with tri-Pp-DO3A **198** afforded the protected DOTA compound **236**, also in good yield (Scheme 79). Deprotection and couplings with a nitroxide for instance are underway.

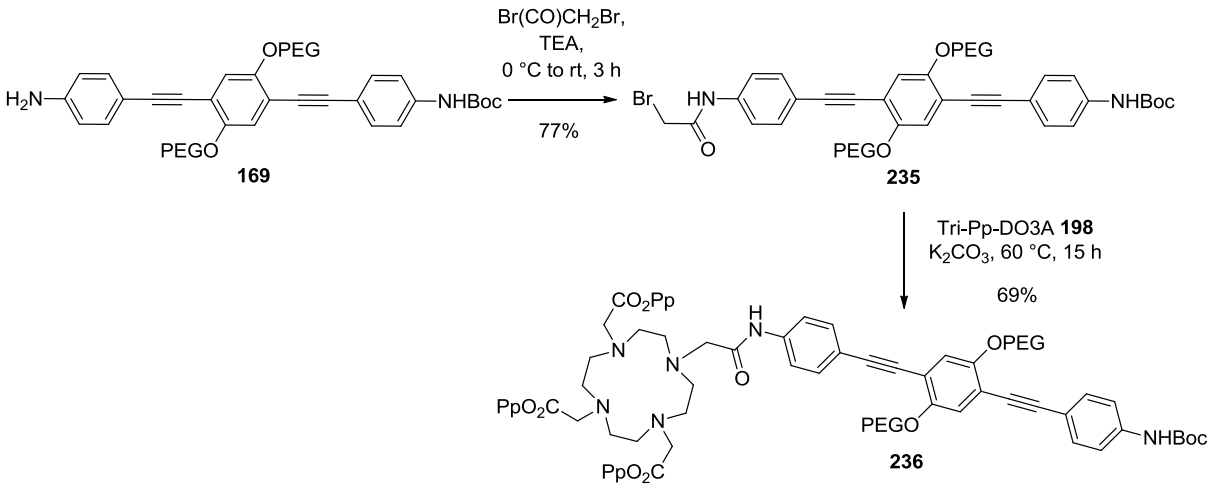

Scheme 79: Synthesis of the mono-DOTA platform **236**

CONCLUSION

To conclude, Mn^{II} complexes that possess a high-field EPR spectrum displaying a narrow central transition have been synthesized. Among them, Mn^{II}-DOTA appeared promising as its peak-to-trough linewidth is comparable to that of $Mn(H_2O)_6^{2+}$. Synthetic methodologies were developed to build various kinds of symmetric and dissymmetric linkers with an end-to-end distance of a few nanometers. Ligands were then grafted on these spacers to obtain platforms with a constrained distance between two high-spin Mn^{II} centers. PELDOR measurements on these platforms will be detailed in the next chapter.

Chapter II – PELDOR distance measurements between two high-spin Mn^{II} centers

In Chapter I, we synthesized a set of platforms incorporating a central rigid rod connected to two ligands for Mn^{II}. Some of these platforms were selected for Mn^{II}-Mn^{II} PELDOR distance measurements as their central transition displayed a narrow hyperfine sextet, as shown by J-band (285 GHz) *cw*-HFEPR. Here, we will present PELDOR experiments on nine modules: the bis-(Tpy)Mn^{II}(PhTpy)-Ph$(OPEG)_2$ **176**, the Mn^{II} complexes of the bis-DOTA-polyprolines platforms $DOTA_2P_n$ (**209**, **210** and **211**, with n = 6, 9 and 12, respectively), and the Mn^{II} complexes of the rigid platforms bis-DOTA-$PhPip_n$ (**149** and **150**, with n = 1 and 2, respectively) and bis-DOTA-OPE_n (**202**, **203** and **204**, with n = 1, 2 or 3, respectively) (see Figure 87, p. 135).

In a first part, G-band (180 GHz) PELDOR measurements on the bis(Mn^{II}-bis(Tpy)) complex **176** will be presented. No PELDOR oscillations could be detected, and several hypotheses will be proposed to explain this observation. These preliminary measurements showed that high-field PELDOR measurements between two high-spin Mn^{II} complexes are far from being trivial. Experiments on this complex were not further investigated because in the meantime, bis-DOTA platforms became available and appeared more promising, as their Mn^{II} complexes are water-soluble and display narrower EPR lines.

In a second part, we will present the PELDOR measurements we performed on the Mn^{II} complexes of $DOTA_2P_n$ **209**, **210** and **211** at W-band (95 GHz). After the determination of the ZFS parameters of Mn^{II}-DOTA, we will discuss the optimal parameters that led to the accurate determination of Mn^{II}-Mn^{II} distances in the 2.8 - 4.5 nm range. We will also compare the distance distribution profiles obtained with Tikhonov regularization with the results from molecular dynamics. For certain combinations of pump and detect frequencies, additional features appear in the frequency-domain spectra, which translate into shorter components in the distance distributions. These results will be rationalized using spin-Hamiltonian calculations, and we will show that they likely arise from contributions of the pseudo-secular term of the dipolar Hamiltonian. This interaction is significant when the pumped and detected spins are similar, and a large distribution of the ZFS parameters was found to be crucial for the experiment. As the $DOTA_2P_n$ modules are quite flexible, these pseudo-secular effects were found to be noticeable but weak, so the shape of the distance distributions could be safely interpreted.

In a third part, experiments performed on the Mn^{II} complexes of the phenyl-piperazine- and OPE-based bis-DOTA rigid platforms will be described. We will show that manifestations of the pseudo-secular term are much more visible on these systems, because they are both shorter and more rigid. For the bis-DOTA-$PhPip_n$ modules **149** and **150**, the PELDOR data could not be reliably processed using conventional implementation of the Tikhonov regularization. This is most probably because of a large pseudo-secular interaction at this short distance range. However interestingly, preliminary MD calculations were in agreement with the most probable distance obtained from the ill-fitting analysis. On the other hand, the bis-DOTA-OPE_n modules with n = 2 and 3 (**203** and **204**,

respectively) also proved difficult to be studied, possibly due to aggregative behavior. However, PELDOR data which could be processed in the conventional manner was obtained for the Mn^{II} complex of bis-DOTA-OPE_1 **202** showing that accurate distance measurements are possible for distances starting from 2.6 nm. Nevertheless, the distance distribution was found to be broader than expected if one consider the stiffness of the OPE linkers as indicated by the preliminary MD calculations. This suggested that for these rigid systems, the consequence of neglecting the pseudo-secular interaction during data analysis leads to the broadening of the distance distribution. Furthermore, the Mn-Mn distance obtained from MD calculations was also longer than the PELDOR value. This discrepancy was assigned to the possibility of an octacoordinated Mn^{II}-DOTA in solution. To confirm this hypothesis, the Gd^{III} complex of the bis-DOTA-OPE_1 platform **202** was investigated, and the same metal-metal distance was obtained. The pseudo-secular-induced broadening was found to be much higher this Gd^{III}-Gd^{III} system. To compare high-spin metal complexes with the more commonly used nitroxide labels, the bis-TEMPO-OPE platform **225** was studied, and orientation selection was found at W-band, as expected. This work shows the complementarities of Mn^{II}, Gd^{III} and nitroxide tags for PELDOR distance measurements.

1. GENERAL SAMPLE PREPARATION FOR PELDOR MEASUREMENTS

PELDOR measurements described in this part have been performed at CEA on a commercial pulsed EPR Bruker Elexsys II 680 EPR spectrometer operating at W-band (95 GHz), or at Goethe-Universität on a home-built pulsed EPR spectrometer operating at G-band (180 GHz). For the bis(Mn^{II}-bis(Tpy)) complex **176**, the concentration was 200 µM in 2-Me-THF with 50 eq of NaBARF. For the bis-DOTA polyprolines $DOTA_2P_n$ **209**, **210** and **211**, the concentration was 250 µM in pH 8 100 mM HEPES buffer with 20% glycerol, and 200 mM NaCl was added to prevent aggregation of the peptides.[216,217] These conditions are typically employed for measurements on biomolecules: glycerol plays the role of a cryoprotectant and allows the formation of a good glass. The ligands were then metallated with 1.8 eq of $Mn(ClO_4)_2 \bullet 6H_2O$ to ensure that the majority of the DOTA sites are occupied and that no excess free Mn^{II} is observed, which may complicate the measurements. The corresponding Mn^{II} complexes are written $MnDOTA_2P_n$. For the rigid bis-DOTA platforms bis-DOTA-$PhPip_n$ **149** and **150** and bis-DOTA-OPE_n **202**, **203** and **204**, unless otherwise stated, the concentration was 100 µM in pH 8 100 mM HEPES buffer with 10% glycerol. The ligands were also metallated with 1.8 eq of $Mn(ClO_4)_2 \bullet 6H_2O$ to form the corresponding Mn^{II} complexes $MnDOTA_2PhPip_n$ and $MnDOTA_2OPE_n$. Bis-DOTA-OPE_1 was also metallated with 1.8 eq $GdCl_3$ to form $GdDOTA_2OPE_1$. The concentration of the bis-TEMPO-OPE platform **225** was 100 µM in 1:1 toluene/$CHCl_3$. The solutions containing the Mn^{II} complexes were loaded into quartz capillaries (inner diameter 0.5 mm, outer diameter 0.9 mm, length 4 mm). The capillaries were then mounted at the extremity of a stick, shock-frozen in liquid nitrogen and inserted into the spectrometer until they reach the cavity. Explanations concerning the standard procedure of a PELDOR measurement can be found in Annex 2 (p. 205). Explanations about the standard data analysis procedure using DeerAnalysis can be found in Annex 3 (p. 206).

2. MEASUREMENTS ON THE BIS-MN-TPY PLATFORMS 176

PELDOR experiments on bis(Mn^{II}-bis(Tpy)) platform **176** were performed at G-band in Goethe-Universität by Dmitry Akhmetzyanov. The T_2 value was equal to 0.8 µs. The ED-EPR spectrum is displayed in Figure 100, showing the expected 6-lines pattern without any free Mn^{II}. However, the three first lines are split, which seem to indicate that the A-tensor is anisotropic. Such a behavior would be observed for compounds with very high ZFS parameters, which is not the case here (D = -1800 MHz and E = 300 MHz for Mn^{II}-bis(Tpy) **58** in MeCN.[129] A more likely explanation is the presence of two different species in solution with slightly different ZFS parameters, as it has been shown above and in the literature[129] that Mn^{II}-bis(Tpy) complexes can partially decoordinate in solution.

A PELDOR experiment was performed, where the pump pulse was set on top of the 4th line and the detection pulse at the bottom of this line (60 MHz offset). As shown in Figure 100, no clear PELDOR oscillations could be detected. An explanation could be the large ZFS parameters of Mn^{II}-bis(Tpy) compounds, which led to quite broad lines, implying that not enough spins could be inverted. This low modulation depth can also arise from the relatively long pump pulse (32.5 ns). PELDOR modulations are thus maybe too shallow to be observed, and would be obscured by the strong intermolecular background decay. The presence of two species in solution, with two different signatures, could also reduce the modulation depth. However, the high frequency (180 GHz) should compensate for this and additional optimization could certainly lead to discernible modulations, as this is only a first trial. Moreover, $Mn(Tpy)_2^{2+}$-nitroxide measurements[89] were successful and discernible oscillations could be observed on a protein tagged with two Mn^{II}-EDTA tags,[22] which have a very large D-value of 3000 MHz. A second explanation could be the decomposition of the platform to form $Mn(Tpy)_2^{2+}$, which would give a very similar spectrum, and insoluble polymeric species. As the Mn-Mn distance is expected to be quite short (approximately 2.7 nm) and because of the 60 MHz offset, the pseudo-secular part of the dipolar Hamiltonian could also smear out the oscillations. This pseudo-secular contribution will be developed below. Hardware issues due to the complexity of the spectrometer could also have an influence.

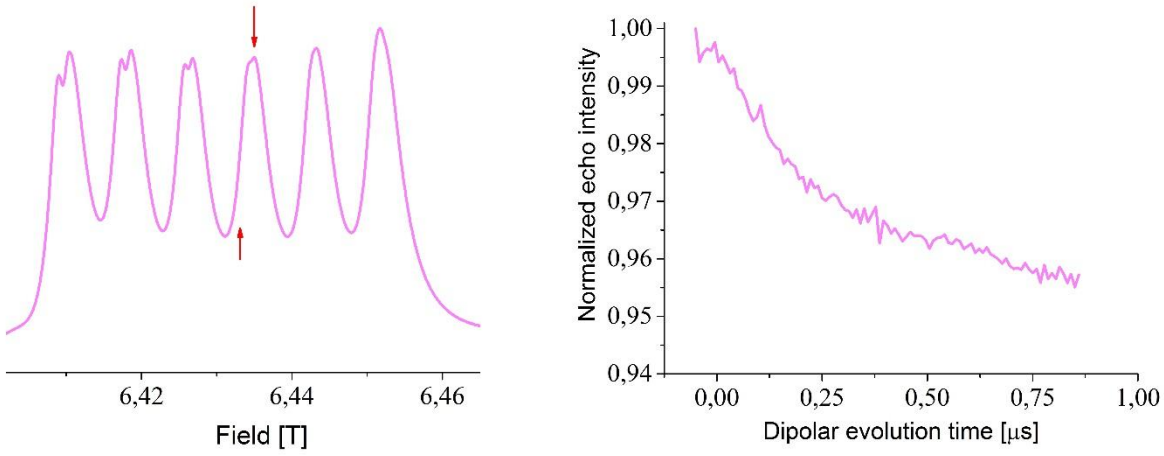

Figure 100: Left: ED-EPR spectrum of platform **176**. Red arrows indicate the pump-detect strategy. Right: Corresponding PELDOR time trace. Conditions: 10 K, 200 µM in 2-Me-THF with 50 eq NaBARF, pump π pulse

32.5 ns, detection π/2 and π pulses 22.5 and 42.5 ns pump 32.5, 1.5 µs dipolar evolution window, 500 shots per point (SPP), 1.1 ms shot repetition time (SRT), 110 scans

Even if the use of this bis-Tpy module was not successful for PELDOR purposes, we can envision other applications such as supramolecular architectures with other metals.[110] These preliminary results show that these unprecedented Mn^{II}-bis(Tpy) – Mn^{II}-bis(Tpy) PELDOR experiments are very difficult, and suggested that two parameters must be optimized: firstly, the solubility or stability of the platform, and secondly lowering the *D*-value which should give better sensitivity. From our results on Chapter I (p. 106 and p. 132), bis-DOTA platforms should comply with these requirements.

3. MEASUREMENTS ON THE POLYPROLINE BIS-DOTA PLATFORMS

3.1 Measurement of the ZFS interaction of Mn-DOTA

As we had first in hands the $DOTA_2P_n$ platforms **209**, **210** and **211**, which displayed satisfactory water solubility, PELDOR measurements were first explored on these systems. The W-band ED-EPR spectrum of $MnDOTA_2P_6$ and the J-band *cw*-HFEPR spectrum of $MnDOTA_2P_{12}$ are depicted in Figure 101.

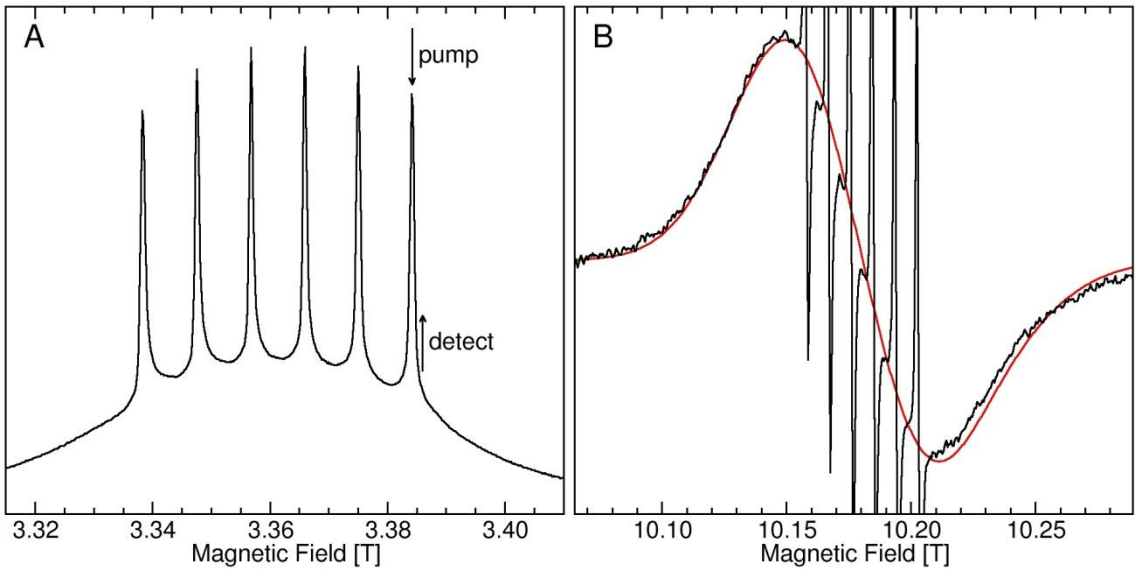

Figure 101: A) W-band ED-EPR spectrum of $MnDOTA_2P_6$ (250 µM, 10 K). B) J-band *cw*-HFEPR spectrum of $MnDOTA_2P_{12}$ (250 µM, 4.2 K) with its simulation (red) that does not include the central transition resonances. The arrows correspond to the pump-detect strategy used in the PELDOR measurements (see below)

The ED-EPR spectrum of $MnDOTA_2P_6$ displays the expected narrow sextet superposed on a broad component. The *g*-value (g = 2.00122) and the hyperfine constant ($|A|$ = 252 MHz) are identical to what was found in Chapter I (p. 82) on Mn^{II}-DOTA using the J-band cw-HFEPR at 23 K. The absence of *g*-anisotropy is confirmed by the invariant linewidth at W- and J-band (average peak-to-trough linewidth of 6.7 ± 0.7 G and 6.4 ± 0.6 G, respectively). The EPR spectra of $MnDOTA_2P_n$ with n = 6, 9 and 12 were identical to each other and to Mn^{II}-DOTA. This confirms that the introduction of an

amide bond in the bis-DOTA-PhPip$_n$ modules compared to a carboxylic acid function in DOTA does not affect the narrowness of the lines, meaning that the influence on the coordination sphere is negligible. The ZFS parameters were determined by fitting the J-band *cw*-HFEPR spectrum, assuming isotropic *g*- and hyperfine interactions and a Gaussian distribution. This led to a *D*-value of 280 MHz and a negligible *E*-value, with Gaussian distributions of 150 MHz for both. The ZFS tensor can thus be considered as axial (p. 11).

3.2 PELDOR results

PELDOR measurements on the MnDOTA$_2$P$_n$ platforms are depicted in Figure 102, as well as the DeerAnalysis results. Parameters and numerical results are displayed in Table 2.

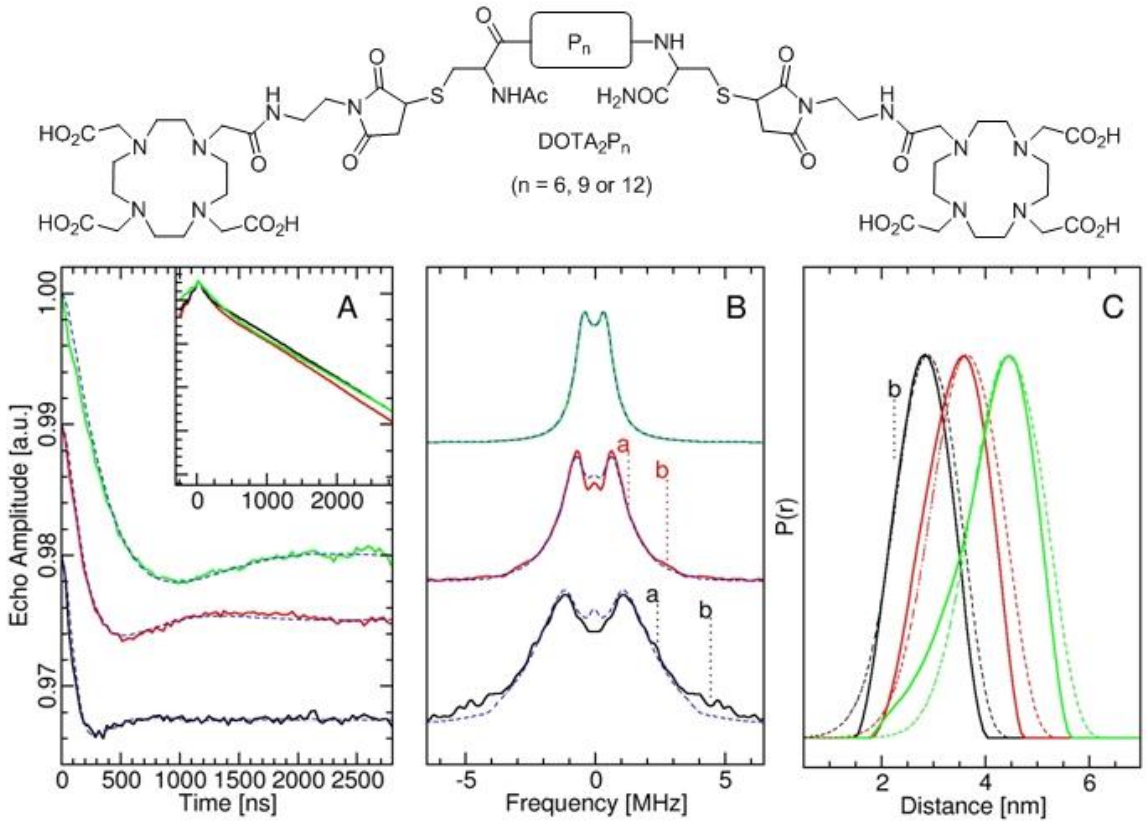

Figure 102: Top: Structure of the DOTA$_2$P$_n$ platforms. Bottom: PELDOR measurements on MnDOTA$_2$P$_n$ platforms (n = 6, black, n = 9, red, n = 12, green) and DeerAnalysis results. A) Experimental PELDOR time traces after background correction (solid lines) and their Tikhonov fits (blue dashed lines) with the inset showing raw data. The traces were arbitrarily shifted. B) Experimental frequency-domain spectra (solid lines) and their Tikhonov fits (blue dashed lines). C) Distance distributions obtained by Tikhonov analysis (solid lines) and from MD/mtsslWizard simulations (dashed lines, see main text for discussion). The description of the dotted markers is discussed in the main text

Table 2: Parameters and numerical results from the PELDOR experiments of Figure 120.

$MnDOTA_2P_n$	n = 6	n = 9	n = 12
Pump pulse (ns)	14	14	14
Detection pulses (ns)	18/36	18/36	18/36
Offset (MHz)	50	50	50
SRT (µs)	440	440	440
Distance (nm)	2.8	3.6	4.5
Half-height distribution	1.3	1.5	1.6

The pump position was set on top of the 6th hyperfine line, and an offset of 50 MHz was used, corresponding to a detection on the high-field side of the 6th hyperfine line (Figure 101). The first PELDOR oscillation can easily be seen in each time trace. The backgrounds are comparable to each other (see inset in Figure 102) and could be adequately modeled using a linear function. An exponential function, which corresponds to the theoretical case, is usually employed, but here the background appears nearly linear due to the low modulations depth.

The simulation of the time- and frequency domains using Tikhonov analysis as implemented in DeerAnalysis are excellent and even if the modulation depths are low (λ = 1.2 to 2%), they are nevertheless about three times higher than the literature,[22] where a Mn^{II}-EDTA (*D*-value of about 3000 MHz) ligand was used. This indicates that spin-labels with small *D*-values effectively lead to an increase in sensitivity, confirming our working hypothesis (p. 56). The much higher symmetry of the coordination sphere of Mn^{II}-DOTA compared to Mn^{II}-EDTA appears to be the main reason for this higher modulation depth. The frequency domains, obtained by Fourier transform, resemble Pake patterns with poorly resolved shoulders at twice the frequency of the “horns” (marked by dotted lines labeled a). The splittings corresponding to the dipolar couplings (frequency range between the center and the “horns” of the Pake patterns) are 1.10, 0.64 and 0.33 MHz for $MnDOTA_2P_6$, $MnDOTA_2P_9$, and $MnDOTA_2P_{12}$, respectively. Tikhonov regularization gave Mn^{II}-Mn^{II} distances of 2.8, 3.6 and 4.5 nm as the number of Pro residues increases (Table 2).

As a control experiment, measurements were performed in the same conditions on Mn^{II}-DOTA. As expected, no modulations could be observed for Mn^{II}-DOTA (Figure 103).

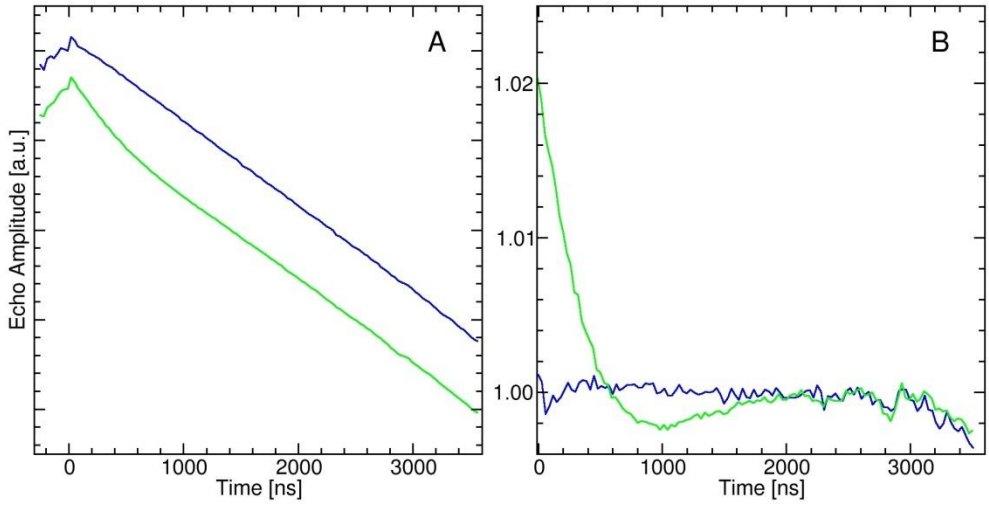

Figure 103: PELDOR measurements on $MnDOTA_2P_{12}$ (green) and Mn-DOTA (blue). A) Raw experimental PELDOR time traces. B) Background-corrected PELDOR time traces. The traces were arbitrarily shifted

We next explored the influence of the offset, and it was shown that the results were not significantly affected by this parameter, as the discrepancy in the most probable extracted distance between two experiments performed at +50 or +150 MHz offset was 0.1 nm (Figure 104 and Table 3). This indicates that the difference in the spectral overlap (which also induces a loss of echo amplitude of 25% with a +50 MHz offset) only plays a minor role.

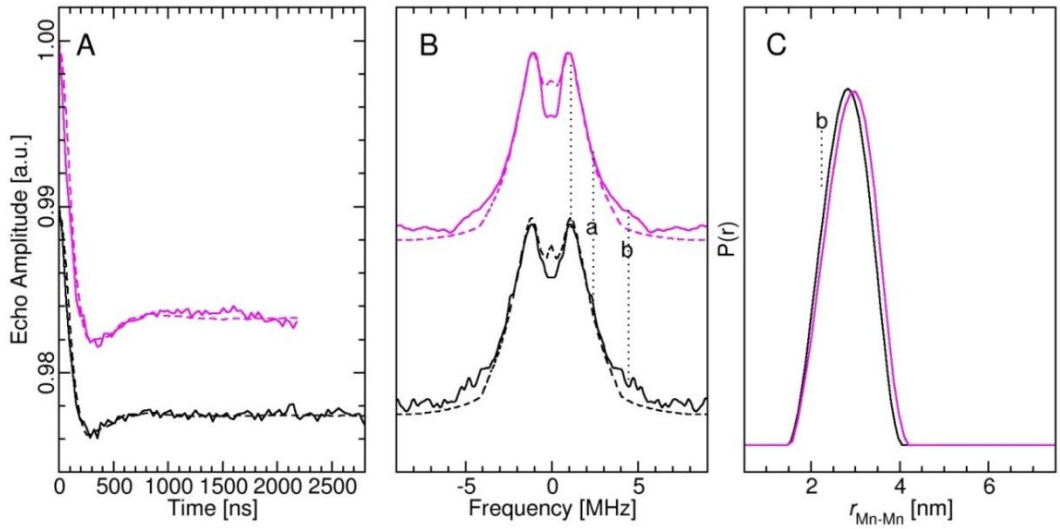

Figure 104: PELDOR measurements of $MnDOTA_2P_6$ with offsets of 50 MHz (black) and 150 MHz (magenta) and DeerAnalysis results. A) Experimental PELDOR time traces after background subtraction (solid lines) and their Tikhonov fits (dashed lines), with arbitrarily shifted traces. B) Experimental frequency-domain spectra (solid lines) and their Tikhonov fits (dashed lines). C) Distance distributions obtained by Tikhonov analysis. The description of the dotted markers is discussed below. For the 150 MHz pump/detect frequency offset experiment, a 30 ns pump pulse, and 22 and 40 ns π/2 and π detection pulses were used

Table 3: Parameters and numerical results from the PELDOR experiments of Figure 104.

Offset (MHz)	50	150
Pump pulse (ns)	14	30
Detection pulses (ns)	18/36	22/40
SRT (us)	440	440
Distance (nm)	2.8	2.9
Half-height distribution	1.3	1.3

As it can be seen from Table 2, the PELDOR-determined length increase per proline residue on the $MnDOTA_2P_n$ systems is approximately 0.3 nm, in good agreement with the crystallographic study of the Wennemers group.[208] Along with the CD results (Figure 86, p. 134), this confirms that the PPII structure is predominant. To determine whether the distance distributions displayed in Figure 120 are realistic pictures, MD calculations in conjunction with mtsslWizard[218,219] (see experimental part for details) were performed to calculate the Mn^{II}-Mn^{II} distance distribution profiles of $MnDOTA_2P_n$ (Figures 102 and 105).

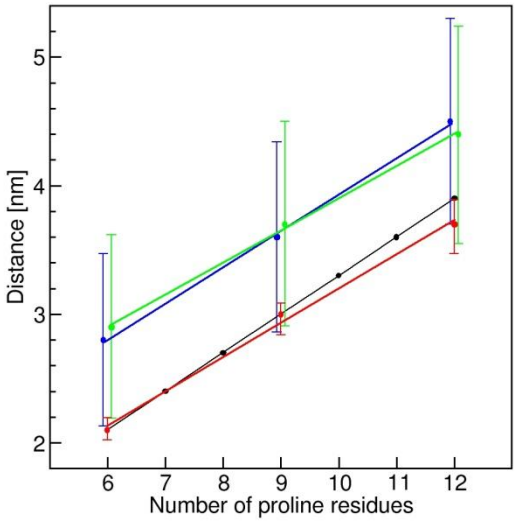

Figure 105: Mn-Mn distances and distributions profiles of $MnDOTA_2P_n$ determined from Tikhonov analysis of the PELDOR measurements (blue) compared to MD/mtsslWizard simulations (green). Also shown are C^{α}_{Cys}-C^{α}_{Cys} distances of unlabeled polyprolines from MD/mtsslWizard simulations (red), and crystallographic model (0.3 nm per residue, black). The lower and upper limits of the vertical bars denote the asymmetric half-widths of the distribution at half height

A first encouraging result, which indicates that MD/mtsslWizard simulations are adequate, is the good agreement between the crystallographic model (black) and the C_{α}^{Cys}-C_{α}^{Cys} distances of unlabeled polyprolines (red), which are also consistent with previously reported results.[209] Figure 105 also proves that the distance distribution profiles from PELDOR measurement (blue) are consistent with the MD/mtsslWizard simulations (green). The incorporation of the two DOTA labels adds 0.8 nm to the C_{α}^{Cys}-C_{α}^{Cys} distances and increases the distance distribution, reflecting the flexibility of the maleimide linker (see structure in Figure 102).

However, the C_α^{Cys}-C_α^{Cys} average distance of the $CP_{12}C$ PPII helix obtained by MD calculations was shorter than that predicted from X-ray crystallographic studies[208] (see red and black curves of Figure 105). This has been attributed to the increasing flexibility as the helices become longer.[85,209,210] This effect is well reflected by the Figure 102,C where in the 1 – 3 nm region, the width of the distance distribution for $MnDOTA_2P_{12}$ is larger than the PELDOR-determined one, whereas the opposite occurs for $MnDOTA_2P_6$. A reason could be the overestimation of the rigidity of polymeric structures by MD simulations.[16,17]

As shown in Figure 102 and Table 2, the increasing broadness of the distance distribution with increasing Mn-Mn distance can be explained by the flexibility of the $MnDOTA_2P_n$ platforms, which comes from the intrinsic flexibility of the PPII backbone and mainly from the flexibility of the maleimide linker. However, this does not account for the additional features observed in the frequency-domain spectra (Figure 102, B, dotted lines labeled b). They appear as shoulders at approximately 4 MHz for $MnDOTA_2P_6$ and 2.5 MHz for $MnDOTA_2P_9$. This translates into shorter components in the distance distribution profiles (Figure 102, C, dotted lines labeled b).

A first hypothesis is the presence of one or more *cis* amide bonds in the PPII structure.[220,221,222,223] As shown by CD experiments (Figure 86, p. 134), polyproline helices never adopt a 100% PPII conformation in aqueous solution. However, the already mentioned report by the group of Jeschke dealing with Gd-nitroxide PELDOR measurements on polyprolines[85] indicated that not more than 2% of *cis*-amide bonds could arise in a very similar environment to the one we used. This value is too small to explain the amplitude of the additional features in the frequency-domain spectra. Another explanation could be the selective pumping or detection of a sub-population of spin pairs. To better understand the origin of these additional features, their field dependence was examined.

3.3 Analysis of the pseudo-secular contribution

The field dependence of the additional features on Figure 102 is depicted in Figure 106.

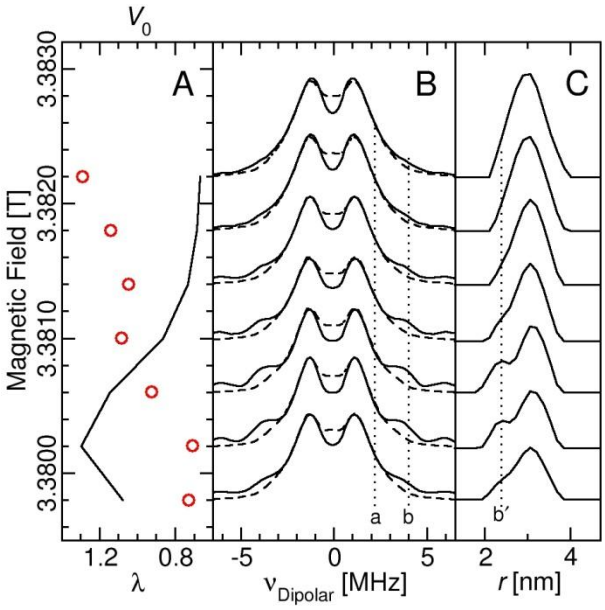

Figure 106: Field dependence of the PELDOR spectra of $MnDOTA_2P_6$. A) Integrated echo amplitude at t = 0 (black) and modulation depth (red circles) at each field point. B) Corresponding experimental frequency-domain spectra (solid lines) and their Tikhonov fits (dashed lines). C) Distance distributions obtained by Tikhonov analysis (solid lines). The description of the dotted markers is discussed below. The amplitudes of frequency-domain spectra have been arbitrarily scaled

In this experiment, the offset was kept constant at +50 MHz. The field point at 3.3822 T corresponds to the pump-detect strategy depicted in Figure 120, *i.e.* when the spins where pumped on top of the 6th hyperfine line. As expected, the largest λ value of 1.3% was observed at this position. The field point at 3.3802 T corresponds to the case where the spins where pumped between the 5th and the 6th line and the observation was resonant with the top of the 6th line, identical to the strategy depicted in Figure 102 but with the positions of the pump and the detection pulses reversed. At this position, the lowest modulation depth was observed, and the 4 MHz feature denoted by the dotted line b in Figure 106, B was the most noticeable in the frequency-domain spectrum. The Tikhonov regularization did not fully account for its amplitude, but a partially resolved 2.4 nm feature became prominent in the distance distribution (denoted by the dotted line b' in Figure 106, C).

The nature of these features can be rationalized by the interplay between the pseudo-secular term of the dipolar Hamiltonian and the ZFS interaction. We will only consider the case where the features were the most prominent in Figure 124, *i.e.* when the detection position was set on top of the 6th hyperfine line with an offset of 50 MHz, corresponding to a pump position about 18 G below, in between the 5th and the 6th lines (3.3802 T point on Figure 106). The specific ZFS interaction experienced by the pumped and detected spins is written D'_A and D'_B, respectively.

Briefly, one can say that the pump pulse is selective for a small number of specific D_A' values, *i.e.* 50 MHz. For Mn^{II} complexes with discrete well-defined ZFS parameters, the pump pulse would have selected molecules with a specific orientation with respect to $\mathbf{B_0}$, like what is observed in the case of orientation selection. However, the ZFS parameters are highly distributed for Mn^{II}-DOTA

(Gaussian distribution of 150 MHz, p. 152), so the size of the ZFS interaction experienced by a particular spin does not depend on the orientation: the pump pulse rather selects spins with a specific ZFS interaction. By contrast, no such selectivity can occur with the detection pulse, because it is set on top of the hyperfine line, where the central transition is mainly detected: this transition is only perturbed by the ZFS in the second order in $\mathbf{B_0}$ (p. 14). This means that all spins, irrespective of the size of their ZFS interactions, will be detected, even those at the extremes of the distributions.

As the *g*- and A-tensors of Mn^{II} complexes are isotropic, the energy difference between a specific pair of pumped and detected spins is largely determined by D_A' and D_B'. As mentioned is the theoretical part (p. 22), the pseudo-secular term of the dipolar Hamiltonian can be neglected if the weak coupling approximation is fulfilled, *i.e.* when the dipolar coupling ω_{dip} is small compared to the energy difference between of the pumped and detected spins. However, in our case, the energy difference can be small compared to ω_{dip}, implying that the pseudo-secular term must be taken into account. This means that for systems where the pumped and detected spins are very similar, as is the case with the bis-Mn^{II}-DOTA platforms, the pseudo-secular contribution of the dipolar Hamiltonian cannot be neglected. More quantitative results were obtained by solving the dipolar Hamiltonian of a Mn^{II} spin pair.[148]

To conclude, these calculations proved that the additional features in the frequency-domain spectra and in the Tikhonov regularization likely arise from the selection of specific ZFS values by the pump pulse. MD/mtsslWizard simulations showed that the $MnDOTA_2P_n$ are quite flexible, mainly due to the flexibility of the maleimide tether: this conformation averaging may mask the contribution of the pseudo-secular term, because the distance distributions are not significantly distorted (see Figure 120), meaning that they are reliable. However, the presence of these additional features indicates that the Tikhonov regularization should be performed with caution.

As this situation appears when the difference between the *g*- and hyperfine interactions of the pumped and detected spins is small, one option is to increase this difference to reduce the pseudo-secular effects. This can be done by careful tuning of the ligand, and we have shown in Chapter I that many Mn^{II} complexes with various ZFS interactions can be synthesized. As we also have in hands dissymmetric linkers, it would be very interesting to prove this hypothesis by building a platform with two different Mn^{II} complexes. Another option is to pump and detect adjacent central-transition hyperfine lines: this would suppress the pseudo-secular interaction because only the central transition would be pumped and detected, and this would also increase the sensitivity. However, the frequency difference between two hyperfine lines (252 MHz) is larger than the maximum value of the offset (200 MHz) available on most spectrometers. A dual-mode cavity[86] would be required to accommodate this large energy difference. These results are consistent with a recent article[34] where a series of bis-Gd^{III}-PyMTA (Figure 19, p. 34) platforms with varying Gd-Gd distances was studied. The role of the pseudo-secular term and a large distribution of the ZFS parameters were also found to be important.

In this part, we have shown that for systems where pumped and detected spins are very similar, as is the case with the Mn-bis-DOTA platforms, the pseudo-secular term of the dipolar Hamiltonian plays a significant role. For certain combinations of pump and detect frequencies, it can induce “shoulders” in the frequency-domain spectra, which translate into shorter components in the

distance distributions, and in general increase its width if conventional application of the Tikhonov analysis is applied.[21,34] However, this phenomenon was found to be small on the $MnDOTA_2P_n$ systems, as shown by the agreement between Tikhonov and MD/mtsslWizard profiles, suggesting that the flexibility of the platform would obscure the pseudo-secular contribution. To verify this hypothesis, PELDOR measurements were performed on the Mn^{II} complexes of the more rigid platforms bis-DOTA-$PhPip_n$ **149** and **150** and bis-DOTA-OPE_n **202**, **203** and **204**.

4. MEASUREMENTS USING RIGID PLATFORMS

4.1 Phenyl-piperazine bis-DOTA platforms 149 and 150

The W-band ED-EPR spectra of the $MnDOTA_2PhPip_n$ platforms **149** and **150** are depicted in Figure 107.

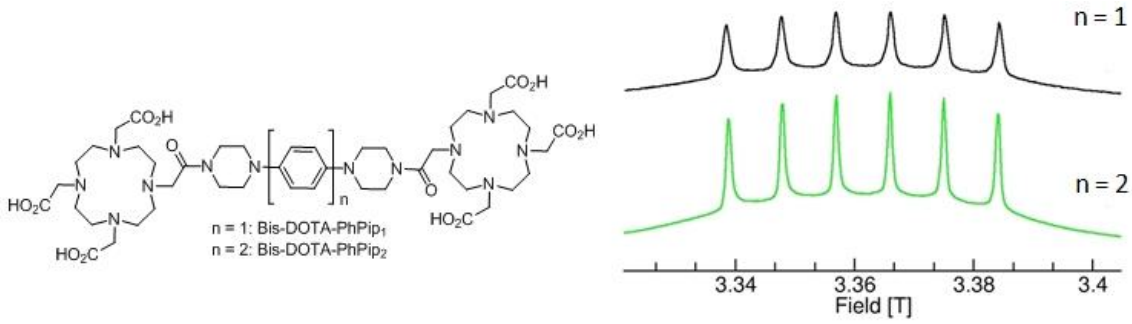

Figure 107: Left: Structure of the bis-DOTA-$PhPip_n$ ligands (n = 1 and 2). Right: W-band ED-EPR spectra of $MnDOTA_2PhPip_n$ (black, n = 1; green, n = 2). Conditions: 125 µM in 50 mM pH 8 HEPES buffer with 10% glycerol at 10 K

As mentioned before (Figure 71, p. 106), when n = 1, the widths of the six EPR lines are twice as broad as for Mn^{II}-DOTA. However, they are as narrow as Mn^{II}-DOTA when n = 2. It shows that in this distance range, a small change in the Mn-Mn distance can have a marked influence on the broadness of the lines: for $MnDOTA_2PhPip_1$, the additional broadening most probably arises from the strong dipolar coupling between the two Mn^{II} centers. In $MnDOTA_2PhPip_2$, this effect is not observed because the Mn^{II}-Mn^{II} distance is longer.

We measured the T_2 of the $MnDOTA_2PhPip_n$ platforms, which represents the spin-spin relaxation rate (p. 17) (Figure 108).

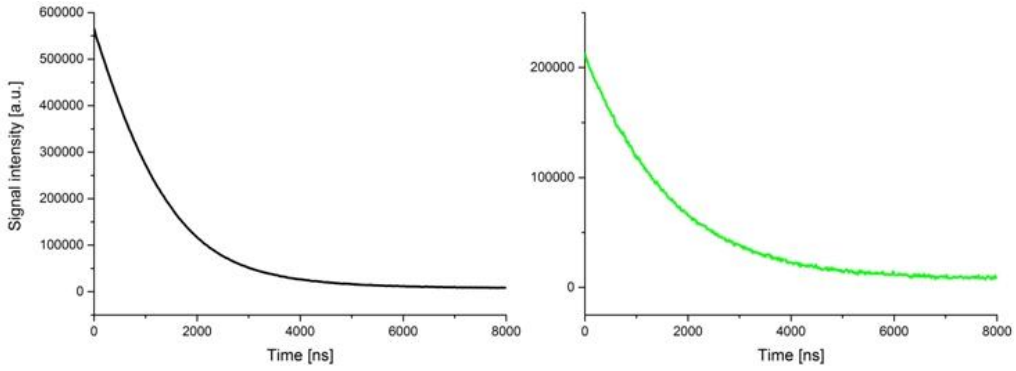

Figure 108: T_2 spectra of the $MnDOTA_2PhPip_n$ platforms (black, n = 1; green, n = 2) at 10 K.

The T_m value for these two compounds is in the 1 – 2 µs range, which allows sufficient time to observe dipolar modulations. As shown in Figure 109, we have chosen the top of the 6th EPR line as the pump position, to excite as many spins as possible. Another line could have been chosen, as there is no A- or *g*-anisotropy. To assess the effect of the offset, we performed PELDOR measurements at four different frequency offsets while keeping the pump pulse at the top of the 6th hyperfine line. A concentration of 250 µM was tested to begin with, in order to obtain a high SNR.

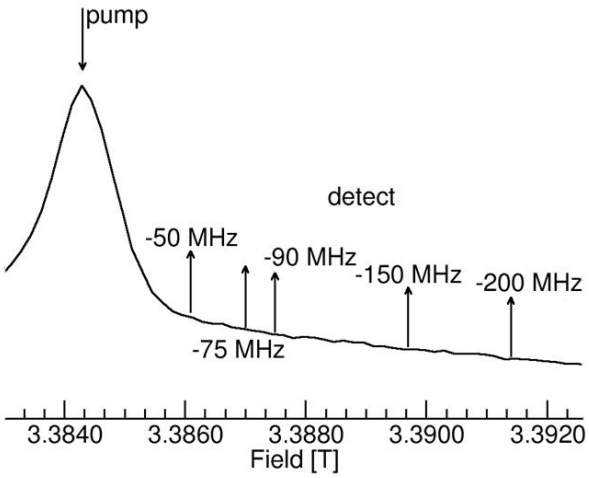

Figure 109: Blow-up of the 6th line of the W-band ED-EPR spectrum of the $MnDOTA_2PhPip_1$ platform showing schematically the pump-detect strategy

The PELDOR measurements are depicted in Figure 110, and the associated parameters and numerical results are compiled in Table 4.

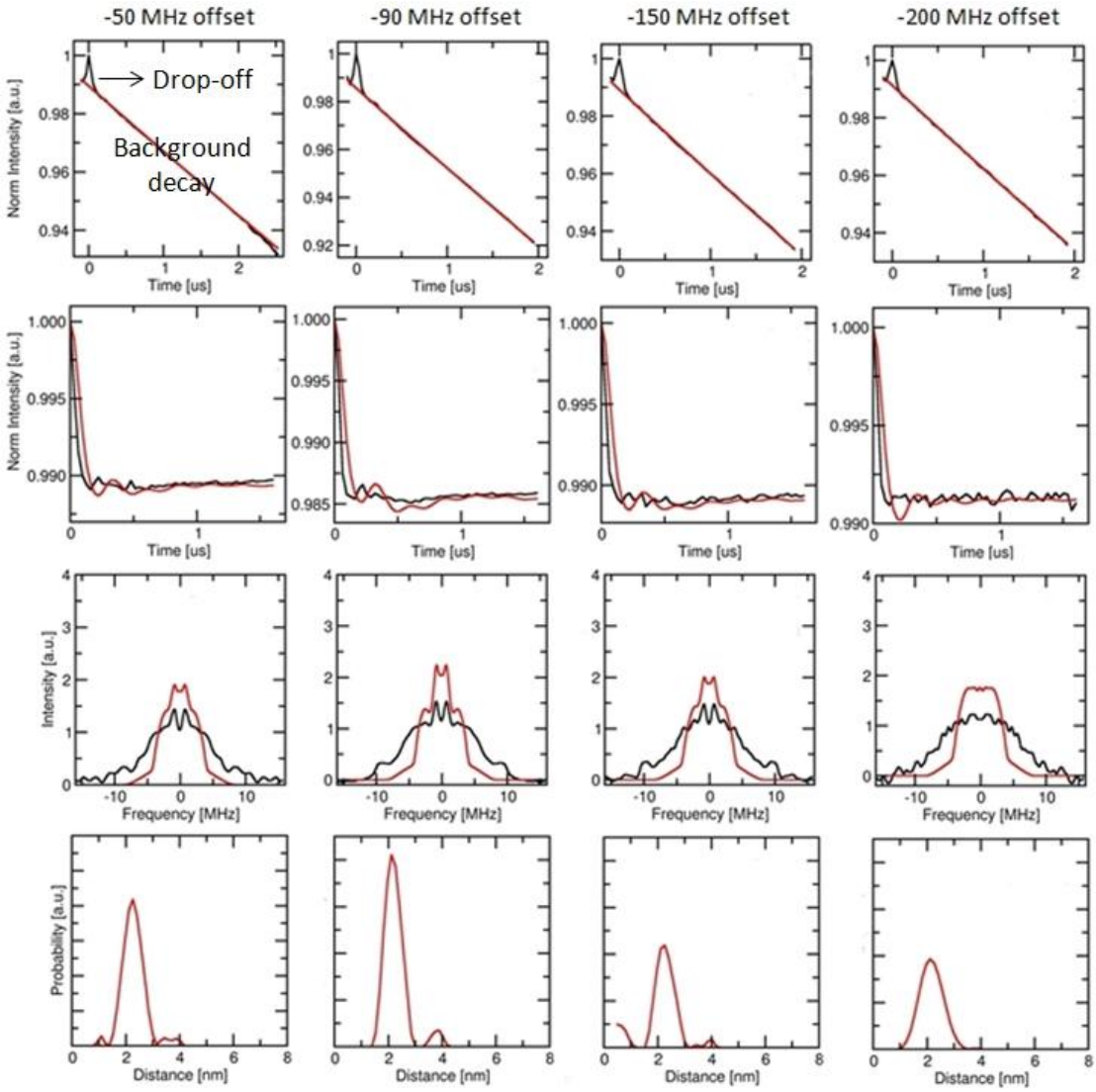

Figure 110: DeerAnalysis results from PELDOR experiments on $MnDOTA_2PhPip_1$ at four different offsets (-50, -90, -150 and -200 MHz). From top to bottom: experimental raw PELDOR time traces (black) and backgrounds (red), experimental PELDOR time traces after background subtraction (black) and their Tikhonov fits (red), experimental frequency-domain spectra (black) and their Tikhonov fits (red), and distance distributions obtained by Tikhonov analysis

Table 4: Parameters and numerical results from the PELDOR experiments of Figure 110.

Offset (MHz)	-50	-90	-150	-200
Pump pulse (ns)	10	26	36	48
Detection pulses (ns)	22/40	16/26	24/46	26/50
Shot per point	100	100	100	100
Scans	438	4055	642	466
Modulation depth (%)	1.1	1.4	1.1	0.9
Distance (nm)	2.3	2.1	2.3	2.1

Short pump pulses were chosen to obtain a high modulation depth λ. Whatever the offset, a first drop-off in the time-domain is clearly visible, which would correspond to a PELDOR modulation, followed by a steep background decay. This steepness is a result of the high concentration and is representative of a strong intermolecular contribution. The background could be adequately fitted with a linear function, as observed for the $MnDOTA_2P_n$ systems. The modulation depth (between 0.9 and 1.4%, maximum for the -90 MHz offset), is also comparable to the $MnDOTA_2P_n$ platforms.

Figure 110 also displays the frequency-domain spectra, obtained by real Fourier transformation. Tikhonov regularization, as implemented in DeerAnalysis, led to the distance distributions with a most probable distance between 2.1 and 2.3 nm. No significant influence of the offset could be detected, as observed for $MnDOTA_2P_n$ platforms. However, as it can be seen from the time- and frequency-domain plots, the Tikhonov analysis could not fully account for the experimental features, especially in the higher frequency components in the frequency-domain traces. The resulting distance distribution profiles also display unexpected additional peaks, and the distance distribution is broader than expected (half-height width of about 1 nm) considering that the phenyl-piperazine linker is expected to be relatively rigid.

We also performed an experiment at 50 µM to reduce the steepness of the background decay, in order to better observe the PELDOR modulations. The offset was -70 MHz, close to the -90 MHz value that led to the highest λ value in Table 4, and the results are displayed in Figure 111. The Tikhonov analysis appears to fit the experimental traces better, but unexpected distance are still present in the distance distribution, showing that these discrepancies do not come from uncertainties in the background removal as the situation is similar for two different concentrations.

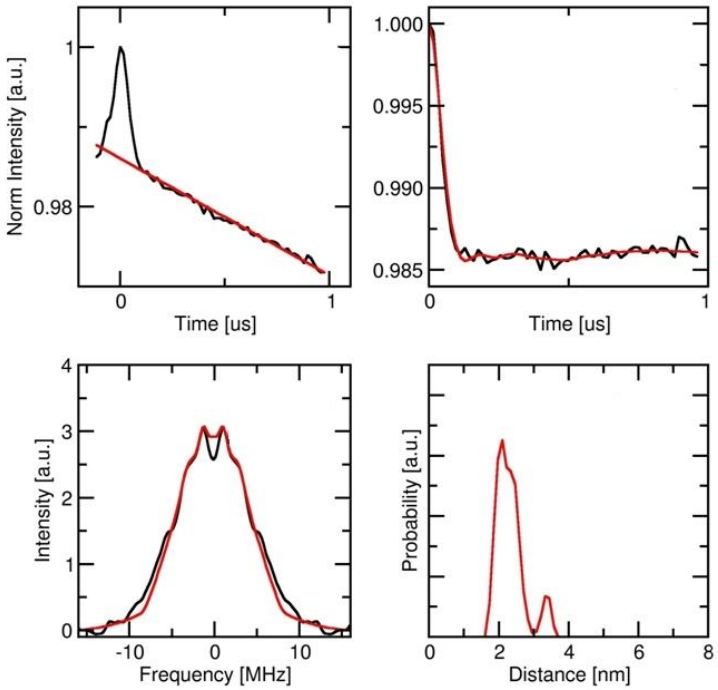

Offset (MHz)	-70
Pump pulse (ns)	14
Detection pulses (ns)	22/44
Shot per point	1000
Scans	70
Modulation depth (%)	1.4
Distance (nm)	2.1

Figure 111: DeerAnalysis results from PELDOR experiments on $MnDOTA_2PhPip_1$ at -70 MHz offset with a concentration of 50 µM. Top, left: experimental raw PELDOR time trace (black) and background (red). Top, right: experimental PELDOR time trace after background subtraction (black) and its Tikhonov fit (red). Bottom,

left: experimental frequency-domain spectrum (black) and its Tikhonov fit (red). Bottom, right: distance distribution obtained by Tikhonov analysis. Table: corresponding parameters and numerical results

These results further illustrate that the pseudo-secular term of the dipolar Hamiltonian cannot be ignored when analyzing data for measuring short distances. Using conventional application of the Tikhonov analysis results in unreliable distances and distributions. Furthermore, for this platform, the relatively large dipolar coupling (from both secular and pseudo-secular interactions) is even noticeable in the broadening of the EPR spectrum, so it is not surprising that the weak coupling approximation is not fulfilled.

In order to approximate the error arising from neglecting the pseudo-secular interaction in the analysis, the Mn-Mn distance as well as its distribution on $MnDOTA_2PhPip_1$ were estimated with MD calculations using the Assisted Model Building with Energy Refinement (AMBER) force field.[224,225,226] A simplified model was used where the DOTA rings where replaced for cyclens, in order to avoid complications linked to the protonation state of the carboxylic acids and due to the difficulty of performing MD calculations with paramagnetic metals. The calculation was run in water, and 500 frames were generated (one for every 10 ps of a 5 ns simulation). A representative conformer is shown in Figure 112, as well as the distributions of three relevant N-N distances which have been extracted using VMD (Visual Molecular Dynamics).[227]

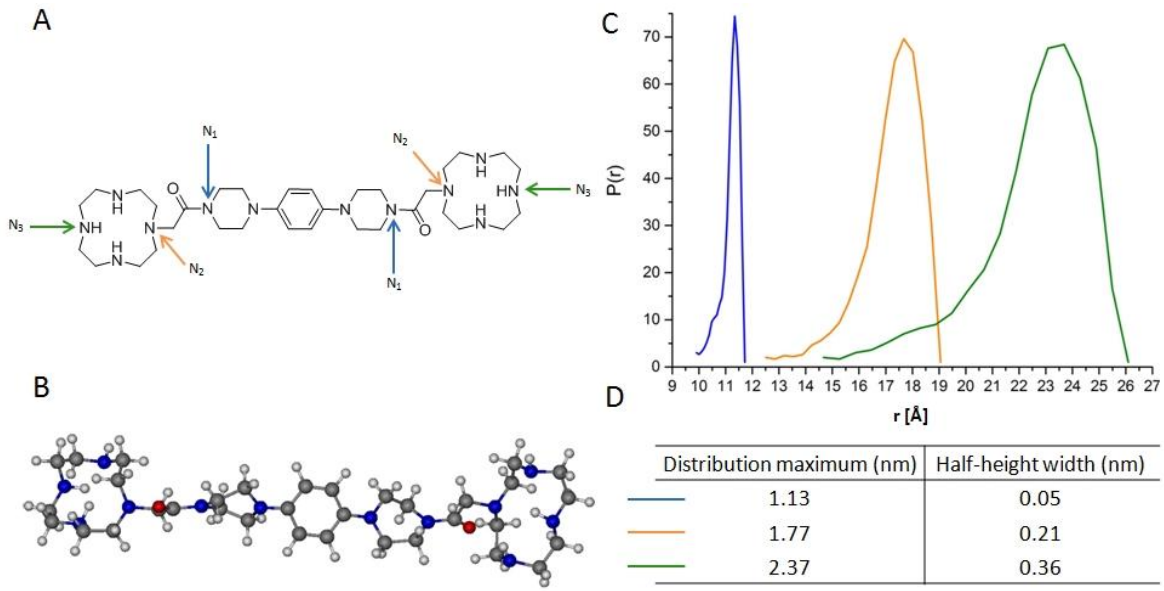

Figure 112: A – Model of $MnDOTA_2PhPip_1$ used for MD calculations showing the three considered distances (N_1-N_1 in blue, N_2-N_2 in orange and N_3-N_3 in green). B – Representative conformer. C – Distance distributions extracted from MD calculations. D – Numerical values of the most probable distances as well as their respective distributions

The width at half-height of the N_1-N_1 distribution is 0.05 nm, confirming the stiffness of the phenyl-piperazine linker. However, by visualizing the MD simulation, the phenyl-piperazine linker appears to adopt many different conformations even if the N_1-N_1 distance stays approximately the same: it can be seen as a "breathing" structure. The maximum of the N_1-N_1 distribution is 1.13 nm, in excellent agreement with the 1.12 and 1.13 nm values from the corresponding N-N distance in the X-

ray structures of compounds **130** and **220**, respectively, and with the 1.13 and 1.14 nm values from the DFT structures of the same molecules (Figures 66, 67, 91 and 92, pp. 97, 98 and 138). As expected, the width of the distance distribution increases with the N-N distance, reflecting the flexibility of the CH_2CO tether and of the cyclen ring.

The Mn-Mn distance can be estimated using the average of the N_2-N_2 and the N_3-N_3 distances. Even if the N-Mn-N bonds are not collinear in crystal structures,[147,149] this averaging still gives a reasonable estimation of the Mn-Mn distance. A value of 2.07 nm was found, in good agreement with the PELDOR values (2.1 – 2.3 nm), suggesting that despite the inadequacy of the Tikhonov analysis, it still yielded a reasonable Mn-Mn distance. This unexpected agreement is not clearly understood. Using the half-height widths of the N_2-N_2 and the N_3-N_3 distances, the distribution of the Mn-Mn distance was estimated to be 0.21 – 0.36 nm at half height. This range would be the upper limit, if we consider the fact that Mn^{II} constrains the cyclen ring. However, even with this simplified model, it is still much narrower than the ≈ 1 nm value obtained from analysis of the PELDOR data.

We surmised that the strong influence of the pseudo-secular interaction which complicates the analysis of the PELDOR data also broadens the central transition in $MnDOTA_2PhPip_1$. We performed the same PELDOR experiments on $MnDOTA_2PhPip_2$, which displays a narrower EPR signal for the central transition. We kept the pump pulse on top of the 6^{th} line and a -50 MHz offset, with two different concentrations (125 and 250 µM) (Figure 113). The influence of the concentration is well reflected by the steepness of the background decay, which is less pronounced at 125 µM than at 250 µM. The Tikhonov analysis appears to better account for the features in the time- and frequency-domain traces. Higher modulation depths (1.7 to 2%) were also observed. However, ghost peaks are still present and the distance distribution is again larger than expected. These ghost peaks cannot be explained by a low SNR and uncertainties in the background removal, as measurements with a higher number of scans (more than 4000, see Table 4) did not change the aspect of the time trace and because the signal was acquired for a long dipolar evolution time (2 µs) so that the background decay can be safely subtracted.

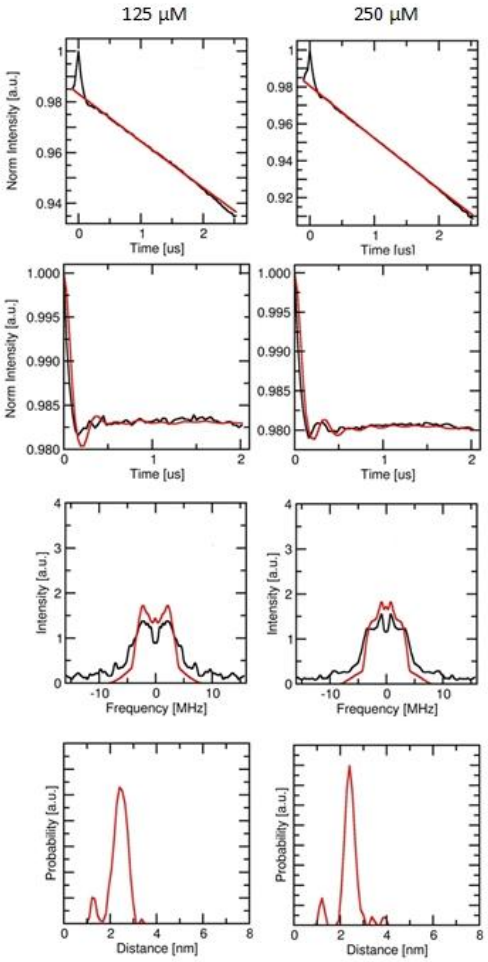

Concentration (µM)	125	250
Pump pulse (ns)	12	12
Detection pulses (ns)	22/36	24/40
Shot per point	100	100
Scans	574	331
Modulation depth (%)	1.7	2
Distance (nm)	2.4	2.4

Figure 113: DeerAnalysis results from PELDOR experiments on $MnDOTA_2PhPip_2$ at two different concentrations (125 and 250 µM). Left, from top to bottom: experimental raw PELDOR time traces (black) and backgrounds (red), experimental PELDOR time traces after background subtraction (black) and their Tikhonov fits (red), experimental frequency-domain spectra (black) and their Tikhonov fits (red), and distance distributions obtained by Tikhonov analysis. Right: Table showing parameters and numerical results

AMBER-based MD calculations were also performed on $MnDOTA_2PhPip_2$ using the same simplified model (Figure 114).

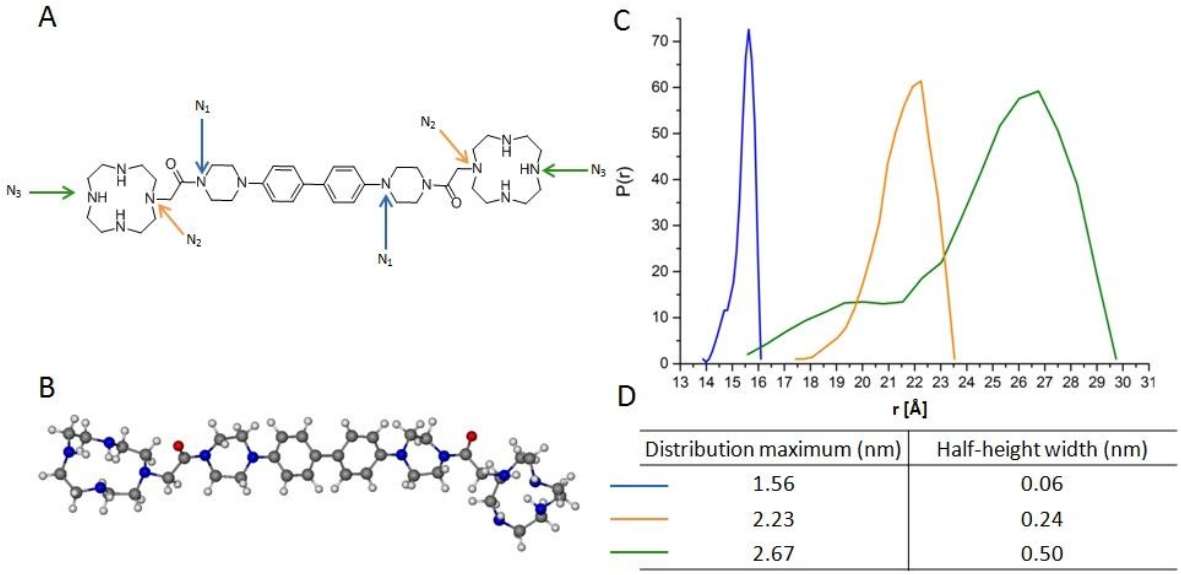

Figure 114: A – Model of $MnDOTA_2PhPip_2$ used for MD calculations showing the three considered distances (N_1-N_1 in blue, N_2-N_2 in orange and N_3-N_3 in green). B – Representative conformer. C – Distance distributions extracted from MD calculations. D – Numerical values of the most probable distances as well as their respective distributions

The situation is quite similar to what was found for bis-DOTA-$PhPip_1$, with a central stiff biphenyl-piperazine linker having the same "breathing" behavior. The N_1-N_1 distance distribution maximum is in excellent agreement with the 1.57 nm value from DFT calculations on compound **140** (Figure 68, p. 101). The average of N_2-N_2 and N_3-N_3 distances is 2.45 nm, again in good agreement with the value obtained from the PELDOR data (2.4 nm). The width of the distance distribution profile is in the 0.24-0.50 nm range, compared to ≈ 1 nm from the Tikhonov analysis of the PELDOR data, indicating that the broadening induced by the pseudo-secular interaction is again clearly visible.

In order to establish a lower distance limit where the influence of the pseudo-secular interaction becomes manageable, we need to increase the distance between the Mn^{II} centers, thus lowering the dipolar coupling. Accordingly, we performed the same experiments with the $MnDOTA_2OPE$ platform.

4.2 OPE bis-DOTA platforms 202, 203 and 204

The W-band ED-EPR spectrum of $MnDOTA_2OPE_1$ is depicted in Figure 115.

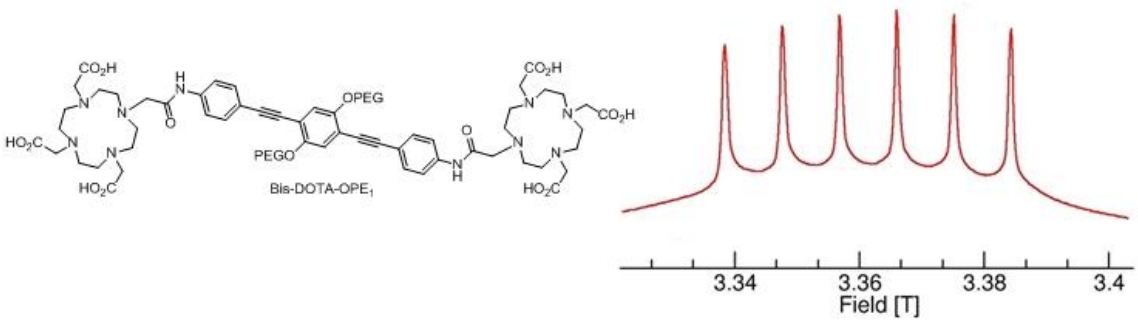

Figure 115: W-band ED-EPR spectrum of $MnDOTA_2OPE_1$. Conditions: 100 µM in 100 mM pH 8 HEPES buffer with 20% glycerol at 10 K

As shown above (Figure 85, p. 132), the hyperfine sextet is as narrow as Mn^{II}-DOTA. The T_2 (spin-spin relaxation) and T_1 (spin-lattice relaxation) values have been measured and are displayed in Figure 116.

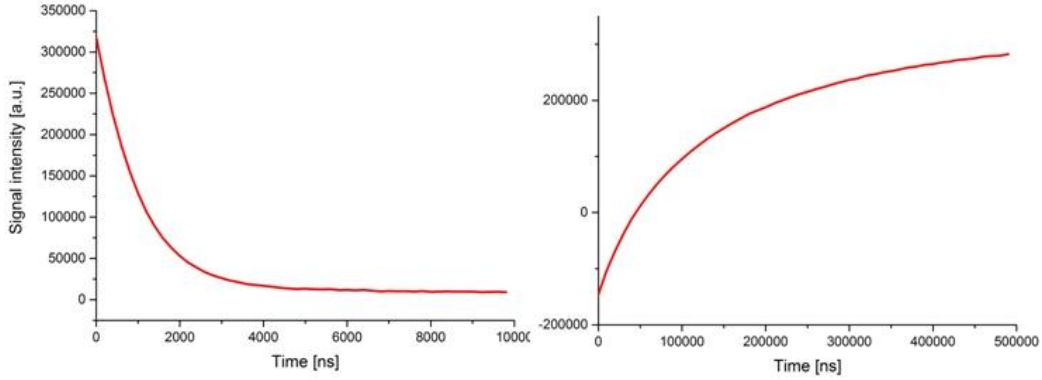

Figure 116: T_2 (left) and T_1 (right) spectra of $MnDOTA_2OPE_1$ at 10 K

The T_m value is around 1.5 µs, similar to $MnDOTA_2PhPip_n$ platforms, and the T_1 is approximately of 2 ms, allowing a fast repetition rate between two acquisitions.

However, when we tried to record the ED-EPR of the longer platforms bis-DOTA-OPE_n with n = 2 and 3, a mixture of the Mn^{II} complex and of hexaaqua Mn^{II} was observed, the latter being present at approximately 95%. This indicates that the DOTA macrocycles have difficulties to coordinate Mn^{II} in these systems. Hence, PELDOR measurements on the $MnDOTA_2OPE_n$ platforms with n = 2 and 3 were not conclusive because of the very low amount of coordinated Mn^{II}. The first modulation could be distinguished but the SNR was very low owing to the high free Mn^{II} concentration. We surmised that the π-stacking of the longer OPE rods could lead to aggregates. Despite numerous attempts (prolonged heating, high NaCl concentration, other solvents, surfactants), the coordination could not be improved. Dynamic Light Scattering (DLS) experiments are in progress to test for the presence of aggregates.

Hence, PELDOR experiments were performed on the $MnDOTA_2OPE_1$ platform only. A set of measurements were performed with pumping on top of the 6th line and detecting around it with two different offets (Figure 117).

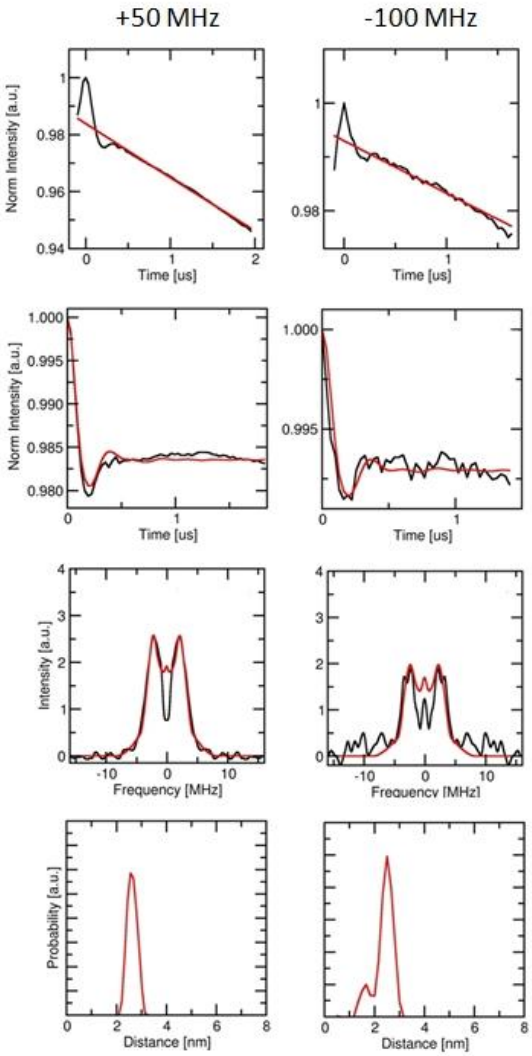

Offset (MHz)	+50	-100
Pump pulse (ns)	16	28
Detection pulses (ns)	10/16	12/22
Shot per point	100	100
Scans	589	17
Modulation depth (%)	1.7	0.7
Distance (nm)	2.6	2.5

Figure 117: DeerAnalysis results from PELDOR experiments on $MnDOTA_2OPE_1$ (250 µM) at two different offsets (+50 and -100 MHz). Left, from top to bottom: experimental raw PELDOR time traces (black) and backgrounds (red), experimental PELDOR time traces after background subtraction (black) and their Tikhonov fits (red), experimental frequency-domain spectra (black) and their Tikhonov fits (red), and distance distributions obtained by Tikhonov analysis. Right: Table showing parameters and numerical results

The difference with platforms $MnDOTA_2PhPip_n$ is striking: the first feature in the time domain corresponds to a complete oscillation and not to a simple drop-off. The Tikhonov analysis appears to fully account for the features in the time- and frequency-domain traces. A clean distance distribution without any ghost peak is observed, with a maximum at 2.5 – 2.6 nm and a half-height width of 0.6 – 0.7 nm (Figure 135). The modulation depth is also high (1.7%). For the experiment with the -100 MHz offset, we acquired the signal for a very short time (17 scans). This shows that the main features are quickly observed. As above for $MnDOTA_2PhPip_n$, the theoretical Mn-Mn distance and its distribution were evaluated using MD calculations (Figure 118).

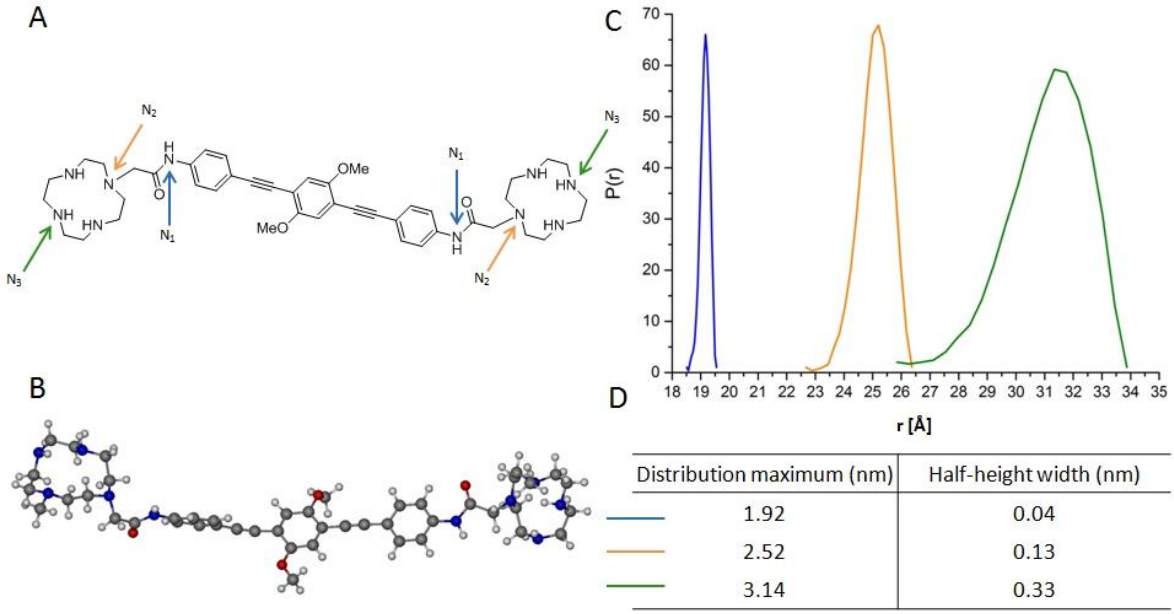

Distribution maximum (nm)	Half-height width (nm)
1.92	0.04
2.52	0.13
3.14	0.33

Figure 118: A – Model of $MnDOTA_2OPE_1$ used for MD calculations showing the three considered distances (N_1-N_1 in blue, N_2-N_2 in orange and N_3-N_3 in green). B – Representative conformer. C – Distance distributions extracted from MD calculations. D – Numerical values of the most probable distances as well as their respective distributions

As expected, the OPE spacer is very rigid, with a half-height width of 0.04 nm. This value is only 0.01 to 0.02 nm smaller than phenyl-piperazine linkers, which can thus be considered as very stiff molecular rods. The N_1-N_1 distance is in excellent agreement with the DFT calculation on OPE-diNH_2 **163** (1.94 nm), and can also be compared to the corresponding C-C distances on OPE-diCOH **161** and OPE-diCCH **164** (1.93 nm for both) (Figures 72 and 73, pp. 111 and 114). The average of the N_2-N_2 and N_3-N_3 distance distributions, in the 0.13 – 0.33 nm range, is again much lower than value obtained from Tikhonov analysis of the PELDOR data (0.6 – 0.7 nm). The flexibility of OPE linkers with nitroxide end groups has been assessed by PELDOR[16,17] and the width of the distance distribution at half-height for a compound of similar length is 0.15 nm.

As explained above, we estimated the Mn-Mn distance as the average value between the N_2-N_2 and N_3-N_3 distances. In this case, the theoretical value (2.83 nm) differs from the experimental PELDOR value (around 2.6 nm). The MD calculations give coherent results: considering that the OPE and the phenyl-piperazine linkers are stiff nanowires, the amido-CH_2-cyclen adds nearly the same distance in both cases (1.24 and 1.22 nm, respectively, *i.e.* the difference between the N_3-N_3 and the N_1-N_1 distances). This apparent discrepancy between the MD and the PELDOR distance values was not observed on the phenyl-piperazine platforms. However, the limitation of the Tikhonov analysis means that these PELDOR results must be considered with caution.

The difference between the MD and the PELDOR value could arise from the fact that the model used from the MD calculations, where the Mn^{II}-DOTA moieties were replaced with cyclen groups, is not appropriate. This means that the coordination sphere of Mn^{II}-DOTA could play a role in bringing together the two cyclens. An explanation could be the coordination of the Mn^{II} to the oxygen of the amide tether. The DOTA rings would be closer together, reducing the Mn^{II}-Mn^{II}

distance by a few angstroms. The crystal structure of Mn^{II}-DOTA indicates a hexacoordinated complex (Figure 58, p. 82):[147] in our case, if Mn^{II} is coordinated to the oxygen of the amide tether, a hexacoordinated complex is not probable as the coordination through two carboxylates is more favorable than coordination through an amido oxygen and a carboxylate (Figure 119). Mn^{II}-DOTA could also be heptacoordinated, but the symmetry loss could not explain the narrowness of the hyperfine sextet. Mn^{II}-DOTA would then be octacoordinated (Figure 119): this possibility was suggested in the first chapter (p. 84) because the J-band *cw*-HFEPR spectra of Mn^{II}-DOTA and Mn^{II}-DOTAM, which are 6- and 8-coordinated in the solid state, where found to be nearly identical. The J-band *cw*-HFEPR spectra of Mn^{II}-DO3A and Mn^{II}-DO2A, with 7 and 6 coordinating groups, respectively, were also found to display much broader EPR lines than Mn^{II}-DOTA (Figures 60 and 61, pp. 83 and 84).

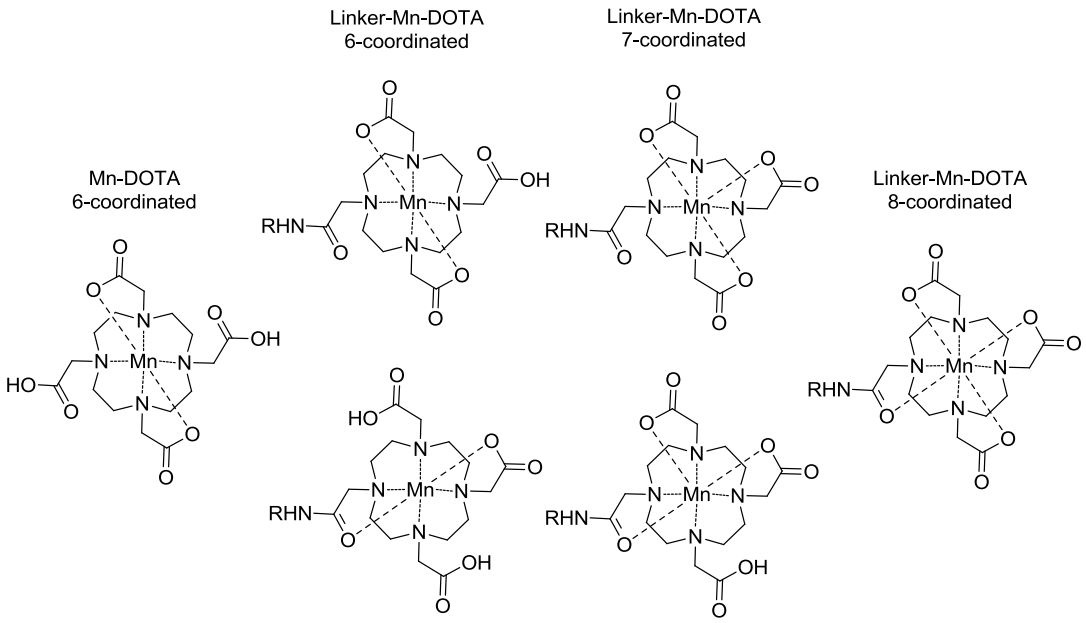

Figure 119: Possible coordination spheres of Mn^{II}-DOTA

PELDOR experiments were thus performed on the same bis-DOTA-OPE_1 ligand but metallated with Gd^{III} instead of Mn^{II} (Figures 120 and 121). As DOTA coordinates Gd^{III} in an octadentate way,[144] the amido oxygen of bis-DOTA-OPE_1 is coordinated to Gd^{III}, as shown in related structures.[197] The Mn^{II}-Mn^{II} and Gd^{III}-Gd^{III} distances determined with PELDOR should thus be identical if we suppose DOTA also coordinates Mn^{II} in an octadentate fashion.

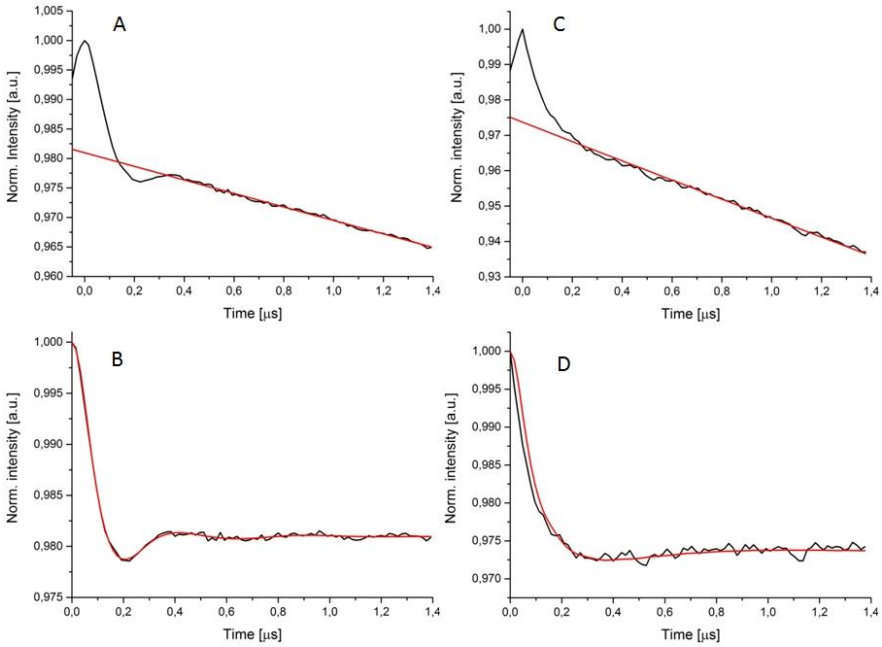

Figure 120: DeerAnalysis results from PELDOR experiments on $MnDOTA_2OPE_1$ (left) and $GdDOTA_2OPE_1$ (right). A – Experimental raw PELDOR time trace (black) and background (red) for $MnDOTA_2OPE_1$. B – Experimental PELDOR time trace after background subtraction (black) and its Tikhonov fit (red) for $MnDOTA_2OPE_1$. C and D – Same as A and B but for $GdDOTA_2OPE_1$

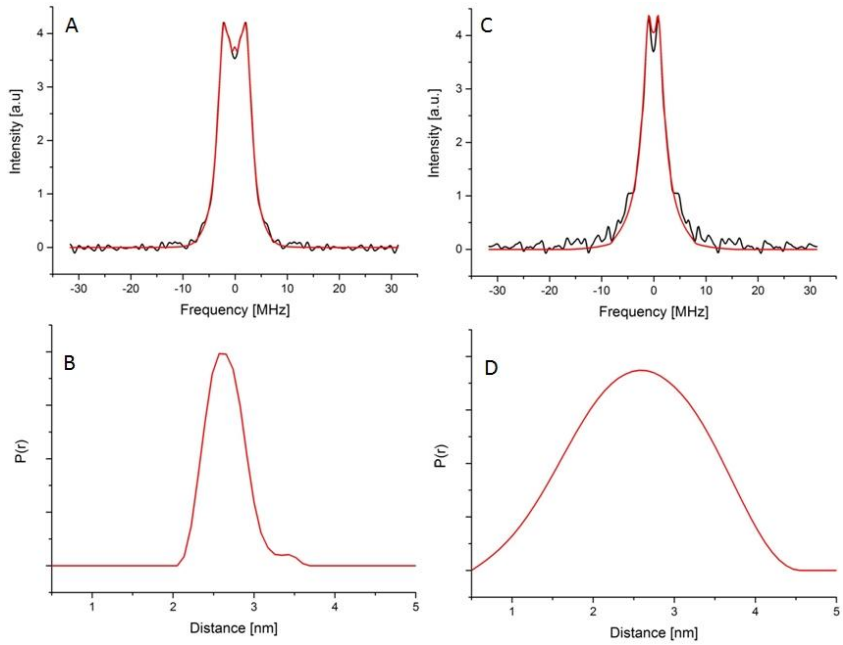

Figure 121: DeerAnalysis results from PELDOR experiments on $MnDOTA_2OPE_1$ (left) and $GdDOTA_2OPE_1$ (right). A – Experimental frequency-domain spectrum (black) and its Tikhonov fit (red) for $MnDOTA_2OPE_1$. B – Distance distribution obtained by Tikhonov analysis for $MnDOTA_2OPE_1$. C and D – Same as A and B but for $GdDOTA_2OPE_1$

To obtain a fair comparison between $MnDOTA_2OPE_1$ and $GdDOTA_2OPE_1$, parameters were kept as similar as possible (pump on top of the 6th hyperfine line, +70 MHz offset, 100 µM). The SRT was set according to the T_1 values, *i.e.* 800 µs for $MnDOTA_2OPE_1$ and 400 µs for $GdDOTA_2OPE_1$,

corresponding to four times T_1. Pump pulses were 24 and 20 ns for $MnDOTA_2OPE_1$ and $GdDOTA_2OPE_1$, respectively. Figure 122 shows the distance distributions obtained with Tikhonov regularization using the same regularization parameter (RP) for $MnDOTA_2OPE_1$ and $GdDOTA_2OPE_1$. The optimal RP corresponds to the corner of the L-curve generated with the Tikhonov regularization as implemented in DeerAnalysis, and is a compromise between the width and the smoothness of the distance distribution (ref interne). Four different RP were used in each case (Figure 122).

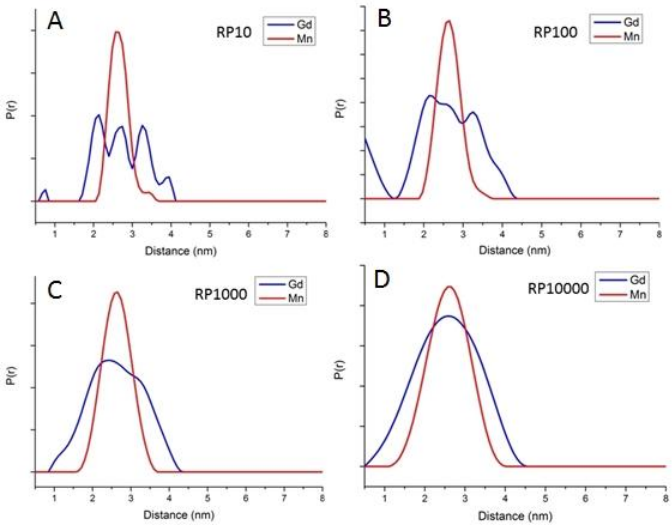

RP	$MnDOTA_2OPE_1$	$GdDOTA_2OPE_1$
10	2.61 (0.58)	n/a
100	2.62 (0.70)	n/a
1000	2.63 (0.93)	n/a
10000	2.61 (1.28)	2.59 (2.13)

Figure 122: Left: Distance distributions for $MnDOTA_2OPE_1$ (red) and $GdDOTA_2OPE_1$ (blue) for four different regularization parameters (RP) of the Tikhonov regularization (A – RP10, B – RP100, C – RP1000, D – RP10000). Right: Table with the most probable distances and the widths at half-height (in nm) for the four RP used

Figure 122 shows that to obtain a good compromise between the smoothness and the width of the distance distribution, a RP of 10 is sufficient for $MnDOTA_2OPE_1$, but the same parameter employed for $GdDOTA_2OPE_1$ gives a non-realistic distribution (Figure 122, A). A RP of 10000 is necessary for $GdDOTA_2OPE_1$ to obtain an acceptable smoothness, but this translates into a broad distance distribution. Figure 123 shows the superposition of the distance distribution profiles for $MnDOTA_2OPE_1$ and $GdDOTA_2OPE_1$, using a RP of 100 for $MnDOTA_2OPE_1$ (so that the tail observed at RP10 does not appear).

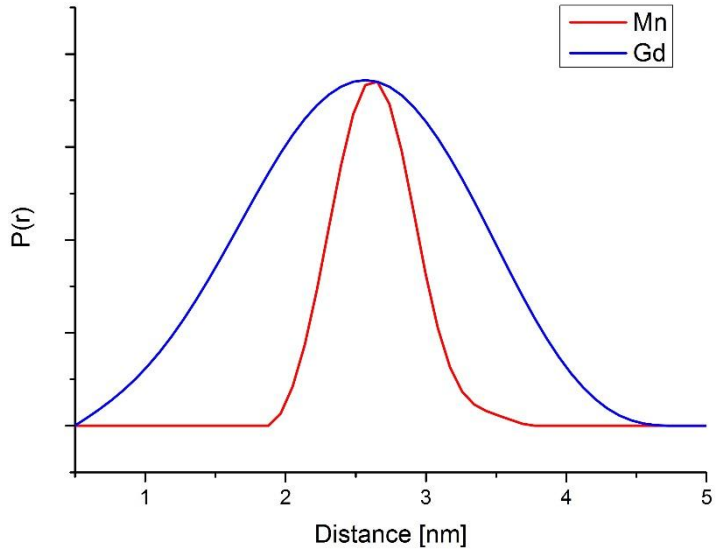

Figure 123: Normalized distance distributions for $MnDOTA_2OPE_1$ (red) and $GdDOTA_2OPE_1$ (blue) obtained with Tikhonov regularization with RP100 for $MnDOTA_2OPE_1$ and RP10000 $GdDOTA_2OPE_1$.

The most probable distance is nearly identical for $MnDOTA_2OPE_1$ and for $GdDOTA_2OPE_1$ (cf table of Figure 122). This confirms our hypothesis and suggests that the coordination sphere is identical for Mn- and Gd-DOTA. These results also show that the influence of the pseudo-secular term is much stronger in the case of $GdDOTA_2OPE_1$, because the distance distribution is much larger than for $MnDOTA_2OPE_1$ (half-height widths of 2.13 nm *vs* 0.59 nm).

To conclude, these preliminary PELDOR studies gave further insights into the parameters for high-spin Mn^{II}-Mn^{II} PELDOR measurements. Short pump pulses associated with a rather low offset seem to give the best results. Pumping on top of a hyperfine line and detecting on its side leads to a good modulation depth: this shows that the influence of the pump-detect pulse overlap is limited and that the resulting loss in echo intensity does not significantly affect the SNR. A concentration of 100 µM appears optimal to minimize the background contribution while keeping the SNR high. These parameters allow for a short measurement time as the main features are observed in a few scans and a time trace with a high SNR can be obtained in a few hours.

The differences between $MnDOTA_2OPE_1$ and $GdDOTA_2OPE_1$ led us to compare these two metal complexes with the more commonly used TEMPO spin labels, to determine the scope and limitations of these three paramagnetic centers. Hence, W-band PELDOR experiments were performed on the bis-TEMPO-OPE platform, which can be seen as the nitroxide analogue of bis-DOTA-OPE_1.

4.3 OPE bis-TEMPO platform 225

The W-band ED-EPR spectrum of the bis-TEMPO-OPE module **225** is depicted in Figure 124.

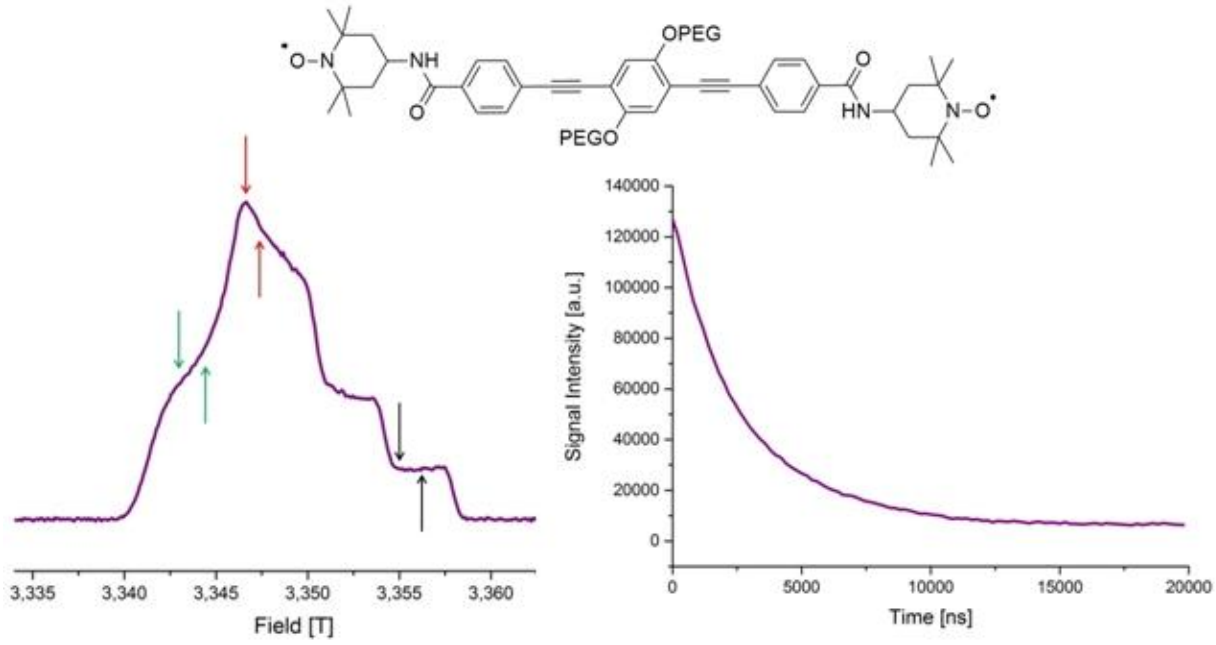

Figure 124: Top: structure of the bis-TEMPO-OPE module **225**. Left: its W-band ED-EPR spectrum showing the pump-probe strategy with green, red and black arrows. Right: its T_2 spectrum. Conditions: 100 µM in 1:1 toluene/$CHCl_3$ at 40 K

This spectrum is typical of a TEMPO moiety, and when derived, resembles the J-band *cw*-HFEPR spectrum of the same compound (Figure 97, p. 142). It is also similar to related bis-TEMPO platforms at the same magnetic field[41,228] At W-band, only the A_z component is resolved, while at J-band the A_x component is partially resolved because of the higher frequency. As expected, the *g*-anisotropy is clearly resolved, so a decrease of the spin flip probability by the pump pulse is to be expected. We can also anticipate orientation selection as observed for structurally related compounds.[41,228] The T_m value is around 2.5 µs, higher than the bis-Mn-DOTA platforms but sufficient to observe a few dipolar oscillations. To confirm this, PELDOR experiments were performed at three different positions of the EPR spectrum, corresponding to g_x, g_y and g_z (indicated on Figure 142 with green, red and black down-pointing arrows, respectively). Conditions were as close as possible as the parameters used for PELDOR experiments with $MnDOTA_2OPE_1$ and $GdDOTA_2OPE_1$. The offset was kept constant at -70 MHz, the DeerAnalysis results are depicted in Figure 125 and the experimental parameters in Table 5.

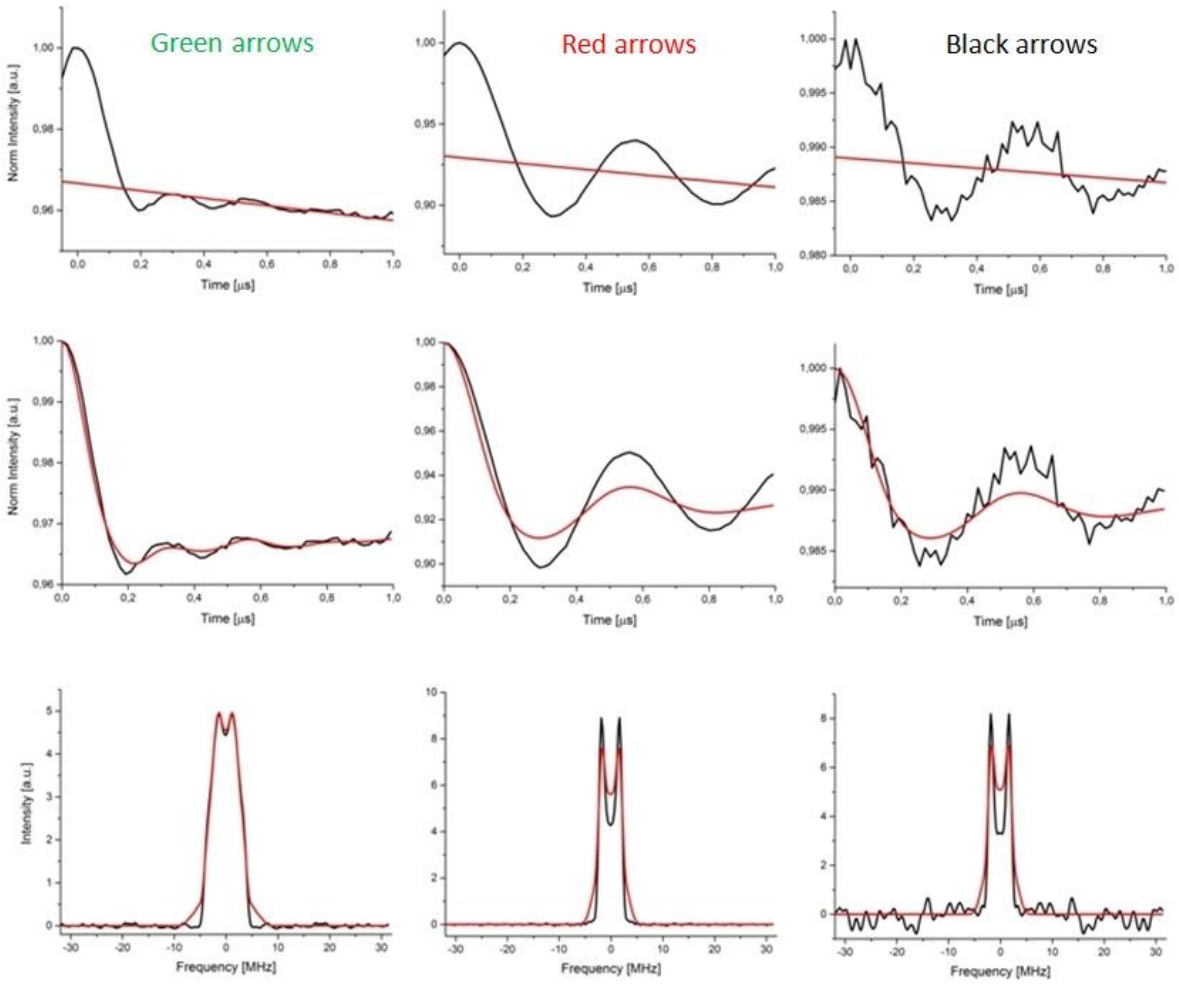

Figure 125: DeerAnalysis results from PELDOR experiments on the bis-TEMPO-OPE module **225** with a -70 MHz offset, corresponding to the green (left side), red (middle) and black (right side) arrows of Figure 124. From top to bottom: experimental raw PELDOR time traces (black) and backgrounds (red), experimental PELDOR time traces after background subtraction (black) and their Tikhonov fits (red), experimental frequency-domain spectra (black) and their Tikhonov fits (red)

Table 5: Parameters and numerical results from the PELDOR experiments of Figure 125

Position on Figure 124	Green	Red	Black
Pump pulse (ns)	80	80	80
Detections pulses (ns)	40/80	40/80	40/80
Shot per point	100	100	100
Scans	28	25	26

The raw PELDOR traces in Figure 125 shows notable differences between the three experiments, indicating orientation selection effects (p. 25). Similarly, the frequency-domain spectra look different: they are shaped like Pake doublets but with a missing parallel component, indicated by the absence of the “feet” that are predicted by the theoretical spectra. Experiments

corresponding to the red and black arrows are similar, the only difference being the lower SNR for the latter because less spins were pumped and detected. As the whole Pake pattern is not observed in these conditions, the distance cannot be extracted. This orientation selection was expected because at W-band, the *g*-anisotropy of nitroxides is resolved, so that only a fraction of biradicals corresponding to a particular orientation are pumped and detected.

To sum up, the broadening induced by the contribution of the pseudo-secular term for Mn^{II} and Gd^{III} is much more prominent for the rigid platforms, as it cannot be compensated by the intrinsic flexibility of the system. This hampers any interpretation of the distance distribution, which will be overestimated. The situation is even worse for short distances, where the additional features cannot be fitted by the Tikhonov regularization, leading to severe distortions of the frequency-domain spectra and distance distribution profiles. These conclusions are consistent with a very recent work[34] on a series of rigid platforms incorporating two Gd-PyMTA labels: the same influence of the pseudo-secular term was observed, and it was also shown that a large distribution of the ZFS parameters was important. The pseudo-secular induced broadening decreases with increasing distances as the flexibility of the system becomes greater.

Compared to Gd^{III}-based spin-labels, Mn^{II}-DOTA appears to be complementary. The broadening induced by the pseudo-secular term is less prominent, and distances from 2.5 – 2.6 nm can be cleanly obtained with a good fit of the frequency-domain spectrum that leads to a clean distance distribution, whereas for Gd-PyMTA spurious peaks in the distance distribution profiles are observed for distances up to 3.4 nm (Figure 126).[34] This indicates that Mn^{II}-DOTA would be more appropriate to measure distances in the 2.5 – 3.5 nm range. However, high distances have been measured with Gd-DOTA and Gd-PyMTA, which may be not reachable with Mn^{II}-DOTA.

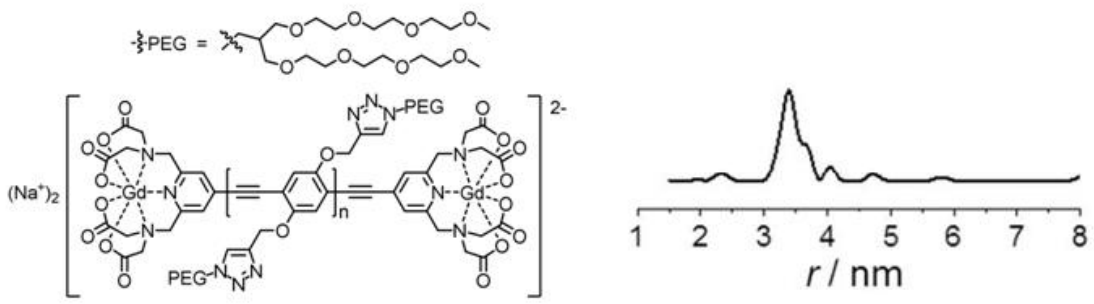

Figure 126: Structure of one of the rigid bis-Gd-PyMTA platforms used by Goldfarb *et al*[34] with an expected Gd-Gd distance of 3.4 nm (right), and distance distribution after DeerAnalysis from Q-band PELDOR (left). The maximum of the main peak is 3.4 nm. Conditions: 100 µM, 10 K, pump pulse 28 ns (set on top of the spectrum), detection pulses 20 and 40 ns, -100 MHz offset. Adapted from [34]

CONCLUSION

In this chapter, we described PELDOR measurements we performed on various platforms that consist in a central linker connected to two high-spin Mn^{II} complexes. Preliminary measurements with Mn^{II}-bis(Tpy) centers proved difficult, but Mn-Mn distances in the 2.6 – 4.8 nm

range were successfully determined with a high SNR when Mn^{II}-DOTA was used instead. It confirms the hypothesis that Mn^{II} complexes with low *D*-values such as Mn^{II}-DOTA are efficient PELDOR spin labels. This work is the first in-depth study on Mn^{II}-Mn^{II} PELDOR measurements using model compounds, highlighting the importance of the choice of a relevant Mn^{II} complex to improve the sensitivity compared to literature.[22] The influence of the pseudo-secular part of the dipolar Hamiltonian on the distance distribution profiles of rigid platforms was analyzed and could be summed up this way:

- In the 1.8 – 2.4 nm range, severe distortions from a Pake pattern are observed in the frequency-domain spectrum, which leads to distance distributions altered with ghost peaks. However, even if the Tikhonov regularization fails to fit the frequency-domain spectrum, the mean distance is still correct.

- Above 2.6 nm, good Tikhonov fits of the frequency-domain spectrum are observed, leading to the correct distance and a clean distance distribution profile, which is nevertheless broadened compared to theoretical results obtained from MD calculations.

- When the distance increases, the broadening decreases as the pseudo-secular interaction becomes less prominent. Above a certain distance, it will be obscured by the intrinsic flexibility of the system, so that the distance distribution profile will reflect the reality. This may be observed on the long platforms $MnDOTA_2OPE_n$ with n = 2 and 3, once an efficient way to make them coordinate Mn^{II} will be found.

These conclusions are not valid for an intrinsically flexible system such as the DOTA-labeled polyprolines, where the flexibility obscures the pseudo-secular contribution even for short distances. The Tikhonov regularization still requires caution, as additional features can appear if specific combinations of pump-detect pulses are used.[148]

These experiments also suggest that Mn^{II}-DOTA could be octacoordinated in solution, in contrast with the reported hexacoordinated structure in the solid state. Discrepancies between the most probable distances obtained from PELDOR experiments and MD calculations, as well as the similar PELDOR-determined metal-metal distance between $MnDOTA_2OPE_1$ and $GdDOTA_2OPE_1$ seem to confirm this hypothesis, and more experiments are underway.

Another conclusion is that the pseudo-secular-induced broadening is much more prominent on $GdDOTA_2OPE_1$ than on $MnDOTA_2OPE_1$: theoretical investigations on why this is the case are underway. It would be also interesting to obtain the distance distribution between the two centers of the cyclens using MD calculations. The amount of pseudo-secular-induced broadening could then be assessed by comparing the distance distribution profiles obtained from PELDOR. Another idea would be to record the X-band EPR spectrum of bis-TEMPO-OPE **225**, which should be free from orientation selection at this frequency. As no pseudo-secular interaction should be noticed, the distance distribution should reflect the reality, and thus should superimpose to the profile obtained by MD calculations. PELDOR measurements on the dissymmetric DOTA-PipPhPip-TEMPO platform **234** (Scheme 78, p. 146) would also be interesting because in this case too, no pseudo-secular interaction should be observed, as the two paramagnetic centers are different. All this work would

be useful to assess the scope, limitations and complementarities of high-spin Mn^{II} and Gd^{III} complexes and nitroxides for PELDOR measurements.

Chapter III – High-field EPR study of persistent substituted trityl radicals

In this last chapter, we will investigate the EPR properties of two different classes of persistent trityl radicals: perchlorotriphenylmethyl (PTM) and tetrathiatriarylmethyl (TAM) families. These radicals drew our attention as the use of TAM derivatives as promising spin-labels for PELDOR measurement was reported three years ago by two independent groups[229,230] TAM radicals display a very narrow single EPR line, which explain their interest for PELDOR measurements as it is today the only spin label that allows a nearly complete inversion of the spins by the pump pulse, achieving very high sensitivity. PTMs also display a single sharp X-band EPR line; this unique feature has been exploited, in the case of PTMs and TAMs, in various active fields, from DNP to EPR-based imaging toward biomedical applications as well as in oxygen and superoxide sensing in biological systems. A focused review of the literature dealing with these persistent trityl radicals will be presented in a first part.

Using the synthetic methodology we developed in the first chapter of this manuscript, we explored the possibility of synthesizing platforms incorporating a central rigid rod with a persistent trityl radical at one end and a Mn^{II}-DOTA complex at the other end. PELDOR measurements on these unreported systems should display a considerably enhanced modulation depth compared to the Mn^{II}-Mn^{II} modules studied in Chapter II, owing to the possibility of pumping on the trityl narrow line and detecting on one of the Mn^{II}-DOTA narrow lines, instead of pumping on top and detecting at the bottom of one Mn^{II} line. They could lead in turn to high-sensitivity PELDOR measurements on native Mn^{II}-containing proteins that would be tagged with a TAM or a PTM spin label. To this end, we developed a revised synthesis of a water-soluble derivative of PTM radicals and attempted its grafting on our previously described linkers and derivatives. This will constitute the second part of this chapter.

The sharp EPR line of persistent trityl radicals implies that they display a very low *g*-anisotropy. As numerous applications of PTM and TAM radicals critically depend on this exceptional narrowness, we envisioned measuring the *g*-tensors of water-soluble PTM and TAM derivatives to see if there is a relationship between a class of trityl radical and its specific applications. An accurate measurement is mandatory, as the differences in the *g*-values of PTM and TAM radicals are expected to be small owing to their very similar structure. J-band *cw*-HFEPR is perfectly suited for this purpose as the high field/frequency allows for an optimal resolution of the EPR spectra. In this third part, we will accurately measure the *g*-tensors of five PTM and TAM derivatives using Mn^{II} as a field standard. By comparing the experimental *g*-tensors with the simulated and DFT-calculated ones, we will show that striking differences can be observed between these two families.

1. PERSISTENT TRITYL RADICALS

1.1 Origins of persistent trityl radicals

In the beginning of the 20th century, a surprising experiment was realized by Moses Gomberg. Having successfully prepared tetraphenylmethane, Gomberg attempted the preparation of hexaphenylethane using a Wurtz reaction between triphenylchloromethane and silver (Scheme 80).[231] However, the white crystalline compound he obtained was not the expected product: elemental analyses indicated the presence of oxygen. When the same experiment was performed under an inert gas, the results were even more curious: a yellow solution, which color increased on heating and faded on cooling was obtained. The elemental analyses of the product obtained after evaporation of the yellow solution were different from the former case. After numerous investigations, Gomberg concluded that the white crystalline compound was the peroxide of triphenylmethane (peroxide dimer), and that the yellow solution was constituted of two products in equilibrium: the expected hexaphenylethane and triphenylmethyl (trityl) radical. This was the first instance of a persistent organic radical with a trivalent carbon. It was later shown that in fact, the trityl radical (Gomberg's trityl) was in equilibrium with its quinoid dimer and not hexaphenylethane (Scheme 80).

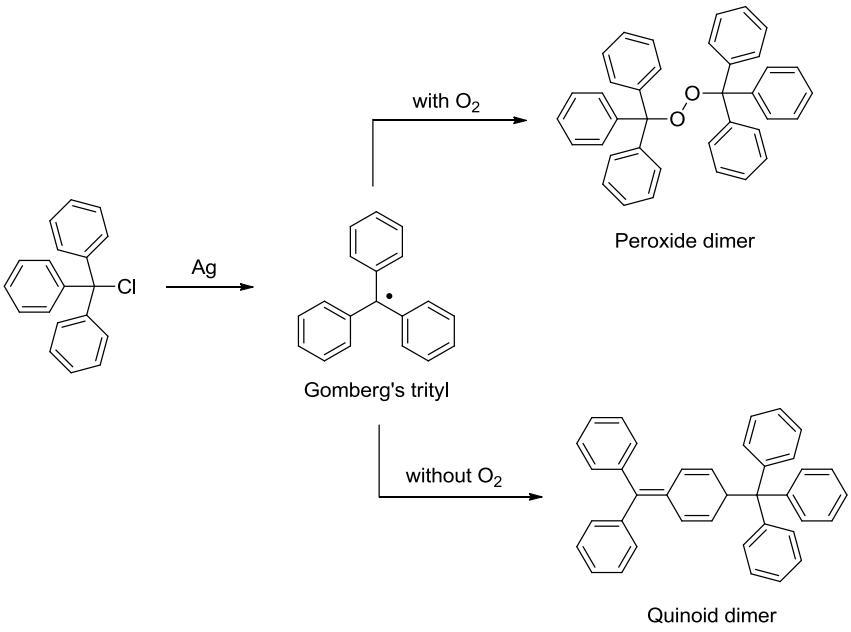

Scheme 80: Synthesis of Gomberg's trityl

In the beginning of the 1970's, the team of M. Ballester reported the synthesis of a number of highly chlorinated derivatives of Gomberg's trityl.[232] The use of the so-called BMC (Ballester-Molinet-Castañer) reagent,[233] a combination of S_2Cl_2 and $AlCl_3$ in boiling SO_2Cl_2, allowed efficient aromatic perchlorination of numerous compounds including triphenylmethane **237**, to give the corresponding αH-quasi-perchloro compound **238**. Generation of the corresponding anion with NaOH in DMSO/Et_2O, and subsequent oxidation with iodine afforded the PTM radical **239** as a red

solid (Scheme 81). This compound and its derivatives were found to be extremely stable, withstanding very harsh conditions (concentrated acids and bases, oxidants, temperatures up to 300 °C) and having half-lives of decades. The shielding of the central carbon by the chlorine atoms, hampering dimerization, was proposed as an explanation for the exceptional stability of the PTM radical **239**.

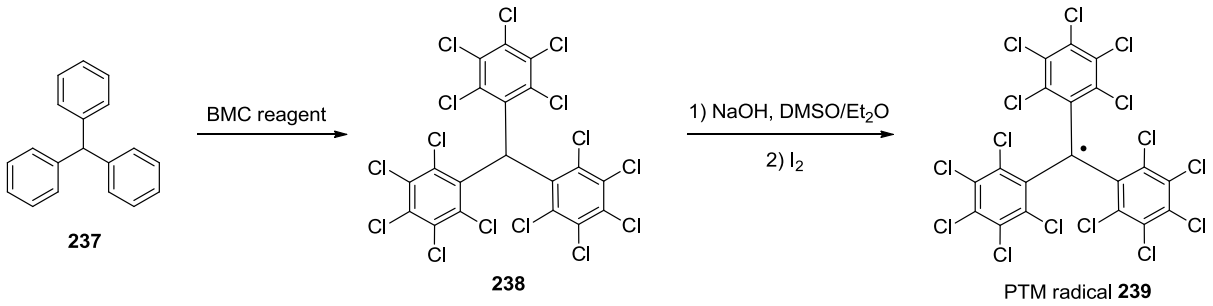

Scheme 81: Synthesis of the PTM radical **239**

A water-soluble derivative incorporating three carboxylate moieties in the *para* position, known as PTMTC (PTM-tricarboxylate), as well as its ethyl ester counterpart PTMTE **246** (PTM-triethylester), have been synthesized and used in many applications (Figure 127). These compounds as well as many PTM derivatives display a single EPR line, because no hyperfine coupling to the unpaired electron can occur: only weak satellite lines arising from the adjacent ^{13}C can be observed. This line is also very narrow (540 mG for a DMSO solution of PTMTE **246** at X-band[234], see Figure 127), which is related to the fact that chlorine has a low gyromagnetic ratio. This concept of shielding with nuclei having a low gyromagnetic ratio was extended to sulfur, as persistent trityl radicals with narrow EPR lines can be obtained by removing all sources of hyperfine contribution to the central carbon by isolating it with low-gamma nuclei. Accordingly, substituted trityl radicals incorporating dithiolane moieties known as TAM radicals were developed by Nycomed Innovation (now part of GE Healthcare) for use as MRI imaging agents.[235,236] As expected, these radicals were found to display a very narrow EPR line (111 mG for an aqueous solution of FT at X-band[237], see Figure 127), thus making them interesting candidates as alternative spin labels in PELDOR measurements. Among these sulfur-containing trityl radicals, the so-called FT (Finland Trityl) and an even more water-soluble compound, OX63, are the most commonly used (Figure 127).

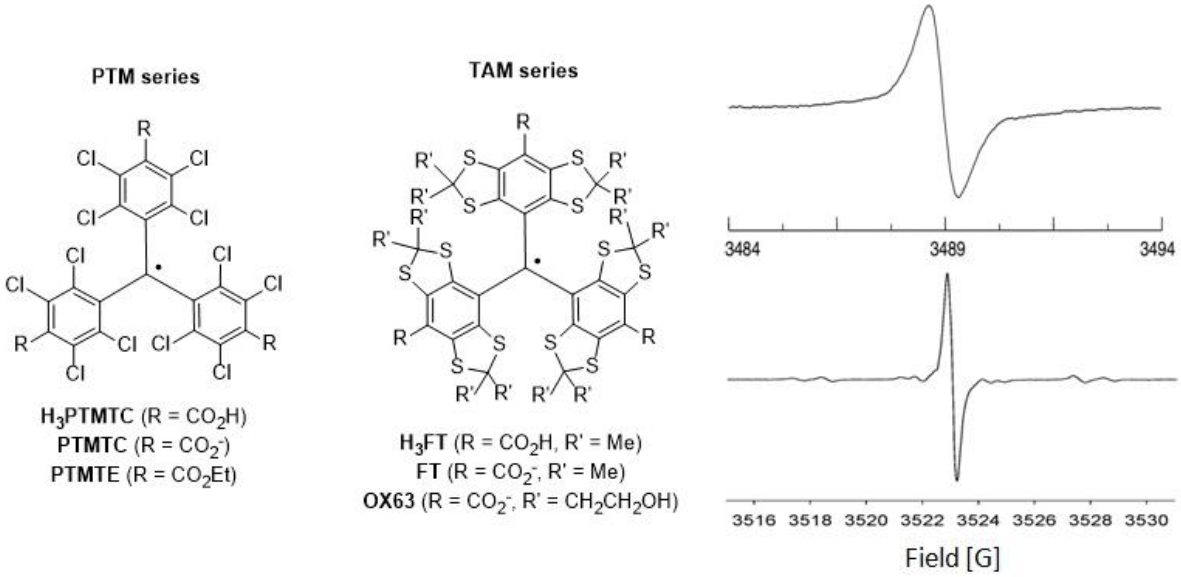

Figure 127: Left side: structures of commonly used members of the PTM and TAM families. Right side: X-band *cw*-EPR spectra of PTMTE **246** (in DMSO, top[234]) and FT (in H_2O, bottom[237])

PTM and TAM are thus the two main classes of trityl radicals. Their synthesis and unique applications will be detailed in the next part.

1.2 Reported synthesis and applications of PTM radicals

1.2.1 Synthesis

As discussed above, the PTM **239** radical has been synthesized by perchlorination of triphenylmethyl **237** with the BMC reagent followed by anion formation and subsequent iodine oxidation. A more convenient route to obtain *para*-substituted derivatives of PTM is the triple Friedel-Crafts reaction between chloroform and 1,2,4,5-tetrachlorobenzene **240**,[238] giving the corresponding dodeca-chlorinated trityl **241** in 61% yield. This overcrowded trityl is a very useful intermediate. Another Friedel-Crafts reaction with excess chloroform resulted in the introduction of three dichloromethyl groups to give intermediate **242**, which was subsequently oxidized in the presence of fuming sulfuric acid at high temperature to furnish tricarboxylic acid **243**. This precursor was finally converted into H_3PTMTC **244** using the NaOH/I_2 procedure.[239] Surprisingly, the route to PTMTE described in the literature is very different. Treatment of trityl **241** with *n*-BuLi and TMEDA and quenching of the resulting trianion with ethyl chloroformate resulted in the formation of triester **245**, which was then transformed into PTMTE **246** with NaOH and I_2.[234] Other functionalizations have been described: reaction of **241** with fuming sulfuric acid gave the trisulfonic trityl **247**, which was converted into the corresponding radical H_3TSPTM **248** (PTM-trisulfonic acid) with KOH and chloranil.[240] Finally, nitration of **241** with HNO_3/H_2SO_4 gave the trinitro derivative **249**, and treatment with *n*-Bu_4NOH and chloranil afforded the radical TNPTM **250** (PTM-trinitro) (Scheme 82).[241]

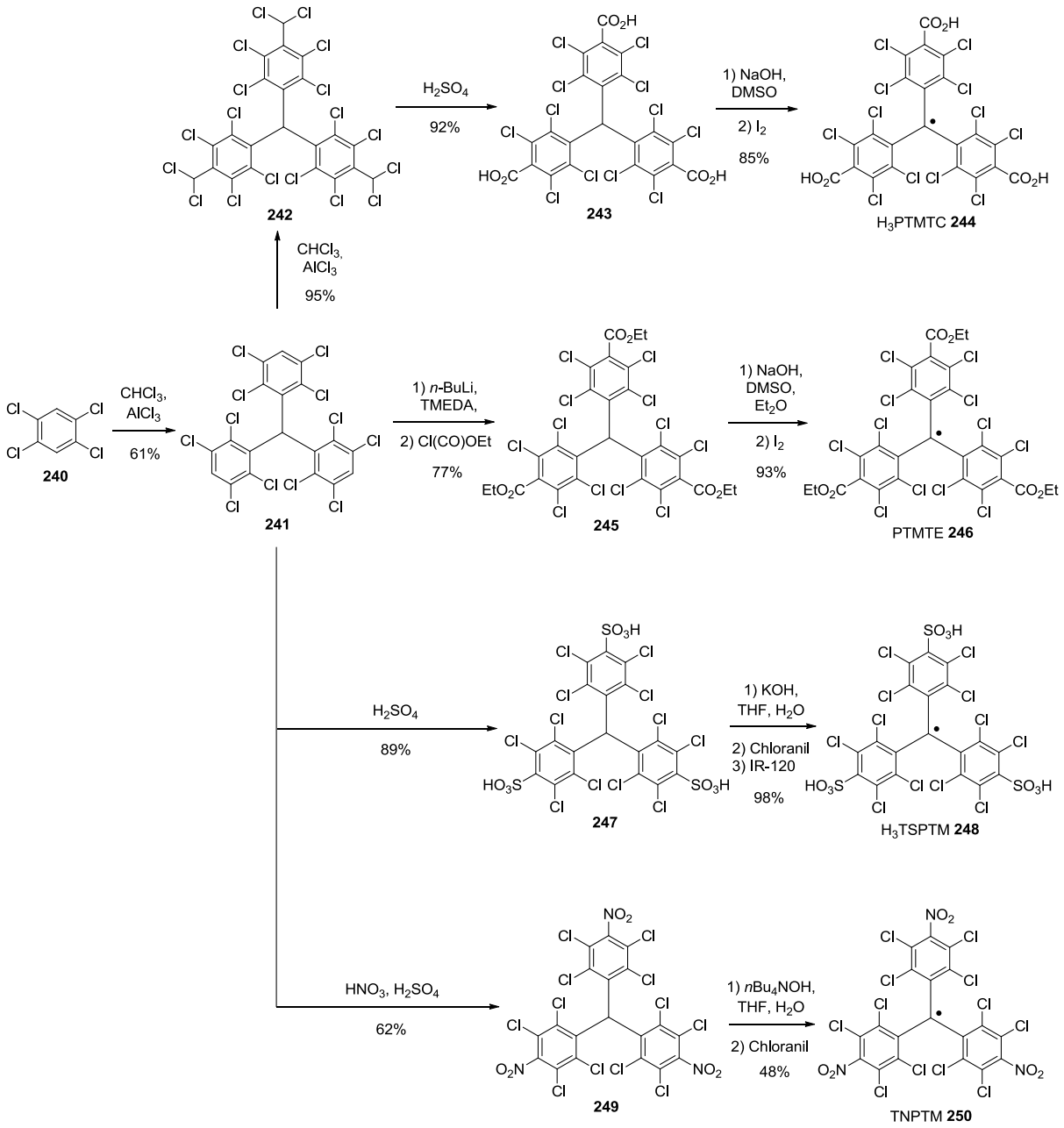

Scheme 82: Described syntheses of trityl radicals derived from intermediate **241**

Graftable monofunctionalized derivatives of PTM have also been synthesized. The Grignard reagent from *p*-bromotoluene **251** added on benzophenone to give **252**, which was reduced to **253** with formic acid. Aromatic perchlorination of this compound with the BMC reagent gave the tetradecachloro derivative **254**, which was photobrominated to afford **255**. An Arbuzov reaction with $P(OEt)_3$ gave the graftable trityl phosphonate **256**,[242] which can be converted to the corresponding radicals using methods described above (Scheme 83).

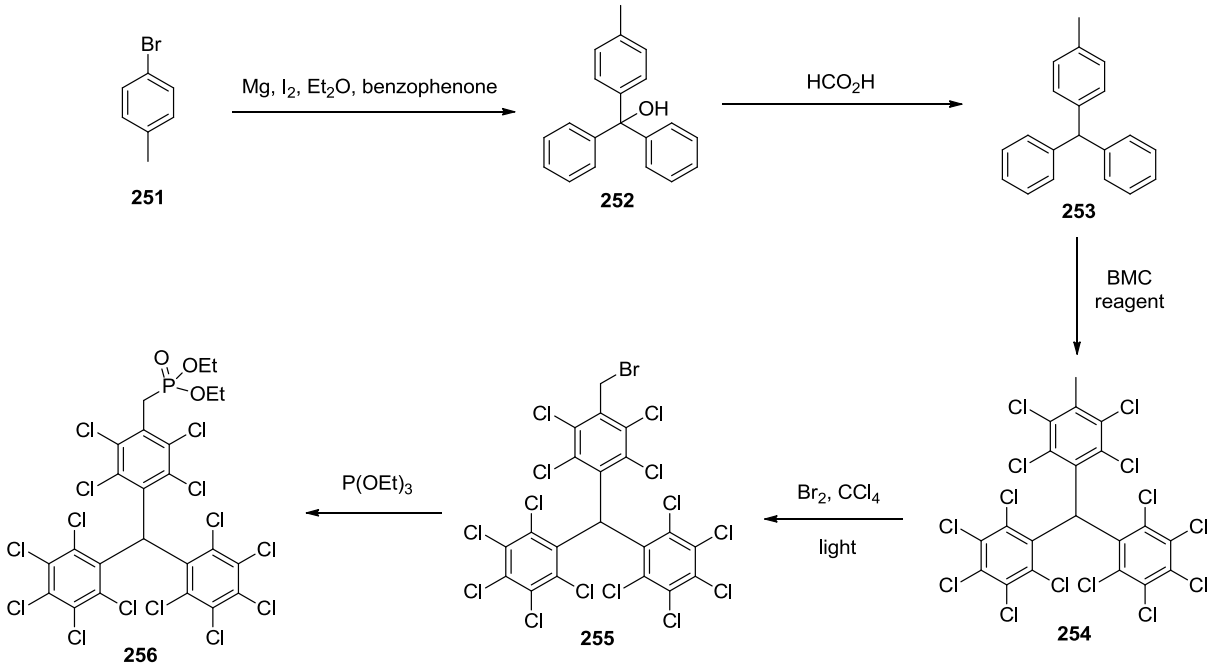

Scheme 83: Synthesis of the graftable trityl phosphonate **256**

It is worth noting that functionalizations in the *para* position of persistent trityl radicals must be carefully designed to keep a single-line EPR spectrum. Hydrogen or nitrogen atoms give rise to hyperfine couplings, adding numerous lines.[243,244,245] Carbon atoms, especially incorporated in carboxylate moieties, are often the preferred option as they even provide good water-solubility.

1.2.2 Applications

Compound **256** has been coupled to numerous compounds giving rise to many applications. Coupling with acetylated maltose gave rise to derivatives soluble in alcoholic solvents aimed at sensoring natural antioxidants in biological fluids.[246] A PTM derivative bearing long alkyl chains has proved to form micro-capsules that can encapsulate polar molecules and release them upon UV irradiation.[247] Dyads with ferrocene derivatives were used as bistable materials[248,249] since it is possible to reversibly switch between the radical and the anion form. This bistability was further exploited towards surface molecular devices when PTM derivatives bearing thioacetate or disulfide moities were anchored on gold substrates[250,251] or were designed to form columnar thin films on SiO_2 or TiO_2.[252] This ultimately led to the development of a non-volatile memory device using SAM (self-assembled monolayers) of PTM deposited on ITO (indium tin oxide).[253]

Electron transfer phenomena were also studied using systems with a PTM radical as an electron acceptor and arylamines as electron donors. These were the first neutral mixed-valence compounds,[254,255] followed by PTM-TTF (tetrathiafulvalene) dyads.[256] Long-range electron transfers were also demonstrated in systems incorporating OPE or oligo(phenylene-vinylidene) (OPV) nanowires grafted at the end with two PTM radicals.[257,258,259]

The PTMTC radical was also used in the construction of supramolecular assemblies with unique magnetic properties. It forms an open-framework magnetic nanoporous structure in the crystalline state.[260,261,262] Coordination through carboxylic groups with lanthanides[263] or transition metals such as Cu[264] or Co[265] gave rise to complex networks.

Other applications of PTMTC include its use as a DNP agent[266,267,268] as well as a superoxide sensor in roots[269] as its single-line narrow EPR signal clearly decreases as $O_2^{\bullet-}$ is produced because a diamagnetic adduct is progressively formed. PTMTE **246** has also been used as a superoxide and/or oxygen sensor in biological systems[234,270,271] with additional fluorescence detection,[272] its EPR linewidth increasing proportionally to the partial pressure of O_2. The sharp and single EPR peak of PTMTC and PTMTE **246** allows their detection at very low concentration.

Finally, H_3TSPTM and TNPTM have been used to measure the electron-donating capacity of polyphenolic antioxidants, as they are only active in electron-transfer reactions.[273] To the best of our knowledge, no EPR-based nanometric distance measurement using PTM derivatives as spin labels has been reported. This could be explained by the narrower linewidth of TAM radicals at W-band (see below) and by the difficult multi-step synthesis of the graftable PTM **256**, while OX63 is commercially available from Oxford Instruments Molecular Biotools.

1.3 Reported synthesis and applications of TAM radicals

1.3.1 Synthesis

The synthesis route to TAM radicals is very different from the PTM one. Starting from the same precursor, 1,2,4,5-tetrachlorobenzene **240**, aromatic nucleophilic substitution with *tert*-butylthiol in the presence of sodium gave intermediate **257**, which was converted to thioacetonide **258** with acetone and HBF_4•Et_2O or, more efficiently, using BF_3•Et_2O with camphorsulfonic acid (CSA).[274] Two equivalents of compound **258** were lithiated with *n*-BuLi and were added on methyl chloroformate (or diethyl carbonate) to generate alcohol **259**. The corresponding triesters **260** and **261** were then synthesized with *n*-BuLi and diethyl or di-*tert*-butyl carbonate, respectively. Starting from triethyl ester **260**, carbocation was generated using BF_3•Et_2O or TFA and reduced with $SnCl_2$ to give the radical **262**, which was hydrolyzed with KOH and acidified with aq. HCl to give H_3FT **263**.[275] It was later shown that the intermediate purification of radical **262** was not necessary.[274] An alternative pathway consisted in the direct synthesis of tricarboxylic acid **264** from alcohol **259** (*n*-BuLi then solid CO_2) and subsequent generation of H_3FT **263** with TFA and $SnCl_2$.[274] This synthesis scheme could be refined to allow a high-scale synthesis of H_3FT. Deprotection of tri-^{t}Bu-ester **261** with neat TFA generated H_3FT **263** at the same time.[276] It was later found that this formal one-electron reduction gave in fact a mixture of FT and quinone methide **265** (Scheme 84).[274]

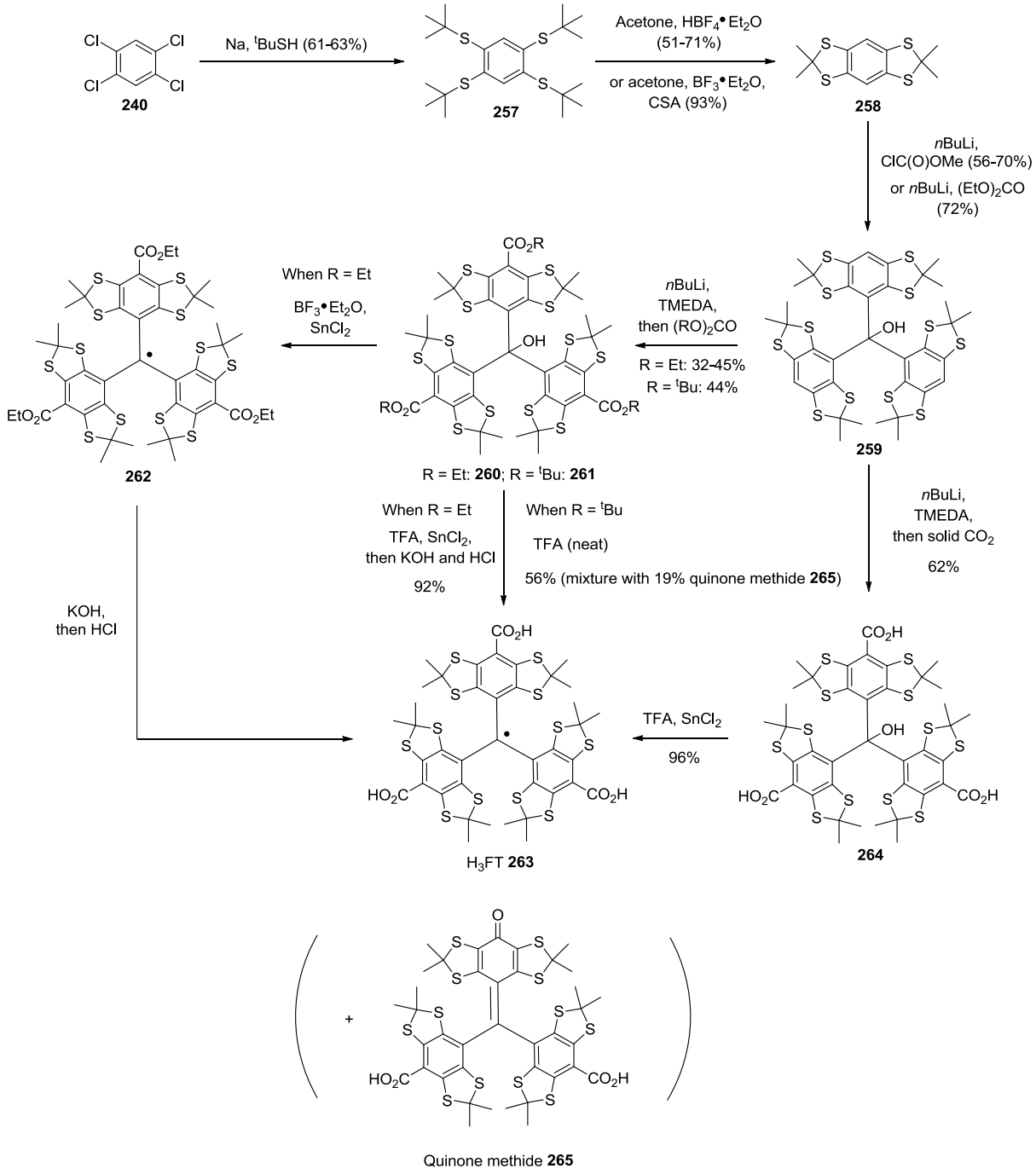

Scheme 84: Synthetics pathways to H_3FT **263**

A route to synthesizing a monocarboxylic FT derivative could be the separation of the monoester byproduct generated in the synthesis of compound **260**.[237] However, the yield of the desired compound was very low (9%). This can explain why, contrary to PTMs, the grafting of TAM derivatives is often performed starting from a symmetric radical like FT or H_3FT **263**, by reacting it with one equivalent of an amine in the presence of a coupling agent such as (benzotriazol-1-yloxy)tris(dimethylamino)phosphonium hexafluorophosphate (BOP) to form a single amide bond.[229,277,278,279,280] Another option is the synthesis of the triacyl chloride **266**[281,282,283] which can react

with one equivalent of an amino compound to form the expected monoamide product. Purification by reversed-phase HPLC is then performed (Scheme 85).

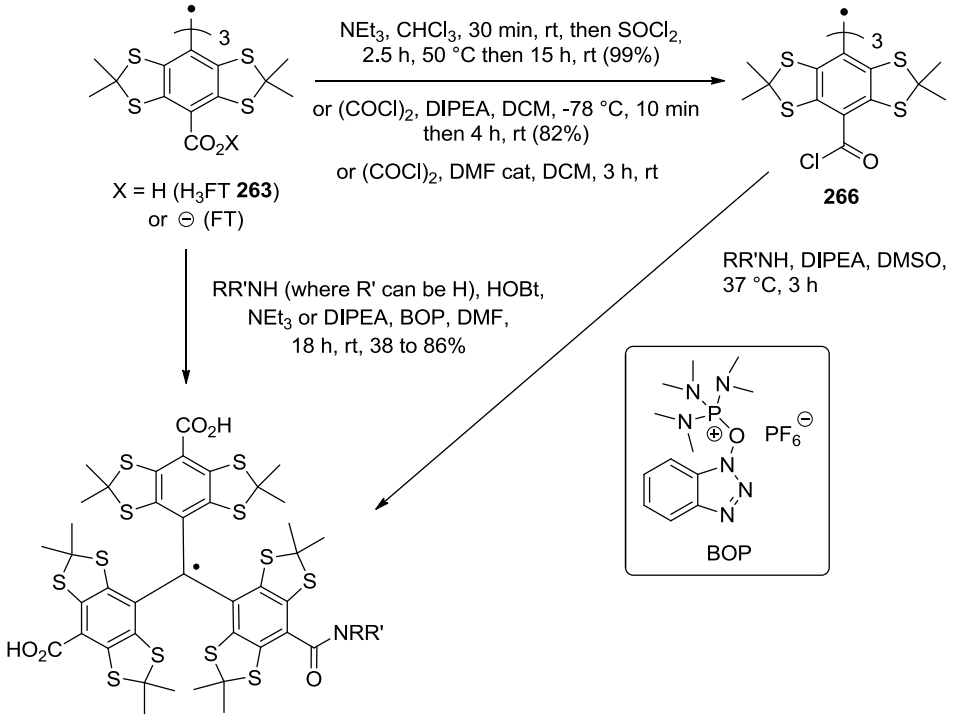

Scheme 85: Synthesis of monoamide derivatives of FT

Other options exist in the literature to synthesize mono-coupled TAM derivatives. The selective reduction of triethyester **260** with one equivalent of $LiAlH_4$[245] generated the mono-reduced alcohol **267** in 45% yield, along with 15% of the doubly reduced product. A nucleophilic substitution with the mesyl chloride of compound **267** could then be performed. A related method is the limited basic hydrolysis of the triethylester **260** to afford the corresponding monocarboxylic acid **268**[230,284] in acceptable yield after flash chromatography on silica gel. Compound **268** can be converted to the corresponding radical and coupled to the compound of interest, or the coupling step can be performed before the conversion to the radical form. The opposite strategy[285] has also been used: starting from H_3FT **263**, it was possible to couple two equivalents of an alkyl bromide to generate the corresponding diester in 31% yield, along with 39% of the triester (Scheme 86).

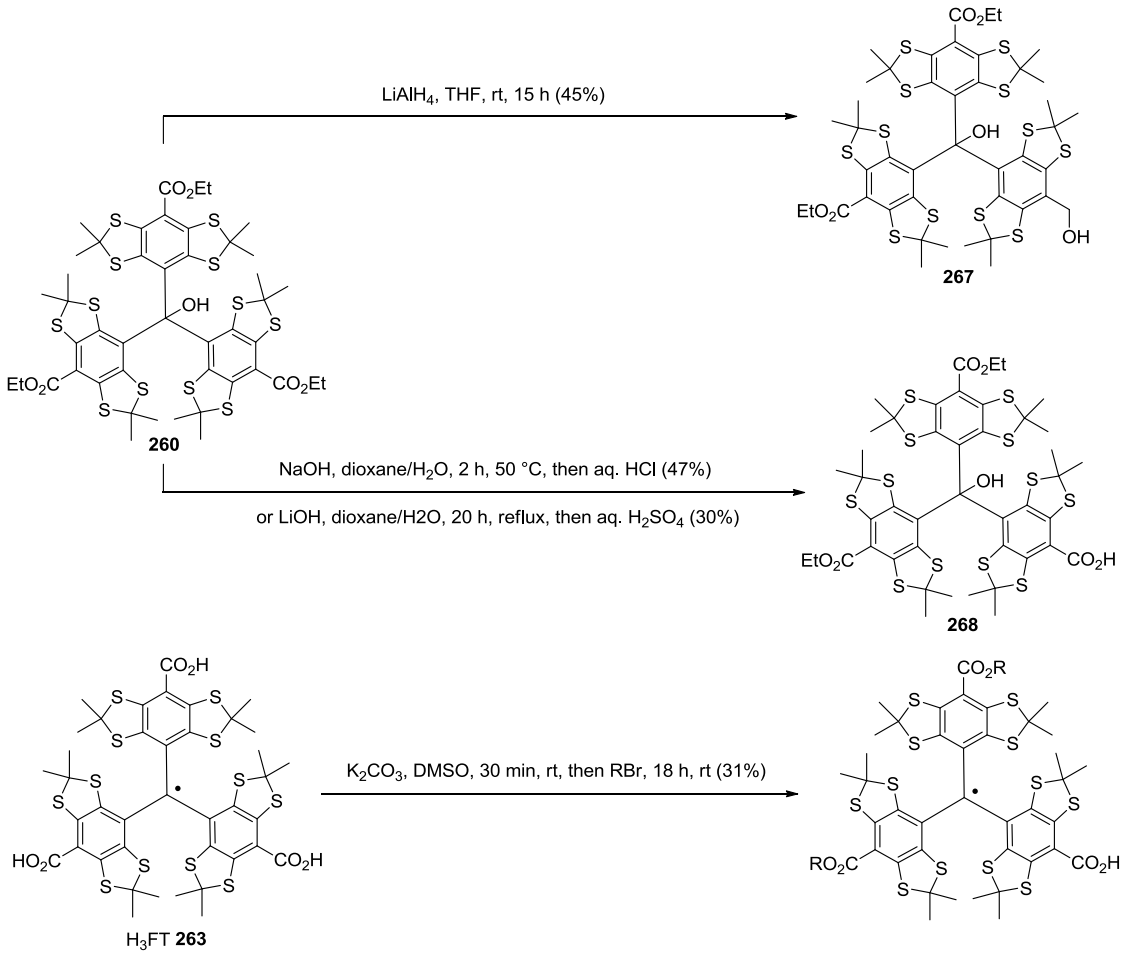

Scheme 86: Synthesis of monofunctionalized FT derivatives by desymmetrization

An elegant method[286] that allows the synthesis of monofunctionalized FT derivatives consists in the generation of the cations from triarylmethanols **259** or **264** with CF_3SO_3H, which can react with a variety of nucleophiles to obtain the corresponding monosubstituted trityl radicals. Another original methodology[243] is the *ipso* aromatic nucleophilic substitution on the cation of FT, obtained with two equivalents of K_2IrCl_6. This allowed the replacement of a carboxylate group with various nucleophiles (Scheme 87).

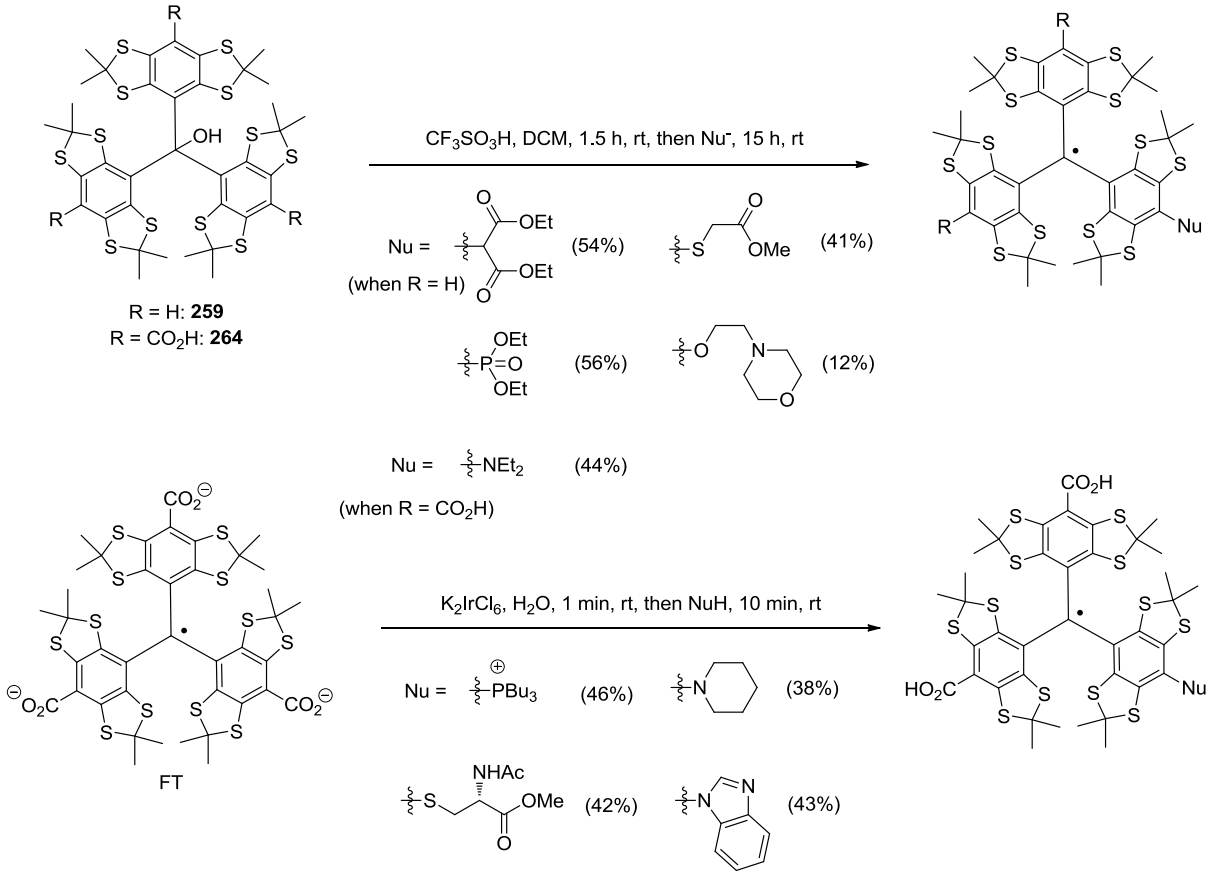

Scheme 87: Synthesis of various monosubstituted FT derivatives by aromatic nucleophilic substitution

1.3.2 Applications

FT and derivatives share numerous applications with the PTM series. Notably, they have also been used as DNP agents[266,287,288] as the outstanding increase of the NMR signal-to-noise ratio induced by OX63 is directly correlated to its extremely narrow single EPR line, smaller than the nuclear Larmor frequency.[289] Their use as superoxide[290,291] and oxygen sensors[237,292,293] when conjugated to a peptidomimetic[284] or derivatized[279,285] is well described. They have even been employed as simultaneous pH and O_2 probes[244,245] because shifts in their *g*-values upon pH variation, which could be linked to aggregation phenomena as shown in the third part, are easily detected.

Structural properties of FT derivatives have been investigated, such as their propeller shape inducing chiral properties.[294,295,296] Multifrequency EPR studies have been performed,[267,288,297] thermomagnetic[298] and electron spin relaxation[299,300] properties have been determined and the metabolism of these radicals is known.[301,302]

Unique applications of TAMs also include EPR imaging, notably in biological samples.[303,304,305] TAMs can be seen as an ideal imaging label: its single narrow line leads to EPR images with resolutions of up to 100 µm while its solubility and stability in aqueous solution is perfectly suited for biological systems. High-resolution imaging of tissue oxygenation using Overhauser-enhanced magnetic resonance imaging (OMRI) was also made possible.[306,307]

Finally, distance measurements with TAM radicals using PELDOR and/or other pulse sequences like DQC have been reported: the narrowness of the EPR signal allows for the inversion of nearly all spin centers by the pump pulse, greatly improving the sensitivity. It can be anticipated that single-frequency techniques such as DQC would be more adequate than PELDOR because the EPR line of TAMs is so narrow that a strong overlap between the pump and the detection pulses would be very detrimental. To the best of our knowledge, only four papers have been published since the first occurrences in 2012, where two groups reported the use of TAM radicals, one concerning biological systems, the other dealing with synthetic model systems.

The former constituted the very first report.[229] Two double mutants of the T4 lysozyme incorporating two Cys residues were immobilized on a sepharose gel and reacted with two TAM derivatives containing a graftable 2,2'-dithiopyridine moiety, synthesized in three steps starting from H_3FT. DQC experiments were then performed at 17.2 GHz, and the mean distances of 1.8 and 2.1 nm were in accordance with the crystal structure. This immobilization strategy is very promising as it allows measurements at 4 °C in the liquid state. The only drawback is the short accessible range (not more than 2.5 nm) because the T_m of the TAM derivative is significantly reduced when the protein is attached on a solid support, even if it is still one order of magnitude more than for a nitroxide under the same conditions.

The second report[230] dealt with two synthetic platforms constituted of two FT derivatives or one TEMPO and one FT center linked to a central OPE rod, obtained by esterification of the trityl monocarboxylic acid **268** with the linker. As expected, X-band PELDOR measurements on the bis-FT compound proved difficult because of the strong pulse overlap, but DQC experiments gave an excellent SNR with pronounced modulations, even at 100 K where no spin echo could be observed for a bis-TEMPO. The distance was 4.9 nm, in accordance with calculations. Concerning the FT-TEMPO module, X-band PELDOR experiments led to a modulation depth of 90% when pumping on top of the narrow FT line. Orientation selection was present, so the time traces for 7 different offsets were summed to extract the distance. DQC measurements on this module led to the same distance (3.5 nm).

This study was extended to other bis-FT compounds with a shorter length.[308] It was shown that for these short distances (2 to 2.4 nm), the weak coupling approximation was not verified: the pseudo-secular term of the dipolar Hamiltonian must be taken into account. The point-dipole approximation was also no longer valid because the spin delocalization deeply affects the distance for such small lengths. However, accurate distances up to 2.5 nm can be extracted by X-band *cw*-EPR: this would be impossible with bis-TEMPO modules for such distances. DQC measurements on the short bis-FT compounds led to distances that were 0.3 nm shorter than the expected value determined from molecular mechanics. Including the pseudo-secular coupling improved the fit of the simulated DQC time trace to the experimental one, and taking into account the spin delocalization led to a nearly perfect fit.

PELDOR experiments were performed again on the small bis-FT compound, setting the pump pulse on top of the EPR spectrum and the detection pulses on the region of the ^{13}C satellites (15 MHz offset). Clear modulations were observed but with a poor SNR, even if the correct distance could be obtained by including the pseudo-secular and spin delocalization contributions. A similar setup was

used for the long bis-FT compound used in before[230], and this time clear modulations that led to the expected distance were observed. This shows that PELDOR on bis-FT compounds is feasible.

Finally, a recent paper[281] reported the first DQC measurement at room temperature, on a doubly FT-tagged DNA duplex where a 4.6 nm distance could be obtained. The triacyl chloride **266** was reacted with a piperazine moiety previously attached on the oligonucleotide strand. The spin-labeled duplex was adsorbed on an ion-exchange sorbent (NucleosilDMA). This procedure led to a two-fold improvement of the phase memory time T_m compared to Hubbell et al,[229] maybe because of the more rigid immobilization of the FT label, which explains the longer measurable distance range. DQC (80 and 310 K) and PELDOR (80 K) measurements (with detection on the ^{13}C satellite lines) led to comparable distances in the 4.5 – 4.6 nm range as well as similar distance distributions, in excellent agreement with molecular dynamics.

To conclude this part, we can mention TAM-TEMPO biradicals, which have been used for structural studies,[278] to simultaneously measure redox status and oxygenation[277] and to measure thiol concentration.[280]

2. TOWARDS TAM/PTM – Mn^{II}-DOTA MODEL SYSTEMS

The synthesis of modules that consist of a trityl radical connected to a DOTA moiety would open the way to very high-sensitivity PELDOR measurements. By combining the narrow line of a PTM or a TAM moiety with the narrow sextet of Mn^{II}-DOTA, one could imagine different possibilities where the pump pulse could be set on top of the trityl spectrum and the detection pulses on the Mn^{II}-DOTA EPR lines, or vice versa. Such a system would be more efficient than a bis-trityl compound, because detecting on the ^{13}C satellite lines, which are very weak, greatly lowers the SNR, reducing the potential of trityl spin labels for PELDOR measurements. A trityl-Mn^{II}-DOTA platform would give a much higher modulation depth, resulting in high sensitivity. Noteworthy, as the EPR linewidth of PTMTE is about five times larger than FT at X-band, we can anticipate that PELDOR measurements with PTM derivatives would be more efficient because the pulse overlap would be reduced.

2.1 Synthesis of PTMTE and PTMTC

To obtain modules that consist in a trityl radical connected to a DOTA moiety, a first step is to synthesize the trityl part. TAM derivatives have already been studied as described above, but their multi-step synthesis is long and difficult, as it can be inferred from the numerous reports dealing with it.[274,275,276] We decided to tackle to the synthesis of H_3PTMTC **244**, which have never been used for PELDOR purposes. A sample of the tricarboxylate potassium salt of FT was kindly provided by Yun Xu-Li (Collège de France).

In order to obtain both the PTMTE **246** and the H_3PTMTC **244** radicals in one unique pathway, we surmised that the latter could be obtained by saponification of the triester. Using a literature procedure[238], the triple Friedel-Crafts alkylation between chloroform and 1,2,4,5-tetrachlorobenzene **240** in a high-pressure tube gave dodeca-chlorinated intermediate **241** in modest yield. In our hands,

the purification proved very tedious. Even a lengthy column chromatography using kilogram amounts of SiO_2 was not able to totally separate tetrachlorobenzene from the product owing to their similar migration. However, we found that washing the product repeatedly with pentane after column chromatography gave pure **241** in a reasonable 37% yield on gram scale (Scheme 88).

Lithiation with *n*-BuLi followed by addition of ethyl chloroformate afforded intermediate **245** in good yield. A scale-up of this step proved inefficient, affording a mixture of unreacted **241** and mono-, di- and triaddition products. Generation of the corresponding anion using NaOH followed by iodine oxidation afforded PTMTE **246** radical as a red solid, again in good yield (Scheme 88).[234]

The last hydrolysis step proved more difficult than anticipated, as the common saponification conditions (LiOH, THF/H_2O) only afforded the desired product at a very slow rate (two weeks). Replacing LiOH with NaOH or KOH did not improve the saponification rate. The problem was solved by using refluxing methanolic potash, affording the desired radical H_3PTMTC **244** in good yield after two days (Scheme 88).

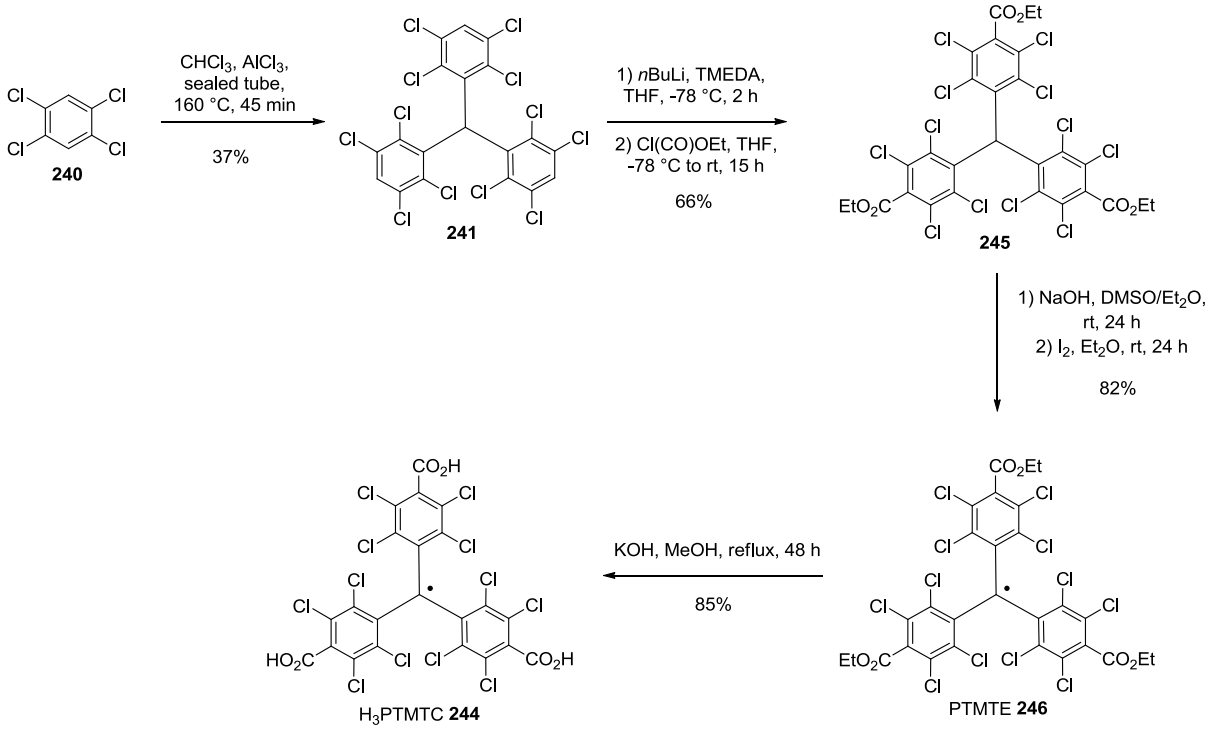

Scheme 88: Synthesis of PTMTE **246** and H_3PTMTC **244**

Red crystals of PTMTE **246** suitable for X-ray diffraction were grown by slow evaporation from a chloroform/methanol solution. This compound crystallizes in the P-1 space group (triclinic system), with an asymmetric unit constituted of four PTMTE molecules. The three aromatic rings are twisted from each other in a so-called propeller conformation, which is expected owing to the very important steric constraints imposed by the chlorine substituents. The packing is structured by halogen bonds (mean distance of 3 Å) between chlorine atoms and the oxygen from the keto group of the ester moiety (Figure 128).

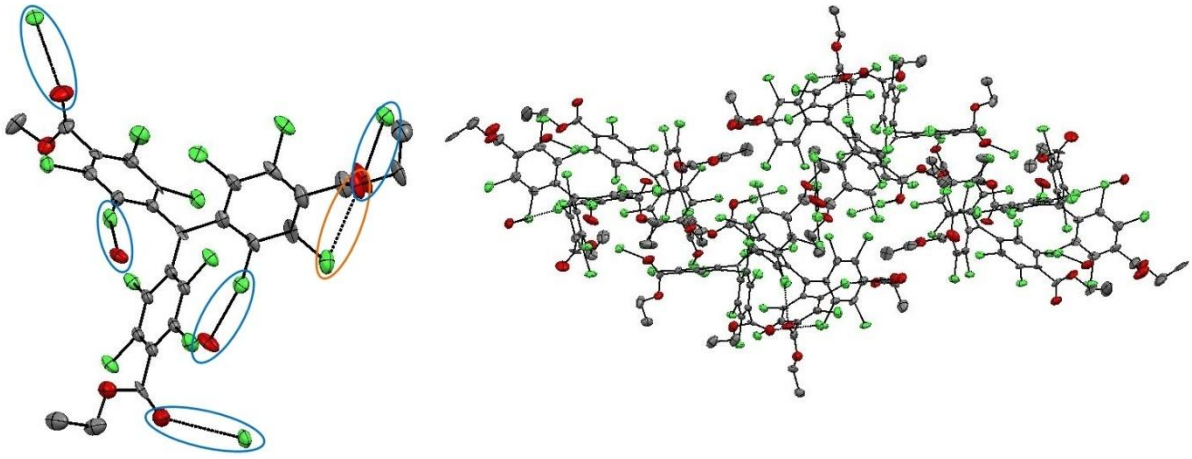

Figure 128: ORTEP drawings of PTMTE **246**. Hydrogen atoms have been omitted for clarity. Left: structure of one of the molecule of the asymmetric unit showing intermolecular (blue) and intramolecular (orange) halogen bonds, right: view of the packing

2.2 Attempted couplings of PTM and TAM radicals

Different strategies were envisioned to couple PTM and TAM derivatives on the rigid OPE and phenyl-piperazine linkers synthesized in Chapter I. As trityl radicals are available in small quantities, and as a mono-coupling is anticipated to be difficult owing to the low yields often described in the literature (pp. 186 – 189), the grafting of a PTM and TAM derivatives should be the last synthetic step.

The first attempts were performed with H_3PTMTC **244** and compounds **228**, **233** or **229** (after Boc cleavage using TFA[278]) (Schemes 76 and 78, pp. 144 and 146) using literature methodologies (BOP/HOBt).[229,277,278,279,280] Under these conditions, no product could be detected with HPLC. A reason could be the poor reactivity induced by the shielding of the numerous chloro groups. FT was reacted with **233** in the same conditions but this attempt was also unsuccessful. To enhance the reactivity of the trityl radical, the triacyl chloride **266** was generated from FT[281] and reacted with **233**, but again the expected product could not be isolated (Scheme 89).

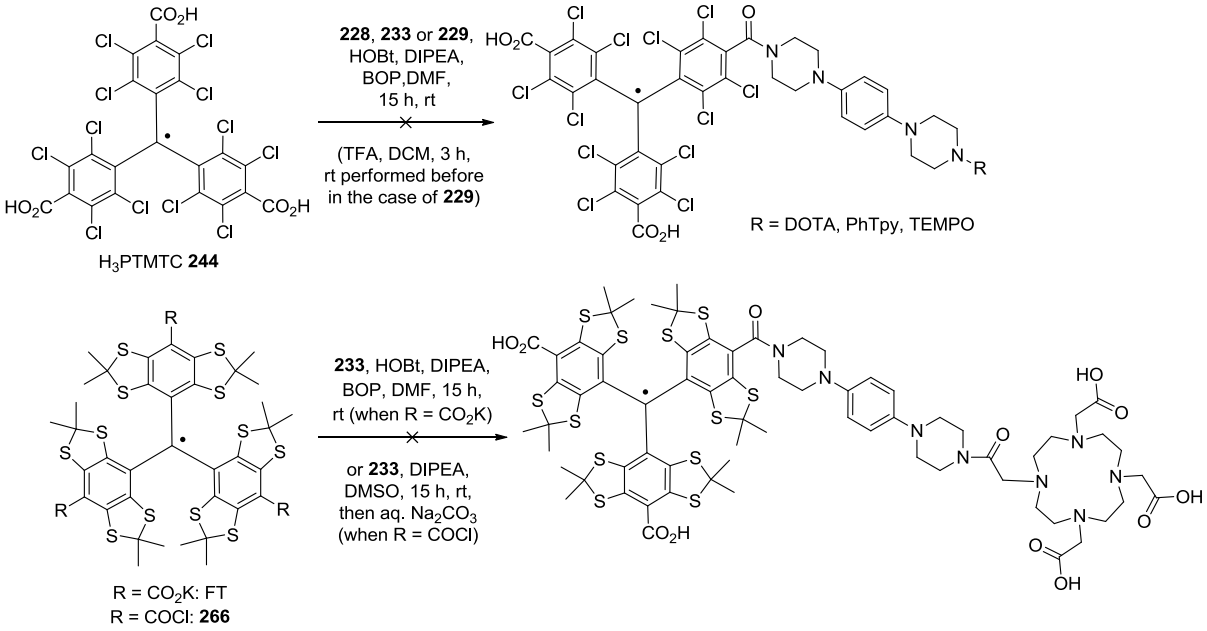

Scheme 89: Attempted couplings of H_3PTMTC **244** and FT on **228**, **233** or the amine of **229**

These couplings are still underway, and numerous other methods could be envisioned, for instance using the monofunctionalized PTM or TAM derivatives mentioned above (pp. 184 – 189). In the meantime, we moved toward in-depth structural studies of these two classes of radicals, as we became interested in the relationship between their structure and their specific applications.

3. ACCURATE MEASUREMENT OF THE *G*-ANISOTROPY OF SUBSTITUTED TRITYL RADICALS

As shown in the first part of this chapter, many of the numerous applications of PTM and TAM radicals are related to their narrower linewidths compared to other organic radicals, meaning that trityl radicals often have low *g*-anisotropies. The spectral resolution over *g*-values is proportional to the frequency, so the use of *cw*-HFEPR is particularly useful to accurately determine the *g*-tensors of persistent trityl radicals. Only a handful of studies on PTMs and TAMs have been performed at high field (*i.e.* above 95 GHz), for purely structural purposes[297] or to understand their efficiency as DNP agents.[267,288] We were interested in carrying out the accurate measurement of the *g*-tensors of FT, its protonated form H_3FT **263**, PTMTC, its protonated form H_3PTMTC **244**, and PTMTE **246** (see Figure 145) using J-band *cw*-HFEPR, as most of the studies involving EPR experiments on trityl radicals have been performed at fields below 95 GHz. The accuracy of the measurements is essential as PTM and TAM radicals display similar g_{iso} values. The results we obtained indicated that, despite their structural similarities, the PTM and the TAM families display very different electronic properties. This observation was supported by DFT calculations, which showed that TAM radicals do not behave like classical π radicals. These findings could lead to a better understanding of the exact role of the electronic structure of trityl radicals in numerous active domains.

3.1 Design of the experimental setup

To accurately measure *g*-tensors, we decided to use the *cw*-HFEPR spectrum of Mn^{II} as a reference. The EPR spectra are more resolved at a high frequency of 285 GHz. The use of Mn^{II} as a "field ruler" is justified by the fact that its six hyperfine transitions spanning over 500 G provide six data points to estimate the error on the measurement. The *g*-value of a Mn^{II} powder sample (0.02% in MgO) has been measured with high precision at X-band using a NMR gaussmeter and a microwave frequency counter[309] and was found to be equal to 2.00101 ± 0.00005. The cavity-less design of the 285 GHz spectrometer we used, offering high sample volume, allows the introduction of the Mn^{II} field standard coaxially with the sample[28]. Another advantage is the high performance of the magnet: the uncertainty of the measurements was determined to be about 0.9 G or 0.00008 in *g*.

It would have been possible to directly use Mn^{II} as a reference, but because its six hyperfine transitions are superimposed on the spectrum of the trityl radicals (Figure 129), a more convenient method is to use Gd^{III} as a second reference as its unresolved hyperfine transition is far from the transitions of trityl radicals.

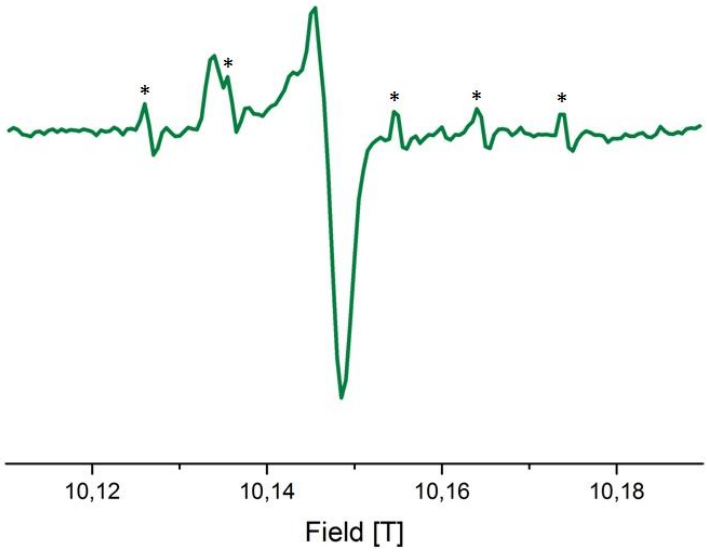

Figure 129: J-band *cw*-HFEPR spectrum of H_3PTMTC (20 mM in 2-Me-THF) superposing Mn^{II} (from 2 µM $MnCl_2$ in 8:2 H_2O/glycerol) at 8 K. Asterisks denote Mn^{II} peaks

Accordingly, the experimental setup consists of an Eppendorf tube coaxially mounted within a PET cryotube. A $GdCl_3$ solution in 9:1 H_2O/glycerol was added to the Eppendorf tube, while the cryotube contained either a $MnCl_2$ solution in 8:2 H_2O/glycerol or the trityl radical samples. This two-tubes setup was loaded with Mn^{II} and Gd^{III}, and using Mn^{II} as a *g*-standard (g = 2.00101), the g_{iso} of $GdCl_3$ was precisely measured (g_{iso} = 1.99128). The reference spectra obtained this way display both the Mn^{II} six-lines and the Gd^{III} single-line. Then Mn^{II} was replaced by the sample of interest. Aligning the Gd^{III} line of the spectrum obtained on the Gd^{III} line of the reference spectrum allowed direct reading of the *g*-values of the trityl radicals (Figure 130).

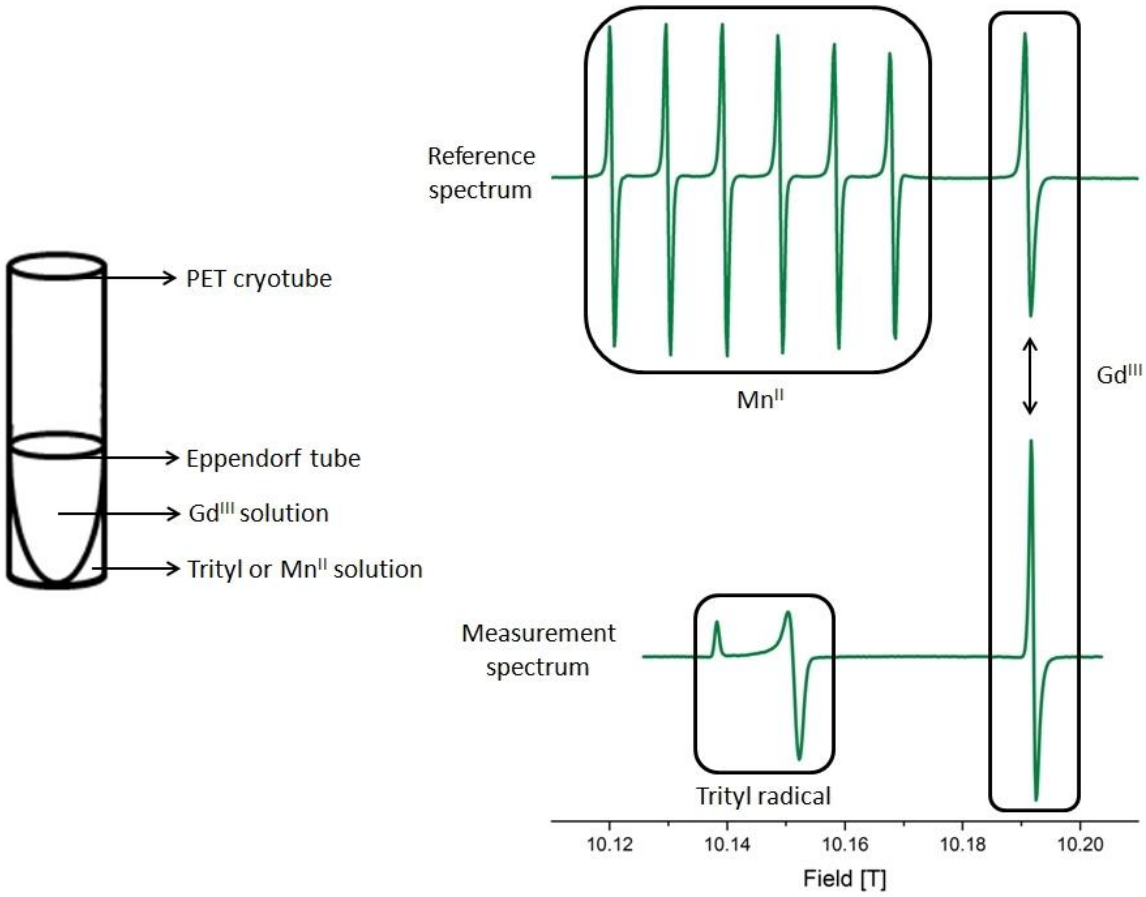

Figure 130: Process for the accurate measurement of *g*-tensors. Left: scheme of the experimental setup showing the two-tubes assembly, right: example of *g*-tensor measurement showing the reference spectrum (top) and the measurement spectrum in the case of PTMTE **246** (bottom). See experimental part for details

3.2 Results and discussion

The J-band *cw*-HFEPR spectra of FT, H_3FT **263**, PTMTC, H_3PTMTC **244** and PTMTE **246** have been recorded and calibrated using the method described above (Figure 131).

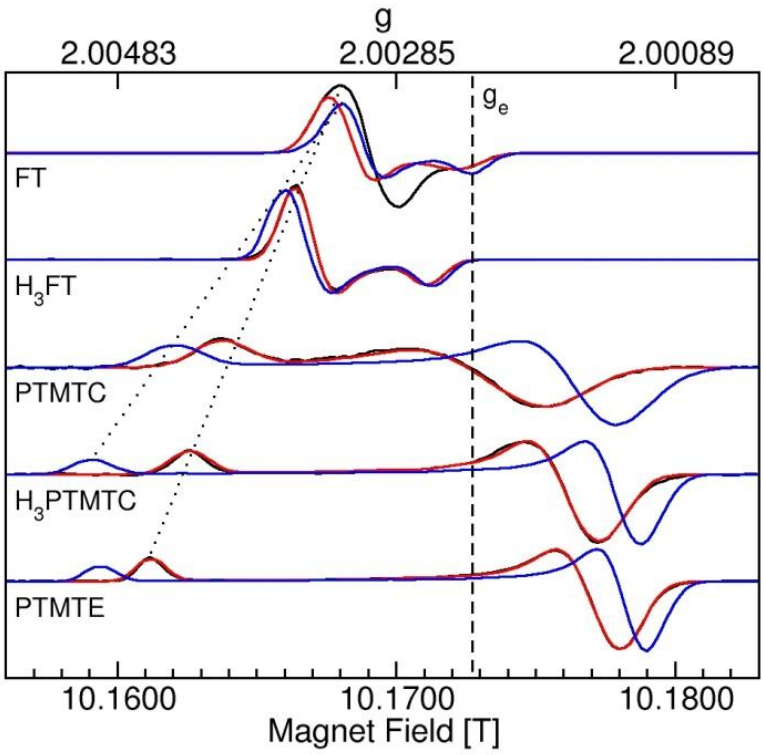

Figure 131: Calibrated J-band cw-HFEPR spectra of FT, H_3FT **263**, PTMTC, H_3PTMTC **244**, and PTMTE **246**. Experimental spectra are in black, fitted spectra are in red and DFT simulations are in blue. Dotted black lines are guides for the eyes. See experimental part for details

As shown in Figure 131, the *g*-anisotropy was resolved for all spectra, showing the striking difference with the X-band spectra depicted in Figure 127: at 285 GHz, trityl radicals cannot be considered as species displaying a sharp single EPR line. This increase in spectral resolution with magnetic field can be compared with the broadening of the EPR lineshape of TEMPO derivatives. This also shows that the use of high fields could be beneficial for PELDOR measurements on bis-trityl modules, as their broader but still narrow linewidth would reduce pulse overlap. The experimental spectra displayed in Figure 131 were fitted using a model that assumed Gaussian distributions for the *g*-values,[131] which was able to account for all the spectral features, with the exception of FT (see black and red lines). A summary of the obtained *g*-values using the convention $g_x \geq g_y \geq g_z$ is presented in Table 6.

Table 6: Experimental and calculated *g*-tensors of PTM and TAM radicals

Radical	g_x	g_y	g_z	g_{iso}	g_x-g_z
Gomberg's trityl					
calculated	2.00243	2.00243	2.00208	2.00231	0.00035
FT					
measured	2.00339 (0.00006)	2.00301 (0.00008)	2.00233 (0.00012)	2.00291	0.00106
calculated	2.00320	2.00309	2.00228	2.00286	0.00092
H_3FT **263**					
measured	2.00358 (0.00002)	2.00340 (0.00004)	2.00262 (0.00004)	2.00320	0.00096
calculated	2.00367	2.00344	2.00259	2.00323	0.00108
PTMTC					
measured	2.00410 (0.00001)	2.00236 (0.00026)	2.00176 (0.00021)	2.00274	0.00234
calculated:	2.00443	2.00149	2.00148	2.00247	0.00295
H_3PTMTC **244**					
measured	2.00429 (0.00004)	2.00168 (0.00011)	2.00132 (0.00011)	2.00243	0.00297
calculated	2.00498	2.00120	2.00116	2.00245	0.00382
PTMTE **246**					
measured	2.00458 (0.00001)	2.00156 (0.00011)	2.00125 (0.00010)	2.00246	0.00333
calculated	2.00494	2.00122	2.00117	2.00244	0.00377

For the spectrum of 1 mM 9:1 H_2O/glycerol solution of FT the model was used to fit the high and low field edges of the spectrum. Subtraction of the fit from the experimental spectrum gave a trace where the *g*-anisotropy was poorly resolved (Figure 132, green trace). One possible explanation for the multiple spectral contributions was the presence of aggregates in the sample due to the lipophilicity of the molecule. This was supported by the spectrum of a 1 mM aqueous solution of FT (Figure 132), where in this more polar solvent that would favor aggregation, was also poorly resolved and resembled the unresolved component of the first spectrum.

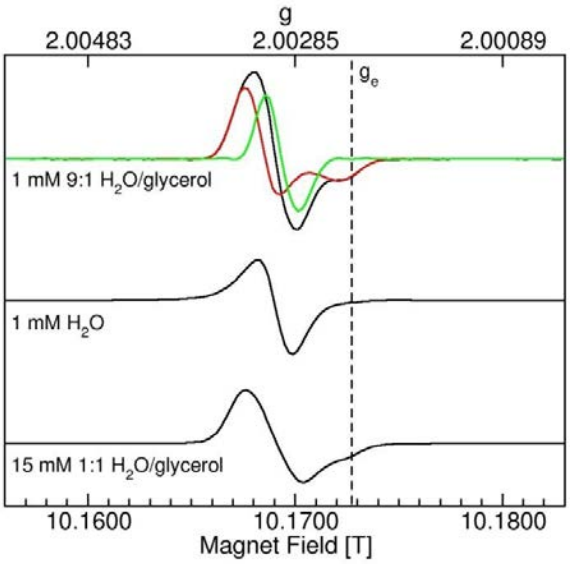

Figure 132: J-band *cw*-HFEPR spectra of FT in different conditions. Top: experimental (black), and fitted (red) spectra of FT in 9:1 H_2O/glycerol, and subtraction of the fit from the experimental (green). Middle: spectrum of FT in aqueous solution (without glycerol). Bottom: spectrum of FT in typical DNP conditions[288] (15 mM 1:1 H_2O/glycerol solution)

Under typical DNP sample conditions (Merritt *et al.*[288]), the spectrum of FT also appeared to contain an unresolved aggregation component. The *g*-tensor observed in this sample was similar to that which was reported for a FT derivative, OX63, obtained at 239.2 GHz under the same sample conditions (Table 7).[288]

Table 7: Comparison of the *g*-tensors of FT and OX63 in typical DNP conditions

Radical	g_x	g_y	g_z	g_{iso}	g_x-g_z	Reference
FT						
J-band, 15 mM, 1:1 H_2O/glycerol	2.00327 (0.00001)	2.00301 (0.00015)	2.00266 (0.00027)	2.00298	0.00061	this work
J-band, 1 mM, H_2O	2.00331	2.00298	2.00287	2.00305	0.00044	this work
OX63						
pulsed EPR, 239.2 GHz, 15 mM, 1:1 H_2O/glycerol	2.00319(3)	2.00319(3)	2.00258(3)	2.00299	0.00061	Merritt *et al.*

For the TAM radicals the g_y values were closer to the g_x values, and the *g*-tensor was above the free electron *g*-value (g_e = 2.00232), while for the PTM radicals the g_y values were instead closer to the g_z values, and the *g*-tensor straddled g_e. Also the TAM radicals were found to be less anisotropic than the PTM radicals, where the g_z is always below g_e, contrary to FT. These trends were consistent with those reported in the literature (Table 8).[267,288,297]

Table 8: Comparison of the g-tensors of PTM and TAM radicals determined in this work with literature data (Goldfarb *et al*,[267] Merritt *et al*,[288] Eaton *et al*[297])

Radical	g_x	g_y	g_z	g_{iso}	g_x-g_z	Reference
Gomberg's trityl						
calculated	2.00243	2.00243	2.00208	2.00231	0.00035	this work
FT						
J-band, 1 mM, 9:1 H_2O/glycerol	2.00339 (0.00006)	2.00301 (0.00008)	2.00233 (0.00012)	2.00291	0.00106	this work
calculated	2.00320	2.00309	2.00228	2.00286	0.00092	this work
cw-EPR, 94 GHz, 200 mM, 1:1 H_2O/glycerol	2.0030	2.0027	2.0021	2.0026	0.00090	Eaton *et al.*
H_3FT **263**						
J-band, 1 mM, 2-Me-THF	2.00358 (0.00002)	2.00340 (0.00004)	2.00262 (0.00004)	2.00320	0.00096	this work
calculated	2.00367	2.00344	2.00259	2.00323	0.00108	this work
OX63						
cw-EPR, 94 GHz, 200 mM, 1:1 H_2O/glycerol	2.0031	2.0027	2.0022	2.0027	0.0009	Eaton *et al.*
pulsed EPR, 239.2 GHz, 15 mM, 1:1 H_2O/glycerol	2.00319(3)	2.00319(3)	2.00258(3)	2.00299	0.00061	Merritt *et al.*
PTMTC						
J-band, 1 mM, 9:1 H_2O/glycerol	2.00410 (0.00001)	2.00236 (0.00026)	2.00176 (0.00021)	2.00274	0.00234	this work
calculated	2.00443	2.00149	2.00148	2.00247	0.00295	this work
pulsed EPR, 95 GHz, 15 mM, 1:1 H_2O/DMSO	2.00271	2.00005	2.00005	2.00094	0.00266	Goldfarb *et al.*
H_3PTMTC **244**						
J-band, 1 mM, 2-Me-THF	2.00429 (0.00004)	2.00168 (0.00011)	2.00132 (0.00011)	2.00243	0.00297	this work
calculated	2.00498	2.00120	2.00116	2.00245	0.00382	this work
PTMTE **246**						
J-band, 1 mM, 2-Me-THF	2.00458 (0.00001)	2.00156 (0.00011)	2.00125 (0.00010)	2.00246	0.00333	this work
calculated	2.00494	2.00122	2.00117	2.00244	0.00377	this work
pulsed EPR, 95 GHz, 15 mM, 1:1 H_2O/DMSO	2.00415	2.00121	2.00121	2.00219	0.00294	Goldfarb *et al.*

For both TAM and PTM radicals the g_x values were higher upon protonation of the carboxylate groups. This suggests that the *g*-anisotropy is sensitive to the nature of the substituent in *para* position even for a slight change, which can only be detected using HFEPR.

At first glance, we expected the FT and PTM radicals to display similar properties owing to their structural resemblance, but as shown in Figure 131 and Table 6, their electronic properties are very different. We investigated the nature of these differences by performing DFT calculations (B3LYP/6-31G*). The molecular structures of the radicals as determined by DFT calculations were in agreement with the X-ray crystallographic structural determination of PTMTE **246** and those that have been reported in the literature[239,285] (Table 9). The DFT-calculated EPR spectra do not perfectly fit the experimental ones, but the trend in the shift of g_x toward low field was reproduced.

Table 9: Comparison of distances (in Å) and dihedral angles (in °) between X-ray structures and DFT calculations for PTM and TAM radicals. X-ray diffraction data for H_3PTMTC **246** are from Veciana *et al,*[239] and X-ray diffraction data from the trimethylester of FT are from Zweier *et al*.[285]

H_3PTMTC **246**	Central C-C	C-Cl ortho	C-Cl meta	C-C ortho	C-C meta	C-C para	Distal C-C	C=O	C-O	O-H	Dihedral angle
X-ray	1.473	1.724	1.718	1.407	1.395	1.396	1.502	1.237	1.288	0.966	83.1
DFT	1.481	1.741	1.742	1.419	1.401	1.397	1.510	1.208	1.347	0.974	81.9
PTMTE **244**	Central C-C	C-Cl ortho	C-Cl meta	C-C ortho	C-C meta	C-C para	Distal C-C	C=O	C-O	O-C	Dihedral angle
X-ray	1.474	1.724	1.728	1.416	1.395	1.391	1.515	1.200	1.322	1.467	81.2
DFT	1.481	1.742	1.744	1.419	1.403	1.398	1.512	1.210	1.339	1.446	81.9
FT triMe ester	Central C-C	C-S ortho	C-S meta	C-C ortho	C-C meta	C-C para	Distal C-C	C=O	C-O		Dihedral angle
X-ray	1.449	1.758	1.767	1.417	1.395	1.407	1.480	1.207	1.335		76.1
DFT (H_3FT)	1.473	1.776	1.777	1.422	1.406	1.414	1.480	1.219	1.355		76.7

To account for this trend, we analyzed the HOMO orbitals of each trityl radical (Figure 133). Despite the structural similarity of PTM and FT, as it can be inferred from Figure 127 (p. 182), striking differences can be pointed out. The picture is very regular for PTM, with a standard alternating bonding-antibonding orbitals, but the situation is more complex for FT, with noticeable density on the sulfur atoms compared to the chlorine moieties of PTM. This suggests that PTM is behaving more like a classic π- radical (like the glycyl radical for instance) than FT, which is confirmed by the fact that its g_z value is below g_e.

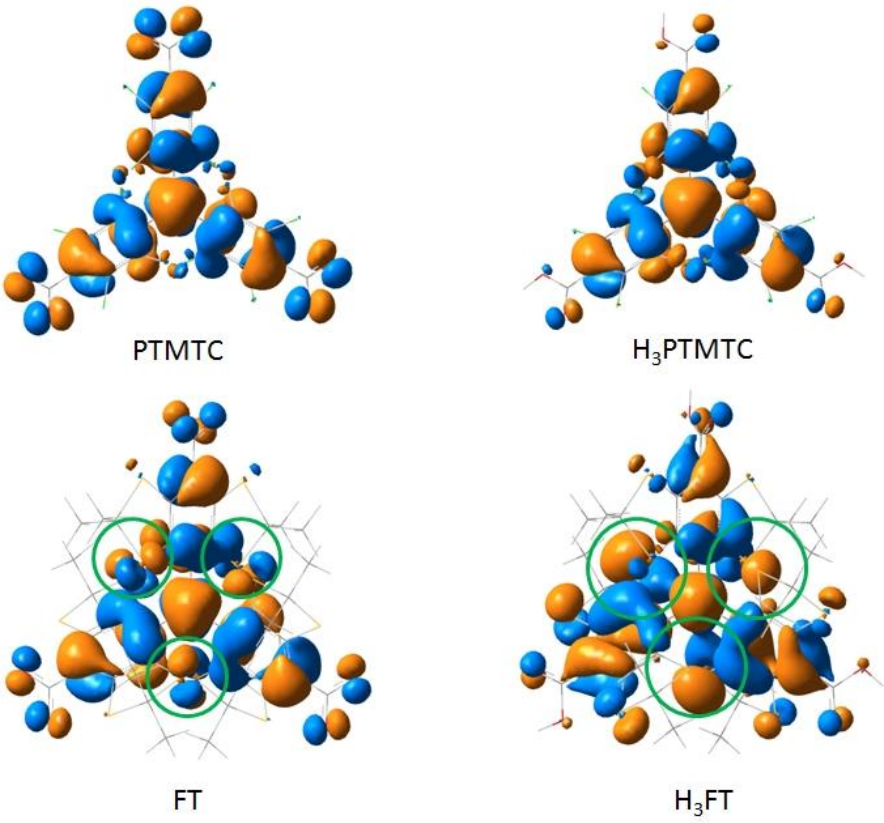

Figure 133: HOMO orbitals of trityl radicals. Density on sulfur atoms is indicated by green circles

The protonation-induced shift of *g*-values implies that the carboxyl group is involved in the delocalization, which can also be seen from Figure 131. It is worth noting that the spin density on the central carbon stays nearly unaffected (0.64 for FT, 0.78-0.80 for PTM). Nevertheless, this small difference can be rationalized by comparing the ^{13}C chemical shifts of the C-S (135.7 ppm)[275] and C-Cl (131.7 ppm) bonds of the aromatic rings of FT and PTM, respectively: this means that the S atom is more electron-withdrawing than the Cl atom on these systems, so the unpaired electron is more delocalized on FT than on PTM, implying less spin density on FT than on PTM. However, this does not explain the extra shift observed for PTMTE as the HOMO orbitals are identical. More investigations are ongoing to better understand the exact differences between the PTM and the TAM radicals.

CONCLUSION

In this chapter, we have studied two classes of persistent substituted trityl radicals: PTMs and TAMs. We synthesized a tricarboxylic derivative of PTM and attempted its coupling with rigid linkers. The coupling of a tricarboxylic derivative of TAM (FT) was also attempted: these reactions are still underway. We also accurately measured the *g*-tensors of five trityl derivatives. Despite the structural similarities between PTMs and TAMs, their electronic properties appeared to be very different. Analysis of the DFT calculations are in progress to better understand this difference, which could be linked to the fact that FT cannot be considered as a classical π radical.

General conclusion and perspectives

Through this work, nanometric distance measurements between high-spin Mn^{II} centers using high-field PELDOR have been explored. Our working hypothesis was that the sensitivity of PELDOR measurements using high-spin metal complexes could be improved by using complexes with narrow EPR lines, meaning that their ZFS parameters must be as low as possible. In a first chapter, we developed an approach based on the screening of selected ligands with a symmetric coordination sphere, which should generate sharp hyperfine transitions in the corresponding Mn^{II} complexes. This procedure led to the identification of DOTA as a very promising candidate. In the meantime, a set of linkers covering the 1.5 – 5.5 nm range was synthesized and attractive ligands were grafted on them using various methodologies to generate a set of "Mn standards" with various Mn-Mn distances. In the second chapter, PELDOR measurements were performed on these platforms. The Mn-Mn could be reliably and accurately extracted, provided that it is not too short, and the interplay between the pseudo-secular interaction and the ZFS parameters of Mn^{II}-DOTA was analyzed in details. In the third chapter, persistent trityl radicals were studied using *cw*-HFEPR and DFT calculations were performed to understand the relationship between their structure and their electronic properties.

In a more general context, this work led to the development of synthetic methodologies that can be used to quickly assemble long and stiff molecular rods, for example the OPE linkers that are used in many domains. A new molecular rod, the phenyl-piperazine linker, was also designed: preliminary MD simulations tend to show that it is very stiff, and it would be interesting to find an efficient elongation methodology, by using more sophisticated catalysts for C-N bond formation for instance, as non-conjugated linear nanowires are not very common. A new pyridine-based ligand, PyMDPDA, was developed and it could be interesting to study its properties and coordination with other metals. Related ligands grafted with an extended aromatic moiety could be efficient probes to detect cations by fluorescence. The platforms that were synthesized could be employed as construction elements in the design of supramolecular assemblies. Finally, the high-field EPR study of PTM and TAM radicals suggested that the latter displays unique electronic properties. This investigation is of major importance as TAMs are widely employed.

The ligand screening procedure showed that the relationship between the ZFS parameters and the coordination sphere of a metal complex appears to be poorly understood, even if the symmetry plays a major role. The exceptional narrowness of the hyperfine sextet of Mn^{II}-DOTA cannot be clearly rationalized. It could be linked to the 8-coordination of Mn^{II}-DOTA in solution: this has been suggested by both *cw*-HFEPR and PELDOR experiments. It would be interesting to record the EPR spectra of other 8-coordinated Mn^{II} complexes (like DOTA derivatives including pyridyl or pyrazyl moieties instead of carboxylate groups) to see if the EPR signal is still sharp.

The sensitivity of Mn-Mn PELDOR distance measurements was improved using Mn-DOTA as a spin label, showing that high-spin Mn^{II} complexes with low *D*-values are efficient and promising. This paves the way to biological applications: proteins incorporating a native Mn^{II} center could be tagged with a Mn^{II}-DOTA center or a trityl radical and the interspin distance would be measured by PELDOR with excellent sensitivity. As these paramagnetic centers tolerate the reducing environment of a cell,

in vivo applications would be possible. Besides trityl-Mn^{II}-DOTA platforms, we can also envision multi-spin systems, for instance star-shaped objects with a central trityl core and three Mn^{II}-DOTA complexes, to see if the trityl-trityl and the trityl-DOTA distances can be independently measured. Systems with Mn^{II} complexes with higher ZFS parameters, or including two different Mn^{II} complexes with different ZFS parameters, or including a Mn^{II} complex and a Gd^{III} complex, could be worth trying, as recent results using Gd^{III} complexes suggested that bigger ZFS parameters could be beneficial for short distance measurements.

It would be also very interesting to definitely assess the precise contribution of the pseudo-secular interaction for the high-spin Mn-Mn or Gd-Gd systems. Additional features in the distance distribution profiles, such as shorter components, ghost peaks or broadened distributions show that the kernel in DeerAnalysis is not always adapted for these systems. A future version that would take into account the pseudo-secular interaction would be highly desirable. Moreover, the pseudo-secular interaction appears to increase the broadening of the distance distribution much more for Gd^{III} than for Mn^{II} in the case of DOTA, a finding that have not been rationalized yet. Comparing the advantages and drawbacks of all spin labels that are known at the moment (radicals like nitroxides or trityls and high-spin Gd^{III} or Mn^{II} complexes) would be very useful to select the optimal tool for PELDOR-based investigations of biological systems.

Annexes

1. GLASSING AGENTS

Glassing Agents		
Pure Substance		
3-methylpentane	sulfuric acid	sugar (.4 M sucrose)
methylcyclopentane	phosphoric acid	triethanolamine
paraffin oil (Nujol)	ethanol	2-methyltetrahydrofuan
isopentane	isopropanol	di-n-propyl ether
methylcyclohexane	1-propanol	decalin
isooctane	1-butanol	triacetin
boric acid	glycerol	toluene
Mixtures		
Components		*Ratio A:B:C...*
hydrocarbon		
3-methylpentane/isopentane		1:1
isopentane/methylcyclohexane		1:6
methylcyclopentane/methylcyclohexane		1:1
3-methylpentane/isopentane		1:2
alcohol		
ethanol/methanol		4:1, 5:2, 1:9
isopropanol/isopentane		3:7
ethanol/ispopentane/diethyl ether		2:5:5
isopentane/n-butanol		7:3
isopentane/isopropanol		8:2
diethyl ether/isooctane/isopropanol (or ethanol)		3:3:1
diethyl ether/isopropanol (or ethanol)		3:1
diethyl ether/toluene/ethanol		2:1:1
butanol/diethyl ether		2:5
aromatic		
toluene/methylene chloride		1:1 or excess toluene
toluene/acetone		1:1 or excess toluene
toluene/EtOH or MeOH		1:1 or excess toluene
toluene/acetonitrile		1:1 or excess toluene
toluene/chloroform		1:1 or excess toluene
water		
water/propylene glycol		1:1
water/glycerol		4:1 to 1:4
water/(poly)ethylene glycol		4:1 to 1:4

*Adapted from: Drago, R. S. Physical methods for chemists; 2nd ed.; Saunders College Pub: Ft. Worth, 1992.

2. PELDOR MEASUREMENT PROCESS

When the temperature is set to the measurement value (usually 10 K for Mn^{II} complexes or 40 K for bis-TEMPO platforms), the cavity was tuned and critically coupled. A Hahn echo sequence was used and the magnetic field position, the *mw* pulses duration and the attenuator level were adjusted to maximize the spin echo intensity. The phase is then adjusted to maximize the signal in the real part. An ED-EPR spectrum can be acquired, by setting the π/2 and π-pulses durations, the time delay between them, the repetition time, and the sweep width.

For PELDOR experiments, the cavity was overcoupled. Nutation experiments were performed at the two frequencies to determine the respective length of the π-pulses. The relevant parameters were the pump π-pulse, the detection π/2 and π-pulses, their position and offset, and the repetition rate which are described in the main text.

3. DATA ANALYSIS

The data analysis process can be performed using DeerAnalysis[33], written by G. Jeschke (ETH Zürich) and running on MATLAB. The raw PELDOR data from the spectrometer can be directly read. Concerning the background subtraction (*i.e.* the extraction of the form factor), four parameters can be modified:

- The zero time must be set in the maximum of the first PELDOR decay. Usually it is very close from it and only need minor adjustment.
- The phase must be set to zero. This is the case where the imaginary part of the signal does not contain any oscillation. Usually, because of the phase cycling, this value is already close to zero.
- The cutoff excludes points at the end of the data set from analysis. It is useful when artifacts arising from the timing of gating pulses are present.
- The background is set after the last PELDOR oscillation to select only the portion of the signal that decays due to intermolecular interaction.

Either the time-domain or the frequency-domain can be displayed to assess the reliability of the fit. The number of dimensions can be set (usually to 3), as well as the background decay model (usually exponential, or linear when the background is very steep).

The Tikhonov regularization is then performed. An important value is the regularization parameter (RP). The optimal RP is at the corner of the L-curve which is generated with the Tikhonov regularization. Other models (Gaussian or double Gaussian fits) can also be employed but great care must be taken concerning the interpretation of the results. It must be emphasized that the data analysis is a crucial step and deeply affects the shape of the distance distribution.

4. FINAL PRODUCTS

Bis-Mn^{II}-bis(terpyridine)s

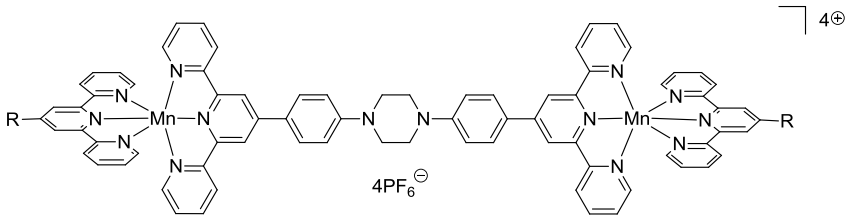

R = H: Bis-(Tpy)Mn^{II}(PhTpy)-Pip **143**
R = Cl: Bis-(*p*ClTpy)Mn^{II}(PhTpy)-Pip **144**

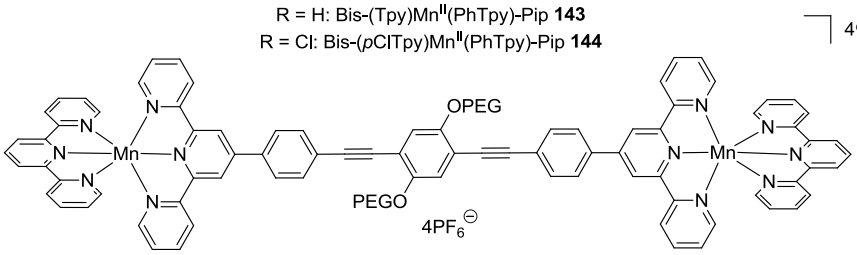

Bis-(Tpy)Mn^{II}(PhTpy)-CC$_2$Ph(OPEG)$_2$ **174**

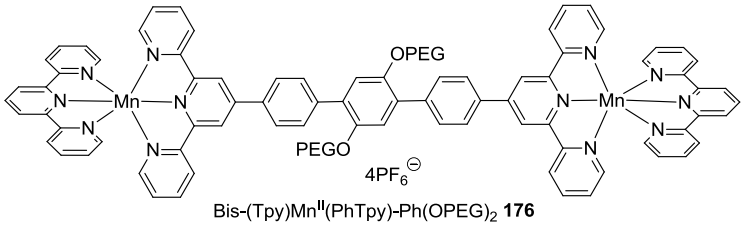

Bis-(Tpy)Mn^{II}(PhTpy)-Ph(OPEG)$_2$ **176**

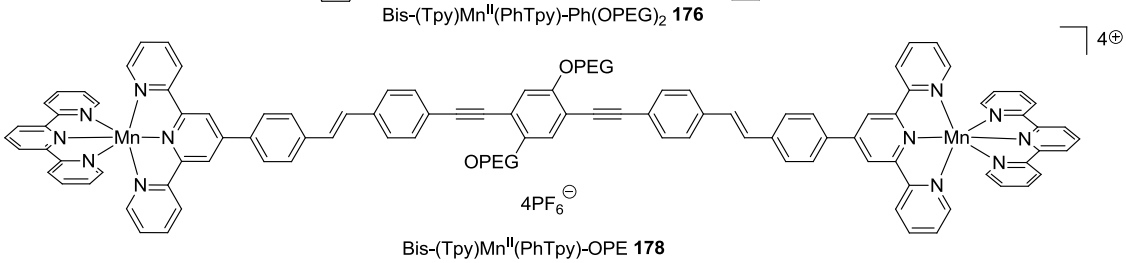

Bis-(Tpy)Mn^{II}(PhTpy)-OPE **178**

Bis-DPA and bis-PyMTA platforms

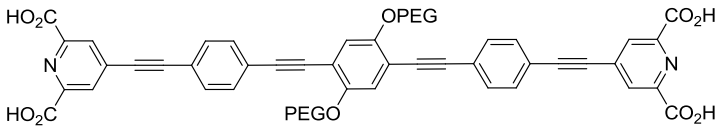

Bis-DPA-OPE**181**

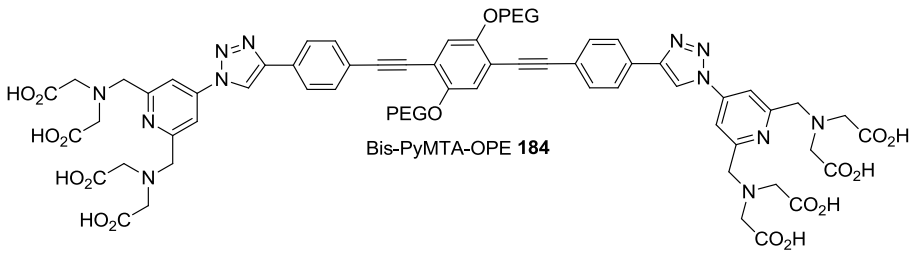

Bis-PyMTA-OPE **184**

Bis-DO3A and bis-DOTA platforms

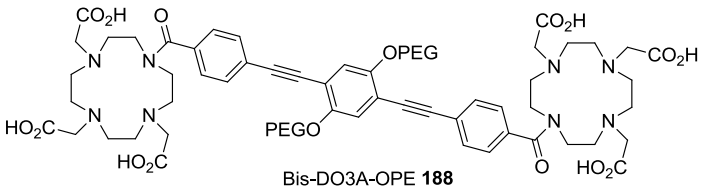

Bis-DO3A-OPE **188**

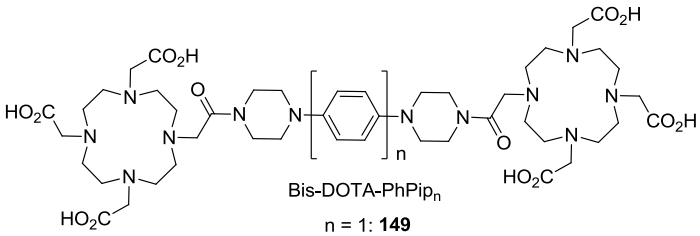

Bis-DOTA-PhPip$_n$

n = 1: **149**
n = 2: **150**

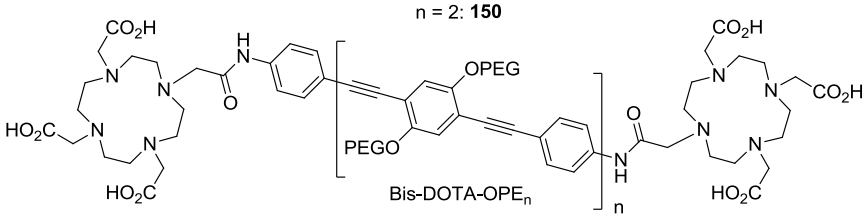

Bis-DOTA-OPE$_n$

n = 1: **202**
n = 2: **203**
n = 3: **204**

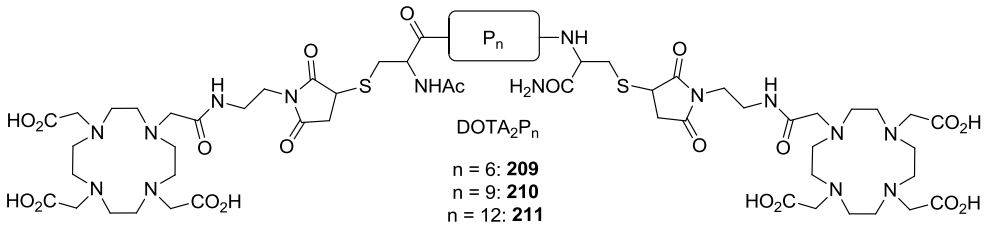

DOTA$_2$P$_n$

n = 6: **209**
n = 9: **210**
n = 12: **211**

Bis-TEMPO

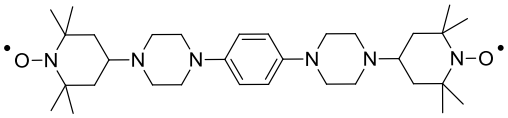

Bis-TEMPO **219**

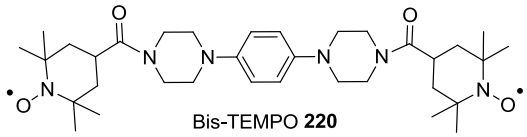

Bis-TEMPO **220**

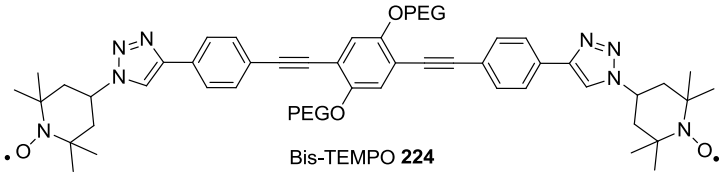

Bis-TEMPO **224**

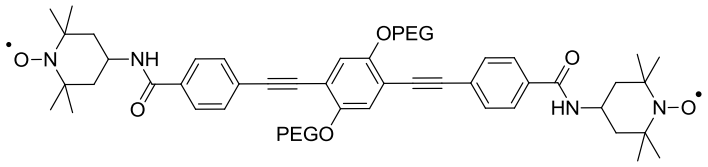

Bis-TEMPO-OPE **225**

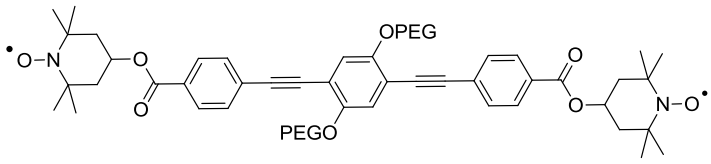

Bis-TEMPO **226**

Dissymmetric platforms

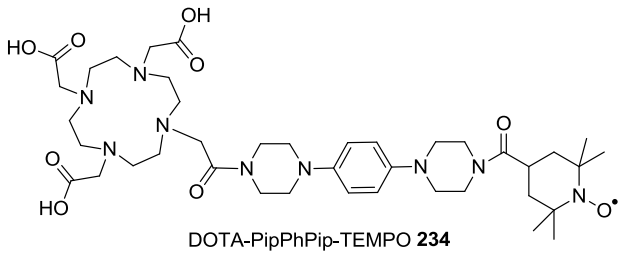

DOTA-PipPhPip-TEMPO **234**

PTM derivatives

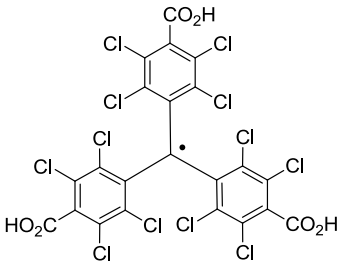

H_3PTMTC **244**

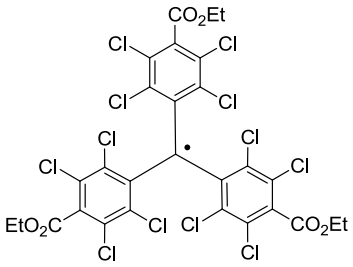

PTMTE **246**

5. LIST OF PUBLICATIONS

Accepted for publication

H. Y. Vincent Ching, Paul Demay-Drouhard, Hélène C. Bertrand, Clotilde Policar, Leandro C. Tabares and Sun Un, Nanometric distance measurements between Mn^{II}DOTA centers, *Phys. Chem. Chem. Phys.* **2015**, *17*, 23368–23377.

In preparation

PELDOR measurements with rigid bis-DOTA platforms

Paul Demay-Drouhard, H. Y. Vincent Ching, Hélène C. Bertrand, Yun Xu-Li, Régis Guillot, Clotilde Policar and Sun Un, High-field EPR study of persistent trityl radicals

Experimental part

1. SYNTHESIS

NMR: ^{1}H and ^{1}3C NMR spectra were recorded on a Bruker Avance 300 or 600 (300 or 400 MHz) spectrometer at Ecole Normale Supérieure (ENS) in the Laboratoire des Biomolécules (LBM, UMR 7203) or at UPMC (Université Pierre et Marie Curie) in IPCM (Institut Parisien de Chimie Moléculaire, UMR 7201), using solvent residuals as internal references.[310] The following abbreviations are used: singlet (s), doublet (d), doublet of doublets (dd), doublet of doublets of doublets (ddd), triplet (t), triplet of doublets (td), doublet of triplets (dt), triplet of triplets (tt), quadruplet (q), quadruplet of doublets (qd), doublet of quadruplets (dq), doublet of quadruplets of doublets (dqd), heptuplet (hept), multiplet (m) and broad (br). δ indicates chemical shifts in parts per million (ppm), and *J* are coupling constants in Hz. For ^{13}C spectra, the assignment of the number of hydrogen atoms linked to the carbon atoms was done using DEPT 135 (Distortionless Enhanced Polarization Transfer) and/or HSQC (Heteronuclear Single Quantum Coherence) experiments. C_q stands for quaternary carbons.

Mass spectrometry: HRMS (High Resolution Mass Spectrometry) using ESI (Electrospray Ionization) or APCI (Atmospheric Pressure Chemical Ionization) methods was performed at Université Paris Sud in the Service de Spectrométrie de masse of the ICMMO (Institut de Chimie Moléculaire et des Matériaux d'Orsay) by Delphine Arquier and Tanya Inceoglu. ESI-HRMS was also performed at UPMC (IPCM) by Claude Charvy and Hristo Nedev. MALDI-TOF MS (Matrix-Assisted Laser Desorption Ionization – Time of Flight Mass Spectrometry) was performed at UPMC in the Plate-forme de Spectrométrie de masse et Protéomique by Gilles Clodic and Gérard Bolbach. The matrix was a saturated solution of HCCA (α-cyano-4-hydroxycinnamic acid) in MeCN/H_2O 1:1 + 0.1% TFA.

Chromatography: Analytical TLC (Thin Layer Chromatography) analysis was carried out on silica gel (Merck 60F-254) with UV visualization at 254 and 366 nm and revelation using $KMnO_4$ or vanillin solutions. Preparative column chromatography was carried out with Merck silica gel (Si 60, 40−63µm). Analytical HPLC (High Performance Liquid Chromatography) measurements were run on a Dionex Ultimate 3000 instrument using C18A ACE columns. Preparative HPLC was performed on a Waters 600 instrument using an XBridgeTM Prep C18 OBDTM column. Gradients of MeCN in H_2O, both containing 0.1% TFA, were employed. Products were monitored with UV detection.

IR spectroscopy: IR (Infra-red) spectra were recorded on a Perkin-Elmer Spectrum 100 FT-IR spectrometer.

Materials: Unless otherwise stated, all syntheses were performed under inert atmosphere (argon or nitrogen). Reagents and chemicals were purchased from Sigma-Aldrich, Alfa Aesar, Strem Chemicals or Chematech. Dry solvents (DCM, MeCN, toluene, THF, dioxane, DMF, DMSO) were purchased from Sigma and used without further purification. AcOEt, DCE, CCl_4, piperidine and TEA were dried with CaH_2, distilled under argon and stored over 4 Å molecular sieves under argon. Catalytic hydrogenation under pressure was performed with a H-Cube hydrogenator.

Diethyl pyridine-2,6-dicarboxylate (Dipicolinic acid diethyl ester **2**)

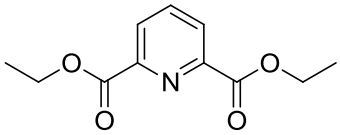

Dipicolinic acid (DPA **1**) (6.00 g, 35.9 mmol, 1.0 eq) was dissolved in a mixture of EtOH (120 mL) and toluene (80 mL). PTSA•H_2O (1.02 g, 5.4 mmol, 0.15 eq) was then added, and the resulting mixture was refluxed for 15 h and concentrated to ≈ 30 mL. Sat. aq. $NaHCO_3$ was added, and the mixture was extracted with Et_2O (3×). The combined organic layers were washed with sat. aq. NaCl (1×), dried over Na_2SO_4 and concentrated to afford Dipicolinic acid diethyl ester **2** (7.07 g, 31.7 mmol, 88%) as a white solid.

Molecular formula: $C_{11}H_{13}NO_4$
MW: 223.2 g.mol^{-1}
^{1}H-NMR (CDCl$_3$, 300 MHz): δ 8.26 (dd, *J* = 7.8, 1.1 Hz, 2H), 8.03–7.94 (m, 1H), 4.47 (qd, *J* = 7.1, 1.2 Hz, 4H), 1.43 (td, *J* = 7.8, 1.2 Hz, 6H).
^{13}C-NMR (CDCl$_3$, 75 MHz): δ 164.7 (C_q), 148.6 (C_q), 138.3 (CH), 127.9 (CH), 62.4 (CH_2), 14.3 (CH_3).
HRMS (ESI): *m/z* = 224.0907 $[M+H]^+$ (found), 224.0917 calcd. for $C_{11}H_{14}NO_4^+$, 246.0731 $[M+Na]^+$ (found), 246.0737 calcd. for $C_{11}H_{13}NNaO_4^+$, 218.0416 $[M+Na\text{-}Et]^+$ (found), 218.0424 calcd. for $C_9H_9NNaO_4^+$.

1,1'-(Pyridine-2,6-diyl)diethanone (Diacetylpyridine, DAP **3**)

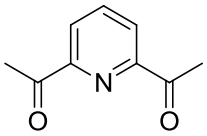

Method 1: Dipicolininc acid diethyl ester **2** (3.55 g, 15.9 mmol, 1.0 eq) was dissolved in dry AcOEt (30 mL). Sodium ethoxide (5.46 g, 80.2 mmol, 5.0 eq) was then added, and the resulting mixture was refluxed for 24 h and cooled to 0 °C. Aq. 37% HCl (35 mL) was added and the resulting mixture was refluxed for 24 h and cooled to rt. H_2O (100 mL) was added and the mixture was extracted with DCM (3×). The combined organic layers were washed with sat. aq. Na_2CO_3 (3×), dried over Na_2SO_4, filtered and concentrated. Column chromatography (SiO_2, 90:10 Cy/AcOEt) afforded DAP **3** (1.19 g, 7.3 mmol, 46%) as a white solid.
Method 2: CuI (2.48 g, 13.03 mmol, 2.66 eq) was suspended in a mixture of dry THF (15 mL) and dry Et_2O (5 mL). The resulting suspension was stirred at −50 °C for 5 min. Methyllithium (1.6 M in THF, 8.5 mL, 13.62 mmol, 2.78 eq) was added dropwise. The temperature was then raised to −20 °C for 15 min, and the mixture was cooled back to −50°C. Dipicolinic acid dichloride **4** (1.0 g, 4.9 mmol, 1.0 eq) was added portionwise and the resulting mixture was stirred at −50 °C for 2.5 h. Sat. aq. NH_4Cl was added, the mixture was allowed to warm to rt and filtered over a pad of celite (washed with Et_2O then DCM). The organic layer was recovered, and the aqueous layer was extracted with Et_2O (2×) and with DCM (1×). The combined organic layers were dried over Na_2SO_4, filtered and concentrated. Column chromatography (SiO_2, 90:10 Cy/AcOEt) afforded DAP **3** (320 mg, 1.96 mmol, 40%) as a white solid.
Method 3: Diamide **5** (2 g, 7.33 mmol, 1.0 eq) was dissolved in dry THF (15 mL). The resulting solution was cooled to 0 °C, and methylmagnesium chloride (3 M in THF, 9 mL, 27.0 mmol, 3.7 eq) was added dropwise. The resulting mixture was allowed to warm to rt for 3 h, aq. 2 M HCl (30 mL) was added

and the mixture was extracted with DCM (3×). The combined organic layers were dried over Na_2SO_4, filtered and concentrated. Column chromatography (SiO_2, 90:10 Cy/AcOEt) afforded DAP **3** (380 mg, 2.33 mmol, 32%) as a white solid.

Molecular formula: $C_9H_9NO_2$
MW: 163.2 g.mol^{-1}
^{1}H-NMR ($CDCl_3$, 300 MHz): δ 8.25–8.18 (m, 2H), 7.99 (dd, *J* = 8.2, 7.3 Hz, 1H), 2.79 (s, 6H). NMR
^{13}C-NMR ($CDCl_3$, 75 MHz): δ 199.3 (C_q), 152.7 (C_q), 138.0 (CH), 124.7 (CH), 25.5 (CH_3).
HRMS (ESI): *m/z* = 164.0708 $[M+H]^+$ (found), 164.0706 calcd. for $C_9H_{10}NO_2^+$, 186.0533 $[M+Na]^+$ (found), 186.0525 calcd. for $C_9H_9NNaO_2^+$.

Pyridine-2,6-dicarbonyl dichloride (Dipicolinic acid dichloride **4**)

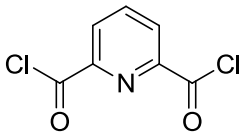

Dipicolinic acid **1** (5 g, 29.9 mmol) was dissolved in thionyl chloride (50 mL). The resulting solution was refluxed for 15 h and concentrated to afford Dipicolinic acid dichloride **4** (6.04 g, 29.6 mmol, 99%) as a reddish solid.

Molecular formula: $C_7H_3Cl_2NO_2$
MW: 204 g.mol^{-1}
^{1}H-NMR ($CDCl_3$, 300 MHz): δ 8.39–8.34 (m, 2H), 8.17 (dd, *J* = 8.3, 7.2 Hz, 1H).
^{13}C-NMR ($CDCl_3$, 75 MHz): δ 169.5 (C_q), 149.3 (C_q), 139.6 (CH), 129.2 (CH).

Pyridine-2,6-diylbis(pyrrolidin-1-ylmethanone) (**5**)

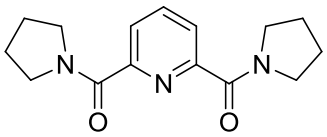

Dipicolinic acid dichloride **4** (6.04 g, 29.6 mmol, 1.0 eq) was dissolved in dry DCM (18 mL). The resulting solution was cooled to 0°C and pyrrolidine (11.1 mL, 133 mmol, 4.5 eq) in dry DCM (30 mL) was added dropwise. The resulting mixture was allowed to warm to rt for 2 h, aq. 5% HCl (70 mL) was added, and the mixture was extracted with DCM (3×). The combined organic layers was dried over Na_2SO_4, filtered and concentrated to afford **5** (7.39 g, 27 mmol, 91%) as an off-white solid.

Molecular formula: $C_{15}H_{19}N_3O_2$
MW: 273.3 g.mol^{-1}
^{1}H-NMR ($CDCl_3$, 300 MHz): δ 7.93–7.82 (m, 3H), 3.74–3.60 (m, 8H), 2.00–1.84 (m, 8H).
^{13}C-NMR ($CDCl_3$, 75 MHz): δ 165.7 (C_q), 152.7 (C_q), 137.5 (CH), 124.5 (CH), 48.8 (CH_2), 46.6 (CH_2), 26.3 (CH_2), 23.7 (CH_2).
HRMS (ESI): *m/z* = 274.1534 $[M+H]^+$ (found), 274.1550 calcd. for $C_{15}H_{20}N_3O_2^+$, 296.1354 $[M+Na]^+$ (found), 296.1369 calcd. for $C_{15}H_{19}N_3NaO_2^+$.

Diethyl 4-hydroxypyridine-2,6-dicarboxylate (Chelidamic acid diethyl ester **7**)

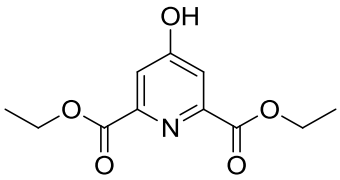

Chelidamic acid monohydrate **6** (5.0 g, 24.9 mmol, 1.0 eq) was suspended in abs. EtOH (100 mL). Concentrated H_2SO_4 (265 µL, 4.98 mmol, 0.2 eq) was the added, and the resulting mixture was refluxed for 15h and concentrated. H_2O (100 mL) and AcOEt (200 mL) were added, and the mixture was extracted with AcOEt (3×). The combined organic layers were dried over Na_2SO_4, filtered and concentrated. Column chromatography (SiO_2, 98:2 to 95:5 DCM/MeOH) afforded Chelidamic acid diethyl ester **7** (4.44 g, 18.6 mmol, 75%) as a white solid.

Molecular formula: $C_{11}H_{13}NO_5$
MW: 239.2 g.mol^{-1}
^{1}H-NMR (MeOD, 300 MHz): δ 7.57 (s, 2H), 4.43 (q, *J* = 7.1 Hz, 4H), 1.42 (t, *J* = 7.1 Hz, 6H).
^{13}C-NMR (MeOD, 75 MHz): δ 169.9 (C_q), 165.3 (C_q), 149.8 (C_q), 116.9 (CH), 63.3 (CH_2), 14.4 (CH_3).
HRMS (ESI): *m/z* = 240.0853 $[M+H]^+$ (found), 240.0866 calcd. for $C_{11}H_{14}NO_5^+$, 262.0673 $[M+Na]^+$ (found), 262.0686 calcd. for $C_{11}H_{13}NNaO_5^+$, 212.0552 $[M+H\text{-}Et]^+$ (found), 212.0553 calcd. for $C_9H_{10}NO_5^+$, 234.0369 $[M+Na\text{-}Et]^+$ (found), 234.0373 calcd. for $C_9H_9NNaO_5^+$.

Diethyl 4-chloropyridine-2,6-dicarboxylate (**8**)

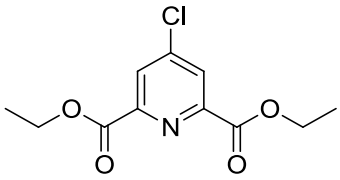

Chelidamic acid diethyl ester **7** (1.0 g, 4.18 mmol, 1.0 eq) was dissolved in $CHCl_3$ (12 mL). The resulting solution was cooled to 0 °C, and thionyl chloride (3.05 mL, 41.8 mmol, 10.0 eq) was added dropwise, followed by a few drops of DMF. The resulting mixture was refluxed for 48 h and concentrated. Aq. 10% $NaHCO_3$ (10 mL) was added and the mixture was extracted with DCM (3×). The combined organic layers were washed with H_2O (2×), dried over Na_2SO_4, filtered and concentrated. Column chromatography (SiO_2, 80:20 Cy/AcOEt) afforded **8** (814 mg, 3.16 mmol, 73%) as a white solid.

Molecular formula: $C_{11}H_{12}ClNO_4$
MW: 257.7 g.mol^{-1}
^{1}H-NMR ($CDCl_3$, 300 MHz): δ 8.26 (s, 2H), 4.49 (q, *J* = 7.1 Hz, 4H), 1.45 (t, *J* = 7.1 Hz, 6H).
^{13}C-NMR ($CDCl_3$, 75 MHz): δ 163.8 (C_q), 150.0 (C_q), 146.7 (C_q), 128.2 (CH), 62.9 (CH_2), 14.3 (CH_3).
HRMS (ESI): *m/z* = 258.0511 $[M+H]^+$ (found), 258.0528 calcd. for $C_{11}H_{13}ClNO_4^+$, 280.0328 $[M+Na]^+$ (found), 280.0347 calcd. for $C_{11}H_{12}ClNNaO_4^+$, 230.0206 $[M+H\text{-}Et]^+$ (found), 230.0215 calcd. for $C_9H_9ClNO_4^+$, 201.9901 $[M+H\text{-}2Et]^+$ (found), 201.9902 calcd. for $C_7H_5ClNO_4^+$.

Diethyl 4-bromopyridine-2,6-dicarboxylate (**9**)

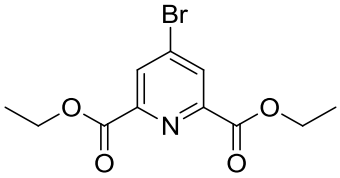

Chelidamic acid diethyl ester **7** (5.66 g, 23.7 mmol, 1.0 eq) was dissolved in $CHCl_3$ (20 mL). PBr_5 (10.2 g, 23.7 mmol, 1.0 eq) was added, and the resulting solution was refluxed for 15h and cooled to rt. NaOH (10 g) dissolved in H_2O (130 mL) was added cautiously and the resulting mixture was extracted with AcOEt (3×). The combined organic layers were dried over Na_2SO_4, filtered and concentrated to afford **9** (6.09 g, 20.2 mmol, 85%) as a white solid.

Molecular formula: $C_{11}H_{12}BrNO_4$
MW: 302.1 g.mol^{-1}
^{1}H-NMR ($CDCl_3$, 300 MHz): δ 8.43 (s, 2H), 4.49 (q, *J* = 7.1 Hz, 4H), 1.45 (t, *J* = 7.1 Hz, 6H).
^{13}C-NMR ($CDCl_3$, 75 MHz): δ 163.5 (C_q), 149.6 (C_q), 134.9 (C_q), 131.1 (CH), 62.7 (CH_2), 14.2 (CH_3).
MS (ESI): *m/z* (%) = 302.0028 $[M+H]^+$ (%), 323.9850 $[M+Na]^+$, 273.9714 $[M+H-Et]^+$
HRMS (ESI): *m/z* = 302.0028 $[M+H]^+$ (found), 302.0022 calcd. for $C_{11}H_{13}BrNO_4^+$, 323.9850 $[M+Na]^+$ (found), 323.9842 calcd. for $C_{11}H_{12}BrNNaO_4^+$

1,1'-(4-Chloropyridine-2,6-diyl)diethanone (*p*ClDAP **10**)

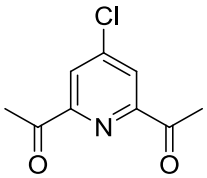

Compound **8** (369 mg, 1.43 mmol, 1.0 eq) was dissolved in dry AcOEt (9 mL). NaOEt (487 mg, 7.15 mmol, 5 eq) was added, and the resulting mixture was refluxed for 24 h and cooled to 0 °C. Aq. 37% HCl (3.2 mL) was added and the resulting mixture was refluxed for 24 h and cooled to rt. H_2O (10 mL) was added and the mixture was extracted with DCM (3×). The combined organic layers were washed with sat. aq. Na_2CO_3 (3×), dried over Na_2SO_4, filtered and concentrated. Column chromatography (SiO_2, 90:10 Cy/AcOEt) afforded *p*ClDAP **10** (151 mg, 0.76 mmol, 53%) as a white solid.

Molecular formula: $C_9H_8ClNO_2$
MW: 197.6 g.mol^{-1}
^{1}H-NMR ($CDCl_3$, 300 MHz): δ 8.19 (s, 2H), 2.78 (s, 6H).
^{13}C-NMR ($CDCl_3$, 75 MHz): δ 198.3 (C_q), 154.0 (C_q), 147.1 (C_q), 125.1 (CH), 25.8 (CH_3).

1,1'-(4-Bromopyridine-2,6-diyl)diethanone (*p*BrDAP **11**)

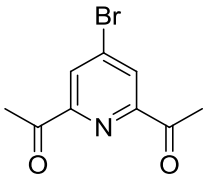

Compound **9** (2.47 g, 8.18 mmol, 1.0 eq) was dissolved in dry AcOEt (70 mL). NaOEt (2.78 g, 40.9 mmol, 5.0 eq) was added, and the resulting mixture was refluxed for 24 h and cooled to 0 °C. Aq.

37% HCl (18.3 mL) was added and the resulting mixture was refluxed for 24 h and cooled to rt. H_2O (52 mL) was added and the mixture was extracted with DCM (3×). The combined organic layers were washed with sat. aq. Na_2CO_3 (3×), dried over Na_2SO_4, filtered and concentrated. Column chromatography (SiO_2, 95:5 Cy/AcOEt) afforded *p*BrDAP **11** (700 mg, 2.89 mmol, 35%) as a white solid.

Molecular formula: $C_9H_8BrNO_2$
MW: 242.1 g.mol^{-1}
^{1}H-NMR ($CDCl_3$, 300 MHz): δ 8.18 (s, 2H), 2.78 (s, 6H).
^{13}C-NMR ($CDCl_3$, 75 MHz): δ 198.3 (C_q), 154.0 (C_q), 147.1 (C_q), 125.1 (CH), 25.8 (CH_3).

General procedure A: synthesis of BImPs

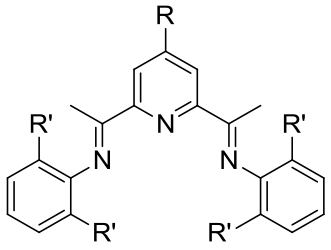

A diacetylpyridine (**3**, **10** or **11**) and an aniline (**12**, **13** or **14**) were dissolved in EtOH or MeOH. A few drops of AcOH or HCO_2H were added, the resulting mixture was refluxed and cooled to 10 °C. The precipitate was filtered, washed with cold EtOH or MeOH and dried to afford the corresponding BImP as a yellow solid.

(*N*,*N*'*E*,*N*,*N*'*E*)-*N*,*N*'-(Pyridine-2,6-diylbis(ethan-1-yl-1-ylidene))dianiline (H-BImP **15**, R = R' = H)

Using the general procedure A with DAP **3** (75 mg, 0.46 mmol, 1.0 eq) and aniline **12** (84 µL, 0.92 mmol, 2.0 eq) in EtOH (4 mL) with AcOH, H-BImP **15** (80 mg, 0.26 mmol, 58%) was obtained after 48 h of reflux, a month of cooling and EtOH washings.

Molecular formula: $C_{21}H_{19}N_3$
MW: 313.4 g.mol^{-1}
^{1}H-NMR ($CDCl_3$, 300 MHz): δ 8.35 (d, *J* = 7.8 Hz, 2H), 7.88 (t, *J* = 7.8 Hz, 1H), 7.39 (t, *J* = 7.5 Hz, 4H), 7.13 (t, *J* = 7.5 Hz, 2H), 6.85 (d, *J* = 7.5 Hz, 4H), 2.41 (s, 6H).
^{13}C-NMR ($CDCl_3$, 75 MHz): δ 167.5, 155.6, 151.4, 137.0, 129.2, 123.8, 122.5, 119.4, 16.4.
HRMS (ESI): *m/z* = 336.1471 $[M+Na]^+$ (found), 336.1471 calcd. for $C_{21}H_{19}N_3Na^+$.

(*N*,*N*'*E*,*N*,*N*'*E*)-*N*,*N*'-(Pyridine-2,6-diylbis(ethan-1-yl-1-ylidene))bis(2,6-dimethylaniline) (Me-BImP **16**, R = H and R' = Me)

Using the general procedure A with DAP **3** (250 mg, 1.53 mmol, 1.0 eq) and 2,6-xylidine **13** (568 µL, 4.59 mmol, 3.0 eq) in MeOH (4.5 mL) with HCO_2H, Me-BImP **16** (466 mg, 1.26 mmol, 82%) was obtained after 24 h of reflux, a few days of cooling and MeOH washings.

Molecular formula: $C_{25}H_{27}N_3$
MW: 369.5 g.mol^{-1}
^{1}H-NMR ($CDCl_3$, 300 MHz): δ 8.39 (d, *J* = 7.8 Hz, 2H), 7.83 (t, *J* = 7.8 Hz, 1H), 6.99 (d, *J* = 7.5 Hz, 4H), 6.85 (dd, *J* = 8.5, 6.8 Hz, 2H), 2.15 (s, 6H), 1.96 (s, 12H).

^{13}C-NMR ($CDCl_3$, 75 MHz): δ 167.3, 155.3, 148.9, 137.0, 128.0, 125.6, 123.2, 122.4, 18.1, 16.6.
HRMS (ESI): *m/z* = 370.2282 $[M+H]^+$ (found), 370.2278 calcd. for $C_{25}H_{28}N_3^+$, 392.2093 $[M+Na]^+$ (found), 392.2097 calcd. for $C_{25}H_{27}N_3Na^+$.

(*N*,*N*′*E*,*N*,*N*′*E*)-*N*,*N*′-(Pyridine-2,6-diylbis(ethan-1-yl-1-ylidene))bis(2,6-diisopropylaniline) (^{i}Pr-BImP **17**, R = H and R' = ^{i}Pr)

Using the general procedure A with DAP **3** (250 mg, 1.53 mmol, 1.0 eq) and 2,6-diisopropylaniline **14** (866 µL, 4.59 mmol, 3.0 eq) in MeOH (4.5 mL) with HCO_2H, ^{i}Pr-BImP **17** (722 mg, 1.50 mmol, 98%) was obtained after 24 h of reflux, a few days of cooling and MeOH washings.

Molecular formula: $C_{33}H_{43}N_3$
MW: 481.7 g.mol^{-1}
^{1}H-NMR ($CDCl_3$, 300 MHz): δ 8.49 (d, *J* = 7.8 Hz, 2H), 7.94 (t, *J* = 7.8 Hz, 1H), 7.23–7.15 (m, 4H), 7.15–7.07 (m, 2H), 2.78 (hept, *J* = 6.9 Hz, 4H), 2.28 (s, 6H), 1.17 (d, *J* = 6.9 Hz, 24H).
^{13}C-NMR ($CDCl_3$, 75 MHz): δ 167.1, 155.3, 146.6, 137.0, 135.9, 123.7, 123.1, 122.3, 28.5, 23.4, 23.1, 17.3.
HRMS (ESI): *m/z* = 482.3505 $[M+H]^+$ (found), 482.3530 calcd. for $C_{33}H_{44}N_3^+$.

(*N*,*N*′*E*,*N*,*N*′*E*)-*N*,*N*′-((4-Chloropyridine-2,6-diyl)bis(ethan-1-yl-1-ylidene))bis(2,6-dimethylaniline) (*p*Cl-Me-BImP **18**, R = Cl and R' = Me)

Using the general procedure A with *p*ClDAP **10** (176 mg, 0.89 mmol, 1.0 eq) and 2,6-xylidine **13** (330 µL, 2.67 mmol, 3.0 eq) in MeOH (2.6 mL) with HCO_2H, *p*Cl-Me-BImP **18** (201 mg, 0.50 mmol, 56%) was obtained after 24 h of reflux, a few days of cooling and MeOH washings.

Molecular formula: $C_{25}H_{26}ClN_3$
MW: 404 g.mol^{-1}
^{1}H-NMR ($CDCl_3$, 300 MHz): δ 8.49 (d, *J* = 0.7 Hz, 2H), 7.09 (d, *J* = 7.4 Hz, 4H), 6.96 (dd, *J* = 8.2, 6.8 Hz, 2H), 2.22 (d, *J* = 0.7 Hz, 6H), 2.05 (s, 12H).
^{13}C-NMR ($CDCl_3$, 75 MHz): δ 166.4 (C_q), 156.6 (C_q), 148.5 (C_q), 145.5 (C_q), 128.1 (CH), 125.4 (C_q), 123.4 (CH), 122.5 (CH), 18.1 (CH_3), 16.7 (CH_3).
HRMS (ESI): *m/z* = 404.1874 $[M+H]^+$ (found), 404.1888 calcd. for $C_{25}H_{27}ClN_3^+$, 426.1692 $[M+Na]^+$ (found), 426.1707 calcd. for $C_{25}H_{26}ClN_3Na^+$.

(*N*,*N*′*E*,*N*,*N*′*E*)-*N*,*N*′-((4-Chloropyridine-2,6-diyl)bis(ethan-1-yl-1-ylidene))bis(2,6-diisopropylaniline) (*p*Cl-^{i}Pr-BImP **19**, R = Cl and R' = ^{i}Pr)

Using the general procedure A with *p*ClDAP **10** (104 mg, 0.53 mmol, 1.0 eq) and 2,6-diisopropylaniline **14** (300 µL, 2.76 mmol, 3.0 eq) in MeOH (2 mL) with HCO_2H, *p*Cl-^{i}Pr-BImP **18** (223 mg, 0.43 mmol, 81%) was obtained after 24 h of reflux, a few days of cooling and MeOH washings.

Molecular formula: $C_{33}H_{42}ClN_3$
MW: 516.2 g.mol^{-1}
^{1}H-NMR ($CDCl_3$, 300 MHz): δ 8.48 (s, 2H), 7.23–7.16 (m, 4H), 7.16–7.08 (m, 2H), 2.74 (hept, *J* = 6.9 Hz, 4H), 2.26 (s, 6H), 1.17 (dd, *J* = 6.9, 4.2 Hz, 24H).
^{13}C-NMR ($CDCl_3$, 75 MHz): δ 166.2 (C_q), 156.6 (C_q), 146.2 (C_q), 145.6 (C_q), 135.8 (C_q), 124.0 (CH), 123.2 (CH), 122.4 (CH), 28.5 (CH), 23.4 (CH_3), 23.1 (CH_3), 17.4 (CH_3).
HRMS (ESI): *m/z* = 516.3136 $[M+H]^+$ (found), 516.3140 calcd. for $C_{33}H_{43}ClN_3^+$.

(*N*,*N'E*,*N*,*N'E*)-*N*,*N'*-((4-Bromopyridine-2,6-diyl)bis(ethan-1-yl-1-ylidene))bis(2,6-dimethylaniline) (*p*Br-Me-BImP **20**, R = Br and R' = Me)

Using the general procedure A with *p*BrDAP **11** (63 mg, 0.26 mmol, 1.0 eq) and 2,6-xylidine **13** (96 µL, 0.78 mmol, 3.0 eq) in MeOH (1.5 mL) with HCO_2H, *p*Br-Me-BImP **20** (146 mg, 0.26 mmol, 100%) was obtained after 24 h of reflux, a few days of cooling and MeOH washings.

Molecular formula: $C_{33}H_{42}BrN_3$
MW: 560.6 g.mol^{-1}
^{1}H-NMR ($CDCl_3$, 300 MHz): δ 8.48 (s, 2H), 7.09 (d, *J* = 7.4 Hz, 4H), 6.96 (dd, *J* = 8.2, 6.7 Hz, 2H), 2.22 (s, 6H), 2.05 (s, 12H).
^{13}C-NMR ($CDCl_3$, 75 MHz): δ 166.4 (C_q), 156.6 (C_q), 148.5 (C_q), 145.5 (C_q), 128.1 (CH), 125.4 (C_q), 123.4 (CH), 122.5 (CH), 18.1 (CH_3), 16.7 (CH_3).

(*N*,*N'E*,*N*,*N'E*)-*N*,*N'*-((4-Bromopyridine-2,6-diyl)bis(ethan-1-yl-1-ylidene))bis(2,6-diisopropylaniline) (*p*Br-^{i}Pr-BImP **21**, R = Br and R' = ^{i}Pr)

Using the general procedure A with *p*BrDAP **11** (63 mg, 0.26 mmol, 1.0 eq) and 2,6-diisopropylaniline **14** (147 µL, 0.78 mmol, 3.0 eq) in MeOH (1.5 mL) with HCO_2H, *p*Br-^{i}Pr-BImP **21** (223 mg, 0.43 mmol, 81%) was obtained after 24 h of reflux, a few days of cooling and MeOH washings.

Molecular formula: $C_{33}H_{42}ClN_3$
MW: 516.2 g.mol^{-1}
^{1}H-NMR ($CDCl_3$, 300 MHz): δ 8.48 (s, 2H), 7.23–7.16 (m, 2H), 7.16–7.08 (m, 4H), 2.74 (hept, *J* = 6.9 Hz, 4H), 2.26 (s, 6H), 1.17 (dd, *J* = 6.9, 4.1 Hz, 24H).
^{13}C-NMR ($CDCl_3$, 75 MHz): δ 166.2 (C_q), 156.6 (C_q), 146.2 (C_q), 145.5 (C_q), 135.8 (C_q), 124.0 (CH), 123.2 (CH), 122.4 (CH), 28.5 (CH), 23.4 (CH_3), 23.1 (CH_3), 17.4 (CH_3).

General procedure B: synthesis of Mn-BImP complexes

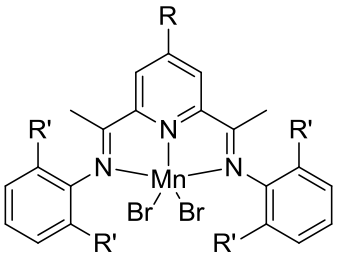

Equimolar quantities of BImP (**15**-**21**) and $MnBr_2$ were suspended in abs. EtOH (2 mL). The resulting mixture was refluxed for 1 h and kept at 10 °C overnight. The resulting precipitate was filtered, washed with cold EtOH and dried to afford the corresponding Mn-BImP as an orange solid.

Mn-H-BImP (**22**, R = R' = H)

Using the general procedure B with H-BImP **15** (75 mg, 0.24 mmol) and $MnBr_2$ (51.5 mg, 0.24 mmol), 93 mg (0.176 mmol, 73%) of Mn-H-BIMP **22** were obtained.

Molecular formula: $C_{21}H_{19}Br_2MnN_3$
MW: 528.2 g.mol^{-1}

HRMS (ESI): *m/z* = 447.0133 $[MnBrL]^+$ (found), 447.0137 calcd. for $C_{21}H_{19}BrMnN_3^+$, 680.2456 $[MnL_2-H]^+$ (found), 680.2455 calcd. for $C_{42}H_{37}MnN_6^+$, 340.6303 $[MnL_2]^{2+}$ (found), 340.6264 calcd. for $C_{42}H_{38}MnN_6^{2+}/2$, 314.1660 $[L+H]^+$ (found), 314.1652 calcd. for $C_{21}H_{20}N_3^+$, 336.1482 $[L+Na]^+$ (found), 336.1471 calcd. for $C_{21}H_{19}N_3Na^+$, 369.1034 $[MnL+H]^+$ (found), 369.1032 calcd. for $C_{21}H_{20}MnN_3^+$.

Mn-Me-BImP (**23**, R = H and R' = Me)

Using the general procedure B with Me-BImP **16** (75 mg, 0.20 mmol) and $MnBr_2$ (43 mg, 0.20 mmol), 101 mg (0.173 mmol, 87%) of Mn-Me-BIMP **23** were obtained.

Molecular formula: $C_{25}H_{27}Br_2MnN_3$
MW: 584.3 $g.mol^{-1}$
HRMS (ESI): *m/z* = 503.0748 $[MnBrL]^+$ (found), 503.0763 calcd. for $C_{25}H_{27}BrMnN_3^+$, 370.2296 $[L+H]^+$ (found), 370.2278 calcd. for $C_{25}H_{28}N_3^+$, 392.2093 $[L+Na]^+$ (found), 392.2097 calcd. for $C_{25}H_{27}NaN_3^+$.

Mn-^{i}Pr-BImP (**24**, R = H and R' = ^{i}Pr)
Using the general procedure B with ^{i}Pr-BImP **17** (75 mg, 0.156 mmol) and $MnBr_2$ (33.5 mg, 0.156 mmol), 92 mg (0.132 mmol, 85%) of Mn-^{i}Pr-BIMP **24** were obtained.

Molecular formula: $C_{33}H_{43}Br_2MnN_3$
MW: 696.5 $g.mol^{-1}$
HRMS (ESI): *m/z* = 482.3560 $[L+H]^+$ (found), 482.3530 calcd. for $C_{33}H_{44}N_3^+$, 504.3336 $[L+Na]^+$ (found), 504.3349 calcd. for $C_{33}H_{43}N_3Na^+$.

Mn-pCl-Me-BImP (**25**, R = Cl and R' = Me)

Using the general procedure B with *p*Cl-Me-BImP **18** (75 mg, 0.186 mmol) and $MnBr_2$ (40 mg, 0.156 mmol), 75 mg (0.121 mmol, 65%) of Mn-*p*Cl-Me-BIMP **25** were obtained.

Molecular formula: $C_{25}H_{26}Br_2ClMnN_3$
MW: 618.7 $g.mol^{-1}$
HRMS (ESI): *m/z* = 404.1900 $[L+H]^+$ (found), 404.1888 calcd. for $C_{25}H_{27}ClN_3^+$, 426.1694 $[L+Na]^+$ (found), 426.1707 calcd. for $C_{25}H_{26}ClN_3Na^+$.

Mn-pBr-Me-BImP (**26**, R = Br and R' = Me)

Using the general procedure B with *p*Br-Me-BImP **20** (65 mg, 0.145 mmol) and $MnBr_2$ (31.2 mg, 0.145 mmol), 47 mg (0.07 mmol, 49%) of Mn-*p*Br-Me-BIMP **26** were obtained.

Molecular formula: $C_{25}H_{26}Br_3MnN_3$
MW: 663.2 $g.mol^{-1}$

4-((Trimethylsilyl)ethynyl)benzaldehyde (**28**)

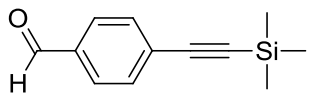

4-Bromobenzaldehyde **27** (10.0 g, 54.05 mmol, 1.0 eq) was dissolved in dry THF (40 mL) and dry TEA (20 mL). $Pd(PPh)_3Cl_2$ (380 mg, 0.541 mmol, 0.01 eq) and CuI (103.3 mg, 0.541 mmol, 0.01 eq) were

added, and argon was bubbled for 15 min. TMSA (9.2 mL, 64.86 mmol, 1.2 eq) was added dropwise, the resulting mixture was refluxed for 24 h and then cooled to rt. DCM (200 mL) was added, the organic layer was recovered and washed with H_2O (1×), aq. 10% HCl (1×), and H_2O again (1×), dried over Na_2SO_4, filtered and concentrated. Column chromatography (SiO_2, 100% Cy to 90:10 Cy/AcOEt) afforded **28** (9.31 g, 46.02 mmol, 85%) as a yellow solid.

Molecular formula: $C_{12}H_{14}OSi$
MW: 202.3 g.mol^{-1}
^{1}H-NMR ($CDCl_3$, 300 MHz): δ 9.99 (s, 1H), 7.81 (d, 2H, *J* = 8.3 Hz), 7.60 (d, 2H, *J* = 8.3 Hz), 0.27 (s, 9H).
^{13}C-NMR ($CDCl_3$, 75 MHz): δ 191.5 (CH), 135.7 (C_q), 132.6 (CH), 129.6 (CH), 129.5 (C_q), 104.0 (C_q), 99.2 (C_q), 0.1 (CH_3).
HRMS (ESI): *m/z* = 203.0886 $[M+H]^+$ (found), 203.0887 calcd. for $C_{12}H_{15}OSi^+$, 225.0668 $[M+Na]^+$ (found), 225.0706 calcd. for $C_{12}H_{14}NaOSi^+$.

4-Ethynylbenzaldehyde (**29**)

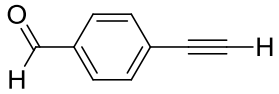

Compound **28** (9.31 g, 46.02 mmol, 1.0 eq) was dissolved in MeOH (450 mL). K_2CO_3 (4.77 g, 34.5 mmol, 0.75 eq) was then added, and the resulting suspension was stirred at rt for 30 min. Sat. aq. NH_4Cl was added and the mixture was extracted with DCM (3×). The combined organic layers were washed with H_2O (1×), dried over Na_2SO_4, filtered and concentrated. Column chromatography (SiO_2, 100% Cy to 90:10 Cy/AcOEt) afforded **29** (5.87 g, 45.12 mmol, 98%) as a brown solid.

Molecular formula: C_6H_9O
MW: 130.1 g.mol^{-1}
^{1}H-NMR ($CDCl_3$, 300 MHz): δ 10.02 (s, 1H), 7.87–7.81 (m, 2H), 7.67–7.60 (m, 2H), 3.29 (s, 1H).
^{13}C-NMR ($CDCl_3$, 75 MHz): δ 191.5 (CH), 136.1 (C_q), 132.9 (CH), 129.6 (CH), 128.5 (C_q), 82.8 (C_q), 81.2 (CH).
HRMS (APCI): *m/z* = 131.0493 $[M+H]^+$ (found), 131.0491 calcd. for $C_6H_7O_9^+$.

4-Azidobenzaldehyde (**31**)

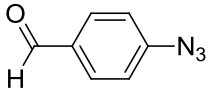

4-Nitrobenzaldehyde **30** (1.8 g, 11.9 mmol, 1.0 eq) and NaN_3 (1.55 g, 23.8 mmol, 2.0 eq) were dissolved in HMPA (30 mL). The resulting mixture was stirred protected from light at rt for 5 d. H_2O was added and the mixture was extracted with Et_2O (3×). The combined organic layers were washed with H_2O (3×), dried over Na_2SO_4, filtered and concentrated to afford **31** (1.65 g, 11.2 mmol, 94%) as an orange oil.

Molecular formula: $C_7H_5N_3O$
MW: 147.1 g.mol^{-1}
^{1}H-NMR ($CDCl_3$, 300 MHz): δ 9.94 (s, 1H), 7.91–7.84 (m, 2H), 7.19–7.11 (m, 2H).
^{13}C-NMR ($CDCl_3$, 75 MHz): δ 190.7 (CH), 146.4 (C_q), 133.4 (C_q), 131.7 (CH), 119.6 (CH).

General procedure C: synthesis of substituted para*-phenylterpyridines*

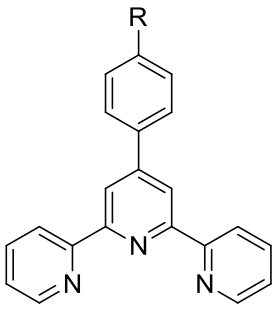

A *para*-substituted benzaldehyde (**27**, **29**, **31**-**34**) (1.0 eq) was dissolved in abs. EtOH. 2-Acetylpyridine **35** (2.0 eq) was added, followed by powdered KOH (2.0 eq) and aq. 28% NH_4OH. The resulting mixture was stirred at rt for 4 h under atmospheric oxygen. The suspension was filtered, washed with cold EtOH (3× 50 mL), taken up in DCM and concentrated. Recrystallization from EtOH afforded the corresponding substituted para-phenylterpyridine.

4'-(4-Bromophenyl)-2,2':6',2''-terpyridine (*p*BrPhTpy **36**, R = Br)

Using the general procedure C with 4-bromobenzaldehyde **27** (10.0 g, 54.05 mmol), 2-acetylpyridine **35** (12.1 mL, 108.1 mmol), powdered KOH (6.06 g, 108.1 mmol), abs. EtOH (250 mL) and aq. 28% NH_4OH (150 mL), *p*BrPhTpy **36** (4.37 g, 11.25 mmol, 21%) was obtained as a white solid.

Molecular formula: $C_{21}H_{14}BrN_3$
MW: 388.3 g.mol^{-1}
^{1}H-NMR (CDCl$_3$, 300 MHz): δ 8.77–8.70 (m, 4H), 8.67 (dt, *J* = 7.9, 1.1 Hz, 2H), 7.89 (td, *J* = 7.9, 1.8 Hz, 2H), 7.81–7.75 (m, 2H), 7.68–7.60 (m, 2H), 7.36 (ddd, *J* = 7.5, 4.8, 1.1 Hz, 2H).
^{13}C-NMR (CDCl$_3$, 75 MHz): δ 156.2 (Cq), 156.1 (Cq), 149.2 (Cq), 149.2 (CH), 137.5 (Cq), 137.1 (CH), 132.2 (CH), 129.0 (CH), 124.1 (CH), 123.6 (Cq), 121.5 (CH), 118.7 (CH).
HRMS (ESI): *m/z* = 388.0437 $[M+H]^+$ (found), 388.0444 calcd. for $C_{21}H_{15}BrN_3^+$, 410.0260 $[M+Na]^+$ (found), 410.0263 calcd. for $C_{21}H_{14}BrN_3Na^+$.

4'-(4-Ethynylphenyl)-2,2':6',2''-terpyridine (*p*CCHPhTpy **37**, R = CCH)

Using the general procedure C with **29** (6.0 g, 46.1 mmol), 2-acetylpyridine **35** (10.4 mL, 92.2 mmol), powdered KOH (5.17 g, 92.2 mmol), abs. EtOH (300 mL) and aq. 28% NH_4OH (125 mL), *p*CCHPhTpy **37** (2.34 g, 7.02 mmol, 15%) was obtained as pale orange needles.

Molecular formula: $C_{23}H_{15}N_3$
MW: 333.4 g.mol^{-1}
^{1}H-NMR (CDCl$_3$, 300 MHz): δ 8.77 (s, 2H), 8.75 (ddd, *J* = 4.8, 1.8, 1.0 Hz, 2H), 8.70 (dt, *J* = 7.9, 1.0 Hz, 2H), 7.96–7.87 (m, 4H), 7.67–7.61 (m, 2H), 7.39 (ddd, *J* = 7.9, 4.8, 1.0 Hz, 2H), 3.19 (s, 1H).
^{13}C-NMR (CDCl$_3$, 75 MHz): δ 155.9 (C_q), 155.8 (C_q), 149.6 (C_q), 149.0 (CH), 138.8 (C_q), 137.5 (CH), 132.9 (CH), 127.4 (CH), 124.2 (CH), 122.9 (C_q), 121.8 (CH), 119.2 (CH), 83.5 (C_q), 78.7 (CH).
HRMS (ESI): *m/z* = 334.1331 $[M+H]^+$ (found), 334.1339 calcd. for $C_{23}H_{16}N_3^+$, 356.1144 $[M+Na]^+$ (found), 356.1158 calcd. for $C_{23}H_{15}N_3Na^+$.

4'-(4-Azidophenyl)-2,2':6',2''-terpyridine (*p*N_3PhTpy **38**, R = N_3)

Using the general procedure C with **31** (1.6 g, 10.88 mmol), 2-acetylpyridine **35** (2.44 mL, 21.76 mmol), powdered KOH (1.22 g, 21.76 mmol), abs. EtOH (50 mL) and aq. 28% NH_4OH (30 mL), *p*N_3PhTpy **38** (623 mg, 1.78 mmol, 16%) was obtained as an orange solid.

Molecular formula: $C_{21}H_{14}N_6$
MW: 350.4 g.mol^{-1}
^{1}H-NMR ($CDCl_3$, 300 MHz): δ 8.77–8.70 (m, 4H), 8.68 (dt, *J* = 8.0, 1.2 Hz, 2H), 7.96–7.85 (m, 4H), 7.37 (ddd, *J* = 7.5, 4.7, 1.2 Hz, 2H), 7.20–7.13 (m, 2H).
^{13}C-NMR ($CDCl_3$, 75 MHz): δ 156.4 (C_q), 155.9 (C_q), 150.3 (C_q), 149.2 (CH), 139.2 (C_q), 137.0 (CH), 136.0 (C_q), 129.8 (CH), 127.3 (CH), 123.9 (CH), 121.5 (CH), 118.8 (CH).
HRMS (ESI): *m/z* = 373.1176 $[M+Na]^+$ (found), 373.1172 calcd. for $C_{21}H_{14}N_6Na^+$, 345.1112 $[M+Na-N_2]^+$ (found), 345.1111 calcd. for $C_{21}H_{14}N_4Na^+$, 323.1286 $[M+H-N_2]^+$ (found), 323.1291 calcd. for $C_{21}H_{15}N_4^+$.

4'-(4-Chlorophenyl)-2,2':6',2''-terpyridine (*p*ClPhTpy **39**, R = Cl)

Using the general procedure C with 4-chlorobenzaldehyde **32** (2.28 g, 16.2 mmol), 2-acetylpyridine **35** (3.63 mL, 32.4 mmol), powdered KOH (1.82 g, 32.4 mmol), abs. EtOH (75 mL) and aq. 28% NH_4OH (45 mL), *p*ClPhTpy **39** (1.353 g, 3.94 mmol, 24%) was obtained as a white solid.

Stepwise method: **42** (365 mg, 1.5 mmol, 1.0 eq), **43** (489 mg, 1.5 mmol, 1.0 eq) and NH_4OAc (2.89 g, 37.5 mmol, 25 eq) were suspended in AcOH (5 mL). The resulting mixture was refluxed for 15 h under atmospheric oxygen. Aq. 10 M NaOH (10 mL) was added, the mixture was extracted with DCM (5×), the organic layer was filtered over a pad of celite, dried over Na_2SO_4, filtered and concentrated. Recrystallization from EtOH afforded *p*ClPhTpy **39** (196 mg, 0.57 mmol, 38%) as a light grey solid.

Molecular formula: $C_{21}H_{14}ClN_3$
MW: 343.8 g.mol^{-1}
^{1}H-NMR ($CDCl_3$, 300 MHz): δ 8.77–8.61 (m, 6H), 7.94–7.78 (m, 4H), 7.48 (d, *J* = 8.2 Hz, 2H), 7.40–7.31 (m, 2H).
^{13}C-NMR ($CDCl_3$, 75 MHz): δ 156.1 (Cq), 149.2 (Cq), 149.2 (CH), 137.1 (CH), 137.0 (Cq), 135.4 (Cq), 129.3 (CH), 128.7 (CH), 124.1 (CH), 121.2 (CH), 118.8 (CH).
HRMS (ESI): *m/z* = 344.0959 $[M+H]^+$ (found), 344.0949 calcd. for $C_{21}H_{15}ClN_3^+$.

4'-(*p*-Tolyl)-2,2':6',2''-terpyridine (*p*MePhTpy **40**, R = Me)

Using the general procedure C with *p*-tolualdehyde **33** (5.0 g, 41.63 mmol), 2-acetylpyridine **35** (9.33 mL, 83.26 mmol), powdered KOH (4.69 g, 83.26 mmol), abs. EtOH (195 mL) and aq. 28% NH_4OH (115 mL), *p*MePhTpy (2.23 g, 6.90 mmol, 17%) was obtained as a white solid.

Molecular formula: $C_{22}H_{17}N_3$
MW: 323.4 g.mol^{-1}
^{1}H-NMR ($CDCl_3$, 300 MHz): δ 8.78–8.71 (m, 4H), 8.68 (d, *J* = 8.0 Hz, 2H), 7.88 (td, *J* = 7.8, 1.8 Hz, 2H), 7.83 (d, *J* = 8.0 Hz, 2H), 7.40–7.29 (m, 4H), 2.44 (s, 3H).
^{13}C-NMR ($CDCl_3$, 75 MHz): δ 156.5, 156.0, 150.3, 149.2, 139.2, 137.0, 135.6, 129.8, 127.3, 123.9, 121.5, 118.8, 21.4.
HRMS (ESI): *m/z* = 324.1503 $[M+H]^+$ (found), 324.1495 calcd. for $C_{22}H_{18}N_3^+$, 346.1305 $[M+Na]^+$ (found), 346.1315 calcd. for $C_{22}H_{17}N_3Na^+$.

4'-(4-Fluorophenyl)-2,2':6',2''-terpyridine (*p*FPhTpy **41**)

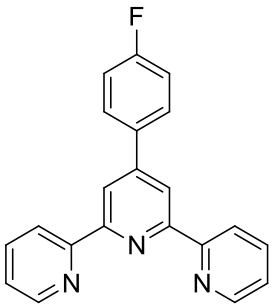

4-fluorobenzaldehyde **34** (0.86 mL, 8.06 mmol, 1.0 eq) was dissolved in MeOH (180 mL). 2-acetylpyridine **35** (1.81 mL, 16.12 mmol, 2.0 eq) was added, followed by powdered NaOH (322 mg, 8.06 mmol, 1.0 eq) and aq. 28% NH_4OH (45 mL). The resulting mixture was refluxed for 72 h under atmospheric oxygen, cooled to rt, and stirred at rt for 3 h. The suspension was filtered, washed with cold MeOH and cold H_2O, taken up in DCM and concentrated to afford *p*FPhTpy **41** (625 mg, 1.91 mmol, 24%) as a white solid.

Molecular formula: $C_{21}H_{14}FN_3$
MW: 327.4 g.mol^{-1}
^{1}H-NMR (CDCl$_3$, 300 MHz): δ 8.77–8.71 (m, 4H), 8.69 (dt, *J* = 8.0, 1.1 Hz, 2H), 7.95–7.85 (m, 4H), 7.37 (ddd, *J* = 7.5, 4.8, 1.1 Hz, 2H), 7.25–7.16 (m, 2H).
^{13}C-NMR (CDCl$_3$, 75 MHz): δ 163.6 (C_q, *J* = 248.7 Hz), 156.1 (C_q, *J* = 12.3 Hz), 149.3 (C_q), 149.2 (CH), 136.9 (CH), 134.7 (C_q, *J* = 3.3 Hz), 129.2 (CH, *J* = 8.4 Hz), 123.9 (CH), 121.5 (CH), 118.8 (CH), 116.0 (CH, *J* = 21.5 Hz). One C_q is missing.
HRMS (ESI): *m/z* = 328.1233 $[M+H]^+$ (found), 328.1245 calcd. for $C_{21}H_{15}FN_3^+$, 350.1051 $[M+Na]^+$ (found), 350.1064 calcd. for $C_{21}H_{14}FN_3Na^+$.

(*E*)-3-(4-Chlorophenyl)-1-(pyridin-2-yl)prop-2-en-1-one (**42**)

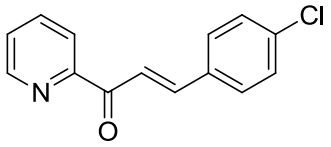

4-Chlorobenzaldehyde **32** (1.406 g, 10 mmol, 1.0 eq) was suspended in MeOH (22.5 mL). Aq. 1 M NaOH (7.5 mL) was added, followed by 2-acetylpyridine **35** (1.18 mL, 10.5 mmol, 1.05 eq). The resulting mixture was stirred at rt for 20 min and the precipitate was filtered, redissolved in DCM, washed with H_2O (3×), dried over Na_2SO_4, filtered and concentrated. Column chromatography (SiO_2, 95:5 Cy/AcOEt) afforded **42** (1.223 g, 5.02 mmol, 50%) as a pale yellow solid.

Molecular formula: $C_{14}H_{10}ClNO$
MW: 243.7 g.mol^{-1}
^{1}H-NMR (CDCl$_3$, 300 MHz): δ 8.73 (ddd, *J* = 4.8, 1.7, 1.0 Hz, 1H), 8.28 (d, *J* = 16.1 Hz, 1H), 8.18 (dt, *J* = 7.8, 1.0 Hz, 1H), 7.92–7.82 (m, 2H), 7.69–7.61 (m, 2H), 7.49 (ddd, *J* = 7.6, 4.8, 1.3 Hz, 1H), 7.41–7.34 (m, 2H).

1-(2-Oxo-2-(pyridin-2-yl)ethyl)pyridin-1-ium iodide (**43**)

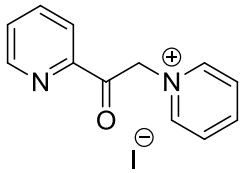

Iodine (2.538 g, 10 mmol, 1.0 eq) was dissolved in pyridine (11 mL). 2-acetylpyridine **35** (1.12 mL, 10 mmol, 1.0 eq) was added dropwise, and the resulting mixture was refluxed for 3 h and cooled to rt. The precipitate was filtered, washed thoroughly with cold pyridine, and dried to afford **43** (924 mg, 2.83 mmol, 28%) as a black solid.

Molecular formula: $C_{12}H_{11}IN_2O$
MW: 326.1 g.mol^{-1}
^{1}H-NMR (acetone-d$_6$, 300 MHz): δ 9.34–9.26 (m, 2H), 8.91 (tt, *J* = 7.8, 1.4 Hz, 1H), 8.87–8.83 (m, 1H), 8.48–8.39 (m, 2H), 8.17–8.08 (m, 2H), 7.81 (ddd, *J* = 6.8, 4.7, 2.3 Hz, 1H), 6.83 (s, 2H).

4'-(4-(Bromomethyl)phenyl)-2,2':6',2''-terpyridine (**44**)

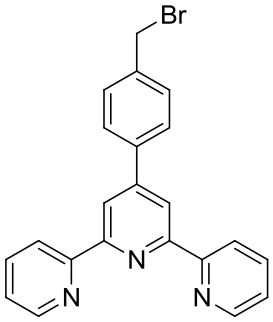

*p*BrPhTpy **36** (5.23 g, 16.18 mmol, 1.0 eq) was dissolved in dry and degassed CCl_4 (40 mL). NBS (3.46 g, 19.44 mmol, 1.2 eq) was added, followed by AIBN (266 mg, 1.62 mmol, 0.1 eq). The resulting mixture was refluxed for 5 h, filtered while hot and concentrated. Recrystallization from a 2/1 EtOH/acetone mixture afforded **44** (3.40 g, 8.46 mmol, 52%) as a pale yellow solid.

Molecular formula: $C_{22}H_{16}BrN_3$
MW: 402.3 g.mol^{-1}
^{1}H-NMR (CDCl$_3$, 300 MHz): δ 8.77–8.71 (m, 4H), 8.71–8.65 (m, 2H), 7.94–7.85 (m, 4H), 7.57–7.51 (m, 2H), 7.36 (ddd, *J* = 7.5, 4.8, 1.2 Hz, 2H), 4.57 (s, 2H).
^{13}C-NMR (CDCl$_3$, 75 MHz): δ 156.2 (C_q), 156.0 (C_q), 149.7 (C_q), 149.2 (CH), 138.8 (C_q), 138.7 (C_q), 137.2 (CH), 129.8 (CH), 127.9 (CH), 124.1 (CH), 121.6 (CH), 119.1 (CH), 33.1 (CH_2).
HRMS (ESI): *m/z* = 402.0587 $[M+H]^+$ (found), 402.0600 calcd. for $C_{22}H_{17}BrN_3^+$, 424.0409 $[M+Na]^+$ (found), 424.0420 calcd. for $C_{22}H_{16}BrN_3Na^+$, 324.1493 $[M+2H-Br]^+$ (found), 324.1495 calcd. for $C_{22}H_{18}N_3^+$.

Diethyl 4-([2,2':6',2''-terpyridin]-4'-yl)benzylphosphonate (**45**)

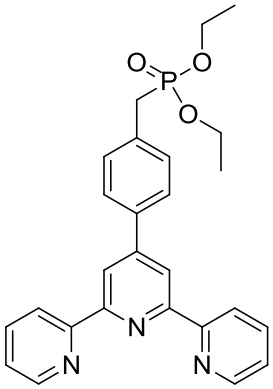

Compound **44** (3.47 g, 8.62 mmol, 1.0 eq) was dissolved in $P(OEt)_3$ (5.6 mL). The resulting solution was refluxed for 30 min and concentrated under heating and high vacuum to afford **45** (3.76 g, 8.19 mmol, 95%) as a very viscous brown oil.

Molecular formula: $C_{26}H_{26}N_3O_3P$
MW: 459.5 $g.mol^{-1}$
^{1}H-NMR ($CDCl_3$, 300 MHz): δ 8.70–8.65 (m, 4H), 8.64–8.58 (m, 2H), 7.87–7.77 (m, 4H), 7.38 (dd, *J* = 8.3, 2.4 Hz, 2H), 7.30 (ddd, *J* = 7.5, 4.8, 1.2 Hz, 2H), 4.03–3.92 (m, 4H), 3.16 (d, *J* = 21.8 Hz, 2H), 1.20 (t, *J* = 7.3 Hz, 6H).
^{13}C-NMR ($CDCl_3$, 75 MHz): δ 156.1 (C_q), 155.8 (C_q), 150.0 (C_q), 148.9 (CH), 137.1 (CH), 137.0 (CH), 137.0 (CH), 132.9 (C_q), 132.8 (C_q), 130.4 (CH), 130.4 (CH), 127.5 (CH), 127.5 (CH), 123.9 (CH), 121.5 (CH), 118.9 (CH), 62.3 (CH_2), 62.2 (CH_2), 34.6 (CH_2), 32.8 (CH_2), 16.5 (CH_3), 16.4 (CH_3).
HRMS (ESI): *m/z* = 460.1764 $[M+H]^+$ (found), 460.1785 calcd. for $C_{26}H_{27}N_3O_3P^+$, 482.1576 $[M+Na]^+$ (found), 482.1604 calcd. for $C_{26}H_{26}N_3NaO_3P^+$, 941.3283 $[2M+Na]^+$ (found), 941.3316 calcd. for $C_{52}H_{52}N_6NaO_6P_2^+$.

4'-(4-(4,4,5,5-Tetramethyl-1,3,2-dioxaborolan-2-yl)phenyl)-2,2':6',2''-terpyridine (**46**)

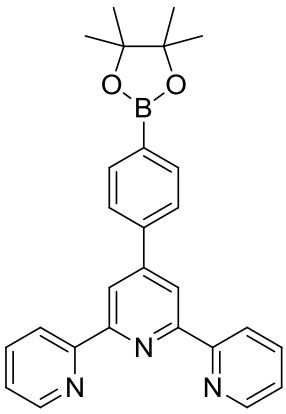

pBrPhTpy **36** (1.09 g, 2.8 mmol, 1.0 eq) was suspended in dry dioxane (14 mL). Bis(pinacolato)diboron (859 mg, 3.36 mmol, 1.2 eq) was added, followed by $PdCl_2$ (25 mg, 0.14 mmol, 0.05 eq), dppf (78 mg, 0.14 mmol, 0.05 eq) and KOAc (412 mg, 4.2 mmol, 1.5 eq). The resulting mixture was heated at 80 °C for 24 h and concentrated. $CHCl_3$ was added, the mixture was washed with aq. 0.1 M EDTA (3×) and the combined aqueous layers were extracted with DCM (3×). The combined organic layers were dried over Na_2SO_4, filtered and concentrated. Column chromatography (SiO_2, 80:20 Cy/AcOEt) afforded **46** (998 mg, 2.29 mmol, 82%) as a white solid.

Molecular formula: $C_{27}H_{26}BN_3O_2$
MW: 435.3 g.mol^{-1}
^{1}H-NMR ($CDCl_3$, 300 MHz): δ 8.78 (ddt, *J* = 4.1, 2.3, 1.1 Hz, 2H), 8.71 (s, 2H), 8.68 (dt, *J* = 8.0, 1.1 Hz, 2H), 8.06 (td, *J* = 7.7, 1.8 Hz, 2H), 7.94–7.88 (m, 2H), 7.82–7.76 (m, 2H), 7.55 (ddd, *J* = 7.5, 4.8, 1.1 Hz, 2H), 1.18 (s, 12H).
^{13}C-NMR ($CDCl_3$, 75 MHz): δ 156.0 (C_q), 149.3 (C_q), 149.1 (CH), 137.5 (C_q), 137.3 (CH), 132.3 (CH), 129.1 (CH), 124.2 (CH), 123.7 (C_q), 121.6 (CH), 118.8 (CH), 83.7 (C_q), 25.2 (CH_3). One C_q missing.
HRMS (ESI): *m/z* = 458.2000 $[M+Na]^+$ (found), 458.2010 calcd. for $C_{27}H_{26}BN_3NaO_2^+$, 436.2196 $[M+H]^+$ (found), 436.2191 calcd. for $C_{27}H_{27}BN_3O_2^+$.

$MnTpyCl_2$ (**49**)

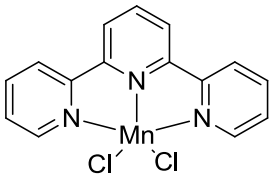

Tpy **47** (500 mg, 2.14 mmol, 1.0 eq) was suspended in acetone (75 mL). The resulting mixture was heated to 50 °C until total dissolution, and $MnCl_2$•$4H_2O$ (2.163 g, 10.93 mmol, 5.1 eq) dissolved in MeOH (25 mL) was added. The resulting mixture was heated at 50 °C for 3 h and cooled to rt. The precipitate was filtered, washed with a 1/4 MeOH/acetone mixture, then thoroughly with Et_2O, and dried to afford $MnTpyCl_2$ **49** (764 mg, 2.12 mmol, 99%) as a yellow solid.

Molecular formula: $C_{15}H_{11}Cl_2MnN_3$
MW: 359.1 g.mol^{-1}
HRMS (ESI): *m/z* = 380.9601 $[MnLCl_2+Na]^+$ (found), 380.9603 calcd. for $C_{15}H_{11}Cl_2MnN_3Na^+$, 323.0012 $[MnLCl]^+$ (found), 323.0022 calcd. for $C_{15}H_{11}ClMnN_3^+$, 234.1027 $[L+H]^+$ (found), 234.1026 calcd. for $C_{15}H_{12}N_3^+$, 289.0408 $[MnL+H]^+$ (found), 289.0406 calcd. for $C_{15}H_{12}MnN_3^+$, 260.5663 $[MnL_2]^{2+}$ (found), 260.5638 calcd. for $C_{30}H_{22}MnN_6^{2+}/2$.

***p*ClMnTpyCl$_2$** (**50**)

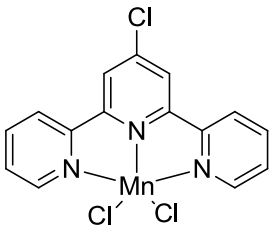

*p*ClTpy **48** (115 mg, 0.43 mmol, 1.0 eq) was suspended in acetone (20 mL). The resulting mixture was heated to 50 °C until total dissolution, and $MnCl_2$•$4H_2O$ (435 mg, 2.2 mmol, 5.1 eq) dissolved in MeOH (5 mL) was added. The resulting mixture was heated at 50 °C for 3 h and cooled to rt. The precipitate was filtered, washed with a 1/4 MeOH/acetone mixture, then copiously with Et_2O, and dried to afford *p*ClMnTpyCl_2 **50** (155 mg, 0.394 mmol, 92%) as a pale orange solid.

Molecular formula: $C_{15}H_{10}Cl_3MnN_3$
MW: 393.6 g.mol^{-1}

HRMS (ESI): *m/z* = 414.9205 $[MnLCl_2+Na]^+$ (found), 414.9213 calcd. for $C_{15}H_{10}Cl_3MnN_3Na^+$, 356.9628 $[MnLCl]^+$ (found), 356.9632 calcd. for $C_{15}H_{10}Cl_2MnN_3^+$, 323.0016 $[MnL+H]^+$ (found), 323.0017 calcd. for $C_{15}H_{11}ClMnN_3^+$, 268.0640 $[L+H]^+$ (found), 268.0636 calcd. for $C_{15}H_{11}ClN_3^+$, 290.0453 $[L+Na]^+$ (found), 290.0455 calcd. for $C_{15}H_{10}ClN_3^+$, 294.5251 $[MnL_2]^{2+}$ (found), 294.5248 calcd. for $C_{30}H_{20}Cl_2MnN_6^{2+}/2$.

General procedure D: synthesis of PhTpyMnBr$_2$ complexes

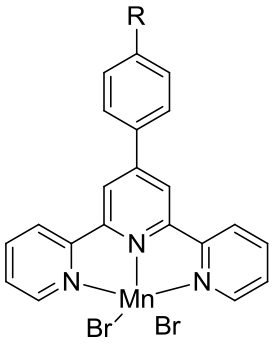

A PhTpy (**36**, **37**, **39** or **41**) (1.0 eq) was suspended in MeCN. The resulting mixture was heated to 60 °C until total dissolution, and aq. $MnBr_2$ (8.15 eq) was added. The resulting mixture was refluxed for 3 h and cooled to rt. The precipitate was filtered, washed with cold aq. 0.1 M $MnBr_2$, cold MeCN, then thoroughly with Et_2O, and dried to afford the corresponding MnPhTpyBr$_2$.

pBrPhTpyMnBr$_2$ (**51**, R = Br)

Using the general procedure D with *p*BrPhTpy **36** (200 mg, 0.515 mmol) and $MnBr_2$ (903 mg, 4.2 mmol, 1.4 mL) in MeCN (1.4 mL), 275 mg (0.456 mmol, 89%) of *p*BrPhTpyMnBr$_2$ **51** were obtained as a yellow solid.

Molecular formula: $C_{21}H_{14}Br_3MnN_3$
MW: 603.0 g.mol^{-1}
HRMS (ESI): *m/z* = 520.8909 $[MnLBr]^+$ (found), 520.8929 calcd. for $C_{21}H_{14}Br_2MnN_3^+$, 388.0424 $[L+H]^+$ (found), 388.0444 calcd. for $C_{21}H_{15}BrN_3^+$, 415.5033 $[MnL_2]^{2+}$ (found), 415.5046 calcd. for $C_{42}H_{28}Br_2MnN_6^{2+}/2$.

***p*CCHPhTpyMnBr$_2$** (**52**, R = CCH)
Using the general procedure D with *p*HCCPhTpy **37** (70 mg, 0.210 mmol) and $MnBr_2$ (368 mg, 1.71 mmol, 3 mL) in MeCN (3 mL), 94 mg (0.172 mmol, 82%) of *p*CCHPhTpyMnBr$_2$ **52** were obtained as an orange solid.

Molecular formula: $C_{23}H_{15}Br_2MnN_3$
MW: 548.1 g.mol^{-1}
HRMS (APCI): *m/z* = 466.9835 $[MnLBr]^+$ (found), 466.9824 calcd. for $C_{23}H_{15}BrMnN_3^+$, 334.1357 $[L+H]^+$ (found), 333.1339 calcd. for $C_{23}H_{16}N_3^+$.

pClPhTpyMnBr$_2$ (**53**, R = Cl)

Using the general procedure D with *p*ClPhTpy **39** (200 mg, 0.582 mmol) and $MnBr_2$ (1.02 g, 4.74 mmol, 6 mL) in MeCN (6 mL), 286 mg (0.512 mmol, 88%) of *p*ClPhTpyMnBr_2 **53** were obtained as an ochre solid.

Molecular formula: $C_{21}H_{14}Br_2ClMnN_3$
MW: 558.6 g.mol^{-1}
HRMS (ESI): *m/z* = 476.9424 $[MnLBr]^+$ (found), 476.9435 calcd. for $C_{21}H_{14}BrClMnN_3^+$, 344.0940 $[L+H]^+$ (found), 344.0940 calcd. for $C_{21}H_{15}ClN_3^+$.

pFPhTpyMnBr_2 (**54**, R = F)

Using the general procedure D with *p*FPhTpy **41** (200 mg, 0.611 mmol) and $MnBr_2$ (1.07 g, 4.98 mmol, 5 mL) in MeCN (5 mL), 221 mg (0.408 mmol, 67%) of *p*FPhTpyMnBr_2 **54** were obtained as an orange solid.

Molecular formula: $C_{21}H_{14}Br_2FMnN_3$
MW: 542.1 g.mol^{-1}
HRMS (APCI): *m/z* = 460.9738 $[MnLBr]^+$ (found), 460.9730 calcd. for $C_{21}H_{14}BrFMnN_3^+$, 328.1274 $[L+H]^+$ (found), 328.1245 calcd. for $C_{21}H_{15}FN_3^+$.

General procedure E: synthesis of Mn(Tpy)$_2^{2+}$, 2PF$_6^-$ complexes

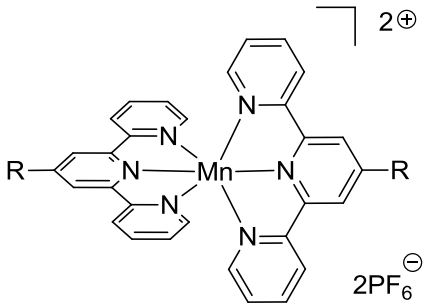

A Tpy (**40**, **41**, **47**, **48** or **55**) (2.0 eq) was dissolved in acetone. Aq. $MnCl_2$ (1 eq) was added, and the resulting mixture was stirred at rt for 30 min. Aq. NH_4PF_6 (10.0 eq) was added, and the resulting precipitate was stirred at rt for 15 min, filtered, washed with a cold 1/1 acetone/H_2O mixture, dissolved in MeCN, reprecipitated by slow addition of Et_2O, filtered again and dried to afford the corresponding Mn(Tpy)$_2^{2+}$, 2PF$_6^-$.

(pMePhTpy)$_2^{2+}$, 2PF$_6^-$ (**56**, R = tolyl)

Using the general procedure E with *p*MePhTpy **40** (100 mg, 0.309 mmol) and $MnCl_2$ (19.5 mg, 0.155 mmol, 5 mL) in acetone (10 mL) after precipitation with NH_4PF_6 (253 mg, 1.55 mmol, 7.5 mL), 86 mg (0.087 mmol, 56%) of (pMePhTpy)$_2^{2+}$, 2PF$_6^-$ **56** were obtained as a pale yellow solid.

Molecular formula: $C_{44}H_{34}F_{12}MnN_6P_2$
MW: 991.7 g.mol^{-1}
HRMS (ESI): *m/z* = 351.1095 $[MnL_2+H]^{2+}$ (found), 351.1146 calcd. for $C_{44}H_{35}MnN_6^{2+}/2$, 324.1489 $[L+H]^+$ (found), 324.1495 calcd. for $C_{22}H_{18}N_3^+$, 346.1318 $[L+Na]^+$ (found), 346.1315 calcd. for $C_{22}H_{17}N_3Na^+$.

(pFPhTpy)$_2^{2+}$, 2PF$_6^-$ (**57**, R = *p*-fluorophenyl)

Using the general procedure E with *p*FPhTpy **41** (100 mg, 0.305 mmol) and $MnCl_2$ (19.5 mg, 0.153 mmol, 5 mL) in acetone (10 mL) after precipitation with NH_4PF_6 (250 mg, 1.53 mmol, 7.5 mL), 124 mg (0.124 mmol, 80%) of $(pFPhTpy)_2^{2+}$, $2PF_6^-$ **57** were obtained as a pale yellow solid.

Molecular formula: $C_{42}H_{28}F_{14}MnN_6P_2$
MW: 999.6 g.mol^{-1}

Tpy_2^{2+}, $2PF_6^-$ (**58**, R = H)

Using the general procedure E with Tpy **47** (100 mg, 0.429 mmol) and $MnCl_2$ (26.9 mg, 0.214 mmol, 5 mL) in acetone (10 mL) after precipitation with NH_4PF_6 (349 mg, 2.14 mmol, 7.5 mL), 122 mg (0.15 mmol, 70%) of Tpy_2^{2+}, $2PF_6^-$ **58** were obtained as a pale yellow solid.

Molecular formula: $C_{30}H_{22}F_{12}MnN_6P_2$
MW: 811.4 g.mol^{-1}
HRMS (ESI): *m/z* = 260.5649 $[MnL_2]^{2+}$ (found), 260.5638 calcd. for $C_{30}H_{22}MnN_6^{2+}/2$, 234.1009 $[L+H]^+$ (found), 234.1026 calcd. for $C_{15}H_{12}N_3^+$, 256.0830 $[L+Na]^+$ (found), 256.0845 calcd. for $C_{15}H_{11}N_3Na^+$, 289.0389 $[MnL+H]^+$ (found), 289.0406 calcd. for $C_{15}H_{12}MnN_3^+$.

$(pClTpy)_2^{2+}$, $2PF_6^-$ (**59**, R = Cl)

Using the general procedure E with *p*ClTpy **48** (100 mg, 0.374 mmol) and $MnCl_2$ (23.5 mg, 0.187 mmol, 5 mL) in acetone (10 mL) after precipitation with NH_4PF_6 (305 mg, 1.87 mmol, 7.5 mL), 121 mg (0.137 mmol, 73%) of $(pClTpy)_2^{2+}$, $2PF_6^-$ **59** were obtained as a pale yellow solid.

Molecular formula: $C_{30}H_{20}Cl_2F_{12}MnN_6P_2$
MW: 880.3 g.mol^{-1}
HRMS (ESI): *m/z* = 294.5263 $[MnL_2]^{2+}$ (found), 294.5248 calcd. for $C_{30}H_{20}Cl_2MnN_6^{2+}/2$, 268.0649 $[L+H]^+$ (found), 268.0636 calcd. for $C_{15}H_{11}ClN_3^+$, 323.0024 $[MnL+H]^+$ (found), 323.0017 calcd. for $C_{15}H_{11}ClMnN_3^+$,

$(pPyrrTpy)_2^{2+}$, $2PF_6^-$ (**60**, R = pyrrolidinyl)

Using the general procedure E with *p*PyrrTpy **55** (50 mg, 0.165 mmol) and $MnCl_2$ (10.4 mg, 0.083 mmol, 2.5 mL) in acetone (5 mL) after precipitation with NH_4PF_6 (135 mg, 0.83 mmol, 3.8 mL), 63 mg (0.066 mmol, 79%) of $(pPyrrTpy)_2^{2+}$, $2PF_6^-$ **60** were obtained as a pale yellow solid.

Molecular formula: $C_{38}H_{36}F_{12}MnN_8P_2$
MW: 949.6 g.mol^{-1}
HRMS (ESI): *m/z* = 329.6257 $[MnL_2]^{2+}$ (found), 329.6216 calcd. for $C_{38}H_{36}MnN_8^{2+}/2$, 303.1613 $[L+H]^+$ (found), 303.1604 calcd. for $C_{19}H_{19}N_4^+$, 804.2091 $[MnL_2+PF_6]^+$ (found), 804.2080 calcd. for $C_{38}H_{36}F_6MnN_8P^+$.

General procedure F: Synthesis of $Mn(PhTpy)(Tpy)^{2+}$, $2PF_6^-$ complexes

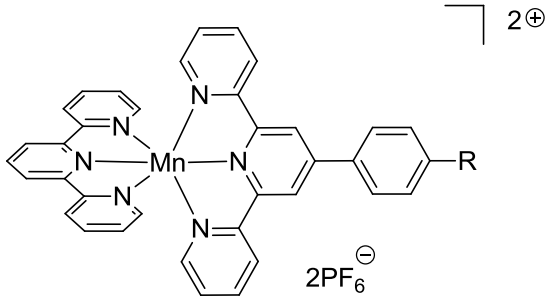

A PhTpyMnBr$_2$ (**51** or **54**) (1.0 eq) was suspended in MeCN. The resulting suspension was refluxed until total dissolution, Tpy **47** (1.0 eq) was added, and the reflux was continued for 15 h. The mixture was cooled to rt, aq. 0.2 M NH_4PF_6 was added, and the mixture was stirred at rt for 1 h, filtered over a pad of celite and washed with H_2O and Et_2O. The celite was then rinced with acetone and the filtrate was concentrated to afford Mn(PhTpy)(Tpy)$^{2+}$, 2PF$_6^-$.

Mn(pBrPhTpy)(Tpy)$^{2+}$, 2PF$_6^-$ (**61**, R = Br)

Using the general procedure F with *p*BrPhTpyMnBr$_2$ **51** (70 mg, 0.116 mmol) and Tpy **47** (27 mg, 0.116 mmol) in MeCN (40 mL) after precipitation with NH_4PF_6 (25 mL), 72.5 mg (0.075 mmol, 65%) of Mn(*p*BrPhTpy)(Tpy)$^{2+}$, 2PF$_6^-$ **61** were obtained as a pale yellow solid.

Molecular formula: $C_{36}H_{25}BrF_{12}MnN_6P_2$
MW: 966.4 g.mol^{-1}

Mn(pFPhTpy)(Tpy)$^{2+}$, 2PF$_6^-$ (**62**, R = F)

Using the general procedure F with *p*FPhTpyMnBr$_2$ **54** (50 mg, 0.092 mmol) and Tpy **47** (21.4 mg, 0.092 mmol) in MeCN (100 mL) after precipitation with NH_4PF_6 (20 mL), 51 mg (0.056 mmol, 61%) of Mn(*p*FPhTpy)(Tpy)$^{2+}$, 2PF$_6^-$ **62** were obtained as a pale yellow solid.

Molecular formula: $C_{36}H_{25}F_{13}MnN_6P_2$
MW: 905.5 g.mol^{-1}

2,6-Bis(bromomethyl)pyridine (**64**)

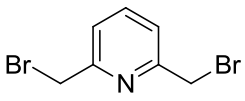

2,6-Pyridinedimethanol **63** (2.0 g, 14.37 mmol, 1.0 eq) was dissolved in aq. 48% HBr (20 mL). The resulting solution was refluxed for 6h and cooled to rt. H_2O (50 mL) was added, followed by solid $NaHCO_3$ until pH ≈ 8. The resulting mixture was extracted with DCM (3×) and the combined organic layers were dried over Na_2SO_4, filtered and concentrated. Column chromatography (SiO_2, 90/10 to 80:20 Cy/AcOEt) afforded **64** (1.54 g, 5.82 mmol, 41%) as a white solid.

Molecular formula: $C_7H_7Br_2N$
MW: 264.9 g.mol^{-1}
^{1}H-NMR (CDCl$_3$, 300 MHz): δ 7.71 (t, *J* = 7.8 Hz, 1H), 7.38 (d, *J* = 7.8 Hz, 2H), 4.54 (s, 4H).
^{13}C-NMR (CDCl$_3$, 75 MHz): δ 156.7 (C_q), 138.2 (CH), 122.9 (CH), 33.6 (CH_2).

HRMS (ESI): *m/z* = 263.9810 $[M+H]^+$ (found), 263.9810 calcd. for $C_7H_8Br_2N^+$, 285.8835 $[M+Na]^+$ (found), 285.8837 calcd. for $C_7H_7Br_2NNa^+$.

Tetraethyl 2,2',2'',2'''-((pyridine-2,6-diylbis(methylene))bis(azanetriyl))tetraacetate (Et-PyMTA **65**)

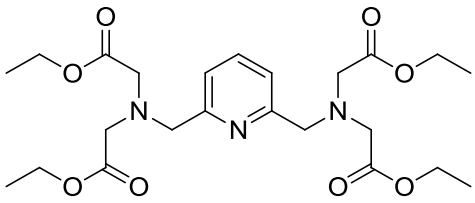

Compound **64** (500 mg, 1.89 mmol, 1.0 eq) was dissolved in dry MeCN (15 mL). Ethyl iminodiacetate (680 µL, 3.78 mmol, 2.0 eq) was added, followed by Na_2CO_3 (2 g, 18.9 mmol, 10.0 eq). The resulting mixture was stirred at rt for 15h, filtered and concentrated. The residue was dissolved in DCM and washed with H_2O (1×) and sat. aq. NaCl (1×). The organic layer was dried over Na_2SO_4, filtered and concentrated. Column chromatography (SiO_2, 80:20 to 50:50 Cy/AcOEt) afforded Et-PyMTA **65** (690 mg, 1.43 mmol, 76%) as a colourless oil.

Molecular formula: $C_{23}H_{35}N_3O_8$
MW: 481.5 g.mol^{-1}
^{1}H-NMR ($CDCl_3$, 300 MHz): δ 7.66 (t, *J* = 7.6 Hz, 1H), 7.48 (d, *J* = 7.6 Hz, 2H), 4.15 (q, *J* = 7.2 Hz, 8H), 4.03 (s, 4H), 3.59 (s, 8H), 1.25 (t, *J* = 7.2 Hz, 12H).
^{13}C-NMR ($CDCl_3$, 75 MHz): δ 171.3 (C_q), 158.3 (C_q), 137.6 (CH), 121.5 (CH), 60.7 (CH_2), 59.9 (CH_2), 55.1 (CH_2), 14.4 (CH_3).
HRMS (ESI): *m/z* = 482.2482 $[M+H]^+$ (found), 482.2497 calcd. for $C_{23}H_{36}N_3O_8^+$, 504.2297 $[M+Na]^+$ (found), 504.2316 calcd. for $C_{23}H_{35}N_3NaO_8^+$.

2,2',2'',2'''-((Pyridine-2,6-diylbis(methylene))bis(azanetriyl))tetraacetic acid (PyMTA **66**)

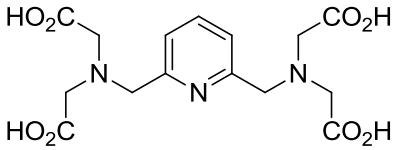

Et-PyMTA **65** (463 mg, 0.962 mmol, 1.0 eq) was dissolved in a mixture of THF (6 mL) and H_2O (6 mL). LiOH (277 mg, 11.54 mmol, 12.0 eq) was added and the resulting mixture was stirred at rt for 15 h. Exchange resin Amberlite IR-120 (H-form) was then added to the solution, which was further stirred for 15 h at rt, filtered and concentrated to afford PyMTA **66** (329 mg, 0.89 mmol, 93%) as a colourless oil.

Molecular formula: $C_{15}H_{19}N_3O_8$
MW: 369.3 g.mol^{-1}

Mn complex of PyMTA (**67**)

PyMTA **66** (388 mg, 1.05 mmol, 1.0 eq) was dissolved in H_2O (19 mL). Argon was bubbled for 10 min, and the pH was adjusted to 6.5 with solid $NaHCO_3$. The mixture was cooled to 0 °C, and $MnCl_2$ (158 mg, 1.26 mmol, 1.2 eq) dissolved in degassed H_2O (50 mL) was slowly added while keeping the pH between 5 and 7 with solid $NaHCO_3$. The mixture was allowed to warm to rt for 15 h and the pH was

adjusted to 8.5 with aq. 0.1 M NaOH. Acetone (700 mL) was added and the resulting precipitate was stirred at rt for 15 min, filtered and washed with acetone. The solid was reprecipitated from H_2O with acetone, filtered and dried to afford the Mn complex of PyMTA **67** (355 mg, 0.845 mmol, 80%) as a white solid.

Molecular formula: $C_{15}H_{15}MnN_3O_8$
MW: 420.2 g.mol^{-1}

(4-Bromopyridine-2,6-diyl)dimethanol (**68**)

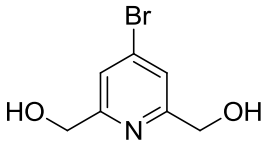

Compound **9** (4.74 g, 15.7 mmol, 1.0 eq) was dissolved in abs. EtOH (200 mL). $NaBH_4$ (2.67 g, 70.7 mmol, 4.5 eq) was added portionwise, and the resulting mixture was stirred for 2 h at rt, refluxed for 15 h and concentrated. Sat. aq. $NaHCO_3$ (25 mL) was added and the resulting mixture was refluxed for 5 min. H_2O (35 mL) was then added, the suspension was cooled to rt, filtered and extracted with DCM containing a small quantity of MeOH (3×). The combined organic layers were dried over Na_2SO_4, filtered and concentrated to afford **68** (2.85 g, 13.1 mmol, 83%) as a white solid.

Molecular formula: $C_7H_8BrNO_2$
MW: 218.1 g.mol^{-1}
^{1}H-NMR ($CDCl_3$, 300 MHz): δ 7.61 (s, 2H), 4.65 (s, 4H).
^{13}C-NMR ($CDCl_3$, 75 MHz): δ 163.7 (C_q), 135.8 (C_q), 123.2 (CH), 65.0 (CH_2).
HRMS (ESI): *m/z* = 217.9816 $[M+H]^+$ (found), 217.9816 calcd. for $C_7H_9BrNO_2^+$, 239.9634 $[M+Na]^+$ (found), 239.9631 calcd. for $C_7H_8BrNNaO_2^+$, 140.0709 $[M-Br+2H]^+$ (found), 140.0706 calcd. for $C_7H_{10}NO_2^+$.

4-Bromo-2,6-bis(bromomethyl)pyridine (**69**)

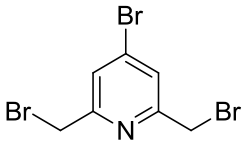

Compound **68** (2.85 g, 13.1 mmol, 1.0 eq) was dissolved in $CHCl_3$ (80 mL). PBr_3 (1.84 mL, 19.6 mmol, 2.8 eq) dissolved in $CHCl_3$ (40 mL) was added dropwise, and the resulting solution was refluxed for 15h and cooled to rt. Aq. 5% NaHCO3 (80 mL) was then added and the resulting mixture was extracted with $CHCl_3$ (3×). The combined organic layers were dried over Na_2SO_4, filtered and concentrated. Column chromatography (SiO_2, 95:5 Cy/AcOEt) afforded **69** (2.37 g, 6.89 mmol, 53%) as a white solid.

Molecular formula: $C_7H_6Br_3N$
MW: 343.8 g.mol^{-1}
^{1}H-NMR ($CDCl_3$, 300 MHz): δ 7.55 (s, 2H), 4.48 (s, 4H).
^{13}C-NMR ($CDCl_3$, 75 MHz): δ 158.0 (C_q), 134.3 (C_q), 126.2 (CH), 32.5 (CH_2).

HRMS (ESI): *m/z* = 341.8117 $[M+H]^+$ (found), 341.8123 calcd. for $C_7H_7Br_3N^+$, 363.7939 $[M+Na]^+$ (found), 363.7943 calcd. for $C_7H_6Br_3NNa^+$.

Tetraethyl 2,2',2'',2'''-(((4-bromopyridine-2,6-diyl)bis(methylene))bis(azanetriyl))tetraacetate (Et-*p*BrPyMTA **70**)

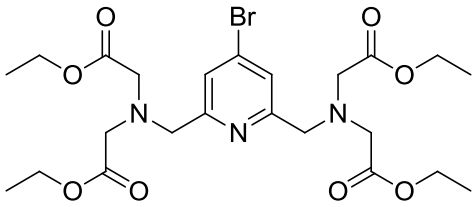

Compound **69** (1.00 g, 2.91 mmol, 1.0 eq) was dissolved in dry MeCN (25 mL). Ethyl iminodiacetate (1.04 mL, 5.82 mmol, 2.0 eq) was added, followed by Na_2CO_3 (3.08 g, 29.1 mmol, 10.0 eq). The resulting mixture was stirred at rt for 15h, filtered and concentrated. The residue was dissolved in DCM and washed with H_2O (1×) and sat. aq. NaCl (1×). The organic layer was dried over Na_2SO_4, filtered and concentrated. Column chromatography (SiO_2, 80:20 to 50:50 Cy/AcOEt) afforded Et-pBrPyMTA **70** (1.44 g, 2.58 mmol, 88%) as a colourless oil.

Molecular formula: $C_{23}H_{34}BrN_3O_8$
MW: 560.4 g.mol^{-1}
^{1}H-NMR (CDCl$_3$, 300 MHz): δ 7.70 (s, 2H), 4.16 (q, *J* = 7.1 Hz, 8H), 3.99 (s, 4H), 3.58 (s, 8H), 1.26 (t, *J* = 7.1 Hz, 12H).
^{13}C-NMR (CDCl$_3$, 75 MHz): δ 171.2 (C_q), 160.2 (C_q), 134.7 (C_q), 124.6 (CH), 60.8 (CH_2), 59.6 (CH_2), 55.1 (CH_2), 14.4 (CH_3).
HRMS (ESI): *m/z* = 560.1602 $[M+H]^+$ (found), 560.1602 calcd. for $C_{23}H_{35}BrN_3O_8^+$, 582.1425 $[M+Na]^+$ (found), 582.1421 calcd. for $C_{23}H_{34}BrN_3NaO_8^+$.

Tetra-*tert*-butyl 2,2',2'',2'''-(((4-bromopyridine-2,6-diyl)bis(methylene))bis(azanetriyl))tetraacetate (^{t}Bu-*p*BrPyMTA **71**)

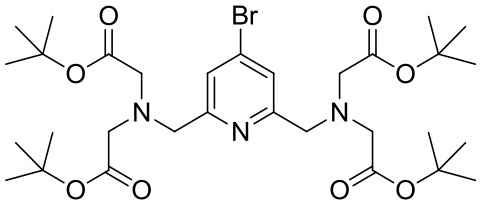

Compound **69** (492 mg, 1.43 mmol, 1.0 eq) was dissolved in dry MeCN (12 mL). *Tert*-butyl iminodiacetate (700 mg, 2.85 mmol, 2.0 eq) was added, followed by Na_2CO_3 (1.51g, 14.3 mmol, 10 eq). The resulting mixture was stirred at rt for 15h, filtered and concentrated. The residue was dissolved in DCM and washed with H_2O (1×) and sat. aq. NaCl (1×). The organic layer was dried over Na_2SO_4, filtered and concentrated. Column chromatography (SiO_2, 95:5 to 80:20 Cy/AcOEt) afforded ^{t}Bu-*p*BrPyMTA **71** (864 mg, 1.29 mmol, 88%) as a colourless oil.

Molecular formula: $C_{31}H_{50}BrN_3O_8$
MW: 672.7 g.mol^{-1}
^{1}H-NMR (CDCl$_3$, 300 MHz): δ 7.72 (s, 2H), 3.98 (s, 4H), 3.46 (s, 8H), 1.45 (s, 36H).

^{13}C-NMR ($CDCl_3$, 75 MHz): δ 170.5 (C_q), 160.7 (C_q), 134.7 (C_q), 124.3 (CH), 81.3 (C_q), 59.6 (CH_2), 56.0 (CH_2), 28.3 (CH_3).
HRMS (ESI): *m/z* = 672.2858 $[M+H]^+$ (found), 672.2854 calcd. for $C_{31}H_{51}BrN_3O_8^+$, 694.2685 $[M+Na]^+$ (found), 694.2673 calcd. for $C_{31}H_{50}BrN_3NaO_8^+$.

2,2',2'',2'''-(((4-Bromopyridine-2,6-diyl)bis(methylene))bis(azanetriyl))tetraacetic acid (*p*BrPyMTA **72**)

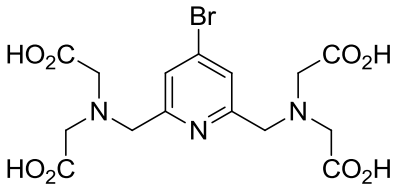

^{t}Bu-*p*BrPyMTA **71** (118.0 mg, 0.175 mmol, 1.0 eq) was dissolved in DCM (2.0 mL). TFA (4.0 mL) was added, and the resulting mixture was stirred at rt for 2.5 h and concentrated. The residue was taken up in Et_2O, and the resulting solid was filtered, washed with Et_2O and dried. Purification by HPLC (5 to 35% MeCN) afforded *p*BrPyMTA **72** as a white solid.

Molecular formula: $C_{15}H_{18}BrN_3O_8$
MW: 448.2 $g.mol^{-1}$
^{1}H-NMR (D_2O, 300 MHz): δ 7.79 (s, 2H), 4.67 (s, 4H), 4.17 (s, 8H).
^{13}C-NMR (MeOD, 75 MHz): δ 173.6, 158.4, 138.1, 127.5, 59.0, 56.4.
HPLC: 5.28 min (5 to 100% MeCN in 30 min, > 95%)
HRMS (ESI): *m/z* = 446.0200 $[M-H]^-$ (found), 446.0205 calcd. for $C_{15}H_{17}BrN_3O_8^-$.

Mn complex of BrPyMTA 73

*p*BrPyMTA **72** (27.0 mg, 0.048 mmol, 1.0 eq) was dissolved in H_2O (1.4 mL). Argon was bubbled for 10 min, and the pH was adjusted to 6.5 with solid $NaHCO_3$. The mixture was cooled to 0 °C, and $MnCl_2$ (7.3 mg, 0.058 mmol, 1.2 eq) dissolved in degassed H_2O (50 mL) was slowly added while keeping the pH between 5 and 7 with solid $NaHCO_3$. The mixture was allowed to warm to rt for 15 h, and the pH was adjusted to 8.5 with aq. 0.1 M NaOH. Acetone (69 mL) was added and the resulting precipitate was stirred at rt for 15 min, filtered and washed with acetone. The solid was reprecipitated from H_2O (3 mL) with acetone (65 mL), filtered and dried to afford the Mn complex of BrPyMTA **73** (25 mg, 0.050 mmol, 100%) as a white solid.

Molecular formula: $C_{15}H_{14}BrMnN_3O_8$
MW: 499.13 $g.mol^{-1}$
HRMS (ESI): *m/z* = 566.9027 $[M+3Na]^-$ (found), 566.9043 calcd. for $C_{15}H_{14}BrMnN_3Na_3O_8^-$.

Tetraethyl 2,2',2'',2'''-(((4-azidopyridine-2,6-diyl)bis(methylene))bis(azanetriyl))tetraacetate (Et-*p*N_3PyMTA **74**)

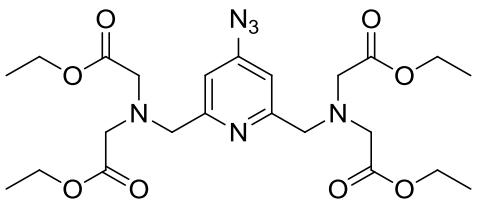

Et-*p*BrPyMTA **70** (467 mg, 0.833 mmol, 1.0 eq) and NaN_3 (542 mg, 8.33 mmol, 10.0 eq) were dissolved in dry DMF (6 mL). The resulting mixture was heated at 100 °C for 48 h and cooled to rt. H_2O was added and the mixture was extracted with AcOEt (3×). The combined organic layers were dried over Na_2SO_4, filtered and concentrated. Column chromatography (SiO_2, 70:30 Cy/AcOEt) afforded Et-*p*N_3PyMTA **74** (305 mg, 0.584 mmol, 70%) as a yellow oil.

Molecular formula: $C_{23}H_{34}N_6O_8$
MW: 522.6 g.mol^{-1}
^{1}H-NMR (CDCl$_3$, 300 MHz): δ 7.22 (s, 2H), 4.16 (q, *J* = 7.1 Hz, 8H), 4.00 (s, 4H), 3.59 (s, 8H), 1.26 (t, *J* = 7.1 Hz, 12H).
^{13}C-NMR (CDCl$_3$, 75 MHz): δ 171.2 (C_q), 160.8 (C_q), 150.5 (C_q), 111.6 (CH), 60.8 (CH_2), 59.9 (CH_2), 55.1 (CH_2), 14.4 (CH_3).
HRMS (ESI): *m/z* = 523.2490 $[M+H]^+$ (found), 523.2511 calcd. for $C_{23}H_{35}N_6O_8^+$, 545.2307 $[M+Na]^+$ (found), 545.2330 calcd. for $C_{23}H_{34}N_6NaO_8^+$, 495.2430 $[M-N_2+H]^+$ (found), 495.2449 calcd. for $C_{23}H_{35}N_4O_8^+$, 517.2242 $[M-N_2+Na]^+$ (found), 517.2269 calcd. for $C_{23}H_{34}N_4NaO_8^+$.

Tetra-*tert*-butyl 2,2',2'',2'''-(((4-azidopyridine-2,6-diyl)bis(methylene))bis(azanetriyl))tetraacetate (^{t}Bu-*p*N_3PyMTA **75**)

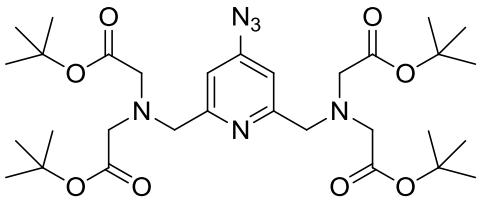

^{t}Bu-*p*BrPyMTA **71** (200 mg, 0.297 mmol, 1.0 eq) and NaN_3 (193 mg, 2.97 mmol, 10.0 eq) were dissolved in dry DMF (2.5 mL). The resulting mixture was heated at 100 °C for 48 h and cooled to rt. H_2O was added and the mixture was extracted with AcOEt (3×). The combined organic layers were dried over Na_2SO_4, filtered and concentrated. Column chromatography (SiO_2, 60:40 to 50:50 Cy/AcOEt) afforded ^{t}Bu-*p*N_3PyMTA **75** (126 mg, 0.199 mmol, 67%) as a yellow oil.

Molecular formula: $C_{31}H_{50}N_6O_8$
MW: 634.8 g.mol^{-1}
^{1}H-NMR (CDCl$_3$, 300 MHz): δ 7.30 (s, 2H), 4.03 (s, 4H), 3.46 (s, 8H), 1.45 (s, 36H).
^{13}C-NMR (CDCl$_3$, 75 MHz): δ 170.5 (C_q), 160.9 (C_q), 111.7 (CH), 81.4 (C_q), 59.5 (CH_2), 56.1 (CH_2), 28.3 (CH_3). A C_q is missing around 150 ppm.
HRMS (ESI): *m/z* = 635.3774 $[M+H]^+$ (found), 635.3763 calcd. for $C_{31}H_{51}N_6O_8^+$, 657.3578 $[M+Na]^+$ (found), 657.3582 calcd. for $C_{31}H_{50}N_6NaO_8^+$, 607.3693 $[M-N_2+H]^+$ (found), 607.3701 calcd. for $C_{31}H_{51}N_4O_8^+$.

Tetraethyl 2,2',2'',2'''-(((4-(4-phenyl-1*H*-1,2,3-triazol-1-yl)pyridine-2,6-diyl)bis(methylene))bis (azanetriyl))tetraacetate (Et-PhTPyMTA **75**)

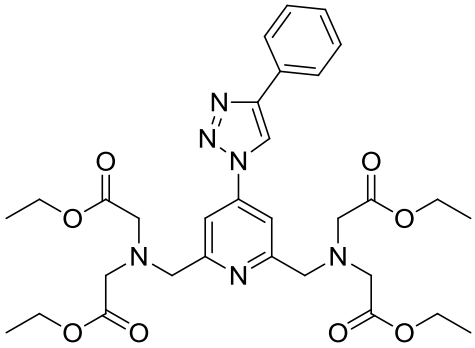

Et-*p*N_3PyMTA **74** (305 mg, 0.584 mmol, 1.0 eq), phenylacetylene (77 µL, 0.701 mmol, 1.2 eq) and CuI (11.2 mg, 0.058 mmol, 0.1 eq) were suspended in dry MeCN (3 mL). The resulting mixture was refluxed for 15h and cooled to rt. Aq. 10% EDTA (5 mL) was then added, the resulting mixture was stirred at rt for 1 h and extracted with AcOEt (3×). The combined organic layers were dried over Na_2SO_4, filtered and concentrated. Column chromatography (SiO_2, 50:50 Cy/AcOEt) afforded Et-PhTPyMTA **76** (247 mg, 0.396 mmol, 68%) as a yellow oil.

Molecular formula: $C_{31}H_{40}N_6O_8$
MW: 624.7 g.mol^{-1}
^{1}H-NMR (CDCl$_3$, 300 MHz): δ 8.44 (s, 1H), 8.12 (s, 2H), 7.97–7.89 (m, 2H), 7.51–7.43 (m, 2H), 7.42–7.34 (m, 1H), 4.23–4.11 (m, 12H), 3.64 (s, 8H), 1.26 (t, *J* = 7.1 Hz, 12H).
^{13}C-NMR (CDCl$_3$, 75 MHz): δ 171.3 (C_q), 161.8 (C_q), 148.8 (C_q), 144.8 (C_q), 130.0 (C_q), 129.1 (CH), 128.8 (CH), 126.1 (CH), 117.3 (CH), 111.2 (CH), 60.8 (CH_2), 60.1 (CH_2), 55.3 (CH_2), 14.4 (CH_3).
HRMS (ESI): *m/z* = 625.2965 $[M+H]^+$ (found), 625.2980 calcd. for $C_{31}H_{41}N_6O_8^+$, 647.2799 $[M+Na]^+$ (found), 647.2800 calcd. for $C_{31}H_{40}N_6NaO_8^+$, 597.2902 $[M+H-N_2]^+$ (found), 597.2919 calcd. for $C_{31}H_{41}N_4O_8^+$, 619.2723 $[M+Na-N_2]^+$ (found), 619.2744 calcd. for $C_{31}H_{40}N_4NaO_8^+$.

2,2',2'',2'''-(((4-(4-Phenyl-1*H*-1,2,3-triazol-1-yl)pyridine-2,6-diyl)bis(methylene))bis(azanetriyl)) tetraacetic acid (PhTPyMTA **77**)

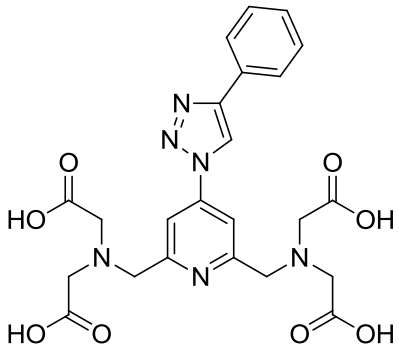

Et-PhTPyMTA **76** (240 mg, 0.384 mmol, 1.0 eq) was suspended in a mixture of THF (10 mL) and H_2O (10 mL). LiOH (111 mg, 4.61 mmol, 12.0 eq) was added, and the resulting mixture was stirred at rt for 24 h. Exchange resin Amberlite IR-120 (H-form) was then added to the pale yellow solution, which was further stirred for 15 h at rt. The white precipitate was then withdrawn *via* Pasteur pipette and concentrated to afford PhTPyMTA **77** (162 mg, 0.316 mmol, 82%) as a white solid.

Molecular formula: $C_{23}H_{24}N_6O_8$
MW: 512.5 g.mol^{-1}

^{1}H-NMR ($CDCl_3$, 300 MHz): δ 12.51 (s, 4H), 9.40 (s, 1H), 8.06 (s, 2H), 8.02–7.95 (m, 2H), 7.57–7.48 (m, 2H), 7.46–7.37 (m, 1H), 4.10 (s, 4H), 3.57 (s, 8H).
HRMS (ESI): *m/z* = 511.1578 $[M-H]^-$ (found), 511.1583 calcd. for $C_{23}H_{23}N_6O_8^-$.

Mn complex of PhTPyMTA 78

PhTPyMTA **77** (70 mg, 0.137 mmol, 1 eq) was dissolved in H_2O (5 mL). Argon was bubbled for 10 min, and the pH was adjusted to 6.5 with solid $NaHCO_3$. The mixture was cooled to 0 °C, and $MnCl_2$ (20.6 mg, 0.164 mmol, 1.2 eq) dissolved in degassed H_2O (6.5 mL) was slowly added while keeping the pH between 5 and 7 with solid $NaHCO_3$. The mixture was allowed to warm to rt for 15 h, and the pH was adjusted to 8.5 with aq. 0.1 M NaOH. Acetone was added until precipitation and the resulting precipitate was stirred at rt for 15 min, filtered and washed with acetone. The solid was reprecipitated from H_2O with acetone, filtered and dried to afford the Mn complex of PhTPyMTA **78** (66.1 mg, 0.117 mmol, 85%) as a pale brown solid.

Molecular formula: $C_{23}H_{20}MnN_6O_8$
MW: 563.4 g.mol^{-1}

Diethyl 4-(((trifluoromethyl)sulfonyl)oxy)pyridine-2,6-dicarboxylate (**79**)

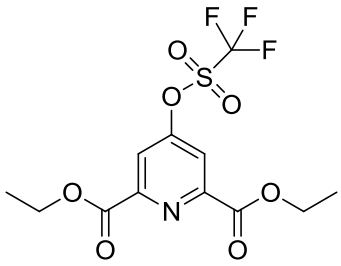

Compound **7** (4.00 g, 16.72 mmol, 1.0 eq) was dissolved in dry DCM (35 mL). The resulting solution was cooled to 0 °C, and 2,6-lutidine (2.91 mL, 25.08 mmol, 1.5 eq) was added, followed by Tf_2O (3.29 mL, 20.06 mmol, 1.2 eq) dropwise. The resulting mixture was allowed to warm to rt for 1h and washed with sat. aq. $NaHCO_3$ (1×), aq. 10% citric acid (2×) and sat. aq. NaCl (1×). The organic layer was dried over Na_2SO_4, filtered and concentrated. Column chromatography (SiO_2, 80:20 Cy/AcOEt) afforded **79** (5.22 g, 14.05 mmol, 84%) as a white solid.

Molecular formula: $C_{12}H_{12}F_3NO_7S$
MW: 371.3 g.mol^{-1}
^{1}H-NMR ($CDCl_3$, 300 MHz): δ 8.17 (s, 2H), 4.52 (q, *J* = 7.1 Hz, 4H), 1.47 (t, *J* = 7.1 Hz, 6H).
^{13}C-NMR ($CDCl_3$, 75 MHz): δ 163.2 (C_q), 157.8 (C_q), 151.8 (C_q), 120.3 (CH), 118.7 (q, *J* = 321.3 Hz, CF_3), 63.2 (CH_2), 14.3 (CH_3).
HRMS (ESI): *m/z* = 372.0342 $[M+H]^+$ (found), 372.0359 calcd. for $C_{12}H_{13}F_3NO_7S^+$, 394.0181 $[M+Na]^+$ (found), 394.0179 calcd. for $C_{12}H_{12}F_3NNaO_7S^+$, 765.0448 $[2M+Na]^+$ (found), 765.0465 calcd. for $C_{24}H_{24}F_6N_2NaO_{14}S_2^+$.

Diethyl 4-(naphthalen-2-yl)pyridine-2,6-dicarboxylate (**80**)

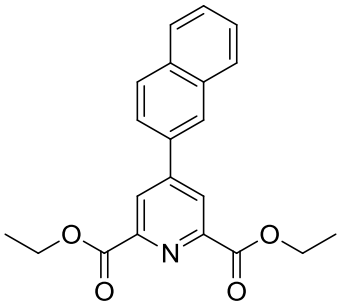

Compound **79** (2.00 g, 5.39 mmol, 1.0 eq) and 2-naphtylboronic acid (1.02 g, 5.93 mmol, 1.1 eq) were dissolved in dry DMF (50 mL). DIPEA (2.02 mL, 11.9 mmol, 2.2 eq) was then added, followed by $Pd(PPh_3)_4$ (312 mg, 0.27 mmol, 0.05 eq). The resulting mixture was heated at 90 °C for 15 h and concentrated. AcOEt was added and the mixture was washed with H_2O (2×) and sat. aq. NaCl (1×). The organic layer was dried over Na_2SO_4, filtered and concentrated. Column chromatography (SiO_2, 80:20 Cy/AcOEt) afforded **80** (1.536 g, 4.40 mmol, 82%) as a light brown solid.

Molecular formula: $C_{21}H_{19}NO_4$
MW: 349.4 g.mol^{-1}
^{1}H-NMR (CDCl$_3$, 300 MHz): δ 8.65 (s, 2H), 8.28–8.24 (m, 1H), 8.01 (d, *J* = 8.6 Hz, 1H), 7.99–7.88 (m, 2H), 7.85 (dd, *J* = 8.6, 1.9 Hz, 1H), 7.62–7.53 (m, 2H), 4.54 (q, *J* = 7.1 Hz, 4H), 1.50 (t, *J* = 7.1 Hz, 6H).
^{13}C-NMR (CDCl$_3$, 75 MHz): δ 165.1 (C_q), 151.1 (C_q), 149.4 (C_q), 134.0 (C_q), 133.6 (C_q), 133.5 (C_q), 129.5 (CH), 128.8 (CH), 127.9 (CH), 127.6 (CH), 127.2 (CH), 127.2 (CH), 125.8 (CH), 124.3 (CH), 62.6 (CH_2), 14.4 (CH_3).
HRMS (ESI): *m/z* = 350.1379 $[M+H]^+$ (found), 350.1387 calcd. for $C_{21}H_{20}NO_4^+$, 372.1209 $[M+Na]^+$ (found), 372.1206 calcd. for $C_{21}H_{19}NNaO_4^+$, 721.2511 $[2M+Na]^+$ (found), 721.2520 calcd. for $C_{42}H_{38}N_2NaO_8^+$.

(4-(Naphthalen-2-yl)pyridine-2,6-diyl)dimethanol (**81**)

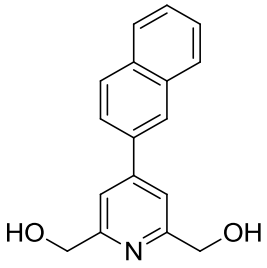

Compound **80** (1.336 g, 3.82 mmol, 1.0 eq) was suspended in abs. EtOH (30 mL). $NaBH_4$ (722 mg, 19.1 mmol, 5.0 eq) was added portionwise, the resulting mixture was refluxed for 4h and cooled to rt. Na_2CO_3 (4 g) was added, the resulting suspension was stirred at rt for 30 min, filtered and concentrated. Column chromatography (SiO_2, 90:10 to 80:20 AcOEt/MeOH) afforded **81** (769 mg, 2.90 mmol, 76%) as a white solid.

Molecular formula: $C_{17}H_{15}NO_2$
MW: 265.3 g.mol^{-1}
^{1}H-NMR (MeOD, 300 MHz): δ 8.31–8.28 (m, 1H), 8.04–7.96 (m, 2H), 7.96–7.90 (m, 1H), 7.88 (dd, *J* = 8.6, 1.9 Hz, 1H), 7.84 (t, *J* = 0.7 Hz, 2H), 7.59–7.52 (m, 2H), 4.78 (s, 4H).
HRMS (ESI): *m/z* = 266.1172 $[M+H]^+$ (found), 266.1176 calcd. for $C_{17}H_{16}NO_2^+$, 288.0992 $[M+Na]^+$ (found), 288.0995 calcd. for $C_{17}H_{15}NNaO_2^+$.

2,6-Bis(chloromethyl)-4-(naphthalen-2-yl)pyridine (**82**)

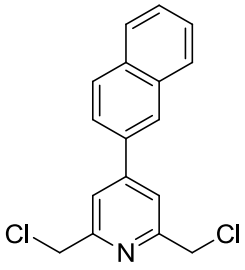

Compound **81** (765 mg, 2.88 mmol, 1.0 eq) was dissolved in dry THF (20 mL). $SOCl_2$ (1.04 mL, 14.4 mmol, 5.0 eq) dissolved in dry THF (5 mL) was added dropwise. The resulting solution was stirred at rt for 6 h, sat. aq. $NaHCO_3$ was added, and the mixture was extracted with $CHCl_3$ (3×). The combined organic layers were dried over Na_2SO_4, filtered and concentrated. Column chromatography (SiO_2, 90:10 Cy/AcOEt) afforded **82** (803 mg, 2.66 mmol, 92%) as a white solid.

Molecular formula: $C_{17}H_{13}Cl_2N$
MW: 302.2 g.mol^{-1}
^{1}H-NMR ($CDCl_3$, 300 MHz): δ 8.17–8.13 (m, 1H), 8.01–7.86 (m, 3H), 7.80–7.73 (m, 3H), 7.61–7.52 (m, 2H), 4.76 (s, 4H).
^{13}C-NMR ($CDCl_3$, 75 MHz): δ 157.0 (C_q), 151.1 (C_q), 134.8 (C_q), 133.8 (C_q), 133.5 (C_q), 129.3 (CH), 128.7 (CH), 127.9 (CH), 127.3 (CH), 127.0 (CH), 126.9 (CH), 124.5 (CH), 120.6 (CH), 46.6 (CH_2).
HRMS (ESI): *m/z* = 302.0491 $[M+H]^+$ (found), 302.0498 calcd. for $C_{17}H_{14}Cl_2N^+$, 324.0307 $[M+Na]^+$ (found), 324.0317 calcd. for $C_{17}H_{13}Cl_2NNa^+$.

Tetra-*tert*-butyl 2,2',2'',2'''-(((4-(naphthalen-2-yl)pyridine-2,6-diyl)bis(methylene))bis(azanetriyl)) tetraacetate (^{t}Bu-NpPyMTA **83**)

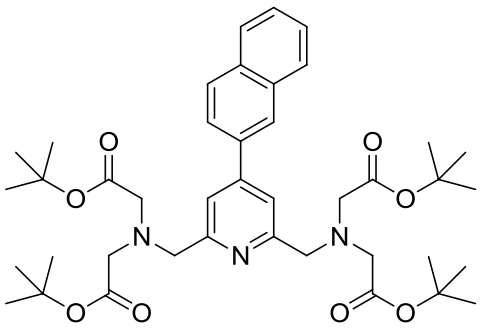

Compound **82** (72 mg, 0.238 mmol, 1.0 eq) and K_2CO_3 (329 mg, 2.38 mmol, 10.0 eq) were mixed in dry MeCN (3 mL). *tert*-Butyl iminodiacetate (117 mg, 0.476 mmol, 2.0 eq) dissolved in dry MeCN (5 mL) was added dropwise, and the resulting mixture was refluxed for 24h, filtered and concentrated. The residue was dissolved in DCM and washed with H_2O (1×) and sat. aq. NaCl (1×). The organic layer was dried over Na_2SO_4, filtered and concentrated. Column chromatography (SiO_2, 90:10 to 70:30 Cy/AcOEt) afforded ^{t}Bu-NpPyMTA **83** (62 mg, 0.086 mmol, 36%) as a colourless oil.

Molecular formula: $C_{41}H_{57}N_3O_8$
MW: 719.9 g.mol^{-1}

^{1}H-NMR ($CDCl_3$, 300 MHz): δ 8.27–8.18 (m, 1H), 7.97–7.88 (m, 4H), 7.88–7.80 (m, 2H), 7.55–7.46 (m, 2H), 4.13 (s, 4H), 3.55 (s, 8H), 1.45 (s, 36H).
^{13}C-NMR ($CDCl_3$, 75 MHz): δ 170.7 (C_q), 159.5 (C_q), 149.5 (C_q), 135.9 (C_q), 133.6 (C_q), 133.5 (C_q), 128.7 (CH), 128.6 (CH), 127.8 (CH), 126.6 (CH), 126.6 (CH), 126.5 (CH), 125.1 (CH), 119.1 (CH), 81.1 (C_q), 60.1 (CH_2), 56.0 (CH_2), 51.0 (CH_2), 28.3 (CH_3).
HRMS (ESI): *m/z* = 720.4214 $[M+H]^+$ (found), 720.4218 calcd. for $C_{41}H_{58}N_3O_8^+$, 742.4019 $[M+Na]^+$ (found), 742.4038 calcd. for $C_{41}H_{57}N_3NaO_8^+$.

2,2',2'',2'''-(((4-(Naphthalen-2-yl)pyridine-2,6-diyl)bis(methylene))bis(azanetriyl))tetraacetic acid (NpPyMTA **84**)

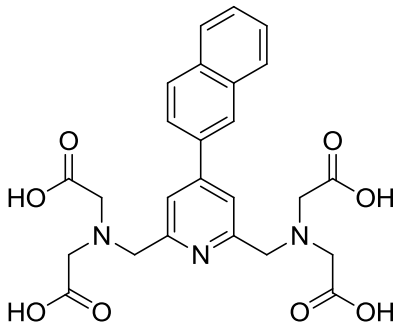

^{t}Bu-NpPyMTA **83** (62 mg, 0.086 mmol, 1.0 eq) was dissolved in dry DCM (1 mL). TFA (1 mL) was added dropwise, and the resulting mixture was stirred at rt for 15 h, concentrated without heating, triturated with Et_2O, filtered and dried to afford NpPyMTA **84** (40.0 mg, 0.081 mmol, 94%) as a white solid.

Molecular formula: $C_{25}H_{25}N_3O_8$
MW: 495.5 g.mol^{-1}

Ethyl 2-((pyridin-2-ylmethyl)amino)acetate (**86**)

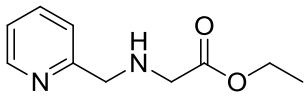

2-Picolylamine **85** (1.91 mL, 18.51 mmol, 2.0 eq) was dissolved in dry THF (12 mL). The resulting solution was cooled to 0 °C, and ethyl bromoacetate (1.02 mL, 9.25 mmol, 1.0 eq) dissolved in dry THF (12 mL) was added dropwise. The resulting mixture was allowed to warm to rt for 15 h, filtered and concentrated. The residue was distilled over reduced pressure (0.47 torr, 135 °C) to afford **86** (1.125 g, 5.79 mmol, 63%) as a colourless oil.

Molecular formula: $C_{10}H_{14}N_2O_2$
MW: 194.2 g.mol^{-1}
^{1}H-NMR ($CDCl_3$, 300 MHz): δ 8.53 (ddd, *J* = 4.9, 1.9, 1.0 Hz, 1H), 7.62 (td, *J* = 7.7, 1.9 Hz, 1H), 7.31 (d, *J* = 7.7 Hz, 1H), 7.18–7.10 (m, 1H), 4.17 (q, *J* = 7.1 Hz, 2H), 3.93 (s, 2H), 3.45 (s, 2H), 2.38 (s, 1H), 1.25 (t, *J* = 7.1 Hz, 3H).
^{13}C-NMR ($CDCl_3$, 75 MHz): δ 172.1 (C_q), 159.1 (C_q), 149.2 (CH), 136.4 (CH), 122.0 (CH), 121.9 (CH), 60.6 (CH_2), 54.5 (CH_2), 50.3 (CH_2), 14.1 (CH_3).
HRMS (ESI): *m/z* = 195.1116 $[M+H]^+$ (found), 195.1128 calcd. for $C_{10}H_{15}N_2O_2^+$, 217.0938 $[M+Na]^+$ (found), 217.0947 calcd. for $C_{10}H_{14}N_2NaO_2^+$.

Diethyl 2,2'-(((4-bromopyridine-2,6-diyl)bis(methylene))bis((pyridin-2-ylmethyl)azanediyl)) diacetate (Et-*p*BrPyMDPDA **87**)

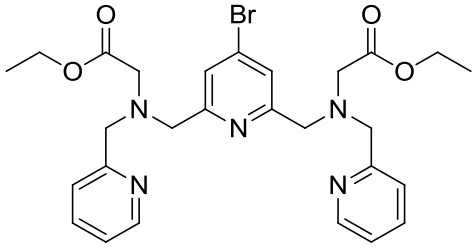

Compound **69** (800 mg, 2.33 mmol, 1.0 eq) was dissolved in dry MeCN (20 mL). Compound **86** (905 mg, 4.66 mmol, 2 eq) was added, followed by Na_2CO_3 (2.47 g, 23.3 mmol, 10.0 eq). The resulting mixture was stirred at rt for 15h, filtered and concentrated. The residue was dissolved in DCM and washed with H_2O (3×) and sat. aq. NaCl (1×). The organic layer was dried over Na_2SO_4, filtered and concentrated to afford Et-*p*BrPyMDPDA **87** (1.23 g, 2.16 mmol, 93%) as a yellow oil.

Molecular formula: $C_{27}H_{32}BrN_5O_4$
MW: 570.5 g.mol^{-1}
^{1}H-NMR ($CDCl_3$, 300 MHz): δ 8.51 (ddd, *J* = 4.9, 1.8, 1.0 Hz, 2H), 7.70–7.59 (m, 4H), 7.50 (d, *J* = 7.7 Hz, 2H), 7.14 (ddd, *J* = 7.7, 4.9, 1.3 Hz, 2H), 4.15 (q, *J* = 7.1 Hz, 4H), 3.98 (s, 4H), 3.93 (s, 4H), 3.45 (s, 4H), 1.25 (t, *J* = 7.1 Hz, 6H).
^{13}C-NMR ($CDCl_3$, 75 MHz): δ 171.2 (C_q), 160.3 (C_q), 158.9 (C_q), 149.2 (CH), 136.7 (CH), 134.3 (C_q), 124.6 (CH), 123.3 (CH), 122.3 (CH), 60.7 (CH_2), 60.2 (CH_2), 59.7 (CH_2), 55.3 (CH_2), 14.4 (CH_3).
HRMS (ESI): *m/z* = 570.1697 $[M+H]^+$ (found), 570.1710 calcd. for $C_{27}H_{33}BrN_5O_4^+$, 592.1514 $[M+Na]^+$ (found), 592.1530 calcd. for $C_{27}H_{32}BrN_5NaO_4^+$.

2,2'-(((4-bromopyridine-2,6-diyl)bis(methylene))bis((pyridin-2-ylmethyl)azanediyl))diacetic acid (*p*BrPyMDPDA **88**)

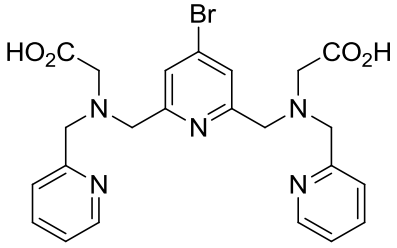

Et-*p*BrPyMDPDA **87** (135.0 mg, 0.24 mmol, 1.0 eq) was dissolved in aq. 0.1 M NaOH (9.6 mL, 0.95 mmol, 4.0 eq) and acetone (2 mL), and the resulting solution was heated at 60 °C for 3 d. Completion of the reaction was monitored by TLC (DCM/MeOH 95/5). The solution was then washed with DCM, the aqueous layer was acidified to pH 1 with aq. 37% HCl and washed with DCM. The aqueous phase was freeze-dried and purified by HPLC to afford *p*BrPyMDPDA **88** (52.0 mg, 0.070 mmol, 30%) as a colourless oil.

Molecular formula: $C_{23}H_{24}BrN_5O_4$
MW: 514.4 g.mol^{-1}
^{1}H-NMR (D_2O, 300MHz): δ 8.65 (m, 2H), 8.44 (td, *J* = 1.5, 7.8 Hz, 2H), 7.94 (d, *J* = 7.8 Hz, 2H), 7.90–7.83 (m, 4H), 4.38 (s, 4H), 4.28 (s, 4H), 3.64 (s, 4H).

HPLC: 4.14 min (5 to 100% MeCN in 10 min, 82%)

2-Nitro-*N*,*N*-bis(2-(2-nitrophenylsulfonamido)ethyl)benzenesulfonamide (**90**)

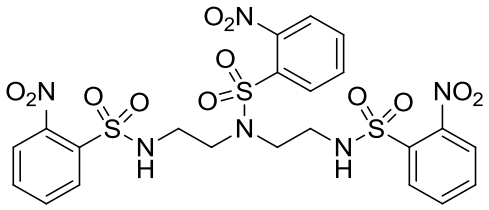

Diethylenetriamine **89** (2.50 g, 24.30 mmol, 1.0 eq) was dissolved in THF (200 mL). $NaHCO_3$ (6.42 g, 76.30 mmol, 3.15 eq) was added, and the resulting suspension was cooled to 0 °C. Nosyl chloride (16.9 g, 76.30 mmol, 3.15 eq) in THF (400 mL) was added, and the mixture was stirred at rt for 15 h, filtered and concentrated. Column chromatography (SiO_2, 100% DCM to 95:5 DCM/MeOH) afforded **90** (1.92 g, 2.92 mmol, 12%) as a white solid.

Molecular formula: $C_{22}H_{22}N_6O_{12}S_3$
MW: 658.6 g.mol^{-1}
^{1}H-NMR (DMSO-d$_6$, 300 MHz): δ 8.22 (br s, 2H), 8.00–7.82 (m, 12H), 3.38 (t, *J* = 6.9 Hz, 4H), 3.06 (t, J = 6.9 Hz, 4H).
^{13}C-NMR (DMSO-d$_6$, 75 MHz): δ 147.65, 147.64, 134.8, 134.3, 132.9, 132.7, 132.5, 131.2, 129.8, 129.5, 124.7, 124.6, 48.1, 41.4.

Macrocycle 91

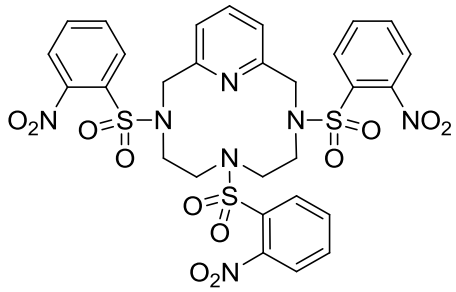

Compound **90** (300.0 mg, 0.456 mmol, 1.0 eq) was dissolved in DMF (3.0 mL). Na_2CO_3 (193.2 mg, 1.822 mmol, 4.0 eq) was added, and the resulting suspension was heated to 100 °C. Compound **64** (120.7 mg, 0.456 mmol, 1.0 eq) dissolved in DMF (3.0 mL) was added dropwise, and the heating was continued for 15 h. The mixture was concentrated, taken up in DCM and washed with aq. 0.1 M NaOH (2×). The organic layer was dried over Na_2SO_4, filtered and concentrated. Column chromatography (SiO_2, 100% DCM to 50:50 DCM/MeOH) afforded **91** (334.0 mg, 0.438 mmol, 96%) as a colourless foam.

Molecular formula: $C_{29}H_{27}N_7O12_4S_3$
MW: 761.8 g.mol^{-1}
^{1}H-NMR (CDCl$_3$, 300 MHz): δ 8.10–8.07 (m, 2H), 8.01–7.99 (m, 2H), 7.89 (t, *J* = 7.8 Hz, 1H), 7.77–7.74 (m, 4H), 7.72–7.63 (m, 4H), 7.56 (d, *J* = 7.8 Hz, 2H), 4.70 (s, 4H), 3.55–3.46 (m, 4H), 3.33–3.25 (m, 4H).
HRMS (ESI): *m/z* = 784.0770 $[M+Na]^+$ (found), 784.0772 calcd. for $C_{29}H_{27}N_7NaO_{12}S_3^+$.

***N*^{1}-benzyl-*N*^{2}-(2-(benzylamino)ethyl)ethane-1,2-diamine** (**92**)

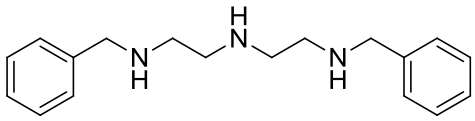

Diethylenetriamine **89** (509.0 mg, 4.93 mmol, 1.0 eq) and benzaldehyde (985 µL, 9.87 mmol, 2.0 eq) were dissolved in dry MeOH (10 mL). The resulting solution was refluxed for 15 h and cooled to 0 °C. $NaBH_4$ (1.306 g, 34.53 mmol, 7.0 eq) was added portionwise and the resulting mixture was allowed to warm to rt for 4 h and concentrated. The residue was taken up in DCM and washed with sat. aq. $NaHCO_3$ (2×). The organic layer was dried over Na_2SO_4, filtered and concentrated to ≈ 35 mL. Aq. 37% HCl (1.25 mL) was added dropwise while stirring. The resulting solid was filtered, washed with DCM and Et_2O and dried to afford **92**•3HCl (1.336 g, 3.40 mmol, 69%) as a white solid.

Molecular formula: $C_{18}H_{25}N_3$
MW: 283.4 g.mol^{-1} (392.8 g.mol^{-1} with 3HCl)
^{1}H-NMR (D_2O, 300 MHz): δ 7.52–7.40 (m, 10H), 4.31–4.22 (m, 4H), 3.26 (t, *J* = 6.0 Hz, 4H), 3.11 (t, *J* = 6.0 Hz, 4H).
^{13}C-NMR (D_2O, 75 MHz): δ 130.4, 129.8, 129.78, 129.3, 128.9, 51.2, 44.9, 43.9.

Di-*tert*-butyl 2,2'-((((2-(tert-butoxy)-2-oxoethyl)azanediyl)bis(ethane-2,1-diyl)) bis (benzylazanediyl))diacetate (**93**)

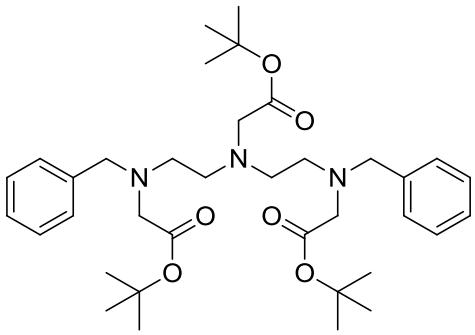

Compound **92**•3HCl (600.0 mg, 1.53 mmol, 1.0 eq) was dissolved in MeCN (16.0 mL). K_2CO_3 (6.4 g, 46.3 mmol, 30.0 eq) was added, followed by bromo-*tert*-butylacetate (1.34 mL, 9.16 mmol, 6.0 eq) in MeCN (10 mL) dropwise. The resuting mixture was refluxed for 1 h, stirred at rt for 15 h, filtered and concentrated. Column chromatography (SiO_2, 90:10 to 80:20 DCM/MeCN) afforded **93** (490.0 mg, 0.783 mmol, 51%) as a colourless oil.

Molecular formula: $C_{36}H_{55}N_3O_6$
MW: 625.8 g.mol^{-1}
^{1}H-NMR ($CDCl_3$, 300 MHz): δ 7.36–7.23 (m, 10H), 3.79 (s, 4H), 3.33 (s, 2H), 3.25 (s, 4H), 2.77 (s, 8H), 1.48 (s, 18H), 1.44 (s, 9H).
^{13}C-NMR ($CDCl_3$, 75 MHz): δ 170.9, 139.2, 129.0, 128.2, 127.0, 80.68, 80.61, 58.4, 56.1, 55.2, 53.5, 52.6, 52.0, 28.25, 28.2.
Rf (SiO_2): 0.24 (80:20 DCM/MeCN)

Di-*tert*-butyl 2,2'-((((2-(tert-butoxy)-2-oxoethyl)azanediyl)bis(ethane-2,1-diyl)) bis (azanediyl)) diacetate (**94**)

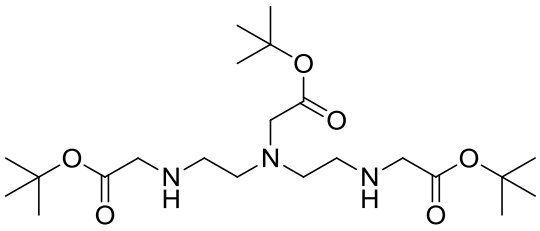

Compound **93** (491.0 mg, 0.780 mmol, 1.0 eq) was dissolved in MeOH (13 mL). Pd/C (20%w, 98.0 mg) was added, and the resulting suspension was hydrogenated (3 bar) at rt for 15h. The resulting mixture was filtered over a pad of celite, washed with MeOH and concentrated to afford **94** (337.0 mg, 0.757 mmol, 97%) as a colourless oil.

Molecular formula: $C_{22}H_{43}N_3O_6$
MW: 445.6 g.mol^{-1}
^{1}H-NMR (CDCl$_3$, 300 MHz): δ 3.33 (s, 6H), 2.82 (t, *J* = 5.4 Hz, 4H), 2.68 (t, *J* = 5.4 Hz, 4H), 1.44 (s, 27H).
^{13}C-NMR (CDCl$_3$, 75 MHz): δ 170.2, 166.6, 83.2, 81.6, 51.6, 50.9, 48.3, 42.3, 28.1, 27.9.

***N*,*N'*-(Azanediylbis(ethane-2,1-diyl))bis(2-nitrobenzenesulfonamide)** (**95**)

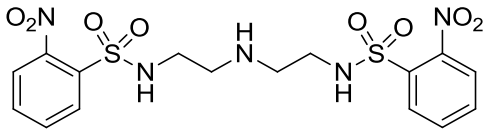

Diethylenetriamine **89** (1.00 g, 9.70 mmol, 1.0 eq) was dissolved in THF (100 mL). $NaHCO_3$ (3.26 g, 38.80 mmol, 4.0 eq) was added, and the resulting suspension was cooled to 0 °C. Nosyl chloride (4.30 g, 19.40 mmol, 2.0 eq) dissolved in THF (200 mL) was added and the resulting mixture was stirred at rt for 15 h, filtered, and concentrated. Column chromatography (SiO_2, 100% DCM to 95:5 DCM/MeOH) afforded **95** (1.01 g, 2.13 mmol, 22%) as a white solid.

Molecular formula: $C_{16}H_{19}N_5O_8S_2$
MW: 473.5 g.mol^{-1}
^{1}H-NMR (Acetone-d$_6$, 300MHz): δ 8.13–8.10 (m, 2H), 7.97–7.86 (m, 6H), 3.10 (t, *J* = 6.0 Hz, 4H), 2.66 (t, *J* = 6.0 Hz, 4H).

***tert*-Butyl 2-(bis(2-(2-nitrophenylsulfonamido)ethyl)amino)acetate** (**96**)

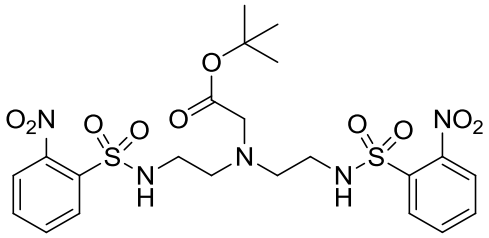

Compound **95** (300 mg, 0.634 mmol, 1.0 eq) and TEA (530 μL, 3.80 mmol, 6.0 eq) were dissolved in THF (8 mL). Chloro-*tert*-butylacetate (272 μL, 1.90 mmol, 3.0 eq) was added, and the resulting solution was refluxed for 15 h and cooled to rt. Sat. aq. NH_4Cl (16 mL) was added and the mixture was extracted with DCM (2×). The combined organic layers were dried over Na_2SO_4, filtered and concentrated. The residue was purified by column chromatography (SiO_2, 94:6 DCM/MeOH). The

desired fractions were concentrated, the residue was taken up in Et_2O, the solvent was discarded and the resulting product was dried to afford **96** (168.0 mg, 0.285 mmol, 45%) as a beige solid.

Molecular formula: $C_{22}H_{29}N_5O_{10}S_2$
MW: 587.6 g.mol^{-1}
^{1}H-NMR ($CDCl_3$, 300 MHz): δ 7.99–7.96 (m, 2H), 7.74–7.64 (m, 6H), 5.97 (t, *J* = 5.7 Hz, 2H), 3.07 (s, 2H), 2.98 (q, *J* = 5.7 Hz, 4H), 2.65 (t, *J* = 5.7 Hz, 4H), 1.30 (s, 9H).

^{t}Bu-2Ns-PCMA (**97**)

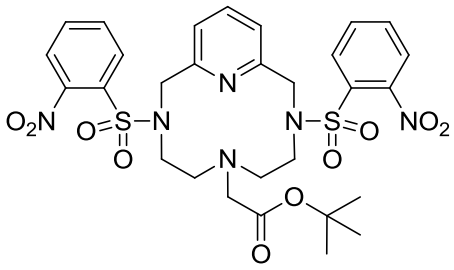

Compound **96** (168.0 mg, 0.286 mmol, 1.0 eq) was dissolved in DMF (4.0 mL). Na_2CO_3 (121.2 mg, 1.143 mmol, 4.0 eq) was added, and the resulting suspension was heated to 100 °C. Compound **64** (75.7 mg, 0.286 mmol, 1.0 eq) dssolved in DMF (4.0 mL) was added dropwise, and heating was continued for 15 h. The mixture was concentrated, taken up in DCM and washed with aq. 0.1 M NaOH (2×). The organic layer was dried over Na_2SO_4, filtered and concentrated. Column chromatography (SiO_2, 50:50 to 20:80 Cy/AcOEt) afforded ^{t}Bu-2Ns-PCMA **97** (108.0 mg, 0.157 mmol, 55%) as a colourless foam.

Molecular formula: $C_{29}H_{34}N_6O_{10}S_2$
MW: 690.7 g.mol^{-1}
^{1}H-NMR ($CDCl_3$, 300 MHz): δ 8.02–7.99 (m, 2H), 7.79–7.63 (m, 7H), 7.42 (d, *J* = 7.5 Hz, 2H), 4.55 (s, 4H), 3.29 (t, *J* = 7.5 Hz, 4 H), 3.17 (s, 2H), 2.56 (t, *J* = 7.5 Hz, 4H), 1.40 (s, 9H).

^{t}Bu-PCMA (**98**)

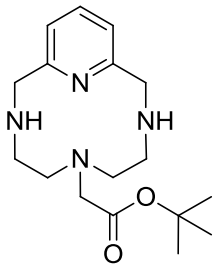

^{t}Bu-2Ns-PCMA **97** (108.0 mg, 0.160 mmol, 1.0 eq) was dissolved in dry DMF (3.0 mL). Thiophenol (40 µL, 0.39 mmol, 2.5 eq) was added, followed by Na_2CO_3 (132.6 mg, 1.25 mmol, 8.0 eq). The resulting suspension was stirred at rt for 24 h. The mixture was diluted with H_2O and extracted with DCM (3×). The combined organic layers were dried over Na_2SO_4, filtered and concentrated. The residue was purified by column chromatography (Al_2O_3, neutral, 99/1 to 90/10 DCM/MeOH). The desired fractions were concentrated and the residue was taken up in $CHCl_3$. The suspension was filtered and the resulting solid was taken up in MeOH and concentrated to afford ^{t}Bu-PCMA **98** (29.0 mg, 0.092 mmol, 58%) as a colourless sticky solid.

Molecular formula: $C_{17}H_{28}N_4O_2$
MW: 320.4 g.mol^{-1}
^{1}H-NMR (MeOD, 300 MHz): δ 7.94 (t, *J* = 7.8 Hz, 1H), 7.45 (d, *J* = 7.8 Hz, 2H), 4.52 (s, 4H), 3.57 (s, 2H), 3.08–3.02 (m, 4H), 3.00–2.92 (m, 4H), 1.50 (s, 9H).

PCMA (**99**)

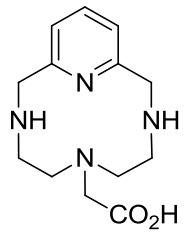

^{t}Bu-PCMA **98** (20.0 mg, 0.062 mmol, 1.0 eq) was dissolved in DCM (1.0 mL). TFA (1.0 mL) was added, and the resulting solution was stirred at rt under for 15 h. Et_2O was added and the resulting solid was filtered, washed with Et_2O and dried to afford PCMA **99** (9.0 mg, 0.034 mmol, 55%) as a colourless solid.

Molecular formula: $C_{13}H_{20}N_4O_2$
MW: 264.3 g.mol^{-1}
^{1}H-NMR (D_2O, 300 MHz): δ 7.94 (t, *J* = 7.8 Hz, 1H), 7.44 (d, *J* = 7.8 Hz, 2H), 4.62 (s, 4H), 3.63 (s, 2H), 3.23–3.17 (m, 4H), 3.03–2.97 (m, 4H).

1-Benzylpiperidin-4-one (**101**)

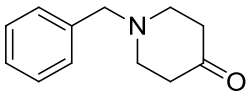

4-Piperidone monohydrate hydrochloride **100** (10.0 g, 65.1 mmol, 1.0 eq) was dissolved in MeCN (170 mL). Benzyl bromide (9.3 mL, 78.1 mmol, 1.2 eq) was added, followed by K_2CO_3 (22.5 g, 162.7 mmol, 2.5 eq). The resulting mixture was refluxed for 15 h, cooled to rt, filtered and concentrated. Column chromatography (SiO_2, 90:10 to 50:50 Cy/AcOEt) afforded **101** (8.48 g, 44.8 mmol, 69%) as a yellow oil.

Molecular formula: $C_{12}H_{15}NO$
MW: 189.3 g.mol^{-1}
^{1}H-NMR ($CDCl_3$, 300 MHz): δ 7.40–7.26 (m, 5H), 3.62 (s, 2H), 2.75 (t, *J* = 6.2 Hz, 4H), 2.46 (t, *J* = 6.2 Hz, 4H).
^{13}C-NMR ($CDCl_3$, 75 MHz): δ 209.5 (C_q), 138.3 (C_q), 129.0 (CH), 128.5 (CH), 127.5 (CH), 62.1 (CH_2), 53.1 (CH_2), 41.5 (CH_2).
HRMS (ESI): *m/z* = 190.1221 $[M+H]^+$ (found), 190.1226 calcd. for $C_{12}H_{16}NO^+$, 212.1047 $[M+Na]^+$ (found), 212.1046 calcd. for $C_{12}H_{15}NNaO^+$, 222.1486 $[M+H+MeOH]^+$ (found), 222.1489 calcd. for $C_{13}H_{20}NO_2^+$, 91.0535 [Tropylium], 91.0542 calcd. for $C_7H_7^+$.

Benzyl 4-oxopiperidine-1-carboxylate (**102**)

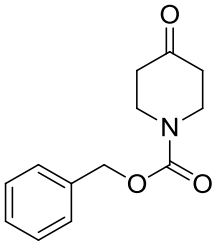

4-Piperidone monohydrate hydrochloride **100** (11.87 g, 77.3 mmol, 1.5 eq) and Na_2CO_3 (10.96 g, 103.0 mmol, 2.0 eq) were dissolved in H_2O (80 mL). CbzOSu (12.84 g, 51.5 mmol, 1.0 eq) dissolved in dioxane (170 mL) was then added, and the resulting mixture was stirred at rt for 15 h and concentrated. H_2O (300 mL) and AcOEt (300 mL) were added, the organic layer was recovered, washed with H_2O (2×), dried over Na_2SO_4, filtered and concentrated to afford **101** (10.95 g, 47.0 mmol, 91%) as a colourless oil.

Molecular formula: $C_{13}H_{15}NO_3$
MW: 233.3 g.mol^{-1}
^{1}H-NMR ($CDCl_3$, 300 MHz): δ 7.43–7.29 (m, 5H), 5.18 (s, 2H), 3.80 (t, *J* = 6.3 Hz, 4H), 2.46 (t, *J* = 6.3 Hz, 4H).
HRMS (ESI): *m/z* = 256.0944 $[M+Na]^+$ (found), 256.0944 calcd. for $C_{13}H_{15}NNaO_3^+$, 288.1198 $[M+Na+MeOH]^+$ (found), 288.1206 calcd. for $C_{14}H_{19}NNaO_4^+$.

8-(1-Benzylpiperidin-4-yl)-1,4-dioxa-8-azaspiro[4.5]decane (**104**)

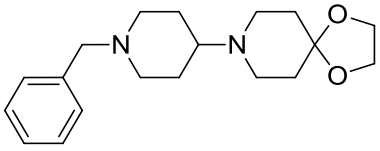

Compound **101** (8.48 g, 44.8 mmol, 1.0 eq), 4-piperidone ethylene ketal **103** (5.74 mL, 44.8 mmol, 1.0 eq) and glacial AcOH (5 mL, 89.6 mmol, 2.0 eq) were dissolved in dry DCE (50 mL). $NaBH(OAc)_3$ (13.3 g, 62.7 mmol, 1.4 eq) was added portionwise and the resulting mixture was stirred at rt for 48h. Aq. 1 M NaOH was added until pH ≈ 12 and the resulting mixture was extracted with DCM (3×). The combined organic layers were dried over Na_2SO_4, filtered and concentrated. Column chromatography (SiO_2, 90:10 to 70:30 AcOEt/MeOH) afforded **104** (9.79 g, 30.9 mmol, 69%) as a light orange solid.

Molecular formula: $C_{19}H_{28}N_2O_2$
MW: 316.4 g.mol^{-1}
^{1}H-NMR ($CDCl_3$, 300 MHz): δ 7.40–7.18 (m, 5H), 3.94 (s, 4H), 3.49 (s, 2H), 2.95 (dt, *J* = 12.8, 3.5 Hz, 2H), 2.75 (t, *J* = 6.2 Hz, 1H), 2.66 (dd, *J* = 6.8, 4.6 Hz, 2H), 2.46 (t, *J* = 6.2 Hz, 1H), 2.38 (ddt, *J* = 11.5, 7.6, 3.8 Hz, 1H), 1.97 (td, *J* = 11.8, 2.4 Hz, 2H), 1.82–1.70 (m, 6H), 1.61 (qd, *J* = 12.1, 3.8 Hz, 2H).

Benzyl 4-(1,4-dioxa-8-azaspiro[4.5]decan-8-yl)piperidine-1-carboxylate (**105**)

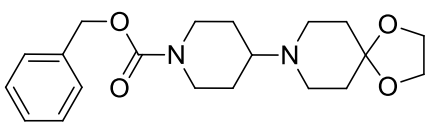

Compound **102** (11.51 g, 49.4 mmol, 1.0 eq), 4-piperidone ethylene ketal **103** (6.33 mL, 49.4 mmol, 1.0 eq) and glacial AcOH (2.73 mL, 49.4 mmol, 1.0 eq) were dissolved in dry DCE (60 mL). $NaBH(OAc)_3$ (14.66 g, 69.2 mmol, 1.4 eq) was added portionwise and the resulting mixture was stirred at rt for 72h. Aq. 1 M NaOH was added until pH ≈ 12 and the resulting mixture was extracted with DCM (3×). The combined organic layers were dried over Na_2SO_4, filtered and concentrated. Column chromatography (SiO_2, 90:10 to 80:20 AcOEt/MeOH) afforded **105** (13.3 g, 36.9 mmol, 75%) as a white solid.

Molecular formula: $C_{20}H_{28}N_2O_4$
MW: 360.5 g.mol^{-1}
^{1}H-NMR (MeOD, 300 MHz): δ 7.40–7.26 (m, 5H), 5.10 (s, 2H), 4.21 (dt, *J* = 13.5, 2.6 Hz, 2H), 3.92 (s, 4H), 2.95–2.73 (m, 2H), 2.68 (t, *J* = 5.7 Hz, 4H), 2.56 (tt, *J* = 11.6, 3.6 Hz, 1H), 1.88 (d, *J* = 12.8 Hz, 2H), 1.73 (t, *J* = 5.7 Hz, 4H), 1.40 (qd, *J* = 12.4, 4.3 Hz, 2H).
^{13}C-NMR (MeOD, 75 MHz): δ 156.8 (C_q), 138.2 (C_q), 129.5 (CH), 129.1 (CH), 128.9 (CH), 107.9 (C_q), 68.3 (CH_2), 65.3 (CH_2), 62.7 (CH_2), 48.0 (CH), 44.6 (CH_2), 35.6 (CH_2), 29.0 (CH_2).
HRMS (ESI): *m/z* = 361.2110 $[M+H]^+$ (found), 361.2122 calcd. for $C_{20}H_{29}N_2O_4^+$, 383.1927 $[M+Na]^+$ (found), 383.1941 calcd. for $C_{20}H_{28}N_2NaO_4^+$.

8-(piperidin-4-yl)-1,4-dioxa-8-azaspiro[4.5]decane (**106**)

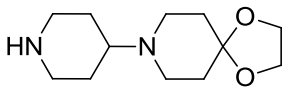

Compound **105** (4.85 g, 13.5 mmol, 1.0 eq) was dissolved in EtOH (50 mL). Pd/C (10%w, 485 mg) was added and the resulting suspension was hydrogenated (10 bar) at rt for 4h. The resulting mixture was filtered over a pad of celite and concentrated to afford **106** (3.0 g, 13.3 mmol, 99%) as an off-white solid.

Molecular formula: $C_{12}H_{22}N_2O_2$
MW: 226.3 g.mol^{-1}
^{1}H-NMR (MeOD, 300 MHz): δ 3.93 (s, 4H), 3.17–3.05 (m, 2H), 2.73–2.64 (m, 4H), 2.58 (td, *J* = 12.6, 2.5 Hz, 2H), 2.47 (tt, *J* = 11.6, 3.6 Hz, 1H), 1.93–1.81 (m, 2H), 1.73 (t, *J* = 5.7 Hz, 4H), 1.45 (qd, *J* = 12.4, 4.0 Hz, 2H).
^{13}C-NMR (MeOD, 75 MHz): δ 108.0 (C_q), 65.2 (CH_2), 62.8 (CH), 47.8 (CH_2), 46.6 (CH_2), 35.7 (CH_2), 29.6 (CH_2).
HRMS (ESI): *m/z* = 227.1747 $[M+H]^+$ (found), 227.1754 calcd. for $C_{12}H_{23}N_2O_2^+$, 249.1567 $[M+Na]^+$ (found), 249.1573 calcd. for $C_{12}H_{22}N_2NaO_2^+$.

Benzyl 4-oxo-[1,4'-bipiperidine]-1'-carboxylate (**107**)

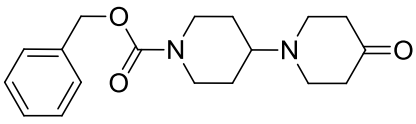

Compound **105** (1.77 g, 4.92 mmol, 1.0 eq) was dissolved in cold aq. 4 M HCl (50 mL). The resulting mixture was allowed to warm to rt for 7 d and cooled to 0°C. DCM (30 mL) was added, followed by dropwise aq. 33% NaOH until pH ≈ 14. The mixture was extracted with DCM (3×) and the combined organic layers were dried over Na_2SO_4, filtered and concentrated. Column chromatography (SiO_2, 90:10 to 70:30 AcOEt/MeOH) afforded **107** (1.46 g, 4.62 mmol, 94%) as a pale yellow oil.

Molecular formula: $C_{18}H_{24}N_2O_3$
MW: 316.4 g.mol^{-1}
^{1}H-NMR (MeOD, 300 MHz): δ 7.40–7.26 (m, 5H), 5.11 (d, *J* = 1.5 Hz, 2H), 4.21 (dq, *J* = 13.7, 2.4 Hz, 2H), 2.88 (t, *J* = 6.1 Hz, 4H), 2.78–2.46 (m, 3H), 2.42 (t, *J* = 6.1 Hz, 2H), 1.88 (d, *J* = 12.6 Hz, 2H), 1.77 (t, *J* = 5.7 Hz, 2H), 1.42 (dqd, *J* = 16.8, 12.6, 4.5 Hz, 2H).
^{13}C-NMR (MeOD, 75 MHz): δ 211.1 (C_q), 156.7 (C_q), 156.7 (C_q), 138.1 (C_q), 129.5 (CH), 129.1 (CH), 128.9 (CH), 68.3 (CH_2), 62.8 (CH), 62.0 (CH), 49.8 (CH_2), 47.3 (CH_2), 44.5 (CH_2), 44.5 (CH_2), 42.1 (CH_2), 36.0 (CH_2).
HRMS (ESI): *m/z* = 317.1848 $[M+H]^+$ (found), 317.1860 calcd. for $C_{18}H_{25}N_2O_3^+$, 339.1664 $[M+Na]^+$ (found), 339.1679 calcd. for $C_{18}H_{24}N_2NaO_3^+$, 349.2104 $[M+H+MeOH]^+$ (found), 349.2122 calcd. for $C_{19}H_{29}N_2O_4^+$, 371.1924 $[M+Na+MeOH]^+$ (found), 371.1941 calcd. for $C_{19}H_{28}N_2NaO_4^+$.

1'-Benzyl-[1,4'-bipiperidin]-4-one (**108**)

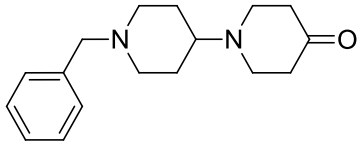

Compound **104** (9.79 g, 30.9 mmol, 1.0 eq) was dissolved in aq. 4 M HCl (250 mL). The resulting mixture was allowed to warm to rt for 7 d and cooled to 0°C. DCM (50 mL) was added followed by dropwise aq. 33% NaOH until pH ≈ 14. The mixture was extracted with DCM (3×) and the combined organic layers were dried over Na_2SO_4, filtered and concentrated. Column chromatography (SiO_2, 80:20 AcOEt/MeOH) afforded **108** (7.64 g, 28 mmol, 91%) as an orange oil.

Molecular formula: $C_{17}H_{24}N_2O$
MW: 272.4 g.mol^{-1}
^{1}H-NMR ($CHCl_3$, 300 MHz): δ 7.38–7.20 (m, 5H), 3.49 (s, 2H), 3.02–2.91 (m, 2H), 2.84 (t, *J* = 5.8 Hz, 4H), 2.49–2.39 (m, 5H), 1.98 (td, *J* = 11.7, 2.6 Hz, 2H), 1.82–1.71 (m, 2H), 1.61 (qd, *J* = 12.0, 3.8 Hz, 2H).
HRMS (ESI): *m/z* = 273.1986 $[M+H]^+$ (found), 273.1961 calcd. for $C_{17}H_{25}N_2O^+$, 305.2245 $[M+H+MeOH]^+$ (found), 305.2224 calcd. for $C_{18}H_{29}N_2O_2^+$.

Benzyl 4-(1,4-dioxa-8-azaspiro[4.5]decan-8-yl)-[1,4':1',4''-terpiperidine]-1''-carboxylate (**109**)

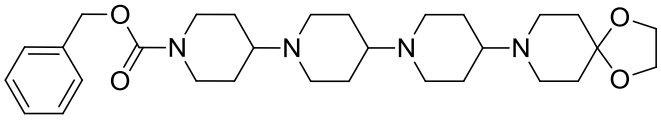

Compound **107** (193 mg, 0.61 mmol, 1.0 eq), compound **106** (138 mg, 0.61 mmol, 1.0 eq) and $Ti(O^iPr)_4$ (325 µL, 1.1 mmol, 1.8 eq) were stirred at rt for 1 h. Abs. EtOH (3 mL) was then added, followed by $NaBH_3CN$ (26 mg, 0.41 mmol, 0.67 eq) and the resulting mixture was stirred at rt for 15 h. Aq. 0.1 M NaOH (100 mL) was added and the mixture was extracted with DCM (3×). The combined organic layers were dried over Na_2SO_4, filtered and concentrated. Column chromatography (SiO_2, 70:30 AcOEt/MeOH) afforded **109** (89 mg, 0.17 mmol, 28%) as a white solid.

Molecular formula: $C_{30}H_{46}N_4O_4$
MW: 526.7 g.mol^{-1}

^{1}H-NMR ($CDCl_3$, 300 MHz): δ 7.40–7.28 (m, 5H), 5.11 (s, 2H), 4.33–4.11 (m, 2H), 3.95 (s, 4H), 3.13 (d, *J* = 10.9 Hz, 2H), 2.96–2.69 (m, 4H), 2.63 (t, *J* = 5.7 Hz, 4H), 2.52–2.25 (m, 4H), 2.23–2.06 (m, 3H), 1.87 (d, *J* = 12.0 Hz, 2H), 1.83–1.62 (m, 9H), 1.62–1.35 (m, 5H).
^{13}C-NMR ($CDCl_3$, 75 MHz): δ 155.3 (C_q), 136.9 (C_q), 128.6 (CH), 128.1 (CH), 128.0 (CH), 107.5 (C_q), 67.2 (CH_2), 64.4 (CH_2), 61.5 (CH), 61.5 (CH), 47.2 (CH_2), 46.8 (CH_2), 45.8 (CH_2), 43.6 (CH_2), 35.3 (CH_2), 34.6 (CH_2), 31.1 (CH), 28.5 (CH_2), 28.3 (CH_2).
HRMS (ESI): *m/z* = 525.3430 $[M-H]^+$ (found), 525.3435 calcd. for $C_{30}H_{45}N_4O_4^+$.

Benzyl 4-hydroxy-[1,4'-bipiperidine]-1'-carboxylate (**110**)

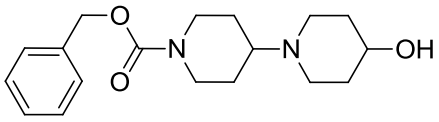

Compound **107** (730 mg, 2.31 mmol, 1.0 eq) was dissolved in abs. EtOH (12 mL). The resulting solution was cooled to 0 °C and $NaBH_4$ (96 mg, 2.54 mmol, 1.1 eq) was added portionwise. The resulting mixture was allowed to warm to rt for 2 h, sat. aq. NH_4Cl was added and the mixture was extracted with DCM (3×). The combined organic layers was washed with H_2O (1×) and sat. aq. NaCl (1×), dried over Na_2SO_4, filtered and concentrated to afford **110** (664 mg, 2.09 mmol, 90%) as a pasty white solid.

Molecular formula: $C_{18}H_{26}N_2O_3$
MW: 318.4 $g.mol^{-1}$
^{1}H-NMR (MeOD, 300 MHz): δ 7.40–7.25 (m, 5H), 5.10 (s, 2H), 4.20 (dt, *J* = 13.5, 2.4 Hz, 2H), 3.60 (tt, *J* = 8.6, 4.1 Hz, 1H), 2.95–2.70 (m, 4H), 2.49 (tt, *J* = 11.6, 3.6 Hz, 1H), 2.34 (ddd, *J* = 12.0, 10.3, 2.9 Hz, 2H), 1.95–1.79 (m, 4H), 1.56 (ddt, *J* = 13.0, 9.5, 4.8 Hz, 2H), 1.39 (qd, *J* = 12.4, 4.3 Hz, 2H).
^{13}C-NMR (MeOD, 75 MHz): δ 156.8 (C_q), 138.2 (C_q), 129.5 (CH), 129.1 (CH), 128.9 (CH), 68.4 (CH), 68.3 (CH_2), 63.0 (CH), 47.8 (CH_2), 44.6 (CH_2), 35.0 (CH_2), 29.0 (CH_2).
HRMS (ESI): *m/z* = 319.2013 $[M+H]^+$ (found), 319.2016 calcd. for $C_{18}H_{27}N_2O_3^+$, 341.1828 $[M+Na]^+$ (found), 341.1836 calcd. for $C_{18}H_{26}N_2NaO_3^+$.

Benzyl 4-((methylsulfonyl)oxy)-[1,4'-bipiperidine]-1'-carboxylate (**111**)

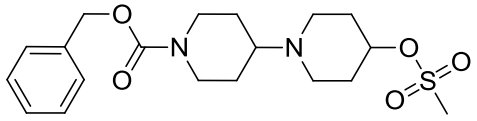

Compound **110** (618 mg, 1.94 mmol, 1.0 eq) was dissolved in dry pyridine (1.5 mL). The resulting solution was cooled to 0 °C and mesyl chloride (300 µL, 3.88 mmol, 2.0 eq) was added dropwise. The resulting mixture was allowed to warm to rt for 4 h, sat. aq. Na_2CO_3 was added, and the mixture was extracted with DCM (3×). The combined organic layers were washed with sat. aq. Na_2CO_3 (1×), H_2O (1×), and sat. aq. NaCl (1×), dried over Na_2SO_4, filtered and concentrated to afford **111** (769 mg, 1.94 mmol, 100%) as a black oil.

Molecular formula: $C_{19}H_{28}N_2O_5S$
MW: 360.5 $g.mol^{-1}$
^{1}H-NMR (MeOD, 300 MHz): δ 7.40–7.26 (m, 5H), 5.11 (s, 2H), 4.76 (tt, *J* = 7.7, 3.9 Hz), 4.22 (dp, *J* = 13.8, 2.2 Hz, 2H), 3.09 (s, 3H), 2.98–2.75 (m, 4H), 2.75–2.56 (m, 3H), 2.15–2.01 (m, 2H), 1.99–1.82 (m, 4H), 1.44 (qd, *J* = 12.3, 4.3 Hz, 2H).

^{13}C-NMR (MeOD, 75 MHz): δ 156.7 (C_q), 156.6 (C_q), 138.1 (C_q), 138.0 (C_q), 134.0 (CH), 129.6 (CH), 129.6 (CH), 129.2 (CH), 129.2 (CH), 129.0 (CH), 129.0 (CH), 119.1 (CH_2), 91.1 (CH_2), 77.5 (C_q), 68.5 (CH_2), 68.5 (CH_2), 63.5 (CH), 56.3 (CH), 46.9 (CH_2), 45.1 (CH_2), 44.2 (CH_2), 43.3 (CH_2), 39.5 (CH), 38.4 (CH), 31.8 (CH_2), 31.7 (CH_2), 29.6 (CH_2), 28.5 (CH_2).
HRMS (ESI): *m/z* = 397.1786 $[M+H]^+$ (found), 397.1792 calcd. for $C_{19}H_{29}N_2O_5S^+$, 319.2020 $[M+2H-Ms]^+$ (found), 319.2016 calcd. for $C_{18}H_{27}N_2O_3^+$, 303.2068 $[M+2H-OMs]^+$ (found), 303.2067 calcd. for $C_{18}H_{27}N_2O_2^+$.

((4-Bromophenyl)ethynyl)trimethylsilane (**113**)

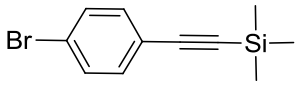

$Zn(OTf)_2$ (51 mg, 0.14 mmol, 0.05 eq) was suspended in dry DCM (11 mL). TEA (0.59 mL, 4.23 mmol, 1.5 eq) was then added, followed by 1-bromo-4-ethynylbenzene **112** (511 mg, 2.82 mmol, 1.0 eq) and TMSOTf (0.77 mL, 4.23 mmol, 1.5 eq). The resulting mixture was stirred at rt for 15 h, sat. aq. NH_4Cl was added, and the mixture was extracted with Et_2O (3×). The combined organic layers were dried over Na_2SO_4, filtered and concentrated. Column chromatography (SiO_2, 100% Cy) afforded **113** (645 mg, 2.55 mmol, 90%) as a white solid.

Molecular formula: $C_{11}H_{13}BrSi$
MW: 253.2 g.mol^{-1}
^{1}H-NMR ($CDCl_3$, 300 MHz): δ 7.46–7.40 (m, 2H), 7.35–7.29 (m, 2H), 0.24 (s, 9H).

8-(1-(4-((Trimethylsilyl)ethynyl)phenyl)piperidin-4-yl)-1,4-dioxa-8-azaspiro[4.5]decane (**114**)

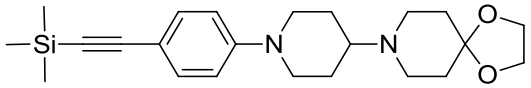

Compound **113** (100 mg, 0.395 mmol, 1.0 eq) and compound **106** (107 mg, 0.474 mmol, 1.2 eq) were dissolved in dry toluene (2 mL). NaO^tBu (53 mg, 0.553 mmol, 1.4 eq) was added, followed by $Pd_2(dba)_3$ (3.7 mg, 0.004 mmol, 0.01 eq) and BINAP (7.5 mg, 0.012 mmol, 0.03 eq). The resulting mixture was refluxed for 48 h and cooled to rt. Et_2O (6 mL) was added, the mixture was filtered over a pad of celite and concentrated. Column chromatography (SiO_2, 95:5 to 90:10 AcOEt/MeOH) afforded **114** (80 mg, 0.201 mmol, 51%) as a yellow solid.

Molecular formula: $C_{23}H_{34}N_2O_2Si$
MW: 398.6 g.mol^{-1}
^{1}H-NMR (MeOD, 300 MHz): δ 7.31–7.23 (m, 2H), 6.92–6.84 (m, 2H), 3.93 (s, 4H), 3.85 (d, *J* = 12.7 Hz, 2H), 2.79–2.64 (m, 6H), 2.51 (tt, *J* = 11.2, 3.1 Hz, 1H), 1.96 (d, *J* = 12.0 Hz, 2H), 1.74 (t, *J* = 5.7 Hz, 4H), 1.61 (qd, *J* = 12.2, 4.1 Hz, 2H), 0.20 (s, 9H).
HRMS (ESI): *m/z* = 399.2449 $[M+H]^+$ (found), 399.2462 calcd. for $C_{23}H_{35}N_2O_2Si^+$, 421.2269 $[M+Na]^+$ (found), 421.2282 calcd. for $C_{23}H_{34}N_2NaO_2Si^+$.

8-(1-(4-Ethynylphenyl)piperidin-4-yl)-1,4-dioxa-8-azaspiro[4.5]decane (**115**)

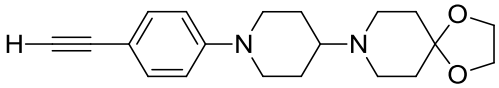

Compound **114** (77 mg, 0.193 mmol, 1.0 eq) was dissolved in DCM (2.5 mL) and MeOH (2.5 mL). K_2CO_3 (34.6 mg, 0.251 mmol, 1.3 eq) was added, the resulting mixture was heated at 40 °C for 24 h and concentrated. DCM was added, and the mixture was washed with H_2O (1×), dried over Na_2SO_4, filtered and concentrated. Column chromatography (SiO_2, 95:5 AcOEt/MeOH) afforded **115** (55 mg, 0.169 mmol, 88%) as a white solid.

Molecular formula: $C_{20}H_{26}N_2O_2$
MW: 326.4 g.mol^{-1}
^{1}H-NMR (MeOD, 300 MHz): δ 7.33–7.26 (m, 2H), 6.94–6.86 (m, 2H), 3.93 (s, 4H), 3.85 (d, *J* = 12.8 Hz, 2H), 3.27 (s, 1H), 2.84–2.62 (m, 6H), 2.50 (tt, *J* = 11.6, 3.7 Hz, 1H), 1.97 (d, *J* = 12.4 Hz, 2H), 1.74 (t, *J* = 5.6 Hz, 4H), 1.62 (qd, *J* = 12.0, 3.3 Hz, 2H).
^{13}C-NMR (MeOD, 75 MHz): δ 152.5 (C_q), 134.0 (CH), 116.6 (CH), 113.5 (C_q), 107.9 (C_q), 85.0 (C_q), 76.5 (C_q), 65.3 (CH_2), 62.9 (CH), 49.6 (CH_2), 48.1 (CH_2), 35.6 (CH_2), 28.8 (CH_2).

(4-Bromopyridine-2,6-diyl)bis(pyrrolidin-1-ylmethanone) (**116**)

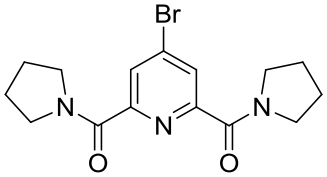

Chelidamic acid monohydrate **6** (2.0 g, 10 mmol, 1.0 eq) was suspended in toluene (15 mL). PBr_5 (12.9 g, 30.0 mmol, 3.0 eq) was added, the resulting mixture was refluxed for 24 h and concentrated. Dry DCM (5 mL) was added, the mixture was cooled to 0 °C, and pyrrolidine (4.17 mL, 50 mmol, 5.0 eq) dissolved in dry DCM (10 mL) was added dropwise. The resulting mixture was allowed to warm to rt for 15 h, aq. 2 M HCl was added until pH ≈ 1, and the mixture was extracted with DCM (3×). The combined organic layers were dried over Na_2SO_4, filtered and concentrated. Column chromatography (SiO_2, 50:50 Cy/AcOEt to 100% AcOEt) afforded **116** (793 mg, 2.25 mmol, 23%) as a white solid.

Molecular formula: $C_{15}H_{18}BrN_3O_2$
MW: 352.2 g.mol^{-1}
^{1}H-NMR ($CDCl_3$, 300 MHz): δ 8.03 (s, 2H), 3.71–3.60 (m, 8H), 1.97–1.84 (m, 8H).

(4-(4-(1,4-Dioxa-8-azaspiro[4.5]decan-8-yl)piperidin-1-yl)pyridine-2,6-diyl)bis(pyrrolidin-1-ylmethanone) (**117**)

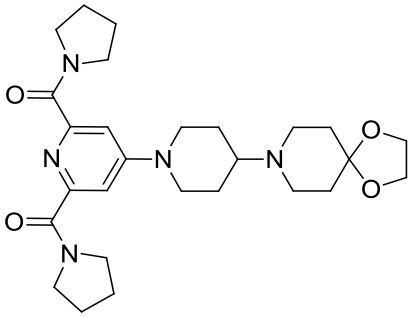

Compound **116** (790 mg, 2.24 mmol, 1 eq) and compound **106** (608 mg, 2.69 mmol, 1.2 eq) were dissolved in dry toluene (9 mL). NaO^{t}Bu (302 mg, 3.14 mmol, 1.4 eq) was added, followed by

$Pd_2(dba)_3$ (20 mg, 0.022 mmol, 0.01 eq) and BINAP (48 mg, 0.067 mmol, 0.03 eq). The resulting mixture was refluxed for 24 h, cooled to rt, and sat. aq. NH_4Cl was added. The mixture was extracted with DCM (3×), dried over Na_2SO_4, filtered and concentrated. Column chromatography (SiO_2, 90:10 to 40:60 Cy/AcOEt) afforded **117** (822 mg, 1.65 mmol, 74%) as a white solid.

Molecular formula: $C_{27}H_{39}N_5O_4$
MW: 497.6 g.mol^{-1}
^{1}H-NMR (CDCl$_3$, 300 MHz): δ 7.17 (s, 2H), 4.01 (d, *J* = 13.1 Hz, 2H), 3.95 (s, 4H), 3.64 (t, *J* = 6.6 Hz, 8H), 2.96–2.81 (m, 2H), 2.63 (t, *J* = 5.6 Hz, 4H), 2.56 (tt, *J* = 10.9, 3.3 Hz, 1H), 1.98–1.80 (m, 10 H), 1.73 (t, *J* = 5.6 Hz, 4H), 1.55 (qd, *J* = 12.2, 4.0 Hz, 2H).
^{13}C-NMR (CDCl$_3$, 75 MHz): δ 167.3 (C_q), 155.6 (C_q), 154.3 (C_q), 108.7 (CH), 107.4 (C_q), 64.4 (CH), 61.6 (CH_2), 49.2 (CH_2), 47.2 (CH_2), 46.8 (CH_2), 46.1 (CH_2), 35.3 (CH_2), 27.9 (CH_2), 26.7 (CH_2), 24.2 (CH_2).

(4-(4-oxo-[1,4'-bipiperidin]-1'-yl)pyridine-2,6-diyl)bis(pyrrolidin-1-ylmethanone) (**118**)

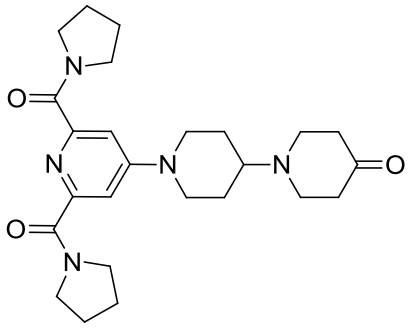

Compound **117** (822 mg, 1.65 mmol, 1.0 eq) was dissolved in aq. 4 M HCl (14 mL). The resulting mixture was allowed to warm to rt for 7 d and cooled to 0°C. DCM (5 mL) was added followed by dropwise aq. 33% NaOH until pH ≈ 14. The mixture was extracted with DCM (3×) and the combined organic layers were dried over Na_2SO_4, filtered and concentrated. Column chromatography (SiO_2, 90:10 to 80:20 AcOEt/MeOH) afforded **118** (464 mg, 1.02 mmol, 62%) as a white solid.

Molecular formula: $C_{25}H_{35}N_5O_3$
MW: 453.6 g.mol^{-1}
^{1}H-NMR (CDCl$_3$, 300 MHz): δ 7.18 (s, 2H), 4.03 (d, *J* = 13.4 Hz, 2H), 3.63 (td, *J* = 6.4, 3.4 Hz, 8H), 2.92 (td, *J* = 12.8, 2.7 Hz, 2H), 2.84 (t, *J* = 5.9 Hz, 4H), 2.70 (tt, *J* = 11.4, 3.6 Hz, 1H), 2.53 (t, *J* = 5.9 Hz, 4H), 1.98–1.79 (m, 10 H), 1.56 (qd, *J* = 12.2, 4.0 Hz, 2H).
HRMS (ESI): *m/z* = 454.2805 $[M+H]^+$ (found), 454.2813 calcd. for $C_{25}H_{36}N_5O_3^+$, 476.2628 $[M+Na]^+$ (found), 476.2632 calcd. for $C_{25}H_{35}N_5NaO_3^+$, 907.5558 $[2M+H]^+$ (found), 907.5553 calcd. for $C_{50}H_{71}N_{10}O_6^+$, 929.5361 $[2M+Na]^+$ (found), 929.5372 calcd. for $C_{50}H_{70}N_{10}NaO_6^+$, 486.3067 $[M+H+MeOH]^+$ (found), 486.3075 calcd. for $C_{26}H_{40}N_5O_4^+$, 508.2893 $[M+Na+MeOH]^+$ (found), 508.2894 calcd. for $C_{26}H_{39}N_5NaO_4^+$, 939.5819 $[2M+H+MeOH]^+$ (found), 939.5815 calcd. for $C_{51}H_{75}N_{10}O_7^+$, 961.5621 $[2M+Na+MeOH]^+$ (found), 961.5634 calcd. for $C_{51}H_{74}N_{10}NaO_7^+$, 971.6066 $[2M+H+2MeOH]^+$ (found), 971.6077 calcd. for $C_{52}H_{79}N_{10}O_8^+$, 993.5883 $[2M+Na+2MeOH]^+$ (found), 993.5896 calcd. for $C_{52}H_{78}N_{10}NaO_8^+$.

8-(1-(4-([2,2':6',2''-Terpyridin]-4'-yl)phenyl)piperidin-4-yl)-1,4-dioxa-8-azaspiro[4.5]decane (**119**)

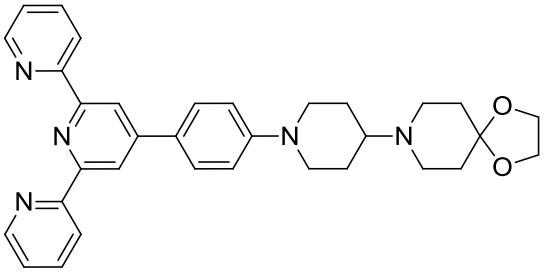

*p*BrPhTpy **36** (2 g, 5.15 mmol, 1.0 eq) and compound **106** (1.4 g, 6.18 mmol, 1.2 eq) were dissolved in dry toluene (20 mL). NaO^tBu (692 mg, 7.21 mmol, 1.4 eq) was added, followed by $Pd_2(dba)_3$ (50 mg, 0.052 mmol, 0.01 eq) and BINAP (97 mg, 0.155 mmol, 0.03 eq). The resulting mixture was refluxed for 48 h and concentrated. Column chromatography (Al_2O_3, basic, activated, Brockmann I, 100% DCM to 98:2 DCM/MeOH) afforded **119** (2.685 g, 5.03 mmol, 98%) as an orange solid.

Molecular formula: $C_{33}H_{35}N_5O_2$
MW: 533.7 g.mol^{-1}
^{1}H-NMR ($CDCl_3$, 300 MHz): δ 8.73 (ddd, *J* = 4.8, 1.8, 0.9 Hz, 2H), 8.70 (s, 2H), 8.66 (dt, *J* = 8.0, 1.1 Hz, 2H), 7.87 (td, *J* = 7.3, 1.4 Hz, 4H), 7.34 (ddd, *J* = 7.5, 4.8, 1.2 Hz), 7.08–6.99 (m, 2H), 3.97 (s, 4H), 3.89 (d, *J* = 12.5 Hz, 2H), 2.80 (td, *J* = 12.2, 1.9 Hz, 2H), 2.69 (t, *J* = 5.7 Hz, 4H), 2.54 (tt, *J* = 11.4, 3.3 Hz, 1H), 1.94 (d, *J* = 12.6 Hz, 2H), 1.77 (t, *J* = 5.6 Hz, 4H), 1.74–1.68 (m, 2H).
^{13}C-NMR ($CDCl_3$, 75 MHz): δ 156.7 (C_q), 155.9 (C_q), 152.0 (C_q), 149.9 (C_q), 149.2 (CH), 137.0 (CH), 128.3 (C_q), 128.2 (CH), 123.8 (CH), 121.5 (CH), 117.9 (CH), 116.0 (CH), 107.5 (C_q), 64.4 (CH_2), 61.9 (CH), 48.9 (CH_2), 47.1 (CH_2), 35.4 (CH_2), 28.1 (CH_2).
HRMS (ESI): *m/z* = 534.2842 $[M+H]^+$ (found), 534.2864 calcd. for $C_{33}H_{36}N_5O_2^+$, 556.2650 $[M+Na]^+$ (found), 556.2683 calcd. for $C_{33}H_{35}N_5NaO_2^+$, 310.1328 $[M\text{-}2pipketal+2H]^+$ (found), 310.1339 calcd. for $C_{21}H_{16}N_3^+$, 332.1137 $[M\text{-}2pipketal+H+Na]^+$ (found), 332.1158 calcd. for $C_{21}H_{15}N_3Na^+$.

1'-(4-([2,2':6',2''-terpyridin]-4'-yl)phenyl)-[1,4'-bipiperidin]-4-one (**120**)

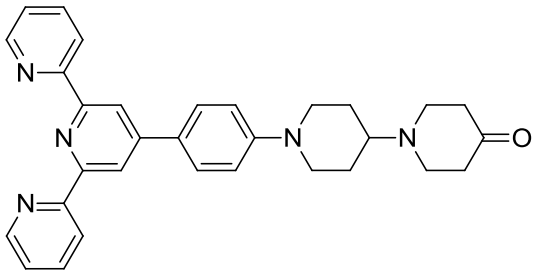

Compound **119** (2.685 g, 5.03 mmol, 1.0 eq) was dissolved in cold aq. 4 M HCl (40 mL). The resulting mixture was allowed to warm to rt for 7 d and cooled to 0°C. DCM (30 mL) was added, followed by dropwise aq. 33% NaOH until pH ≈14. The mixture was extracted with DCM (3×) and the combined organic layers were dried over Na_2SO_4, filtered and concentrated. Column chromatography (Al_2O_3, basic, activated, Brockmann I, 100% DCM to 99:1 DCM/MeOH) afforded **120** (2.01 g, 4.11 mmol, 82%) as an orange solid.

Molecular formula: $C_{31}H_{31}N_5O$
MW: 489.6 g.mol^{-1}
^{1}H-NMR ($CDCl_3$, 300 MHz): δ 8.73 (ddd, *J* = 4.8, 1.8, 0.9 Hz, 2H), 8.71 (s, 2H), 8.67 (dt, *J* = 8.0, 1.1 Hz, 2H), 7.91–7.83 (m, 4H), 7.34 (ddd, *J* = 7.5, 4.8, 1.2 Hz, 2H), 7.07–7.00 (m, 2H), 3.90 (d, *J* = 12.7 Hz, 2H),

2.90 (t, *J* = 6.0 Hz, 4H), 2.82 (dd, *J* = 12.2, 2.6 Hz, 2H), 2.67 (tt, *J* = 11.5, 3.7 Hz, 1H), 2.48 (t, *J* = 6.0 Hz, 4H), 1.95 (d, *J* = 12.3 Hz, 2H), 1.74 (qd, *J* = 12.1, 4.0 Hz, 2H).
^{13}C-NMR ($CDCl_3$, 75 MHz): δ 209.6 (C_q), 156.6 (C_q), 155.9 (C_q), 151.8 (C_q), 149.8 (C_q), 149.2 (CH), 137.0 (CH), 128.5 (C_q), 128.2 (CH), 123.9 (CH), 121.5 (CH), 117.9 (CH), 116.0 (CH), 61.5 (CH), 49.1 (CH_2), 48.8 (CH_2), 42.0 (CH_2), 28.2 (CH_2).
HRMS (ESI): *m/z* = 490.2586 $[M+H]^+$ (found), 490.2601 calcd. for $C_{31}H_{32}N_5O^+$, 512.2409 $[M+Na]^+$ (found), 512.2421 calcd. for $C_{31}H_{31}N_5NaO^+$, 522.2848 $[M+H+MeOH]^+$ (found), 522.2864 calcd. for $C_{32}H_{36}N_5O_2^+$, 544.2673 $[M+Na+MeOH]^+$ (found), 544.2683 calcd. for $C_{32}H_{35}N_5NaO_2^+$, 310.1343 $[M-2pipketal+2H]^+$ (found), 310.1339 calcd. for $C_{21}H_{16}N_3^+$, 332.1152 $[M-2pipketal+H+Na]^+$ (found), 332.1158 calcd. for $C_{21}H_{15}N_3Na^+$.

Benzyl 4-(4-(((trifluoromethyl)sulfonyl)oxy)-5,6-dihydropyridin-1(2*H*)-yl)piperidine-1-carboxylate (**121**)

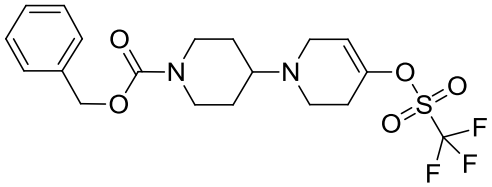

Compound **107** (1.185 g, 3.75 mmol, 1.0 eq) was dissolved in dry THF (10 mL). The resulting solution was cooled to -78 °C and LDA (2 M in THF/heptane/ethylbenzene, 2.25 mL, 4.5 mmol, 1.2 eq) was added dropwise. The resulting mixture was stirred at -78 °C for 20 min and $PhNTf_2$ (1.474 g, 4.13 mmol, 1.1 eq) dissolved in dry THF (10 mL) was added dropwise. The resulting mixture was allowed to warm to rt for 3 h, sat. aq. NH_4Cl was added and the mixture was extracted with AcOEt (3×). The combined organic layers were dried over Na_2SO_4, filtered and concentrated. Column chromatography (SiO_2, 90:10 to 80:20 AcOEt/MeOH) afforded **121** (697 mg, 1.55 mmol, 41%) as a pasty beige solid.

Molecular formula: $C_{19}H_{23}F_3N_2O_5S$
MW: 448.5 g.mol^{-1}
^{1}H-NMR (MeOD, 300 MHz): δ 7.39–7.23 (m, 5H), 5.88–5.80 (m, 1H), 3.59 (s, 2H), 3.27 (q, *J* = 2.9 Hz, 2H), 3.02 (dt, *J* = 13.1, 3.1 Hz, 2H), 2.83 (t, *J* = 5.7 Hz, 2H), 2.54–2.38 (m, 3H), 2.14 (t, *J* = 10.8 Hz, 2H), 1.94–1.80 (m, 2H), 1.61 (qd, *J* = 12.2, 3.8 Hz, 2H).
^{13}C-NMR (MeOD, 75 MHz): δ 148.7 (C_q), 137.2 (C_q), 130.9 (CH), 129.4 (CH), 128.7 (CH), 120.8 (C_q), 117.9 (CH), 63.6 (CH_2), 61.5 (CH), 53.7 (CH_2), 47.7 (CH_2), 46.8 (CH_2), 29.6 (CH_2), 28.6 (CH_2).

1-(1-Benzylpiperidin-4-yl)-1,2,3,6-tetrahydropyridin-4-yl trifluoromethanesulfonate (**122**)

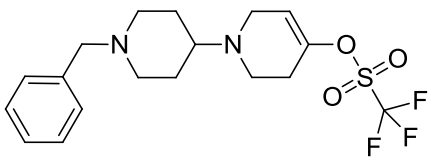

Compound **108** (1.5 g, 5.51 mmol, 1.0 eq) was dissolved in dry THF (15 mL). The resulting solution was cooled to -78 °C and LDA (2 M in THF/heptane/ethylbenzene, 3.31 mL, 6.61 mmol, 1.2 eq) was added dropwise. The resulting mixture was stirred at -78 °C for 20 min and $PhNTf_2$ (2.16 g, 4.13 mmol, 1.1 eq) dissolved in dry THF (15 mL) was added dropwise. The resulting mixture was allowed to warm to rt for 3 h, sat. aq. NH_4Cl was added and the mixture was extracted with AcOEt (3×). The

combined organic layers were dried over Na_2SO_4, filtered and concentrated. Column chromatography (SiO_2, 90:10 to 80:20 AcOEt/MeOH) afforded **122** (1.09 g, 2.7 mmol, 49%) as a pasty beige solid.

Molecular formula: $C_{18}H_{23}F_3N_2O_3S$
MW: 404.4 g.mol^{-1}
^{1}H-NMR ($CHCl_3$, 300 MHz): δ 7.35–7.24 (m, 5H), 5.74 (td, *J* = 3.5, 1.8 Hz, 1H), 3.53 (s, 2H), 3.23 (q, J = 3.1 Hz, 2H), 2.98 (d, *J* = 11.3 Hz, 2H), 2.78 (t, *J* = 5.6 Hz, 2H), 2.49–2.38 (m, 3H), 2.02 (t, *J* = 11.3 Hz, 2H), 1.82–1.72 (m, 2H), 1.63 (qd, *J* = 11.9, 3.8 Hz, 2H).
HRMS (ESI): *m/z* = 405.1434 $[M+H]^+$ (found), 405.1454 calcd. for $C_{18}H_{24}F_3N_2O_3S^+$, 91.0536 [Tropylium], 91.0542 calcd. for $C_7H_7^+$.

Benzyl 4-hydrazono-[1,4'-bipiperidine]-1'-carboxylate (**123**)

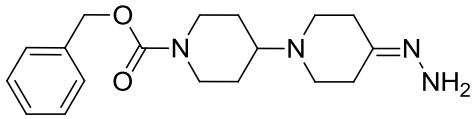

Hydrazine monohydrate (1.53 mL, 31.6 mmol, 20.0 eq) was dissolved in dry MeOH (4 mL). Activated 4 Å molecular sieve (840 mg) was added and the resulting mixture was stirred at rt for 30 min. Compound **107** (500 mg, 1.58 mmol, 1.0 eq) dissolved in dry MeOH (2 mL) was then added and the resulting mixture was stirred at rt for 3 h, filtered over a pad of celite and concentrated to afford **123** (522 mg, 1.58 mmol, 100%) as a pale yellow solid.

Molecular formula: $C_{18}H_{26}N_4O_2$
MW: 330.4 g.mol^{-1}
^{1}H-NMR ($CDCl_3$, 300 MHz): δ 7.40–7.27 (m, 5H), 5.11 (s, 2H), 4.37–4.11 (m, 2H), 2.77 (t, *J* = 12.9 Hz, 2H), 2.64 (q, *J* = 5.9 Hz, 4H), 2.52 (tt, *J* = 11.4, 3.4 Hz, 1H), 2.35 (q, *J* = 5.6 Hz, 4H), 1.87–1.68 (m, 2H), 1.44 (qd, *J* = 12.1, 3.9 Hz, 2H).
^{13}C-NMR ($CDCl_3$, 75 MHz): δ 164.2 (C_q), 155.2 (C_q), 136.9 (C_q), 128.6 (CH), 128.1 (CH), 127.9 (CH), 67.2 (CH_2), 61.7 (CH), 49.9 (CH_2), 48.8 (CH_2), 43.7 (CH_2), 35.4 (CH_2), 28.5 (CH_2), 28.2 (CH_2).
HRMS (ESI): *m/z* = 331.2118 $[M+H]^+$ (found), 331.2129 calcd. for $C_{18}H_{27}N_4O_2^+$, 353.1933 $[M+Na]^+$ (found), 353.1948 calcd. for $C_{18}H_{26}N_4NaO_2^+$.

Benzyl 4-hydroxy-4-phenyl-[1,4'-bipiperidine]-1'-carboxylate (**124**)

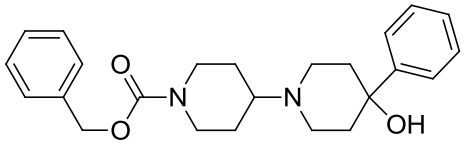

Magnesium turnings (77 mg, 3.16 mmol, 2.0 eq) were suspended in dry THF (1 mL). Five drops of bromobenzene were added, followed by one drop of 1,2-dibromoethane. The reaction was initiated with a heatgun and then dry THF (2.5 mL) and the remaining bromobenzene (332 µL, 3.16 mmol, 2.0 eq overall) were added alternatively to keep the suspension boiling. This mixture was then refluxed until total consumption of the magnesium and cooled to 0 °C. Compound **107** (500 mg, 1.58 mmol, 1.0 eq) dissolved in dry THF (2.5 mL) was added dropwise and the resulting mixture was stirred at rt for 24 h. Sat. aq. NH_4Cl was added and the mixture was extracted with DCM (3×). The combined organic layers were dried over Na_2SO_4, filtered and concentrated. Column chromatography (SiO_2, 95:5 AcOEt/MeOH) afforded **124** (333 mg, 0.844 mmol, 53%) as a white solid.

Molecular formula: $C_{24}H_{30}N_2O_3$
MW: 394.5 g.mol^{-1}
^{1}H-NMR (MeOD, 300 MHz): δ 7.53–7.46 (m, 2H), 7.41–7.27 (m, 7H), 7.26–7.17 (m, 1H), 5.12 (s, 2H), 4.24 (dq, *J* = 11.3, 2.5 Hz, 2H), 2.97–2.64 (m, 6H), 2.58 (ddd, *J* = 14.7, 11.6, 3.6 Hz, 1H), 2.19–2.03 (m, 2H), 2.03–1.82 (m, 2H), 1.82–1.67 (m, 2H), 1.46 (qd, *J* = 12.4, 4.1 Hz, 2H).
^{13}C-NMR (MeOD, 75 MHz): δ 156.8 (C_q), 150.0 (C_q), 138.2 (C_q), 129.6 (CH), 129.2 (CH), 129.1 (CH), 128.9 (CH), 127.7 (CH), 125.7 (CH), 71.8 (C_q), 68.3 (CH_2), 63.2 (CH), 46.3 (CH_2), 44.6 (CH_2), 39.0 (CH_2), 35.7 (CH_2), 29.0 (CH_2).

Benzyl 4-(4-phenyl-5,6-dihydropyridin-1(2H)-yl)piperidine-1-carboxylate (**125**)

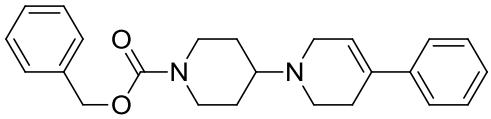

Compound **124** (317 mg, 0.804 mmol, 1.0 eq) was dissolved in dry DCM (7 mL). TFA (1.85 mL, 24.12 mmol, 30.0 eq) was added dropwise, the resulting solution was refluxed for 48 h and cooled to rt. Aq. 5 M NaOH (4 mL) was added and the mixture was extracted with DCM (3×). The combined organic layers were washed with sat. aq. NaCl (1×), dried over Na_2SO_4, filtered and concentrated. Column chromatography (SiO_2, 98:2 AcOEt/MeOH) afforded **125** (210 mg, 0.558 mmol, 69%) as a white solid.

Molecular formula: $C_{24}H_{28}N_2O_2$
MW: 376.5 g.mol^{-1}
^{1}H-NMR ($CDCl_3$, 300 MHz): δ 7.43–7.19 (m, 10H), 6.08 (t, *J* = 3.8 Hz, 1H), 5.14 (s, 2H), 4.27 (br s, 2H), 3.30 (q, *J* = 3.0 Hz, 2H), 2.92–2.78 (m, 2H), 2.79 (t, *J* = 6.1 Hz, 2H), 2.63–2.49 (m, 3H), 1.91 (d, *J* = 12.6 Hz, 2H), 1.53 (qd, *J* = 12.2, 4.2 Hz, 2H).
^{13}C-NMR ($CDCl_3$, 75 MHz): δ 155.3 (C_q), 140.9 (C_q), 137.0 (C_q), 135.3 (C_q), 128.6 (CH), 128.4 (CH), 128.1 (CH), 128.0 (CH), 127.1 (CH), 125.1 (CH), 122.1 (CH), 67.2 (CH_2), 61.4 (CH), 49.3 (CH_2), 46.3 (CH_2), 43.7 (CH_2), 28.7 (CH_2).

4-phenyl-1,4'-bipiperidine (**126**)

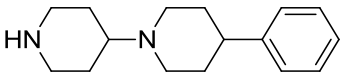

Compound **125** (177 mg, 0.47 mmol, 1.0 eq) was dissolved in EtOH (25 mL). Pd/C (10%w, 17.7 mg) was added and the resulting suspension was hydrogenated (10 bar) at rt for 3h. The resulting mixture was filtered over a pad of celite and concentrated to afford **126** (105 mg, 0.43 mmol, 91%) as a white solid.

Molecular formula: $C_{16}H_{24}N_2$
MW: 244.4 g.mol^{-1}
^{1}H-NMR (MeOD, 300 MHz): δ 7.32–7.11 (m, 5H), 3.10 (t, *J* = 11.7 Hz, 4H), 2.59 (td, *J* = 12.4, 2.3 Hz, 2H), 2.57–2.43 (m, 2H), 2.38 (td, *J* = 11.7, 3.3 Hz, 2H), 1.97–1.81 (m, 4H), 1.81–1.69 (m, 2H), 1.49 (qd, *J* = 12.4, 4.0 Hz, 2H).
^{13}C-NMR (MeOD, 75 MHz): δ 147.4 (C_q), 129.5 (CH), 127.8 (CH), 127.2 (CH), 63.5 (CH), 50.8 (CH_2), 46.7 (CH_2), 43.9 (CH), 34.4 (CH_2), 29.5 (CH_2).
HRMS (ESI): *m/z* = 245.2004 $[M+H]^+$ (found), 245.2012 calcd. for $C_{16}H_{25}N_2^+$.

***tert*-Butyl piperazine-1-carboxylate** (Boc-Pip **127**)

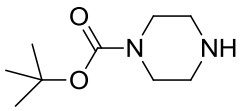

Piperazine (25.0 g, 290.4 mmol, 2.5 eq) was dissolved in a mixture of H_2O (350 mL) and *tert*-butyl alcohol (350 mL). The solution was cooled to 0 °C and NaOH (10.22 g, 255.6 mmol, 2.2 eq) dissolved in H_2O (50 mL) was added, followed by Boc_2O (25.35 g, 116.2 mmol, 1.0 eq). The resulting mixture was stirred for 15 h at rt, concentrated to ≈ 300 mL and filtered. The filtrate was extracted with DCM (3×) and the combined organic layers were washed with sat. aq. NaCl (1×), dried over Na_2SO_4, filtered and concentrated to afford Boc-Pip **127** (13.34 g, 71.6 mmol, 62 %) as a white solid.

Molecular formula: $C_9H_{18}N_2O_2$
MW: 186.3 g.mol^{-1}
^{1}H-NMR ($CDCl_3$, 300 MHz): δ 3.38 (dd, *J* = 6.3, 3.9 Hz, 4H), 2.79 (t, *J* = 5.1 Hz, 4H), 1.83 (s, 1H), 1.44 (s, 9H).
^{13}C-NMR ($CDCl_3$, 75 MHz): δ 154.9 (C_q), 79.7 (C_q), 46.0 (CH_2), 44.5 (CH_2, br), 28.5 (CH_3).
HRMS (ESI): *m/z* = 187.1441 $[M+H]^+$ (found), 187.1441 calcd. for $C_9H_{18}N_2O_2^+$, 209.1263 $[M+Na]^+$ (found), 209.1260 calcd. for $C_9H_{18}N_2NaO_2^+$, 131.0818 $[M–{}^tBu+2H]^+$ (found), 131.0815 calcd. for $C_5H_{11}N_2O_2^+$, 87.0917 [M–Boc+2H]$^+$ (found), 89.0917 calcd. for $C_4H_{11}N_2^+$.

1-Benzylpiperazine (Bn-Pip **128**)

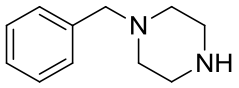

Piperazine (27.2 g, 316 mmol, 4.0 eq) was suspended in toluene (50 mL). Benzyl chloride (9.1 mL, 79 mmol, 1.0 eq) was added dropwise and the resulting mixture was heated at 85 °C for 5 h, filtered, and concentrated. Aq. 2 M HCl (50 mL) was added and the mixture was extracted with DCM (3×). The pH of the aqueous layer was adjusted to ≈ 14 with aq. NaOH, and the aqueous layer was extracted again with DCM (3×). The combined organic layer were washed with sat. aq. NaCl (1×) and H_2O (1×), dried over Na_2SO_4, filtered and concentrated. Column chromatography (SiO_2, 90:10 DCM/MeOH to 100% MeOH) afforded Bn-Pip **128** (10.48 g, 59.4 mmol, 75%) as an oily white solid.

Molecular formula: $C_{11}H_{16}N_2$
MW: 126.3 g.mol^{-1}
^{1}H-NMR ($CDCl_3$, 300 MHz): δ 7.35–7.20 (m, 5H), 3.48 (s, 2H), 2.88 (t, *J* = 4.9 Hz, 4H), 2.30–2.50 (m, 4H), 1.72 (s, 1H).
^{13}C-NMR ($CDCl_3$, 75 MHz): δ 138.1 (C_q), 129.3 (CH), 128.3 (CH), 127.2 (CH), 67.8 (CH_2), 54.4 (CH_2), 46.1 (CH_2).
HRMS (ESI): *m/z* = 177.1382 $[M+H]^+$ (found), 177.1386 calcd. for $C_{11}H_{17}N_2^+$, 91.0536 [Tropylium] (found), 91.0542 calcd. for $C_7H_7^+$.

Di-*tert*-butyl 4,4'-(1,4-phenylene)bis(piperazine-1-carboxylate) (**130**)

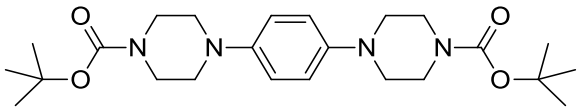

1,4-Dibromobenzene **129** (200 mg, 0.848 mmol, 1.0 eq) and Boc-Pip **127** (395 mg, 2.12 mmol, 2.5 eq) were dissolved in dry toluene (5 mL). NaO^tBu (163 mg, 1.70 mmol, 2.0 eq) was then added, followed by $Pd_2(dba)_3$ (15.5 mg, 0.017 mmol, 0.02 eq) and BINAP (31.7 mg, 0.051 mmol, 0.06 eq). The resulting mixture was refluxed for 72 h, cooled to rt, filtered over a pad of celite and concentrated. Column chromatography (SiO_2, 70/30 Cy:AcOEt) afforded **130** (300 mg, 0.972 mmol, 79%) as a yellow solid.

Molecular formula: $C_{24}H_{38}N_4O_4$
MW: 446.6 g.mol^{-1}
^{1}H-NMR ($CDCl_3$, 300 MHz): δ 6.98–6.81 (m, 4H), 3.57 (t, *J* = 5.0 Hz, 8H), 3.14–2.90 (m, 8H), 1.48 (s, 18H).
^{13}C-NMR ($CDCl_3$, 75 MHz): δ 154.9 (C_q), 118.4 (CH), 80.0 (C_q), 50.6 (CH_2), 43.7 (CH_2, br), 28.6 (CH_3).
HRMS (ESI): *m/z* = 447.2949 $[M+H]^+$ (found), 447.2966 calcd. for $C_{24}H_{39}N_4O_4^+$, 469.2777 $[M+Na]^+$ (found), 469.2785 calcd. for $C_{24}H_{38}N_4NaO_4^+$, 391.2328 $[M-^tBu+2H]^+$ (found), 391.2340 calcd. for $C_{20}H_{31}N_4O_4^+$, 413.2153 $[M-^tBu+H+Na]^+$ (found), 413.2159 calcd. for $C_{20}H_{30}N_4NaO_4^+$, 335.1703 $[M-2^tBu+3H]^+$ (found), 335.1714 calcd. for $C_{16}H_{23}N_4O_4^+$, 291.1806 $[M-^tBu-Boc+3H]^+$ (found), 291.1816 calcd. for $C_{15}H_{23}N_4O_2^+$, 269.1725 $[M-2Boc+2H+Na]^+$ (found), 269.1737 calcd. for $C_{14}H_{22}C_4Na^+$, 369.2247 $[M-Boc+H+Na]^+$ (found), 369.2261 calcd. for $C_{19}H_{30}N_4NaO_2^+$, 347.2424 $[M-Boc+2H]^+$ (found), 347.2442 calcd. for $C_{19}H_{31}N_4O_2^+$.

1,4-Di(piperazin-1-yl)benzene (PipPhPip **131**)

Compound **130** (292 mg, 0.654 mmol, 1.0 eq) was dissolved in dry DCM (4 mL) and the resulting solution was cooled to 0 °C. TFA (1 mL) was added dropwise, and the resulting mixture was allowed to warm to rt for 3h. Aq. NaOH was added until pH ≈ 14 and the mixture was then extracted with DCM (3×). The combined organic layers were dried over Na_2SO_4, filtered and concentrated to afford PipPhPip **131** (140 mg, 0.568 mmol, 87%) as an orange solid.

Molecular formula: $C_{14}H_{22}N_4$
MW: 246.4 g.mol
^{1}H-NMR ($CDCl_3$, 300 MHz): δ 6.92–6.88 (m, 4H), 3.08–2.99 (m, 16H), 1.60 (s, 2H).
^{13}C-NMR ($CDCl_3$, 75 MHz): δ 146.1 (C_q), 117.9 (CH), 51.8 (CH_2), 46.4 (CH_2).
HRMS (ESI): *m/z* = 247.1917 $[M+H]^+$ (found), 247.1917 calcd. for $C_{14}H_{23}N_4^+$.

***tert*-Butyl 4-(4-bromophenyl)piperazine-1-carboxylate** (**133**)

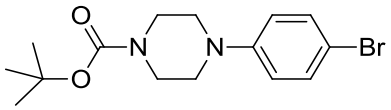

1-Bromo-4-iodobenzene **132** (1.47 g, 5.19 mmol, 1.0 eq) and Boc-Pip **127** (1.16 g, 6.23 mmol, 1.2 eq) were dissolved in dry THF (18 mL). NaO^tBu (697 mg, 7.26 mmol, 1.4 eq), dibenzo-18-crown-6 (2.618 g, 7.26 mmol, 1.4 eq), $Pd_2(dba)_3$ (119 mg, 0.130 mmol, 0.025 eq) and BINAP (242 mg, 0.389 mmol, 0.075 eq) were then added, and the resulting mixture was refluxed for 15 h. The suspension was

then cooled to rt, filtered over a pad of celite and concentrated. Column chromatography (SiO_2, 90:10 to 70:30 Cy/AcOEt) afforded **133** (1.611 g, 4.72 mmol, 91 %) as a pale orange solid.

Molecular formula: $C_{15}H_{21}BrN_2O_2$
MW: 341.2 g.mol^{-1}
^{1}H-NMR ($CDCl_3$, 300 MHz): δ 7.38–7.31 (m, 2H), 6.83–6.74 (m, 2H), 3.57 (t, *J* = 5.1 Hz, 4H), 3.09 (t, *J* = 5.1 Hz, 4H), 1.48 (s, 9H).
^{13}C-NMR ($CDCl_3$, 75 MHz): δ 154.8 (C_q), 150.4 (C_q), 132.1 (CH), 118.3 (CH), 112.6 (C_q), 80.2 (C_q), 49.4 (CH_2), 43.7 (CH_2, br), 28.6 (CH_3).
HRMS (ESI): *m/z* = 341.0843 $[M+H]^+$ (found), 341.0859 calcd. for $C_{15}H_{22}BrN_2O_2^+$, 363.0660 $[M+Na]^+$ (found), 363.0679 calcd. for $C_{15}H_{21}BrN_2NaO_2^+$, 285.0223 $[M-{}^tBu+2H]^+$ (found), 285.0223 calcd. for $C_{11}H_{14}BrN_2O_2^+$, 263.0148 [M-Boc+H+Na]$^+$, 263.0154 calcd. for $C_{10}H_{31}BrN_2Na^+$, 241.0326 $[M-Boc+2H]^+$ (found), 241.0335 calcd. for $C_{10}H_{14}BrN_2^+$, 163.1229 $[M-Boc-Br+3H]^+$ (found), 163.1230 calcd. for $C_{10}H_{15}N_2^+$.

1-Benzyl-4-(4-bromophenyl)piperazine (**134**)

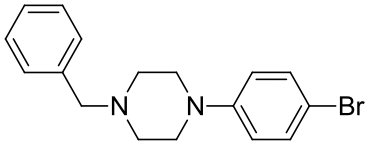

1-Bromo-4-iodobenzene **132** (2.0 g, 7.07 mmol, 1.0 eq) and Bn-Pip **128** (1.5 g, 8.48 mmol, 1.2 eq) were dissolved in dry THF (25 mL). NaO^tBu (950 mg, 9.90 mmol, 1.4 eq), dibenzo-18-crown-6 (3.57 g, 9.90 mmol, 1.4 eq), $Pd_2(dba)_3$ (162 mg, 0.177 mmol, 0.025 eq) and BINAP (330 mg, 0.530 mmol, 0.075 eq) were then added, and the resulting mixture was refluxed for 15 h. The suspension was then cooled to rt, filtered over a pad of celite and concentrated. Column chromatography (SiO_2, 90:10 to 70:30 Cy/AcOEt) afforded **134** (1.925 g, 5.81 mmol, 82 %) as a pale orange solid.

Molecular formula: $C_{17}H_{19}BrN_2$
MW: 331.3 g.mol^{-1}
^{1}H-NMR ($CDCl_3$, 300 MHz): δ 7.38–7.24 (m, 7H), 6.82–6.74 (m, 2H), 3.57 (s, 2H), 3.17 (t, *J* = 5.0 Hz, 4H), 2.60 (t, *J* = 5.0 Hz, 4H).
^{13}C-NMR ($CDCl_3$, 75 MHz): δ 150.5 (C_q), 138.0 (C_q), 132.0 (CH), 129.3 (CH), 128.4 (CH), 127.3 (CH), 117.7 (CH), 111.8 (C_q), 63.2 (CH_2), 53.0 (CH_2), 49.1 (CH_2).
HRMS (ESI): *m/z* = 331.0799 $[M+H]^+$ (found), 331.0804 calcd. for $C_{17}H_{20}BrN_2^+$, 252.1615 $[M-Br+H]^+$ (found), 252.1621 calcd. for $C_{17}H_{20}N_2^+$, 240.0249 $[M-Bn+H]^+$ (found), 240.0257 calcd. for $C_{10}H_{13}BrN_2^+$.

***tert*-Butyl 4-(4-(4-benzylpiperazin-1-yl)phenyl)piperazine-1-carboxylate** (BocPipPhPipBn **135**)

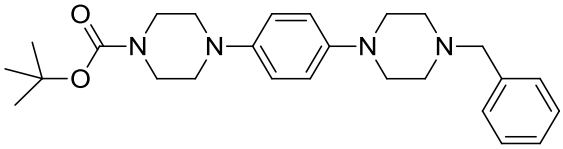

Method 1: Compound **133** (1.00 g, 2.93 mmol, 1.0 eq) and Bn-Pip **128** (517 mg, 2.93 mmol, 1.0 eq) were dissolved in dry dioxane (15 mL). Cs_2CO_3 (1.91 g, 5.86 mmol, 2.0 eq) was added, followed by $Pd_2(dba)_3$ (134 mg, 0.147 mmol, 0.05 eq) and XPhos (140 mg, 0.293 mmol, 0.10 eq). The resulting

suspension was refluxed for 36 h, cooled to rt, filtered over a pad of celite and concentrated. Column chromatography (SiO_2, 80:20 to 60:40 Cy/AcOEt) afforded BocPipPhPipBn **135** (842 mg, 1.93 mmol, 66%) as a yellow solid.
Method 2: Compound **134** (1.00 g, 3.02 mmol, 1.0 eq) and Boc-Pip **127** (675 mg, 3.62 mmol, 1.2 eq) were dissolved in dry toluene (15 mL). NaO^tBu (406 mg, 4.23 mmol, 1.4 eq) was then added, followed by $Pd_2(dba)_3$ (28 mg, 0.030 mmol, 0.01 eq) and BINAP (57 mg, 0.091 mmol, 0.03 eq). The resulting mixture was refluxed for 48 h, cooled to rt, filtered over a pad of celite and concentrated. Column chromatography (SiO_2, 80:20 to 60:40 Cy/AcOEt) afforded BocPipPhPipBn **135** (423 mg, 0.969 mmol, 32%) as a yellow solid.

Molecular formula: $C_{26}H_{36}N_4O_2$
MW: 436.6 g.mol^{-1}
^{1}H-NMR ($CDCl_3$, 300 MHz): δ 7.38–7.26 (m, 5H), 6.91–6.86 (m, 4H), 3.61–3.52 (m, 6H), 3.12 (t, *J* = 5.0 Hz, 4H), 3.01 (t, *J* = 5.0 Hz, 4H), 2.62 (t, *J* = 5.0 Hz, 4H), 1.48 (s, 9H).
^{13}C-NMR ($CDCl_3$, 75 MHz): δ 154.9 (C_q), 146.0 (C_q), 145.3 (C_q), 129.4 (CH), 128.4 (CH), 127.3 (CH), 118.4 (CH), 117.7 (CH), 79.9 (C_q), 63.2 (CH_2), 53.3 (CH_2), 50.7 (CH_2), 50.3 (CH_2), 44.0 (CH_2, br), 28.6 (CH_3).
HRMS (ESI): *m/z* = 437.2904 $[M+H]^+$ (found), 437.2911 calcd. for $C_{26}H_{37}N_4O_2^+$, 381.2275 $[M-^tBu+2H]^+$ (found), 381.2285 calcd. for $C_{22}H_{29}N_4O_2^+$, 346.2358 $[M-Bn+H]^+$ (found), 346.2363 calcd. for $C_{19}H_{30}N_4O_2^+$.

1-Benzyl-4-(4-(piperazin-1-yl)phenyl)piperazine (BnPipPhPip **136**)

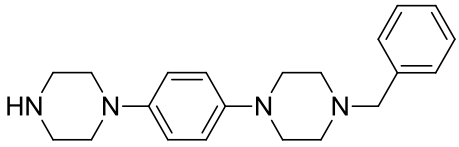

BocPipPhPipBn **135** (750 mg, 1.718 mmol, 1.0 eq) was dissolved in dry DCM (10 mL) and the resulting solution was cooled to 0 °C. TFA (2.5 mL) was added dropwise and the resulting mixture was allowed to warm to rt for 3h. Aq. NaOH was added until pH ≈ 14 and the mixture was then extracted with DCM (3×). The combined organic layers were dried over Na_2SO_4, filtered and concentrated to afford BnPipPhPip **136** (570 mg, 1.694 mmol, 99%) as an orange solid.

Molecular formula: $C_{21}H_{28}N_4$
MW: 336.5 g.mol^{-1}
^{1}H-NMR ($CDCl_3$, 300 MHz): δ 7.38–7.27 (m, 5H), 6.91–6.87 (m, 4H), 3.57 (s, 2H), 3.11 (t, *J* = 4.9 Hz, 4H), 3.07–2.99 (m, 8H), 2.61 (t, *J* = 4.9 Hz, 4H), 1.78 (s, 1H).
^{13}C-NMR ($CDCl_3$, 75 MHz): δ 145.8 (C_q), 145.7 (C_q), 138.2 (C_q), 129.4 (CH), 128.4 (CH), 127.2 (CH), 118.0 (CH), 117.8 (CH), 63.2 (CH_2), 53.4 (CH_2), 51.5 (CH_2), 50.4 (CH_2), 46.2 (CH_2).
HRMS (ESI): *m/z* = 337.2386 $[M+H]^+$ (found), 337.2387 calcd. for $C_{21}H_{29}N_4^+$, 246.1840 $[M-Bn+H]^+$ (found), 246.1839 calcd. for $C_{14}H_{22}N_4^+$, 91.0539 [Tropylium] (found), 91.0542 calcd. for $C_7H_7^+$.

***tert*-Butyl 4-(4-(piperazin-1-yl)phenyl)piperazine-1-carboxylate** (BocPipPhPip **137**)

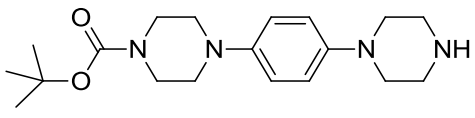

BocPipPhPipBn **135** (1.5 g, 3.44 mmol, 1.0 eq) was dissolved in MeOH (30 mL). NH_4HCO_2 (1.085 g, 17.2 mmol, 5.0 eq) and Pd/C (10%w, 150 mg) were then added, the mixture was refluxed for 24 h, cooled to rt, filtered over a pad of celite and concentrated. The residue was dissolved in DCM and washed with sat. aq. $NaHCO_3$ (1×). The organic layer was dried over Na_2SO_4, filtered and concentrated to afford BocPipPhPip **137** (1.158 g, 3.34 mmol, 97%) as a light brown solid.

Molecular formula: $C_{19}H_{30}N_4O_2$
MW: 346.5 g.mol^{-1}
^{1}H-NMR (CDCl$_3$, 300 MHz): δ 6.95–6.86 (m, 4H), 3.57 (t, *J* = 5.1 Hz, 4H), 3.15–3.09 (m, 2H), 3.09–3.05 (m, 4H), 3.05–2.97 (m, 4H), 2.72–2.64 (m, 2H), 1.78 (s, 1H), 1.48 (s, 9H).
^{13}C-NMR (CDCl$_3$, 75 MHz): δ 154.9 (C_q), 146.5 (C_q), 145.3 (C_q), 118.4 (CH), 117.7 (CH), 79.9 (C_q), 51.6 (CH_2), 50.7 (CH_2), 46.4 (CH_2), 43.8 (CH_2, br), 28.6 (CH_3).
HRMS (ESI): *m/z* = 347.2436 $[M+H]^+$ (found), 347.2442 calcd. for $C_{19}H_{31}N_4O_2^+$, 369.2250 $[M+Na]^+$ (found), 369.2261 calcd. for $C_{19}H_{30}N_4NaO_2^+$, 291.1814 $[M-^tBu+2H]^+$ (found), 291.1816 calcd. for $C_{15}H_{23}N_4O_2^+$, 247.1912 $[M-Boc+2H]^+$ (found), 247.1917 calcd. for $C_{14}H_{23}N_4^+$.

***tert*-Butyl 4-(4'-bromo-[1,1'-biphenyl]-4-yl)piperazine-1-carboxylate** (**139**)

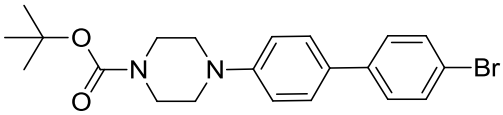

p-Dibromobiphenyl **138** (209 mg, 0.67 mmol, 1.0 eq) and Boc-Pip **127** (312 mg, 1.674 mmol, 2.5 eq) nd were suspended in dry toluene (7.0 mL). $Pd_2(dba)_3$ (12.3 mg, 0.013 mmol, 0.02 eq), BINAP (25.0 mg, 0.04 mmol, 0.06 eq) and Cs_2CO_3 (436 mg, 1.34 mmol, 2.0 eq) were added and the resulting mixture was refluxed for 6 d, cooled to 0 °C, fitered over a pad of celite and concentrated. Column chromatography (SiO_2, 70:30 Cy/AcOEt) afforded **139** (131 mg, 0.32 mmol, 47%) as a yellow solid.

Molecular formula: $C_{21}H_{25}BrN_2O_2$
MW: 417.3 g.mol^{-1}
^{1}H-NMR (CDCl$_3$, 300 MHz): δ 7.54–7.38 (m, 6H), 6.96 (d, *J* = 8.0 Hz, 2H), 3.60 (t, *J* = 5.0 Hz, 4H), 3.18 (t, *J* = 5.0 Hz, 4H), 1.50 (s, 9H).
^{13}C-NMR (CDCl$_3$, 100 MHz): δ 154.9 (C_q), 150.6 (C_q), 140.9 (C_q), 133.0 (CH), 128.8 (CH), 127.9 (CH), 126.7 (CH), 116.7 (CH), 80.0 (C_q), 49.3 (CH_2), 43.8 (CH_2, br), 28.6 (CH_3).

Di-*tert*-butyl 4,4'-([1,1'-biphenyl]-4,4'-diyl)bis(piperazine-1-carboxylate) (**140**)

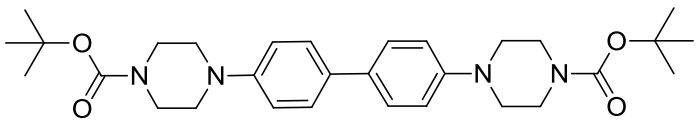

Compound **139** (70.9 mg, 0.170 mmol, 1.0 eq) and Boc-Pip **127** (34.8 mg, 0.187 mmol, 1.1 eq) were suspended in dry dioxane (5 mL). $Pd_2(dba)_3$ (6.2 mg, 0.007 mmol, 0.04 eq), XPhos (9.8 mg, 0.020 mmol, 0.12 eq) and Cs_2CO_3 (111 mg, 0.34 mmol, 2.0 eq) were added and the resulting mixture was refluxed for 2 d and cooled to rt. H_2O was added and the mixture was extracted with DCM (3×). The combined organic layers were dried over Na_2SO_4, filtered and concentrated. Column chromatography (SiO_2, 70:30 Cy/AcOEt) afforded **140** (48.4 mg, 0.093 mmol, 55%) as a yellow solid.

Molecular formula: $C_{30}H_{42}N_4O_4$

MW: 522.7 g.mol^{-1}
^{1}H-NMR (CDCl$_3$, 300 MHz): δ 7.48 (d, *J* = 8.2 Hz, 4H), 6.95 (d, *J* = 8.2 Hz, 4H), 3.59 (t, *J* = 5.1 Hz, 8H), 3.16 (t, *J* = 5.1 Hz, 8H), 1.49 (s, 18H).
^{13}C-NMR (CDCl$_3$, 100 MHz): δ 154.9 (C_q), 150.2 (C_q), 132.8 (C_q), 127.3 (CH), 120.3 (C_q), 116.9 (CH), 80.0 (C_q), 49.5 (CH_2), 43.4 (CH_2, br), 28.6 (CH_3).

4,4'-Di(piperazin-1-yl)-1,1'-biphenyl (PipPh$_2$Pip **141**)

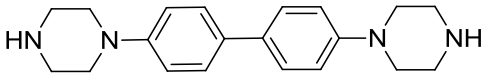

Compound **140** (48.4 mg, 0.093 mmol, 1.0 eq) was dissolved in dry DCM (4.5 mL) and the resulting solution was cooled to 0 °C. TFA (1.5 mL) was added dropwise and the resulting mixture was allowed to warm to rt for 3h. Aq. NaOH was added until pH ≈ 14 and the mixture was then extracted with DCM (3×). The combined organic layers were dried over Na_2SO_4, filtered and concentrated to afford PipPh$_2$Pip **141** (24.4 mg, 0.076 mmol, 82%) as a yellow solid.

Molecular formula: $C_{20}H_{26}N_4$
MW: 322.4 g.mol^{-1}
^{1}H-NMR (CDCl$_3$, 300 MHz): δ 7.49–7.44 (m, 4H), 7.26 (s, 2H), 7.00–6.94 (m, 4H), 3.19–3.14 (m, 8H), 3.06–3.01 (m, 8H).

1,4-Bis(4-([2,2':6',2''-terpyridin]-4'-yl)phenyl)piperazine (Bis-PhTpy-Pip **142**)

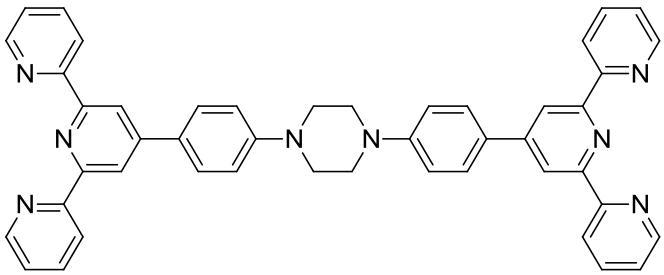

Piperazine (11 mg, 0.129 mmol, 1.0 eq) and *p*BrPhTpy **36** (100 mg, 0.258 mmol, 2.0 eq) were dissolved in dry toluene (3 mL). NaO^{t}Bu (35 mg, 0.361 mmol, 2.8 eq), BINAP (5 mg, 0.0078 mmol, 0.06 eq) and $Pd_2(dba)_3$ (2.5 mg, 0.0026 mmol, 0.02 eq) were then added, the resulting mixture was refluxed for 24 h and concentrated. Column chromatography (Al_2O_3, basic, activated, Brockmann I, 100% DCM to 99:1 DCM/MeOH) afforded Bis-PhTpy-Pip **142** (37 mg, 0.0053 mmol, 41%) as a pale yellow solid.

Molecular formula: $C_{46}H_{36}N_8$
MW: 700.8 g.mol^{-1}
^{1}H-NMR (DMSO-d$_6$, 300 MHz): δ 8.78 (d, 4H, *J* = 4.7 Hz), 8.70 (s, 4H), 8.67 (d, 4H, *J* = 8.0 Hz), 8.03 (td, 4H, *J* = 8.0, 1.6 Hz), 7.87 (d, 4H, *J* = 8.0 Hz), 7.53 (dd, 4H, *J* = 8.0, 4.7 Hz), 7.21 (d, 4H, *J* = 8.0 Hz), 3.49 (s, 8H).

Bis-(Tpy)-Mn^{II}-(PhTpy)-Pip (**143**)

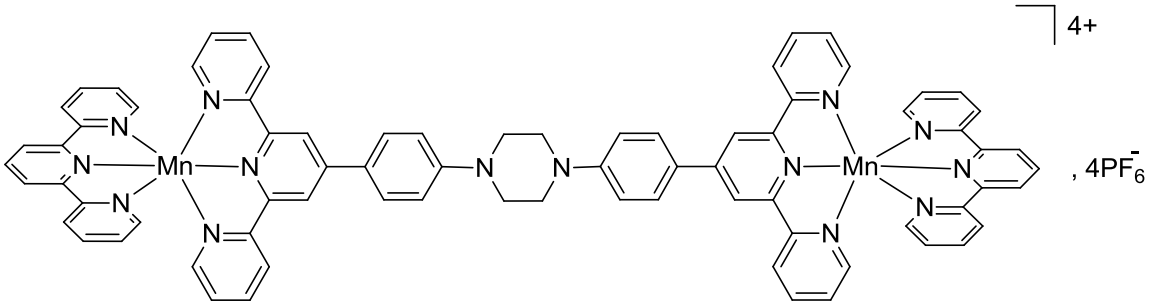

Bis-PhTpy-Pip **142** (35 mg, 0.0499 mmol, 1.0 eq) and $TpyMnCl_2$ **49** (35.9 mg, 0.0998 mmol, 2.0 eq) were dissolved in toluene (100 mL). The resulting solution was refluxed for 15 h and cooled to rt. NH_4PF_6 (81.5 mg, 0.499 mmol, 10 eq) dissolved in MeOH (10 mL) was then added, and the resulting mixture was stirred at rt for 15 h, concentrated to ≈ 20 mL, filtered, thoroughly washed with Et_2O and H_2O and dried to afford Bis-(Tpy)-Mn^{II}-(PhTpy)-Pip **143** (81.7 mg, 0.0424 mmol, 80%) as an orange solid.

Molecular formula: $C_{76}H_{56}Cl_2F_{24}Mn_2N_{14}P_4$
MW: 1926.0 g.mol^{-1}

Bis-(*p*ClTpy)-Mn^{II}-(PhTpy)-Pip (**144**)

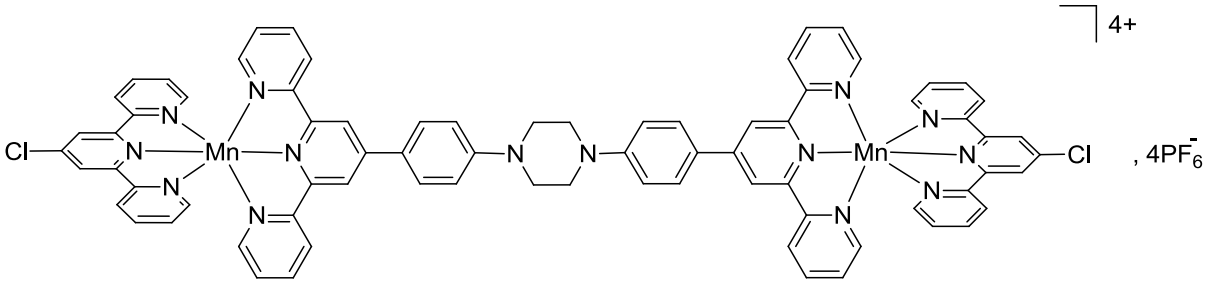

Bis-PhTpy-Pip **142** (35 mg, 0.0499 mmol, 1.0 eq) and *p*ClTpy$MnCl_2$ **50** (39.3 mg, 0.0998 mmol, 2.0 eq) were dissolved in toluene (100 mL). The resulting solution was refluxed for 15 h and cooled to rt. NH_4PF_6 (81.5 mg, 0.499 mmol, 10.0 eq) dissolved in MeOH (10 mL) was then added, and the resulting mixture was stirred at rt for 15 h, concentrated to ≈ 20 mL, filtered, thoroughly washed with Et_2O and H_2O and dried to afford Bis-(*p*ClTpy)-Mn^{II}-(PhTpy)-Pip **144** (74 mg, 0.0398 mmol, 85%) as an orange solid.

Molecular formula: $C_{76}H_{58}F_{24}Mn_2N_{14}P_4$
MW: 1857.1 g.mol^{-1}

***tert*-Butyl 4-(4-([2,2':6',2''-terpyridin]-4'-yl)phenyl)piperazine-1-carboxylate** (**144**)

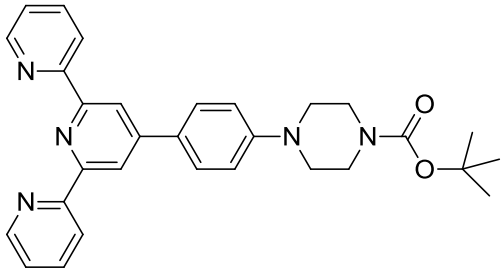

*p*BrPhTpy **36** (1.5 g, 3.87 mmol, 1.0 eq) and Boc-Pip **127** (864 mg, 4.64 mmol, 1.2 eq) were dissolved in dry toluene (25 mL). NaO^tBu (520 mg, 5.42 mmol, 1.4 eq) was added, followed by $Pd_2(dba)_3$ (35 mg, 0.039 mmol, 0.01 eq) and BINAP (72 mg, 0.116 mmol, 0.03 eq). The resulting mixture was refluxed for 3 d and concentrated. Column chromatography (Al_2O_3, basic, activated, Brockmann I, 100% DCM to 98:2 DCM/MeOH) afforded **144** (1.71 g, 3.46 mmol, 89%) as a pale orange solid.

Molecular formula: $C_{30}H_{31}N_5O_2$
MW: 493.6 g.mol^{-1}
^{1}H-NMR ($CDCl_3$, 300 MHz): δ 8.73 (ddd, *J* = 4.8, 1.8, 0.9 Hz, 2H), 8.71 (s, 2H), 8.66 (dt, *J* = 8.0, 1.1 Hz, 2H), 7.92–7.83 (m, 4H), 7.34 (ddd, *J* = 7.5, 4.8, 1.2 Hz, 2H), 7.06–6.99 (m, 2H), 3.62 (t, *J* = 5.2 Hz, 4H), 3.25 (t, *J* = 5.2 Hz, 4H), 1.50 (s, 9H).

4'-(4-(Piperazin-1-yl)phenyl)-2,2':6',2''-terpyridine (**145**)

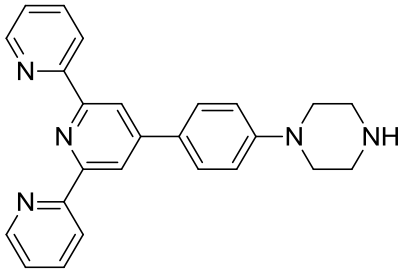

Compound **144** (1.617 g, 3.28 mmol, 1.0 eq) was dissolved in dry DCM (20 mL) and the resulting solution was cooled to 0 °C. TFA (5 mL) was added dropwise and the resulting mixture was allowed to warm to rt for 3h. Aq. NaOH was added until pH ≈ 14 and the mixture was then extracted with DCM (5×). The combined organic layers were dried over Na_2SO_4, filtered and concentrated to afford **145** (1.097 g, 2.79 mmol, 85%) as a pale orange solid.

Molecular formula: $C_{25}H_{23}N_5$
MW: 393.5 g.mol^{-1}
^{1}H-NMR ($CDCl_3$, 300 MHz): δ 8.73 (ddd, *J* = 4.8, 1.8, 0.9 Hz, 2H), 8.71 (s, 2H), 8.66 (dt, *J* = 8.0, 1.1 Hz, 2H), 7.94–7.83 (m, 4H), 7.34 (ddd, *J* = 7.5, 4.8, 1.3 Hz, 2H), 7.06–6.99 (m, 2H), 3.29–3.21 (m, 4H), 3.10–3.02 (m, 4H).
HRMS (ESI): *m/z* = 394.2040 $[M+H]^+$ (found), 394.2026 calcd. for $C_{25}H_{24}N_5^+$, 416.1836 $[M+Na]^+$ (found), 416.1846 calcd. for $C_{25}H_{23}N_5Na^+$, 310.1335 $[M\text{-}Pip+2H]^+$ (found), 310.1339 calcd. for $C_{21}H_{16}N_3^+$.

Protected bis-DOTA 147

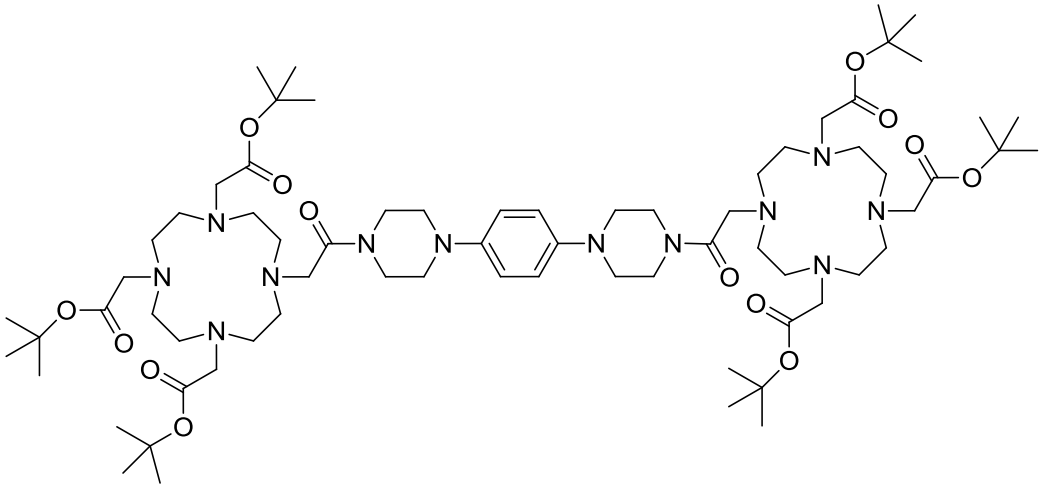

Tri-^{t}Bu-DOTA **146** (88 mg, 0.154 mmol, 2.5 eq) and HATU (63 mg, 0.166 mmol, 2.7 eq) were dissolved in dry DMF (1.5 mL). The resulting mixture was stirred at rt for 10 min and PipPhPip **131** (15 mg, 0.061 mmol, 1.0 eq) was added. The resulting solution was stirred at rt for 20 min and DIPEA (63 µL, 0.368 mmol, 6.0 eq) was added. The resulting mixture was stirred at rt for 24 h and concentrated. DCM was added and the mixture was washed with H_2O (1×) and sat. aq. NaCl (1×). The organic layer was dried over Na_2SO_4, filtered and concentrated. Column chromatography (SiO_2, 98:2 to 95:5 DCM/MeOH) afforded **147** (82 mg, 0.06 mmol, 98%) as a light grey solid.

Molecular formula: $C_{70}H_{122}N_{12}O_{14}$
MW: 1355.8 g.mol^{-1}
^{1}H-NMR ($CDCl_3$, 300 MHz): δ 6.86 (s, 4H), 4.00–1.80 (m, 64H), 1.45 (br s, 27H), 1.43 (br s, 27H).
^{13}C-NMR ($CDCl_3$, 75 MHz): δ 172.9 (C_q), 172.8 (C_q), 172.7 (C_q), 170.2 (C_q), 149.7 (C_q), 145.5 (C_q), 129.9 (C_q), 118.3 (CH), 82.2 (C_q), 81.9 (C_q), 56–41 (CH_2, numerous peaks), 28.2 (CH_3), 28.1 (CH_3).

Protected bis-DOTA 148

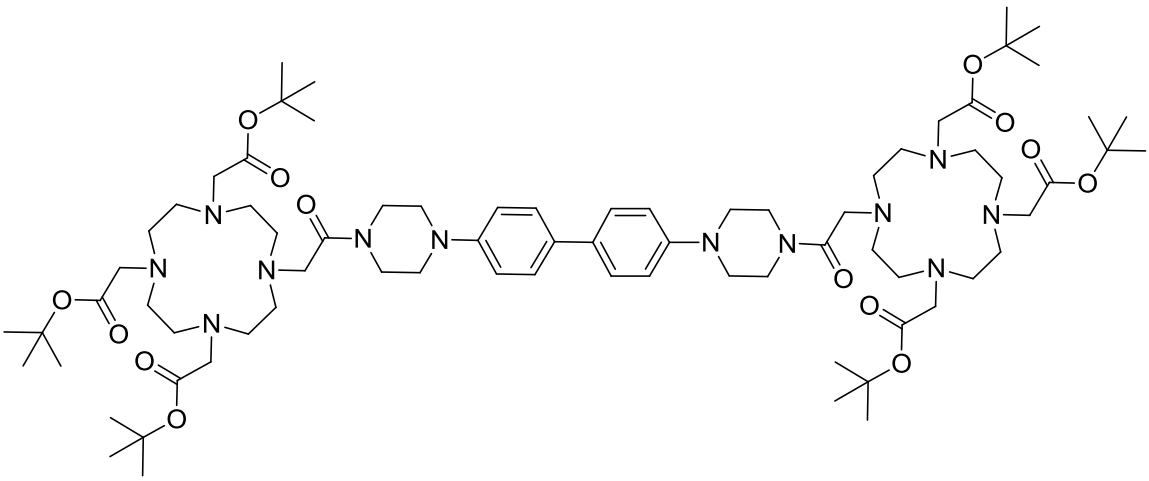

Tri-^{t}Bu-DOTA **146** (54.2 mg, 0.095 mmol, 2.5 eq) and HATU (38.8 mg, 0.102 mmol, 2.7 eq) were dissolved in dry DMF (1.5 mL). The resulting mixture was stirred at rt for 5 min and $PipPh_2Pip$ **141** (12.2 mg, 0.038 mmol, 1.0 eq) was added. The resulting mixture was stirred at rt for 5 min and DIPEA (39.5 µL, 0.227 mmol, 6.0 eq) was added. The resulting mixture was stirred at rt for 24 h and concentrated. DCM was added and the mixture was washed with H_2O (1×) and sat. aq. NaCl (1×). The

organic layer was dried over Na_2SO_4, filtered and concentrated. Column chromatography (SiO_2, 98:2 DCM:MeOH) afforded **148** (45.4 mg, 0.032 mmol, 84%) as a yellow solid.

Molecular formula: $C_{76}H_{126}N_{12}O_{14}$
MALDI-TOF MS (HCCA): 1453.62 $[M+Na]^+$ (found), 1453.94 calcd. for $C_{76}H_{126}N_{12}NaO_{14}^+$.
MW: 1431.9 $g.mol^{-1}$
HPLC: 8.13 min (5 to 100% MeCN in 10 min, 80%)

Bis-DOTA-PhPip$_1$ (**149**)

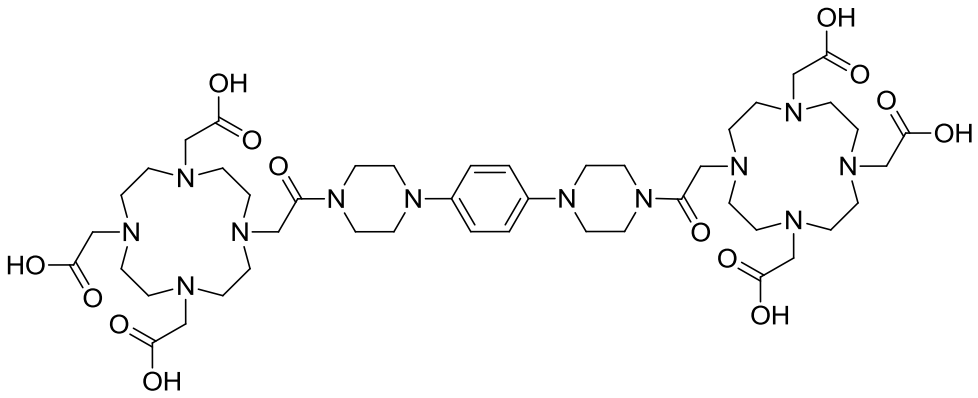

Protected bis-DOTA **147** (50.0 mg, 0.037 mmol, 1.0 eq) was dissolved in dry DCM (2 mL). The resulting solution was cooled to 0 °C, and TFA (2 mL) was added dropwise. The resulting mixture was allowed to warm to rt for 15 h, concentrated without heating, redissolved in MeOH and concentrated again. The residue was dissolved again in MeOH, precipitated by slow addition of Et_2O, filtered and dried. The crude product was purified by preparative HPLC (0 to 20% MeCN) to afford Bis-DOTA-PhPip$_1$ **149** as a light blue solid.

Molecular formula: $C_{46}H_{74}N_{12}O_{14}$
MW: 1019.2 $g.mol^{-1}$
MALDI-TOF MS (HCCA): 1019.57 $[M+H]^+$ (found), 1019.55 calcd. for $C_{46}H_{75}N_{12}O_{14}^+$.

Bis-DOTA-PhPip$_2$ (**150**)

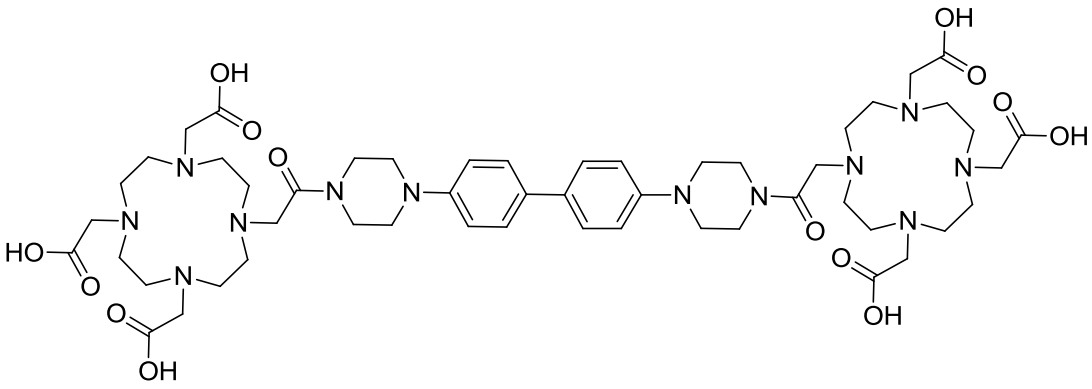

Protected bis-DOTA **149** (45.4 mg, 0.032 mmol, 1.0 eq) was dissolved in dry DCM (2 mL). The resulting solution was cooled to 0 °C, and TFA (2 mL) was added dropwise. The resulting mixture was allowed to warm to rt for 15 h and concentrated. DCM was added and the product was precipitated

with Et_2O and centrifugated. Purification by preparative HPLC (10 to 30% MeCN) afforded Bis-DOTA-$PhPip_2$ **150** as a yellow solid.

Molecular formula: $C_{52}H_{78}N_{12}O_{14}$
MW: 1095.2 g.mol^{-1}
HPLC: 5.32 min (10 to 30% MeCN in 10 min, >95%)

2-(2-Methoxyethoxy)ethyl 4-methylbenzenesulfonate (**152**)

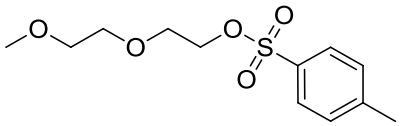

Diethylene glycol monomethyl ether **151** (39.1 mL, 332.7 mmol, 1.0 eq) was dissolved in THF (110 mL). The resulting solution was cooled to 0 °C and NaOH (26.44 g, 661.0 mmol, 2.0 eq) dissolved in H_2O (110 mL) was added dropwise, followed by tosyl chloride (95.16 g, 499.0 mmol, 1.5 eq) dissolved in THF (110 mL) dropwise. The resulting mixture was stirred at rt for 2 h and H_2O (400 mL) was added. The organic layer was recovered and washed without shaking with aq. 1 M NaOH (2×) and H_2O (1×), dried over Na_2SO_4, filtered and concentrated to afford **152** (72.95 g, 266.2 mmol, 80%) as a colourless oil.

Molecular formula: $C_{12}H_{18}O_5S$
MW: 274.3 g.mol^{-1}
^{1}H-NMR ($CDCl_3$, 300 MHz): δ 7.80 (d, 2H, *J* = 8.0 Hz), 7.34 (d, 2H, *J* = 8.0 Hz), 4.17 (t, 2H, *J* = 4.8 Hz), 3.69 (t, 2H, *J* = 4.8 Hz), 3.61–3.54 (m, 2H), 3.51–3.44 (m, 2H), 3.35 (s, 3H), 2.44 (s, 3H).
^{13}C-NMR ($CDCl_3$, 75 MHz): δ 144.9 (C_q), 133.0 (C_q), 129.9 (CH), 128.1 (CH), 71.9 (CH_2), 70.8 (CH_2), 69.3 (CH_2), 68.8 (CH_2), 59.2 (CH_3), 21.8 (CH_3).
HRMS (ESI): *m/z* =275.0950 $[M+H]^+$ (found), 275.0948 calcd. for $C_{12}H_9O_5S^+$, 297.0766 $[M+Na]^+$ (found), 275.0767 calcd. for $C_{12}H_{18}NaO_5S^+$.

1,4-bis(2-(2-methoxyethoxy)ethoxy)benzene ($Ph(OPEG)_2$ **153**)

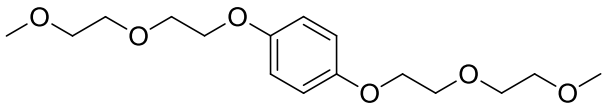

Hydroquinone (14.64 g, 133.1 mmol, 1.0 eq) and K_2CO_3 (73.47 g, 532.4 mmol, 4.0 eq) were suspended in MeCN (1.1 L). The resulting suspension was refluxed for 30 min and cooled to rt. Compound **152** (72.95 g, 266.2 mmol, 2.0 eq) dissolved in MeCN (220 mL) was added dropwise. The resulting mixture was refluxed for 72 h, cooled to rt, filtered and concentrated. Column chromatography (SiO_2, 90:10 Cy/AcOEt to 50:50 Cy/AcOEt) afforded $Ph(OPEG)_2$ **153** (32.81 g, 104.5 mmol, 79%) as an orange oil.

Molecular formula: $C_{16}H_{26}O_6$
MW: 314.4 g.mol^{-1}
^{1}H-NMR ($CDCl_3$, 300 MHz): δ 6.83 (s, 4H), 4.11–4.05 (m, 4H), 3.86–3.80 (m, 4H), 3.74–3.68 (m, 4H), 3.60–3.54 (m, 4H), 3.39 (s, 6H).
^{13}C-NMR ($CDCl_3$, 75 MHz): δ 153.2 (C_q), 115.6 (CH), 72.1 (CH_2), 70.9 (CH_2), 70.0 (CH_2), 68.1 (CH_2), 59.2 (CH_3).

HRMS (ESI): *m/z* = 315.1796 $[M+H]^+$ (found), 315.1802 calcd. for $C_{16}H_{27}O_6^+$, 337.1617 $[M+Na]^+$ (found), 337.1622 calcd. for $C_{16}H_{26}NaO_6^+$.

1,4-Diiodo-2,5-bis(2-(2-methoxyethoxy)ethoxy)benzene ($Ph(OPEG)_2I_2$ **154**)

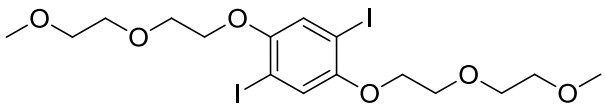

$Ph(OPEG)_2$ **153** (25.0 g, 79.6 mmol, 1.0 eq), iodine (22.3 g, 87.6 mmol, 1.1 eq) and KIO_3 (6.8 g, 31.8 mmol, 0.4 eq) were dissolved in glacial AcOH (250 mL) and H_2O (25 mL). Conc. H_2SO_4 (3.3 mL) was added, the resulting mixture was refluxed for 48 h and cooled to rt. DCM and aq. 10% $Na_2S_2O_3$ were added, the organic layer was recovered and washed with sat. aq. $NaHCO_3$ (1×), H_2O (1×), sat. aq. NaCl (1×), dried over Na_2SO_4, filtered and concentrated. Recrystallization from EtOH afforded $Ph(OPEG)_2I_2$ **154** (27.27 g, 48.1 mmol, 60%) as a white solid.

Molecular formula: $C_{16}H_{24}I_2O_6$
MW: 566.2 $g.mol^{-1}$
^{1}H-NMR (CDCl$_3$, 300 MHz): δ 7.23 (s, 2H), 4.14–4.07 (m, 4H), 3.92–3.86 (m, 4H), 3.80–3.74 (m, 4H), 3.61–3.55 (m, 4H), 3.40 (s, 6H).
^{13}C-NMR (CDCl$_3$, 75 MHz): δ 153.2 (C_q), 123.6 (CH), 86.5 (C_q), 72.2 (CH_2), 71.2 (CH_2), 70.5 (CH_2), 69.8 (CH_2), 59.3 (CH_3).
HRMS (ESI): *m/z* = 566.9707 $[M+H]^+$ (found), 566.9735 calcd. for $C_{16}H_{25}I_2O_6^+$, 588.9544 $[M+Na]^+$ (found), 588.9554 calcd. for $C_{16}H_{24}I_2NaO_6^+$, 440.0670 $[M+H-I]^+$ (found), 440.0690 calcd. for $C_{16}H_{25}IO_6^+$.

((4-Bromophenyl)ethynyl)triisopropylsilane (**156**)

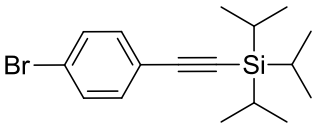

1-Bromo-4-iodobenzene **155** (3 g, 10.6 mmol, 1.0 eq) was suspended in dry piperidine (10 mL). PPh_3 (139 mg, 0.53 mmol, 0.05 eq) was added, followed by $Pd(PPh_3)_2Cl_2$ (186 mg, 0.265 mmol, 0.025 eq) and CuI (101 mg, 0.53 mmol, 0.05 eq). Argon was bubbled for 15 min and TIPSA (2.37 mL, 10.6 mmol, 1.0 eq) was added dropwise. The resulting suspension was stirred at rt for 15 h, sat. aq. NH_4Cl was added, and the mixture was extracted with DCM (3×). The combined organic layers were dried over Na_2SO_4, filtered and concentrated. Column chromatography (SiO_2, 100% Cy) afforded **156** (3.48 g, 10.3 mmol, 97%) as a pale yellow oil.

Molecular formula: $C_{17}H_{25}BrSi$
MW: 337.4 $g.mol^{-1}$
^{1}H-NMR (CDCl$_3$, 300 MHz): δ 7.46–7.40 (m, 2H), 7.36–7.30 (m, 2H), 1.12 (s, 21H).
^{13}C-NMR (CDCl$_3$, 75 MHz): δ 133.6 (CH), 131.6 (CH), 122.6 (Cq), 122.6 (Cq), 106.0 (Cq), 92.2 (Cq), 18.8 (CH3), 11.4 (CH).

4-((Triisopropylsilyl)ethynyl)benzaldehyde (**157**)

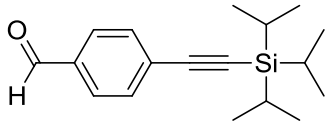

4-Bromobenzaldehyde **27** (10.0 g, 54.05 mmol, 1.0 eq) was dissolved in dry THF (50 mL) and dry TEA (50 mL). PPh_3 (227 mg, 0.865 mmol, 0.016 eq) was added, followed by $Pd(PPh_3)_2Cl_2$ (254 mg, 0.362 mmol, 0.0067 eq) and CuI (69 mg, 0.362 mmol, 0.0067 eq). Argon was bubbled for 15 min, TIPSA (12.1 mL, 54.05 mmol, 1.0 eq) was added, and the resulting mixture was refluxed for 15 h and cooled to rt. Sat. aq. NH_4Cl was added and the mixture was extracted with DCM (3×). The combined organic layers were dried over Na_2SO_4, filtered and concentrated. Column chromatography (SiO_2, 100% Cy to 98:2 Cy/AcOEt) afforded **157** (14.87 g, 51.89 mmol, 96%) as a pale yellow oil.

Molecular formula: $C_{18}H_{26}OSi$
MW: 286.5 g.mol^{-1}
^{1}H-NMR (CDCl$_3$, 300 MHz): δ 10.00 (s, 1H), 7.85–7.79 (m, 2H), 7.64–7.58 (m, 2H), 1.14 (s, 21H).
^{13}C-NMR (CDCl$_3$, 75 MHz): δ 191.6 (CH), 135.6 (C_q), 132.7 (CH), 129.9 (C_q), 129.6 (CH), 106.0 (C_q), 95.9 (C_q), 18.8 (CH_3), 11.4 (CH).
HRMS (ESI): *m/z* = 287.1833 $[M+H]^+$ (found), 287.1826 calcd. for $C_{18}H_{27}OSi^+$, 309.1640 $[M+Na]^+$ (found), 309.1645 calcd. for $C_{18}H_{26}NaOSi^+$.

((4-(2,2-Dibromovinyl)phenyl)ethynyl)triisopropylsilane (**158**)

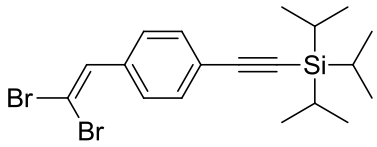

CBr_4 (52.0 g, 157.0 mmol, 5.0 eq) and powdered zinc (10.3 g, 157.0 mmol, 5.0 eq) were suspended in dry DCM (500 mL). The resulting suspension was cooled to 0 °C and PPh_3 (41.2 g, 157.0 mmol, 5.0 eq) was added portionwise. The resulting mixture was allowed to warm to rt for 24 h and cooled again to 0 °C. Compound **157** (9.0 g, 31.4 mmol, 1.0 eq) dissolved in dry DCM (40 mL) was added in one portion. The mixture was stirred at rt for 15 h, concentrated to ≈ 100 mL, filtered over a small pad of silica gel (eluting with DCM) and concentrated again. Column chromatography (SiO_2, 100% Cy) afforded **158** (13.75 g, 31.1 mmol, 99%) as a pale yellow oil.

Molecular formula: $C_{19}H_{26}Br_2Si$
MW: 442.3 g.mol^{-1}
^{1}H-NMR (CDCl$_3$, 300 MHz): δ 7.47 (s, 4H), 7.46 (s, 1H), 1.13 (s, 21H).
^{13}C-NMR (CDCl$_3$, 75 MHz): δ 136.4 (CH), 135.2 (C_q), 132.2 (CH), 128.3 (CH), 123.8 (C_q), 106.8 (C_q), 92.5 (C_q), 90.5 (C_q), 18.8 (CH_3), 11.4 (CH).
HRMS (APCI): *m/z* = 441.0236 $[M+H]^+$ (found), 441.0243 calcd. for $C_{19}H_{27}Br_2Si^+$.

((4-Ethynylphenyl)ethynyl)triisopropylsilane (**159**)

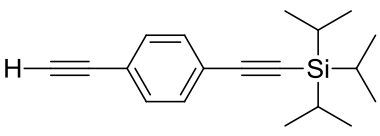

Compound **158** (13.06 g, 29.52 mmol, 1.0 eq) was dissolved in dry THF (400 mL). The resulting solution was cooled to -78 °C and LDA (2 M in THF/heptane/ethylbenzene, 60.5 mL, 121 mmol, 4.1 eq) was added dropwise. The resulting mixture was stirred at -78 °C for 3h, sat. aq. NH_4Cl was added and the mixture was allowed to warm to rt. Cy was added, the organic layer was recovered, washed with H_2O (3×), dried over Na_2SO_4, filtered and concentrated. Column chromatography (SiO_2, 100% Cy) afforded a mixture of the desired product and BrTIPS-diethynylbenzene. This mixture (8.19 g) was dissolved in dry THF (230 mL). The resulting solution was cooled to -78 °C and *tert*-BuLi (1.7 M in pentane, 20 mL) was added dropwise. The resulting mixture was stirred at -78 °C for 2 h, H_2O (30 mL) was added, and the mixture was allowed to warm to rt for 15 h and extracted with DCM (3×). The combined organic layers were washed with sat. aq. NaCl (1×), dried over Na_2SO_4, filtered and concentrated. Column chromatography (SiO_2, 100% Cy) afforded **159** (7.08 g, 25.06 mmol, 85%) as a pale yellow oil.

Molecular formula: $C_{19}H_{26}Si$
MW: 282.5 g.mol^{-1}
^{1}H-NMR ($CDCl_3$, 300 MHz): δ 7.42 (s, 4H), 3.16 (s, 1H), 1.13 (s, 21H).

General procedure G: synthesis of OPE linkers

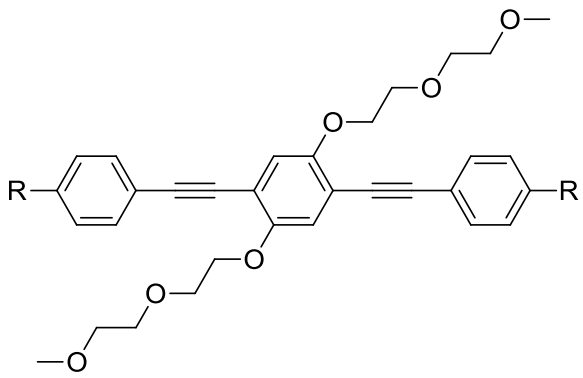

$Ph(OPEG)_2I_2$ **154** (1.0 eq) and a *para*-substituted benzaldehyde (**29**, **159** or **160**) (2.0 eq) were dissolved in dry THF and dry TEA. Argon was bubbled for 15 min and then $Pd(PPh_3)_2Cl_2$ (0.1 eq) and CuI (0.2 eq) were added. The resulting suspension was stirred for 24 h at rt, sat. aq. NH_4Cl was added and the mixture was extracted with DCM (3×). The combined organic layers were dried over Na_2SO_4, filtered and concentrated. Column chromatography afforded the corresponding OPE linker as an orange solid.

4,4'-((2,5-Bis(2-(2-methoxyethoxy)ethoxy)-1,4-phenylene)bis(ethyne-2,1-diyl))dibenzaldehyde
(OPE-diCHO **161**, R = CHO)

Using the general procedure G with $Ph(OPEG)_2I_2$ **154** (639 mg, 1.15 mmol), compound **29** (300 mg, 2.31 mmol), $Pd(PPh_3)_2Cl_2$ (81 mg, 0.115 mmol) and CuI (44 mg, 0.23 mmol) dissolved in dry THF (5 mL) and dry TEA (5 mL), OPE-diCHO **161** (528 mg, 0.925 mmol, 80%) was obtained after column chromatography (SiO_2, 80:20 Cy/AcOEt to 100% AcOEt).

Molecular formula: $C_{34}H_{34}O_8$
MW: 570.6 g.mol^{-1}
^{1}H-NMR ($CDCl_3$, 300 MHz): δ 10.03 (s, 2H), 7.91–7.84 (m, 4H), 7.72–7.64 (m, 4H), 7.08 (s, 2H), 4.27–4.21 (m, 4H), 3.98–3.92 (m, 4H), 3.83–3.77 (m, 4H), 3.58–3.53 (m, 4H), 3.37 (s, 6H).

^{13}C-NMR ($CDCl_3$, 75 MHz): δ 191.4 (CH), 153.9 (C_q), 135.6 (C_q), 132.2 (CH), 129.7 (CH), 129.6 (C_q), 117.5 (CH), 114.3 (C_q), 94.5 (C_q), 89.9 (C_q), 72.1 (CH_2), 71.2 (CH_2), 69.9 (CH_2), 69.7 (CH_2), 59.2 (CH_3).
HRMS (ESI): *m/z* = 571.2315 $[M+H]^+$ (found), 571.2326 calcd. for $C_{34}H_{35}O_8^+$, 593.2134 $[M+Na]^+$ (found), 593.2146 calcd. for $C_{34}H_{34}NaO_8^+$.

((((2,5-Bis(2-(2-methoxyethoxy)ethoxy)-1,4-phenylene)bis(ethyne-2,1-diyl))bis(4,1-phenylene)) bis(ethyne-2,1-diyl))bis(triisopropylsilane) (OPE-diCCTIPS **162**, R = CCTIPS)

Using the general procedure G with $Ph(OPEG)_2I_2$ **154** (6.97 g, 12.53 mmol), compound **159** (7.08 g, 25.06 mmol), $Pd(PPh_3)_2Cl_2$ (880 mg, 1.25 mmol) and CuI (479 mg, 2.51 mmol) dissolved in dry THF (100 mL) and dry TEA (100 mL), OPE-diCCTIPS **162** (5.02 g, 5.74 mmol, 46%) was obtained after column chromatography (SiO_2, 95:5 to 85:15 Cy/AcOEt).

Molecular formula: $C_{54}H_{74}O_6Si_2$
MW: 875.4 g.mol^{-1}
^{1}H-NMR ($CDCl_3$, 300 MHz): δ 7.45 (s, 8H), 7.04 (s, 2H), 4.21 (t, *J* = 4.9 Hz, 4H), 3.93 (t, *J* = 4.9 Hz, 4H), 3.84–3.77 (m, 4H), 3.57–3.51 (m, 4H), 3.37 (s, 6H), 1.13 (s, 42H).
^{13}C-NMR ($CDCl_3$, 75 MHz): δ 153.8 (C_q), 132.1 (CH), 131.5 (CH), 123.6 (C_q), 123.3 (C_q), 117.4 (CH), 114.3 (C_q), 106.8 (C_q), 95.0 (C_q), 93.1 (C_q), 87.7 (C_q), 72.2 (CH_2), 71.3 (CH_2), 69.9 (CH_2), 69.7 (CH_2), 59.2 (CH_3), 18.8 (CH_3), 11.4 (CH).
HRMS (ESI): *m/z* = 897.4912 $[M+Na]^+$ (found), 897.4916 calcd. for $C_{54}H_{74}NaO_6Si_2^+$.

4,4'-((2,5-Bis(2-(2-methoxyethoxy)ethoxy)-1,4-phenylene)bis(ethyne-2,1-diyl))dianiline (OPE-diNH_2 **163**, R = NH_2)

Using the general procedure G with $Ph(OPEG)_2I_2$ **154** (2.78 g, 5.0 mmol), compound **160** (1.17 g, 10.0 mmol), $Pd(PPh_3)_2Cl_2$ (351 mg, 0.5 mmol) and CuI (191 mg, 1.0 mmol) dissolved in dry THF (20 mL) and dry TEA (20 mL), OPE-diNH_2 **163** (1.41 g, 2.59 mmol, 52%) was obtained after column chromatography (SiO_2, 50:50 Cy/AcOEt to 100% AcOEt).

Molecular formula: $C_{32}H_{36}N_2O_6$
MW: 544.6 g.mol^{-1}
^{1}H-NMR ($CDCl_3$, 300 MHz): δ 7.32 (d, *J* = 8.4 Hz, 4H), 6.99 (s, 2H), 6.63 (d, *J* = 8.4 Hz, 4H), 4.20 (t, *J* = 5.0 Hz, 4H), 3.92 (t, *J* = 5.0 Hz, 4H), 3.86–3.77 (m, 8H), 3.57–3.50 (m, 4H), 3.36 (s, 6H).
^{13}C-NMR ($CDCl_3$, 75 MHz): δ 153.5 (C_q), 146.9 (C_q), 133.1 (CH), 117.5 (CH), 114.9 (CH), 114.5 (C_q), 112.9 (C_q), 95.1 (C_q), 84.0 (C_q), 72.2 (CH_2), 71.2 (CH_2), 69.9 (CH_2), 69.9 (CH_2), 59.2 (CH_3).
HRMS (ESI): *m/z* = 545.2609 $[M+H]^+$ (found), 545.2646 calcd. for $C_{32}H_{37}N_2O_6^+$, 567.2443 $[M+Na]^+$ (found), 567.2466 calcd. for $C_{32}H_{36}N_2NaO_6^+$.

4,4'-((2,5-Bis(2-(2-methoxyethoxy)ethoxy)-1,4-phenylene)bis(ethyne-2,1-diyl))bis(ethynylbenzene) (OPE-diCCH **164**)

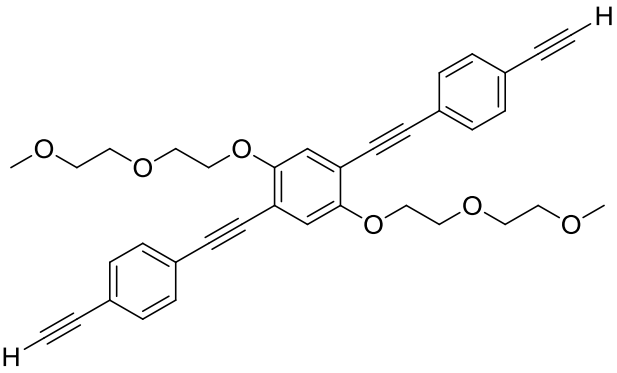

OPE-diCCTIPS **162** (5.16 g, 5.89 mmol, 1.0 eq) was dissolved in dry THF (150 mL). The resulting solution was cooled to 0 °C and TBAF (1M in THF, 11.78 mL, 11.78 mmol) was added dropwise. The resulting solution was allowed to warm to rt for 3 h, H_2O was added, and the mixture was extracted with DCM (3×). The combined organic layers were dried over Na_2SO_4, filtered and concentrated. Column chromatography (SiO_2, 90:10 to 70:30 Cy/AcOEt) afforded OPE-diCCH **164** (2.71 g, 4.81 mmol, 82%) as a yellow solid.

Molecular formula: $C_{36}H_{34}O_6$
MW: 562.7 g.mol^{-1}
^{1}H-NMR (CDCl$_3$, 300 MHz): δ 7.47 (s, 8H), 7.04 (s, 2H), 4.22 (t, J = 5.0 Hz, 4H), 3.93 (t, J = 5.0 Hz, 4H), 3.83–3.77 (m, 4H), 3.57–3.51 (m, 4H), 3.37 (s, 6H), 3.19 (s, 2H).
^{13}C-NMR (CDCl$_3$, 75 MHz): δ 153.8 (C_q), 132.2 (CH), 131.6 (CH), 123.9 (C_q), 122.1 (C_q), 117.4 (CH), 114.3 (C_q), 94.8 (C_q), 87.9 (C_q), 83.4 (C_q), 79.2 (C_q), 72.2 (CH2), 71.2 (CH2), 69.9 (CH2), 69.7 (CH2), 59.2 (CH3).
HRMS (ESI): *m/z* = 585.2246 $[M+Na]^+$ (found), 585.2248 calcd. for $C_{36}H_{34}NaO_6^+$.

4,4'-((2,5-bis(2-(2-methoxyethoxy)ethoxy)-1,4-phenylene)bis(ethyne-2,1-diyl))dibenzoic acid (OPE-diCO_2H **165**)

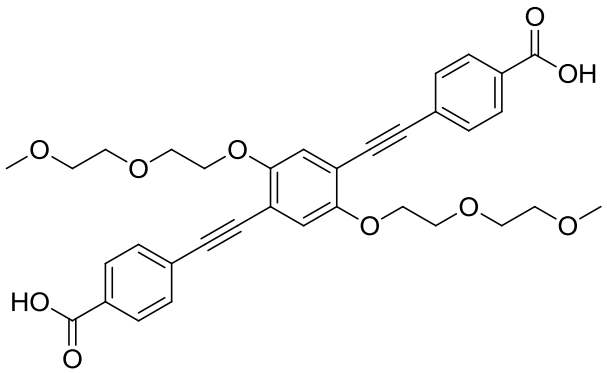

OPE-diCHO **161** (1.5 g, 2.63 mmol, 1.0 eq) was suspended in dry DMF (65 mL). $KHSO_5$•$KHSO_4$•K_2SO_4 (Oxone®, 3.23 g, 5.26 mmol, 2.0 eq) was added and the resulting suspension was stirred at rt for 24 h. H_2O was added, the resulting precipitate was filtered and dried to afford OPE-diCO_2H **165** (1.294 g, 2.15 mmol, 82%) as a yellow solid.

Molecular formula: $C_{34}H_{34}O_{10}$
MW: 602.6 g.mol^{-1}
^{1}H-NMR (DMSO-d$_6$, 300 MHz): δ 13.13 (s, 2H), 8.03–7.94 (m, 4H), 7.68–7.60 (m, 4H), 7.27 (s, 2H), 4.20 (t, *J* = 4.5 Hz, 4H), 3.80 (t, *J* = 4.5 Hz, 4H), 3.71–3.64 (m, 4H), 3.48–3.41 (m, 4H), 3.21 (s, 6H).

^{13}C-NMR (DMSO-d_6, 75 MHz): δ 166.7 (C_q), 153.2 (C_q), 131.4 (CH), 130.6 (C_q), 129.6 (CH), 126.8 (C_q), 116.9 (CH), 113.1 (C_q), 94.3 (C_q), 88.8 (C_q), 71.4 (CH_2), 70.1 (CH_2), 69.1 (CH_2), 69.0 (CH_2), 58.1 (CH_3).
HRMS (ESI): *m/z* = 601.2076 $[M-H]^-$ (found), 601.2079 calcd. for $C_{34}H_{33}O_{10}^-$, 300.1022 $[M-2H]^{2-}$ (found), 300.1003 calcd. for $C_{34}H_{32}O_{10}^{2-}/2$.

4,4'-((2,5-Bis(2-(2-methoxyethoxy)ethoxy)-1,4-phenylene)bis(ethyne-2,1-diyl))bis(azidobenzene) (OPE-diN_3 **166**)

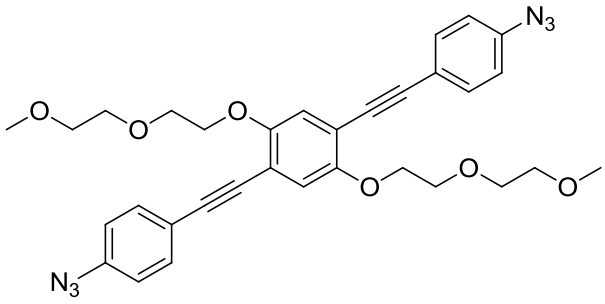

OPE-diNH_2 **163** (70 mg, 0.129 mmol, 1.0 eq) was suspended in H_2O (2 mL). The resulting mixture was cooled to 0 °C and aq. 37% HCl (630 µL) was added, followed by $NaNO_2$ (25 mg, 0.361 mmol, 2.8 eq) dissolved in H_2O (2 mL). The resulting red solution was stirred at 0 °C for 45 min and NaN_3 (22 mg, 0.335 mmol, 2.6 eq) dissolved in H_2O (2 mL) was added. The resulting orange suspension was stirred at 0 °C for 45 min, filtered, washed with H_2O and dried to afford OPEdiN_3 **166** (63 mg, 0.106 mmol, 82%) as an orange solid.

Molecular formula: $C_{32}H_{32}N_6O_6$
MW: 596.6 g.mol^{-1}
^{1}H-NMR ($CDCl_3$, 300 MHz): δ 7.55–7.48 (m, 4H), 7.03 (s, 2H), 7.04–6.97 (m, 4H), 4.21 (t, *J* = 4.9 Hz, 4 H), 3.92 (t, *J* = 4.9 Hz, 4H), 3.82–3.77 (m, 4H), 3.58–3.51 (m, 4H), 3.37 (s, 6H).
^{13}C-NMR ($CDCl_3$, 75 MHz): δ 153.8 (C_q), 140.2 (C_q), 133.2 (CH), 120.1 (CH), 119.2 (C_q), 117.6 (CH), 114.3 (C_q), 94.6 (C_q), 86.3 (C_q), 72.2 (CH_2), 71.2 (CH_2), 69.9 (CH_2), 69.8 (CH_2), 59.2 (CH_3).
HRMS (ESI): *m/z* = 619.2282 $[M+Na]^+$ (found), 619.2276 calcd. for $C_{32}H_{32}N_6NaO_6^+$, 591.2194 $[M+Na-N_2]^+$ (found), 591.2214 calcd. for $C_{32}H_{32}N_4NaO_6^+$, 563.2138 $[M+Na-2N_2]^+$ (found), 563.2153 calcd. for $C_{32}H_{32}N_2NaO_6^+$.

4-((4-Iodo-2,5-bis(2-(2-methoxyethoxy)ethoxy)phenyl)ethynyl)aniline (**167**)

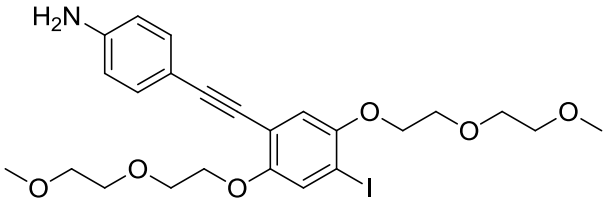

Ph(OPEG)$_2$I$_2$ **154** (1.23 g, 2.21 mmol, 1.0 eq) and *p*-ethynylaniline **160** (195 mg, 1.66 mmol, 0.75 eq) were dissolved in a mixture of dry THF (12 mL) and dry TEA (12 mL). Argon was bubbled for 15 min, and then $Pd(PPh_3)_2Cl_2$ (155 mg, 0.221 mmol, 0.1 eq) and CuI (84 mg, 0.442 mmol, 0.2 eq) were added. The resulting suspension was stirred at rt for 24 h, sat. aq. NH_4Cl was added, and the mixture was extracted with DCM (3×). The combined organic layers were dried over Na_2SO_4, filtered and concentrated. Column chromatography (SiO_2, 60:40 to 30:70 Cy/AcOEt) afforded **167** (477 mg, 0.86 mmol, 52%) as an orange oil.

Molecular formula: $C_{24}H_{30}INO_6$
MW: 555.4 g.mol^{-1}
^{1}H-NMR (CDCl$_3$, 300 MHz): δ 7.32 (s, 1H), 7.31 (d, *J* = 7.9 Hz, 2H), 6.92 (s, 1H), 6.62 (d, *J* = 8.4 Hz, 2H), 4.20–4.09 (m, 4H), 3.93–3.86 (m, 4H), 3.84 (s, 2H), 3.81–3.75 (m, 4H), 3.61–3.56 (m, 2H), 3.56–3.50 (m, 2H), 3.40 (s, 3H), 3.36 (s, 3H).
^{13}C-NMR (CDCl$_3$, 100 MHz): δ 154.2 (C_q), 152.3 (C_q), 147.0 (C_q), 133.0 (CH), 124.8 (CH), 116.8 (CH), 115.0 (C_q), 114.8 (CH), 112.6 (C_q), 95.5 (C_q), 86.5 (C_q), 83.4 (C_q), 72.2 (CH_2), 72.2 (CH_2), 71.2 (CH_2), 71.2 (CH_2), 70.2 (CH_2), 70.1 (CH_2), 69.9 (CH_2), 69.8 (CH_2), 59.2 (CH_3), 59.2 (CH_3).
HRMS (ESI): *m/z* = 578.1003 $[M+H]^+$ (found), 578.1010 calcd. for $C_{24}H_{30}INNaO_6^+$.

***tert*-Butyl (4-ethynylphenyl)carbamate** (**168**)

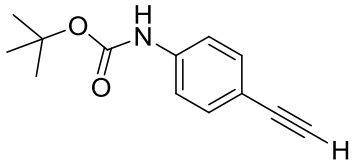

p-Ethynylaniline **160** (1.00 g, 8.53 mmol, 1.0 eq) and Boc_2O (3.72 g, 17.06 mmol, 2.0 eq) were dissolved in dry THF (10 mL). The resulting solution was refluxed for 7 h and concentrated. Column chromatography (SiO_2, 95:5 Cy/AcOEt) afforded **168** (1.644 g, 7.57 mmol, 89%) as a white solid.

Molecular formula: $C_{13}H_{15}NO_2$
MW: 217.3 g.mol^{-1}
^{1}H-NMR (CDCl$_3$, 300 MHz): δ 7.44–7.38 (m, 2H), 7.36–7.28 (m, 2H), 6.61 (s, 1H), 3.01 (s, 1H), 1.51 (s, 9H).
HRMS (ESI): *m/z* = 240.1002 $[M+Na]^+$ (found), 240.0995 calcd. for $C_{13}H_{15}NNaO_2^+$, 184.0378 $[M+Na+H-{}^tBu]^+$ (found), 184.0369 calcd. for $C_9H_7NNaO_2^+$, 162.0557 $[M+2H-{}^tBu]^+$ (found), 162.0550 calcd. for $C_9H_8NO_2^+$.

***tert*-Butyl (4-((4-((4-aminophenyl)ethynyl)-2,5-bis(2-(2-methoxyethoxy)ethoxy)phenyl)ethynyl) phenyl)carbamate** (**169**)

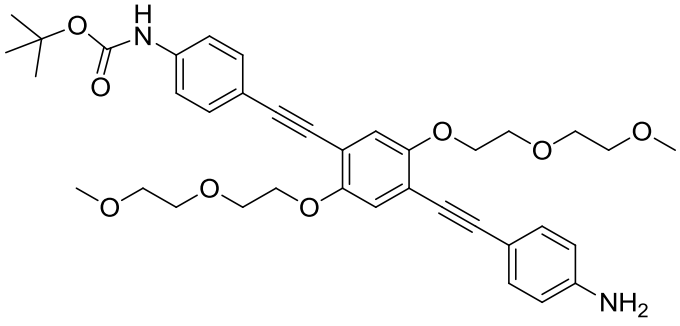

Compound **167** (250 mg, 0.45 mmol, 1.0 eq) and compound **168** (217 mg, 0.45 mmol, 1.0 eq) were dissolved in dry THF (3 mL) and dry TEA (3 mL). Argon was bubbled for 15 min, and then $Pd(PPh_3)_2Cl_2$ (32 mg, 0.045 mmol, 0.1 eq) and CuI (17 mg, 0.09 mmol, 0.2 eq) were added. The resulting suspension was stirred for 24 h at rt, sat. aq. NH_4Cl was added and the mixture was extracted with DCM (3×). The combined organic layers were dried over Na_2SO_4, filtered and concentrated. Column

chromatography (SiO_2, 40:60 to 30:70 Cy/AcOEt) afforded **169** (209 mg, 0.324 mmol, 72%) as an orange solid.

Molecular formula: $C_{37}H_{44}N_2O_8$
MW: 644.8 g.mol^{-1}
^{1}H-NMR ($CDCl_3$, 300 MHz): δ 7.45 (dt, *J* = 9.1, 2.8 Hz, 2H), 7.38–7.29 (m, 4H), 7.01 (s, 1H), 7.00 (s, 1H), 6.65–6.59 (m, 2H), 4.20 (t, *J* = 4.8 Hz, 4H), 3.92 (t, *J* = 4.8 Hz, 4H), 3.84 (s, 2H), 3.83–3.76 (m, 4H), 3.56–3.50 (m, 4H), 3.36 (s, 6H), 1.52 (s, 9H).
HRMS (ESI): *m/z* = 667.2990 $[M+Na]^+$ (found), 667.2990 calcd. for $C_{37}H_{44}N_2NaO_8^+$.

4,4'-(((1,4-phenylenebis(ethyne-2,1-diyl))bis(2,5-bis(2-(2-methoxyethoxy)ethoxy)-4,1-phenylene)) bis(ethyne-2,1-diyl))dianiline (OPE_2-diNH_2 **171**)

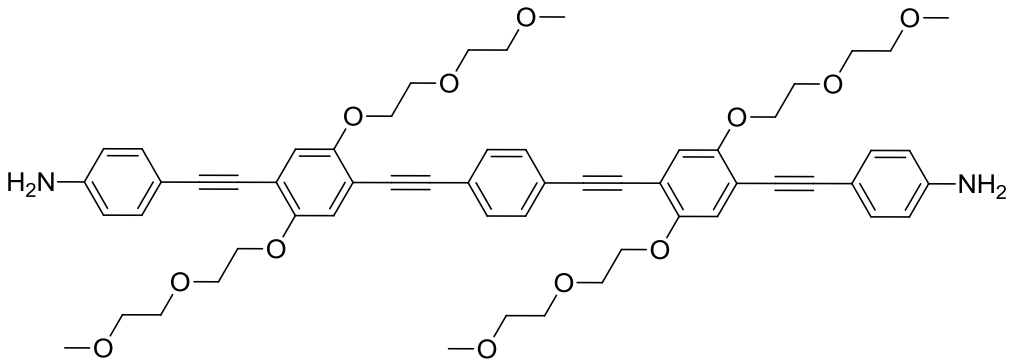

p-Diethynylbenzene **170** (53.4 mg, 0.423 mmol, 1.0 eq) and compound **167** (470 mg, 0.846 mmol, 2 eq) were dissolved in a mixture of dry THF (5 mL) and dry TEA (5 mL). Argon was bubbled for 15 min, and then $Pd(PPh_3)_2Cl_2$ (29.5 mg, 0.042 mmol, 0.1 eq) and CuI (16.3 mg, 0.085 mmol, 0.2 eq) were added. The resulting suspension was stirred at rt for 24 h, sat. aq. NH_4Cl was added, and the mixture was extracted with DCM (3×). The combined organic layers were dried over Na_2SO_4, filtered and concentrated. Column chromatography (SiO_2, 30:70 Cy/AcOEt to 100% AcOEt) afforded OPE_2-diNH_2 **171** (271 mg, 0.276 mmol, 65%) as a pale orange solid.

Molecular formula: $C_{58}H_{64}N_2O_{12}$
MW: 981.2 g.mol^{-1}
^{1}H-NMR ($CDCl_3$, 300 MHz): δ 7.51–7.47 (m, 4H), 7.37–7.29 (m, 4H), 7.03 (s, 2H), 7.02 (s, 2H), 6.67–6.60 (m, 4H), 4.21 (t, *J* = 4.9 Hz, 8H), 3.93 (t, *J* = 4.9 Hz, 8H), 3.85 (s, 4H), 3.84–3.78 (m, 8H), 3.58–3.51 (m, 8H), 3.37 (s, 12H).
^{13}C-NMR ($CDCl_3$, 75 MHz): δ 153.8, 153.4, 147.0, 133.1, 131.5, 123.3, 117.7, 117.3, 115.6, 114.8, 113.2, 112.5, 96.4, 94.6, 88.1, 83.8, 72.1, 71.1, 69.9, 69.8, 59.1, 59.1.
HRMS (ESI): *m/z* = 981.4517 $[M+H]^+$ (found), 981.4532 calcd. for $C_{58}H_{65}N_2O_{12}^+$, 1003.4344 $[M+Na]^+$ (found), 1003.4351 calcd. for $C_{58}H_{64}N_2NaO_{12}^+$, 513.2123 $[M+2Na]^{2+}$ (found), 513.2122 calcd. for $C_{58}H_{64}N_2Na_2O_{12}^{2+}/2$.

4,4'-((((((2,5-Bis(2-(2-methoxyethoxy)ethoxy)-1,4-phenylene)bis(ethyne-2,1-diyl))bis(4,1-phenylene))bis(ethyne-2,1-diyl))bis(2,5-bis(2-(2-methoxyethoxy)ethoxy)-4,1-phenylene)) bis(ethyne-2,1-diyl))dianiline (OPE_3-diNH_2 **172**)

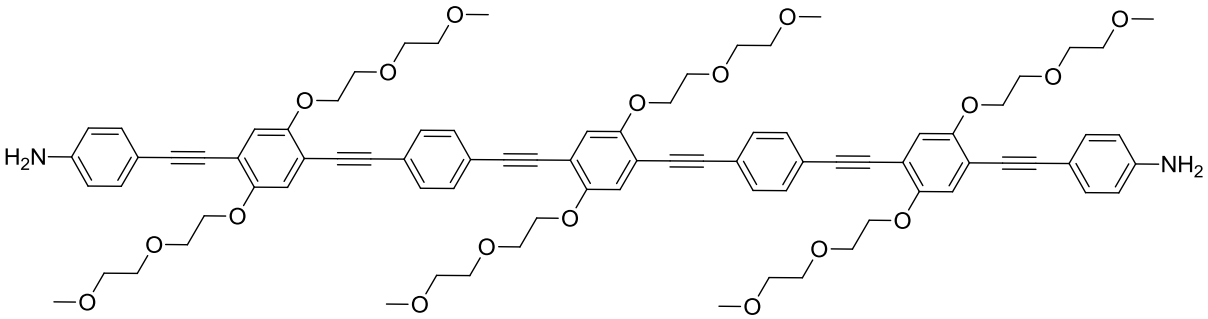

OPE-diCCH **164** (70.3 mg, 0.125 mmol, 1.0 eq) and compound **167** (138.9 mg, 0.25 mmol, 2.0 eq) were dissolved in a mixture of dry THF (3 mL) and dry TEA (3 mL). Argon was bubbled for 15 min, and then $Pd(PPh_3)_2Cl_2$ (8.8 mg, 0.0125 mmol, 0.1 eq) and CuI (4.8 mg, 0.025 mmol, 0.2 eq) were added. The resulting suspension was stirred at rt for 24 h, sat. aq. NH_4Cl was added, and the mixture was extracted with DCM (3×). The combined organic layers were dried over Na_2SO_4, filtered and concentrated. Column chromatography (SiO_2, 100% AcOEt to 95:5 AcOEt/MeOH) afforded OPE_3-diNH_2 **172** (123 mg, 0.087 mmol, 69%) as a dark orange solid.

Molecular formula: $C_{84}H_{92}N_2O_{18}$
MW: 1417.7 g.mol^{-1}
^{1}H-NMR ($CDCl_3$, 300 MHz): δ 7.53–7.48 (m, 8H), 7.37–7.30 (m, 4H), 7.05 (s, 2H), 7.03 (s, 2H), 7.02 (s, 2H), 6.67–6.60 (m, 4H), 4.27–4.18 (m, 12H), 3.98–3.90 (m, 12H), 3.85 (s, 4H), 3.84–3.78 (m, 12H), 3.59–3.52 (m, 12H), 3.38 (s, 6H), 3.37 (s, 6H), 3.37 (s, 6H).
^{13}C-NMR ($CDCl_3$, 75 MHz): δ 153.8 (C_q), 153.7 (C_q), 153.4 (C_q), 147.1 (C_q), 133.0 (CH), 132.5 (CH), 131.6 (CH), 131.5 (CH), 131.5 (CH), 123.5 (C_q), 123.1 (C_q), 117.7 (CH), 117.5 (CH), 117.3 (CH), 115.6 (C_q), 114.7 (CH), 114.3 (C_q), 113.1 (C_q), 112.4 (C_q), 96.5 (C_q), 95.0 (C_q), 94.5 (C_q), 88.2 (C_q), 87.8 (C_q), 83.8 (C_q), 72.1 (CH_2), 71.1 (CH_2), 69.8 (CH_2), 69.7 (CH_2), 69.6 (CH_2), 59.1 (CH_3), 59.1 (CH_3).
HRMS (ESI): *m/z* = 1417.6408 $[M+H]^+$ (found), 1417.6418 calcd. for $C_{84}H_{93}N_2O_{18}^+$, 1439.6235 $[M+Na]^+$ (found), 1439.6237 calcd. for $C_{84}H_{92}N_2NaO_{18}^+$, 731.3074 $[M+2Na]^{2+}$ (found), 731.3065 calcd. for $C_{84}H_{92}N_2Na_2O_{18}^{2+}/2$.

4',4''''-(((2,5-Bis(2-(2-methoxyethoxy)ethoxy)-1,4-phenylene)bis(ethyne-2,1-diyl))bis(4,1-phenylene))di-2,2':6',2''-terpyridine (Bis-CCPhTpy-Ph$(OPEG)_2$ **173**)

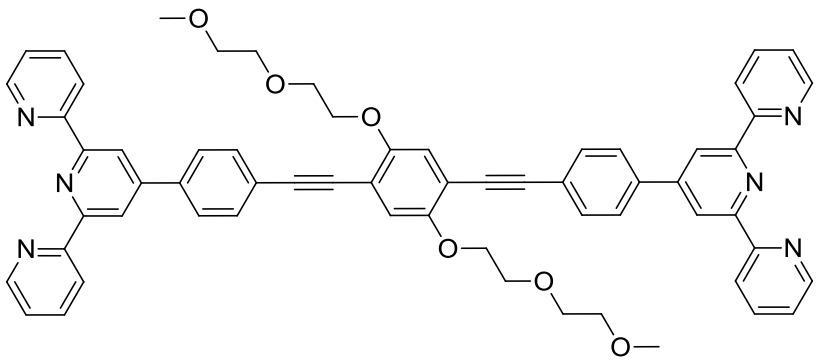

$Ph(OPEG)_2I_2$ **154** (700 mg, 1.26 mmol, 1.0 eq) and *p*CCHPhTpy **37** (840 mg, 2.52 mmol, 2.0 eq) were dissolved in dry THF (30 mL) and dry TEA (15 mL). Argon was bubbled for 15 min, and then $Pd(PPh_3)Cl_2$ (89 mg, 0.126 mmol, 0.1 eq) and CuI (48 mg, 0.252 mmol, 0.2 eq) were added. The resulting mixture was heated at 50 °C for 48 h, sat. aq. NH_4Cl was added and the mixture was

extracted with DCM (3×). The combined organic layers were washed with sat. aq. NaCl, dried over Na_2SO_4, filtered and concentrated. Column chromatography (Al_2O_3, basic, activated, Brockmann I, 100% DCM to 99:1 DCM/MeOH) afforded a solid, which was then suspended in boiling EtOH for 1 h, filtered, washed with EtOH and dried to afford bis-CCPhTpy-Ph(OPEG)$_2$ **173** (449 mg, 0.460 mmol, 37%) as a yellow-orange solid.

Molecular formula: $C_{62}H_{52}N_6O_6$
MW: 977.1 g.mol^{-1}
^{1}H-NMR (CDCl$_3$, 300 MHz): δ 8.79–8.72 (m, 8H), 8.69 (d, 4H, *J* = 8.1 Hz), 7.97–7.84 (m, 8H), 7.68 (d, 4H, *J* = 8.1 Hz), 7.41–7.33 (m, 4H), 7.11 (s, 2H), 4.31–4.24 (m, 4H), 4.02–3.96 (m, 4H), 3.89–3.83 (m, 4H), 3.64–3.57 (m, 4H), 3.39 (s, 6H).
^{13}C-NMR (CDCl$_3$, 75 MHz): 156.2 (C_q), 156.2 (C_q), 153.8 (C_q), 149.5 (C_q), 149.3 (CH), 138.4 (C_q), 137.1 (CH), 133.2 (CH), 132.2 (CH), 127.5 (C_q), 127.4 (CH), 124.2 (C_q), 124.1 (CH), 121.5 (CH), 118.8 (CH), 117.4 (CH), 114.3 (C_q), 95.0 (C_q), 87.5 (C_q), 72.2 (CH_2), 71.3 (CH_2), 69.9 (CH_2), 69.8 (CH_2), 59.3 (CH_3).
HRMS (ESI): *m/z* = 977.4009 $[M+H]^+$ (found), 977.4021 calcd. for $C_{62}H_{53}N_6O_6^+$, 999.3817 $[M+Na]^+$ (found), 999.3841 calcd. for $C_{62}H_{52}N_6NaO_6^+$.

Bis-(Tpy)Mn^{II}(PhTpy)-CC$_2$Ph(OPEG)$_2$ 174

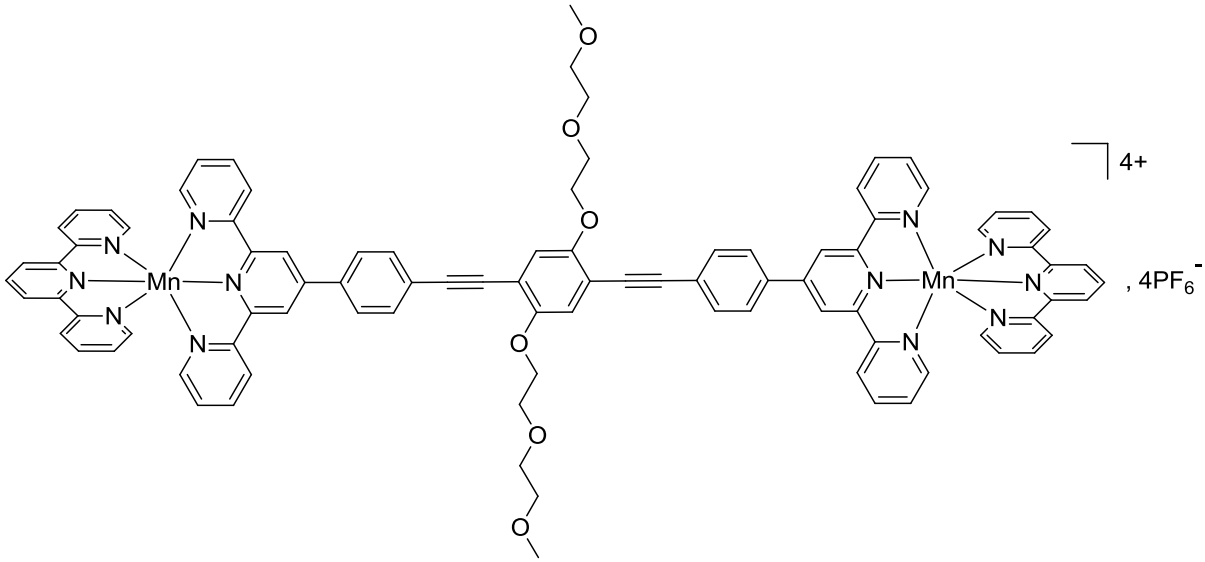

Bis-CCPhTpy-Ph(OPEG)$_2$ **173** (30.0 mg, 0.0307 mmol, 1.0 eq) and TpyMnCl$_2$ (22.1 mg, 0.0614 mmol, 2.0 eq) were dissolved in a 1:1:2 MeCN/MeOH/DCM mixture (80 mL overall). The resulting solution was heated at 80 °C for 48 h and cooled to rt. NH_4PF_6 (50.0 mg, 0.307 mmol, 10.0 eq) dissolved in MeOH (20 mL) was added and the resulting mixture was stirred at rt for 15 h, concentrated to ≈ 20 mL, filtered, thoroughly washed with Et_2O and H_2O and dried to afford bis-(Tpy)Mn^{II}(PhTpy)-CC$_2$Ph(OPEG)$_2$ **174** (36.1 mg, 0.0169 mmol, 55%) as an orange solid.

Molecular formula: $C_{92}H_{74}F_{24}Mn_2N_{12}O_6P_4$
MW: 2133.4 g.mol^{-1}

4',4''''-(2',5'-bis(2-(2-methoxyethoxy)ethoxy)-[1,1':4',1''-terphenyl]-4,4''-diyl)di-2,2':6',2''-terpyridine (bis-PhTpy-Ph(OPEG)$_2$ **175**)

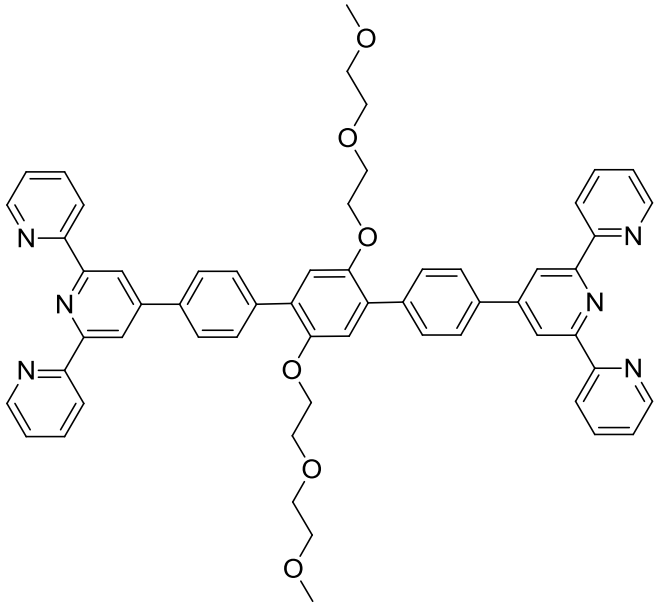

$Ph(OPEG)_2I_2$ **154** (100 mg, 0.18 mmol, 1.0 eq) and compound **46** (157 mg, 0.36 mmol, 2.0 eq) were dissolved in a mixture of toluene (4 mL) and MeOH (0.5 mL). Argon was bubbled for 10 min and Cs_2CO_3 (293 mg, 0.9 mmol, 5.0 eq) was added, followed by $Pd(PPh_3)_4$ (21 mg, 0.018 mmol, 0.1 eq). The resulting mixture was heated at 80 °C for 24 h and cooled to rt. DCM was added and the mixture was washed with H_2O (2×) and sat. aq. NaCl (2×). The organic layer was dried over Na_2SO_4, filtered and concentrated. Column chromatography (Al_2O_3, basic, activated, Brockmann I, 100% DCM to 99:1 DCM/MeOH) afforded bis-PhTpy-$Ph(OPEG)_2$ **175** (153 mg, 0.165 mmol, 92%) as an orange solid.

Molecular formula: $C_{58}H_{52}N_6O_6$
MW: 929.1 $g.mol^{-1}$
^{1}H-NMR ($CDCl_3$, 300 MHz): δ 8.72 (ddd, *J* = 4.8, 1.9, 0.9 Hz, 4H), 8.70 (s, 4H), 8.67 (dt, *J* = 8.0, 1.1 Hz, 4H), 7.89 (ddd, *J* = 8.0, 7.5, 1.8 Hz, 4 H), 7.81–7.75 (m, 4H), 7.66–7.60 (m, 4H), 7.36 (ddd, *J* = 7.5, 4.8, 1.1 Hz, 4H), 6.83 (s, 2H), 4.13–4.03 (m, 4H), 3.85–3.79 (m, 4H), 3.73–3.68 (m, 4H), 3.60–3.54 (m, 4H), 3.39 (s, 6H).
^{13}C-NMR ($CDCl_3$, 75 MHz): 156.1 (C_q), 156.0 (C_q), 149.2 (CH), 149.1 (C_q), 137.4 (C_q), 137.2 (CH), 132.2 (CH), 129.0 (CH), 124.1 (CH), 123.6 (C_q), 121.6 (CH), 118.8 (CH), 115.7 (CH), 72.1 (CH_2), 70.8 (CH_2), 70.0 (CH_2), 68.1 (CH_2), 59.2 (CH_3).

Bis-(Tpy)Mn^{II}(PhTpy)-$Ph(OPEG)_2$ 176

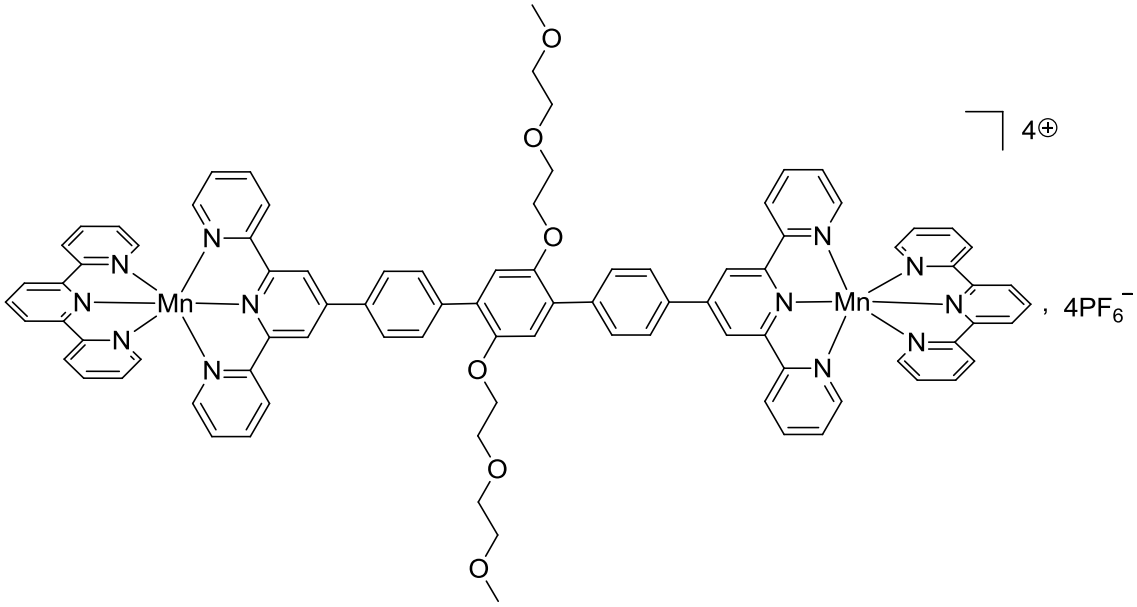

Bis-PhTpy-Ph(OPEG)$_2$ **175** (53.1 mg, 0.057 mmol, 1.0 eq) and TpyMnCl$_2$ **49** (40.0 mg, 0.111 mmol, 2.0 eq) were dissolved in a mixture of MeOH (20 mL) and MeCN (20 mL). The resulting solution was heated at 80 °C for 15 h and cooled to rt. NH_4PF_6 (93.1 mg, 0.571 mmol, 10 eq) dissolved in MeOH (20 mL) was added and the resulting mixture was stirred at rt for 15 h, concentrated to ≈ 15 mL, filtered, thoroughly washed with Et_2O and H_2O and dried to afford bis-(Tpy)Mn^{II}(PhTpy)-Ph(OPEG)$_2$ **176** (45.9 mg, 0.0296 mmol, 52%) as an orange solid.

Molecular formula: $C_{91}H_{82}Mn_2N_{12}O_6$
MW: 1549.6 g.mol^{-1}

4',4''''-(((1*E*,1'*E*)-(((2,5-Bis(2-(2-methoxyethoxy)ethoxy)-1,4-phenylene)bis(ethyne-2,1-diyl))bis(4,1-phenylene))bis(ethene-2,1-diyl))bis(4,1-phenylene))di-2,2':6',2''-terpyridine (bis-PhTpy-OPE **177**)

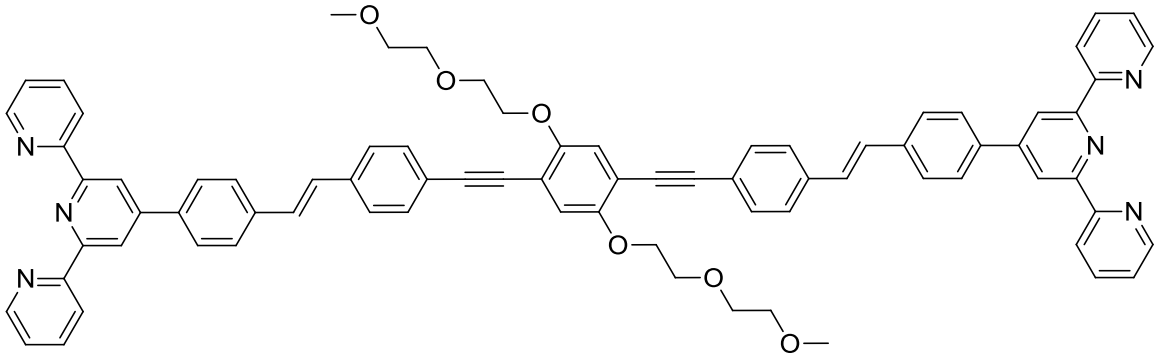

Compound **45** (543 mg, 1.182 mmol, 2.0 eq) was dissolved in dry DMF (17 mL). The resulting solution was cooled to 0 °C and NaH (60% dispersion in mineral oil, 83 mg, 2.07 mmol, 3.5 eq) was added. The suspension was stirred for 20 min at 0 °C and OPE-diCHO **161** (337 mg, 0.591 mmol, 1.0 eq) dissolved in dry THF (29 mL) was added dropwise during 1 h at 0 °C. The resulting mixture was refluxed for 15 h and cooled to rt. H_2O was added and the resulting yellow suspension was extracted with DCM (5×). The combined organic layers were washed with H_2O (1×), dried over Na_2SO_4, filtered and concentrated. Column chromatography (Al_2O_3, basic, activated, Brockmann I, 100% DCM to 99:1 DCM/MeOH) afforded bis-PhTpy-OPE **177** (556 mg, 0.471 mmol, 80%) as an orange solid.

Molecular formula: $C_{78}H_{64}N_6O_6$
MW: 1181.4 g.mol^{-1}
^{1}H-NMR ($CDCl_3$, 300 MHz): δ 8.81–8.76 (m, 4H), 8.75 (d, 4H, *J* = 8.2 Hz), 8.69 (d, 4H, *J* = 8.2 Hz), 7.95 (d, 4H, *J* = 8.2 Hz), 7.89 (td, 4H, *J* = 8.2, 1.8 Hz), 7.67 (d, 4H, *J* = 8.6 Hz), 7.55 (s, 8H), 7.41–7.32 (m, 4H), 7.21 (s, 4H), 7.07 (s, 2H), 4.28–4.23 (m, 4H), 3.99–3.94 (m, 4H), 3.88–3.83 (m, 4H), 3.60–3.55 (m, 4H), 3.40 (s, 6H).
^{13}C-NMR ($CDCl_3$, 75 MHz): δ 156.4 (C_q), 156.1 (C_q), 153.8 (C_q), 149.7 (C_q), 149.3 (CH), 138.0 (C_q), 137.8 (C_q), 137.4 (C_q), 137.0 (CH), 132.1 (CH), 129.1 (CH), 128.9 (CH), 127.8 (CH), 127.3 (CH), 126.7 (CH), 124.0 (CH), 122.7 (C_q), 121.5 (CH), 118.7 (CH), 117.5 (CH), 114.4 (C_q), 95.5 (C_q), 87.1 (C_q), 72.2 (CH_2), 71.3 (CH_2), 69.9 (CH_2), 69.8 (CH_2), 59.3 (CH_3).
HRMS (ESI): *m/z* = 1181.4908 $[M+H]^+$ (found), 1181.4960 calcd. for $C_{78}H_{65}N_6O_6^+$, 1203.4722 $[M+Na]^+$ (found), 1203.4780 calcd. for $C_{78}H_{64}N_6NaO_6^+$.

Bis-(Tpy)Mn^{II}(PhTpy)-OPE 178

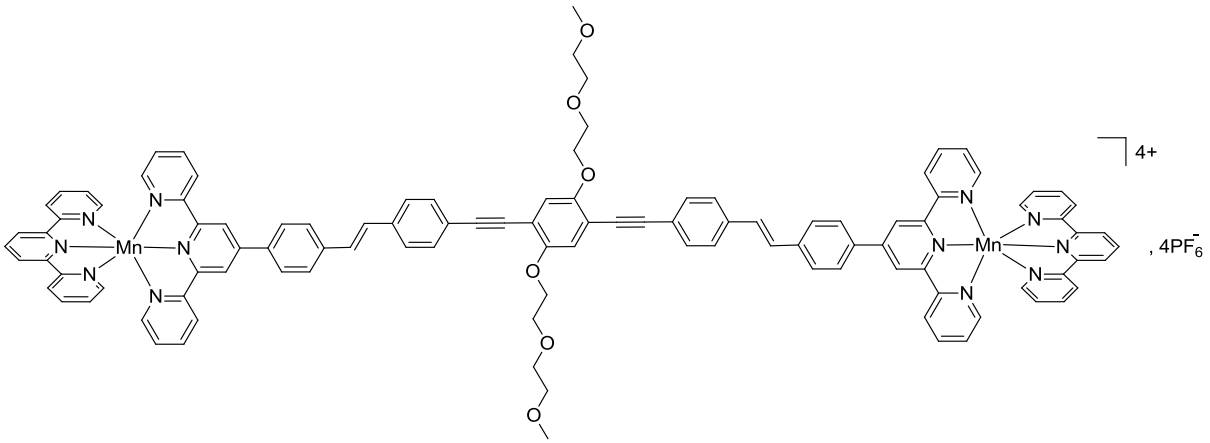

Bis-PhTpy-OPE **177** (30.0 mg, 0.0254 mmol, 1.0 eq) and $TpyMnCl_2$ **49** (18.2 mg, 0.0508 mmol, 2.0 eq) were dissolved in a 1:1:2 MeCN/MeOH/DCM mixture (40 mL overall). The resulting solution was heated at 80 °C for 48 h and cooled to rt. NH_4PF_6 (41.4 mg, 0.254 mmol, 10 eq) dissolved in MeOH (10 mL) was added and the resulting mixture was stirred at rt for 15 h, concentrated to ≈ 20 mL, filtered, thoroughly washed with Et_2O and H_2O and dried to afford bis-(Tpy)Mn^{II}(PhTpy)-OPE **178** (19 mg, 0.0081 mmol, 32%) as an orange solid.

Molecular formula: $C_{108}H_{86}F_{24}Mn_2N_{12}O_6P_4$
MW: 2337.7 g.mol^{-1}

Mn^{II}-bis-PhTpy-OPE (**179**)

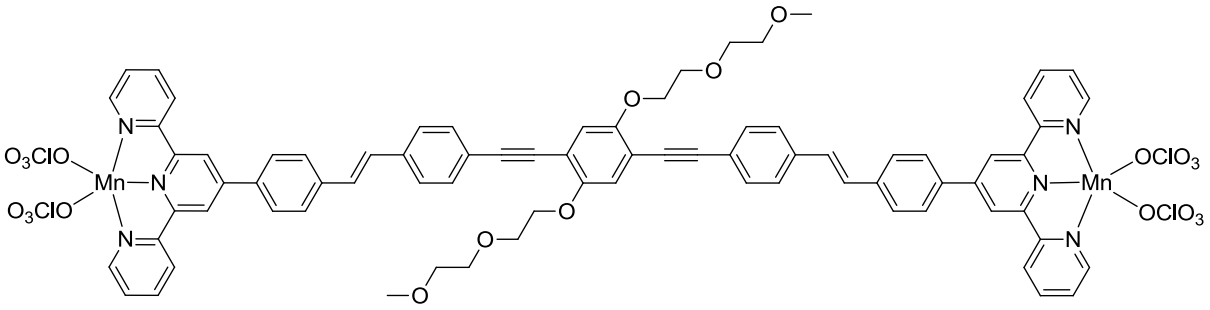

Bis-PhTpy-OPE **177** (20.0 mg, 0.017 mmol, 1.0 eq) was dissolved in $CHCl_3$ (3 mL). $Mn(ClO_4)_2 \bullet 6H_2O$ (61.2 mg, 0.169 mmol, 10.0 eq) dissolved in abs. EtOH (3 mL) was added dropwise. The resulting precipitate was stirred at rt for 5 h, filtered, washed with H_2O and Et_2O, and dried to afford Mn^{II}-bis-PhTpy-OPE **179** (15.2 mg, 0.009 mmol, 51%) as an orange solid.

Molecular formula: $C_{78}H_{64}Cl_4Mn_2N_6O_{22}$
MW: 1689.1 g.mol^{-1}

Tetraethyl 4,4'-((((2,5-bis(2-(2-methoxyethoxy)ethoxy)-1,4-phenylene)bis(ethyne-2,1-diyl))bis(4,1-phenylene))bis(ethyne-2,1-diyl))bis(pyridine-2,6-dicarboxylate) (**180**)

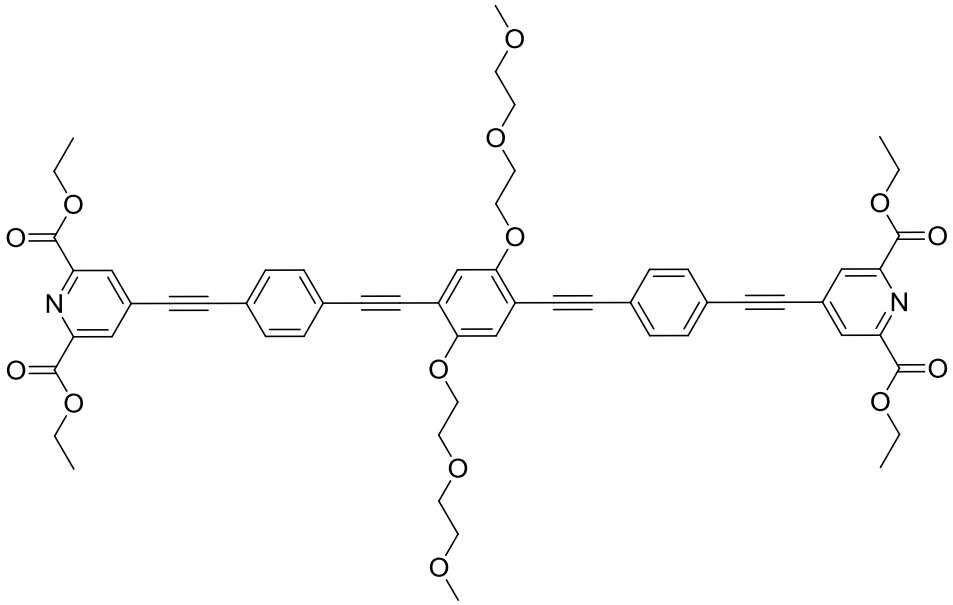

OPE-diCCH **164** (100.0 mg, 0.178 mmol, 1.0 eq) and compound **9** (108.0 mg, 0.356 mmol, 2.0 eq) were dissolved in a mixture of dry DMF (2 mL) and dry TEA (2 mL). Argon was bubbled for 15 min, and $Pd(PPh_3)_2Cl_2$ (12.5 mg, 0.018 mmol, 0.1 eq) and CuI (6.8 mg, 0.036 mmol, 0.2 eq) were added. The resulting mixture was stirred at rt for 60 h and concentrated. DCM and sat. aq. NH_4Cl were added and the mixture was extracted with DCM (3×). The combined organic layers were dried over Na_2SO_4, filtered and concentrated. Column chromatography (SiO_2, 50:50 to 30:70 Cy/AcOEt) afforded **180** (121 mg, 0.120 mmol, 67%) as a yellow solid.

Molecular formula: $C_{58}H_{56}N_2O_{14}$
MW: 1005.1 g.mol^{-1}

^{1}H-NMR (CDCl$_3$, 300 MHz): δ 8.34 (s, 4H), 7.56 (s, 8H), 7.07 (s, 2H), 4.51 (q, *J* = 7.1 Hz, 8H), 4.24 (t, *J* = 5.2 Hz, 4H), 3.95 (t, *J* = 5.2 Hz, 4H), 3.85–3.78 (m, 4H), 3.60–3.53 (m, 4H), 3.38 (s, 6H), 1.47 (t, *J* = 7.1 Hz, 12H).
^{13}C-NMR (CDCl$_3$, 75 MHz): δ 164.4 (C_q), 153.9 (C_q), 149.1 (C_q), 134.1 (C_q), 132.2 (CH), 131.8 (CH), 129.5 (CH), 125.0 (C_q), 121.3 (C_q), 117.5 (CH), 114.3 (C_q), 96.3 (C_q), 94.8 (C_q), 88.7 (C_q), 87.4 (C_q), 72.2 (CH_2), 71.2 (CH_2), 69.9 (CH_2), 69.7 (CH_2), 62.7 (CH_2), 59.3 (CH_3), 14.4 (CH_3).
HRMS (ESI): *m/z* = 1005.3781 $[M+H]^+$ (found), 1005.3804 calcd. for $C_{58}H_{57}N_2O_{14}^+$, 1027.3605 $[M+Na]^+$ (found), 1027.3624 calcd. for $C_{58}H_{56}N_2NaO_{14}^+$, 503.1932 $[M+2H]^{2+}$ (found), 503.1939 calcd. for $C_{58}H_{58}N_2O_{14}^{2+}/2$, 514.1838 $[M+H+Na]^{2+}$ (found), 514.1848 calcd. for $C_{58}H_{57}N_2NaO_{14}^{2+}/2$.

4,4'-((((2,5-Bis(2-(2-methoxyethoxy)ethoxy)-1,4-phenylene)bis(ethyne-2,1-diyl))bis(4,1-phenylene))bis(ethyne-2,1-diyl))bis(pyridine-2,6-dicarboxylic acid) (bis-DPA-OPE **181**)

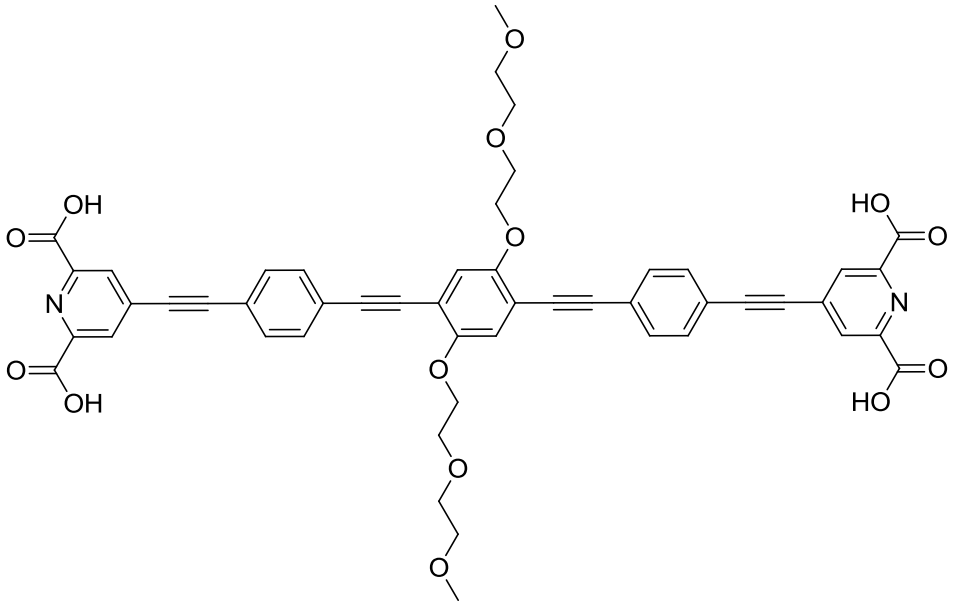

Compound **180** (306 mg, 0.304 mmol, 1.0 eq) was suspended in a mixture of THF (13 mL) and H_2O (13 mL). LiOH (88 mg, 3.65 mmol, 12 eq) was added and the resulting mixture was stirred at rt for 24 h. Exchange resin Amberlite IR-120 (H-form) was then added to the yellow solution, which was further stirred for 15 h at rt. The yellow precipitate was then withdrawn *via* Pasteur pipette and concentrated to afford bis-DPA-OPE **181** (268 mg, 0.300 mmol, 99%) as a yellow solid.

Molecular formula: $C_{50}H_{40}N_2O_{14}$
MW: 892.9 g.mol^{-1}
^{1}H-NMR (DMSO-d$_6$, 300 MHz): δ 13.63 (s, 4H), 8.30 (s, 4H), 7.75 (d, *J* = 8.1 Hz, 4H), 7.63 (d, *J* = 8.1 Hz, 4H), 7.26 (s, 2H), 4.20 (t, *J* = 4.5 Hz, 4H), 3.81 (t, *J* = 4.5 Hz, 4H), 3.69 (t, *J* = 4.5 Hz, 4H), 3.46 (t, *J* = 4.5 Hz, 4H), 3.23 (s, 6H).
^{13}C-NMR (DMSO-d$_6$, 75 MHz): δ 165.4, 153.2, 132.3, 132.0, 132.0, 131.6, 131.5, 131.4, 128.9, 128.7, 123.9, 121.1, 116.9, 113.2, 94.6, 94.4, 88.8, 87.9, 71.4, 70.0, 69.1, 69.0, 58.1.
HRMS (ESI): *m/z* = 891.2437 $[M-H]^-$ (found), 891.2407 calcd. for $C_{50}H_{39}N_2O_{14}^-$.

Mn^{II}-bis-DPA-OPE (**182**)

Bis-DPA-OPE **181** (26 mg, 0.029 mmol, 1 eq) was dissolved in a mixture of THF (5 mL) and H_2O (5 mL). $Mn(ClO_4)_2 \bullet 6H_2O$ (26.4 mg, 0.073 mmol, 2.5 eq) dissolved in H_2O (1 mL) was added dropwise. The

resulting yellow precipitate was stirred at rt for 5 h, filtered, washed with H_2O and dried to afford Mn^{II}-bis-DPA-OPE **182** (25.3 mg, 0.021 mmol, 72%) as a yellow solid.

Molecular formula: $C_{50}H_{36}Cl_4Mn_2N_2O_{30}$
MW: 1396.5 g.mol^{-1}

Octaethyl 2,2',2'',2''',2'''',2''''',2'''''',2'''''''-(((4,4'-(4,4'-(((2,5-bis(2-(2-methoxyethoxy)ethoxy)-1,4-phenylene)bis(ethyne-2,1-diyl))bis(4,1-phenylene))bis(1*H*-1,2,3-triazole-4,1-diyl))bis(pyridine-6,4,2-triyl))tetrakis(methylene))tetrakis(azanetriyl))octaacetate (**183**)

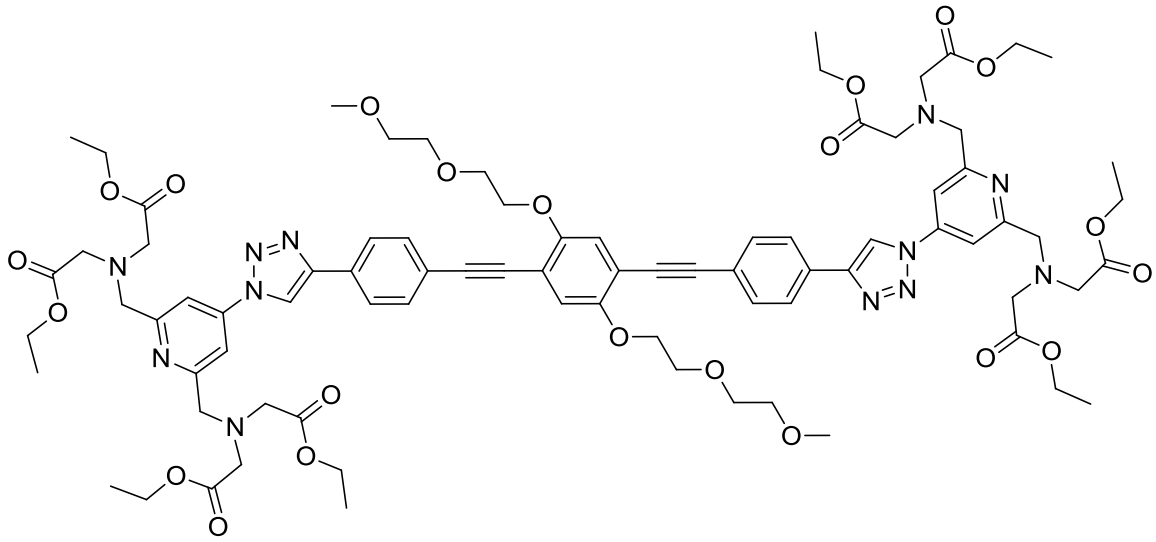

OPE-diCCH **164** (31.5 mg, 0.056 mmol, 1.0 eq), Et-*p*N_3PyMTA **74** (57.0 mg, 0.109 mmol, 2.0 eq) and CuI (2.1 mg, 0.011 mmol, 0.2 eq) were suspended in dry MeCN (2 mL). The resulting mixture was refluxed for 7 h and cooled to rt. Aq. 10% tetrasodium EDTA (2 mL) was added and the resulting mixture was stirred at rt for 1 h. H_2O and DCM were added and the mixture was extracted several times with DCM. The combined organic layers were dried over Na_2SO_4, filtered and concentrated. Column chromatography (SiO_2, 50:50 Cy/AcOEt to 100% AcOEt to 90:10 AcOEt/MeOH) afforded **183** (31.2 mg, 0.023 mmol, 41%) as a light brown oil.

Molecular formula: $C_{82}H_{102}N_{12}O_{22}$
MW: 1607.8 g.mol^{-1}
^{1}H-NMR (CDCl$_3$, 300 MHz): δ 8.49 (s, 2H), 8.13 (s, 4H), 7.93 (d, *J* = 8.2 Hz, 4H), 7.63 (d, *J* = 8.2 Hz, 4H), 7.07 (s, 2H), 4.29–4.10 (m, 28H), 3.96 (t, *J* = 4.8 Hz, 4H), 3.86–3.80 (m, 4H), 3.64 (s, 16H), 3.59–3.53 (m, 4H), 3.37 (s, 6H), 1.26 (t, *J* = 7.2 Hz, 24H).
^{13}C-NMR (CDCl$_3$, 75 MHz): δ 171.3 (C_q), 161.8 (C_q), 153.8 (C_q), 148.2 (C_q), 144.7 (C_q), 132.3 (CH), 129.9 (C_q), 125.9 (CH), 123.6 (C_q), 117.7 (CH), 117.5 (CH), 114.3 (C_q), 111.2 (CH), 95.0 (C_q), 87.1 (C_q), 72.2 (CH_2), 71.2 (CH_2), 69.9 (CH_2), 69.8 (CH_2), 60.8 (CH_2), 60.0 (CH_2), 59.2 (CH_3), 55.3 (CH_2), 14.4 (CH_3).
HRMS (ESI): *m/z* = 804.3633 $[M+2H]^{2+}$ (found), 804.3689 calcd. for $C_{82}H_{104}N_{12}O_{22}^{2+}$/2, 815.3564 $[M+H+Na]^{2+}$ (found), 815.3598 calcd. for $C_{82}H_{103}N_{12}NaO_{22}^{2+}$/2, 826.3477 $[M+2Na]^{2+}$ (found), 826.3508 calcd. for $C_{82}H_{102}N_{12}Na_2O_{22}^{2+}$/2, 801.3538 $[M-4H]^{2+}$ (found), 801.3454 calcd. for $C_{82}H_{98}N_{12}O_{22}^{2+}$/2, 790.3552 $[M+2H-N_2]^{2+}$ (found), 790.3658 calcd. for $C_{82}H_{104}N_{10}O_{22}^{2+}$/2, 776.3571 $[M+2H-2N_2]^{2+}$ (found), 776.3627 calcd. for $C_{82}H_{104}N_8O_{22}^{2+}$/2.

2,2',2'',2''',2'''',2''''',2'''''',2'''''''-(((4,4'-(4,4'-(((2,5-Bis(2-(2-methoxyethoxy)ethoxy)-1,4-phenylene)bis(ethyne-2,1-diyl))bis(4,1-phenylene))bis(1*H*-1,2,3-triazole-4,1-diyl))bis(pyridine-6,4,2-triyl))tetrakis(methylene))tetrakis(azanetriyl))octaacetic acid (bis-PyMTA-OPE **184**)

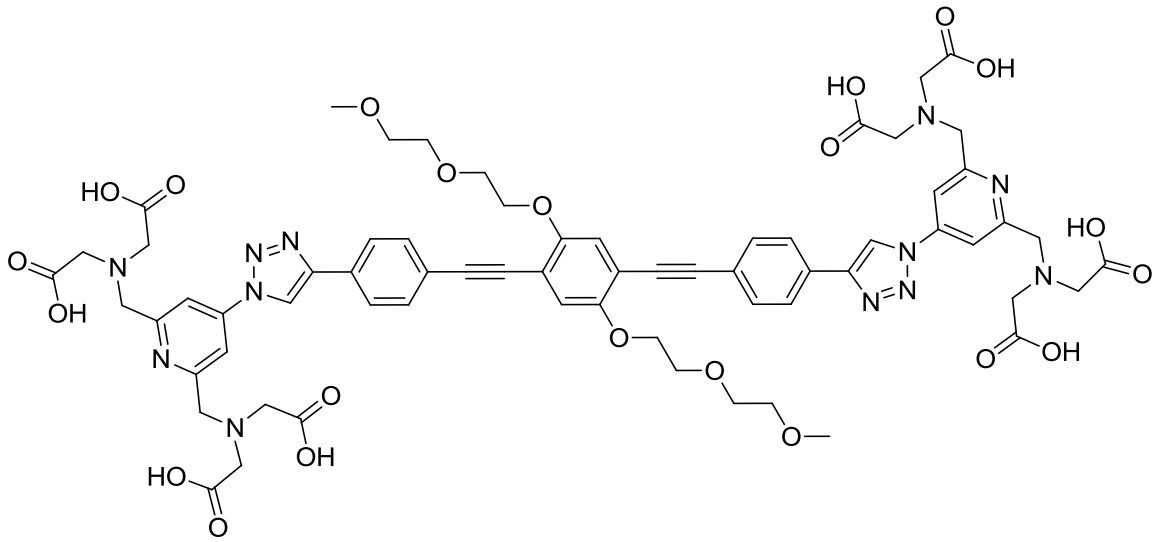

Compound **183** (56 mg, 0.035 mmol, 1.0 eq) was suspended in a mixture of THF (2 mL) and H_2O (2 mL). LiOH (21 mg, 0.87 mmol, 25.0 eq) was added and the resulting mixture was stirred at rt for 24 h. Exchange resin Amberlite IR-120 (H-form) was then added to the yellow solution, which was further stirred for 15 h at rt. The yellow precipitate was then withdrawn *via* Pasteur pipette and concentrated to afford bis-PyMTA-OPE **184** (47 mg, 0.034 mmol, 97%) as a yellow solid.

Molecular formula: $C_{66}H_{70}N_{12}O_{22}$
MW: 1383.3 g.mol^{-1}
^{1}H-NMR (DMSO-d$_6$, 300 MHz): δ 12.70 (br s, 8H), 9.54 (s, 2H), 8.10 (s, 4H), 8.07 (d, *J* = 8.0 Hz, 4H), 7.69 (d, *J* = 8.0 Hz, 4H), 7.27 (s, 2H), 4.27–4.19 (m, 4H), 4.15 (s, 4H), 3.87–3.79 (m, 4H), 3.75–3.68 (m, 4H), 3.62 (s, 16H), 3.51–3.45 (m, 4H), 3.25 (s, 6H).
^{13}C-NMR (DMSO-d$_6$, 75 MHz): δ 172.4, 161.4, 153.2, 147.0, 144.0, 139.2, 132.0, 130.0, 125.7, 124.9, 122.5, 120.0, 116.9, 113.3, 110.9, 94.8, 87.2, 71.4, 70.1, 69.2, 69.1, 59.2, 58.2, 54.6.
HRMS (ESI): *m/z* = 1405.4667 $[M+Na]^+$ (found), 1405.4620 calcd. for $C_{66}H_{70}N_{12}NaO_{22}^+$.

Mn^{II}-bis-PyMTA-OPE (**185**)

Bis-PyMTA-OPE **184** (100 mg, 0.072 mmol, 1.0 eq) was dissolved in H_2O (5 mL). Argon was bubbled for 10 min, and the pH was adjusted to 6.5 with solid $NaHCO_3$. The mixture was cooled to 0 °C, and $MnCl_2$ (22.6 mg, 0.18 mmol, 2.5 eq) dissolved in H_2O (5 mL) was slowly added while keeping the pH between 5 and 7 with solid $NaHCO_3$. The mixture was allowed to warm to rt for 15 h, and the pH was adjusted to 8.5 with aq. 0.1 M NaOH. Acetone (100 mL) was added and the resulting precipitate was stirred at rt for 15 min, filtered and washed with acetone. The solid was reprecipitated from H_2O with acetone, filtered and dried to afford Mn^{II}-bis-PyMTA-OPE **185** (72.5 mg, 0.049 mmol, 68%) as a yellow solid.

Molecular formula: $C_{66}H_{62}Mn_2N_{12}O_{22}$
MW: 1485.2 g.mol^{-1}

HRMS (ESI): *m/z* = 743.1485 $[L+2Mn-6H]^{2-}$ (found), 743.1515 calcd. for $C_{66}H_{64}Mn_2N_{12}O_{22}^{2-}/2$, 485.7629 $[L+2Mn-7H-N_2]^{3-}$ (found), 485.7632 calcd. for $C_{66}H_{63}Mn_2N_{10}O_{22}^{3-}/3$, 357.0700 $[L+2Mn-8H-2N_2]^{4-}$ (found), 357.0690 calcd. for $C_{66}H_{62}Mn_2N_8O_{22}^{4-}/4$.

Protected bis-DO3A 187

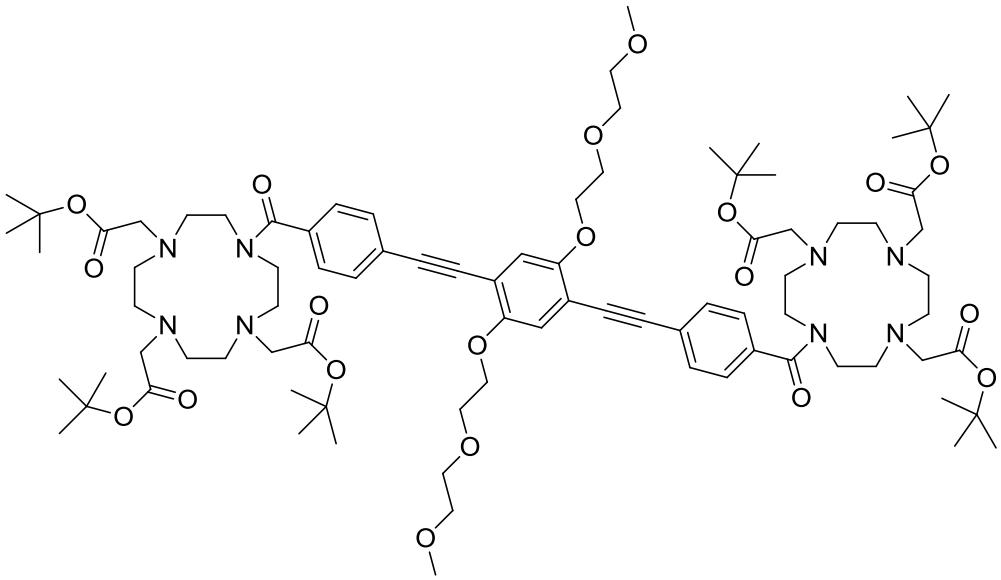

OPE-diCO_2H **165** (23.5 mg, 0.039 mmol, 1.0 eq) and tri-^{t}Bu-DO3A **186** (50.0 mg, 0.097 mmol, 2.5 eq) were dissolved in dry DMF (1 mL). HOBt•H_2O (17.9 mg, 0.117 mmol, 3.0 eq) and DCC (24.1 mg, 0.117 mmol, 3.0 eq) were added, the resulting mixture was stirred at rt for 24h and concentrated. Column chromatography (SiO_2, 95:5 to 90:10 DCM/MeOH) afforded protected bis-DO3A **187** (36.6 mg, 0.023 mmol, 59%) as a yellow solid.

Molecular formula: $C_{86}H_{130}N_8O_{20}$
MW: 1596 g.mol^{-1}
^{1}H-NMR ($CDCl_3$, 300 MHz): δ 7.53 (d, *J* = 7.9 Hz, 4H), 7.37 (d, *J* = 7.9 Hz, 4H), 7.05 (s, 2H), 4.22 (t, *J* = 4.9 Hz, 4H), 3.92 (t, *J* = 4.9 Hz, 4H), 3.83–3.71 (m, 8H), 3.67–3.58 (m, 4H), 3.58–3.61 (m, 4H), 3.36 (s, 6H), 3.34–3.26 (m, 8H), 3.15–3.06 (m, 4H), 3.06–2.98 (m, 4H), 2.97–2.87 (m, 4H), 2.85–2.71 (m, 12H), 2.71–2.61 (m, 4H), 1.45 (br s, 54H).
^{13}C-NMR ($CDCl_3$, 75 MHz): δ 171 (C_q, numerous peaks), 153.8 (C_q), 131.8 (CH), 131.7 (CH), 131.7 (CH), 126.8 (CH), 117.7 (CH), 81 (C_q, numerous peaks), 72.2 (CH_2), 71.2 (CH_2), 69.9 (CH_2), 69.8 (CH_2), 59.2 (CH_3), 59–44 (CH_2, numerous peaks), 28.3 (CH_3).
HRMS (ESI): *m/z* = 1595.9573 $[M+H]^+$ (found), 1595.9474 calcd. for $C_{86}H_{131}N_8O_{20}^+$, 1617.9400 $[M+Na]^+$ (found), 1617.9294 calcd. for $C_{86}H_{130}N_8NaO_{20}^+$.

Bis-DO3A-OPE (**188**)

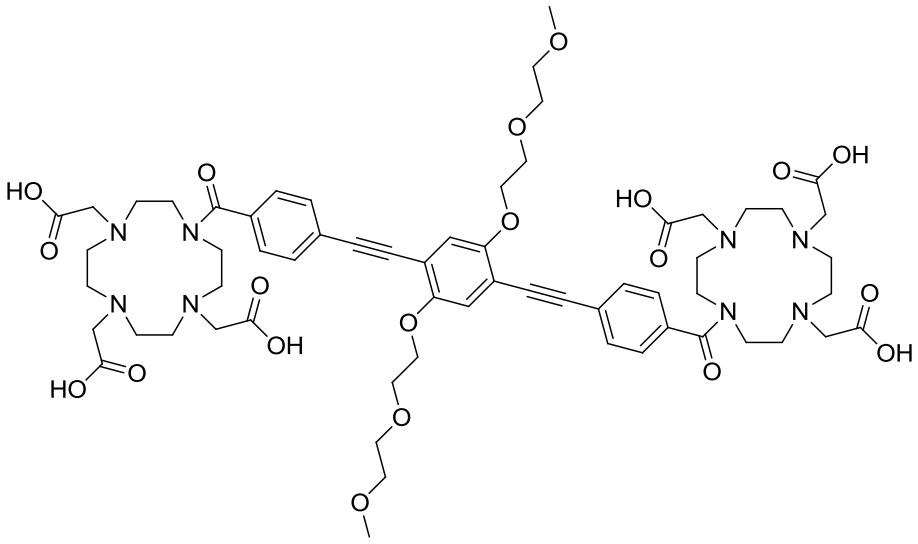

Protected bis-DO3A **187** (47.0 mg, 0.029 mmol, 1.0 eq) was dissolved in dry DCM (2 mL). The resulting solution was cooled to 0 °C and TFA (2 mL) was added dropwise. The resulting mixture was allowed to warm to rt for 15 h, concentrated without heating, redissolved in MeOH and concentrated again. The residue was dissolved again in MeOH, precipitated by slow addition of Et_2O, filtered and dried. The crude product was purified by reversed-phase preparative HPLC (0 to 50% MeCN) to afford Bis-DO3A-OPE **188** as a pale yellow solid.

Molecular formula: $C_{62}H_{82}N_8O_{20}$
MW: 1259.4 g.mol^{-1}
MALDI-TOF MS (HCCA): 1259.35 $[M+H]^+$ (found), 1259.57 calcd. for $C_{62}H_{83}N_8O_{20}^+$.

2-phenylpropan-2-yl 2-bromoacetate (**196**)

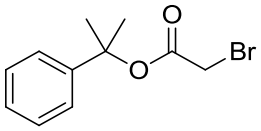

Bromoacetic acid (10.0 g, 72 mmol, 1.0 eq) and 2-phenyl-2-propanol **195** (14.8 g, 109 mmol, 1.5 eq) were dissolved in DCM (100 mL). DMAP (880 mg, 7.2 mmol, 0.1 eq) was added and the resulting mixture was cooled to 0 °C. DCC (15.2 g, 74 mmol, 1.03 eq) was added portionwise and the resulting suspension was allowed to warm to rt for 3 h, filtered and washed with DCM. The filtrate was washed with aq. 0.5 M HCl (2×) and sat. aq. $NaHCO_3$ (1×). The organic layer was dried over Na_2SO_4, filtered and concentrated. Column chromatography (SiO_2, 95:5 Cy/AcOEt) afforded **196** (10.82 g, 42.1 mmol, 58%) as a yellow oil.

Molecular formula: $C_{11}H_{13}BrO_2$
MW: 257.1 g.mol^{-1}
^{1}H-NMR ($CDCl_3$, 300 MHz): δ 7.47–7.24 (m, 5H), 3.80 (s, 2H), 1.84 (s, 6H).
^{13}C-NMR ($CDCl_3$, 100 MHz): δ 165.1 (C_q), 144.6 (C_q), 128.1 (CH), 127.0 (CH), 123.9 (CH), 83.4 (C_q), 28.0 (CH_3), 27.0 (CH_2).
HRMS (ESI): *m/z* = 278.9992 $[M+Na]^+$ (found), 278.9991 calcd. for $C_{11}H_{13}BrNaO_2^+$.

Tris(2-phenylpropan-2-yl) 2,2',2''-(1,4,7,10-tetraazacyclododecane-1,4,7-triyl)triacetate

(tri-Pp-DO3A **198**)

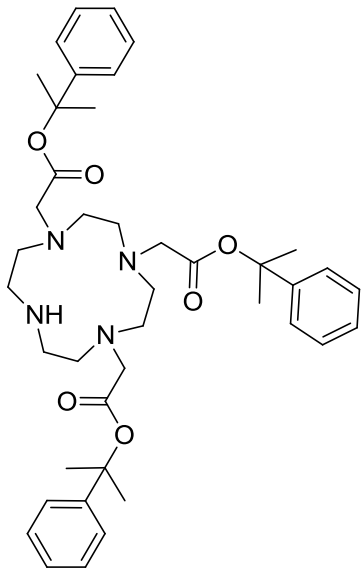

Cyclen **197** (2.41 g, 14 mmol, 1.0 eq) was dissolved in MeCN (150 mL). The resulting solution was cooled to 0 °C and $NaHCO_3$ (3.53 g, 42 mmol, 3.0 eq) was added. Compound **196** (10.8 g, 42 mmol, 3.0 eq) dissolved in MeCN (40 mL) was added dropwise (≈ 30 min). The resulting suspension was allowed to warm to rt for 15 h and concentrated. DCM was added and the mixture was washed with H_2O (1×) and sat. aq. NaCl (1×). The organic layer was dried over Na_2SO_4, filtered and concentrated. Column chromatography (SiO_2, 98:2 to 95:5 DCM/MeOH) afforded tri-Pp-DO3A **198** (2.21 g, 3.15 mmol, 23%) as a light brown foam.

Molecular formula: $C_{41}H_{56}N_4O_6$
MW: 700.9 g.mol^{-1}
^{1}H-NMR ($CDCl_3$, 300 MHz): δ 9.82 (s, 1H), 7.37–7.20 (m, 15H), 3.40–3.35 (m, 4H), 3.31 (s, 2H), 3.06–2.97 (m, 4H), 2.85–2.72 (m, 12H), 1.78 (s, 12H), 1.77 (s, 6H).
^{13}C-NMR ($CDCl_3$, 100 MHz): δ 170.3 (C_q), 169.3 (C_q), 145.4 (C_q), 145.2 (C_q), 128.5 (CH), 127.5 (CH), 127.4 (CH), 124.4 (CH), 124.4 (CH), 82.9 (C_q), 82.8 (C_q), 57.9 (CH_2), 52.1 (CH_2), 51.8 (CH_2), 49.7 (CH_2), 49.3 (CH_2), 47.3 (CH_2), 28.8 (CH_3), 28.8 (CH_3).
HRMS (ESI): *m/z* = 701.4315 $[M+H]^+$ (found), 701.4273 calcd. for $C_{41}H_{57}N_4O_6^+$, 723.4096 $[M+Na]^+$ (found), 723.4092 calcd. for $C_{41}H_{56}N_4NaO_6^+$, 583.3486 $[M+2H-Pp]^+$ (found), 583.3490 calcd. for $C_{32}H_{47}N_4O_6^+$, 465.2698 $[M+3H-2Pp]^+$ (found), 465.2708 calcd. for $C_{23}H_{37}N_4O_6^+$, 347.1915 $[M+4H-3Pp]^+$ (found), 347.1925 calcd. for $C_{14}H_{27}N_4O_6^+$.

General procedure H: Synthesis of dibromo-OPE linkers

An $OPE_n diNH_2$ (**163**, **171** or **172**) (1.0 eq) was dissolved in dry DCM. The resulting solution was cooled to 0 °C, and TEA (2.5 eq) was added, followed by bromoacetyl bromide (2.5 eq) dissolved in dry DCM dropwise. The resulting mixture was allowed to warm to rt for 3 h and washed with sat. aq. $NaHCO_3$ (1×) and sat. aq. NaCl (1×). The organic layer was dried over Na_2SO_4, filtered and concentrated. Column chromatography afforded the corresponding dibromo-OPE linker.

***N*,*N'*-(((2,5-Bis(2-(2-methoxyethoxy)ethoxy)-1,4-phenylene)bis(ethyne-2,1-diyl))bis(4,1-phenylene))bis(2-bromoacetamide)** (**190**)

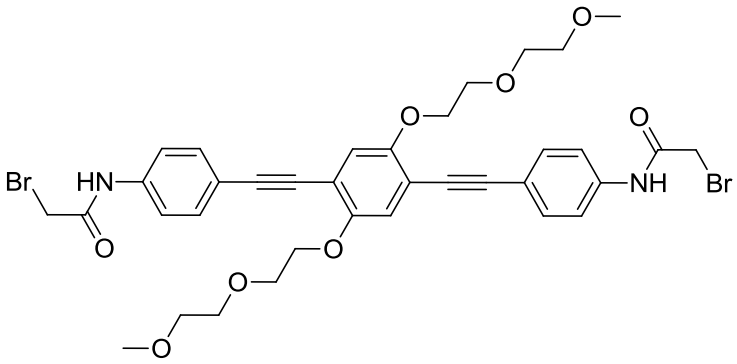

Using the general procedure H with OPEdiNH$_2$ **163** (798 mg, 1.465 mmol), TEA (496 µL, 3.66 mmol) and bromoacetyl bromide (319 µL, 3.66 mmol, dissolved in 3 mL dry DCM) in dry DCM (20 mL), **190** (459 mg, 0.584 mmol, 40%) was obtained after column chromatography (SiO_2, 40:60 to 20:80 Cy/AcOEt) as a pale yellow solid.

Molecular formula: $C_{36}H_{38}Br_2N_2O_8$
MW: 786.5 g.mol^{-1}
^{1}H-NMR (CDCl$_3$, 300 MHz): δ 8.17 (s, 2H), 7.59–7.48 (m, 8H), 7.03 (s, 2H), 4.22 (t, *J* = 4.8 Hz, 4H), 4.04 (s, 4H), 3.93 (t, *J* = 4.8 Hz, 4H), 3.83–3.78 (m, 4H), 3.57–3.52 (m, 4H), 3.37 (s, 6H).
^{13}C-NMR (CDCl$_3$, 75 MHz): δ 163.4 (C_q), 153.7 (C_q), 137.1 (C_q), 132.6 (CH), 120.1 (C_q), 119.7 (CH), 117.6 (CH), 114.3 (C_q), 94.7 (C_q), 86.0 (C_q), 72.2 (CH_2), 71.2 (CH_2), 69.9 (CH_2), 69.8 (CH_2), 59.2 (CH_3), 29.6 (CH_2).
HRMS (ESI): *m/z* = 809.0859 $[M+Na]^+$ (found), 809.0867 calcd. for $C_{36}H_{38}Br_2N_2NaO_8^+$.

***N*,*N*′-((((1,4-Phenylenebis(ethyne-2,1-diyl))bis(2,5-bis(2-(2-methoxyethoxy)ethoxy)-4,1-phenylene))bis(ethyne-2,1-diyl))bis(4,1-phenylene))bis(2-bromoacetamide)** (**191**)

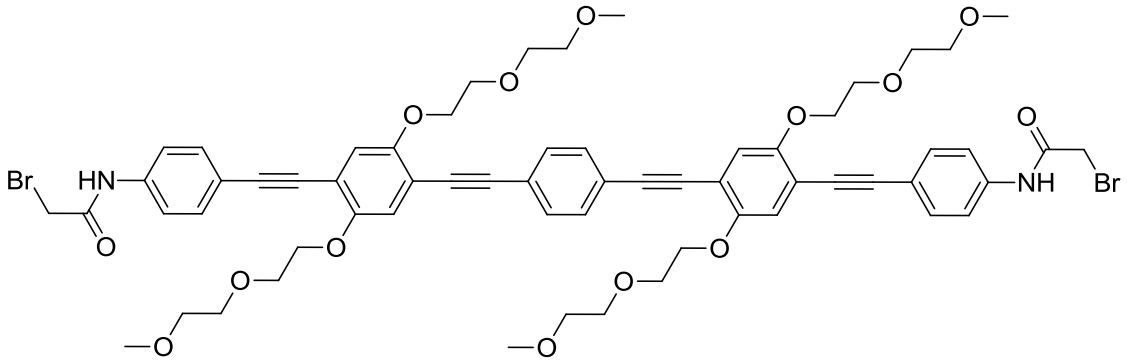

Using the general procedure H with OPE$_2$-diNH$_2$ **171** (231 mg, 0.235 mmol), TEA (78 µL, 0.588 mmol) and bromoacetyl bromide (51 µL, 0.588 mmol, dissolved in 3 mL dry DCM) in dry DCM (3 mL), **191** (192 mg, 0.156 mmol, 66%) was obtained after column chromatography (SiO_2, 20:80 Cy/AcOEt to 100% AcOEt) as a yellow solid.

Molecular formula: $C_{62}H_{66}Br_2N_2O_{14}$
MW: 1223.0 g.mol^{-1}
^{1}H-NMR (CDCl$_3$, 300 MHz): δ 8.26 (s, 2H), 7.58–7.47 (m, 12H), 7.04 (s, 2H), 7.03 (s, 2H), 4.24–4.18 (m, 8H), 4.02 (s, 4H), 3.95–3.90 (m, 8H), 3.83–3.78 (m, 8H), 3.58–3.52 (m, 8H), 3.37 (s, 6H), 3.36 (s, 6H).
^{13}C-NMR (CDCl$_3$, 75 MHz): δ 163.6, 153.8, 153.7, 137.2, 132.6, 131.6, 123.4, 120.0, 119.7, 117.6, 117.5, 114.6, 114.1, 94.9, 94.9, 88.0, 86.0, 72.2, 71.2, 71.1, 69.9, 69.8, 69.8, 59.2, 29.5.

HRMS (ESI): *m/z* = 1243.2746 $[M+Na]^+$ (found), 1243.2773 calcd. for $C_{62}H_{66}Br_2N_2NaO_{14}^+$.

***N*,*N*'-(((((((2,5-Bis(2-(2-methoxyethoxy)ethoxy)-1,4-phenylene)bis(ethyne-2,1-diyl))bis(4,1-phenylene))bis(ethyne-2,1-diyl))bis(2,5-bis(2-(2-methoxyethoxy)ethoxy)-4,1-phenylene))bis(ethyne-2,1-diyl))bis(4,1-phenylene))bis(2-bromoacetamide)** (**192**)

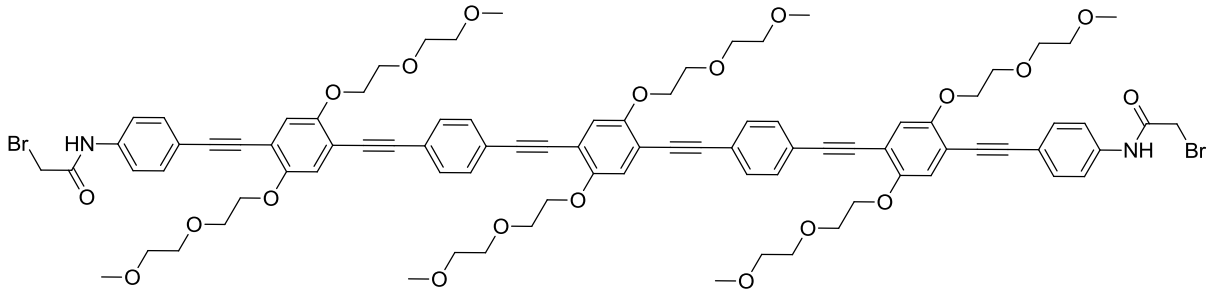

Using the general procedure H with OPE_3-diNH_2 (**172**) (102 mg, 0.072 mmol), TEA (24 µL, 0.18 mmol) and bromoacetyl bromide (16 µL, 0.18 mmol, dissolved in 1 mL dry DCM) in dry DCM (2 mL), **192** (76 mg, 0.05 mmol, 69%) was obtained after column chromatography (SiO_2, 10:90 Cy/AcOEt to 100% AcOEt to 98:2 AcOEt/MeOH) as a yellow solid.

Molecular formula: $C_{88}H_{94}Br_2N_2O_{20}$
MW: 1659.5 g.mol^{-1}
^{1}H-NMR ($CDCl_3$, 300 MHz): δ 8.25 (s, 2H), 7.59–7.47 (m, 16H), 7.05 (s, 2H), 7.04 (s, 2H), 7.04 (s, 2H), 4.26–4.18 (m, 12H), 4.02 (s, 4H), 3.97–3.89 (m, 12H), 3.84–3.77 (m, 12H), 3.59–3.52 (m, 12H), 3.37 (s, 12H), 3.37 (s, 6H).
^{13}C-NMR ($CDCl_3$, 75 MHz): δ 163.5, 153.8, 153.7, 137.2, 132.6, 131.6, 123.4, 123.4, 120.1, 119.7, 117.6, 117.6, 114.6, 114.4, 114.1, 95.1, 94.9, 94.9, 88.0, 88.0, 86.0, 72.2, 71.2, 69.9, 69.8, 69.8, 69.8, 59.2, 29.6.
HRMS (ESI): *m/z* = 1682.4680 $[M+Na]^+$ (found), 1682.4650 calcd. for $C_{88}H_{94}Br_2N_2NaO_{20}^+$, 851.2285 $[M+2Na]^{2+}$ (found), 851.2276 calcd. for $C_{88}H_{94}Br_2N_2Na_2O_{20}^{2+}/2$.

General procedure I: Synthesis of protected bis-DOTA platforms

Linkers **190**, **191** or **192** (1.0 eq) and a DO3A derivative (tri-^{t}Bu-DO3A **186** or tri-Pp-DO3A **198**) (2.5 eq) were mixed in dry MeCN. K_2CO_3 (10.0 eq) was added, and the resulting mixture was heated at 60 °C for 15 h and concentrated. DCM was added and the mixture was washed with H_2O (1×) and sat. aq. NaCl (1×). The combined organic layers were dried over Na_2SO_4, filtered and concentrated. Column chromatography afforded the corresponding protected bis-DOTA-OPE_n as a yellow solid.

^{t}Bu-protected bis-DOTA-OPE_1 (**189**)

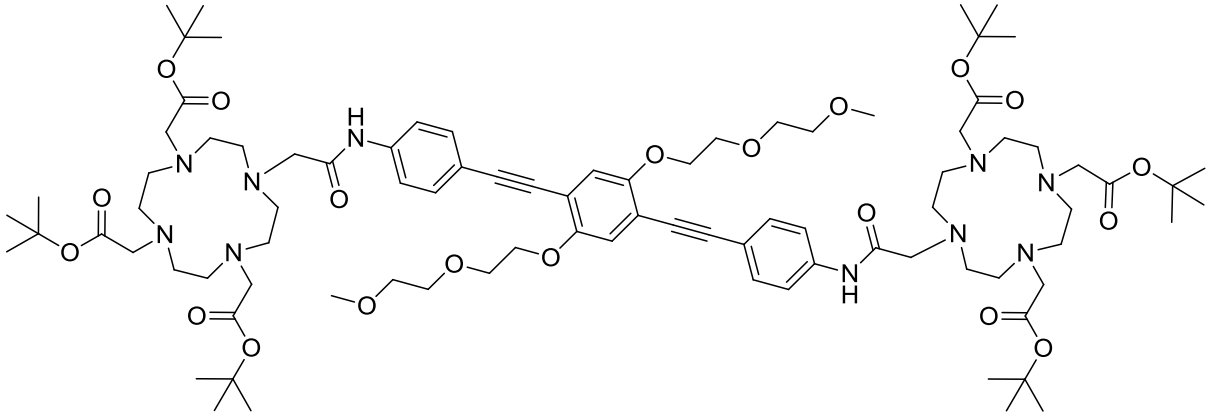

Using the general procedure I with linker **190** (55 mg, 0.07 mmol), tri-^{t}Bu-DO3A **186** (100 mg, 0.174 mmol) and K_2CO_3 (96 mg, 0.7 mmol) in dry MeCN (10 mL), ^{t}Bu-protected bis-DOTA-OPE$_1$ **189** (96 mg, 0.058 mmol, 83%) was obtained after column chromatography (SiO_2, 90:10 to 80:20 DCM/MeOH).
Alternative method: Tri-^{t}Bu-DOTA **146** (50.0 mg, 0.087 mmol, 2.5 eq) and HATU (35.7 mg, 0.094 mmol, 2.7 eq) were dissolved in dry DMF (1 mL). The resulting solution was stirred at rt for 10 min and OPE-diNH$_2$ **163** (19.0 mg, 0.035 mmol, 1.0 eq) was added. The resulting solution was stirred at rt for 15 min and DIPEA (36 µL, 0.209 mmol, 6.0 eq) was added. The resulting mixture was stirred at rt for 15 h and concentrated. DCM was added and the mixture was washed with H_2O (1×) and sat. aq. NaCl (1×). The organic layer was dried over Na_2SO_4, filtered and concentrated. Column chromatography (SiO_2, 95:5 to 80:20 DCM/MeOH) afforded ^{t}Bu-protected bis-DOTA-OPE$_1$ **189** (19 mg, 0.0115 mmol, 33%) as a yellow solid.

Molecular formula: $C_{88}H_{136}N_{10}O_{20}$
MW: 1654.1 g.mol^{-1}
^{1}H-NMR (CDCl$_3$, 300 MHz): δ 11.49 (s, 2H), 7.97 (d, *J* = 8.5 Hz, 4H), 7.34 (d, *J* = 8.5 Hz, 4H), 7.01 (s, 2H), 4.19 (t, *J* = 5.0 Hz, 4H), 3.91 (t, *J* = 5.0 Hz, 4H), 3.83–3.78 (m, 4H), 3.75 (s, 4H), 3.55–3.50 (m, 4H), 3.34 (s, 6H), 3.30–1.85 (m, 44H), 1.48 (s, 18H), 1.43 (s, 36H).
^{13}C-NMR (CDCl$_3$, 75 MHz): δ 172.34 (C_q), 171.6 (C_q), 153.6 (C_q), 140.1 (C_q), 131.8 (CH), 120.2 (CH), 117.6 (C_q), 114.5 (C_q), 95.9 (C_q), 84.7 (C_q), 82.4 (C_q), 82.2 (C_q), 72.2 (CH_2), 71.2 (CH_2), 69.9 (CH_2), 69.9 (CH_2), 59.1 (CH_3), 57.0 (CH_2), 55.9 (CH_2), 55.8 (CH_2), 51.3 (CH_2), 28.2 (CH_3), 28.1(CH_3).
HRMS (ESI): *m/z* = 1675.9832 [M+Na]$^+$ (found), 1675.9825 calcd. for $C_{88}H_{136}N_{10}NaO_{20}^+$.

^{t}Bu-protected bis-DOTA-OPE$_2$ (**193**)

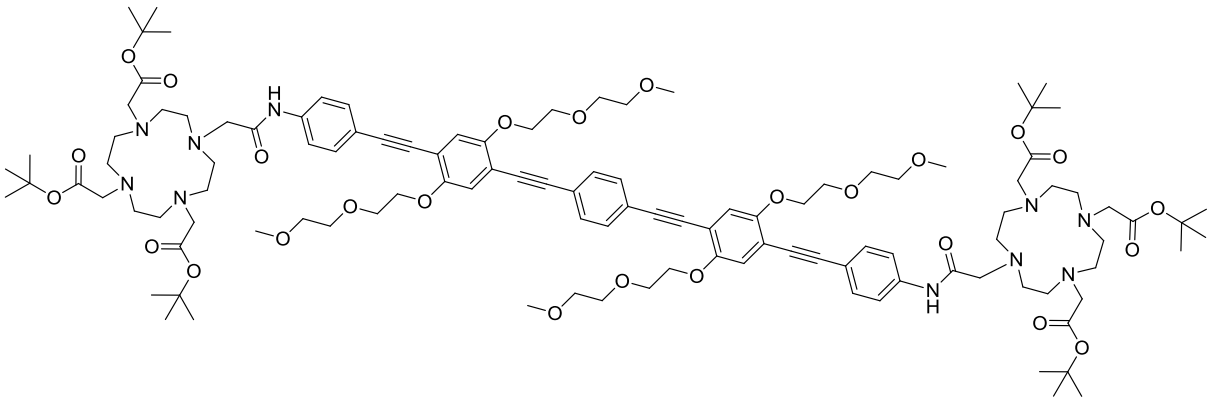

Using the general procedure I with linker **191** (69 mg, 0.056 mmol), tri-^{t}Bu-DO3A **186** (80 mg, 0.14 mmol) and K_2CO_3 (77 mg, 0.56 mmol) in dry MeCN (8 mL), ^{t}Bu-protected bis-DOTA-OPE$_2$ **193** (100 mg, 0.048 mmol, 85%) was obtained after column chromatography (SiO_2, 95:5 to 85:15 DCM/MeOH).

Molecular formula: $C_{114}H_{164}N_{10}O_{26}$
MW: 2090.6 g.mol^{-1}
^{1}H-NMR (CDCl$_3$, 300 MHz): δ 11.41 (s, 2H), 7.96 (d, *J* = 8.4 Hz, 4H), 7.48 (s, 4H), 7.34 (d, *J* = 8.4 Hz, 4H), 7.02 (s, 2H), 7.01 (s, 1H), 4.23–4.15 (m, 8H), 3.95–3.87 (m, 8H), 3.82–3.76 (m, 8H), 3.71 (s, 4H), 3.56–3.48 (m, 8H), 3.35 (s, 6H), 3.33 (s, 6H), 3.25–1.75 (m, 44H), 1.46 (s, 18H), 1.42 (s, 36H).
^{13}C-NMR (CDCl$_3$, 75 MHz): δ 172.4 (C_q), 171.6 (C_q), 153.8 (C_q), 153.6 (C_q), 153.6 (C_q), 140.1 (C_q), 132.2 (C_q), 131.8 (CH), 131.6 (CH), 123.4 (C_q), 123.4 (C_q), 120.1 (CH), 117.6 (CH), 117.6 (CH), 117.5 (CH), 117.3 (C_q), 115.3 (C_q), 113.8 (C_q), 113.6 (C_q), 96.3 (C_q), 95.7 (C_q), 94.7 (C_q), 88.0 (C_q), 85.3 (C_q), 84.6 (C_q), 82.3 (C_q), 82.3 (C_q), 82.1 (C_q), 72.2 (CH_2), 72.1 (CH_2), 71.2 (CH_2), 71.2 (CH_2), 69.9 (CH_2), 69.9 (CH_2), 69.8 (CH_2), 69.7 (CH_2), 59.2 (CH_3), 59.1 (CH_3), 57.0 (CH), 55.9 (C_q), 55.8 (C_q), 53.5–51 (CH_2, broad cluster), 50.5–47.5 (CH_2, broad cluster), 28.3 (CH_3), 28.2 (CH_3), 28.1 (CH_3), 28.1 (CH_3).
HRMS (ESI): *m/z* = 1045.5963 $[M+2H]^{2+}$ (found), 1045.5982 calcd. for $C_{114}H_{166}N_{10}O_{26}^{2+}$/2, 1056.5870 $[M+H+Na]^{2+}$ (found), 1056.5892 calcd. for $C_{114}H_{165}N_{10}NaO_{26}^{2+}$/2, 1068.0794 $[M+2Na]^{2+}$ (found), 1068.0794 calcd. for $C_{114}H_{164}N_{10}Na_2O_{26}^{2+}$/2, 705.0633 $[M+2H+Na]^{3+}$ (found), 705.0630 calcd. for $C_{114}H_{166}N_{10}NaO_{26}^{2+}$/3, 712.3912 $[M+H+2Na]^{3+}$ (found), 712.3903 calcd. for $C_{114}H_{165}N_{10}Na_2O_{26}^{2+}$/3, 719.7189 $[M+3Na]^{3+}$ (found), 719.7176 calcd. for $C_{114}H_{164}N_{10}Na_3O_{26}^{3+}$/3.

^{t}Bu-protected bis-DOTA-OPE$_3$ (194)

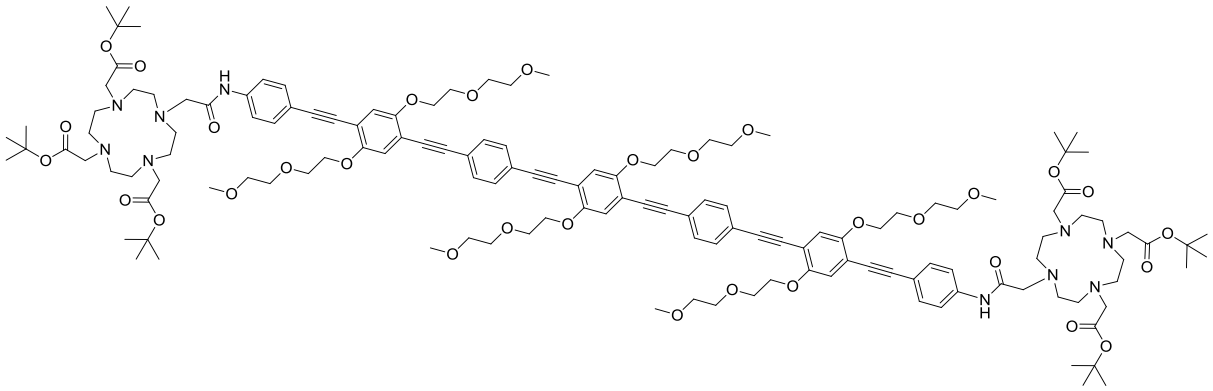

Using the general procedure I with linker **192** (61 mg, 0.037 mmol), tri-^{t}Bu-DO3A **186** (53 mg, 0.092 mmol) and K_2CO_3 (51 mg, 0.37 mmol) in dry MeCN (4 mL), ^{t}Bu-protected bis-DOTA-OPE$_3$ **194** (59 mg, 0.023 mmol, 63%) was obtained after column chromatography (SiO_2, 95:5 to 90:10 DCM/MeOH).

Molecular formula: $C_{140}H_{192}N_{10}O_{32}$
MW: 2527.1 g.mol^{-1}
^{1}H-NMR (CDCl$_3$, 300 MHz): δ 11.38 (s, 2H), 7.96 (d, *J* = 8.4 Hz, 4H), 7.50 (s, 8H), 7.35 (d, *J* = 8.4 Hz, 4H), 7.05 (s, 2H), 7.03 (s, 2H), 7.02 (s, 2H), 4.25–4.17 (m, 12H), 3.97–3.89 (m, 12H), 3.83–3.77 (m, 12H), 3.72 (s, 4H), 3.58–3.50 (m, 12H), 3.25–1.90 (m, 44H), 1.47 (s, 18H), 1.43 (s, 36H).
^{13}C-NMR (CDCl$_3$, 75 MHz): δ 172.3 (C_q), 171.6 (C_q), 153.8 (C_q), 153.6 (C_q), 140.1 (C_q), 131.8 (CH), 131.6 (CH), 123.5 (C_q), 123.3 (C_q), 120.1 (CH), 117.6 (CH), 117.6 (CH), 117.6 (CH), 117.5 (CH), 117.2 (C_q), 115.3 (C_q), 114.4 (C_q), 114.4 (C_q), 113.5 (C_q), 96.4 (C_q), 95.1 (C_q), 94.7 (C_q), 88.1 (C_q), 87.9 (C_q), 84.5 (C_q), 82.3 (C_q), 82.2 (C_q), 72.2 (CH_2), 72.1 (CH_2), 71.2 (CH_2), 71.2 (CH_2), 71.2 (CH_2), 69.9 (CH_2), 69.8 (CH_2), 69.8 (CH_2), 69.7 (CH_2), 59.2 (CH_3), 59.1 (CH_3), 57.0 (C_q), 55.9 (C_q), 55.8 (C_q), 54.5–50.5 (CH_2, broad cluster), 50.5–47.5 (CH_2, broad cluster), 28.1 (CH_3), 28.1 (CH_3).

HRMS (ESI): *m/z* = 1285.6752 $[M+2Na]^{2+}$ (found), 1285.6744 calcd. for $C_{140}H_{192}N_{10}Na_2O_{32}^{2+}/2$, 865.1134 $[M+3Na]^{3+}$ (found), 865.1136 calcd. for $C_{140}H_{192}N_{10}Na_3O_{32}^{2+}/3$.

Pp-protected bis-DOTA-OPE$_1$ (**199**)

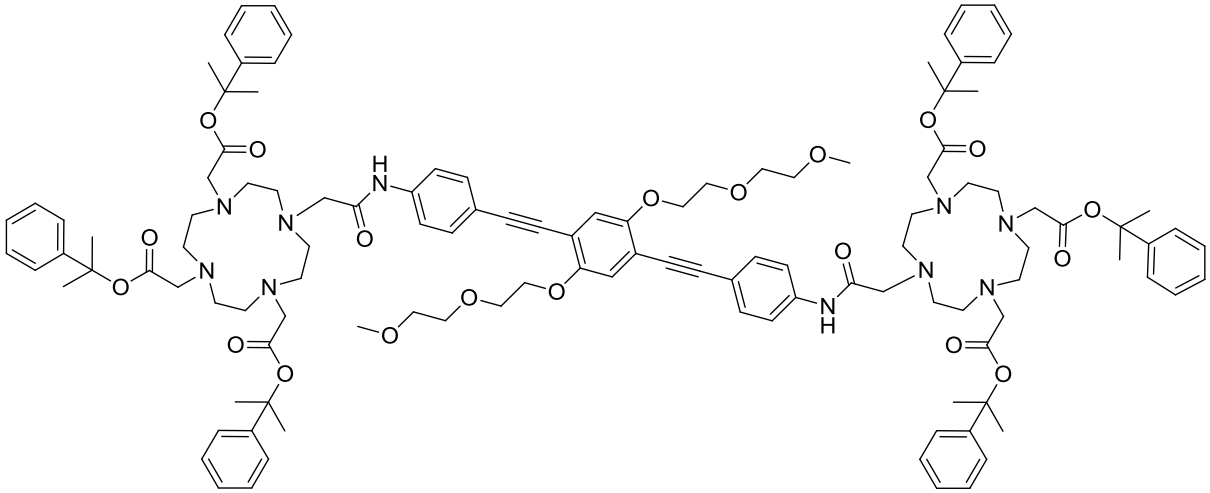

Using the general procedure I with linker **190** (71 mg, 0.09 mmol), tri-Pp-DO3A **198** (161 mg, 0.23 mmol) and K_2CO_3 (124 mg, 0.9 mmol) in dry MeCN (8 mL), Pp-protected bis-DOTA-OPE$_1$ **199** (99 mg, 0.049 mmol, 54%) was obtained after column chromatography (SiO_2, 95:5 to 85:15 DCM/MeOH).

Molecular formula: $C_{118}H_{148}N_{10}O_{20}$
MW: 2026.5 g.mol^{-1}
^{1}H-NMR (CDCl$_3$, 300 MHz): δ 10.95 (s, 2H), 7.91 (d, *J* = 8.4 Hz, 4H), 7.39 (d, *J* = 8.4 Hz, 4H), 7.34–7.08 (m, 30H), 7.04 (s, 2H), 4.21 (t, *J* = 4.9 Hz, 4H), 3.92 (t, *J* = 4.9 Hz, 4H), 3.84–3.76 (m, 4H), 3.56–3.49 (m, 4H), 3.34 (s, 6H), 3.25–1.95 (m, 44H), 1.62 (s, 36H).
^{13}C-NMR (CDCl$_3$, 100 MHz): δ 171.6 (C_q), 171.0 (C_q), 153.6 (C_q), 145.7 (C_q), 140.1 (C_q), 131.8 (CH), 128.4 (CH), 127.2 (CH), 124.2 (CH), 124.1 (CH), 120.1 (CH), 117.6 (CH), 117.4 (C_q), 114.5 (C_q), 95.9 (C_q), 84.8 (C_q), 83.4 (C_q), 83.3 (C_q), 72.2 (CH_2), 71.2 (CH_2), 69.9 (CH_2), 59.1 (CH_3), 56.6 (CH_2), 55.8 (CH_2), 55.7 (CH_2), 54–50.5 (CH_2, broad cluster), 50–47.5 (CH_2, broad cluster), 33–24 (CH_3, broad cluster).
HRMS (ESI): *m/z* = 1035.5329 $[M+2Na]^{2+}$ (found), 1035.5328 calcd. for $C_{118}H_{148}N_{10}Na_2O_{20}^{2+}/2$, 1025.0453 $[M+H+Na]^{2+}$ (found), 1025.0435 calcd. for $C_{118}H_{149}N_{10}NaO_{20}^{2+}/2$.

Pp-protected bis-DOTA-OPE$_2$ (**200**)

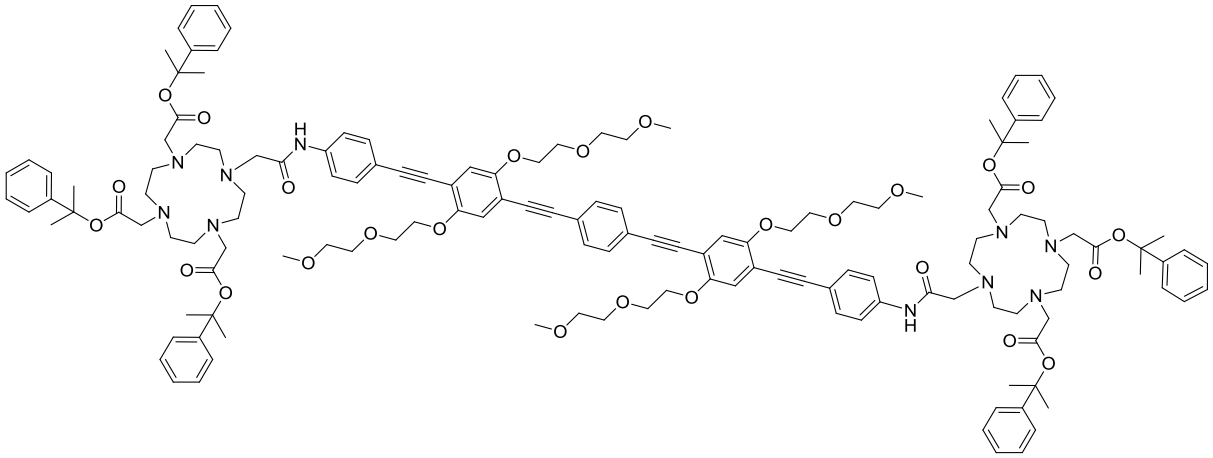

Using the general procedure I with linker **191** (66 mg, 0.054 mmol), tri-Pp-DO3A **198** (95 mg, 0.135 mmol) and K_2CO_3 (75 mg, 0.54 mmol) in dry MeCN (6 mL), Pp-protected bis-DOTA-OPE_2 **200** (65 mg, 0.0264 mmol, 54%) was obtained after column chromatography (SiO_2, 95:5 to 85:15 DCM/MeOH).

Molecular formula: $C_{144}H_{176}N_{10}O_{26}$
MW: 2463.0 g.mol^{-1}
^{1}H-NMR ($CDCl_3$, 300 MHz): δ 10.94 (s, 2H), 7.91 (d, *J* = 8.4 Hz, 4H), 7.50 (s, 4H), 7.40 (s, *J* = 8.4 Hz, 4H), 7.35–7.10 (m, 30H), 7.06 (s, 2H), 7.04 (s, 2H), 4.23 (t, *J* = 4.9 Hz, 8H), 3.94 (t, *J* = 4.9 Hz, 8H), 3.85–3.77 (m, 8H), 3.58–3.51 (m, 8H), 3.37 (s, 6H), 3.35 (s, 6H), 3.15–1.85 (m, 44H), 1.63 (s, 36H).
^{13}C-NMR ($CDCl_3$, 100 MHz): δ 171.6 (C_q), 171.0 (C_q), 153.8 (C_q), 153.6 (C_q), 145.7 (C_q), 140.1 (C_q), 131.8 (CH), 131.6 (CH), 128.5 (CH), 128.4 (CH), 127.2 (CH), 124.4 (CH), 124.3 (CH), 124.1 (CH), 124.1 (CH), 123.4 (C_q), 120.1 (CH), 117.6 (CH), 117.5 (CH), 117.3 (CH), 115.3 (C_q), 113.6 (C_q), 96.3 (C_q), 94.7 (C_q), 88.1 (C_q), 84.7 (C_q), 83.4 (C_q), 83.3 (C_q), 72.2 (CH_2), 72.2 (CH_2), 71.2 (CH_2), 71.2 (CH_2), 69.9 (CH_2), 69.9 (CH_2), 69.7 (CH_2), 59.2 (CH_3), 59.2 (CH_3), 56.6 (CH_2), 55.9–55.6 (C_q, multiple peaks), 53.5–50.5 (CH_2, broad cluster), 50–47.5 (CH_2, broad cluster), 29.8 (CH_3), 28.7 (CH_3).
HRMS (ESI): *m/z* = 1253.6265 $[M+2Na]^{2+}$ (found), 1253.6271 calcd. for $C_{144}H_{176}N_{10}Na_2O_{26}^{2+}/2$, 1242.6363 $[M+H+Na]^{2+}$ (found), 1242.6361 calcd. for $C_{144}H_{177}N_{10}NaO_{26}^{2+}/2$, 843.4142 $[M+3Na]^{3+}$ (found), 843.4145 calcd. for $C_{144}H_{176}N_{10}Na_3O_{26}^{2+}/3$.

Pp-protected bis-DOTA-OPE_3 (**201**)

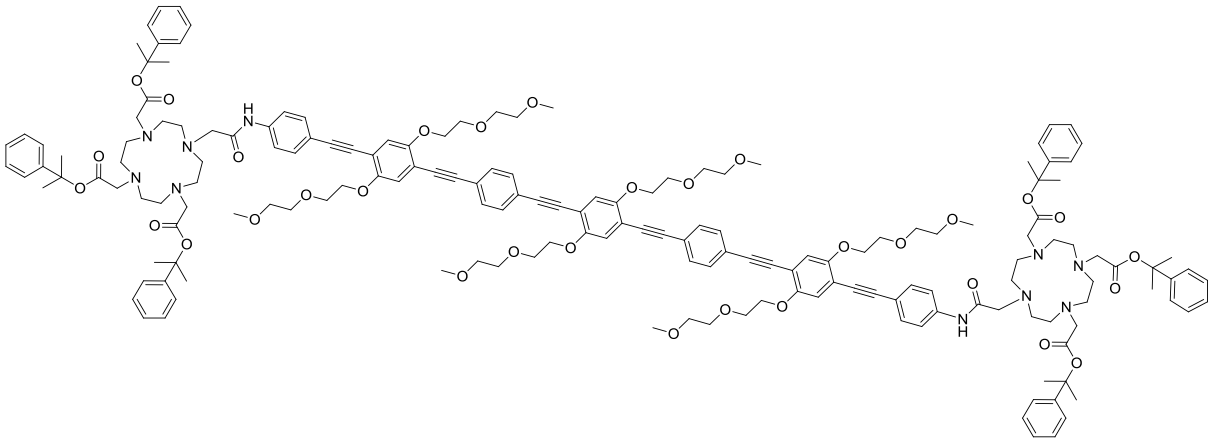

Using the general procedure I with linker **192** (60 mg, 0.036 mmol), tri-Pp-DO3A **198** (56 mg, 0.080 mmol) and K_2CO_3 (50 mg, 0.36 mmol) in dry MeCN (4 mL), Pp-protected bis-DOTA-OPE$_3$ **201** (20 mg, 0.007 mmol, 19%) was obtained after column chromatography (SiO_2, 95:5 to 90:10 DCM/MeOH).

Molecular formula: $C_{170}H_{204}N_{10}O_{32}$
MW: 2899.5 g.mol^{-1}
^{1}H-NMR (CDCl$_3$, 300 MHz): δ 11.01 (s, 2H), 7.92 (d, *J* = 8.4 Hz, 4H), 7.50 (s, 8H), 7.41 (d, *J* = 8.4 Hz, 4H), 7.36–7.10 (m, 30H), 7.06 (s, 2H), 7.05 (s, 2H), 7.04 (s, 2H), 4.23 (t, *J* = 4.8 Hz, 12H), 3.94 (t, *J* = 4.8 Hz, 12H), 3.85–3.77 (m, 12H), 3.58–3.51 (m, 12H), 3.37 (s, 12H), 3.36 (s, 6H), 3.10–1.80 (m, 44H), 1.63 (s, 36H).
^{13}C-NMR (CDCl$_3$, 100 MHz): δ 171.6 (C_q), 171.0 (C_q), 153.8 (C_q), 153.8 (C_q), 153.6 (C_q), 145.7 (C_q), 140.1 (C_q), 131.9 (CH), 131.6 (CH), 129.8 (CH), 128.5 (CH), 128.4 (CH), 128.2 (CH), 127.2 (CH), 124.6 (CH), 124.4 (CH), 124.2 (CH), 124.1 (CH), 123.5 (C_q), 123.3 (C_q), 120.1 (CH), 117.7 (CH), 117.6 (CH), 117.5 (CH), 117.3 (C_q), 115.3 (C_q), 114.4 (C_q), 113.6 (C_q), 96.3 (C_q), 95.1 (C_q), 94.7 (C_q), 88.1 (C_q), 87.9 (Cq), 84.7 (Cq), 72.2 (CH2), 72.2 (CH2), 71.2 (CH2), 71.2 (CH2), 71.2 (CH2), 69.9 (CH2), 69.9 (CH_2), 69.8 (CH_2), 69.7 (CH_2), 68.1 (CH_2), 59.2 (CH_3), 59.2 (CH_3), 56.6 (C_q), 55.9–55.6 (C_q, multiple peaks), 54.5–50.5 (CH_2, broad cluster), 50–47.5 (CH_2, broad cluster), 25.7 (CH_3).
HRMS (ESI): *m/z* = 1471.7348 $[M+2Na]^{2+}$ (found), 1471.7214 calcd. for $C_{170}H_{204}N_{10}Na_2O_{32}^{2+}$/2, 989.1552 $[M+3Na]^{3+}$ (found), 989.1451 calcd. for $C_{170}H_{204}N_{10}Na_3O_{32}^{2+}$/3.

General procedure J: Deprotection of Pp-protected bisDOTA platforms

A Pp-protected bis-DOTA-OPE$_n$ (**199**, **200** or **201**) was dissolved in a mixture of TFA/TIS/DCM (2/2/96, 10 mg.mL^{-1}). The resulting solution was stirred at rt for 4 h and concentrated. MeOH was added, and the product was precipitated by slow addition of Et_2O, filtered and dried. The crude product was purified by preparative HPLC to afford the corresponding bis-DOTA-OPE$_n$ as a yellow solid.

Bis-DOTA-OPE$_1$ (**202**)

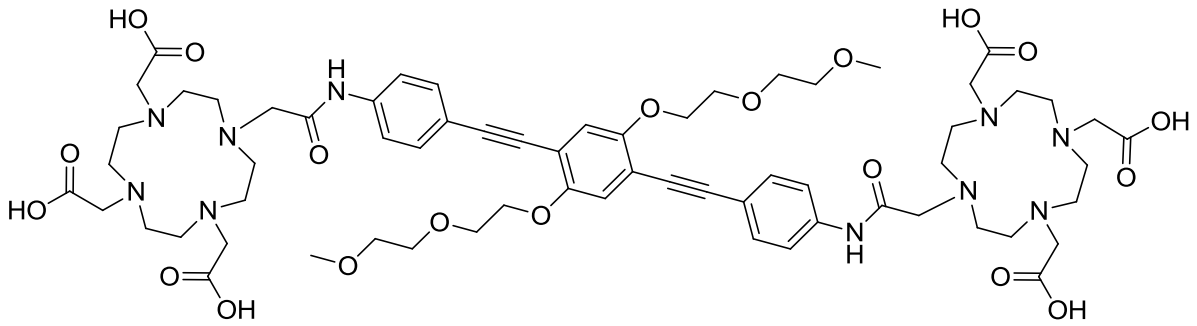

Conditions: 30 to 50% MeCN
Molecular formula: $C_{64}H_{88}N_{10}O_{20}$
MW: 1317.5 g.mol^{-1}
MALDI-TOF MS (HCCA): 1317.43 $[M+H]^+$ (found), 1317.62 calcd. for $C_{64}H_{89}N_{10}O_{20}^+$.

Bis-DOTA-OPE$_2$ (**203**)

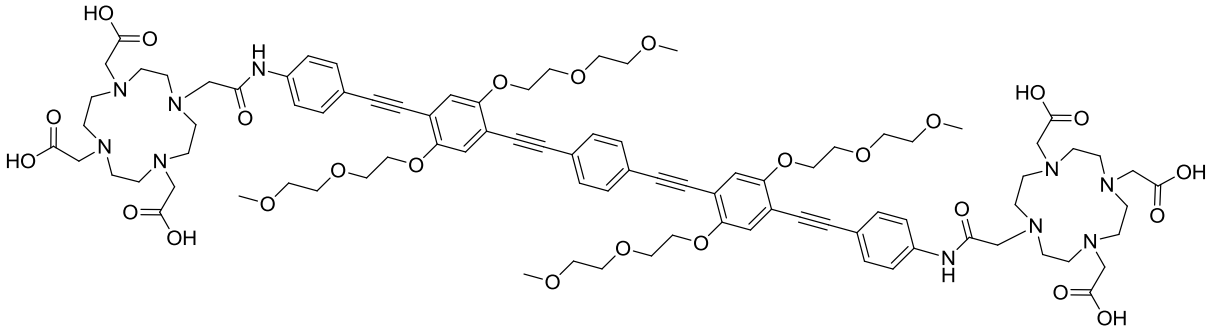

Conditions: 25 to 60% MeCN
Molecular formula: $C_{90}H_{116}N_{10}O_{26}$
MW: 1754.0 g.mol^{-1}
MALDI-TOF MS (HCCA): 1753.72 $[M+H]^+$ (found), 1753.81 calcd. for $C_{90}H_{117}N_{10}O_{26}^+$.

Bis-DOTA-OPE$_3$ (**204**)

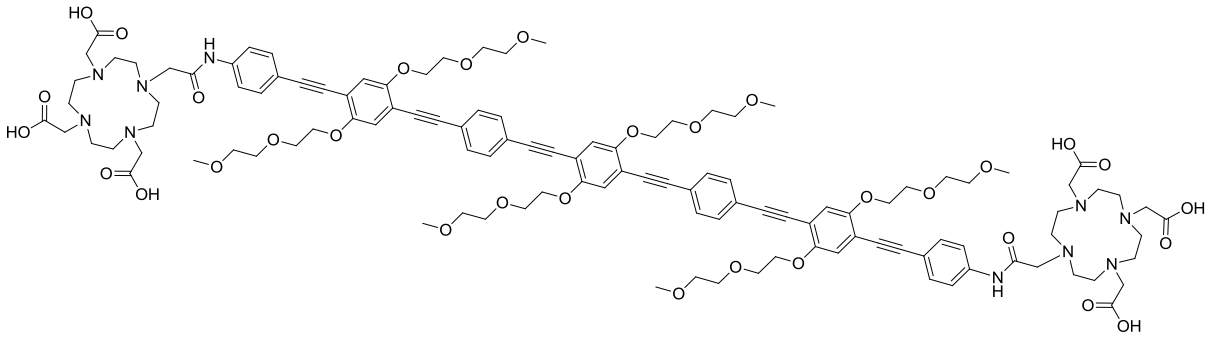

Conditions: 40 to 100% MeCN
Molecular formula: $C_{116}H_{144}N_{10}O_{32}$
MW: 2190.5 g.mol^{-1}
MALDI-TOF MS (HCCA): 2190.10 $[M+H]^+$ (found), 2190.00 calcd. for $C_{116}H_{145}N_{10}O_{32}^+$.

Synthesis of Cys(Pro)$_n$Cys and *(Pro)$_n$Cys (n = 6, 9 or 12)*

Peptides were synthesized according to standard SPPS procedures. Kaiser and Chloranil tests were used to check the coupling efficiencies. Rink Amide MBHA resin was swelled in DCM for 30 min, rinced (3× NMP, 3×DCM, 3×NMP), deprotected (20:80 NMP/piperidine for 1 min, rincing, 20:80 NMP/piperidine for 15 min) and rinced again. The first coupling step was realized with Fmoc-Cys(Trt)-OH (3.1 eq), HATU (3.0 eq) and DIPEA (6.0 eq) in NMP (aminoacid concentration: 120 mg.mL^{-1}) for 2.5 h, after which the resin was rinced, deprotected and rinced again. The next coupling steps were realized with Fmoc-Pro•H_2O-OH (4.1 eq), HBTU (4.0 eq) and DIPEA (8.0 eq) in NMP (aminoacid concentration: 70 mg.mL^{-1}) for 30 min, after which the resin was rinced, deprotected and rinced again. This coupling/rincing/deprotection/rincing sequence was repeated 6, 9 or 12 times. In each case, when the adequate number of prolines was reached, the last coupling step (with Cys) was performed on a determined fraction of the resin using the same conditions as the initial Cys coupling step. The resin was then rinced, deprotected, rinced, and capped (15:85 Ac_2O/DCM) for 30 min. The peptide was cleaved from the resin (degassed 2.5:2.5:2.5:92.5 EDT/TIS/H_2O/TFA for 2 h),

concentrated without heating, precipitated with cold degassed Et_2O, filtered and dried to afford $Cys(Pro)_nCys$ (n = 6, 9, 12) as a white solid.
Alternatively, instead of coupling the last Cys, the peptide was directly cleaved from the resin and precipitated in the same conditions to afford $(Pro)_nCys$ (n = 6, 9, 12) as a white solid.
The efficiency of each coupling step was monitored using color tests on a few beads of the resin. After the introduction of a Cys residue, a Kaiser test (ninhydrin/phenol/KCN) was realized: when the beads are heated, the solution stays yellow when no primary amine is present but turns blue (Ruhemann's purple) when primary amines are still on the beads, indicating that the coupling was incomplete. For secondary amines (after the introduction of a proline residue), a chloranil test (chloranil/acetaldehyde) was performed: a negative result is indicated by a light yellow solution whereas the beads turn dark blue for a positive result (incomplete coupling).

$Cys(Pro)_nCys$

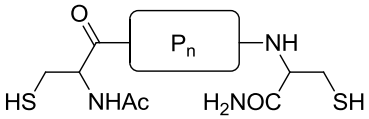

n = 6, 9 or 12

$Cys(Pro)_6Cys$ (**206**, n = 6)

MALDI-TOF MS (HCCA): 870.35 $[M+Na]^+$ (found), 870.36 calcd. for $C_{38}H_{57}N_9NaO_9S_2^+$, 886.32 $[M+K]^+$ (found), 886.34 calcd. for $C_{38}H_{57}KN_9O_9S_2^+$.
HRMS (ESI): *m/z* = 848.3781 $[M+H]^+$ (found), 848.3793 calcd. for $C_{38}H_{58}N_9O_9S_2^+$, 870.3605 $[M+Na]^+$ (found), 870.3613 calcd. for $C_{38}H_{57}N_9NaO_9S_2^+$.

$Cys(Pro)_9Cys$ (**207**, n = 9)

MALDI-TOF MS (HCCA): 1161.57 $[M+Na]^+$ (found), 1161.52 calcd. for $C_{53}H_{78}N_{12}NaO_{12}S_2^+$, 1177.53 $[M+K]^+$ (found), 1177.49 calcd. for $C_{53}H_{78}KN_{12}O_{12}S_2^+$.
HRMS (ESI): *m/z* = 1161.5163 $[M+Na]^+$ (found), 1161.5196 calcd. for $C_{53}H_{78}N_{12}NaO_{12}S_2^+$, 592.2543 $[2M+2Na]^{2+}$ (found), 592.2544 calcd. for $C_{53}H_{78}N_{12}Na_2O_{12}S_2^{2+}/2$.

$Cys(Pro)_{12}Cys$ (**208**, n = 12)

MALDI-TOF MS (HCCA): 1452.73 $[M+Na]^+$ (found), 1452.68 calcd. for $C_{68}H_{99}N_{15}NaO_{15}S_2^+$, 1468.71 $[M+K]^+$ (found), 1468.65 calcd. for $C_{68}H_{99}KN_{15}O_{15}S_2^+$.
HRMS (ESI): *m/z* = 1452.6766 $[M+Na]^+$ (found), 1452.6779 calcd. for $C_{68}H_{99}N_{15}NaO_{15}S_2^+$, 737.8334 $[2M+2Na]^{2+}$ (found), 737.8335 calcd. for $C_{68}H_{99}N_{15}NaO_{15}S_2^{2+}/2$.

$(Pro)_nCys$

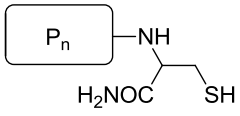

n = 6, 9 or 12

$(Pro)_6Cys$ (**212**, n = 6)

MALDI-TOF MS (HCCA): 703.25 $[M+H]^+$ (found), 703.36 calcd. for $C_{33}H_{51}N_8O_7S^+$, 725.20 $[M+Na]^+$ (found), 725.34 calcd. for $C_{33}H_{50}N_8NaO_7S^+$.
HRMS (ESI): *m/z* = 703.3581 $[M+H]^+$ (found), 703.3596 calcd. for $C_{33}H_{51}N_8O_7S^+$, 725.3402 $[M+Na]^+$ (found), 725.3415 calcd. for $C_{33}H_{50}N_8NaO_7S^+$, 363.1739 $[2M+H+Na]^{2+}$ (found), 363.1744 calcd. for $C_{33}H_{51}N_8NaO_7S^{2+}/2$.

(Pro)$_9$Cys (**213**, n = 9)

MALDI-TOF MS (HCCA): 1016.49 $[M+Na]^+$ (found), 1016.50 calcd. for $C_{48}H_{71}N_{11}NaO_{10}S^+$, 1032.48 $[M+K]^+$ (found), 1032.47 calcd. for $C_{48}H_{71}KN_{11}O_{10}S^+$.
HRMS (ESI): *m/z* = 994.5149 $[M+H]^+$ (found), 994.5179 calcd. for $C_{48}H_{72}N_{11}O_{10}S^+$, 1016.4966 $[M+Na]^+$ (found), 1016.4998 calcd. for $C_{48}H_{71}N_{11}NaO_{10}S^+$, 497.7617 $[2M+2H]^{2+}$ (found), 497.7626 calcd. for $C_{48}H_{73}N_{11}O_{10}S^{2+}/2$, 508.7525 $[2M+H+Na]^{2+}$ (found), 508.7536 calcd. for $C_{48}H_{72}N_{11}NaO_{10}S^{2+}/2$, 519.7436 $[2M+2Na]^{2+}$ (found), 519.7445 calcd. for $C_{48}H_{71}N_{11}Na_2O_{10}S^{2+}/2$.

(Pro)$_{12}$Cys (**214**, n = 12)

MALDI-TOF MS (HCCA): 1307.59 $[M+Na]^+$ (found), 1307.66 calcd. for $C_{63}H_{92}N_{14}NaO_{13}S^+$, 1323.57 $[M+K]^+$ (found), 1323.63 calcd. for $C_{63}H_{92}KN_{14}O_{13}S^+$.
HRMS (ESI): *m/z* = 1285.6843 $[M+H]^+$ (found), 1285.6762 calcd. for $C_{63}H_{93}N_{14}O_{13}S^+$, 1307.6684 $[M+Na]^+$ (found), 1307.6581 calcd. for $C_{63}H_{92}N_{14}NaO_{13}S^+$, 643.3417 $[2M+2H]^{2+}$ (found), 643.3417 calcd. for $C_{63}H_{94}N_{14}O_{13}S^{2+}/2$, 654.3326 $[2M+H+Na]^{2+}$ (found), 654.3327 calcd. for $C_{63}H_{93}N_{14}NaO_{13}S^{2+}/2$, 665.3240 $[2M+2Na]^{2+}$ (found), 665.3237 calcd. for $C_{63}H_{92}N_{14}Na_2O_{13}S^{2+}/2$.

General procedure K: synthesis of DOTA$_2$P$_n$

CysPro$_n$Cys **206**, **207** or **208** (5 µmol, 1 eq) was dissolved in aq. HEPES (200 mM, 1.0 mL, pH 7). TCEP (0.5 M, 20 µL, 10 µmol, 2 eq) was added, and the resulting solution was stirred at rt for 30 min. DOTA-Mal **205** (8.0 mg, 10 µmol, 2 eq) was then added, the strirring was continued for 2 h, and excess TCEP (0.5 M, 10 µL, 5.0 µmol, 1 eq) and DOTA-Mal **205** (16 mg, 20 µmol, 4 eq) were added. The resulting solution was further stirred at rt for 15 h, concentrated and purified by HPLC to afford the corresponding DOTA$_2$P$_n$ as a white solid.

DOTA$_2$P$_6$ (**209,** n = 6)

Using the general procedure K with CysPro$_6$Cys **206** (5.0 mg, 5.9 µmol), DOTA$_2$P$_6$ **209** (6.0 mg, 2.5 µmol, 42%) was obtained.

Molecular formula: $C_{82}H_{125}N_{21}O_{27}S_2$
MW: 1901.2 g.mol^{-1}
HPLC: 4.89 min (10 to 30% MeCN in 10 min, >95%)
MALDI-TOF MS (HCCA): *m/z* = 1901.4 $[M+H]^+$ (found), 1900.9 calcd. for $C_{82}H_{126}N_{21}O_{27}S_2^+$.

DOTA$_2$P$_6$ (**210,** n = 9)

Using the general procedure K with CysPro$_9$Cys **207** (6.0 mg, 5.2 µmol), DOTA$_2$P$_9$ **210** (9.0 mg, 3.4 µmol, 65%) was obtained.

Molecular formula: $C_{97}H_{146}N_{24}O_{30}S_2$
MW: 2192.5 g.mol^{-1}

HPLC: 5.47 min (10 to 30% MeCN in 10 min, >95%)
MALDI-TOF MS (HCCA): *m/z* = 2192.1 $[M+H]^+$ (found), 2192.0 calcd. for $C_{97}H_{147}N_{24}O_{30}S_2^+$.

$DOTA_2P_6$ (**210,** n = 9)

Using the general procedure K with $CysPro_{12}Cys$ **208** (7.3 mg, 5.0 µmol), $DOTA_2P_{12}$ **211** (7.9 mg, 2.7 µmol, 54%) was obtained.

Molecular formula: $C_{112}H_{167}N_{27}O_{33}S_2$
MW: 2483.8 $g.mol^{-1}$
HPLC: 6.06 min (10 to 30% MeCN in 10 min, >95%)
MALDI-TOF MS (HCCA): *m/z* = 2483.3 $[M+H]^+$ (found), 2483.2 calcd. for $C_{112}H_{168}N_{27}O_{33}S_2^+$.

Bis-TEMPO 219

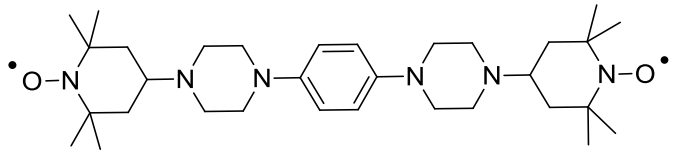

4-oxo-TEMPO **215** (65 mg, 0.381 mmol, 2.0 eq) and $Ti(O^iPr)_4$ (226 µL, 0.762 mmol, 4.0 eq) were stirred at rt for 20 min. PipPhPip **131** (70 mg, 0.286 mmol, 1.5 eq) was added, the resulting mixture was heated at 80 °C for 3 h and cooled to rt. Abs. EtOH (1 mL) and $NaBH_3CN$ (30 mg, 0.476 mmol, 2.5 eq) were added, and the resulting mixture was stirred at rt for 15 h. H_2O was added and the mixture was extracted with DCM (3×). The combined organic layers were dried over Na_2SO_4, filtered and concentrated. Column chromatography (SiO_2, 40:60 Cy/AcOEt to 100% AcOEt to 90:10 AcOEt/MeOH) afforded bis-TEMPO **219** (23 mg, 0.041 mmol, 21%) as an orange solid.

Molecular formula: $C_{32}H_{54}N_6O_2^{2\bullet}$
MW: 554.8 $g.mol^{-1}$
Rf (SiO_2): 0.18 (90:10 AcOEt/MeOH)
HRMS (ESI): *m/z* = 555.4349 $[M+H]^{2\bullet+}$ (found), 555.4381 calcd. for $C_{32}H_{55}N_6O_2^{2\bullet+}$, 577.4176 $[M+Na]^{2\bullet+}$ (found), 577.4200 calcd. for $C_{32}H_{54}N_6NaO_2^{2\bullet+}$.

Bis-TEMPO 220

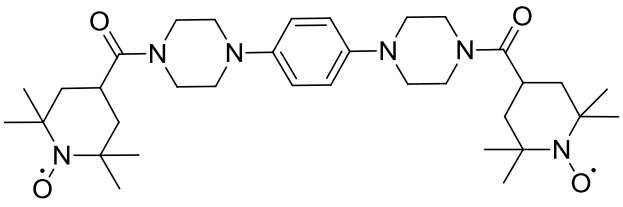

PipPhPip **131** (21.0 mg, 0.086 mmol, 1.0 eq) and 4-CO_2H-TEMPO **217** (37.9 mg, 0.189 mmol, 2.2 eq) were dissolved in dry DMF (1 mL). HOBt•H_2O (28.9 mg, 0.189 mmol, 2.2 eq) and EDC•HCl (39.5 mg, 0.206 mmol, 2.4 eq) were added, followed by DIPEA (43.8 µL, 0.258 mmol, 3.0 eq). The resulting mixture was stirred at rt for 24 h and concentrated. DCM was added and the mixture was washed with H_2O (1×) and sat. aq. NaCl (1×). The organic layer was dried over Na_2SO_4, filtered and concentrated. Column chromatography (SiO_2, 10:90 Cy/AcOEt to 100% AcOEt) afforded bis-TEMPO **220** (27 mg, 0.044 mmol, 51%) as a pale orange solid.

Molecular formula: $C_{34}H_{54}N_6O_4^{2\bullet}$
MW: 610.8 g.mol^{-1}
Rf (SiO_2): 0.16 (100% AcOEt)
HRMS (ESI): *m/z* = 611.4290 $[M+H]^{2\bullet+}$ (found), 611.4279 calcd. for $C_{34}H_{55}N_6O_4^{2\bullet+}$, 633.4119 $[M+Na]^{2\bullet+}$ (found), 633.4099 calcd. for $C_{34}H_{54}N_6NaO_4^{2\bullet+}$.

4-OTf-TEMPO (**221**)

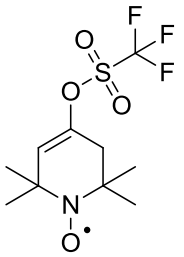

4-oxo-TEMPO **215** (500.0 mg, 2.94 mmol, 1.0 eq) was dissolved in dry THF (10.0 mL). The resulting solution was cooled to -78 °C and LDA (2 M in THF/heptane/ethylbenzene, 3.23 mL, 6.46 mmol, 2.2 eq) was added dropwise, followed by $PhNTf_2$ (1.012 g, 3.08 mmol, 1.05 eq) in THF (5.0 mL) dropwise. The resulting mixture was allowed to warm to rt for 15 h and concentrated. Column chromatography (SiO_2, 90:10 Cy/AcOEt) afforded 4-OTf-TEMPO **221** (435.3 mg, 1.44 mmol, 49%) as a brown oily solid.

Molecular formula: $C_{10}H_{15}F_3NO_4S^{\bullet}$
MW: 302.3 g.mol^{-1}
HPLC: 18.8 min (5 to 100% MeCN in 30 min, 92%)
HRMS: *m/z* = 304.0820 $[M+2H]^{2+}$ (found), 304.0825 calcd. for $C_{10}H_{17}F_3NO_4S^{+}$.

4-OMs-TEMPO (**222**)

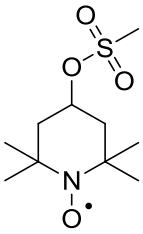

4-OH-TEMPO **216** (500.0 mg, 2.90 mmol, 1.0 eq) was dissolved in pyridine (2.0 mL). The resulting solution was cooled to 0 °C and mesyl chloride (449 µL, 5.80 mmol, 2.0 eq) was added. The resulting mixture was allowed to warm to rt for 6 h, cold sat. aq. Na_2CO_3 was added and the mixture was extracted with DCM (2×). The combined organic layers were washed with sat. aq. Na_2CO_3 (1×) and H_2O (1×), dried over Na_2SO_4, filtered and concentrated to afford 4-OMs-TEMPO **222** (685.0 mg, 2.74 mmol, 94%) as an orange solid.

Molecular formula: $C_{10}H_{20}NO_4S^{\bullet}$
MW: 250.3 g.mol^{-1}
HPLC: 6.63 min (5 to 100% MeCN in 30 min, >95%)
HRMS: *m/z* = 250.1106 $[M]^{+}$ (found), 250.1108 calcd. for $C_{10}H_{20}NO_4S^{+}$.

4-N_3-TEMPO (**223**)

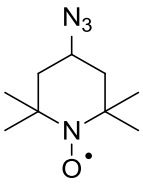

4-OMs-TEMPO **222** (685.0 mg, 2.74 mmol, 1.0 eq) was dissolved in DMF (18 mL). NaN_3 (356.0 mg, 5.47 mmol, 2.0 eq) was added and the resulting mixture was heated at 110 °C for 15 h and concentrated. H_2O was added and the mixture was extracted Et_2O (3×). The combined organic layers were washed with H_2O (2×), dried over Na_2SO_4, filtered and concentrated to afford 4-N_3-TEMPO **223** (370.0 mg, 1.88 mmol, 69%) as orange needles.

Molecular formula: $C_9H_{17}N_4O^{\bullet}$
MW: 197.3 g.mol^{-1}
HPLC: 17.0 min (5 to 100% MeCN in 30 min, 95%)
Rf (SiO_2): 0.38 (100% DCM)
IR: 2095 cm^{-1}

Bis-TEMPO 224

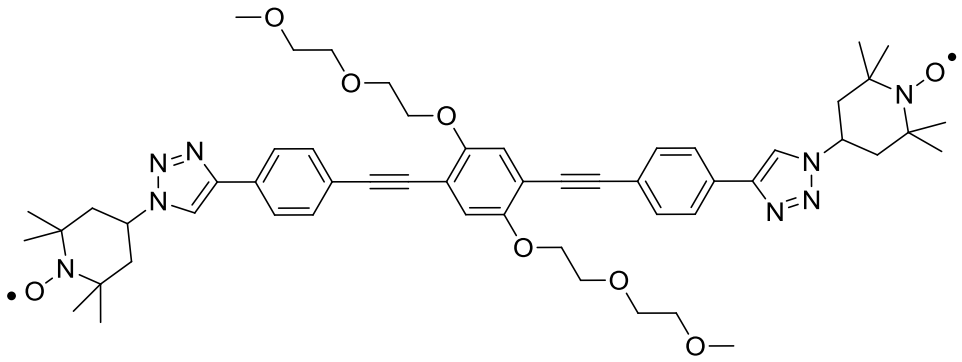

OPE-diCCH **164** (100 mg, 0.178 mmol, 1.0 eq) and 4-N_3-TEMPO **223** (70 mg, 0.355 mmol, 2.0 eq) were dissolved in dry DMSO (5 mL). CuI (27 mg, 0.142 mmol, 0.8 eq) was added, the resulting mixture was heated at 40 °C for 2 h and cooled to rt. H_2O was added and the mixture was extracted with DCM (3×). The combined organic layers were dried over Na_2SO_4, filtered and concentrated. Column chromatography (SiO_2, 30:70 Cy/AcOEt to 100% AcOEt) afforded bis-TEMPO **224** (33 mg, 0.034 mmol, 19%) as a yellow solid.

Molecular formula: $C_{54}H_{68}N_8O_8^{2\bullet}$
MW: 957.2 g.mol^{-1}
^{1}H-NMR ($CDCl_3$, 300 MHz): (all signals broadened and some obscured due to paramagnetism) δ 8.13–7.47 (m, 10H), 7.08 (s, 2H), 4.26 (br s, 4H), 3.97 (br s, 4H), 3.85 (br s, 4H), 3.58 (br s, 4H), 3.39 (s, 6H), 1.59–0.80 (m, 12H).
Rf (SiO_2): 0.76 (90:10 AcOEt/MeOH)
HRMS (ESI): *m/z* = 957.5187 $[M+H]^{2\bullet+}$ (found), 957.5233 calcd. for $C_{54}H_{69}N_8O_8^{2\bullet+}$, 979.5000 $[M+Na]^{2\bullet+}$ (found), 979.5052 calcd. for $C_{54}H_{68}N_8NaO_8^{2\bullet+}$.

Bis-TEMPO-OPE (**225**)

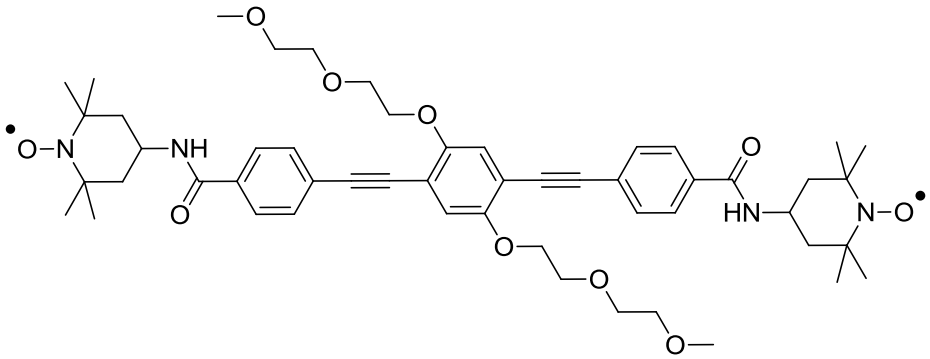

OPE-diCO_2H **165** (57 mg, 0.094 mmol, 1.0 eq) and 4-NH_2-TEMPO **218** (40 mg, 0.234 mmol, 2.5 eq) were dissolved in dry DMF (2 mL). The resulting solution was cooled to 0 °C, HOBt•H_2O (43 mg, 0.282 mmol, 3.0 eq) and DCC (58 mg, 0.282 mmol, 3 eq) were added, and the resulting mixture was stirred at rt for 24 h. H_2O was added and the mixture was extracted with DCM (3×). The combined organic layers were dried over Na_2SO_4, filtered and concentrated. Column chromatography (SiO_2, 30:70 to 20:80 Cy/AcOEt) afforded bis-TEMPO-OPE **226** (79 mg, 0.087 mmol, 93%) as an orange solid.

Molecular formula: $C_{52}H_{68}N_4O_{10}^{2\bullet}$
MW: 909.1 g.mol^{-1}
^{1}H-NMR ($CDCl_3$, 300 MHz): (all signals broadened and some obscured due to paramagnetism) δ 8.05–7.53 (m, 8H), 7.09 (s, 2H), 4.25 (br s, 4H), 3.96 (br s, 4H), 3.82 (br s, 4H), 3.57 (br s, 4H), 3.39 (s, 6H), 2.12–0.79 (m, 32H).
Rf (SiO_2): 0.39 (100% AcOEt)
HPLC: 6.92 min (40 to 100% MeCN in 10 min, 95%)
HRMS (ESI): *m/z* = 909.4968 $[M+H]^{2\bullet+}$ (found), 909.5008 calcd. for $C_{52}H_{69}N_4O_{10}^{2\bullet+}$, 931.4793 $[M+Na]^{2\bullet+}$ (found), 931.4828 calcd. for $C_{52}H_{68}N_4NaO_{10}^{2\bullet+}$.

Bis-TEMPO 226

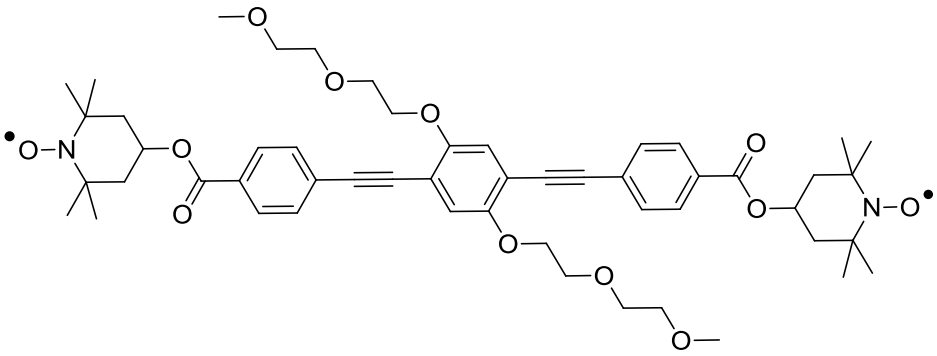

OPE-diCO_2H **165** (40.0 mg, 0.066 mmol, 1.0 eq) was suspended in dry DCM (2 mL). 4-OH-TEMPO **216** (23.0 mg, 0.133 mmol, 2.0 eq), DCC (30.0 mg, 0.146 mmol, 2.2 eq) and DMAP (1.6 mg, 0.013 mmol, 0.2 eq) were added and the resulting solution was stirred at rt for 24 h. H_2O was added and the mixture was extracted with DCM (3×). The combined organic layers were dried over Na_2SO_4, filtered and concentrated. Column chromatography (SiO_2, 70:30 to 60:40 Cy/AcOEt) afforded bis-TEMPO **226** (25.0 mg, 0.027 mmol, 41%) as an orange solid.

Molecular formula: $C_{52}H_{66}N_2O_{12}^{2\bullet}$

MW: 911.1 g.mol^{-1}
^{1}H-NMR (CDCl$_3$, 300 MHz): (all signals broadened and some obscured due to paramagnetism) δ 8.40–7.55 (m, 8H), 7.13 (s, 2H), 4.29 (br s, 4H), 4.00 (br s, 4H), 3.86 (br s, 4H), 3.61 (br s, 4H), 3.43 (s, 6H), 2.42–0.76 (m, 18H).
Rf (SiO$_2$): 0.79 (20:80 Cy/AcOEt)
HRMS (ESI): *m/z* = 933.4458 $[M+Na]^{2\bullet+}$ (found), 933.4508 calcd. for $C_{52}H_{66}N_2NaO_{12}^{2\bullet+}$.

***tert*-Butyl 4-(4-(4-(4-([2,2':6',2''-terpyridin]-4'-yl)phenyl)piperazin-1-yl)phenyl)piperazine-1-carboxylate** (**227**)

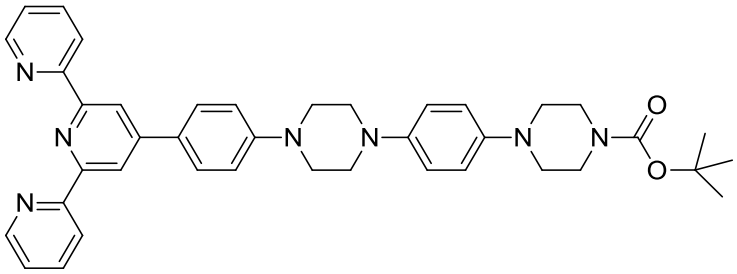

*p*BrPhTpy **36** (80 mg, 0.206 mmol, 1.0 eq) and BocPipPhPip **137** (86 mg, 0.247 mmol, 1.2 eq) were dissolved in dry toluene (2 mL). NaO^{t}Bu (28 mg, 0.288 mmol, 1.4 eq) was added, followed by $Pd_2(dba)_3$ (2.0 mg, 0.002 mmol, 0.01 eq) and BINAP (4.0 mg, 0.006 mmol, 0.03 eq). The resulting mixture was refluxed for 5 d and concentrated. Column chromatography (Al_2O_3, basic, activated, Brockmann I, 100% DCM to 99:1 DCM/MeOH) afforded **227** (116 mg, 0.177 mmol, 86%) as a pale orange solid.

Molecular formula: $C_{40}H_{43}N_7O_2$
MW: 653.8 g.mol^{-1}
^{1}H-NMR (CDCl$_3$, 300 MHz): δ 8.76–8.70 (m, 4H), 8.67 (dt, *J* = 8.0, 1.1 Hz, 2H), 7.94–7.83 (m, 4H), 7.34 (ddd, *J* = 7.5, 4.7, 1.2 Hz, 2H), 7.06 (d, *J* = 8.6 Hz, 2H), 7.01–6.87 (m, 4H), 3.58 (t, *J* = 5.1 Hz, 4H), 3.45 (t, *J* = 5.1 Hz, 4H), 3.28 (t, *J* = 5.1 Hz, 4H), 3.04 (t, *J* = 5.1 Hz, 4H), 1.49 (s, 9H).
HRMS (ESI): *m/z* = 654.3537 $[M+H]^+$ (found), 654.3551 calcd. for $C_{40}H_{44}N_7O_2^+$, 676.3347 $[M+Na]^+$ (found), 676.3370 calcd. for $C_{40}H_{43}N_7NaO_2^+$.

4'-(4-(4-(4-(Piperazin-1-yl)phenyl)piperazin-1-yl)phenyl)-2,2':6',2''-terpyridine (**228**)

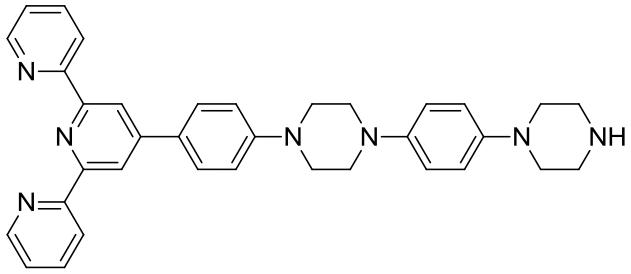

Compound **227** (112 mg, 0.171 mmol, 1.0 eq) was dissolved in dry DCM (5 mL) and the resulting solution was cooled to 0 °C. TFA (0.5 mL) was added dropwise and the resulting mixture was allowed to warm to rt for 3h. Aq. NaOH was added until pH ≈ 14 and the mixture was then extracted with DCM (5×). The combined organic layers were dried over Na_2SO_4, filtered and concentrated to afford **228** (83 mg, 0.150 mmol, 88%) as a pale orange solid.

Molecular formula: $C_{35}H_{35}N_7$
MW: 553.7 g.mol^{-1}
^{1}H-NMR ($CDCl_3$, 300 MHz): δ 8.76–8.70 (m, 4H), 8.67 (dt, *J* = 8.0, 1.1 Hz, 2H), 7.94–7.84 (m, 4H), 7.35 (ddd, *J* = 7.5, 4.8, 1.2 Hz, 2H), 7.08 (d, *J* = 8.8 Hz, 2H), 7.01–6.88 (m, 4H), 3.45 (dd, *J* = 6.5, 3.7 Hz, 4H), 3.28 (dd, *J* = 6.5, 3.7 Hz, 4H), 3.11–2.99 (m, 8H).
HRMS (ESI): *m/z* = 554.3017 $[M+H]^+$ (found), 554.3027 calcd. for $C_{35}H_{36}N_7^+$, 576.2831 $[M+Na]^+$ (found), 576.2846 calcd. for $C_{35}H_{35}N_7Na^+$.

Nitroxide 229

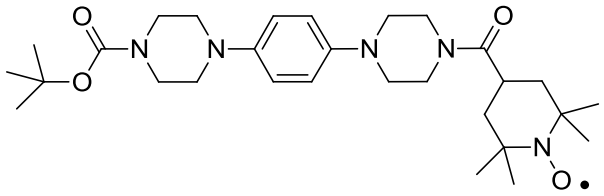

4-CO_2H-TEMPO **217** (25 mg, 0.125 mmol, 1.0 eq) and BocPipPhPip **137** (48 mg, 0.138 mmol, 1.1 eq) were dissolved in dry DMF (1 mL). HOBt•H_2O (21 mg, 0.138 mmol, 1.1 eq) and EDC•HCl (29 mg, 0.150 mmol, 1.2 eq) were added, followed by DIPEA (32 µL, 0.187 mmol, 1.5 eq). The resulting mixture was stirred at rt for 24 h and concentrated. DCM was added and the mixture was washed with H_2O (1×) and sat. aq. NaCl (1×). The organic layer was dried over Na_2SO_4, filtered and concentrated. Column chromatography (SiO_2, 50:50 to 30:70 Cy/AcOEt) afforded nitroxide **229** (49 mg, 0.093 mmol, 74%) as a pale orange solid.

Molecular formula: $C_{29}H_{46}N_5O_4^{\bullet}$
MW: 528.7 g.mol^{-1}
^{1}H-NMR ($CDCl_3$, 300 MHz): (all signals broadened and some obscured due to paramagnetism) δ 6.93 (s, 4H), 3.83 (br s, 4H), 3.59 (t, *J* = 4.9 Hz, 4H), 3.12 (br s, 4H), 3.06 (t, *J* = 5.1 Hz, 4H), 1.50 (s, 9H).
Rf (SiO_2): 0.35 (20:80 Cy/AcOEt)
HRMS (ESI): *m/z* = 529.3636 $[M+H]^{\bullet+}$ (found), 529.3623 calcd. for $C_{29}H_{47}N_5O_4^{\bullet+}$, 551.3460 $[M+Na]^{\bullet+}$ (found), 551.3442 calcd. for $C_{29}H_{46}N_5NaO_4^{\bullet+}$, 473.2991 $[M+2H-{}^tBu]^{\bullet+}$ (found), 473.2997 calcd. for $C_{25}H_{39}N_5O_4^{\bullet+}$, 429.3092 $[M+2H-Boc]^{\bullet+}$ (found), 429.3098 calcd. for $C_{24}H_{39}N_5O_2^{\bullet+}$.

Tri-*tert*-butyl 2,2',2''-(10-(2-(4-(4-(4-(4-([2,2':6',2''-terpyridin]-4'-yl)phenyl)piperazin-1-yl) phenyl)piperazin-1-yl)-2-oxoethyl)-1,4,7,10-tetraazacyclododecane-1,4,7-triyl)triacetate (**230**)

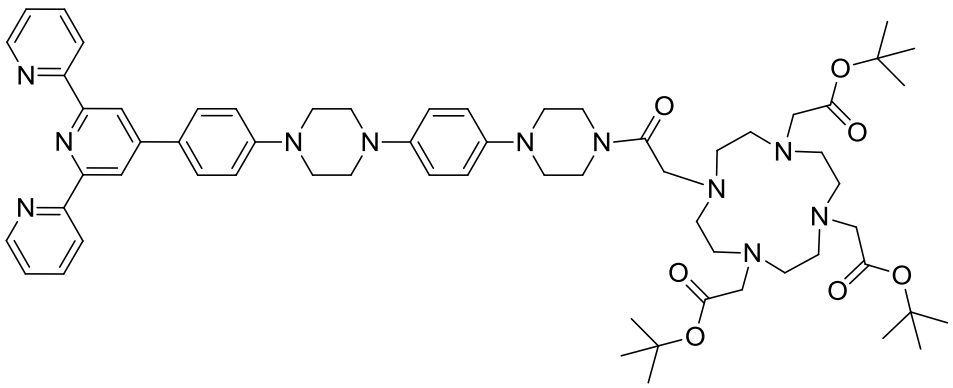

Tri-^{t}Bu-DOTA **146** (37 mg, 0.065 mmol, 1.2 eq) was dissolved in dry DMF (1 mL). HATU (27 mg, 0.070 mmol, 1.3 eq) was added, and the resulting mixture was stirred at rt for 10 min. Compound **228** (30 mg, 0.054 mmol, 1.0 eq) was added, and the resulting mixture was stirred at rt for 20 min. DIPEA (28 µL, 0.163 mmol, 3.0 eq) was added, and the resulting mixture was stirred at rt for 15 h and concentrated. DCM was added and the mixture was washed with H_2O (1×) and sat. aq. NaCl (1×). The organic layer was dried over Na_2SO_4, filtered and concentrated. Column chromatography (Al_2O_3, basic, activated, Brockmann I, 100% DCM to 99:1 DCM/MeOH) afforded compound **230** (45 mg, 0.041 mmol, 74%) as a pale orange solid.

Molecular formula: $C_{63}H_{85}N_{11}O_7$
MW: 1108.4 g.mol^{-1}
^{1}H-NMR ($CDCl_3$, 300 MHz): δ 8.76–8.70 (m, 4H), 8.67 (dt, *J* = 8.0, 1.1 Hz, 2H), 7.93–7.84 (m, 4H), 7.35 (ddd, *J* = 7.5, 4.7, 1.1 Hz, 2H), 7.07 (d, *J* = 8.7 Hz, 2H), 7.02–6.84 (m, 4H), 3.95–1.72 (m, 24H), 3.58 (t, *J* = 5.2 Hz, 8H), 3.03 (t, *J* = 5.3 Hz, 8H), 1.45 (s, 9H), 1.42 (s, 18H).

Nitroxide 231

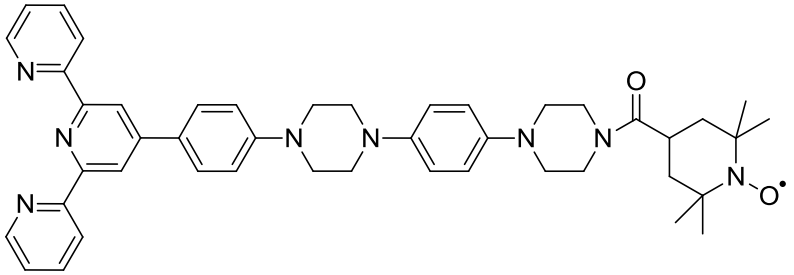

4-CO_2H-TEMPO **217** (15 mg, 0.075 mmol, 1.0 eq) and compound **228** (46 mg, 0.082 mmol, 1.0 eq) were dissolved in dry DMF (1 mL). HOBT•H_2O (13 mg, 0.082 mmol, 1.1 eq), EDC•HCl (17 mg, 0.090 mmol, 1.2 eq) and DIPEA (19 µL, 0.112 mmol, 1.5 eq) were then added and the resulting mixture was stirred at rt for 24 h and concentrated. Column chromatography (Al_2O_3, basic, activated, Brockmann I, 100% DCM to 99:1 DCM/MeOH) afforded nitroxide **231** (39 mg, 0.053 mmol, 71%) as an orange solid.

Molecular formula: $C_{45}H_{51}N_8O_2^{\bullet}$
MW: 735.9 g.mol^{-1}
^{1}H-NMR ($CDCl_3$, 300 MHz): (all signals broadened and some obscured due to paramagnetism) δ 8.76–8.70 (m, 4H), 8.67 (dt, *J* = 8.0, 1.1 Hz, 2H), 7.94–7.83 (m, 4H), 7.35 (ddd, *J* = 7.5, 4.7, 1.2 Hz, 2H), 7.06 (d, *J* = 8.5 Hz, 2H), 7.02–6.87 (m, 4H), 3.83 (br s, 4H), 3.60 (t, *J* = 5.0 Hz, 4H), 3.11 (br s, 4H), 3.06 (t, *J* = 5.1 Hz, 4H).

Tri-*tert*-butyl 2,2',2''-(10-(2-(4-(4-(4-(*tert*-butoxycarbonyl)piperazin-1-yl)phenyl)piperazin-1-yl)-2-oxoethyl)-1,4,7,10-tetraazacyclododecane-1,4,7-triyl)triacetate (**232**)

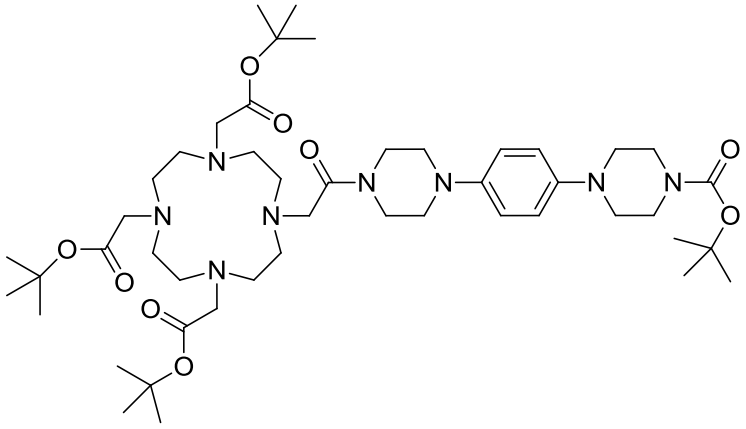

Tri-^{t}Bu-DOTA **146** (70 mg, 0.122 mmol, 1.0 eq) and HATU (51 mg, 0.134 mmol, 1.1 eq) were dissolved and dry DMF (1.5 mL). BocPipPhPip **137** (85 mg, 0.244 mmol, 2.0 eq) was added, followed by DIPEA (62 µL, 0.366 mmol, 3.0 eq). The resulting mixture was stirred for 24 h at rt and concentrated. DCM was added and the mixture was washed with H_2O (1×) and sat. aq. NaCl (1×). The organic layer was dried over Na_2SO_4, filtered and concentrated. Column chromatography (SiO_2, 98:2 DCM/MeOH) afforded **232** (85 mg, 0.094 mmol, 77%) as a pale orange solid.

Molecular formula: $C_{47}H_{80}N_8O_9$
MW: 901.2 g.mol^{-1}
^{1}H-NMR (CDCl$_3$, 300 MHz): δ 6.88 (s, 4H), 3.90–1.80 (m, 24H), 3.57 (t, *J* = 5.1 Hz, 8H), 3.04 (t, *J* = 5.4 Hz, 8H), 1.48 (s, 9H), 1.45 (s, 9H), 1.43 (s, 18H).
^{13}C-NMR (CDCl$_3$, 75 MHz): δ 172.8 (C_q), 105.5 (C_q), 81.9 (C_q), 81.8 (C_q), 80.0 (C_q), 55.8 (CH_2), 38.8 (CH_2), 28.6 (CH_3), 28.2 (CH_3), 28.1 (CH_3).
HRMS (ESI): *m/z* = 901.6171 $[M+H]^+$ (found), 901.6121 calcd. for $C_{47}H_{81}N_8O_9^+$, 923.5933 $[M+Na]^+$ (found), 923.5940 calcd. for $C_{47}H_{80}N_8NaO_9^+$, 801.5583 $[M+2H\text{-}Boc]^+$ (found), 801.5597 calcd. for $C_{42}H_{73}N_8O_7^+$.

2,2',2''-(10-(2-Oxo-2-(4-(4-(piperazin-1-yl)phenyl)piperazin-1-yl)ethyl)-1,4,7,10-tetraazacyclododecane-1,4,7-triyl)triacetic acid (**233**)

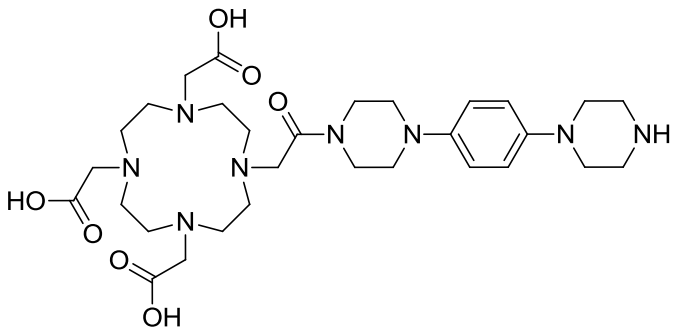

Compound **232** (75 mg, 0.083 mmol, 1.0 eq) was dissolved in dry DCM (2 mL). The resulting solution was cooled to 0 °C and TFA (2 mL) was added dropwise. The resulting mixture was allowed to warm to rt for 15 h, concentrated without heating, redissolved in MeOH and concentrated again. The residue was dissolved again in MeOH, precipitated by slow addition of Et_2O, filtered and dried to afford **233** (43 mg, 0.068mmol, 82%) as a light grey solid.

Molecular formula: $C_{30}H_{48}N_8O_7$

MW: 632.8 g.mol^{-1}
HRMS (ESI): *m/z* = 633.3715 $[M+H]^+$ (found), 633.3719 calcd. for $C_{30}H_{49}N_8O_7^+$, 655.3537 $[M+Na]^+$ (found), 655.3738 calcd. for $C_{30}H_{48}N_8NaO_7^+$, 328.1809 $[M+H+Na]^{2+}$, 328.1805 calcd. for $C_{30}H_{49}N_8NaO_7^{2+}/2$, 317.1899 $[M+2H]^{2+}$ (found), 317.1896 calcd. for $C_{30}H_{50}N_8O_7^{2+}/2$.

DOTA-PipPhPip-TEMPO (**234**)

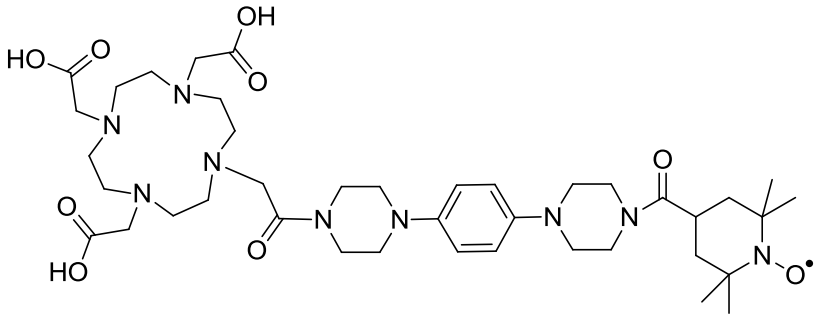

4-CO_2H-TEMPO **217** (7.0 mg, 0.035 mmol, 1.0 eq) and HATU (14.8 mg, 0.039 mmol, 1.1 eq) were dissolved in dry DMF (1 mL). The resulting solution was stirred at rt for 10 min and compound **233** (33.5 mg, 0.053 mmol, 1.5 eq) was added. The resulting solution was stirred at rt for 15 min and DIPEA (27 µL, 0.158 mmol, 4.5 eq) was added. The resulting mixture was stirred at rt for 15 h and concentrated. Purification by preparative HPLC (0 to 30% MeCN) afforded DOTA-PipPhPip-TEMPO **234** as an orange solid.

Molecular formula: $C_{40}H_{64}N_9O_9^{\bullet}$
MW: 815.0 g.mol^{-1}
HPLC: 5.15 min (0 to 30% MeCN in 10 min, 87%)

***tert*-Butyl (4-((4-((4-(2-bromoacetamido)phenyl)ethynyl)-2,5-bis(2-(2-methoxyethoxy) ethoxy) phenyl)ethynyl)phenyl)carbamate** (**235**)

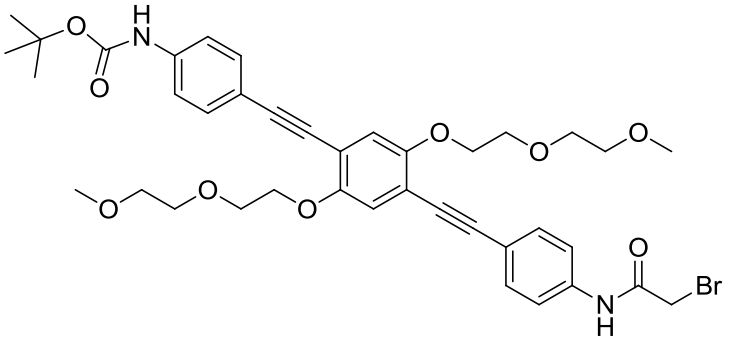

Compound **169** (200 mg, 0.31 mmol, 1.0 eq) was dissolved in dry DCM (5 mL). The resulting solution was cooled to 0 °C and TEA (50 µL, 0.37 mmol, 1.2 eq) was added, followed by bromoacetyl bromide (32 µL, 0.37 mmol, 1.2 eq) dissolved in dry DCM (1 mL) dropwise. The resulting mixture was allowed to warm to rt for 3h and washed with sat. aq. $NaHCO_3$ (1×) and sat. aq. NaCl (1×). The organic layer was dried over Na_2SO_4, filtered and concentrated. Column chromatography (SiO_2, 50:50 to 40:60 Cy/AcOEt) afforded **235** (182 mg, 0.238 mmol, 77%) as a yellow solid.

Molecular formula: $C_{39}H_{45}BrN_2O_9$

MW: 765.7 g.mol^{-1}
^{1}H-NMR (CDCl$_3$, 300 MHz): δ 8.20 (s, 1H), 7.58–7.48 (m, 4H), 7.48–7.42 (m, 2H), 7.39–7.32 (m, 2H), 7.02 (s, 1H), 7.02 (s, 1H), 6.57 (s, 1H), 4.24–4.18 (m, 4H), 4.03 (s, 2H), 3.95–3.89 (m, 4H), 3.83–3.77 (m, 4H), 3.57–3.51 (m, 4H), 3.36 (s, 6H), 1.52 (s, 9H).
HRMS (ESI): *m/z* = 787.2203 [M+Na]$^+$ (found), 787.2201 calcd. for $C_{39}H_{45}BrN_2NaO_9^+$.

Tris(2-phenylpropan-2-yl) 2,2',2''-(10-(2-((4-((4-((4-((*tert*-butoxycarbonyl)amino)phenyl)ethynyl)-2,5-bis(2-(2-methoxyethoxy)ethoxy)phenyl)ethynyl)phenyl)amino)-2-oxoethyl)-1,4,7,10-tetraazacyclododecane-1,4,7-triyl)triacetate (**236**)

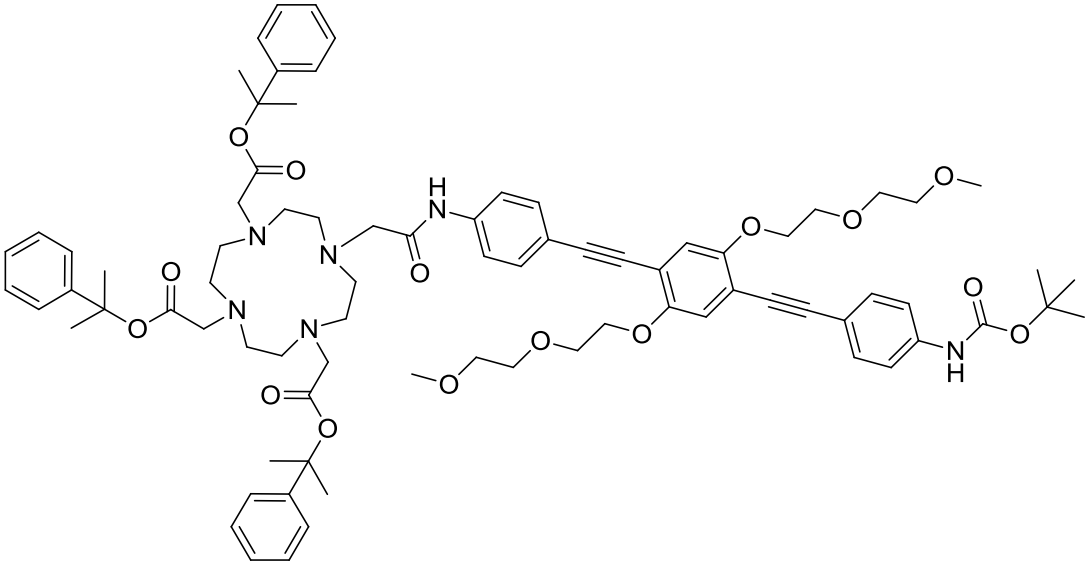

Compound **235** (172 mg, 0.225 mmol, 1.0 eq) and tri-Pp-DO3A **198** (205 mg, 0.293 mmol, 1.3 eq) were mixed in dry MeCN (10 mL). K_2CO_3 (156 mg, 1.13 mmol, 5.0 eq) was added, the resulting mixture was heated at 60 °C for 15 h and concentrated. DCM was added and the mixture was washed with H_2O (1×) and sat. aq. NaCl (1×). The organic layer was dried over Na_2SO_4, filtered and concentrated. Column chromatography (SiO_2, 95:5 to 90:10 DCM/MeOH) afforded **236** (214 mg, 0.154 mmol, 69%) as a yellow solid.

Molecular formula: $C_{80}H_{100}N_6O_{15}$
MW: 1385.7 g.mol^{-1}
^{1}H-NMR (CDCl$_3$, 300 MHz): δ 11.12 (s, 1H), 7.98–7.90 (m, 2H), 7.48–7.38 (m, 6H), 7.33–7.10 (m, 15H), 7.04 (s, 1H), 7.02 (s, 1H), 6.64 (s, 1H), 4.25–4.17 (m, 4H), 3.95–3.88 (m, 4H), 3.84–3.77 (m, 4H), 3.57–3.50 (m, 4H), 3.36 (s, 3H), 3.35 (s, 3H), 2.95–1.95 (m, 24H), 1.63 (s, 18H), 1.52 (s, 9H).
HRMS (ESI): *m/z* = 1407.7102 [M+Na]$^+$ (found), 1407.7139 calcd. for $C_{80}H_{100}N_6NaO_{15}^+$.

Tris(2,3,5,6-tetrachlorophenyl)methane (**241**)

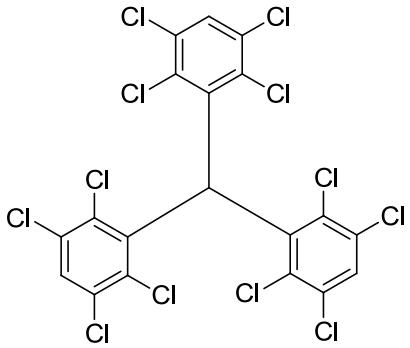

1,2,4,5-Tetrachlorobenzene **240** (9.6 g, 44 mmol, 9.0 eq), $AlCl_3$ (730 mg, 5.2 mmol, 1.06 eq) and chloroform (0.4 mL, 4.9 mmol, 1.0 eq) were mixed in a sealed high-pressure tube. The resulting mixture was heated at 160 °C for 45 min and cooled to rt. CH_2Cl_2 was added and the black suspension was sonicated for 30 min and washed with aq. 0.1 M HCl (1×), H_2O (1×), and sat. aq. NaCl (1×). The organic layer was dried over Na_2SO_4, filtered and concentrated. Column chromatography (SiO_2, 1300 g, Ø 9 cm, 100% Cy) followed by pentane washings afforded **241** (1.181 g, 1.796 mmol, 37%) as a white solid.

Molecular formula: $C_{19}H_4Cl_{12}$
MW: 657.6 g.mol^{-1}
^{1}H-NMR (CDCl$_3$, 300 MHz): δ 7.65 (s, 3H), 6.98 (s, 1H).
^{13}C-NMR (CDCl$_3$, 75 MHz): δ 138.7 (C_q), 134.5 (C_q), 133.7 (C_q), 133.4 (C_q), 132.6 (C_q), 130.5 (CH), 56.2 (CH).
HRMS (APCI): *m/z* = 616.6886 $[M\text{-}Cl]^+$ (found), 616.6881 calcd. for $C_{19}H_4Cl_{11}^+$.

Triethyl 4,4',4''-methanetriyltris(2,3,5,6-tetrachlorobenzoate) (**245**)

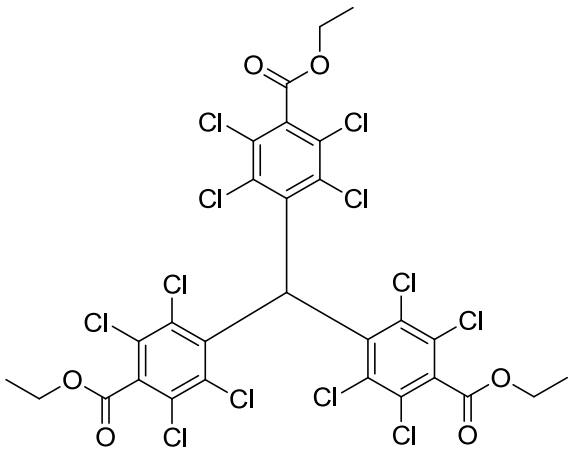

Compound **241** (730 mg, 1.11 mmol, 1.0 eq) was dissolved in dry THF (70 mL). TMEDA (530 µL, 3.55 mmol, 3.2 eq) was added and the resulting solution was cooled to -78 °C. *n*-BuLi (1.6 M in THF, 2.36 mL, 3.77 mmol, 3.4 eq) was added in one portion and the resulting mixture was stirred at -78 °C for 2h. Ethyl chloroformate (1.06 mL, 11.1 mmol, 10.0 eq) was added dropwise and the resulting solution was allowed to warm to rt for 15h and concentrated. H_2O was added and the mixture was extracted with DCM (3×). The combined organic layers were dried over Na_2SO_4, filtered and concentrated. Column chromatography (99:1 to 90:10 Cy/AcOEt) afforded **245** (640 mg, 0.732 mmol, 66%) as a white solid.

Molecular formula: $C_{28}H_{16}Cl_{12}O_6$
MW: 873.8 g.mol^{-1}
^{1}H-NMR ($CDCl_3$, 300 MHz): δ 7.00 (s, 1H), 4.49 (q, *J* = 7.1 Hz, 6H), 1.43 (t, *J* = 7.1 Hz, 9H).
HRMS (APCI): *m/z* = 868.7303 $[M+H]^+$ (found), 868.7282 calcd. for $C_{28}H_{17}Cl_{12}O_6^+$.

PTMTE (**246**)

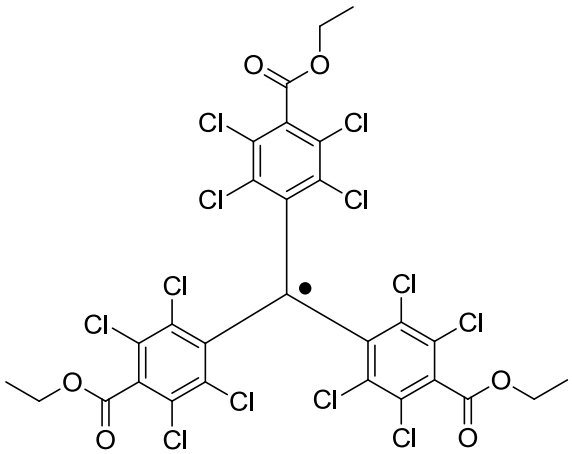

Compound **245** (820 mg, 0.938 mmol, 1.0 eq) was dissolved in a mixture of dry DMSO (30 mL) and dry Et_2O (135 mL), and then powdered NaOH (750 mg, 18.8 mmol, 20.0 eq) was added. The resulting mixture was stirred at rt for 24 h protected from light and filtered to a solution containing iodine (1.05 g) dissolved in dry Et_2O (55 mL). The resulting solution was left undisturbed protected from light for 24 h and washed with sat. aq. $NaHCO_3$ (1×), sat. aq. NaCl (1×), and H_2O (2×). The organic layer was dried over Na_2SO_4, filtered and concentrated. Column chromatography (95:5 to 80:20 Cy/AcOEt) afforded PTMTE **246** (672 mg, 0.770 mmol, 82%) as a red solid.

Molecular formula: $C_{28}H_{15}Cl_{12}O_6^{\bullet}$
MW: 872.8 g.mol^{-1}
Rf (SiO_2): 0.65 (80:20 Cy/AcOEt)
HRMS (ESI): *m/z* = 889.7008 $[M+Na]^{\bullet+}$ (found), 889.7023 calcd. for $C_{28}H_{15}Cl_{12}NaO_6^{\bullet+}$.

H_3PTMTC (**244**)

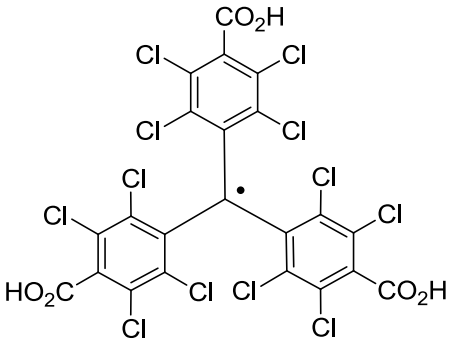

PTMTE **246** (260 mg, 0.298 mmol, 1.0 eq) was dissolved in MeOH (5 mL). KOH (836 mg, 14.9 mmol, 50.0 eq) was added and the resulting mixture was refluxed for 48 h and cooled to rt. H_2O was added, the mixture was washed with Et_2O (3×) and acidified with aq. 1 M HCl to obtain a red precipitate. This

mixture was extracted with Et_2O (3×) and the combined organic layers were dried over Na_2SO_4, filtered and concentrated to afford H_3PTMTC **244** (200 mg, 0.253 mmol, 85%) as a red solid.

Molecular formula: $C_{22}H_3Cl_{12}O_6^{\bullet}$
MW: 788.7 g.mol^{-1}
This product has been characterized by J-band *cw*-HFEPR and waits for elemental analysis.

2. ITC

ITC were performed using a TA instrument Nano-ITC calorimeter operating with a reference power of 166 µJ.s^{-1} and a stirring speed of 1000 rpm. Triplicate titrations were performed. The data was processed using the inbuilt software. Experimental details are provided in the main text.

3. CD

CD spectra were recorded on a Jasco J-815 spectropolarimeter using a 0.1 mm pathlength quartz cuvette at IPCM with the help of Christophe Desmarets. Measurements were conducted with a scanning speed of 20 nm/min. Reported spectra were averaged on 5 scans, smoothed, and corrected for buffer contributions. Experimental details are provided in the main text.

4. EPR

Continuous-wave EPR: J-band *cw*-HFEPR spectra were recorded at CEA in the group of Biological High-field Magnetic Resonance (BHMR) in the Institute for Integrative Biology of the Cell (I2BC) (Department of Biochemistry, Biophysics and Structural Biology, Université Paris-Saclay, CEA, CNRS UMR 9198) on a locally constructed spectrometer[28] under nonsaturating conditions. Simulations of the *cw*-HFEPR spectra were carried out using locally written programs.[131]

Pulsed EPR: W-band pulsed EPR experiments (ED-EPR spectra, T_1 and T_2 measurements and PELDOR time traces) were performed at the SB2SM using a Bruker Elexsys II 680 EPR spectrometer equipped with a Bruker "power upgrade 2" and an Oxford Instruments CF935 flow cryostat.

Sample preparation: Spin echo detected EPR spectra were taken at 10 K using a Hahn-echo sequence with π/2 and π pulse durations of 10 and 20 ns (for Mn-DOTA and $MnDOTA_2P_n$ platforms) or 16 and 30 ns (for $MnDOTA_2PhPip_n$ and $MnDOTA_2OPE_n$ platforms) or 40 and 80 ns (for the bis-TEMPO-OPE platform **225**), respectively, an inter-pulse delay time of 3000 ns (1500 ns for bis-TEMPO-OPE **225**), repetition time of 800 µs (5100 µs for bis-TEMPO-OPE **225**) , and a sweep width of 1000 G. For $MnDOTA_2PhPip_n$, T_m was on the order of 1500 ns. PELDOR experimental details are provided in the main text.

For trityl radicals, all samples are prepared under ambient oxygen concentration, and unless otherwise stated their concentration was 1 mM. FT samples (1 or 15 mM) were prepared by dissolving K_3FT in H_2O with 10% glycerol, H_2O, or H_2O with 50% glycerol. The H_3FT **263** sample was prepared by addition of one drop of concentrated HCl (12 M) to an aqueous solution of FT (1 mM,

500 µL). The precipitate was isolated by centrifugation and dissolved in 2-MeTHF (500 µL). The PTMTC sample was prepared *in situ* by deprotonation of H_3PTMTC **244** using excess NaOH (20 eq.) in H_2O with 10% glycerol. The H_3PTMTC **244** and PTMTE **246** samples were prepared by dissolving in 2-MeTHF.

With the exception of PTMTC, 285 GHz *cw*-HFEPR spectra were obtained at 15 K with modulation of 5 G under non-saturating conditions. For PTMTC, the cryostat was set at 100 K and 10 G modulation was used to achieve non-saturation.

The experimental setup consists of a 0.6 mL Eppendorf tube coaxially mounted within a 2 mL PET cryotube. A 85 µL solution of 50 µM $GdCl_3$ in H_2O with 10% glycerol was added to the Eppendorf tube, while the cryotube contained 300 µL solution of either 50 µM $MnCl_2$ in H_2O with 20% glycerol or the radical samples.

5. COMPUTATIONAL METHODS

DFT calculations: DFT calculations were performed on the *Gaussian 09* program package.[173] Geometries were optimized using the hybrid unrestricted open-shell UB3LYP functional and the 6-31G*, 6-311G* or 6-311G** basis set for all atoms, or the HF/STO-3G functional. Vibrational harmonic frequency analysis of the optimized geometries was used to ensure that there were true local minima with no imaginary frequencies.

Molecular dynamics: For $MnDOTA_2P_n$ platforms, MD simulations were performed for $CysPro_nCys$, with n = 6, 9, 10, 12 or 15. The starting conformation was obtained using the angular parameters derived from the crystal structure of a hexaproline PPII helix.[208] All simulations were performed using the GROMACS simulation package version 5.0.4.[311] The coordinate and topology for simulations were generated by the pdb2gmx protocol of GROMACS using the OPLS-AA/L force field. For solvation, the spc216 explicit water model was used. Simulations were carried out at constant temperature and pressure (300 K, 1 atm) in a periodic cubic box whose length was 2 nm longer than the fully extended peptides (n = 6, 46 Å, 3130 water molecules; n = 9, 55 Å, 5335 water molecules; n = 10, 58 Å, 6190 water molecules; n = 12, 64 Å, 8737 water molecules; n = 15, 73 Å, 12506 water molecules). Charges were neutralized and salt adjusted to 150 mM using NaCl. MD simulations were carried out for 20 ns and sampled every 20 ps. Atomic coordinates were saved every 10 ps. The distance distribution profiles from the N-terminal N_{Cys} to the C-terminal S_{Cys} atoms for n = 10 and 15 were comparable to those reported previously for $GlyPro_nCys$ peptides.[209] Although it has been shown that PPII simulation using different force fields produces slightly different distance distribution profiles,[312] the discrepancies were minor in comparison to the additional contribution from the spin-labels. For each sampled MD structure, the program mtsslWizard[218,219] was used to generate a distribution of possible positions of the Mn-DOTA spin-labels by carrying out a accessible space analysis. The program was modified to accommodate the structure of MnDOTA-maleimide which was derived from the crystal structure of Mn-DOTA[147] and the "loose" and "thorough search" options were used to generate 200 possible positions of each label. The structures from the combined MD/mtsslWizard simulations were then used to generate the final Mn-Mn distance distribution profiles for the $MnDOTA_2P_n$ platforms.

For the simplified models of the rigid platforms bis-DOTA-$PhPip_n$ and bis-DOTA-OPE_n, compounds were parameterised for MD simulation from the corresponding pdb files (generated using Chem3D, Perkin Elmer) using the gaff forcefield[225] and bcc charge model from the Antechamber program,[226]

part of the AmberTools14 software suite.[224] The compounds were solvated with a 10.0 Å TIP3P water octahedral solvent box using xleap. The resulting solvated systems were energy minimised then the system was heated to 300 K with restraints applied to the solute using the PMEMD module from Amber14. The restraints were relaxed over eight steps then a 5 ns molecular dynamics trajectory was acquired for subsequent analysis.

Analyses of distances and distance distributions were performed using VMD[227] software (http://www.ks.uiuc.edu/Research/vmd/) and the distance.tcl script available online at http://www.ks.uiuc.edu/Training/Tutorials/vmd/vmd-tutorial-files/ with a number of bins of 20 for the distribution. Spectra were smoothed (adjacent averaging on 5 points).

6. X-RAY CRYSTALLOGRAPHY

X-ray diffraction was performed on compounds **25**, **80**, **120**, **130**, **161**, **164**, **225** and **246** by Régis Guillot at ICMMO (Orsay). Data were collected by using a Kappa X8 Appex II Bruker diffractometer with graphite-monochromated Mo Kα radiation (λ = 0.71073 Å). Crystals were mounted on a CryoLoop (Hampton Research) with Paratone-N (Hampton Research) as cryoprotectant and then flash-frozen under a nitrogen gas stream at 100 K. The temperature of the crystal was maintained at the selected value (100 K) by means of a 700 series Cryostream cooling device to within an accuracy of ±1 K. The data were corrected for Lorentz−polarization and absorption effects. The structures were solved by direct methods using SHELXS-97[313] and refined against F^2 by full-matrix least-squares techniques using SHELXL-97[314] with anisotropic displacement parameters for all non-hydrogen atoms. Hydrogen atoms were located on a difference Fourier map and introduced into the calculations as a riding model with isotropic thermal parameters. All calculations were performed by using the Crystal Structure crystallographic software package WinGX.[315] The structure of PTMTE **246** was deposited to the Cambridge Crystallographic Data Centre (CCDC 1420702).

X-ray diffraction was performed on compounds **180** and **220** by Lise-Marie Chamoreau at IPCM (UPMC). Data were collected by using a Kappa-APEXII Bruker diffractometer with graphite-monochromated Mo Kα radiation (λ = 0.71073 Å). Crystals were mounted on a CryoLoop (Hampton Research) with Paratone-N (Hampton Research) as cryoprotectant and placed in the cold flow produced with an Oxford Cryocooling device. Data collection was performed with the APEX2 suite.[316] Unit-cell parameters refinement, integration and data reduction were carried out with the SAINT program.[316] SADABS[316] was used for multi-scan absorption corrections. In the WinGX[315] suite of programs, the structure was solved by direct methods with SHELXS-97[313] and refined by full-matrix least-squares methods using SHELXL-97.[313] Almost all non-hydrogen atoms were refined anisotropically, only atoms of solvent molecules or disordered parts were refined isotropically. Hydrogen atoms were placed at calculated positions and refined with a reding model.

The summary of diffraction data on these ten compounds can be found in Table 10.

Table 10: X-ray diffraction data

	Mn-BImP **25**	Diester **80**	Tpy **120**	Linker **130**	OPE-diCOH **161**
Crystal system	Triclinic	Monoclinic	Monoclinic	Monoclinic	Triclinic
Space group	P-1	$P2_1/c$	Cc	$P2_1/m$	P-1
Cell lengths					
a	13.6656(4)	15.4882(13)	14.2915(6)	6.43450(10)	8.0566(3)
b	15.4616(5)	7.0925(6)	14.7087(6)	37.5483(7)	10.0504(4)
c	16.4234(5)	16.9628(13)	12.3618(5)	10.2795(2)	10.2709(4)
Cell angles					
α	68.004(1)	90.00	90.00	90.00	61.8080(10)
β	66.828(1)	113.077(3)	103.7340(10)	92.4370(10)	74.3230(10)
γ	80.166(1)	90.00	90.00	90.00	81.4180(10)
Cell volume	2956.86	1714.26	2524.27	2481.33	705.501
Z and Z'		4 and 0	4 and 0	4 and 0	1 and 0
R-factor (%)		4.12	3.48	3.81	4.91

	OPE-diCCH **164**	Tetraester **180**	Bis-TEMPO **220**	Bis-TEMPO **225**	PTMTE **246**
Crystal system	Monoclinic	Triclinic	Triclinic	Monoclinic	Triclinic
Space group	P21	P-1	P-1	$P2_1/m$	P-1
Cell lengths					
a	7.3179(3)	8.7756(2)	6.02840(10)	12.3531(8)	12.8632(11)
b	19.8711(9)	10.7516(2)	9.7096(2)	14.0252(10)	20.872(2)
c	20.7472(9)	14.4110(3)	15.9256(3)	16.2862(11)	28.298(3)
Cell angles					
α	90.00	80.3820(10)	89.6020(10)	90.00	69.293(2)
β	90.656(2)	81.6100(10)	85.5390(10)	100.597(2)	85.748(2)
γ	90.00	70.2660(10)	82.7150(10)	90.00	78.335(2)
Cell volume	3016.75	1255.98	921.849	2773.54	6959.87
Z and Z'	4 and 0	1 and 0	1 and 0	2 and 0	8 and 0
R-factor (%)	6.17	4.7	4.2	9.77	14.86

References

(1) Kendrew, J. C.; Bodo, G.; Dintzis, H. M.; Parrish, R. G.; Wyckoff, H.; Phillips, D. C. *Nature* **1958**, *181* (4610), 662–666.
(2) Wüthrich, K. *Nat. Struct. Biol.* **2001**, *8* (11), 923–925.
(3) Ban, N.; Freeborn, B.; Nissen, P.; Penczek, P.; Grassucci, R. A.; Sweet, R.; Frank, J.; Moore, P. B.; Steitz, T. A. *Cell* **1998**, *93* (7), 1105–1115.
(4) Fernández, C.; Wüthrich, K. *FEBS Lett.* **2003**, *555* (1), 144–150.
(5) Wüthrich, K. *J. Biol. Chem.* **1990**, *265* (36), 22059–22062.
(6) Schiemann, O.; Prisner, T. F. *Q. Rev. Biophys.* **2007**, *40* (1), 1–53.
(7) Zheng. J. *Methods in Molecular Biology vol. 337*, Humana Press, 65–77.
(8) Jeschke, G. *Annu. Rev. Phys. Chem.* **2012**, *63* (1), 419–446.
(9) Klare, J. P.; Steinhoff, H. J. *Photosynth. Res.* **2009**, *102* (2), 377–390.
(10) Jeschke, G. *ChemPhysChem* **2002**, *3* (11), 927–932.
(11) Hilger, D.; Jung, H.; Padan, E.; Wegener, C.; Vogel, K.-P.; Steinhoff, H.-J.; Jeschke, G. *Biophys. J.* **2005**, *89* (2), 1328–1338.
(12) Endeward, B.; Butterwick, J. A.; MacKinnon, R.; Prisner, T. F. *J. Am. Chem. Soc.* **2009**, *131* (42), 15246–15250.
(13) Schiemann, O.; Weber, A.; Edwards, T. E.; Prisner, T. F.; Sigurdsson, S. T. *J. Am. Chem. Soc.* **2003**, *125* (12), 3434–3435.
(14) Schiemann, O.; Piton, N.; Mu, Y.; Stock, G.; Engels, J. W.; Prisner, T. F. *J. Am. Chem. Soc.* **2004**, *126* (18), 5722–5729.
(15) Schiemann, O.; Piton, N.; Plackmeyer, J.; Bode, B. E.; Prisner, T. F.; Engels, J. W. *Nat. Protoc.* **2007**, *2* (4), 904–923.
(16) Godt, A.; Schulte, M.; Zimmermann, H.; Jeschke, G. *Angew. Chem. Int. Ed.* **2006**, *45* (45), 7560–7564.
(17) Jeschke, G.; Sajid, M.; Schulte, M.; Ramezanian, N.; Volkov, A.; Zimmermann, H.; Godt, A. *J. Am. Chem. Soc.* **2010**, *132* (29), 10107–10117.
(18) Jeschke, G.; Godt, A. *ChemPhysChem* **2003**, *4* (12), 1328–1334.
(19) Pievo, R.; Casati, C.; Franchi, P.; Mezzina, E.; Bennati, M.; Lucarini, M. *ChemPhysChem* **2012**, *13* (11), 2659–2661.
(20) Goldfarb, D. *Struct. Bond.* **2014**, *152*, 163–204.
(21) Raitsimring, A. M.; Gunanathan, C.; Potapov, A.; Efremenko, I.; Martin, J. M. L.; Milstein, D.; Goldfarb, D. *J. Am. Chem. Soc.* **2007**, *129* (46), 14138–14139.
(22) Banerjee, D.; Yagi, H.; Huber, T.; Otting, G.; Goldfarb, D. *J. Phys. Chem. Lett.* **2012**, *3*, 157−160.
(23) Bock, C. W.; Katz, A. K.; Markham, G. D.; Glusker, J. P. *J. Am. Chem. Soc.* **1999**, *121* (32), 7360–7372.
(24) Bertrand, P. La Spectroscopie de Résonance Paramagnétique Electronique - Fondements, **2010**, EDP Sciences, 1–124.
(25) Reed, H. G.; Markham, G. D. *Biological Magnetic Resonance vol. 6*, Plenum Press, 73–142.
(26) Un, S. *Inorg. Chem.* **2013**, *52* (7), 3803–3813.
(27) Stich, T. A.; Lahiri, S.; Yeagle, G.; Dicus, M.; Brynda, M.; Gunn, A.; Aznar, C.; DeRose, V. J.; Britt, R. D. *Appl. Magn. Reson.* **2007**, *31* (1-2), 321–341.
(28) Un, S.; Dorlet, P.; Rutherford, A. W. *Appl. Magn. Reson.* **2001**, *21* (3-4), 341–361.
(29) Blume, R. J. *Phys. Rev.* **1958**, *109* (6), 1867–1873.
(30) Milov, A. D.; Ponomarev, A. B.; Tsvetkov, Y. D. *Chem. Phys. Lett.* **1984**, *110* (1), 67–72.
(31) Tsvetkov, Y. D.; Milov, A. D.; Maryasov, A G. *Russ. Chem. Rev.* **2008**, *77* (6), 487–520.

(32) Martin, R. E.; Pannier, M.; Diederich, F.; Gramlich, V.; Hubrich, M.; Spiess, H. W. *Angew. Chem. Int. Ed.* **1998**, *37* (20), 2833–2837.
(33) Jeschke, G.; Chechik, V.; Ionita, P.; Godt, A.; Zimmermann, H.; Banham, J.; Timmel, C. R.; Hilger, D.; Jung, H. *Appl. Magn. Reson.* **2006**, *30*, 473–498.
(34) Dalaloyan, A.; Qi, M.; Ruthstein, S.; Vega, S.; Godt, A.; Feintuch, A.; Goldfarb, D. *Phys. Chem. Chem. Phys.* **2015**.
(35) Goldfarb, D. *Phys. Chem. Chem. Phys.* **2014**, *16* (21), 9685–9699.
(36) Jeschke, G.; Polyhach, Y. *Phys. Chem. Chem. Phys.* **2007**, *9* (16), 1895–1910.
(37) Sajid, M.; Jeschke, G.; Wiebcke, M.; Godt, A. *Chem. Eur. J.* **2009**, *15* (47), 12960–12962.
(38) Prisner, T. F.; Marko, a.; Sigurdsson, S. T. *J. Magn. Reson.* **2015**, *252*, 187–198.
(39) Qi, M.; Groβ, A.; Jeschke, G.; Godt, A.; Drescher, M. *J. Am. Chem. Soc.* **2014**, *136*, 15366–15378.
(40) Lovett, J. E.; Hoffmann, M.; Cnossen, A.; Shutter, A. T. J.; Hogben, H. J.; Warren, J. E.; Pascu, S. I.; Kay, C. W. M.; Timmel, C. R.; Anderson, H. L. *J. Am. Chem. Soc.* **2009**, *131* (38), 13852–13859.
(41) Polyhach, Y.; Godt, A.; Bauer, C.; Jeschke, G. *J. Magn. Reson.* **2007**, *185* (1), 118–129.
(42) Bode, B. E.; Margraf, D.; Plackmeyer, J.; Dürner, G.; Prisner, T. F.; Schiemann, O. *J. Am. Chem. Soc.* **2007**, *129* (21), 6736–6745.
(43) Jeschke, G.; Wegener, C.; Nietschke, M.; Jung, H.; Steinhoff, H.-J. *Biophys. J.* **2004**, *86* (4), 2551–2557.
(44) Tsvetkov, Y. D. *J. Struct. Chem.* **2013**, *54* (S1), 42–72.
(45) Denysenkov, V. P.; Prisner, T. F.; Stubbe, J.; Bennati, M. *Proc. Natl. Acad. Sci.* **2006**, *103* (36), 13386–13390.
(46) Denysenkov, V. P.; Biglino, D.; Lubitz, W.; Prisner, T. F.; Bennati, M. *Angew. Chem. Int. Ed.* **2008**, *47* (7), 1224–1227.
(47) Ji, M.; Ruthstein, S.; Saxena, S. *Acc. Chem. Res.* **2014**, *47* (2), 688–695.
(48) Yang, Z.; Becker, J.; Saxena, S. *J. Magn. Reson.* **2007**, *188* (2), 337–343.
(49) Yang, Z.; Ji, M.; Saxena, S. *Appl. Magn. Reson.* **2010**, *39* (4), 487–500.
(50) Amsterdam, I. M. C. Van; Ubbink, M.; Canters, G. W.; Huber, M. *Angew. Chem. Int. Ed* **2003**, *42* (1), 62–64.
(51) Kay, C. W. M.; El Mkami, H.; Cammack, R.; Evans, R. W. *J. Am. Chem. Soc.* **2007**, *129* (16), 4868–4869.
(52) Van Wonderen, J. H.; Kostrz, D. N.; Dennison, C.; MacMillan, F. *Angew. Chem. Int. Ed.* **2013**, *52* (7), 1990–1993.
(53) Yang, Z.; Kise, D.; Saxena, S. *J. Phys. Chem. B* **2010**, *114* (18), 6165–6174.
(54) Sarver, J.; Silva, K. I.; Saxena, S. *Appl. Magn. Reson.* **2013**, *44* (5), 583–594.
(55) Narr, E.; Godt, A.; Jeschke, G. *Angew. Chem. Int. Ed.* **2002**, *41* (20), 3907–3910.
(56) Bode, B. E.; Plackmeyer, J.; Prisner, T. F.; Schiemann, O. *J. Phys. Chem. A* **2008**, *112* (23), 5064–5073.
(57) Merz, G. E.; Borbat, P. P.; Pratt, A. J.; Getzoff, E. D.; Freed, J. H.; Crane, B. R. *Biophys. J.* **2014**, *107* (7), 1669–1674.
(58) Yang, Z.; Kurpiewski, M. R.; Ji, M.; Townsend, J. E.; Mehta, P.; Jen-Jacobson, L.; Saxena, S. *Proc. Natl. Acad. Sci.* **2012**, *109* (17), E993–E1000.
(59) Abdullin, D.; Florin, N.; Hagelueken, G.; Schiemann, O. *Angew. Chemie Int. Ed.* **2015**, *54* (6), 1827–1831.
(60) Becker, J. S.; Saxena, S. *Chem. Phys. Lett.* **2005**, *414* (1-3), 248–252.
(61) Ruthstein, S.; Ji, M.; Mehta, P.; Jen-Jacobson, L.; Saxena, S. *J. Phys. Chem. B* **2013**, *117*, 6227–6230.
(62) Elsässer, C.; Brecht, M.; Bittl, R. *J. Am. Chem. Soc.* **2002**, *124* (42), 12606–12611.

(63) Astashkin, A. V.; Seravalli, J.; Mansoorabadi, S. O.; Reed, G. H.; Ragsdale, S. W. *J. Am. Chem. Soc.* **2006**, *128* (12), 3888–3889.
(64) Astashkin, A. V; Rajapakshe, A.; Cornelison, M. J.; Johnson-Winters, K.; Enemark, J. H. *J. Phys. Chem. B* **2012**, 116, 1942–1950.
(65) Codd, R.; Astashkin, A. V.; Pacheco, A.; Raitsimring, A. M.; Enemark, J. H. *J. Biol. Inorg. Chem.* **2002**, *7* (3), 338–350.
(66) Hara, H.; Kawamori, A.; Astashkin, A. V.; Ono, T. A. *Biochim. Biophys. Acta - Bioenerg.* **1996**, *1276* (2), 140–146.
(67) Kawamori, A. *Appl. Magn. Reson.* **2007**, *31*, 205–220.
(68) Gunanathan, C.; Diskin-Posner, Y.; Milstein, D. *Cryst. Growth Des.* **2010**, *10* (10), 4235–4239.
(69) Potapov, A.; Song, Y.; Meade, T. J.; Goldfarb, D.; Astashkin, A. V.; Raitsimring, A. *J. Magn. Reson.* **2010**, *205* (1), 38–49.
(70) Raitsimring, A.; Astashkin, A. V.; Enemark, J. H.; Kaminker, I.; Goldfarb, D.; Walter, E. D.; Song, Y.; Meade, T. J. *Appl. Magn. Reson.* **2013**, *44* (6), 649–670.
(71) Doll, A.; Qi, M.; Pribitzer, S.; Wili, N.; Yulikov, M.; Godt, A.; Jeschke, G. *Phys. Chem. Chem. Phys.* **2015**, *17*, 7334–7344.
(72) Potapov, A.; Yagi, H.; Huber, T.; Jergic, S.; Dixon, N. E.; Otting, G.; Goldfarb, D. *J. Am. Chem. Soc.* **2010**, *132*, 9040–9048.
(73) Gordon-Grossman, M.; Kaminker, I.; Gofman, Y.; Shai, Y.; Goldfarb, D. *Phys. Chem. Chem. Phys.* **2011**, *13* (22), 10771–10780.
(74) Edwards, D. T.; Huber, T.; Hussain, S.; Stone, K. M.; Kinnebrew, M.; Kaminker, I.; Matalon, E.; Sherwin, M. S.; Goldfarb, D.; Han, S. *Structure* **2014**, *22* (11), 1677–1686.
(75) Song, Y.; Meade, T. J.; Astashkin, A. V.; Klein, E. L.; Enemark, J. H.; Raitsimring, A. *J. Magn. Reson.* **2011**, *210* (1), 59–68.
(76) Yagi, H.; Banerjee, D.; Graham, B.; Huber, T.; Goldfarb, D.; Otting, G. *J. Am. Chem. Soc.* **2011**, *133*, 10418–10421.
(77) Matalon, E.; Huber, T.; Hagelueken, G.; Graham, B.; Frydman, V.; Feintuch, A.; Otting, G.; Goldfarb, D. *Angew. Chem. Int. Ed.* **2013**, *52* (45), 11831–11834.
(78) Martorana, A.; Bellapadrona, G.; Feintuch, A.; Elbaum, M.; Di Gregorio, E.; Aime, S.; Goldfarb, D. *J. Am. Chem. Soc.* **2014**, *136*, 16458–13465.
(79) Wojciechowski, F.; Groß, A.; Holder, I. T.; Knörr, L.; Drescher, M.; Hartig, J. S. *Chem. Comm.* **2015**.
(80) Lueders, P.; Jeschke, G.; Yulikov, M. *J. Phys. Chem. Lett.* **2011**, *2* (6), 604–609.
(81) Yulikov, M.; Lueders, P.; Farooq Warsi, M.; Chechik, V.; Jeschke, G. *Phys. Chem. Chem. Phys.* **2012**, *14* (30), 10732.
(82) Kaminker, I.; Yagi, H.; Huber, T.; Feintuch, A.; Otting, G.; Goldfarb, D. *Phys. Chem. Chem. Phys.* **2012**, *14* (13), 4355.
(83) Lueders, P.; Jäger, H.; Hemminga, M. A.; Jeschke, G.; Yulikov, M. *J. Phys. Chem. B* **2013**, *117* (7), 2061–2068.
(84) Garbuio, L.; Bordignon, E.; Brooks, E. K.; Hubbell, W. L.; Jeschke, G.; Yulikov, M. *J. Phys. Chem. B* **2013**, *117* (11), 3145–3153.
(85) Garbuio, L.; Lewandowski, B.; Wilhelm, P.; Ziegler, L.; Yulikov, M.; Wennemers, H.; Jeschke, G. *Chem. Eur. J.* **2015**, *21*, 10747–10753.
(86) Kaminker, I.; Tkach, I.; Manukovsky, N.; Huber, T.; Yagi, H.; Otting, G.; Bennati, M.; Goldfarb, D. *J. Magn. Reson.* **2013**, *227*, 66–71.
(87) Razzaghi, S.; Qi, M.; Nalepa, A. I.; Godt, A.; Jeschke, G.; Savitsky, A.; Yulikov, M. *J. Phys. Chem. Lett.* **2014**, *5*, 3970–3975.
(88) Sezer, D.; Prandolini, M. J.; Prisner, T. F. *Phys. Chem. Chem. Phys.* **2009**, *11* (31), 6626–6637.
(89) Akhmetzyanov, D.; Plackmeyer, J.; Endeward, B.; Denysenkov, V.; Prisner, T. F. *Phys. Chem. Chem. Phys.* **2015**, *17* (10), 6760–6766.

(90) Kaminker, I.; Bye, M.; Mendelman, N.; Gislason, K.; Sigurdsson, S. T.; Goldfarb, D. *Phys. Chem. Chem. Phys.* **2015**, *17* (23), 15098–15102.
(91) Small, B. L. *Acc. Chem. Res.* **2015**, 10.1021/acs.accounts.5b00252, ASAP
(92) Small, B. L.; Brookhart, M.; Bennett, A. M. A. *J. Am. Chem. Soc.* **1998**, *120* (16), 4049–4050.
(93) Tondreau, A. M.; Atienza, C. C. H.; Weller, K. J.; Nye, S. A.; Lewis, K. M.; Delis, J. G. P.; Chirik, P. J. *Science* **2012**, *335*, 567–570.
(94) Sylvester, K. T.; Chirik, P. J. *J. Am. Chem. Soc.* **2009**, 8772–8774.
(95) Monfette, S.; Turner, Z. R.; Semproni, S. P.; Chirik, P. J. *J. Am. Chem. Soc.* **2012**, *134* (10), 4561–4564.
(96) Esteruelas, M. A.; López, A. M.; Méndez, L.; Oliván, M.; Oñate, E. *Organometallics* **2003**, *22* (3), 395–406.
(97) Reardon, D.; Conan, F.; Gambarotta, S.; Yap, G.; Wang, Q. *J. Am. Chem. Soc.* **1999**, *121* (40), 9318–9325.
(98) Reardon, D.; Aharonian, G.; Gambarotta, S.; Yap, G. P. A. *Organometallics* **2002**, *21* (5), 786–788.
(99) Fan, R.-Q.; Zhu, D.-S.; Mu, Y.; Li, G.-H.; Yang, Y.-L.; Su, Q.; Feng, S.-H. *Eur. J. Inorg. Chem.* **2004**, *2004* (24), 4891–4897.
(100) Fan, R.; Yang, Y.; Yin, Y.; Hasi, W.; Mu, Y. *Inorg. Chem.* **2009**, *48* (13), 6034–6043.
(101) Fan, R.-Q.; Wang, P.; Yang, Y.-L.; Zhang, Y.-J.; Yin, Y.-B.; Hasi, W. *Polyhedron* **2010**, *29* (14), 2862–2866.
(102) Jurca, T.; Gorelsky, S. I.; Korobkov, I.; Richeson, D. S. *Dalton Trans.* **2011**, *40* (17), 4394–4396.
(103) Gallagher, M.; Wieder, N. L.; Dioumaev, V. K.; Carroll, P. J.; Berry, D. H. *Organometallics* **2010**, *29* (3), 591–603.
(104) Edwards, D. A.; Mahon, M. F.; Martin, W. R.; Molloy, K. C.; Fanwick, P. E.; Walton, R. A. *J. Chem. Soc. Dalton Trans.* **1990**, *1*, 3161–3168.
(105) Pérez, C. M.; Rodríguez-Delgado, A.; Palma, P.; Álvarez, E.; Gutiérrez-Puebla, E.; Cámpora, J. *Chem. Eur. J.* **2010**, *16* (46), 13834–13842.
(106) Farouk, H.; El, A.; Omar, M. M.; Mohamed, G. G.; El, M. A.; Sayed, E. *Eur. J. Chem.* **2011**, *2* (2), 178–188.
(107) Su, B.; Zhao, J.; Cui, Y.; Sun, W. *Synth. Comm.* **2005**, *3*5, 2317–2324.
(108) Xie, G.; Ai, H.; Lei, L.; Zhang, D. *J. Chem. Soc. Pak.* **2009**, *31* (4).
(109) Ivchenko, P. V.; Nifant'Ev, I. E.; Buslov, I. V. *Tet. Lett.* **2013**, *54* (3), 217–219.
(110) Schultz, A.; Li, X.; Barkakaty, B.; Moorefield, C. N.; Wesdemiotis, C.; Newkome, G. R. *J. Am. Chem. Soc.* **2012**, *134* (18), 7672–7675.
(111) Chung, S.-K.; Tseng, Y.-R.; Chen, C.-Y.; Sun, S.-S. *Inorg. Chem.* **2011**, *50*, 2711–2713.
(112) Constable, E. C.; Housecroft, C. E.; Schneider, G. E.; Zampese, J. A.; Bolink, H. J.; Pertegás, A.; Roldan-Carmona, C. *Dalton Trans.* **2014**, *43*, 4653.
(113) Bertrand, H.; Monchaud, D.; De Cian, A.; Guillot, R.; Mergny, J.-L.; Teulade-Fichou, M.-P. *Org. Biomol. Chem.* **2007**, *5* (16), 2555–2559.
(114) Bertrand, H.; Bombard, S.; Monchaud, D.; Talbot, E.; Guédin, A.; Mergny, J.-L.; Grünert, R.; Bednarski, P. J.; Teulade-Fichou, M.-P. *Org. Biomol. Chem.* **2009**, *7* (14), 2864–2871.
(115) Cargill Thompson, A. M. W. W. *Coord. Chem. Rev.* **1997**, *160*, 1–52.
(116) Wang, J.; Hanan, G. S. *Synlett* **2005**, *8*, 1251–1254.
(117) Eryazici, I.; Moorefield, C. N.; Durmus, S.; Newkome, G. R. *J. Org. Chem.* **2006**, *71*, 1009–1014.
(118) Wang, Z.; Yuan, S.; Mason, A.; Reprogle, B.; Liu, D. J.; Yu, L. *Macromolecules* **2012**, *45* (18), 7413–7419.
(119) Herner, A.; Nikić, I.; Kállay, M.; Lemke, E. A.; Kele, P. *Org. Biomol. Chem.* **2013**, *11* (20), 3297–3306.
(120) Chen, H.; Tagore, R.; Das, S.; Incarvito, C.; Faller, J. W.; Crabtree, R. H.; Brudvig, G. W. *Inorg. Chem.* **2005**, *44* (21), 7661–7670.

(121) Tu, S.; Jia, R.; Jiang, B.; Zhang, J.; Zhang, Y.; Yao, C.; Ji, S. *Tetrahedron* **2007**, *63* (2), 381–388.
(122) Cave, G. W. V; Raston, C. L. *J. Chem. Soc. Perkin Trans. 1* **2001**, No. 24, 3258–3264.
(123) Korall, P.; Börje, A.; Norrby, P.-O.; Åkermark, B.; Robinson, W. T.; Wood, B. R.; Robinson, W. T.; Roos, B. O.; Vallance, C.; Wood, B. R. *Acta Chem. Scand.* **1997**, 760–766.
(124) Winter, A.; Egbe, D. a M.; Schubert, U. S. *Org. Lett.* **2007**, 9 (*12*), 2345–2348.
(125) Yuan, S. C.; Chen, H. B.; Zhang, Y.; Pei, J. *Org. Lett.* **2006**, *8* (25), 5701–5704.
(126) Mantel, C.; Baffert, C.; Romero, I.; Deronzier, A.; Pécaut, J.; Collomb, M. N.; Duboc, C. *Inorg. Chem.* **2004**, *43* (20), 6455–6463.
(127) Osorio, E. A.; Moth-Poulsen, K.; Van Der Zant, H. S. J.; Paaske, J.; Hedegård, P.; Flensberg, K.; Bendix, J.; Bjørnholm, T. *Nano Lett.* **2010**, *10* (1), 105–110.
(128) Karmakar, S.; Maity, D.; Mardanya, S.; Baitalik, S. *Inorg. Chem*. **2014**, *53*, 12036–12049.
(129) Gätjens, J.; Sjöden, M.; Pecoraro, V. L.; Un, S. *J. Am. Chem. Soc.* **2007**, *129*, 13825–13827.
(130) Brücher, E.; Tircsó, G.; Baranyai, Z.; Kovács, Z.; Sherry, A. D. *Stability and Toxicity of Contrast Agents***,** in "Chemistry of Contrast Agents in Medical Magnetic Resonance Imaging" 2nd edition, Chapter 5, ed. A. E. Merbach, E. Tóth and L. Helm, John Wiley & Sons, 157–208.
(131) Tabares, L. C.; Gätjens, J.; Hureau, C.; Burrell, M. R.; Bowater, L.; Pecoraro, V. L.; Bornemann, S.; Un, S. *J. Phys. Chem. B* **2009**, *113* (26), 9016–9025.
(132) Pellegatti, L.; Zhang, J.; Drahoš, B.; Villette, S.; Suzenet, F.; Guillaumet, G.; Petoud, S.; Tóth, E. *Chem. Comm.* **2008**, *60* (48), 6591–6593.
(133) Drahoš, B.; Lukeš, I.; Tóth, E. *Eur. J. Inorg. Chem.* **2012**, *12*, 1975–1986.
(134) Takalo, H.; Pasanen, P.; Kankare, J.; Undheim, K.; Wittman, G.; Gera, L.; Bartók, M.; Pelczer, I.; Dombi, G. *Acta Chem. Scand.* **1988**, 373–377.
(135) Bonnet, C. S.; Buron, F.; Caillé, F.; Shade, C. M.; Drahoš, B.; Pellegatti, L.; Zhang, J.; Villette, S.; Helm, L.; Pichon, C.; Suzenet, F.; Petoud, S.; Tóth, E. *Chem. Eur. J.* **2012**, *18* (5), 1419–1431.
(136) Pouessel, J.; Abada, S.; Le Bris, N.; Elhabiri, M.; Charbonnière, L. J.; Tripier, R. *Dalton Trans.* **2013**, *42* (14), 4859–4872.
(137) Valeur, B.; Czarnik, A. W.; *Topics in Fluorescence Spectroscopy, vol. 4*, ed. J. R. Lakowicz, 21–68.
(138) Tzanopoulou, S.; Pirmettis, I. C.; Patsis, G.; Paravatou-Petsotas, M.; Livaniou, E.; Papadopoulos, M.; Pelecanou, M. *J. Med. Chem.* **2006**, *49* (18), 5408–5410.
(139) Siaugue, J.-M.; Segat-Dioury, F.; Favre-Réguillon, A.; Madic, C.; Foos, J.; Guy, A. *Tet. Lett.* **2000**, *41* (39), 7443–7446.
(140) Galaup, C.; Couchet, J. M.; Bedel, S.; Tisnès, P.; Picard, C. *J. Org. Chem.* **2005**, *70* (6), 2274–2284.
(141) Siaugue, J.-M.; Segat-Dioury, F.; Sylvestre, I.; Favre-Réguillon, A.; Foos, J.; Madic, C.; Guy, A. *Tetrahedron* **2001**, *57* (22), 4713–4718.
(142) Stetter, H.; Frank, W. *Angew. Chem* **1976**, *15* (11), 686.
(143) Viola-Villegas, N.; Doyle, R. P. *Coord. Chem. Rev.* **2009**, *253* (13-14), 1906–1925.
(144) Caravan, P.; Ellison, J. J.; McMurry, T. J.; Lauffer, R. B. *Chem. Rev.* **1999**, *99*, 2293–2352.
(145) Bianchi, A.; Calabi, L.; Giorgi, C.; Losi, P.; Mariani, P.; Palano, D.; Paoli, P.; Rossi, P.; Valtancoli, B. *J. Chem. Soc. Dalton Trans.* **2001**, No. 6, 917–922.
(146) Drahoš, B.; Kubíček, V.; Bonnet, C. S.; Hermann, P.; Lukeš, I.; Tóth, E. *Dalton Trans.* **2011**, *40* (9), 1945–1951.
(147) Wang, S.; Westmoreland, T. D. *Inorg. Chem.* **2009**, *48* (2), 719–727.
(148) Ching, H. Y. V.; Demay-Drouhard, P.; Bertrand, H. C.; Policar, C.; Tabares, L. C.; Un, S. *Phys. Chem. Chem. Phys.* **2015**, *17*, 23368–23377.
(149) Yang, C. T.; Li, Y.; Liu, S. *Inorg. Chem.* **2007**, *46* (21), 8988–8997.
(150) Stasiuk, G. J.; Smith, H.; Wylezinska-Arridge, M.; Tremoleda, J. L.; Trigg, W.; Luthra, S. K.; Iveson, V. M.; Gavins, F. N. E.; Long, N. J. *Chem. Comm.* **2012**, *49* (6), 564–566.

(151) Natrajan, L. S.; Villaraza, A. J. L.; Kenwright, A. M.; Faulkner, S. *Chem. Comm.* **2009**, No. 40, 6020–6022.
(152) Li, W.-S.; Luo, J.; Chen, Z.-N. *Dalton Trans.* **2011**, *40* (2), 484–488.
(153) Saini, N.; Varshney, R.; Tiwari, A. K.; Kaul, A.; Allard, M.; Ishar, M. P. S.; Mishra, A. K. *Dalton Trans.* **2013**, *42* (14), 4994–5003.
(154) Norante, G. D. M.; Vaira, M. Di; Mani, F.; Mazzi, S.; Stoppioni, P. *Inorg. Chem.* **1990**, *29*, 2822–2829.
(155) Bu, X. H.; Chen, W.; Mu, L. J.; Zhang, Z. H.; Zhang, R. H.; Clifford, T. *Polyhedron* **2000**, *19*, 2095–2100.
(156) Liu, G. F.; Filipović, M.; Heinemann, F. W.; Ivanović-Burmazović, I. *Inorg. Chem.* **2007**, *46* (21), 8825–8835.
(157) Hureau, C.; Blanchard, S.; Nierlich, M.; Blain, G.; Rivière, E.; Girerd, J.-J.; Anxolabéhère-Mallart, E.; Blondin, G. *Inorg. Chem.* **2004**, *43* (14), 4415–4426.
(158) Semetey, V.; Moustakas, D.; Whitesides, G. M. *Angew. Chem. Int. Ed.* **2006**, *45* (4), 588–591.
(159) Fray, M. J.; Allen, P.; Bradley, P. R.; Challenger, C. E.; Closier, M.; Evans, T. J.; Lewis, M. L.; Mathias, J. P.; Nichols, C. L.; Po-Ba, Y. M.; Snow, H.; Stefaniak, M. H.; Vuong, H. V. *Tetrahedron* **2006**, *62* (29), 6869–6875.
(160) Abdel-Magid, A. F.; Carson, K. G.; Harris, B. D.; Maryanoff, C. A.; Shah, R. D. *J. Org. Chem.* **1996**, *61* (11), 3849–3862.
(161) Rahaim, R. J.; Shaw, J. T. *J. Org. Chem.* **2008**, *73* (7), 2912–2915.
(162) Wolfe, J. P.; Wagaw, S.; Buchwald, S. L. *J. Am. Chem. Soc.* **1996**, *118* (30), 7215–7216.
(163) Wolfe, J. P.; Buchwald, S. L. *J.Org. Chem.* **2000**, *64*, 1144–1157.
(164) McMurry, J. E. *Chem. Rev.* **1989**, *89* (7), 1513–1524.
(165) Duan, X. F.; Zeng, J.; Lü, J. W.; Zhang, Z. Bin. *J. Org. Chem.* **2006**, *71* (26), 9873–9876.
(166) Bursavich, M. G.; West, C. W.; Rich, D. H. *Org. Lett.* **2001**, *3* (15), 2317–2320.
(167) Eastwood, P. R. *Tet. Lett.* **2000**, *41* (19), 3705–3708.
(168) Ghosez, A.; Göbel, T.; Giese, B. *Chem. Ber.* **1988**, *121*, 1807–1811.
(169) Takeda, T.; Sasaki, R.; Yamauchi, S.; Fujiwara, T. *Tetrahedron* **1997**, *53* (2), 557–566.
(170) Darwish, A.; Chong, J. M. *J. Org. Chem.* **2007**, *72* (4), 1507–1509.
(171) Biannic, B.; Bozell, J. J. *Org. Lett.* **2013**, *15* (11), 2730–2733.
(172) Lim, M. J.; Murray, C. A.; Tronic, T. A.; Kathryn, E.; Ley, A. N.; Jordan, C.; Pike, R. D.; Lu, H.; Patterson, H. H. *Inorg. Chem.* **2008**, *47* (15), 6931–6947.
(173) Frisch, M. J.; Trucks, G. W.; Schlegel, H. B.; Scuseria, G. E.; Robb, M. A.; Cheeseman, J. R.; Scalmani, G.; Barone, V.; Mennucci, B.; Petersson, G. A.; Nakatsuji, H.; Caricato, M.; Li, X.; Hratchian, H. P.; Izmaylov, A. F.; Bloino, J.; Zheng, G.; Sonnenberg, J. L.; Hada, M.; Ehara, M.; Toyota, K.; Fukuda, R.; Hasegawa, J.; Ishida, M.; Nakajima, T.; Honda, Y.; Kitao, O.; Nakai, H.; Vreven, T.; Montgomery, J. A., Jr.; Peralta, J. E.; Ogliaro, F.; Bearpark, M.; Heyd, J. J.; Brothers, E.; Kudin, K. N.; Staroverov, V. N.; Kobayashi, R.; Normand, J.; Raghavachari, K.; Rendell, A.; Burant, J. C.; Iyengar, S. S.; Tomasi, J.; Cossi, M.; Rega, N.; Millam, J. M.; Klene, M.; Knox, J. E.; Cross, J. B.; Bakken, V.; Adamo, C.; Jaramillo, J.; Gomperts, R.; Stratmann, R. E.; Yazyev, O.; Austin, A. J.; Cammi, R.; Pomelli, C.; Ochterski, J. W.; Martin, R. L.; Morokuma, K.; Zakrzewski, V. G.; Voth, G. A.; Salvador, P.; Dannenberg, J. J.; Dapprich, S.; Daniels, A. D.; Farkas, O.; Foresman, J. B.; Ortiz, J. V.; Cioslowski, J.; Fox, D. J. *Gaussian 09*, Gaussian, Inc., Wallingford, CT, 2009.
(174) Maity, P.; König, B. *Org. Lett.* **2008**, *10* (7), 1473–1476.
(175) Wolfe, J. P.; Buchwald, S. L. *J. Org. Chem.* **1997**, *62* (7), 6066–6068.
(176) Zhang, H.; Cai, Q.; Ma, D. *J. Org. Chem.* **2005**, 70, 5164–5173.
(177) Fors, B. P.; Buchwald, S. L. *J. Am. Chem. Soc.* **2010**, *132*, 15914–15917.
(178) Ram. S.; Spicer, D. *Tet. Lett.* **1987**, *28* (5), 515–516.

(179) Barge, A.; Tei, L.; Upadhyaya, D.; Fedeli, F.; Beltrami, L.; Stefanìa, R.; Aime, S.; Cravotto, G. *Org. Biomol. Chem.* **2008**, *6* (7), 1176–1184.
(180) Morrison, D. E.; Aitken, J. B.; de Jonge, M. D.; Ioppolo, J. A.; Harris, H. H.; Rendina, L. M. *Chem. Comm.* **2014**, *50* (18), 2252–2254.
(181) Tour, J. M. *Chem. Rev.* **1996**, *96* (1), 537–554.
(182) Jeschke, G.; Zimmermann, H.; Godt, A. *J. Magn. Reson.* **2006**, *180* (1), 137–146.
(183) Sun, J.; Stone, G. M.; Balsara, N. P.; Zuckermann, R. N. *Macromolecules* **2012**, *45*, 5151–5156.
(184) Zhao, Y.; Shirai, Y.; Slepkov, A. D.; Cheng, L.; Alemany, L. B.; Sasaki, T.; Hegmann, F. A.; Tour, J. M. *Chem. Eur. J.* **2005**, *11* (12), 3643–3658.
(185) Meier, H.; Ickenroth, D.; Stalmach, U.; Koynov, K.; Bahtiar, A.; Bubeck, C. *Eur. J. Org. Chem.* **2001**, *2001* (23), 4431–4443.
(186) Sontag, B.; Rüth, M.; Spiteller, P.; Arnold, N.; Steglich, W.; Reichert, M.; Bringmann, G. *Eur. J. Org. Chem.* **2006**, *2006* (4), 1023–1033.
(187) Nierengarten, J. F.; Zhang, S.; Gégout, A.; Urbani, M.; Armaroli, N.; Marconi, G.; Rio, Y. *J. Org. Chem.* **2005**, *70* (19), 7550–7557.
(188) Burdyńska, J.; Li, Y.; Aggarwal, A. V.; Höger, S.; Sheiko, S. S.; Matyjaszewski, K. *J. Am. Chem. Soc.* **2014**, *136*, 12762–12770.
(189) Swinnen, D.; Jorand-Lebrun, C.; Gerber, P.; Gonzalez, J.; Bombrun, A. Patent PCT WO 2005/09773 A1.
(190) Martos-Maldonado, M. C.; Quesada-Soriano, I.; Casas-Solvas, J. M.; García-Fuentes, L.; Vargas-Berenguel, A. *Eur. J. Org. Chem.* **2012**, No. 13, 2560–2571.
(191) Allen, C. P.; Benkovics, T.; Turek, A. K.; Yoon, T. P. *J. Am. Chem. Soc.* **2009**, *131* (35), 12560–12561.
(192) Mössinger, D.; Jester, S.-S.; Sigmund, E.; Müller, U.; Höger, S. *Macromolecules* **2009**, *42* (20), 7974–7978.
(193) Ponce, J.; Arroyo, C. R.; Tatay, S.; Frisenda, R.; Gavin, P.; Aravena, D.; Ruiz, E.; Zant, H. S. J. Van Der; Coronado, E. *J. Am. Chem. Soc.* **2014**, *136*, 8314–8322.
(194) Wild, A.; Winter, A.; Hager, M. D.; Schubert, U. S. *Chem. Comm.* **2012**, *48* (7), 964.
(195) Spartan
(196) Lee, M.; Tremblay, M. S.; Jockusch, S.; Turro, N. J.; Sames, D. *Org. Lett.* **2011**, *13* (11), 2802–2805.
(197) Fung, Y. O.; Wu, W.; Yeung, C. T.; Kong, H. K.; Wong, K. K. C.; Lo, W. S.; Law, G. L.; Wong, K. L.; Lau, C. K.; Lee, C. S.; Wong, W. T. *Inorg. Chem.* **2011**, *50* (12), 5517–5525.
(198) Wilkinson, A. J.; Maffeo, D.; Beeby, A.; Foster, C. E.; Williams, J. A. G. *Inorg. Chem.* **2007**, *46* (22), 9438–9449.
(199) Luo, J.; Li, W.-S.; Xu, P.; Zhang, L.-Y.; Chen, Z.-N. *Inorg. Chem.* **2012**, *51* (17), 9508–9516.
(200) Laakso, J.; Rosser, G. A.; Szíjjártó, C.; Beeby, A.; Borbas, K. E. *Inorg. Chem.* **2012**, *51* (19), 10366–10374.
(201) Viguier, R. F. H.; Hulme, A. N. *J. Am. Chem. Soc.* **2006**, *128* (35), 11370–11371.
(202) Jamous, M.; Haberkorn, U.; Mier, W. *Molecules* **2013**, *18* (3), 3379–3409.
(203) Jamous, M.; Haberkorn, U.; Mier, W. *Tet. Lett.* **2012**, *53* (50), 6810–6814.
(204) Mier, W.; Graham, K. A. N.; Wang, Q.; Krämer, S.; Hoffend, J.; Eisenhut, M.; Haberkorn, U. *Tet. Lett.* **2004**, *45* (28), 5453–5455.
(205) Bonora, M.; Becker, J.; Saxena, S. *J. Magn. Reson.* **2004**, *170* (2), 278–283.
(206) Gray, E. G. *Nature* **1955**, *175*, 642–643.
(207) Kakinoki, S.; Hirano, Y.; Oka, M. *Polym. Bull.* **2005**, *53* (2), 109–115.
(208) Wilhelm, P.; Lewandowski, B.; Trapp, N.; Wennemers, H. *J. Am. Chem. Soc.* **2014**, *136*, 15829–15832.
(209) Schuler, B.; Lipman, E. A.; Steinbach, P. J.; Kumke, M.; Eaton, W. A. *Proc. Natl. Acad. Sci.* **2005**, *102* (8), 2754–2759.

(210) Hoefling, M.; Lima, N.; Haenni, D.; Seidel, C. A. M.; Schuler, B.; Grubmüller, H. *PLoS One* **2011**, *6* (5).
(211) Rabanal, F.; Ludevid, M. D.; Pons, M.; Giralt, E. *Biopolymers* **1993**, *33* (7), 1019–1028.
(212) Traub, W. *Nature* **1963**, *198*, 1165–1166.
(213) Rucker, A. L.; Creamer, T. P. *Protein Sci.* **2002**, *11* (4), 980–985.
(214) Braslau, R.; Rivera, F.; Lilie, E.; Cottman, M. *J. Org. Chem.* **2013**, *78* (2), 238–245.
(215) Yin, W.; Chu, C.; Lu, Q.; Tao, J.; Liang, X.; Liu, R. *Adv. Synth. Catal.* **2010**, *352* (1), 113–118.
(216) Schleich, T. *Biopolymers* **1973**, *12*, 993–1010.
(217) Tooke, L.; Duitch, L.; Measey, T. J.; Schweitzer-Stenner, R. *Biopolymers* **2010**, *93* (5), 451–457.
(218) Hagelueken, G.; Ward, R.; Naismith, J. H.; Schiemann, O. *Appl. Magn. Reson.* **2012**, *42* (3), 377–391.
(219) Hagelueken, G.; Abdullin, D.; Ward, R.; Schiemann, O. *Mol. Phys.* **2013**, *111* (18-19), 2757–2766.
(220) Schimmel, P.R.; Flory, P. J. *Proc. Nat. Acad. Sci.* **1967**, *58*, 52–59.
(221) Mattice, L M.; Mandelkern, L. *J. Am. Chem. Soc.* **1984**, *93* (7), 115–118.
(222) Watkins, L. P.; Chang, H.; Yang, H. *J. Phys. Chem. A* **2006**, *110* (15), 5191–5203.
(223) Best, R. B.; Merchant, K. A.; Gopich, I. V; Schuler, B.; Bax, A.; Eaton, W. A. *Proc. Natl. Acad. Sci.* **2007**, *104* (48), 18964–18969.
(224) Case, D.A.; Berryman, J.T.; Betz, R.M.; Cerutti, D.S.; Cheatham, T.E.; Darden, T.A.; Duke, R.E.; Giese, T.J.; Gohlke, H.; Goetz, A.W.; Homeyer, N.; Izadi, S.; Janowski, P.; Kaus, J.; Kovalenko, A.; Lee, T.S.; LeGrand, S.; Li, P.; Luchko, T.; Luo, R.; Madej, B.; Merz, K.M.; Monard, G.; Needham, P.; Nguyen, H.; Nguyen, H.T.; Omelyan, I.; Onufriev, A.; Roe, D.R.; Roitberg, A.; Salomon-Ferrer, R.; Simmerling, C.L.; Smith, W.; Swails, J.; Walker, R.C.; Wang, J.; Wolf, R.M.; Wu, X.; York, D.M.; Kollman, P.A. *AMBER 2015*, University of California, San Francisco, 2015.
(225) Wang, J. M.; Wolf, R. M.; Caldwell, J. W.; Kollman, P. A; Case, D. A. *J. Comput. Chem.* **2004**, *25* (9), 1157–1174.
(226) Wang, J.; Wang, W.; Kollman, P. A.; Case, D. A. *J. Mol. Graph. Model.* **2006**, *25* (2), 247–260.
(227) Humphrey, W.; Dalke, A.; Schulten, K. *J. Mol. Graph.* **1996**, *14* (1), 33–38.
(228) Goldfarb, D.; Lipkin, Y.; Potapov, A.; Gorodetsky, Y.; Epel, B.; Raitsimring, A. M.; Radoul, M.; Kaminker, I. *J. Magn. Reson.* **2008**, *194* (1), 8–15.
(229) Yang, Z.; Liu, Y.; Borbat, P.; Zweier, J. L.; Freed, J. H.; Hubbell, W. L. *J. Am. Chem. Soc.* **2012**, *134* (24), 9950–9952.
(230) Reginsson, G. W.; Kunjir, N. C.; Sigurdsson, S. T.; Schiemann, O. *Chem. Eur. J.* **2012**, *18* (43), 13580–13584.
(231) Gomberg, M. *J. Am. Chem. Soc.* **1900**, *22* (11), 752–757.
(232) Ballester, M.; Riera, J.; Castañer, J.; Badia, C.; Monso, J. M. *J. Am. Chem. Soc.* **1971**, *9*3 (9), 2215–2225.
(233) Ballester, M.; Molinet, C.; Castañer, J. *J. Am. Chem. Soc.* **1960**, *82* (16), 4254–4258.
(234) Dang, V.; Wang, J.; Feng, S.; Buron, C.; Villamena, F. A.; Wang, P. G.; Kuppusamy, P. *Bioorganic Med. Chem. Lett.* **2007**, *17* (14), 4062–4065.
(235) Jorgensen, M.; Rise, F.; Andersson, S.; Almén, T.; Aabye, A.; Wikstrom, H.; Golman, K.; Servin, R.; Michelsen, P. Patent PCT WO 91/12024.
(236) Andersson, S.; Rydbeck, A.; Servin, R.; Wistrand, L.-G.; Radner, F. Patent PCT WO 96/39367.
(237) Xia, S.; Villamena, F. A.; Hadad, C. M.; Kuppusamy, P.; Li, Y.; Zhu, H.; Zweier, J. L. *J. Org. Chem.* **2006**, *71* (19), 7268–7279.
(238) Ballester, M.; Veciana, J.; Riera, J.; Castañer, J.; Concepción, R.; Armet, O. *J. Org. Chem.* **1986**, *51* (12), 2472–2480.
(239) Maspoch, D.; Domingo, N.; Roques, N.; Wurst, K.; Tejada, J.; Rovira, C.; Ruiz-Molina, D.; Veciana, J. *Chem. Eur. J.* **2007**, *13* (29), 8153–8163.

(240) Mesa, J. A.; Velázquez-Palenzuela, A.; Brillas, E.; Torres, J. L.; Juliá, L. *Tetrahedron* **2011**, *67* (17), 3119–3123.
(241) Torres, J. L.; Carreras, A.; Jiménez, A.; Brillas, E.; Torrelles, X.; Rius, J.; Juliá, L. *J. Org. Chem.* **2007**, *72* (10), 3750–3756.
(242) Munoz-Gomez, J.-L.; Marin-Montesinos, I.; Lloveras, V.; Pons, M.; Vidal-Gancelo, J.; Veciana, J. *Org. Lett.* **2014**, *16*, 5402–5405.
(243) Decroos, C.; Prangé, T.; Mansuy, D.; Boucher, J.-L.; Li, Y. *Chem. Comm.* **2011**, *47* (16), 4805–4807.
(244) Bobko, A. A.; Dhimitruka, I.; Zweier, J. L.; Khramtsov, V. V. *J. Am. Chem. Soc.* **2007**, *129* (23), 7240–7241.
(245) Dhimitruka, I.; Bobko, A. A.; Hadad, C. M.; Zweier, J. L.; Khramtsov, V. V. *J. Am. Chem. Soc.* **2008**, *130* (32), 10780–10787.
(246) Mesa, J. A.; Velázquez-Palenzuela, A.; Brillas, E.; Coll, J.; Torres, J. L.; Juliá, L. *J. Org. Chem.* **2012**, *77* (2), 1081–1086.
(247) Vera, F.; Mas-Torrent, M.; Avci, C.; Arbiol, J.; Esquena, J.; Rovira, C.; Veciana, J. *Chem. Comm.* **2013**, *49* (71), 7827–7829.
(248) Guasch, J.; Grisanti, L.; Jung, S.; Morales, D.; D'Avino, G.; Souto, M.; Fontrodona, X.; Painelli, A.; Renz, F.; Ratera, I.; Veciana, J. *Chem. Mater.* **2013**, *25* (5), 808–814.
(249) Sporer, C.; Ratera, I.; Ruiz-Molina, D.; Zhao, Y.; Vidal-Gancedo, J.; Wurst, K.; Jaitner, P.; Clays, K.; Persoons, A.; Rovira, C.; Veciana, J. *Angew. Chem. Int. Ed.* **2004**, *43* (39), 5266–5268.
(250) Crivillers, N.; Mas-Torrent, M.; Vidal-Gancedo, J.; Veciana, J.; Rovira, C. *J. Am. Chem. Soc.* **2008**, *130* (16), 5499–5506.
(251) Mas-Torrent, M.; Veciana, J. *Nano Lett.* **2011**, 4382–4385.
(252) Oliveros, M.; González-García, L.; Mugnaini, V.; Yubero, F.; Roques, N.; Veciana, J.; González-Elipe, A. R.; Rovira, C. *Langmuir* **2011**, *27* (8), 5098–5106.
(253) Simão, C.; Mas-Torrent, M.; Crivillers, N.; Lloveras, V.; Artés, J. M.; Gorostiza, P.; Veciana, J.; Rovira, C. *Nat. Chem.* **2011**, *3* (5), 359–364.
(254) Heckmann, A.; Lambert, C.; Goebel, M.; Wortmann, R. *Angew. Chem. Int. Ed.* **2004**, *43* (43), 5851–5856.
(255) Heckmann, A.; Lambert, C. *J. Am. Chem. Soc.* **2007**, *129* (17), 5515–5527.
(256) Guasch, J.; Grisanti, L.; Lloveras, V.; Vidal-Gancedo, J.; Souto, M.; Morales, D. C.; Vilaseca, M.; Sissa, C.; Painelli, A.; Ratera, I.; Rovira, C.; Veciana, J. *Angew. Chem. Int. Ed.* **2012**, *51* (44), 11024–11028.
(257) Elsner, O.; Ruiz-Molina, D.; Vidal-Gancedo, J.; Rovira, C.; Veciana, J. *Nano Lett.* **2001**, *1* (3), 117–120.
(258) Bonvoisin, J.; Launay, J.-P.; Rovira, C.; Veciana, J. *Angew. Chem. Int. Ed.* **1994**, *33* (20), 2106–2109.
(259) Lloveras, V.; Vidal-Gancedo, J.; Figueira-Duarte, T. M.; Nierengarten, J. F.; Novoa, J. J.; Mota, F.; Ventosa, N.; Rovira, C.; Veciana, J. *J. Am. Chem. Soc.* **2011**, *133* (15), 5818–5833.
(260) Maspoch, D.; Domingo, N.; Ruiz-Molina, D.; Wurst, K.; Vaughan, G.; Tejada, J.; Rovira, C.; Veciana, J. *Angew. Chem. Int. Ed.* **2004**, *43* (14), 1828–1832.
(261) Roques, N.; Maspoch, D.; Wurst, K.; Ruiz-Molina, D.; Rovira, C.; Veciana, J. *Chem. Eur. J.* **2006**, *12* (36), 9238–9253.
(262) Datcu, A.; Roques, N.; Jubera, V.; Imaz, I.; Maspoch, D.; Sutter, J. P.; Rovira, C.; Veciana, J. *Chem. Eur. J.* **2011**, *17* (13), 3644–3656.
(263) Roques, N.; Maspoch, D.; Imaz, I.; Datcu, A.; Sutter, J.-P.; Rovira, C.; Veciana, J. *Chem. Comm.* **2008**, No. 27, 3160–3162.
(264) Roques, N.; Güell, M.; Mugnaini, V.; Gómez, L.; Imaz, I.; Datcu, A.; Solà, M.; Luis, J. M.; Veciana, J.; Ribas, X.; Costas, M. *Dalton Trans.* **2008**, *3* (13), 1679–1682.

(265) Maspoch, D.; Domingo, N.; Ruiz-Molina, D.; Wurst, K.; Hernández, J.-M.; Vaughan, G.; Rovira, C.; Lloret, F.; Tejada, J.; Veciana, J. *Chem. Comm.* **2005**, *40*, 5035–5037.
(266) Gabellieri, C.; Mugnaini, V.; Paniagua, J. C.; Roques, N.; Oliveros, M.; Feliz, M.; Veciana, J.; Pons, M. *Angew. Chem. Int. Ed.* **2010**, *49* (19), 3360–3362.
(267) Banerjee, D.; Paniagua, J. C.; Mugnaini, V.; Veciana, J.; Feintuch, A.; Pons, M.; Goldfarb, D. *Phys. Chem. Chem. Phys.* **2011**, *13* (41), 18626.
(268) Paniagua, J. C.; Mugnaini, V.; Gabellieri, C.; Feliz, M.; Roques, N.; Veciana, J.; Pons, M. *Phys. Chem. Chem. Phys.* **2010**, *12* (22), 5741–5751.
(269) Warwar, N.; Mor, A.; Fluhr, R.; Pandian, R. P.; Kuppusamy, P.; Blank, A. *Biophys. J.* **2011**, *101* (6), 1529–1538.
(270) Meenakshisundaram, G.; Eteshola, E.; Blank, A.; Lee, S. C.; Kuppusamy, P. *Biosens. Bioelectron.* **2010**, *25* (10), 2283–2289.
(271) Bratasz, A.; Kulkarni, A. C.; Kuppusamy, P. *Biophys. J.* **2007**, *92* (8), 2918–2925.
(272) Wang, J.; Dang, V.; Zhao, W.; Lu, D.; Rivera, B. K.; Villamena, F. A.; Wang, P. G.; Kuppusamy, P. *Bioorganic Med. Chem.* **2010**, *18* (2), 922–929.
(273) Jiménez, A.; Selga, A.; Torres, J. L.; Julià, L. *Org. Lett.* **2004**, *6* (24), 4583–4586.
(274) Rogozhnikova, O. Y.; Vasiliev, V. G.; Troitskaya, T. I.; Trukhin, D. V.; Mikhalina, T. V.; Halpern, H. J.; Tormyshev, V. M. *Eur. J. Org. Chem.* **2013**, No. 16, 3347–3355.
(275) Reddy, T. J.; Iwama, T.; Halpern, H. J.; Rawal, V. H. *J. Org. Chem.* **2002**, *67* (14), 4635–4639.
(276) Dhimitruka, I.; Velayutham, M.; Bobko, A. A.; Khramtsov, V. V.; Villamena, F. A.; Hadad, C. M.; Zweier, J. L. *Bioorganic Med. Chem. Lett.* **2007**, *17* (24), 6801–6805.
(277) Liu, Y.; Villamena, F. A.; Rockenbauer, A.; Zweier, J. L. *Chem. Comm.* **2010**, *46* (4), 628–630.
(278) Liu, Y.; Villamena, F. A.; Rockenbauer, A.; Song, Y.; Zweier, J. L. *J. Am. Chem. Soc.* **2013**, *135*, 2350–2356.
(279) Liu, Y.; Villamena, F. A.; Song, Y.; Sun, J.; Rockenbauer, A.; Zweier, J. L. *J. Org. Chem.* **2010**, *75* (22), 7796–7802.
(280) Liu, Y.; Song, Y.; Rockenbauer, A.; Sun, J.; Hemann, C.; Villamena, F. A.; Zweier, J. L. *J. Org. Chem.* **2011**, *76* (10), 3853–3860.
(281) Shevelev, G. Y.; Krumkacheva, O. A.; Lomzov, A. A.; Kuzhelev, A. A.; Rogozhnikova, O. Y.; Trukhin, D. V; Troitskaya, T. I.; Tormyshev, V. M.; Fedin, M. V; Pyshnyi, D. V; Bagryanskaya, E. G. *J. Am. Chem. Soc.* **2014**, *136*, 9874–9877.
(282) Driesschaert, B.; Levêque, P.; Gallez, B.; Marchand-Brynaert, J. *Tet. Lett.* **2013**, *54* (44), 5924–5926.
(283) Liu, Y.; Villamena, F. A.; Zweier, J. L. *Chem. Comm.* **2008**, No. 36, 4336–4338.
(284) Driesschaert, B.; Levêque, P.; Gallez, B.; Marchand-Brynaert, J. *Eur. J. Org. Chem.* **2014**, 8077–8084.
(285) Liu, Y.; Villamena, F. A.; Sun, J.; Xu, Y.; Dhimitruka, I.; Zweier, J. L. *J. Org. Chem.* **2008**, *73* (4), 1490–1497.
(286) Tormyshev, V. M.; Rogozhnikova, O. Y.; Bowman, M. K.; Trukhin, D. V.; Troitskaya, T. I.; Vasiliev, V. G.; Shundrin, L. A.; Halpern, H. J. *Eur. J. Org. Chem.* **2014**, *2014* (2), 371–380.
(287) Ardenkjaer-Larsen, J. H.; Fridlund, B.; Gram, A.; Hansson, G.; Hansson, L.; Lerche, M. H.; Servin, R.; Thaning, M.; Golman, K. *Proc. Natl. Acad. Sci.* **2003**, *100* (18), 10158–10163.
(288) Lumata, L.; Kovacs, Z.; Sherry, A. D.; Malloy, C.; Hill, S.; van Tol, J.; Yu, L.; Song, L.; Merritt, M. E. *Phys. Chem. Chem. Phys.* **2013**, *15* (24), 9800–9807.
(289) Haze, O.; Corzilius, B.; Smith, A. A.; Griffin, R. G.; Swager, T. M. *J. Am. Chem. Soc.* **2012**, *134* (35), 14287–14290.
(290) Rizzi, C.; Samouilov, A.; Kumar Kutala, V.; Parinandi, N. L.; Zweier, J. L.; Kuppusamy, P. *Free Radic. Biol. Med.* **2003**, *35* (12), 1608–1618.
(291) Decroos, C.; Li, Y.; Bertho, G.; Frapart, Y.; Mansuy, D.; Boucher, J.-L. *Chem. Comm.* **2009**, 11, 1416–1418.

(292) Liu, Y.; Villamena, F. A.; Sun, J.; Wang, T. Y.; Zweier, J. L. *Free Radic. Biol. Med.* **2009**, *46* (7), 876–883.
(293) Decroos, C.; Balland, D.; Boucher, J.; Bertho, G.; Xu-Li, Y.; Mansuy, D. *Chem. Res. Toxicol.* **2013**, *26*, 1561–1569.
(294) Driesschaert, B.; Robiette, R.; Lucaccioni, F.; Gallez, B.; Marchand-Brynaert, J. *Chem. Comm.* **2011**, *47* (16), 4793–4795.
(295) Tormyshev, V. M.; Genaev, A. M.; Sal'Nikov, G. E.; Rogozhnikova, O. Y.; Troitskaya, T. I.; Trukhin, D. V.; Mamatyuk, V. I.; Fadeev, D. S.; Halpern, H. J. *Eur. J. Org. Chem.* **2012**, No. 3, 623–629.
(296) Driesschaert, B.; Robiette, R.; Le Duff, C. S.; Collard, L.; Robeyns, K.; Gallez, B.; Marchand-Brynaert, J. *European J. Org. Chem.* **2012**, No. 33, 6517–6525.
(297) Fielding, A. J.; Carl, P. J.; Eaton, G. R.; Eaton, S. S. *Appl. Magn. Reson.* **2005**, *28* (3-4), 231–238.
(298) Cage, B.; McNeely, J. H.; Russek, S. E.; Halpern, H. J. *J. Appl. Phys.* **2009**, *105* (4), 1–6.
(299) Yong, L.; Harbridge, J.; Quine, R. W.; Rinard, G. A.; Eaton, S. S.; Eaton, G. R.; Mailer, C.; Barth, E.; Halpern, H. J. *J. Magn. Reson.* **2001**, *152* (1), 156–161.
(300) Owenius, R.; Eaton, G. R.; Eaton, S. S. *J. Magn. Reson.* **2005**, *172* (1), 168–175.
(301) Decroos, C.; Li, Y.; Bertho, G.; Frapart, Y.; Mansuy, D.; Boucher, J. L. *Chem. Res. Toxicol.* **2009**, *22* (7), 1342–1350.
(302) Decroos, C.; Boucher, J.; Mansuy, D.; Xu-Li, Y. *Chem. Res. Toxicol.* **2014**, *27*, 627–636.
(303) He, G.; Deng, Y.; Li, H.; Kuppusamy, P.; Zweier, J. L. *Magn. Reson. Med.* **2002**, *47* (3), 571–578.
(304) Samouilov, A.; Caia, G. L.; Kesselring, E.; Petryakov, S.; Wasowicz, T.; Zweier, J. L. *Magn. Reson. Med.* **2007**, *58* (1), 156–166.
(305) Kuppusamy, P.; Wang, P.; Chzhan, M.; Zweier, J. L. *Magn. Reson. Med.* **1997**, *37* (4), 479–483.
(306) Krishna, M. C.; English, S.; Yamada, K.; Yoo, J.; Murugesan, R.; Devasahayam, N.; Cook, J. A.; Golman, K.; Ardenkjaer-Larsen, J. H.; Subramanian, S.; Mitchell, J. B. *Proc. Natl. Acad. Sci.* **2002**, *99* (4), 2216–2221.
(307) Ardenkjaer-Larsen, J. H.; Laursen, I.; Leunbach, I.; Ehnholm, G.; Wistrand, L. G.; Petersson, J. S.; Golman, K. *J. Magn. Reson.* **1998**, *133* (1), 1–12.
(308) Kunjir, N. C.; Reginsson, G. W.; Schiemann, O.; Sigurdsson, S. T. *Phys. Chem. Chem. Phys.* **2013**, *15* (45), 19673–19685.
(309) Burghaus, O.; Rohrer, M.; Gotzinger, T.; Plato, M.; Mobius, K. *Meas. Sci. Technol.* **1999**, *3* (8), 765–774.
(310) Gottlieb, H. E.; Kotlyar, V.; Nudelman, A. *J. Org. Chem.* **1997**, *62* (3), 7512–7515.
(311) Pronk, S.; Páll, S.; Schulz, R.; Larsson, P.; Bjelkmar, P.; Apostolov, R.; Shirts, M. R.; Smith, J. C.; Kasson, P. M.; Van Der Spoel, D.; Hess, B.; Lindahl, E. *Bioinformatics* **2013**, *29* (7), 845–854.
(312) Zagrovic, B.; Lipfert, J.; Sorin, E. J.; Millett, I. S.; van Gunsteren, W. F.; Doniach, S.; Pande, V. S. *Proc. Natl. Acad. Sci.* **2005**, *102* (33), 11698–11703.
(313) Sheldrick, G. M. *SHELXS-97, Program for Crystal Structure Solution*, University of Göttingen, Göttingen, Germany, 1997.
(314) Sheldrick, G. M. *SHELXL-97, Program for the Refinement of Crystal Structures from Diffraction Data*, University of Göttingen, Göttingen, Germany, 1997.
(315) Farrugia, L. J. *J. Appl. Crystallogr.* **1999**, *32* (4), 837–838.
(316) Bruker AXS Inc, Madison, Wisconsin, USA.

Résumé en français

INTRODUCTION

La complexité des être vivants est à la fois source d'émerveillement et d'inspiration. Parmi les nombreux processus biologiques à l'œuvre dans une cellule, beaucoup impliquent des macromolécules comme les protéines ou les acides nucléiques. Pour comprendre la fonction et les interactions de ces biomacromolécules, il est nécessaire de connaître leur structure. La diffractométrie de rayons X[1] (DRX) et la résonance magnétique nucléaire[2] (RMN) en sont les deux principaux outils d'analyse.

La DRX est une technique puissante puisqu'elle permet d'obtenir les coordonnées de tous les atomes de la molécule étudiée en analysant sa densité électronique. Pour cela, il est nécessaire d'obtenir un cristal de la molécule en question, et la recherche de conditions favorables à la cristallisation est empirique et peut se révéler particulièrement ardue pour certaines protéines. De plus, la structure d'une biomacromolécule cristallisée ne reflète pas nécessairement sa conformation active en milieu biologique. La RMN contourne ce problème puisqu'elle s'applique aux protéines en solution. Par le biais de nombreuses expériences bi- ou tridimensionnelles, il est possible d'identifier chaque atome en étudiant ses corrélations au travers des liaisons ou de l'espace. En reliant ces informations à des contraintes angulaires et de distance, la protéine d'intérêt peut alors être cartographiée. Cette méthode est très efficace pour les objets de petite taille mais l'interprétation des données devient complexe pour des protéines de masse moléculaire supérieure à 50 kDa.

Déterminer précisément de longues distances (de l'ordre de quelques nanomètres) dans les protéines par exemple apparaît alors comme une problématique intéressante, puisque les données ainsi obtenues fournissent des informations précieuses quant à la structure globale de l'objet étudié et complètent efficacement la DRX et la RMN. Obtenir un ensemble de contraintes de distance est également un excellent moyen d'analyser la structure dynamique des biomacromolécules, par exemple en observant des changements de conformation lors d'interactions avec des ligands, ou la formation d'oligomères. Dans cette optique, le transfert d'énergie par résonance de type Förster (FRET) a été largement utilisé, mais il est parfois difficile d'extraire la distance désirée à partir d'une différence d'intensités de fluorescence. Une alternative très prometteuse pour mesurer des distances nanométriques est la résonance paramagnétique électronique (RPE) et tout particulièrement certaines séquences d'impulsions comme le PELDOR (Pulse Electron-Electron Double Resonance), également appelé DEER (Double Electron-Electron Resonance).[3,4]

Lors d'une expérience RPE, un centre paramagnétique de spin électronique S, c'est-à-dire une espèce possédant un (cas des radicaux) ou plusieurs (cas des complexes métalliques en particulier) électrons non-appariés, est placé dans un champ magnétique **B** (les vecteurs sont indiqués en gras). L'interaction entre celui-ci et le moment magnétique $\boldsymbol{\mu}$ du centre paramagnétique fait apparaître un motif de 2S+1 niveaux d'énergie équidistants, pouvant prendre les valeurs M_S = -S, -S+1, … , S, et séparés par :

$$\Delta E = g\beta B \qquad [1]$$

g est appelé facteur *g* et β est le magnéton de Bohr. Cette levée de dégénérescence est connue sous le nom d'effet Zeeman (Figure 1).[5] Pour mesurer le facteur *g*, caractéristique du centre paramagnétique étudié, un rayonnement électromagnétique lui est appliqué. La composante magnétique de ce rayonnement va induire des transitions entre les niveaux d'énergie du centre paramagnétique si l'énergie hν des photons incidents est égale à l'écart d'énergie entre deux niveaux adjacents : c'est la condition de résonance. Dans une expérience de RPE en onde continue, la fréquence ν du rayonnement est fixe, et on fait varier B jusqu'à ce que celui-ci prenne la valeur B_0 telle que (Figure 1) :

$$h\nu = g\beta B_0 \qquad [2]$$

h est la constante de Planck. Ces transitions entraînent une absorption d'énergie, détectée par le spectromètre et convertie en raie de résonance. En RPE en onde continue, la dérivée du signal d'absorption est enregistrée : cela provient d'un procédé, appelé détection synchrone, qui consiste à superposer un petit champ magnétique sinusoïdal parallèle à **B**, ce qui permet l'extraction de la dérivée du signal d'absorption avec un excellent rapport signal sur bruit (RSB).

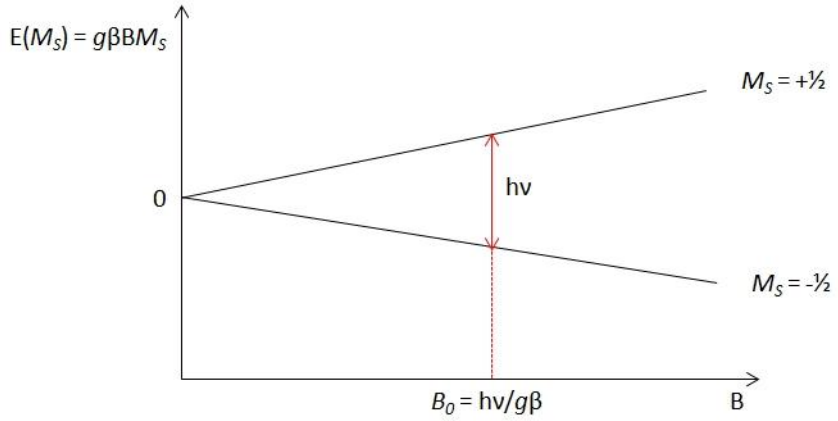

Figure 1 : Effet Zeeman et condition de résonance pour un centre paramagnétique de spin S = 1/2.

La forme d'un spectre RPE est en général bien plus complexe pour plusieurs raisons. Premièrement, l'interaction entre **μ** et **B** peut dépendre de la direction de **B** par rapport aux molécules étudiées, ce qui revient à dire que le facteur *g* doit être remplacé par un tenseur *g* anisotrope. Les électrons non-appariés de l'échantillon peuvent interagir avec le moment magnétique des noyaux : cette interaction dite hyperfine peut également être anisotrope. Enfin, les niveaux d'énergie des centres paramagnétiques de spin supérieur à ½ peuvent être déjà séparés en l'absence de **B** : ce terme d'éclatement en champ nul (ECN) modifie grandement la forme du spectre RPE.

La méthode PELDOR fait partie des techniques RPE dites impulsionnelles, ce qui consiste à appliquer une séquence d'impulsions micro-ondes à l'échantillon. Par exemple, l'enchaînement d'une impulsion π/2 et d'une impulsion π génère un écho de spin (ou écho de Hahn) : ce procédé permet d'enregistrer, avec une excellente sensibilité, un spectre RPE dit spectre d'écho, en mesurant l'intensité de l'écho tout en faisant varier **B**. Des séquences d'impulsions plus sophistiquées comme le PELDOR permettent d'extraire avec précision la distance entre deux centres paramagnétiques

appartenant à la même molécule dans la gamme 1.5 – 8 nm, ainsi que la distribution de cette distance.

Dans le cas des protéines, qui sont souvent diamagnétiques, il est donc nécessaire d'introduire deux centres paramagnétiques en deux positions précises. Cette technique appelée SDSL (Site-Directed Spin Labeling) a été appliquée avec succès depuis quelques dizaines d'années en utilisant un nitroxyde stable, MTSSL (MethaneThioSulfonate Spin Label).[6] Celui-ci réagit avec les résidus cystéine des protéines, natifs ou introduits par mutagenèse dirigée, pour former un pont disulfure (Figure 2). De nombreux nitroxydes stables possédant des fonctionnalités diverses ont été synthétisés de manière à utiliser la séquence PELDOR pour étudier une grande variété de biomolécules : protéines[7], peptides, acides nucléiques[8] ou pour évaluer la flexibilité d'objets purement synthétiques comme des caténanes[9], des rotaxanes[10] ou des espaceurs rigides dont les oligo-phénylène-éthynylène (OPE) notamment.[11] Les mesures sont généralement effectuées en bande X (9.5 GHz).

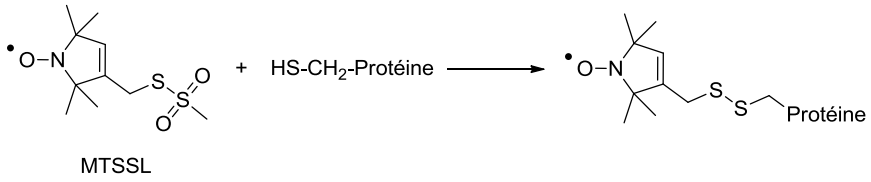

Schéma 1 : Marquage des résidus cystéine d'une protéine par MTSSL.

La méthode PELDOR repose sur l'extraction du couplage dipolaire ω_{dip} entre le moment magnétique de deux centres paramagnétiques, proportionnel à la racine cubique de la distance entre ces deux centres.[3] Ce couplage est très faible et il est masqué par d'autres contributions au spectre RPE comme l'anisotropie du facteur *g* ou le couplage hyperfin. L'énergie de l'interaction dipolaire entre deux centres paramagnétiques est représentée par l'Hamiltonien dipolaire H_{dip} :

$$H_{dip} = (g_1 g_2 \beta^2/R^3)(A+B+C+D+E+F) \quad [3]$$

g_1 et g_2 sont les facteurs *g* des deux centres paramagnétiques, *A* est appelé terme séculaire, *B* est appelé terme pseudo-séculaire et *C*-*F* sont les termes non séculaires. Quand ω_{dip} est faible par rapport à l'interaction Zeeman, quand les tenseurs g_1 et g_2 sont faiblement anisotropes, et dans le cas de l'approximation des couplages faibles (voir plus bas), les termes pseudo- et non séculaires peuvent être négligés. Le couplage dipolaire ω_{dip} s'écrit alors :

$$\omega_{dip} = (D_{dip}/R^3)(1-3\cos^2\theta) \quad [4]$$

D_{dip} est appelée constante de couplage dipolaire, égale à 327 MHz.cm^{-3} quand $g_1 = g_2 = 2$, et θ représente l'angle entre **B** et le vecteur correspondant à la distance R entre les deux centres paramagnétiques, appelé vecteur dipolaire.

La méthode PELDOR opère à deux fréquences différentes, appelées fréquence de détection et fréquence d'inversion, qui correspondent à deux populations de spin sur le spectre d'écho (Figure 2, exemple d'un nitroxyde). Les deux premières impulsions de la séquence de détection vont générer un écho de spin sélectif de la population B au temps $2\tau_1$. La décroissance de cet écho contient de nombreuses interactions dont le couplage dipolaire ω_{dip}. L'impulsion π de la séquence d'inversion va

alors inverser sélectivement les spins de la région A. Un terme $\pm\omega_{dip}$ à la fréquence de Larmor des spins B est ainsi ajouté, en fonction de l'état quantique des spins A, ce qui correspond à un transfert de cohérence. Ceci va provoquer un déphasage des spins B, modifiant l'intensité de leur écho au temps $2(\tau_1+\tau_2)$ généré par la dernière impulsion π. En faisant varier le temps T auquel l'impulsion d'inversion est appliquée, le déphasage des spins B peut être modifié de manière à introduire une modulation périodique de l'intensité de leur écho V(T) selon l'équation :

$$V(T) = V_0(1-\lambda+\lambda\cos(\omega_{dip}T)) \quad [5]$$

V(T) est appelé temps d'évolution dipolaire, V_0 représente l'intensité de l'écho des spins B à T = 0, et le paramètre λ (en %) est appelé profondeur de modulation et correspond à la fraction de spins A excitée par l'impulsion π de la séquence d'inversion. En général, la fréquence d'inversion correspond à la région d'intensité maximale du spectre d'écho de manière à maximiser λ, ce qui maximise également le RSB, tandis que la fréquence de détection est décalée de plusieurs dizaines de MHz pour minimiser le recouvrement spectral des profils d'inversion et de détection (Figure 2). La différence de fréquence entre la fréquence d'inversion et la fréquence de détection est souvent appelée *offset*.

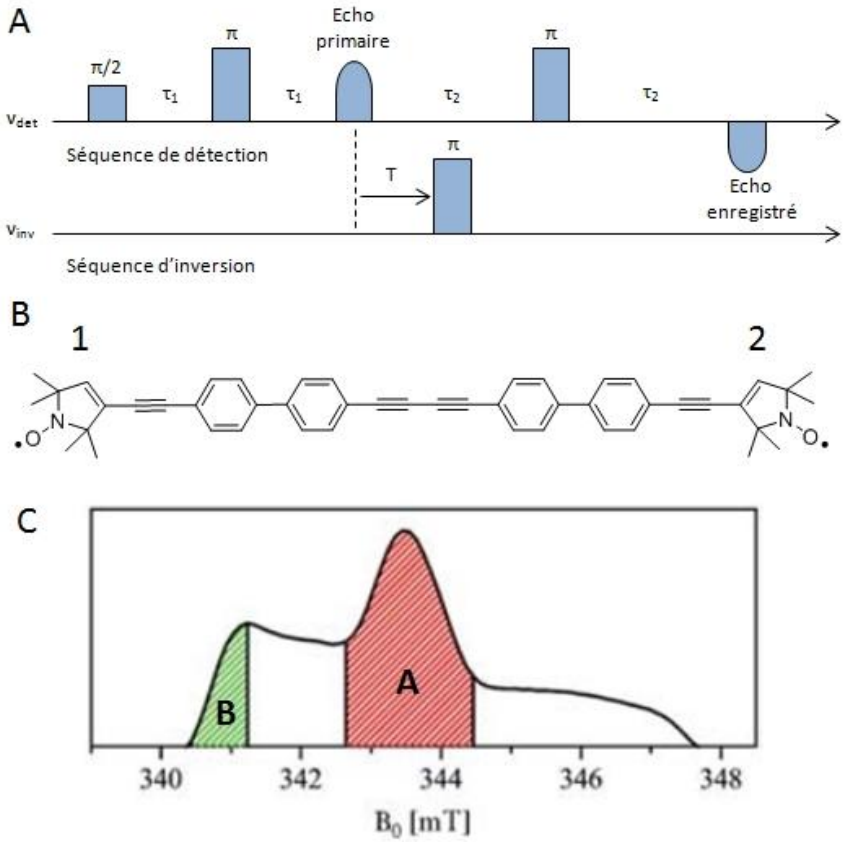

Figure 2 : A – Séquence d'impulsions de la méthode PELDOR. B – Structure d'un système modèle rigide bis-nitroxyde. C – Son spectre d'écho. La portion excitée par la séquence d'inversion est en rouge, celle excitée par la séquence de détection est en vert.

Le temps d'évolution dipolaire V(T) est le produit de deux facteurs : une contribution intramoléculaire F(T), qui représente le couplage dipolaire au sein d'un biradical par exemple, et une

contribution intermoléculaire B(T) qui tient compte des autres biradicaux présents dans l'échantillon. Pour séparer ces deux contributions, B(T) est souvent modélisée par une décroissance exponentielle en supposant une distribution homogène des molécules dans l'échantillon, ce qui permet d'isoler F(T). La transformée de Fourier de F(T) permet de passer d'un spectre en temps à un spectre en fréquence. Si λ ne dépend pas de θ, ce qui est le cas si les deux nitroxydes du biradical étudié sont flexibles, ce spectre en fréquence a la forme d'un doublet de Pake (Figure 3). Un tel spectre représente la superposition des spectres de tous les biradicaux de l'échantillon étudié en solution gelée, correspondant à toutes les orientations possibles du vecteur dipolaire par rapport à **B**.

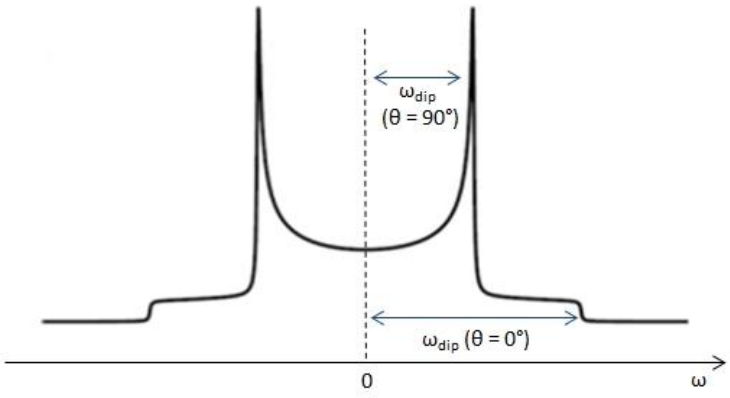

Figure 3 : Doublet de Pake.

Les deux « cornes » du doublet de Pake correspondent aux échantillons alignés perpendiculairement à **B**, tandis que les deux « pieds » correspondent aux échantillons alignés parallèlement à **B**. La distance entre le centre du doublet et les « cornes » est donc égale à ω_{dip} quand θ = 90°, et la distance entre le centre et les « pieds » est égale à ω_{dip} quand θ = 0°. La distance R peut donc être connue en utilisant l'équation [4], mais cette procédure n'est pas fiable car de petites variations du temps d'évolution dipolaire peuvent mener à une grande incertitude sur la valeur de R. Cette situation correspond à un problème mal posé, et la régularisation de Tikhonov est souvent utilisée pour stabiliser la solution, ce qui permet d'obtenir de manière très fiable une distribution des valeurs de R. Cette procédure peut être effectuée grâce au logiciel DeerAnalysis (Figure 4).[12]

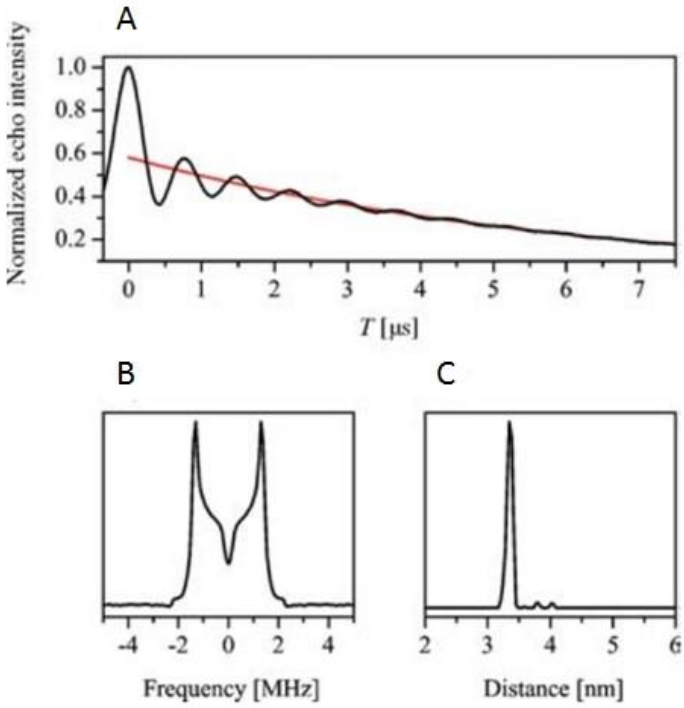

Figure 4 : A – Spectre d'évolution dipolaire V(T) du bis-nitroxyde modèle (en noir) et contribution intermoléculaire B(T) (en rouge). B – Spectre en fréquence obtenu par transformée de Fourier du spectre d'évolution dipolaire, ayant la forme d'un doublet de Pake (« cornes » à 1,3 MHz et « pieds » à 2,3 MHz). C – Distribution de distance obtenue par régularisation de Tikhonov implémentée sous DeerAnalysis.

Comme mentionné plus haut, l'approximation des couplages faibles doit être vérifiée pour pouvoir uniquement considérer le terme séculaire de l'Hamiltonien dipolaire. Cela signifie que ω_{dip} doit être inférieur à la valeur absolue de l'*offset*. Cette condition est souvent vérifiée pour les nitroxydes en bande X, mais la situation est plus complexe pour les complexes de Mn^{II} et Gd^{III} à haut spin.

Malgré le succès de la méthode PELDOR avec des nitroxydes stables,[13] ces derniers présentent plusieurs inconvénients. Les temps d'acquisition sont généralement très longs (de 12 à 24 h) et la concentration de l'échantillon doit être assez élevée (de 0.1 à 1 mM) pour obtenir un bon RSB. Un moyen efficace d'améliorer la sensibilité de la méthode PELDOR est d'augmenter la fréquence du spectromètre RPE, ce qui correspond également à augmenter le champ magnétique. Ce procédé n'est pas adapté pour les nitroxydes car leur spectre RPE s'élargit quand la fréquence augmente : le gain en sensibilité est compensé par une réduction de la profondeur de modulation car l'impulsion d'inversion excite beaucoup moins de spins. De plus, cet élargissement du spectre des nitroxydes à haut champ entraîne également la résolution de l'anisotropie de leur tenseur *g*. L'impulsion d'inversion excite alors uniquement un sous-ensemble de molécules correspondant à une orientation particulière par rapport au champ magnétique, et seules ces molécules vont contribuer au temps d'évolution dipolaire. Ce phénomène est appelé sélection d'orientation : il peut également se produire en bande X quand le mouvement des nitroxydes est contraint. Il conduit à un doublet de Pake déformé, ce qui complique fortement l'analyse car plusieurs expériences doivent être réalisées en changeant la position des profils de détection et d'inversion sur le spectre d'écho. Les nitroxydes sont également rapidement convertis en *N*-hydroxylamines diamagnétiques dans le

milieu réducteur des cellules, ce qui limite fortement leur utilisation pour des expériences de PELDOR *in vivo*.

Il est donc nécessaire de trouver des centres paramagnétiques alternatifs pour la méthode PELDOR, et les complexes métalliques à haut spin, notamment de Gd^{III} (S = 7/2) et de Mn^{II} (S = 5/2), apparaissent très prometteurs.[14] Contrairement aux nitroxydes, la transition centrale de leur spectre RPE devient plus étroite quand la fréquence du spectromètre est plus élevée (comme en bande Q, 34 GHz ; en bande W, 95 GHz, ou en bande G, 180 GHz), augmentant ainsi le nombre de spins pouvant être excités par l'impulsion d'inversion. Les complexes métalliques à haut spin présentent une sélection d'orientation négligeable, du fait de l'isotropie des tenseurs *g* et *A*, de la contribution au second ordre de l'interaction d'ECN à la transition centrale et des paramètres D et E d'éclatement en champ nul très distribués. Enfin, les complexes à haut spin de Gd^{III} et de Mn^{II} sont stables (d'un point de vue redox) en milieu cellulaire.

L'utilisation des complexes de Gd^{III} comme centres paramagnétiques pour la méthode PELDOR a été initiée par le groupe de D. Goldfarb en 2007.[15] En comparaison, les complexes de Mn^{II} ont été très peu étudiés : une seule étude utilisant la méthode PELDOR pour mesurer la distance entre deux complexes de Mn^{II} a été publiée en 2011 par le même groupe.[16] Cela peut s'expliquer par l'interaction hyperfine avec le spin nucléaire du ^{55}Mn (I = 5/2) : la transition centrale des complexes de Mn^{II} se présente alors sous la forme d'un sextuplet couvrant environ 600 G, réduisant ainsi la profondeur de modulation d'un facteur 6. Cependant, l'utilisation des complexes de Mn^{II} est très avantageuse d'un point de vue biologique : ils sont présents dans de nombreuses protéines (comme la superoxyde dismutase, la concanavaline A ou l'oxalate décarboxylase), et l'ion Mn^{II} peut remplacer l'ion Mg^{II} dans les systèmes biologiques car il présente une taille et une charge similaires.[17]

L'objectif de cette thèse est de développer l'utilisation de la méthode PELDOR à haut champ pour mesurer la distance entre deux complexes de Mn^{II} à haut spin. Afin de bénéficier de la meilleure sensibilité possible, le choix du ligand employé est crucial. Pour maximiser le nombre de spins excités par l'impulsion d'inversion, l'utilisation d'un complexe de Mn^{II} présentant des raies RPE étroites est souhaitable : ce signal RPE fin est directement relié à une faible valeur du paramètre d'éclatement en champ nul D, le paramètre E étant le plus souvent négligeable. La relation entre l'ECN et la sphère de coordination d'un complexe de Mn^{II} est mal connue, mais une symétrie élevée de cette sphère de coordination est susceptible de générer un complexe de Mn^{II} présentant un sextuplet hyperfin étroit. Un ligand avec une haute affinité pour le Mn^{II} est préférable pour éviter toute liaison non spécifique avec la protéine étudiée, et la présence d'un site de greffage est également nécessaire.

La méthode PELDOR appliquée à la mesure de la distance entre deux centres Mn^{II} sera d'abord optimisée sur des systèmes modèles, composés d'un espaceur central relié à deux complexes de Mn^{II} sélectionnés pour leur signal RPE étroit (Figure 5). Cet espaceur central devra être rigide et facilement incrémentable pour générer un ensemble de plateformes qui serviront d' « étalons » sur lesquels les paramètres optimaux de la méthode PELDOR entre deux centres Mn^{II} seront déterminés. Dans le premier chapitre, plusieurs ligands équipés d'un site de greffage ont été synthétisés et leurs complexes de Mn^{II} seront étudiés par RPE en onde continue en bande J (285 GHz). Au terme de cette procédure, le complexe de Mn^{II} présentant le signal RPE le plus fin a été retenu. En parallèle, des espaceurs rigides couvrant la gamme 1,5 – 5 nm ont été synthétisés et couplés au ligand le plus prometteur.

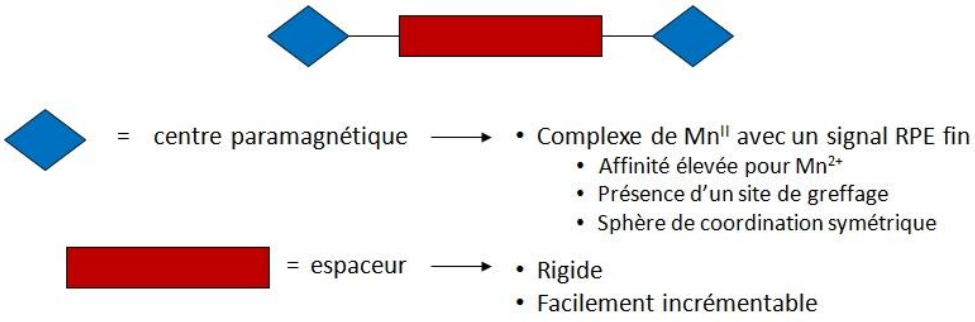

Figure 5 : Structure des systèmes modèles visés.

L'optimisation des paramètres de la méthode PELDOR qui permettent l'extraction précise de la distance Mn^{II}-Mn^{II} avec un bon RSB sur les systèmes modèles synthétisés précédemment est l'objet du deuxième chapitre. Cette distance et sa distribution ont été comparées aux résultats obtenus par modélisation moléculaire, et l'influence du terme pseudo-séculaire de l'Hamiltonien dipolaire sur la distribution de la distance Mn-Mn a été analysée. Une comparaison avec les systèmes bis-Gd^{III} et bis-nitroxydes a également été effectuée. Dans le troisième chapitre, l'étude de centres paramagnétiques alternatifs pour la méthode PELDOR, les radicaux PTM (PerchloroTriphénylMéthyle) et TAM (TétrathiaTriarylMéthyle), a été menée. Ces deux classes de radicaux stables sont des trityls substitués par des groupements soufrés ou chlorés, ce qui leur confère un signal RPE très étroit (largeur de pic d'environ 100 à 600 mG en bande X).[18,19] Cette caractéristique unique explique leur succès dans de nombreux domaines, de l'imagerie RPE[20] à la mesure du pH et/ou du taux d'oxygène *in vivo*.[21] Pour mieux comprendre la relation entre la structure de ces radicaux trityl et l'étroitesse de leur signal RPE, le tenseur *g* de quelques dérivés a été mesuré avec précision par RPE en onde continue en bande J, en utilisant l'ion Mn^{II} comme référence interne. Malgré la similarité de structure entre les radicaux PTM et TAM, ces résultats ont mis en évidence une grande différence entre leurs propriétés électroniques. L'utilisation de calculs DFT (Density Functional Theory) a permis de rationaliser ces observations.

SYNTHESE DES SYSTEMES MODELES

Dans une première partie, la synthèse de nombreux ligands dont la structure est basée sur un cœur pyridine a été réalisée. L'utilisation d'un noyau pyridine équipé d'un groupement halogène en position *para* permet un greffage sur l'espaceur central reposant sur un couplage Pd-catalysé, afin de générer le moins de flexibilité possible. L'acide chélidamique, commercialement disponible et possédant un groupement alcool en position *para*, est un réactif de départ adapté. Les bis(imino)pyridines (BImP)[22] ont constitué une première cible : leur synthèse et un exemple de spectre RPE en bande J d'un complexe BImP-$MnBr_2$ sont présentés Figure 6.

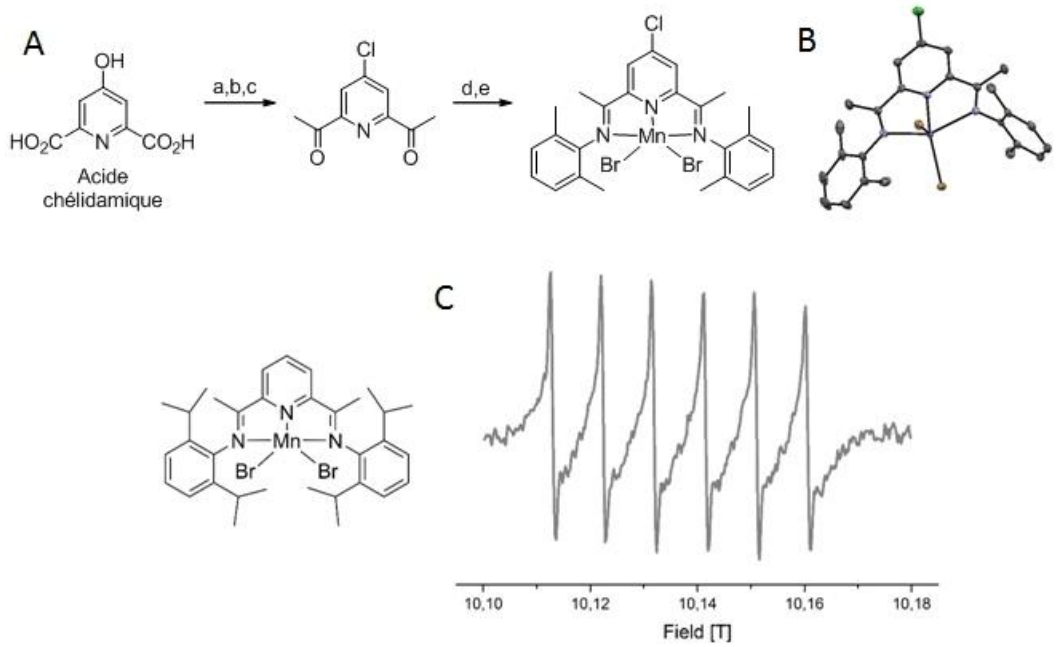

Figure 6 : A – Synthèse d'un complexe BImP-$MnBr_2$. Conditions : a) EtOH, H_2SO_4, reflux, 15 h, 75 % b) $SOCl_2$, DMF, $CHCl_3$, reflux, 48 h, 73 % c) NaOEt, AcOEt, reflux, 24 h, puis HCl, H_2O, 0 °C jusqu'à T_{amb}, 24 h, 53 % d) 2,6-xylidine, AcOH, EtOH, reflux, 24 h, 56 % e) $MnBr_2$, EtOH, reflux, 1 h, 65 %. B – Structure cristallographique du produit obtenu. C – Structure d'un autre complexe BImP-$MnBr_2$ ainsi que son spectre RPE en bande J (1 mM, MeCN, 23 K).

L'analyse du spectre RPE montre que le sextuplet hyperfin attendu est bien observé, mais que la partie étroite correspond au signal du manganèse libre, ce qui témoigne d'une décoordination importante. La partie plus large du spectre pourrait correspondre au signal du complexe ou à des artefacts liés à la précipitation du complexe ou la formation d'un mauvais verre. La synthèse de terpyridines (Tpy), qui forment des complexes de type $Mn(Tpy)_2^{2+}$,[23] a donc été entreprise, ainsi que leur étude par RPE en bande J (Figure 7).

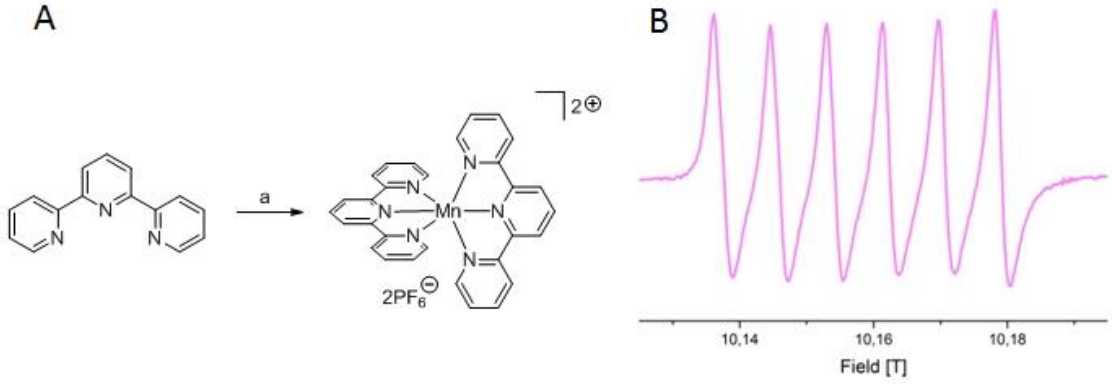

Figure 7 : A – Synthèse d'un complexe $Mn(Tpy)_2^{2+}$. Conditions : a) $MnCl_2$, acétone/H_2O, T_{amb}, 30 min, puis NH_4PF_6, H_2O, T_{amb}, 15 min, 70 %. B – Spectre RPE en bande J du complexe obtenu (2 mM, MeCN avec 100 mM *n*-Bu_4NPF_6, 23 K).

Cette fois, aucune décoordination n'est observée, et six lignes relativement étroites sont obtenues (amplitude crête à creux : 27 G). Ce type de complexe a donc été retenu pour la méthode

PELDOR, mais de nombreux problèmes de solubilité et de stabilité des plateformes bis-$Mn(Tpy)_2^{2+}$ ont rendu l'utilisation du ligand Tpy délicate. L'emploi de complexes solubles en solution aqueuse pourrait permettre de contourner ces difficultés et serait intéressant dans un contexte biologique. Le cœur pyridine a été par la suite modifié de manière à introduire des groupements carboxylate : les ligands PyMTA[24] (Pyridine-diMéthylènenitrilo-TétraAcétate) et PyMDPDA (Pyridine-diMéthylène-DiPyridineDiAcétate) ont été synthétisés, purifiés par HPLC (Chromatographie en phase Liquide à Haute Performance) et le spectre RPE en bande J de leurs complexes de Mn^{II} enregistré (Figure 8). Ces complexes ainsi que tous les suivants sont générés *in situ* par addition de la quantité adéquate de Mn^{II} sous forme de $Mn(ClO_4)_2 \bullet 6H_2O$.

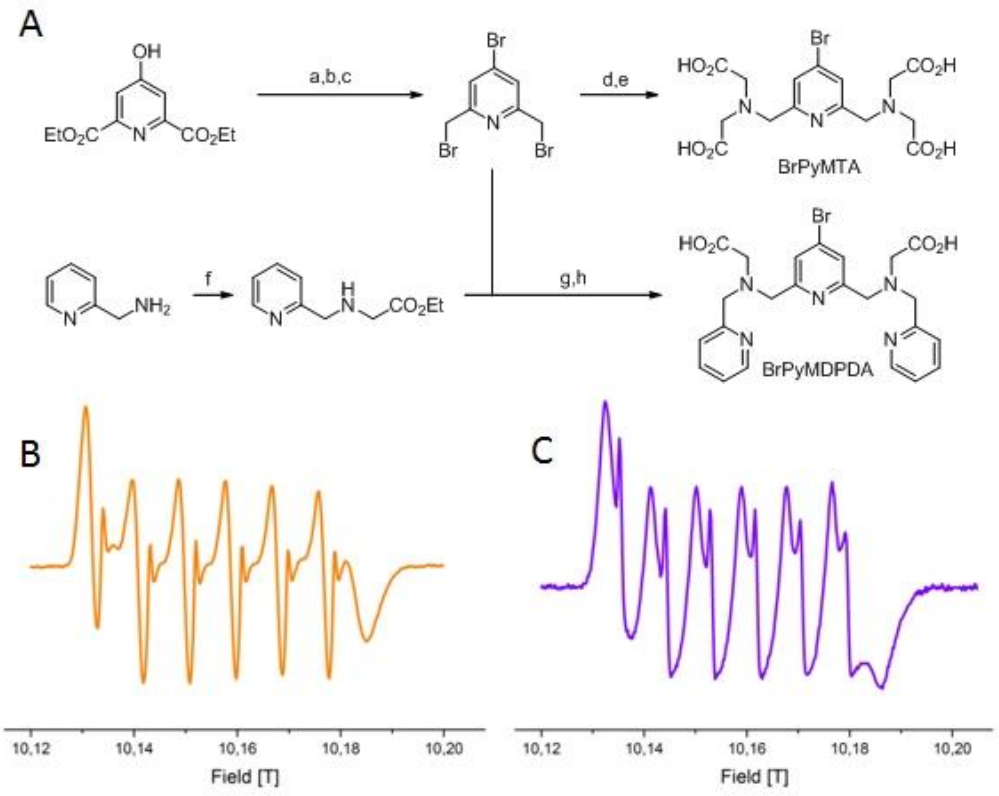

Figure 8 : A – Synthèse des ligands BrPyMTA et BrPyMDPDA. Conditions : a) PBr_5, $CHCl_3$, reflux, 15 h, 85 % b) $NaBH_4$, EtOH, T_{amb} jusqu'au reflux, 17 h, 83 % c) PBr_3, $CHCl_3$, reflux, 15 h, 53 % d) iminodiacétate de *tert*-butyle, Na_2CO_3, MeCN, T_{amb}, 15 h, 88 % e) TFA, DCM, T_{amb}, 2 h f) bromoacétate d'éthyle, THF, 0 °C jusqu'à T_{amb}, 15 h, 63 % g) Na_2CO_3, MeCN, T_{amb}, 15 h, 93 % h) NaOH, acétone/H_2O, T_{amb}, 72 h. B – Spectre RPE en bande J du complexe de Mn^{II} de BrPyMTA (1 mM en ligand, 500 µM en Mn^{II}, en tampon HEPES 100 mM pH 8 avec 20 % de glycérol à 23 K). C – Spectre RPE en bande J du complexe de Mn^{II} de BrPyMDPDA (500 µM en ligand, 440 µM en Mn^{II}, en tampon HEPES 100 mM pH 8 avec 20 % de glycérol à 23 K).

Les complexes de Mn^{II} de PyMTA et PyMDPDA présentent les six lignes attendues (amplitude crête à creux de 21 et 36 G, respectivement). Le signal est dédoublé, ce qui reflète la complexité de la sphère de coordination. Ces complexes sont solubles à pH 8, mais leur signal RPE n'est pas beaucoup plus fin que celui de $Mn(Tpy)_2^{2+}$. La constante d'affinité de PyMTA pour le Mn^{II} a été déterminée par titration par calorimétrie isotherme ($\log K_{MnL}$ = 7,9) : l'utilisation de ligands macrocycliques incorporant un noyau pyridine serait susceptible d'augmenter cette affinité, ce qui pourrait générer un signal RPE plus fin. Un bon exemple est le ligand PCMA[25] (Pyridyltriaza-Cyclododécane-

MonoAcétate), dont la synthèse est présentée Figure 9, ainsi que le ligand PCTA (Pyridyltriaza-Cyclododécane-TriAcétate) fourni par une source extérieure. Les spectres RPE en bande J des complexes de Mn^{II} de PCMA et de PCTA sont également présentés Figure 9.

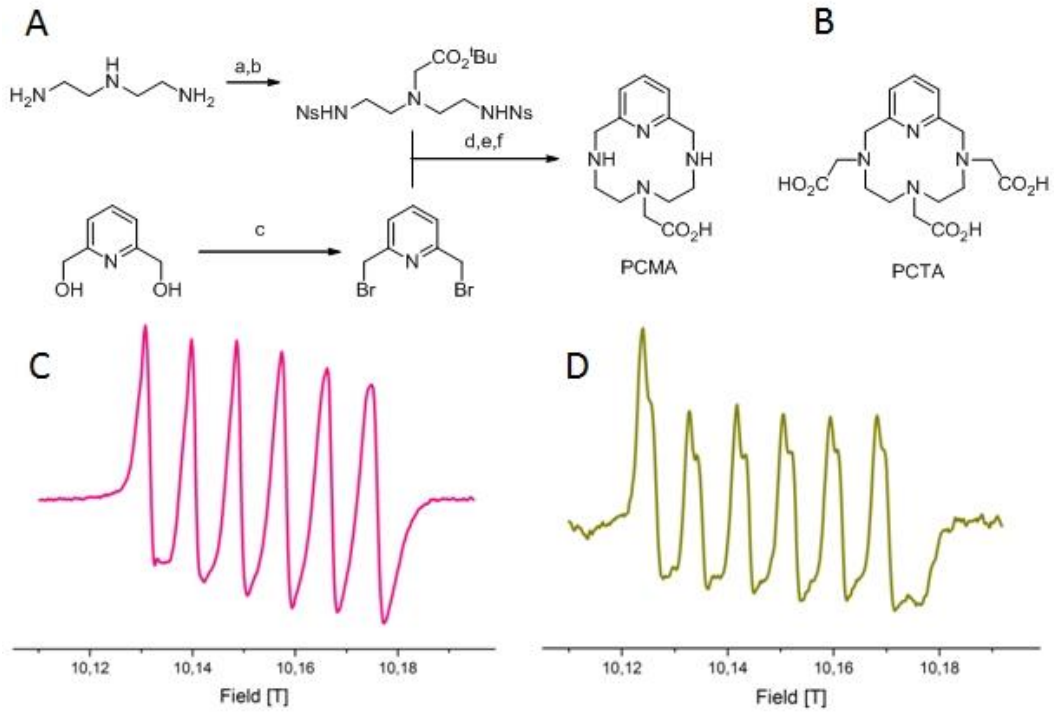

Figure 9 : A – Synthèse du ligand PCMA. Conditions : a) NsCl, $NaHCO_3$, THF, 0 °C jusqu'à T_{amb}, 15 h, 22 % b) chloroacétate de *tert*-butyle, NEt_3, THF, reflux, 15 h, 43 % c) HBr, H_2O, reflux, 6 h, 41 % d) Na_2CO_3, DMF, 100 °C, 15 h, 55 % e) PhSH, Na_2CO_3, DMF, T_{amb}, 24 h, 58 % e) TFA, DCM, T_{amb}, 15 h, 55 %. B – Structure du ligand PCTA. C – Spectre RPE en bande J du complexe de Mn^{II} de PCMA (500 µM en ligand, 450 µM en Mn^{II}, en tampon HEPES 100 mM pH 8 avec 20 % de glycérol à 23 K). D – Spectre RPE en bande J du complexe de Mn^{II} de PCTA (500 µM en ligand, 250 µM en Mn^{II}, en tampon HEPES 100 mM pH 8 avec 20 % de glycérol à 23 K).

L'amplitude crête à creux de ces complexes est de 21 et 32 G, respectivement, ce qui ne représente pas d'amélioration notable par rapport aux complexes acycliques. Le cycle pyridine pourrait être relié à la relative largeur de raie : l'étude du DOTA[26] (tétraazacycloDOdécane-TétraCarboxylate) a donc été entreprise, même si le greffage de ce ligand sur un espaceur central induit plus de flexibilité. La structure du DOTA et le spectre RPE en bande J de son complexe de Mn^{II} sont présentés Figure 10.

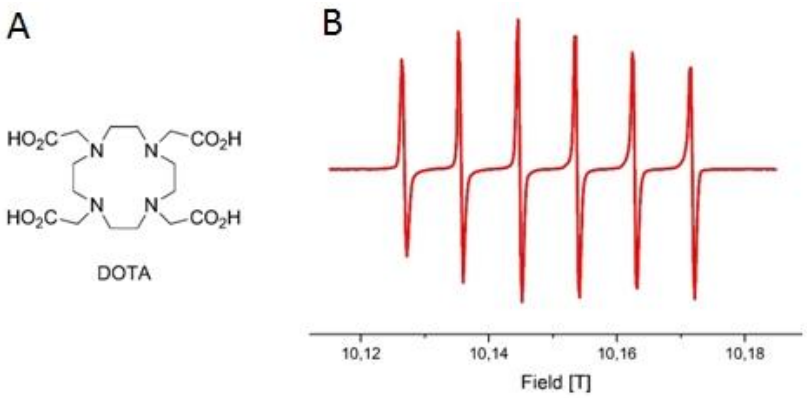

Figure 10 : A – Structure du ligand DOTA. B – Spectre RPE en bande J de son complexe de Mn^{II} (1 mM en ligand, 500 µM en Mn^{II}, en tampon HEPES 100 mM pH 8 avec 20 % de glycérol à 23 K).

Un sextuplet très fin est observé (amplitude crête à creux : 6 G). La sphère de coordination très symétrique ainsi que la constante d'affinité très élevée (K_{MnL} = 19,9) pourraient expliquer cette observation. Le DOTA apparaît donc comme le candidat idéal pour la méthode PELDOR. La structure cristallographique de Mn^{II}-DOTA, connue dans la littérature,[27] révèle un nombre de coordination de 6 avec deux acides carboxyliques non coordinants. Par contre, le nombre de coordination d'un complexe très similaire, Mn^{II}-DOTAM (tétraazacycloDOdécane-TétraCarboxAMide), est de 8 : son spectre RPE en bande J a été enregistré et est quasiment superposable à celui de Mn^{II}-DOTA, qui serait donc plutôt octacoordiné en solution. Pour appuyer cette hypothèse, les spectres RPE en bande J des complexes de Mn^{II} de DO3A et DO2A, avec un nombre de coordination maximal de 7 et de 6, respectivement, ont été enregistrés. Le sextuplet hyperfin est nettement plus large (amplitude crête à creux de 20 et 27 G, respectivement), ce qui confirmerait l'hypothèse d'un complexe Mn^{II}-DOTA octacoordiné (Figure 11). Des études RPE plus poussées sont actuellement en cours pour confirmer cette hypothèse.

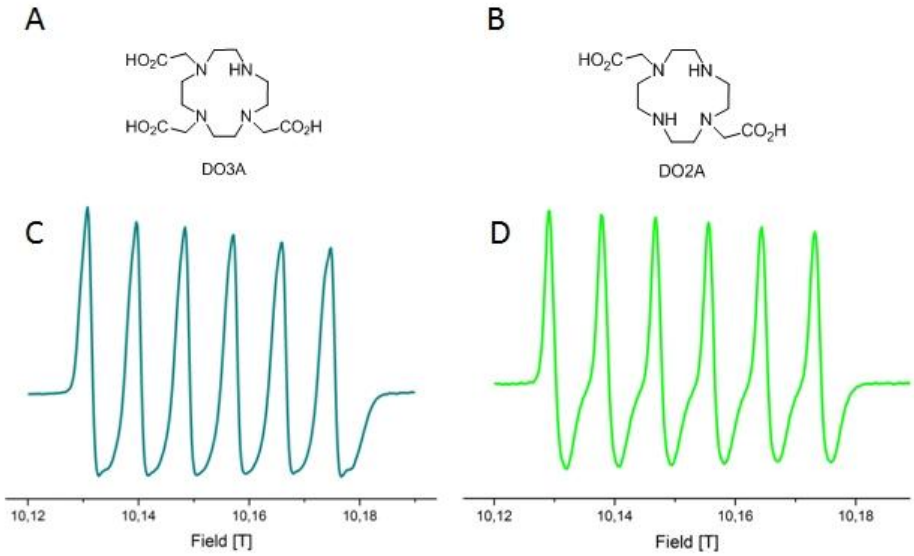

Figure 11 : A – Structure du ligand DO3A. B – Structure du ligand DO2A. C – Spectre RPE en bande J du complexe de Mn^{II} de DO3A (500 µM en ligand, 450 µM en Mn^{II}, en tampon HEPES 100 mM pH 8 avec 20 % de glycérol à 23 K). D – Spectre RPE en bande J du complexe de Mn^{II} de DO2A (500 µM en ligand, 450 µM en Mn^{II}, en tampon HEPES 100 mM pH 8 avec 20 % de glycérol à 23 K).

Le premier espaceur étudié est constitué de deux pipérazines attachées à un noyau benzène en position *para*. L'étape-clef de la synthèse est une double réaction de Hartwig-Buchwald entre le *p*-dibromobenzène et la mono-Boc-pipérazine (Boc-Pip). La structure aux rayons X du produit de couplage a été obtenue : la distance entre les deux carbones des groupes C=O des carbamates vaut 1,37 nm. Un espaceur plus long a également été synthétisé en utilisant le *p*-dibromobiphényle : dans ce cas, deux couplages successifs avec la mono-Boc-pipérazine sont nécessaires (Figure 12). Des calculs DFT sur ces deux espaceurs ont conduit à une distance C-C entre les deux C=O des carbamates de 1,39 et 1,83 nm.

Ces espaceurs ont ensuite été couplés au tri-^{t}Bu-DOTA, un ligand DOTA protégé sous forme de triester de *tert*-butyle, puis une étape de déprotection en milieu acide a permis l'obtention des plateformes bis-DOTA correspondantes après purification par HPLC. Un couplage avec le 4-carboxy-TEMPO (TEtraméthyl-PipéridinylOxyle) a également été réalisé afin d'obtenir l'analogue bis-nitroxyde (Figure 12) : sa structure aux rayons X a été résolue et la distance entre le milieu des deux liaisons N-O vaut 1,98 nm.

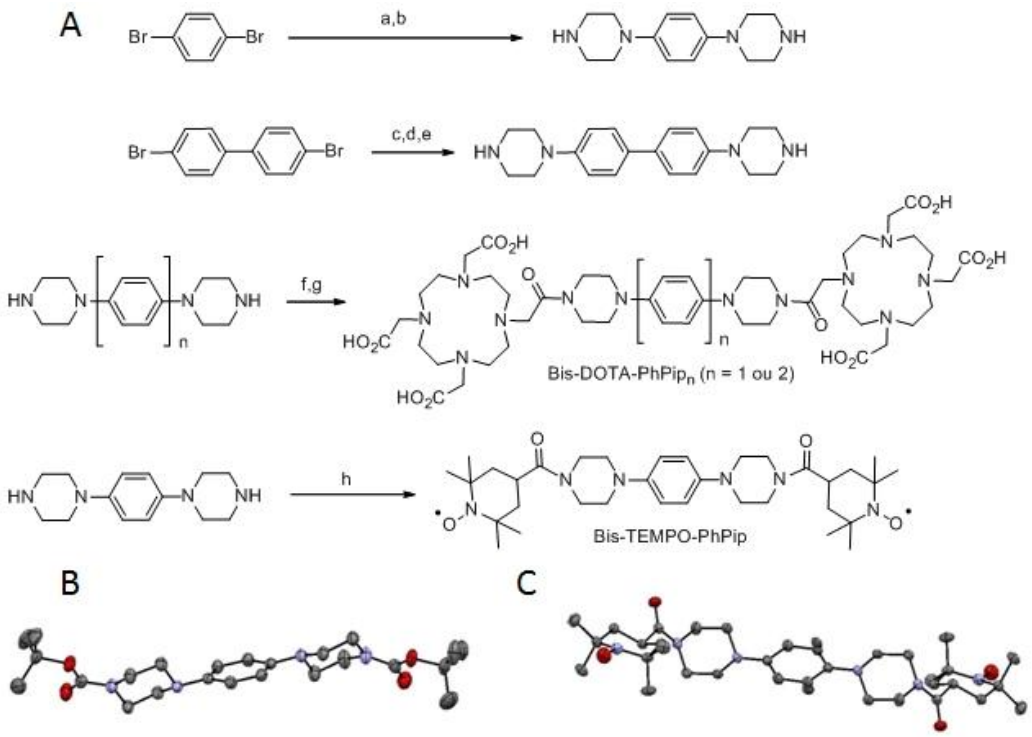

Figure 12 : A – Synthèse des espaceurs phényle-pipérazine et leur couplage. Conditions : a) Boc-Pip, $Pd_2(dba)_3$, BINAP, NaO^tBu, toluène, reflux, 72 h, 79 % b) TFA, DCM, 0 °C jusqu'à T_{amb}, 3 h, 87% c) Boc-Pip, $Pd_2(dba)_3$, BINAP, NaO^tBu, toluène, reflux, 6 j, 47 % d) Boc-Pip, $Pd_2(dba)_3$, XPhos, Cs_2CO_3, dioxane, reflux, 48 h, 55 % e) TFA, DCM, 0 °C jusqu'à T_{amb}, 3 h, 82% f) tri-^{t}Bu-DOTA, HATU, DIPEA, DMF, T_{amb}, 24 h, 98 % (n = 1) ou 84 % (n = 2) g) TFA, DCM, 0 °C jusqu'à T_{amb}, 24 h h) 4-carboxy-TEMPO, HOBt, EDC, DIPEA, DMF, T_{amb}, 24 h, 51 %. B – Structure cristallographique du produit de couplage entre le *p*-dibromobenzène et Boc-Pip. C – Structure cristallographique de bis-TEMPO-PhPip.

L'élaboration d'un espaceur OPE a ensuite été réalisée.[28] L'étape-clef consiste en un double couplage de Sonogashira entre un bloc diiodé central équipé de chaînes éthylène glycol pour permettre une bonne solubilité et un éthynylbenzène substitué en position para par un site de greffage (amine, aldéhyde ou éthynyle protégé). Un mono-couplage entre le bloc diiodé et le *p*-diéthynylbenzène mono-protégé a également été réalisé, et le composé ainsi généré a été couplé avec le *p*-diéthynylbenzène ou l'OPE di-CCH généré précédemment pour donner des espaceurs OPE di-NH_2 avec 5 ou 7 unités phénylène-éthynylène, respectivement (Figure 13). Les structures aux rayons X des OPE di-COH et di-CCH ont été résolues : la distance C-C (entre les deux carbones des groupements aldéhyde ou entre les deux premiers carbones des groupements éthynyle) vaut 1,93 et 1,92 nm, respectivement. Des calculs DFT sur les trois OPE di-NH_2 ont conduit à une distance N-N de 1,94, 3,31 et 4,68 nm.

Les modules bis-DOTA protégés ont été synthétisés par réaction avec le bromure de bromoacétyle puis substitution nucléophile sur le tri-Pp-DO3A (Pp = phényle-isopropyle). L'utilisation du groupe Pp,[29] clivable en milieu acide très peu concentré, est nécessaire car un milieu acide trop concentré entraîne la dégradation des plateformes. L'équivalent bis-nitroxyde a été obtenu par oxydation de l'OPE di-COH et réaction avec le 4-amino-TEMPO (Figure 14) : sa structure aux rayons X a été résolue et la distance entre le milieu des deux liaisons N-O vaut 3,02 nm.

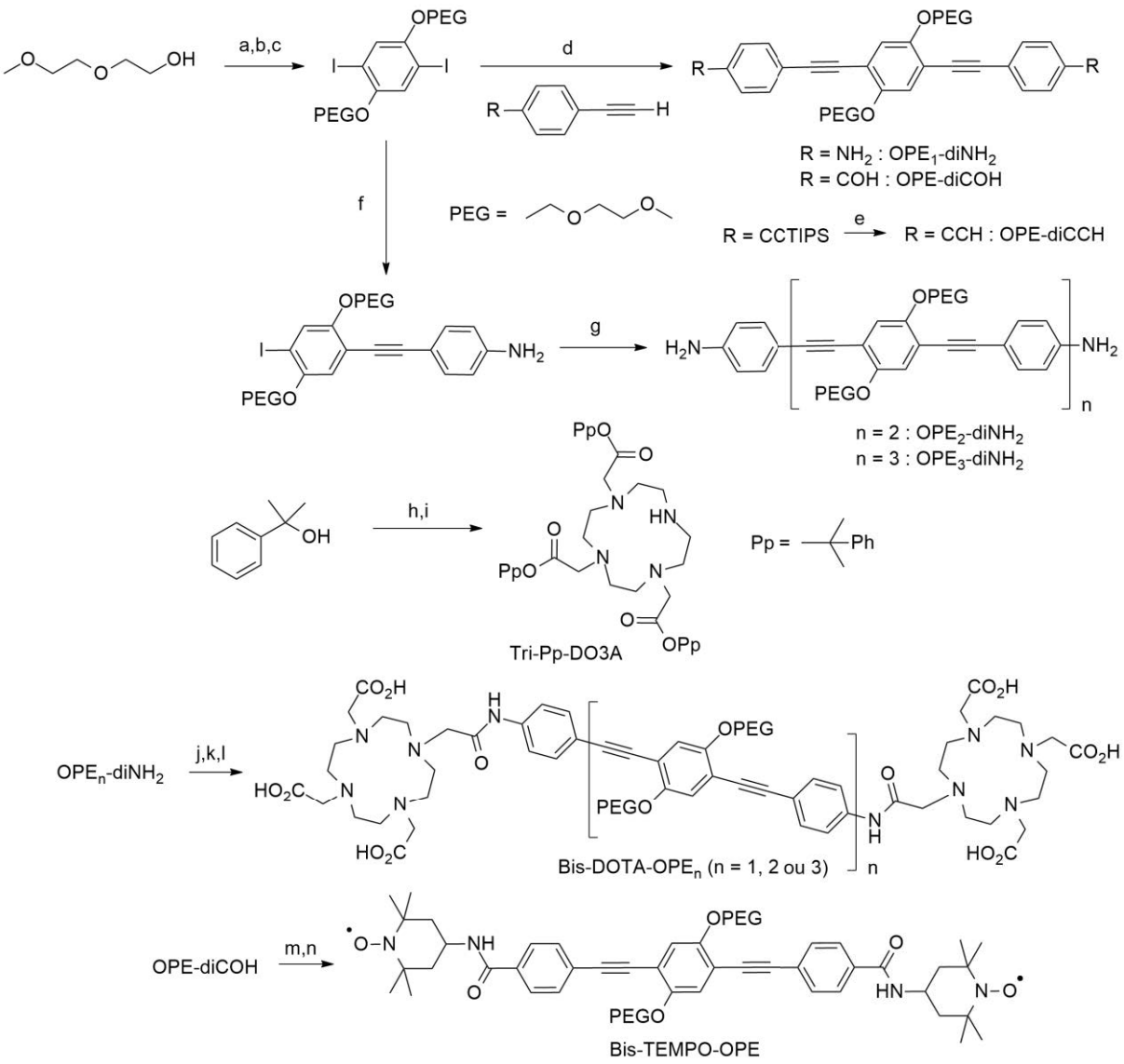

Figure 13 : Synthèse des espaceurs OPE et leur couplage. Conditions : a) TsCl, NaOH, THF/H_2O, 0 °C jusqu'à T_{amb}, 2 h, 80 % b) hydroquinone, K_2CO_3, MeCN, reflux, 72 h, 79 % c) I_2, KIO_3, H_2SO_4, AcOH/H_2O, reflux, 48 h, 60 % d) $Pd(PPh_3)_2Cl_2$, CuI, THF/NEt_3, T_{amb}, 24 h, 47 % (R = CCTIPS), 52 % (R = NH_2) ou 80 % (R = COH) e) TBAF, THF, 0 °C jusqu'à T_{amb}, 3 h, 82 % f) *p*-éthynylaniline (0,75 eq), $Pd(PPh_3)_2Cl_2$, CuI, THF/NEt_3, T_{amb}, 24 h, 52 % g) *p*-diéthynylbenzène (n = 2) ou OPE-diCCH (n = 3), $Pd(PPh_3)_2Cl_2$, CuI, THF/NEt_3, T_{amb}, 24 h, 65 % (n = 2) ou 69 % (n = 3) h) acide bromoacétique, DCC, DMAP, DCM, 0 °C jusqu'à T_{amb}, 3 h, 58 % i) cyclen, $NaHCO_3$, MeCN, 0 °C jusqu'à T_{amb}, 15 h, 23 % j) bromure de bromoacétyle, NEt_3, DCM, 0 °C jusqu'à T_{amb}, 3 h, 40 % (n = 1), 66 % (n = 2) ou 69 % (n = 3) k) tri-Pp-DO3A, K_2CO_3, MeCN, T_{amb}, 15 h, 53 % (n = 1), 49 % (n = 2) ou 19 % (n = 3) l) TFA, TIS, DCM, T_{amb}, 4 h m) oxone, DMF, T_{amb}, 24 h, 82 % n) 4-amino-TEMPO, HOBt, DCC, DMF, 0 °C jusqu'à T_{amb}, 24 h, 93 %.

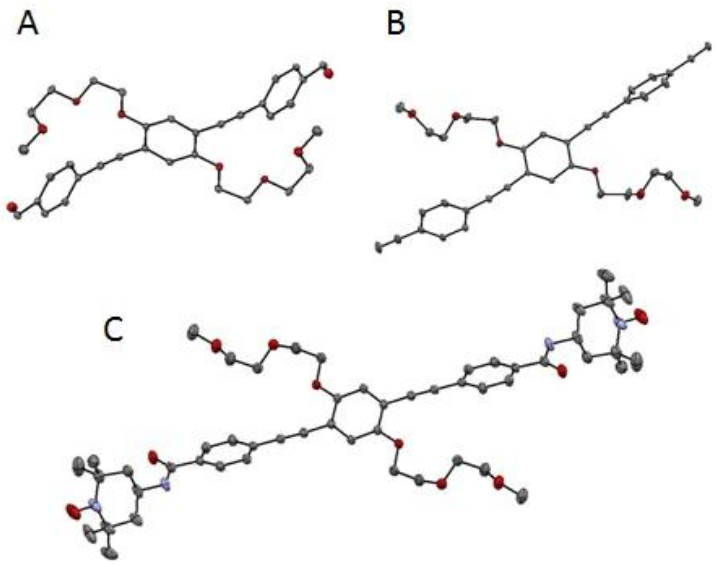

Figure 14 : Structures cristallographiques. A – OPE-diCOH. B – OPE-diCCH. C – Bis-TEMPO-OPE.

Le dernier espaceur étudié est constitué d'un oligomère de prolines. Ces polyprolines adoptent une structure hélicoïdale relativement rigide en solution aqueuse dite PPII (polyproline II), où toutes les liaisons amide sont en conformation *trans*.[30] Trois polyprolines avec la séquence Cys-Pro_n-Cys (n = 6, 9 et 12) ont été obtenues par synthèse peptidique sur support solide en stratégie Fmoc. Les groupements thiol ont ensuite réagi avec le DOTA-Mal pour générer les plateformes $DOTA_2P_n$ correspondantes (Figure 15).

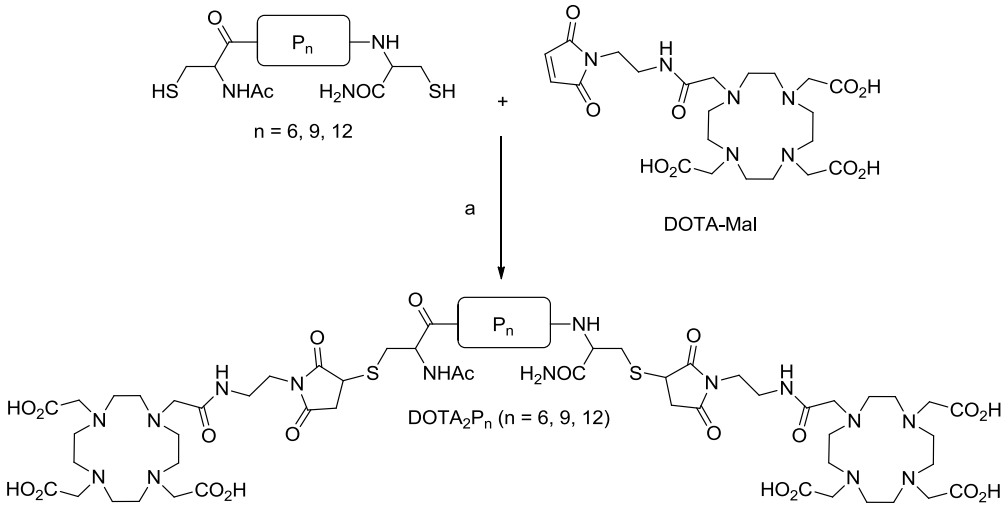

Figure 15 : Couplage des polyprolines au DOTA. Conditions : a) TCEP, tampon HEPES pH 7, T_{amb}, 15 h, 42 % (n = 6), 65 % (n = 9) ou 54 % (n = 12).

Les spectres RPE en bande J des complexes de Mn^{II} des plateformes bis-DOTA-$PhPip_1$, bis-DOTA-OPE_1 et $DOTA_2P_9$, ainsi que celui de la plateforme bis-TEMPO-OPE, sont présentés Figure 16. Les six lignes sont bien obtenues, aussi fines que Mn^{II}-DOTA dans le cas de bis-DOTA-OPE_1 et de $DOTA_2P_9$, mais deux fois plus larges pour bis-DOTA-$PhPip_1$. Ceci traduit la présence d'un couplage dipolaire important à cette courte distance. Le spectre de bis-TEMPO-OPE est typique d'un TEMPO, avec une anisotropie de *g* très résolue.

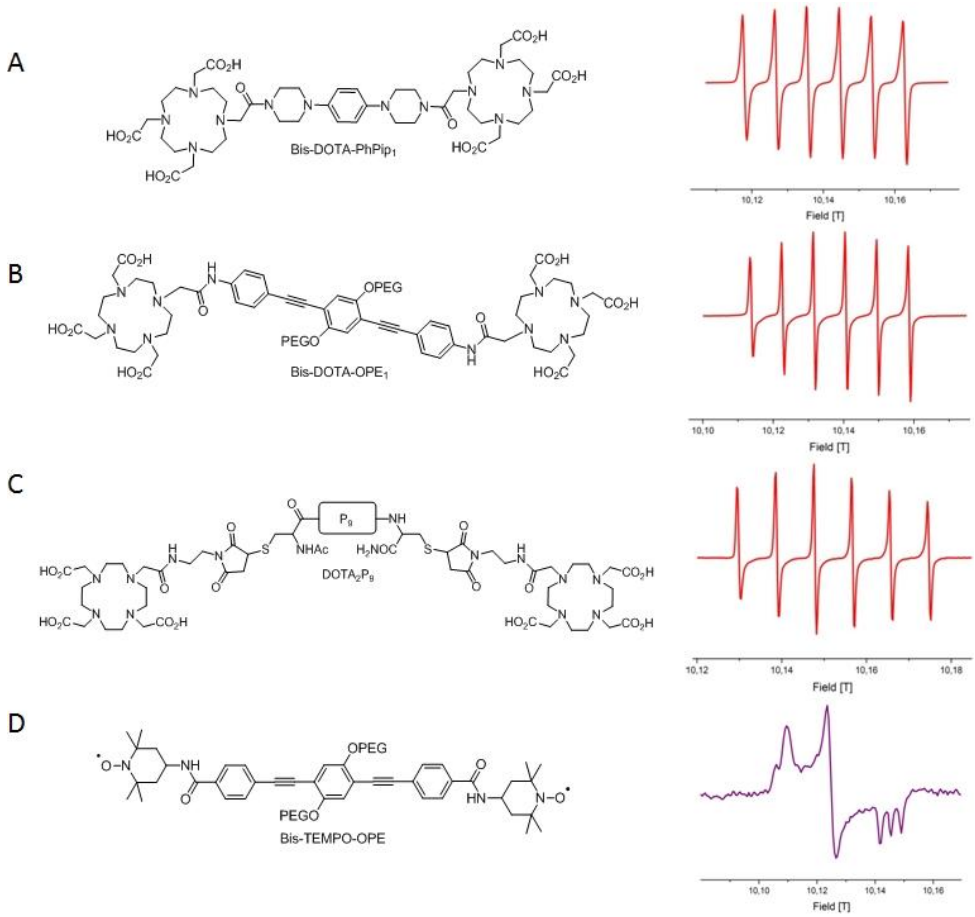

Figure 16 : Spectres RPE en bande J. A – Complexe de Mn^{II} de bis-DOTA-$PhPip_1$ (250 µM, 1,8 eq Mn^{II}, en tampon HEPES 50 mM pH 8 avec 10 % de glycérol, 23 K). B – Complexe de Mn^{II} de bis-DOTA-OPE_1 (250 µM, 1,8 eq Mn^{II}, en tampon HEPES 100 mM pH 8 avec 20 % de glycérol, 23 K). C – Complexe de Mn^{II} de $DOTA_2P_9$ (50 µM, 1,8 eq Mn^{II}, en tampon HEPES pH 8, 200 mM NaCl avec 10 % de glycérol, 23 K). D – Bis-TEMPO-OPE (200 µM, 9/1 MeOH/toluène, 20 K).

MESURE DE LA DISTANCE Mn^{II}-Mn^{II} PAR PELDOR EN BANDE W

Dans un premier temps, les plateformes $MnDOTA_2P_n$ ont été étudiées (Figure 17). Les paramètres d'ECN de Mn^{II}-DOTA ont également été déterminés (D = 280 MHz et E ≈ 0 MHz avec une distribution de 150 MHz pour les deux).[31]

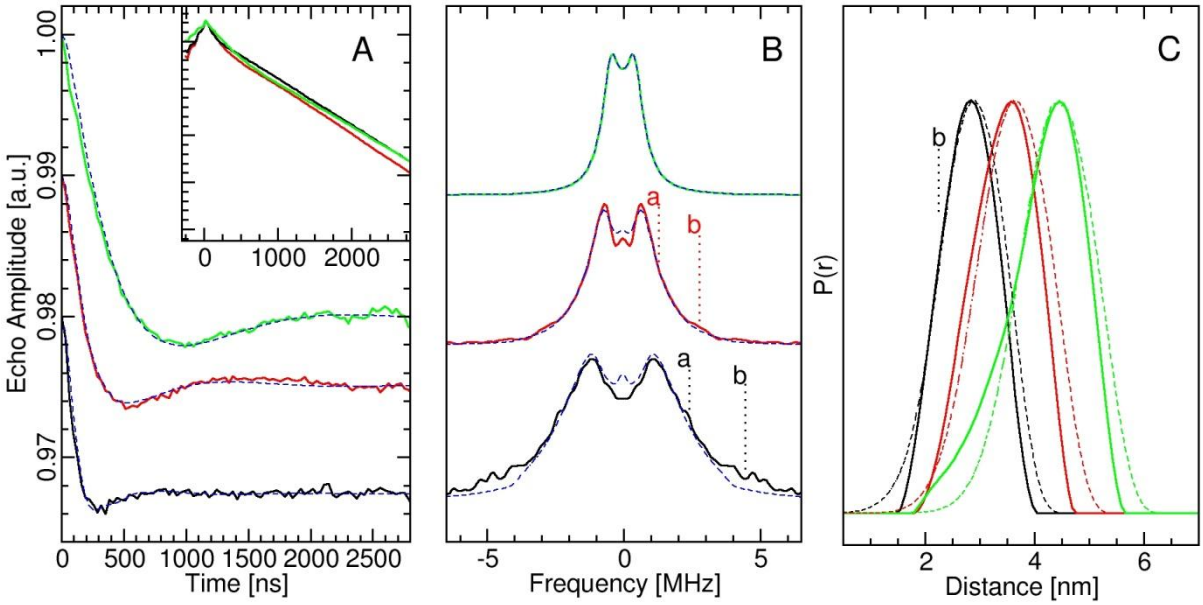

Figure 17 : Résultats PELDOR sur les systèmes $MnDOTA_2P_n$ (n = 6, vert ; n = 9, rouge ; n = 12, noir). A – Spectres d'évolution dipolaire corrigés par la contribution intermoléculaire et leur régularisation de Tikhonov (bleu pointillé). B – Leur transformée de Fourier et leur régularisation de Tikhonov (bleu pointillé). C – Distribution de distance obtenue par régularisation de Tikhonov (lignes pleines) et par modélisation moléculaire (lignes pointillées). Les lignes pointillées marquées a et b sont expliquées dans le texte. Conditions : 250 µM, 1,8 eq Mn^{II}, en tampon HEPES 100 mM pH 8 avec 200 mM NaCl et 10 % de glycérol, 10 K. La position d'inversion correspond au sommet de la 6ème ligne hyperfine et un *offset* de +50 MHz est utilisé.

La régularisation de Tikhonov rend très bien compte des spectres expérimentaux. Le maximum de la distribution de distance est de 2,8, 3,6 et 4,5 nm pour $MnDOTA_2P_n$ avec n = 6, 9 et 12, respectivement. La composante parallèle des doublets de Pake, indiquée par les lignes pointillées marquées a, est visible mais peu résolue. La profondeur de modulation varie entre 1,2 et 2%, ce qui représente un gain d'un facteur 4 par rapport à la littérature.[16] Cela confirme que l'utilisation de complexes de Mn^{II} avec de faibles paramètres d'ECN conduit à une amélioration de la sensibilité. La différence de fréquence entre la position d'inversion et la position de détection n'influe que très légèrement sur les résultats, tandis qu'une concentration de 100 µM et de courtes impulsions d'inversion (14 ns) paraissent optimales. L'augmentation de distance par résidu proline est d'environ 0,3 nm, en bon accord avec les résultats d'études cristallographiques dans la littérature.[32] Ceci indique que les systèmes $MnDOTA_2P_n$ adoptent une structure très majoritairement PPII dans les conditions étudiées. Ce résultat est confirmé par les spectres de dichroïsme circulaire de $MnDOTA_2P_n$, qui présentent la signature d'une hélice PPII,[33] dont la proportion en solution est estimée entre 85 et 92 %.

Les distributions de distance obtenues ont été comparées à des calculs de dynamique moléculaire (MD) (Figure 18).[34] Les résultats de DRX de la littérature (en noir) sont en bon accord avec la distance C_α^{Cys}-C_α^{Cys} obtenue par MD sur les séquences Cys-Pro_n-Cys (en rouge). De même, les distributions de distances obtenues par PELDOR (en bleu) correspondent assez bien aux profils obtenus par MD (en vert). Les deux DOTA-Mal ajoutent 0,8 nm à la distance C_α^{Cys}-C_α^{Cys} et augmentent fortement la largeur de la distribution de distance, ce qui reflète bien la flexibilité de l'espaceur maléimide.

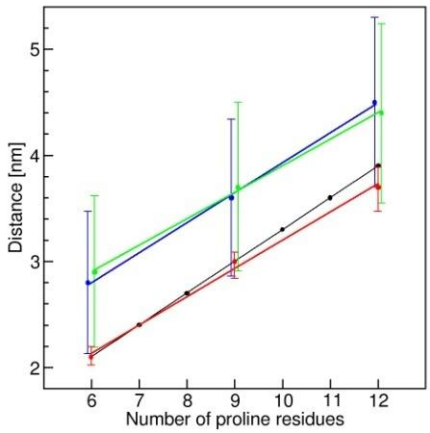

Figure 18 : Distances Mn^{II}-Mn^{II} et leur distribution, indiquant les résultats de DRX de la littérature (en noir), la modélisation moléculaire sur les séquences Cys-Pro_n-Cys (en rouge) et sur les systèmes $MnDOTA_2P_n$ (en vert), ainsi que les résultats obtenus par PELDOR (en bleu).

Cette flexibilité et celle de la structure PPII en elle-même expliquent également l'augmentation de la largeur de la distribution de distance avec la distance Mn-Mn, mais elles ne rendent pas compte des épaulements indiqués par les lignes pointillées marquées b sur la Figure 17, qui se traduisent par une composante plus petite dans la distribution de distance. La dépendance en champ de ces épaulements est représentée Figure 19 pour $MnDOTA_2P_6$.

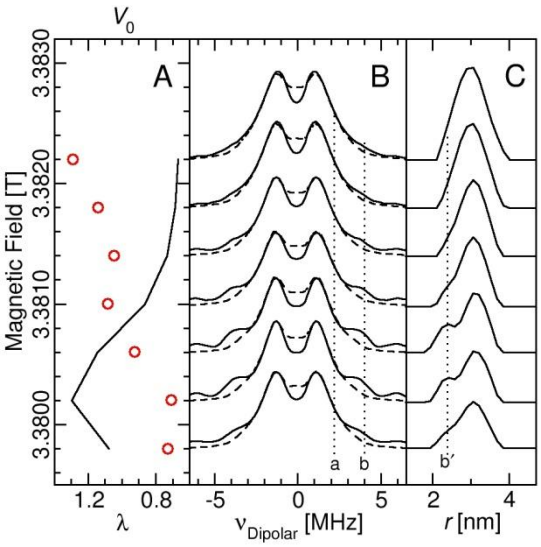

Figure 19 : Dépendance en champ des épaulements observés sur le spectre en fréquence de $MnDOTA_2P_6$. A – Amplitude de l'écho de spin à T = 0 (V_0, en noir) et profondeur de modulation (cercles rouges) pour certaines valeurs de B. B – Transformées de Fourier des spectres d'évolution dipolaire correspondants (lignes pleines) et leur régularisation de Tikhonov (lignes pointillées). C – Distributions de distance correspondantes obtenues par régularisation de Tikhonov. Les lignes pointillées marquées a, b et b' sont expliquées dans le texte. Les conditions sont identiques à celles de la Figure 17, sauf pour la position de l'impulsion d'inversion.

D'après cette figure, l'épaulement (marqué b') est minimal quand la position d'inversion correspond au sommet de la dernière ligne hyperfine, et maximal quand la position de détection correspond au sommet. Ces épaulements peuvent être rationalisés par la sélection de valeurs spécifiques d'ECN par l'impulsion d'inversion. Si les paramètres d'ECN du complexe de Mn^{II} étudié ne

sont pas distribués, l'impulsion d'inversion sélectionne uniquement certaines molécules avec une orientation spécifique par rapport à **B** (phénomène de sélection d'orientation). Dans le cas de Mn^{II}-DOTA, qui présente des paramètres d'ECN très distribués, l'interaction d'ECN ressentie par une molécule ne dépend pas de son orientation : l'impulsion d'inversion va plutôt sélectionner certaines valeurs d'ECN. La différence d'énergie entre les spins inversés et détectés est donc déterminée par leur interaction d'ECN spécifique : comme cette différence d'énergie peut être petite comparée au couplage dipolaire, le terme pseudo-séculaire ne peut pas être négligé. Dans les cas des systèmes $MnDOTA_2P_n$, les distributions de distances obtenues par PELDOR restent en bon accord avec les résultats de MD : cette interaction pseudo-séculaire est donc faible car certainement masquée par la flexibilité intrinsèque du système étudié, mais peut néanmoins conduire à des profils de distance déformés pour certaines positions d'inversion et de détection, ce qui indique que la régularisation de Tikhonov doit être effectuée avec prudence.

Pour explorer l'influence de cette interaction pseudo-séculaire sur des objets où elle devrait être plus visible, les complexes de Mn^{II} des plateformes rigides bis-DOTA-$PhPip_n$ (notés $MnDOTA_2PhPip_n$) ont été étudiés. La fréquence d'inversion est placée au sommet de la dernière ligne hyperfine tandis que la fréquence de détection est placée à une position variable quelques dizaines de gauss plus loin. L'influence de la concentration a également été analysée (Figure 20).

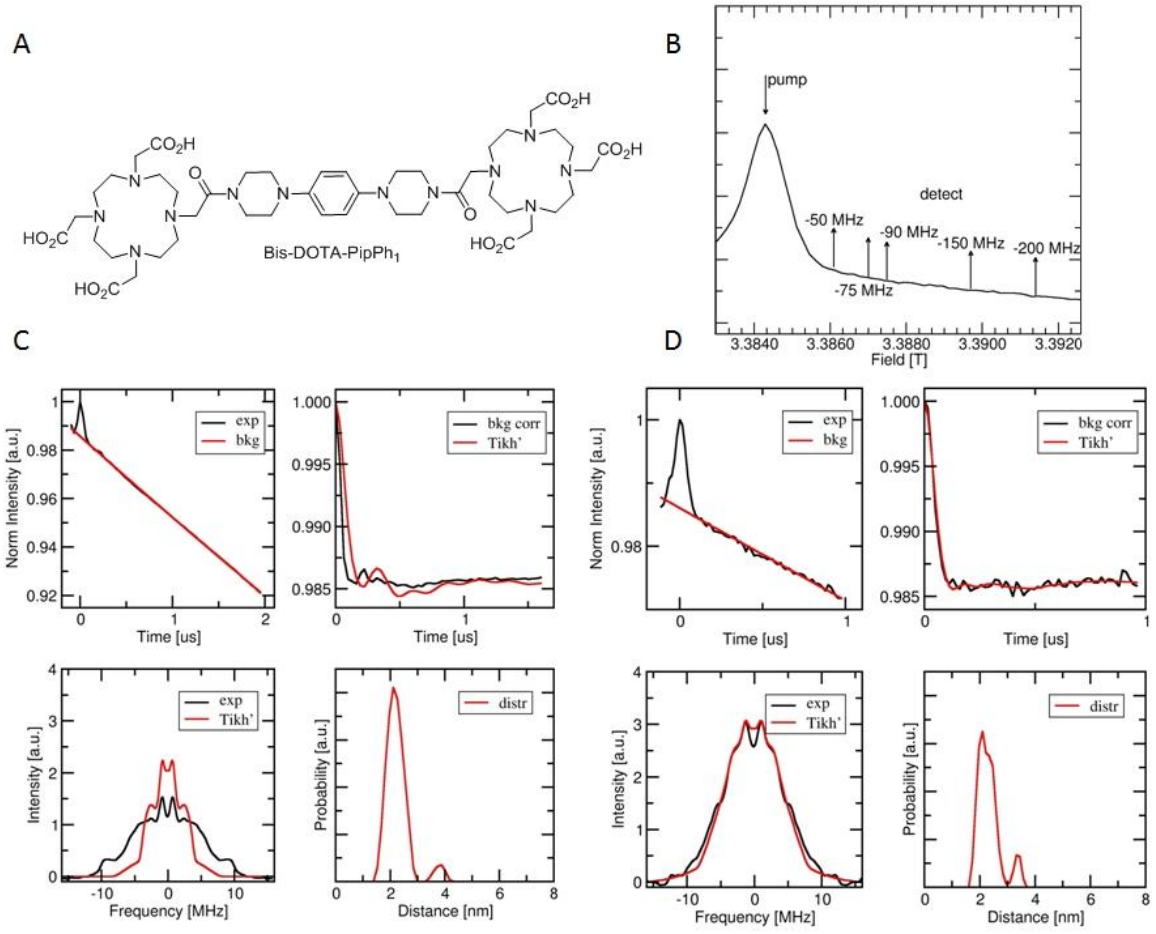

Figure 20 : Résultats de la méthode PELDOR sur $MnDOTA_2PipPh_1$. A – Structure du ligand bis-DOTA-$PipPh_1$. B – Agrandissement du spectre d'écho de $MnDOTA_2PipPh_1$, montrant la 6ème ligne hyperfine ainsi que la position

d'inversion (pump) et les positions de détection. C – Résultats de DeerAnalysis avec une concentration de 250 µM et un *offset* de -90 MHz. D – Résultats de DeerAnalysis avec une concentration de 50 µM et un *offset* de -50 MHz. Ces résultats ainsi que les suivants sont toujours présentés de cette façon : en haut à gauche, le spectre d'évolution dipolaire (en noir) et la contribution intermoléculaire (en rouge) ; en haut à droite, le spectre d'évolution dipolaire corrigé par la contribution intermoléculaire (en noir) et sa régularisation de Tikhonov (en rouge) ; en bas à gauche, la transformée de Fourier du spectre d'évolution dipolaire (en noir) et sa régularisation de Tikhonov (en rouge) ; et en bas à droite, la distribution de distance obtenue par régularisation de Tikhonov. Conditions : 1,8 eq Mn^{II}, en tampon HEPES 100 mM pH 8 avec 20 % de glycérol, 10 K.

Quelles que soient les conditions, le spectre d'évolution dipolaire est constitué d'une première modulation suivie d'une décroissance quasi-linéaire qui correspond à la contribution intermoléculaire. La profondeur de modulation est égale à 1,4 %, comparable aux systèmes $MnDOTA_2P_n$: un bon RSB peut être obtenu en quelques heures à des concentrations de 50 µM. Ici aussi, l'offset ne joue pas de rôle déterminant, et une concentration de 50 µM est préférable à 250 µM pour éviter la forte contribution intermoléculaire. Cependant, l'examen du spectre en fréquence révèle que celui-ci s'écarte fortement d'un doublet de Pake. La régularisation de Tikhonov ne parvient pas à rendre compte des spectres expérimentaux, ce qui se traduit également par une distribution de distance plus large que prévue pour un espaceur aussi rigide et des pics fantômes sans réalité physique. Ceci empêche l'interprétation fiable de la distance obtenue (2,1 nm). Afin de comparer cette valeur à la théorie, des expériences de MD avec le champ de force AMBER[35] (Assisted Model Building with Energy Refinement) ont été menées. Pour éviter certaines complications dues à l'état de protonation des acides carboxyliques et à l'incorporation d'un métal, les complexes Mn^{II}-DOTA ont été remplacés par des cyclens. Curieusement, le maximum de la distribution de distance Mn-Mn obtenue par MD (voir plus bas pour son extraction) vaut 2,07 nm, en bon accord avec la valeur expérimentale obtenue par PELDOR.

Ces problèmes pourraient être liés au fait que le sextuplet hyperfin de $MnDOTA_2PhPip_1$ est élargi par rapport à Mn^{II}-DOTA. Des expériences similaires ont donc été menées avec $MnDOTA_2PhPip_2$, plus long de quelques angströms, qui présente une finesse de raie égale à celle de Mn^{II}-DOTA. L'accord avec les spectres expérimentaux est meilleur, mais toujours loin d'être optimal (Figure 21). Le maximum de la distribution de distance, à 2,4 nm, est encore en accord avec la valeur obtenue sous MD en utilisant le même modèle simplifié (2,45 nm).

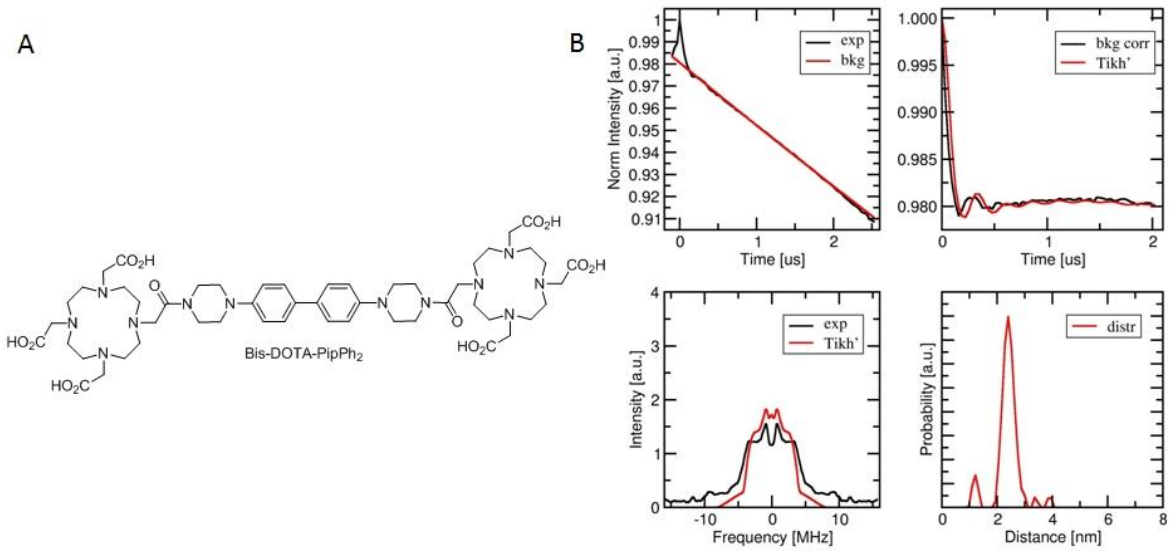

Figure 21 : A – Structure du ligand bis-DOTA-PipPh$_2$. B – Résultats de DeerAnalysis sur MnDOTA$_2$PhPip$_1$ (250 µM, 1,8 eq Mn^{II}, en tampon HEPES 100 mM pH 8 avec 20 % de glycérol, *offset* de -50 MHz, 10 K). La position d'inversion correspond au sommet de la 6ème ligne hyperfine.

Ces expériences montrent que pour de courtes distances, l'interaction pseudo-séculaire empêche l'interprétation fiable des résultats de PELDOR. Ceci s'explique par le fait que la régularisation de Tikhonov implémentée sous DeerAnalysis est optimisée pour un système constitué de deux centres paramagnétiques de spin 1/2 avec un couplage dipolaire faible, cas dans lequel le terme pseudo-séculaire est négligé. Pour réduire le couplage dipolaire, la distance entre les deux centres Mn^{II} peut être augmentée. L'étude des complexes de Mn^{II} de la série bis-DOTA-OPE$_n$ (notés MnDOTA$_2$OPE$_n$), pour laquelle la distance Mn-Mn est plus grande, a donc été entreprise. Les plateformes avec n = 2 et n = 3 n'ont pas pu être utilisées car très peu des complexes de Mn^{II} correspondants ont pu être détectés, ce qui serait peut-être lié à la formation d'agrégats. Les expériences PELDOR sur MnDOTA$_2$OPE$_1$ sont présentés Figure 22.

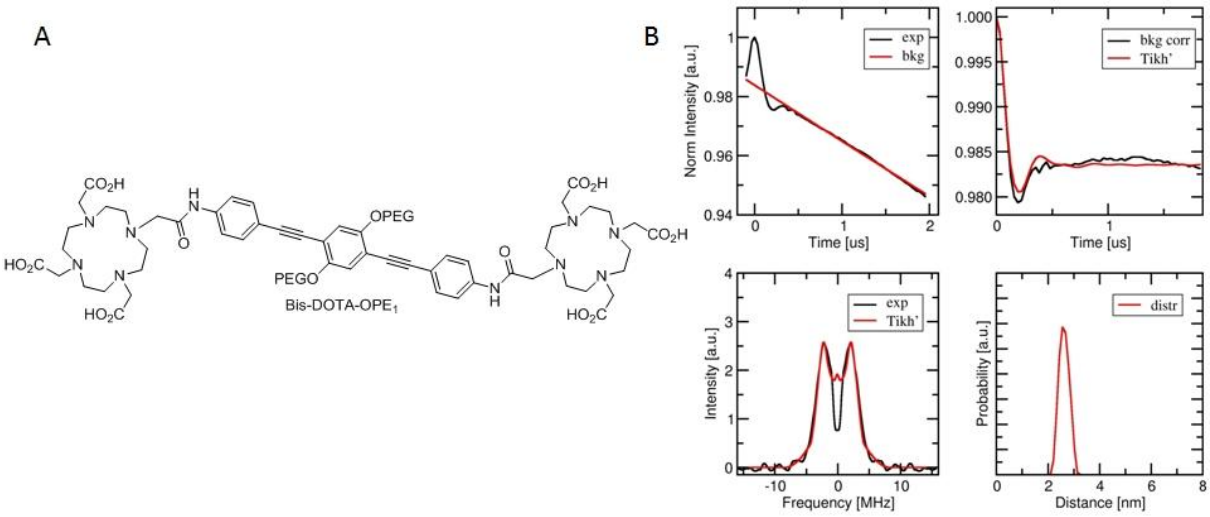

Figure 22 : A – Structure du ligand bis-DOTA-OPE_1. B – Résultats de DeerAnalysis sur $MnDOTA_2OPE_1$ (250 µM, 1,8 eq Mn^{II}, en tampon HEPES 100 mM pH 8 avec 20 % de glycérol, *offset* de +50 MHz, 10 K). La position d'inversion correspond au sommet de la 6ème ligne hyperfine.

Cette fois, la régularisation de Tikhonov rend très bien compte du spectre expérimental, qui a la forme attendue d'un doublet de Pake. La distribution de distance correspondante ne présente pas de pics fantômes, la profondeur de modulation (1.7 %) est comparable aux plateformes précédentes, mais la largeur de la distribution de distances (0,6 nm) est toujours plus importante qu'attendu considérant la rigidité des espaceurs OPE. Les résultats de MD sur le même modèle simplifié de $MnDOTA_2OPE_1$ sont présentés Figure 23.

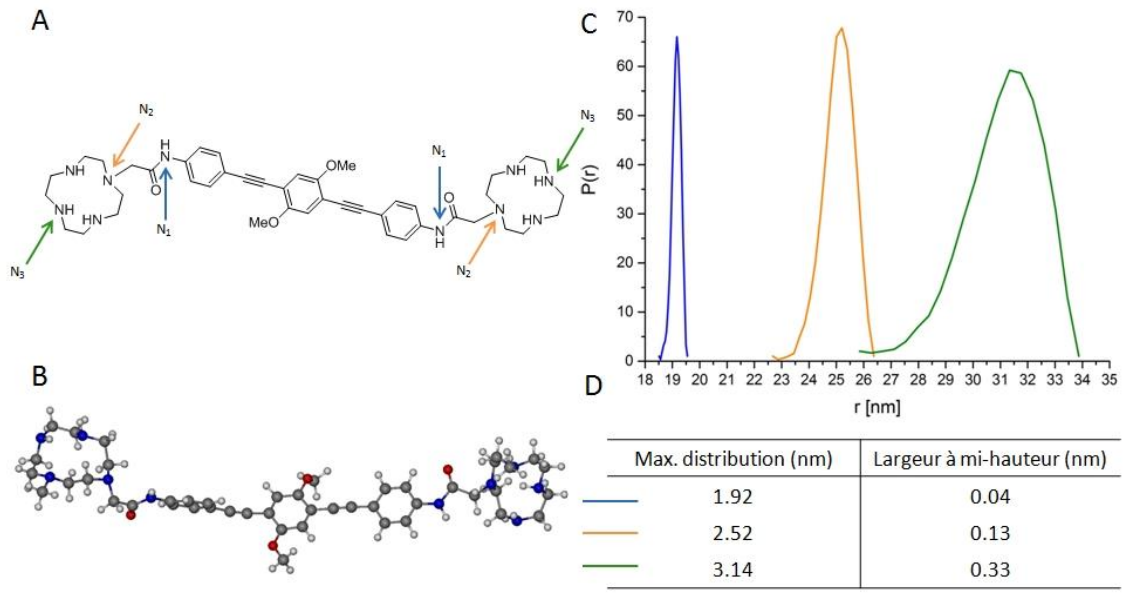

Figure 23 : A – Modèle simplifié de $MnDOTA_2OPE_1$. Les trois distances discutées sont notées N_1-N_1 (en bleu), N_2-N_2 (en orange) et N_3-N_3 (en vert). B – Structure d'un conformère parmi les 500 générés en 5 ns lors des calculs de MD. C – Distributions de distances obtenues par MD. D – Valeurs numériques de la distance moyenne et de la largeur à mi-hauteur pour chacune des trois distances considérées.

Comme attendu, l'espaceur OPE est très rigide (largeur à mi-hauteur de 0,4 nm pour la distance N_1-N_1). La moyennes des distributions de distances N_2-N_2 et N_3-N_3, entre 0,13 et 0,33 nm, est effectivement inférieure à la valeur obtenue par PELDOR (0,6 nm), et pour cette plateforme, la moyenne des maxima de ces deux distances, qui devrait représenter la distance Mn-Mn, est supérieure (2,83 nm) aux résultats de PELDOR (2,6 nm). Cela pourrait s'expliquer par la coordination du Mn^{II} à l'atome d'oxygène du groupement amide connectant le DOTA à l'espaceur OPE, rapprochant ainsi les deux DOTA de quelques angströms : comme des cyclens sont utilisé à la place des DOTAs lors des calculs de MD, il serait cohérent que la distance obtenue soit plus grande qu'en réalité. Il a toujours été supposé que Mn^{II}-DOTA est hexacoordiné, ce qui n'inclut pas de coordination au groupement amide, mais un nombre de coordination de 8 avait été suggéré au premier chapitre. Pour vérifier cette hypothèse, le complexe de Gd^{III} de bis-DOTA-OPE_1 ($GdDOTA_2OPE_1$) a été étudié. Comme DOTA coordonne Gd^{III} de manière octadente, la distance intermétallique devrait être identique entre $MnDOTA_2OPE_1$ et $GdDOTA_2OPE_1$. Les résultats sont présentés Figure 24.

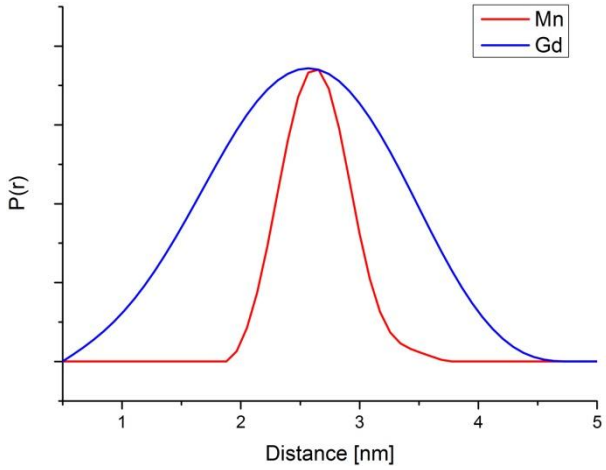

Figure 24 : Distribution de distances obtenues par régularisation de Tikhonov ($MnDOTA_2OPE_1$ en bleu, $GdDOTA_2OPE_1$ en rouge).

Les paramètres expérimentaux ont été gardés aussi proches que possible entre $MnDOTA_2OPE_1$ et $GdDOTA_2OPE_1$. Le maximum de la distribution est comparable dans les deux cas (différence de 0,3 Å en moyenne), ce qui semblerait confirmer l'hypothèse d'un Mn^{II}-DOTA octacoordiné. La largeur de la distribution est bien plus grande pour $GdDOTA_2OPE_1$: cette contribution plus importante de l'interaction pseudo-séculaire par rapport à $MnDOTA_2OPE_1$ reste à rationaliser.

Ces résultats ont été comparés avec le bis-TEMPO-OPE (Figure 25). Comme prévu, une forte sélection d'orientation est observée à cette fréquence, indiquée par la différence d'aspect entre les trois spectres d'évolution dipolaire et l'absence de la composante parallèle des doublets de Pake obtenus. Ceci empêche l'extraction directe de la distance entre les deux nitroxydes, ce qui prouve la supériorité des complexes métalliques à haut spin pour le PELDOR en bande W.

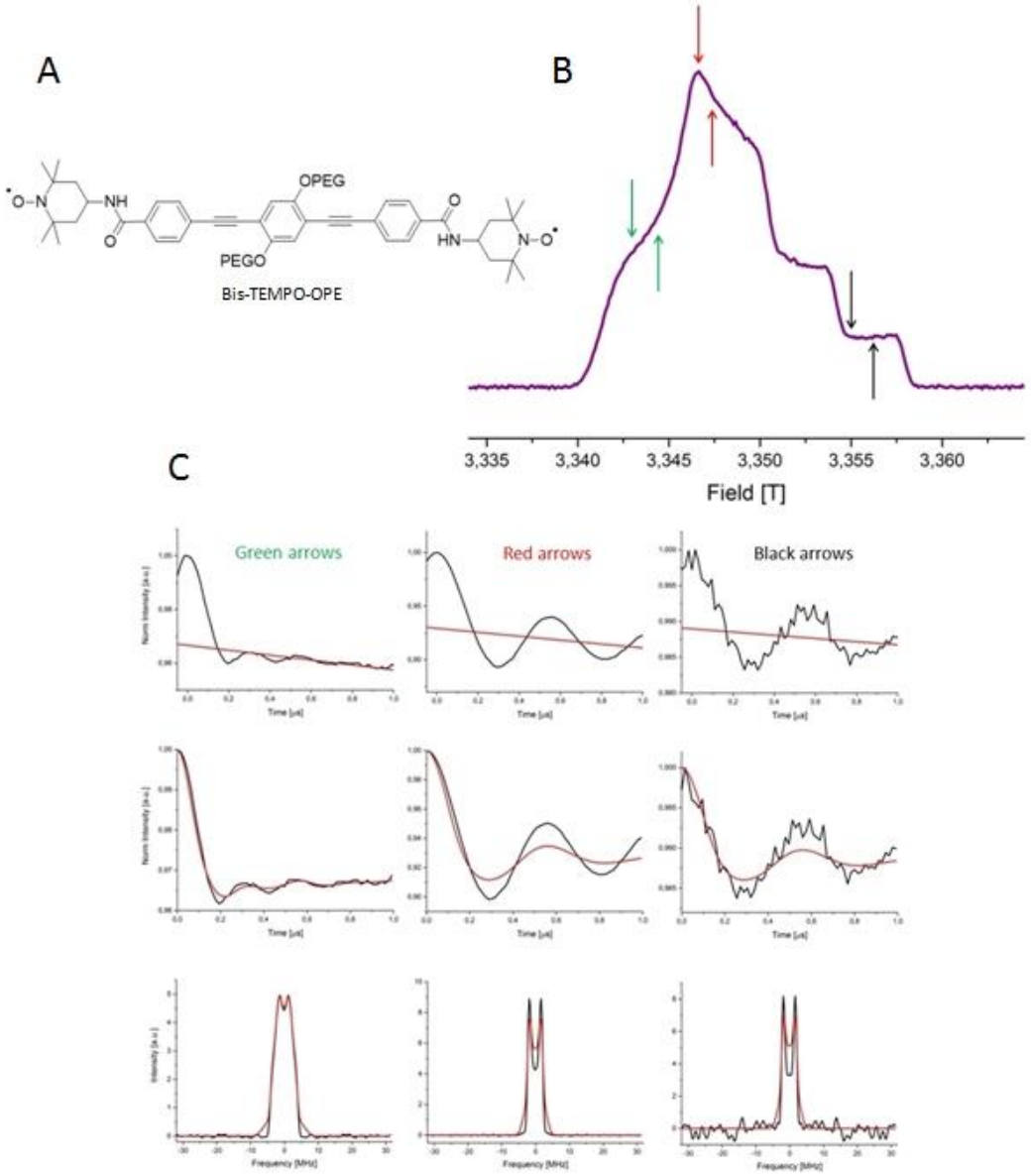

Figure 25 : A – Structure de bis-TEMPO-OPE. B – Son spectre d'écho (100 µM, $CHCl_3$/toluène 1/1, 40 K). Les positions d'inversion sont indiquées par des flèches pointant vers le bas, les positions de détection sont indiquées par des flèches pointant vers le haut. C – Résultats de DeerAnalysis pour les positions indiquées avec un *offset* de -70 MHz.

Pour résumer, l'interaction pseudo-séculaire se traduit différemment en fonction de la distance interspin et de la flexibilité du système :

- Jusqu'à 2,3 nm, la régularisation de Tikhonov ne rend pas compte des spectres expérimentaux. Des doublets de Pake très déformés sont observés, ce qui entraîne une distribution de distance élargie par rapport à la réalité, avec de nombreux pics fantômes. Si le maximum de cette distribution correspond bien à la distance théorique, l'interprétation des données n'est pas fiable.

- A partir de 2,4 nm, la régularisation de Tikhonov rend bien compte des spectres expérimentaux. Le maximum de la distribution de distance peut être interprété de manière fiable. Cette distribution est cependant élargie dans le cas d'un espaceur rigide, et des pics fantômes peuvent apparaître pour certaines positions spécifiques des séquences d'inversion et de détection.

- Quand la distance augmente, le couplage dipolaire diminue, et l'élargissement induit par le terme pseudo-séculaire devient de moins en moins important. A une certaine distance, cet effet est masqué par la flexibilité intrinsèque du système étudié.

ETUDE DE RADICAUX TRITYLS PERSISTANTS PAR RPE A HAUT CHAMP

Une autre alternative aux nitroxydes comme centres paramagnétiques pour la méthode PELDOR a émergé il y a trois ans : les radicaux trityls substitués de type TAM. Ces espèces sont stables et solubles en milieu aqueux lorsqu'elles comprennent des groupements carboxylate en position *para*, ce qui est le cas du Finland Trityl (FT) et du radical OX63.[36] Les radicaux PTM, substitués par des atomes de chlore au lieu de cycles dithiolane, sont également très stables et solubles en milieu aqueux comme le PTM-TC (PTM-tricarboxylate) (Figure 26).[37] Le spectre RPE en bande X de ces composés n'est constitué que d'une seule ligne, car aucun couplage hyperfin n'est possible grâce à la substitution sur l'ensemble de la structure. Les atomes de chlore et de soufre ayant un rapport gyromagnétique faible, cette ligne est étroite (111 mG pour une solution aqueuse de FT et 540 mG pour une solution de PTMTE (PTM-triéthylester) dans le DMSO) (Figure 26).

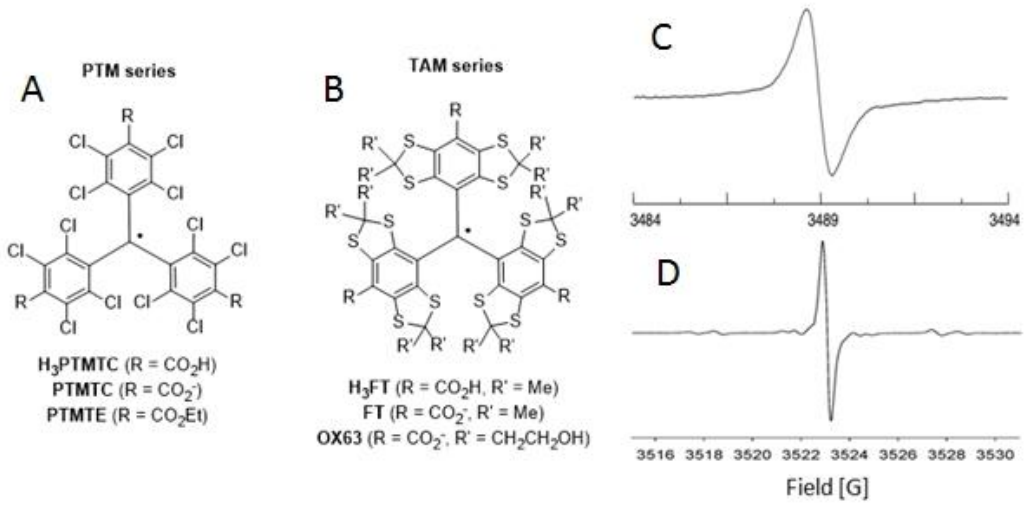

Figure 26 : Structures des principaux représentants de la série PTM (A) et TAM (B), et spectres RPE en bande X d'une solution aqueuse de FT (C) et d'une solution de PTMTE dans le DMSO (D).

Ce signal RPE constitué d'une seule raie fine explique l'intérêt des dérivés TAM et PTM dans de nombreux domaines car il permet leur détection à de très faibles concentrations. Ces espèces sont en effet de très bonnes sondes de l'ion superoxyde (la raie RPE diminue progressivement avec la formation d'un adduit diamagnétique),[38] de l'oxygène (la largeur de raie augmente avec la pression

partielle en O_2)[39] et du pH (reflété par une variation du tenseur *g*) *in vivo*.[40] Ces radicaux sont également d'excellents agents hyperpolarisants, ce qui explique leur succès comme agents DNP (Dynamic Nuclear Polarization),[41] et ont trouvé de nombreuses applications dans l'imagerie par RPE à haute résolution.[20] Cette finesse de raie est aussi la principale raison de leur succès en PELDOR, initié il y a trois ans, car elle permet d'obtenir une profondeur de modulation très élevée.[42] Les radicaux PTMTE et H_3PTMTC ont donc été synthétisés (Figure 27), et le radical FT a été fourni par une source extérieure. Le couplage de ces radicaux à des espaceurs rigides afin d'obtenir des plateformes trityl-DOTA est en cours. De tels systèmes seraient très intéressants : combiner l'étroitesse du signal du trityl avec celui du Mn^{II}-DOTA serait susceptible d'améliorer grandement la sensibilité de la méthode PELDOR.

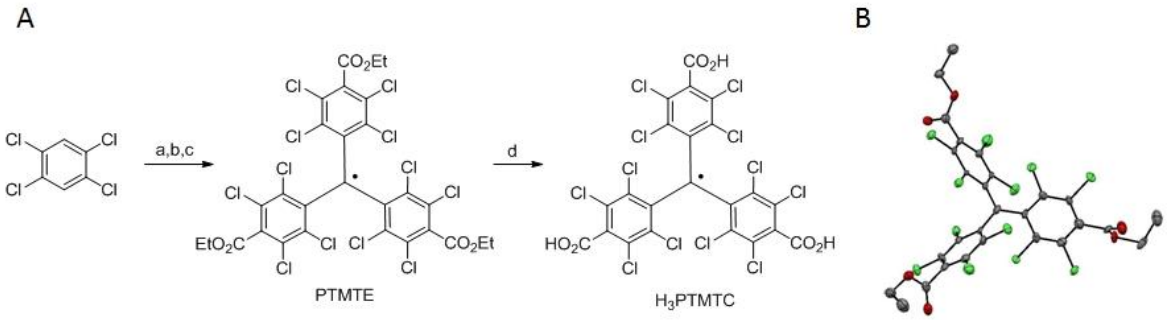

Figure 27 : A – Synthèse des radicaux PTMTE et H_3PTMTC. Conditions : a) $CHCl_3$, $AlCl_3$, tube scellé, 160 °C, 45 min, 37 % b) *n*-BuLi, TMEDA, THF, -78 °C, 2 h, puis Cl(CO)OEt, THF, -78 °C jusqu'à T_{amb}, 15 h, 66 % c) NaOH, DMSO/Et_2O, T_{amb}, 24 h, puis I_2, Et_2O, T_{amb}, 24 h, 82 % d) KOH, MeOH, reflux, 48 h, 85 %. B – Structure cristallographique de PTMTE.

Pour mesurer précisément les tenseurs *g* des radicaux PTM et TAM étudiés, la RPE en bande J est un très bon choix car la résolution de ces tenseurs est maximisée. L'emploi de Mn^{II} comme référence (g = 2,00101 ± 0,00005) procure six points pour estimer l'erreur sur la mesure. La conception du spectromètre utilisé permet d'introduire l'échantillon d'intérêt avec la solution de Mn^{II} dans deux tubes coaxiaux (Figure 28), et assure une incertitude très faible (0,9 G soit 0,00008 en valeur de *g*). Par contre, comme les raies hyperfines de Mn^{II} sont superposées au signal des radicaux trityls, l'emploi d'une deuxième référence est souhaitable. Un spectre de référence a donc été enregistré, qui correspond à un échantillon dans lequel ont été introduits une solution de Mn^{II} et une solution de Gd^{III}. Ceci permet de mesurer très précisément le facteur *g* de Gd^{III} (g = 1,99128), dont le signal est loin de celui des radicaux trityls. En remplaçant la solution de Mn^{II} par le radical étudié et en alignant le spectre obtenu sur le signal de Gd^{III} (Figure 28), les tenseurs *g* de cinq dérivés PTM et TAM ont pu être précisément mesurés.

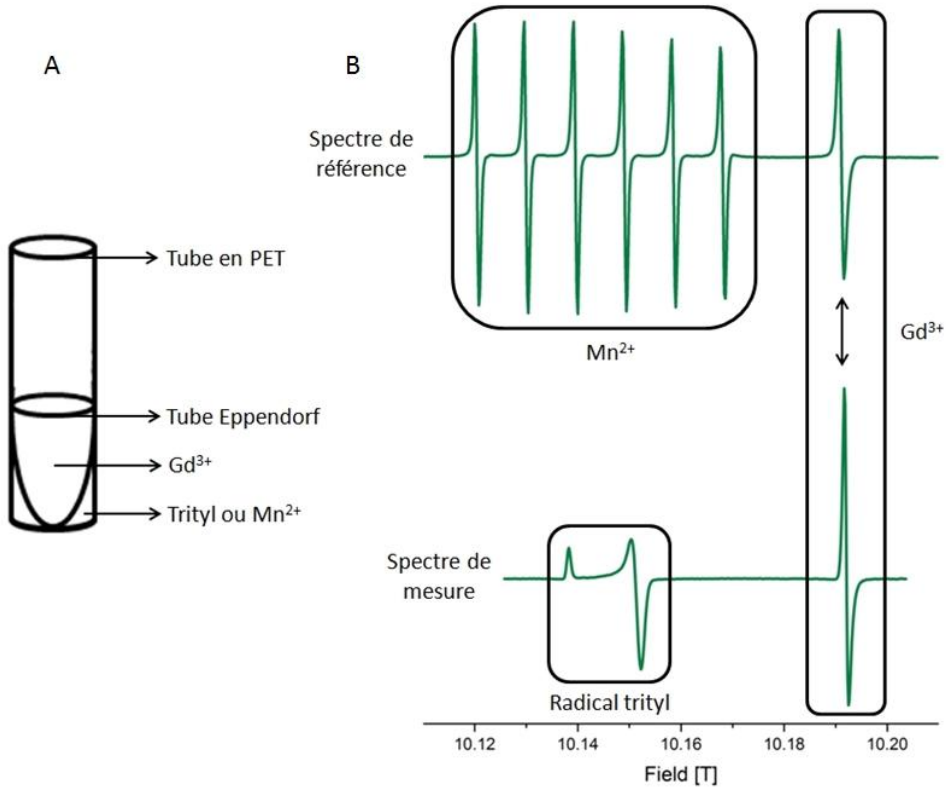

Figure 28 : A – Schéma du dispositif expérimental utilisé. B – Procédé pour mesurer précisément les tenseurs *g* des radicaux trityl étudiés en alignant un spectre de mesure sur le spectre de référence.

Les spectres expérimentaux sont consignés Figure 29 (en noir). L'anisotropie de *g* est clairement résolue pour chaque spectre : à cette fréquence, le signal des radicaux trityls étudiés ne peut plus être considéré comme unique et fin, ce qui illustre bien la différence avec les spectres présentés Figure 26. Chaque spectre a également été simulé (en rouge) avec un modèle supposant une distribution gaussienne des valeurs de *g*, ce qui rend très bien compte des résultats expérimentaux sauf dans le cas de FT. Les tenseurs *g* ont également été extraits des calculs DFT : l'accord avec les spectres expérimentaux n'est pas parfait (en bleu), mais le décalage de g_x vers les champs plus faibles, indiqué par les lignes pointillées noires, est bien reproduit.

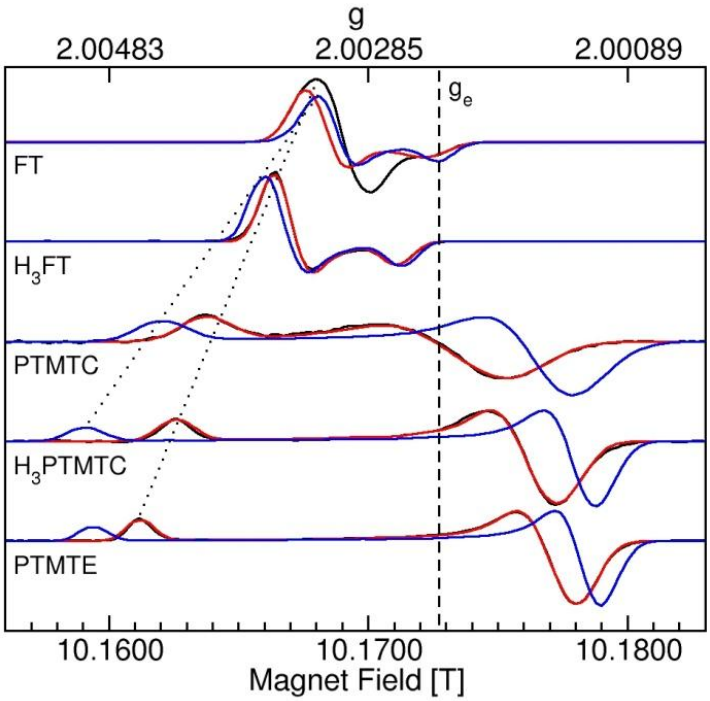

Figure 29 : Spectres RPE calibrés en bande J de FT, H_3FT, PTMTC, H_3PTMTC et PTMTE. Les spectres expérimentaux sont en noir, les spectres simulés sont en rouge et les spectres calculés par DFT sont en bleu. Conditions : 1 mM dans le 2-Me-THF (pour H_3FT, H_3PTMTC et PTMTE) ou dans H_2O avec 10 % de glycérol (pour FT et PTMTC). Température : 15 K sauf pour PTMTC (100 K). Les lignes pointillées noires sont expliquées dans le texte. g_e est le facteur *g* de l'électron libre (g_e = 2,00232).

Pour les radicaux TAM, les valeurs de g_y sont proches des valeurs de g_x, et la valeur de g_e est au-dessus du tenseur *g*. Pour les radicaux PTM, les valeurs de g_y sont proches des valeurs de g_z, et la valeur de g_e est à cheval sur le tenseur *g*. Les radicaux TAM sont moins anisotropes que les radicaux PTM, en accord avec la littérature. Les valeurs de g_x augmentent également avec la protonation, quel que soit le radical étudié, ce qui suggère que l'anisotropie de *g* est sensible à la nature des groupements en position *para*, même pour un très faible changement. Malgré leur structure similaire, les radicaux PTM et TAM sont donc des propriétés électroniques très différentes.

Pour rationaliser ces observations, les orbitales HOMO (Highest Occupied Molecular Orbital) ont été analysées (Figure 30). Pour les radicaux PTM, une alternance classique d'orbitales liantes et antiliantes peut être observée. La situation est plus complexe pour les TAM, où une densité sur les atomes de soufre est notable, contrairement aux atomes de chlore dans le cas des PTMs. Ces résultats suggèrent que les TAMs ne se comportent pas comme des radicaux π classiques, à la différence des PTMs. Des analyses plus détaillées des calculs DFT sont en cours.

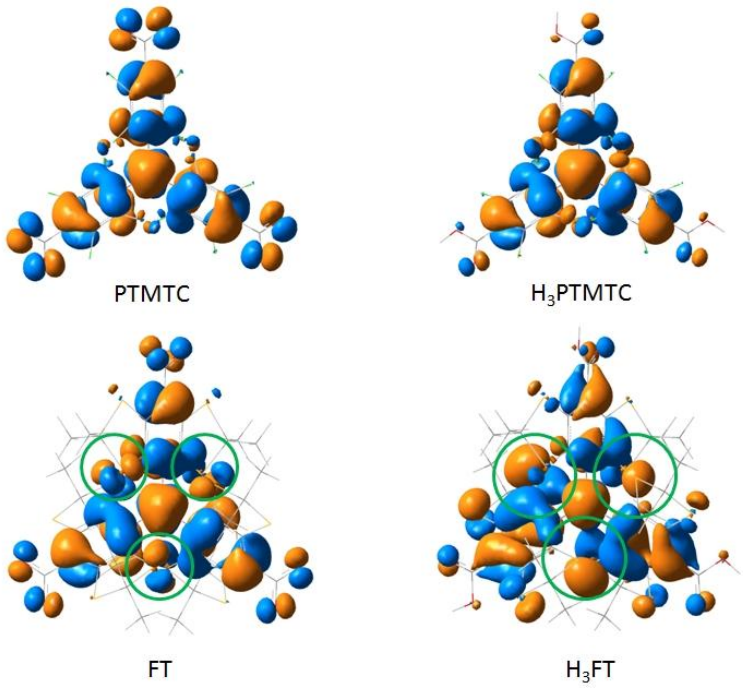

Figure 30 : Orbitales HOMO des radicaux trityls étudiés. La densité sur les atomes de soufre dans le cas de FT et de H_3FT est indiquée par des cercles verts.

CONCLUSION ET PERSPECTIVES

Au cours de ce travail, des plateformes imposant une distance fixée entre deux centres Mn^{II} ont été synthétisées. Trois espaceurs différents ont été utilisés pour couvrir la gamme 2,1 – 4,5 nm. Le ligand DOTA s'est révélé être le meilleur choix pour la coordination du Mn^{II}, car les complexes obtenus présentent un signal RPE très fin. La méthode PELDOR a été appliquée à ces systèmes et la distance Mn-Mn a pu être extraite de manière fiable et précise du moment que la distance n'est pas trop courte (en-dessous de 2,5 nm). Une bonne sensibilité a pu être obtenue, confirmant l'intérêt des complexes de Mn^{II} avec une faible valeur d'éclatement en champ nul *D* comme centre paramagnétique pour la méthode PELDOR à haut champ. Les rôles du terme pseudo-séculaire de l'Hamiltonien dipolaire ainsi que des paramètres d'ECN ont été analysés et leur influence sur la distribution de la distance obtenue a été discutée et mise en relief avec la flexibilité du système étudié. Plusieurs expériences suggèrent que Mn^{II}-DOTA pourrait être octacoordiné et non hexacoordiné en solution. En parallèle, les radicaux trityls stables de type PTM et TAM ont été étudiés par RPE à haut champ. Ce travail a permis de développer l'utilisation des complexes de Mn^{II} à haut spin pour mesurer des distances nanométriques par PELDOR à haut champ, ce qui avait été très peu exploité jusqu'alors.

Ces résultats ouvrent la voie à des applications biologiques, où des complexes Mn^{II}-DOTA ou des radicaux trityls seraient greffés sur des protéines contenant un centre Mn^{II} natif, ce qui permettrait d'extraire la distance entre ces centres paramagnétiques avec une excellente sensibilité.

RÉFÉRENCES

(1) Kendrew, J. C.; Bodo, G.; Dintzis, H. M.; Parrish, R. G.; Wyckoff, H.; Phillips, D. C. *Nature* **1958**, *181* (4610), 662–666.
(2) Wüthrich, K. *Nat. Struct. Biol.* **2001**, *8* (11), 923–925.
(3) Schiemann, O.; Prisner, T. F. *Q. Rev. Biophys.* **2007**, *40* (1), 1–53.
(4) Jeschke, G. *ChemPhysChem* **2002**, *3* (11), 927–932.
(5) Bertrand, P. La Spectroscopie de Résonance Paramagnétique Electronique - Fondements, **2010**, EDP Sciences, 1–124.
(6) Klare, J. P.; Steinhoff, H. J. *Photosynth. Res.* **2009**, *102* (2), 377–390.
(7) Endeward, B.; Butterwick, J. A.; MacKinnon, R.; Prisner, T. F. *J. Am. Chem. Soc.* **2009**, *131* (42), 15246–15250.
(8) Schiemann, O.; Piton, N.; Plackmeyer, J.; Bode, B. E.; Prisner, T. F.; Engels, J. W. *Nat. Protoc.* **2007**, *2* (4), 904–923.
(9) Jeschke, G.; Godt, A. *ChemPhysChem* **2003**, *4* (12), 1328–1334.
(10) Pievo, R.; Casati, C.; Franchi, P.; Mezzina, E.; Bennati, M.; Lucarini, M. *ChemPhysChem* **2012**, *13* (11), 2659–2661.
(11) Godt, A.; Schulte, M.; Zimmermann, H.; Jeschke, G. *Angew. Chem. Int. Ed.* **2006**, *45* (45), 7560–7564.
(12) Jeschke, G.; Chechik, V.; Ionita, P.; Godt, A.; Zimmermann, H.; Banham, J.; Timmel, C. R.; Hilger, D.; Jung, H. *Appl. Magn. Reson.* **2006**, *30*, 473–498.
(13) Tsvetkov, Y. D. *J. Struct. Chem.* **2013**, *54*, 42–72.
(14) Goldfarb, D. *Phys. Chem. Chem. Phys.* **2014**, *16* (21), 9685–9699.
(15) Raitsimring, A. M.; Gunanathan, C.; Potapov, A.; Efremenko, I.; Martin, J. M. L.; Milstein, D.; Goldfarb, D. *J. Am. Chem. Soc.* **2007**, *129* (46), 14138–14139.
(16) Banerjee, D.; Yagi, H.; Huber, T.; Otting, G.; Goldfarb, D. *J. Phys. Chem. Lett.* **2012**, *3*, 157−160.
(17) Bock, C. W.; Katz, A. K.; Markham, G. D.; Glusker, J. P. *J. Am. Chem. Soc.* **1999**, *121* (32), 7360–7372.
(18) Dang, V.; Wang, J.; Feng, S.; Buron, C.; Villamena, F. A.; Wang, P. G.; Kuppusamy, P. *Bioorganic Med. Chem. Lett.* **2007**, *17* (14), 4062–4065.
(19) Xia, S.; Villamena, F. A.; Hadad, C. M.; Kuppusamy, P.; Li, Y.; Zhu, H.; Zweier, J. L. *J. Org. Chem.* **2006**, *71* (19), 7268–7279.
(20) Kuppusamy, P.; Wang, P.; Chzhan, M.; Zweier, J. L. *Magn. Reson. Med.* **1997**, *37* (4), 479–483.
(21) Bobko, A. A.; Dhimitruka, I.; Zweier, J. L.; Khramtsov, V. V. *J. Am. Chem. Soc.* **2007**, *129* (23), 7240–7241.
(22) Edwards, D. A.; Mahon, M. F.; Martin, W. R.; Molloy, K. C.; Fanwick, P. E.; Walton, R. A. *J. Chem. Soc. Dalton Trans.* **1990**, 3161–3168.
(23) Osorio, E. A.; Moth-Poulsen, K.; Van Der Zant, H. S. J.; Paaske, J.; Hedegård, P.; Flensberg, K.; Bendix, J.; Bjørnholm, T. *Nano Lett.* **2010**, *10* (1), 105–110.
(24) Bonnet, C. S.; Buron, F.; Caillé, F.; Shade, C. M.; Drahoš, B.; Pellegatti, L.; Zhang, J.; Villette, S.; Helm, L.; Pichon, C.; Suzenet, F.; Petoud, S.; Tóth, É. *Chem. Eur. J.* **2012**, *18* (5), 1419–1431.
(25) Siaugue, J.-M.; Segat-Dioury, F.; Favre-Réguillon, A.; Madic, C.; Foos, J.; Guy, A. *Tet. Lett.* **2000**, *41* (39), 7443–7446.
(26) Stetter, H., Frank, W. *Angew. Chem* **1976**, *15* (11), 686.
(27) Wang, S.; Westmoreland, T. D. *Inorg. Chem.* **2009**, *48* (2), 719–727.
(28) Tour, J. M. *Chem. Rev.* **1996**, *96* (1), 537–554.
(29) Jamous, M.; Haberkorn, U.; Mier, W. *Tetrahedron Lett.* **2012**, *53* (50), 6810–6814.
(30) Kakinoki, S.; Hirano, Y.; Oka, M. *Polym. Bull.* **2005**, *53* (2), 109–115.
(31) Ching, H. Y. V.; Demay-Drouhard, P.; Bertrand, H. C.; Policar, C.; Tabares, L. C.; Un, S. *Phys. Chem. Chem. Phys.* **2015**, *17*, 23368–23377.

(32) Wilhelm, P.; Lewandowski, B.; Trapp, N.; Wennemers, H. *J. Am. Chem. Soc.* **2014**, 136, 15829–15832.
(33) Rucker, A. L.; Creamer, T. P. *Protein Sci.* **2002**, *11* (4), 980–985.
(34) Hagelueken, G.; Abdullin, D.; Ward, R.; Schiemann, O. *Mol. Phys.* **2013**, *111* (18-19), 2757–2766.
(35) Wang, J. M.; Wolf, R. M.; Caldwell, J. W.; Kollman, P. A.; Case, D. A. *J. Comput. Chem.* **2004**, *25* (9), 1157–1174.
(36) Reddy, T. J.; Iwama, T.; Halpern, H. J.; Rawal, V. H. *J. Org. Chem.* **2002**, *67* (14), 4635–4639.
(37) Datcu, A.; Roques, N.; Jubera, V.; Imaz, I.; Maspoch, D.; Sutter, J. P.; Rovira, C.; Veciana, J. *Chem. Eur. J.* **2011**, *17* (13), 3644–3656.
(38) Rizzi, C.; Samouilov, A.; Kumar Kutala, V.; Parinandi, N. L.; Zweier, J. L.; Kuppusamy, P. *Free Radic. Biol. Med.* **2003**, *35* (12), 1608–1618.
(39) Bratasz, A.; Kulkarni, A. C.; Kuppusamy, P. *Biophys. J.* **2007**, *92* (8), 2918–2925.
(40) Liu, Y.; Villamena, F. A.; Sun, J.; Wang, T. Y.; Zweier, J. L. *Free Radic. Biol. Med.* **2009**, *46* (7), 876–883.
(41) Gabellieri, C.; Mugnaini, V.; Paniagua, J. C.; Roques, N.; Oliveros, M.; Feliz, M.; Veciana, J.; Pons, M. *Angew. Chem. Int. Ed.* **2010**, *49* (19), 3360–3362.
(42) Yang, Z.; Liu, Y.; Borbat, P.; Zweier, J. L.; Freed, J. H.; Hubbell, W. L. *J. Am. Chem. Soc.* **2012**, *134* (24), 9950–9952.

Abstract

In this work, the synthesis of a set of platforms that incorporate a central linker of varying length connected to two high-spin Mn^{II} complexes has been performed. Several ligands were screened and efficient synthetic methodologies were developed to graft them on various spacers covering the 1.5 – 5.5 nm range. These systems were designed to serve as « standards » on which the Mn-Mn distance has been successfully measured using high-field pulsed electron paramagnetic resonance (EPR) spectroscopy, more precisely pulsed electron-electron double resonance (PELDOR). We showed that the use of Mn^{II} complexes with low zero-field splitting (ZFS) parameters led to an improved sensitivity. For flexible polyproline-based platforms, distances and distribution profiles obtained with PELDOR were in good agreement with molecular dynamics (MD) estimations, but additional features in the distance distributions could be observed under specific conditions. These finding were rationalized by taking into account the pseudo-secular term of the dipolar Hamiltonian, which was found to be non-negligible for the studied platforms, where pumped and detected spins are very similar. When the linker was rigid, the influence of the pseudo-secular interaction was much more prominent, leading to distance profiles with a higher width than predicted by MD calculations. Other emergent spin labels for pulsed EPR-based distance measurements such as persistent substituted trityl radicals were studied and their *g*-tensor was accurately measured using high-field EPR with Mn^{II} as an internal reference. Density functional theory (DFT) calculations were performed to better understand the relationship between the structure and the EPR properties of the studied trityl radicals.

Keywords: Manganese, EPR, PELDOR, molecular rod, OPE, trityl, nanometric distance measurement

Résumé

Au cours de ce travail, une série de plateformes constituées d'un espaceur central connecté à deux complexes de Mn^{II} à haut spin a été synthétisée. De nombreux ligands ont été étudiés et greffés sur un ensemble d'espaceurs de longueur variant entre 1,5 et 5,5 nm. La distance Mn-Mn a été mesurée avec succès par résonance paramagnétique électronique (RPE) impulsionnelle à haut champ en utilisant la méthode PELDOR (Pulsed Electron-Electron Double Resonance). L'emploi de complexes de Mn^{II} avec de faibles valeurs d'éclatement en champ nul (ECN) a permis d'améliorer la sensibilité de cette méthode. Pour les plateformes constituées d'un espaceur polyproline, un bon accord a été observé entre la distribution de la distance Mn-Mn obtenue par PELDOR et par dynamique moléculaire, mais des composantes plus courtes dans la distribution ont été détectées pour certains paramètres expérimentaux. Ces observations ont été rationalisées en prenant en compte le terme pseudo-séculaire de l'Hamiltonien dipolaire, non négligeable pour les systèmes étudiés où les spins observés et détectés sont similaires. Lorsqu'un espaceur rigide est employé, l'interaction pseudo-séculaire est nettement plus marquée, ce qui se traduit par une distribution de distances plus large que prévu par la dynamique moléculaire. L'étude de nouveaux centres paramagnétiques pour la méthode PELDOR comme les radicaux trityl persistants a également été entreprise. Le tenseur *g* de ces radicaux a été déterminé avec précision par RPE à haut champ en utilisant Mn^{II} comme référence interne. Des calculs de DFT (Density Functional Theory) ont été effectués pour mieux comprendre la relation entre la structure et le spectre RPE de ces radicaux trityl.

Mots-clef : Manganèse, RPE, PELDOR, espaceur moléculaire, OPE, trityl, mesure de distances nanométriques